# studies in surface science and catalysis
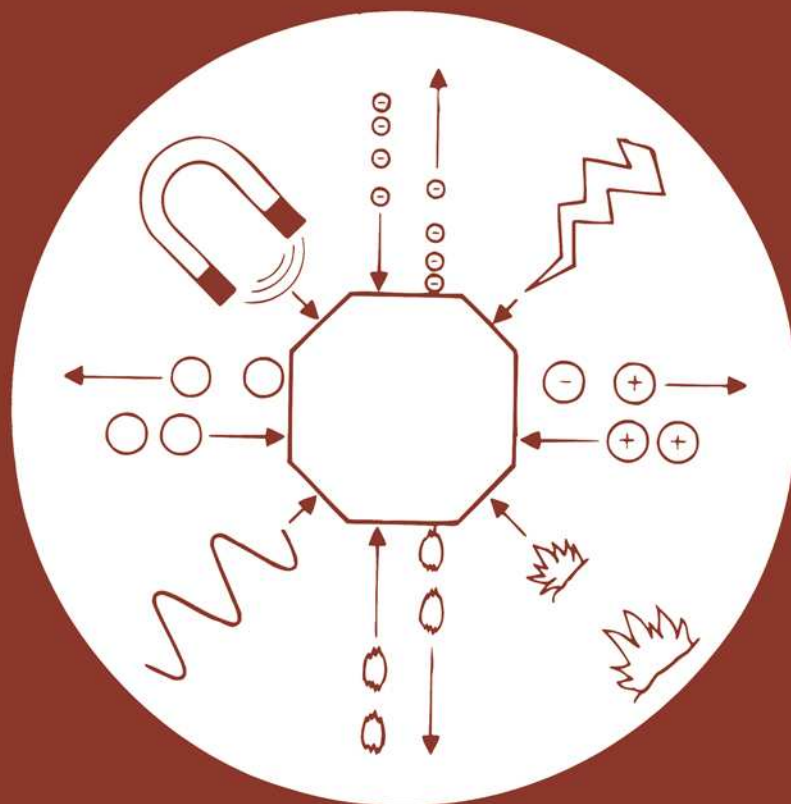


# 138

# SPILLOVER AND MOBILITY
# OF SPECIES ON SOLID SURFACES

## A. Guerrero-Ruiz
## I. Rodríguez-Ramos
### (editors)

elsevier

# SPILLOVER AND MOBILITY OF SPECIES ON SOLID SURFACES

Edited by

**A. Guerrero-Ruiz**
*Dpt. De Química Inorgánica y Técnica, Facultad de Ciencias, UNED,
C/Senda del Rey, s/n. 28040 Madrid, Spain*

**I. Rodríguez-Ramos**
*Instituto de Catálisis y Petroleoquímica, CSIC, Campus de Cantoblanco,
28049 Madrid, Spain*

⊖ The paper used in this publication meets the requirements of ANSI/NISO Z39.48-1992 (Permanence of Paper).
Printed in The Netherlands.

# PREFACE

This volume collects the papers which were presented at the Fifth International Conference on Spillover, either as oral or posters contributions, as well as the summaries of the invited lectures. This congress and its publication in the Studies on Surface Science and Catalysis series follow the tradition of previous conferences on spillover, initiated in Lyon, 1983, and continued in Leipzig, 1989, Kyoto, 1993 and Dalian, 1997. For the present fifth conference, held in S.L. el Escorial (Madrid), the organising committee has attempted to compile representative contributions which illustrate the advances in understanding of the spillover phenomenon since 1997. Spillover is a process taking place during the interaction of gas reactant molecules (mainly hydrogen and oxygen) on solid surfaces. However, different contributions to the more general area of the chemistry at surfaces, related with the mobility and migration of species, diffusion through membranes, fuel cell catalysts, etc., have also been included. In fact the title of the present volume, *Spillover and Mobility of Species on Solid Surfaces*, summaries this attempt to extend the conference topics towards dynamics at surfaces.

Among the 70 contributions received, the 56 accepted papers were selected on the basis of the reports of at least two international reviewers, according to standards comparable to those applied for other specialised journals. These papers are from 21 different countries. We like to thank the members of the Honorary Scientific Committee and of the National and International Advisory Boards for their conscientious revision of manuscripts which ensured the high scientific quality of this volume. Thanks are also extended to the members of the Organising Committee.

It is also with pleasure that we acknowledge the four institutions that contributed financially to the organisation of this meeting. These are, *Universidad Nacional de Educación a Distancia* (UNED), which provided us with 15 free inscription grants for young scientific researchers, *Consejo Superior de Investigaciones Científicas* (CSIC), *Sociedad Española de Catálisis* (SECAT) and *Ministerio de Ciencia y Tecnología*. Also the contributions made by the exhibitors are greatly appreciated.

There is no doubt that the width of topics covered in this volume will give to any interested reader, a state of the art impression with regard to dynamics of processes at surfaces, in general, and, in particular, of the spillover phenomenon. This view is supported by the relevance of the invited scientists and the expertise of the participants.


Madrid, May 2001                                    A. Guerrero-Ruiz
                                                    I. Rodríguez-Ramos

This Page Intentionally Left Blank

# Contents

## Invited Lectures

## Oral Presentations

## Poster Presentations

# HONORARY SCIENTIFIC COMMITTEE

**M. Boudart**. *Stanford University, USA.*
**B. Delmon**. *Université Catholique de Louvain, Belgium.*
**T. Inui**. *Corporate Center for Gas and Chemical Research, Osaka, Japan.*
**G.M. Pajonk**. *Université Claude Bernard Lyon I, France.*


# INTERNATIONAL ADVISORY BOARD

**J.A. Anderson**, *University of Dundee, UK*
**D. Duprez**, *Lab. de Catalyse en Chimie Organique, CNRS-Univ. Poitiers, France*
**K. Fujimoto**, *The University of Tokyo, Japan*
**P. Grange**, *Université Catholique de Louvain, Belgium*
**C. Li**, *State Key Lab. of Catalysis, Dalian, P.R. China*
**H.G. Lintz**, *University of Nancy, France*
**C. Mirodatos**, *Institut des Recherches sur la Catalyse,CNRS,France*
**V.N. Parmon**, *Boreskov Institute of Catalysis, Novosibirsk, Russia*
**V.I. Parvulescu**, *University of Bucharest, Rumania*
**P. Ruiz**, *Université Catholique de Louvain, Belgium*
**M. Schmal**, *Universidade Federal do Rio de Janeiro, Brazil*
**P.A. Sermon**, *University of Surrey, UK*
**C.G. Vayenas**, *University of Patras, Greece*


# NATIONAL ADVISORY BOARD

**M.C. Andrade**. *Inst. de Ciencias de la Construcción, CSIC.*
**T. Blasco**. *Inst. de Tecnologia Química, CSIC.*
**S. Bernal**. *Universidad de Cádiz.*
**A. Caballero**. *Universidad de Sevilla.*
**J.C. Conesa**. *Inst. de Catálisis y Petroleoquímica, CSIC. Madrid.*
**A. Cortés**. *Inst. de Catálisis y Petroleoquímica, CSIC. Madrid.*
**M. Fernández-García**. *Inst. de Catálisis y Petroleoquímica, CSIC. Madrid.*
**P. Ferreira-Aparicio**. *Inst. de Catálisis y Petroleoquímica, CSIC. Madrid.*
**A. Guerrero-Ruiz**. *Universidad Nacional de Educación a Distancia.*
**F. Illas**. *Universidad de Barcelona.*
**F.J. López-Garzón**. *Universidad de Granada.*
**A. Martínez**. *Inst. de Tecnologia Química, CSIC.*
**M. Montes**. *Universidad del Pais Vasco.*
**G. Munuera**. *Universidad de Sevilla.*
**J.A. Navío**. *Universidad de Sevilla.*
**F.J. Pérez**. *Universidad Complutense de Madrid.*

**V. Rives**. *Universidad de Salamanca.*
**A. Rodríguez Gónzalez-Elipe**. *Inst. de Ciencias de Materiales de Sevilla, CSIC.*
**I. Rodríguez-Ramos**. *Inst. de Catálisis y Petroleoquímica, CSIC. Madrid.*
**F. Rodríguez-Reinoso**. *Universidad de Alicante.*
**J. Sanz**. *Inst. de Ciencias de Materiales de Madrid, CSIC.*
**A. Sepúlveda-Escribano**. *Universidad de Alicante.*
**J. Soria**. *Inst. de Catálisis y Petroleoquímica, CSIC. Madrid.*
**J.M.D. Tascón**. *Inst. Nacional del Carbón, CSIC.*

## ORGANIZING COMMITTEE

**A. Guerrero-Ruiz** (Chair). *Universidad Nacional de Educación a Distancia.*
**I. Rodríguez-Ramos** (Co-chair, Scient. Secretary). *Inst. Catálisis y Petrol., CSIC. Madrid.*
**A. Cortés**. *Inst. Catálisis y Petroleoquímica, CSIC. Madrid.*
**M. Fernández-García** (Treasurer). *Inst. Catálisis y Petrol., CSIC. Madrid.*
**A. Sepúlveda-Escribano**. *Universidad de Alicante.*

## SPONSORING

**Universidad Nacional de Educación a Distancia (UNED).**
**Consejo Superior de Investigaciones Científicas (CSIC).**
**Sociedad Española de Catálisis (SECAT).**
**Ministerio de Ciencia y Tecnología.**

1

# Hydrogenation by spillover of hydrogen from metal to acidic support or by reverse spillover of the reactant molecule from the support to the metal

R. Prins

Laboratory for Technical Chemistry, Federal Institute of Technology (ETH), 8092 Zurich, Switzerland

For hydrogen spillover to be effective in catalysis, it must lead to a net transport of hydrogen atoms. The first prerequisite for this to happen is a thermodynamic driving force between the point of hydrogen atom creation by $H_2$ dissociation on the metal particle and the site where the hydrogen is used for hydrogenation. The second prerequisite is a means of transportation of the hydrogen atoms over the support surface. Proof of the existence of spillover came from experiments with reducible supports such as $WO_3$. In a metal/ $WO_3$ catalyst both prerequisites are met. The thermodynamic driving force is the reducibility of the support cations, and they provide at the same time the means of transportation by a redox transfer of the hydrogen atom between neighbouring tungsten cations. Scientists have tried to use the same explanation for systems in which the support metal cations cannot be reduced. Thus, hydrogen-deuterium exchange on a metal/$SiO_2$ catalyst is often quoted as an example of spillover as well. This, however, is a misunderstanding. There is no net hydrogen transport on an ideal metal/$SiO_2$ system, only hydrogen-deuterium exchange. Exchange between a deuterium atom on the metal surface and a hydrogen atom of a silanol group occurs at the metal-support interface by a bending over of a silanol group towards the metal surface. The diffusion of the deuterium atom over the silica surface, away from the metal particle, takes place by exchange of a Si-OD group with a Si-OH group. This is a water-assisted proton and deuteron jump process.

The difference between the two examples is that in the case of the metal/$WO_3$ system there is a genuine transport of hydrogen atoms away from the metal particles. These hydrogen atoms turn into protons by donating an electron to the support surface cations, and the protons combine with the oxygen anions of the support to hydroxyl surface groups. In the case of the metal/$SiO_2$ system, however, hydrogen atoms cannot reduce the Si cations. As a result, there can only be exchange between OH and OD groups, but no net transport of hydrogen away from the metal particles.

With the need to remove more sulfur-containing and aromatic molecules from diesel fuel, interest in metal catalysts supported on acidic carriers has increased.

Pt and Pd on zeolites and amorphous silica-alumina (ASA) have especially attracted attention. An explanation for the increased hydrogenation capacity of such catalysts is a special interaction of the metal atoms with acidic sites, leading to electron deficiency of the metal atoms and a higher sulfur tolerance (1). Recently hydrogen spillover from the metal particles to molecules adsorbed on acidic support sites has been proposed (2, 3). Similar proposals have been put forward for the reaction of synthesis gas to methanol over $Cu/ZrO_2$ and $Cu/ZnO$. $ZrO_2$ is a reducible support, and it is therefore no surprise that formate species, formed on the $ZrO_2$ surface by reaction of CO with hydroxyl groups, were shown to be reduced to methoxy species by hydrogen atoms spilled over from the copper particles (4). The proof for the same reaction in the $Cu/ZnO$ system is less convincing (5), as might be expected from the difficult reducibility of ZnO.

The explanation of enhanced hydrogenation of reactant molecules over metal-on-acidic-support catalysts by spillover is appealing, but spectroscopic proof has not been provided as yet. Also the diffusion of the hydrogen atoms over the support surface is difficult to understand. Alternative explanations will be discussed. A possibility would be that the interaction with the acid support sites leads to a higher concentration of basic reactant molecules on the support surface. For such pre-equilibrium to work, the molecules should, however, not leave the surface, but must move along the surface to the metal particles. An analogy to the precursor state and increased sticking coefficient of molecules on metal surfaces can be made. The acid support functions as a collector for the reactants which then undergo reverse spillover towards the metal.

## REFERENCES

1. R.A. Dalla Betta, M. Boudart, P. Gallezot and R.S. Weber, J. Catal. 69, 524 (1981).
2. L. Simon, J.G. van Ommen, A. Jentys and J.A. Lercher, J. Phys. Chem. B104,11644 (2000).
3. J.Chupin, N.S. Gnep, S. Lacombe and M. Guisnet, Appl. Catal. A 206, 43 (2001).
4. K.D. Jung and A.T. Bell, J. Catal. 193, 207 (2000).
5. S. Fujita, M. Usui, H. Ito and N. Takezawa, J. Catal. 157, 403 (1995).

# Molecular Hydrogen-Originated Protonic Acid Site

Hideshi Hattori

Center for Advanced Research of Energy Technology, Hokkaido University, Sapporo 060-8628, Japan

Formation of surface protons from hydrogen molecule was observed for Pt/SO$_4^{2-}$-ZrO$_2$, and the protons act as catalytically active sites for several acid catalyzed reactions. The surface protons exist only when hydrogen molecules are present in gas phase, and disappear from the surface when hydrogen molecules are removed from gas phase. The proton is formed via dissociative adsorption of hydrogen, spillover of hydrogen atom onto support, surface diffusion of the spiltover hydrogen to Lewis acid site, and donation of an electron from hydrogen atom to Lewis acid site.

Promotive effects of hydrogen on acid-catalyzed reactions are observed not only for the Pt/SO$_4^{2-}$-ZrO$_2$, but also for other catalysts which are composed of hydrogen activation sites and Lewis acid sites. A *molecular hydrogen-riginated protonic acid site* is proposed as a widely applicable concept for generation of protonic acid sites.

## 1. INTRODUCTION

It is established that the active sites of solid acid catalysts for most of the acid-catalyzed reactions are protons located on the surfaces. These protons are believed to be generated intrinsically as the catalysts are prepared. Protons are located on the surface to compensate negative charge generated by, for instance, isomorphous substitution of Si by Al in SiO$_2$ as seen for zeolites and silica-alumina.

Although a proton is formed by heterolytic dissociation of hydrogen molecule, promotion effects of hydrogen on the acid-catalyzed reactions have scarcely been observed. In recent years, several papers have reported the promotion effects of hydrogen. Baba et al. reported that the promotion effects of hydrogen on ethylbenzene disproportionation over Ag-Y zeolite are caused by the formation of proton from hydrogen molecules accompanied by reduction of Ag$^+$ ions to Ag$^0$ in the presence of hydrogen[1, 2]. Prominent effect of hydrogen was reported by Sachtler et al. with Pd-Y zeolite for methylcyclopentane isomerization[3].

Hosoi et al. reported that Pt/SO$_4^{2-}$-ZrO$_2$ persisted a high activity for a long period in alkane isomerization when the reaction was carried out in the presence of hydrogen[4]. They ascribed a high activity and stable activity in the presence of hydrogen to a removal of carbonaceous residues deposited on the catalyst by hydrogenation. We have studied the hydrogen effects on the catalytic activities of Pt/SO$_4^{2-}$-ZrO$_2$, and concluded that the promotion effect of hydrogen is caused by the formation of protons from molecular

4

hydrogen. We propose the concept that the surface proton is formed by the mechanisms as *molecular hydrogen-originated protonic acid site*.

Molecular hydrogen-originated protonic acid site can be applied not only to Pt/SO$_4^{2-}$-ZrO$_2$, but also to the other catalytic systems which are composed of hydrogen activation species and acidic support, and, therefore, is widely applicable concept.

In the present paper, I describe how we could establish the concept of *molecular hydrogen-originated protonic acid site*.

## 2. HYDROGEN EFFECTS ON Pt/SO$_4^{2-}$-ZrO$_2$

### 2.1. Hydrogen effects on catalytic activity

Promotive effect of hydrogen on the catalytic activity was observed for pentane isomerization[5], butane isomerization[5], and cumene cracking[6] over Pt/SO$_4^{2-}$-ZrO$_2$. Pentane did not undergo any reactions at a reaction temperature of 573 K when the reaction was carried out in a nitrogen stream, but undergwent isomerization when the carrier gas was switched from nitrogen into hydrogen. The activity did not change with time on stream in the presence of hydrogen and persisted a long time. Over SO$_4^{2-}$-ZrO$_2$, however, the activity for pentane isomerization quickly decreased with time on stream even in the presence of hydrogen.

Essentially the same hydrogen effect was observed for butane isomerization over Pt/SO$_4^{2-}$-ZrO$_2$. The activity was proportional approximately to square root of the hydrogen partial pressure. If the isomerization proceeded via a metal-acid bifunctional mechanism, the rate equation would have been expressed by a negative order in hydrogen partial pressure.

There are two possible mechanisms for isomerization of alkanes; acid-metal bifunctional mechanism and monofunctional acid-catalyzed mechanism. The positive order in hydrogen for butane isomerization suggests that the reaction proceeds by the monofunctional mechanism. The promotive effect of hydrogen on pentane and butane isomerization suggests that the active sites for acid-catalyzed reactions increase in the presence of hydrogen. To confirm this point, it would be helpful to examine the hydrogen effect on a "pure acid-catalyzed reaction". Cumene cracking is one of the typical acid-catalyzed reactions. Protonic acid sites are believed to promote cumene cracking.

Figure 1 shows the results of cumene cracking over Pt/SO$_4^{2-}$-ZrO$_2$ in a pulse reactor at 423 K. The carrier gas was sequentially switched. In the hydrogen carrier, the activity was high and stable. The activity,
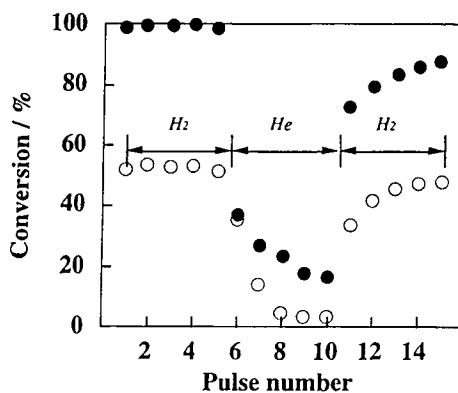


Fig. 1 Promotion effect of hydrogen on the catalytic activity of Pt/SO$_4^{2-}$-ZrO$_2$ for cumene cracking at 423 K (○) and 473 K (●)

however, quickly decreased as the carrier gas was switched to helium. As the carrier gas was switched back to hydrogen, the activity gradually recovered. The promotive effect of hydrogen is reversible. Over $SO_4^{2-}$-$ZrO_2$, the activity markedly decreased with the pulse number in both hydrogen and helium streams. It is stated that the promotive effects of hydrogen on the catalytic activities of acid-catalyzed reaction are rationalized by the formation of protonic acid sites from hydrogen molecules over Pt/$SO_4^{2-}$-$ZrO_2$.

## 2.2. Observation of protonic acid site generation by IR

The formation of protonic acid sites from hydrogen molecules is demonstrated by an IR study of adsorbed pyridine[5, 7]. The IR spectra of pyridine adsorbed on Pt/$SO_4^{2-}$-$ZrO_2$ which was pretreated at 623 K in hydrogen flow followed by evacuation at 673 K showed absorption bands ascribed to pyridinium ions and pyridine coordinated to Lewis acid sites. Heating in the presence of hydrogen resulted in a decrease in the amount of pyridine adsorbed on Lewis acid sites (1450 cm$^{-1}$), and an increase in the amount of pyridine adsorben on protonic acid sites (1540 cm$^{-1}$). Following heating in the presence of hydrogen at 573 K, the sample was cooled to room temperature, and gaseous hydrogen was evacuated with increasing the temperature. The evacuation caused a decrease in the protonic acid sites and a restoration of Lewis acid sites. The changes in the amounts of Lewis acid sites and protonic acid sites are plotted against the temperatures of heating in the presence of hydrogen and under a vacuum in Fig. 2. It is obvious that the change in the surface acid properties of Pt/$SO_4^{2-}$-$ZrO_2$ induced by hydrogen is a reversible process.

The above observation indicates that the surface protons are generated from molecular hydrogen as follows. Hydrogen molecule is dissociated on the platinum species to form hydrogen atoms which spillover onto the support. The spiltover hydrogen atom undergoes surface diffusion on the support to reach Lewis acid site where hydrogen atom loses an electron to form a proton. The proton is stabilized on the
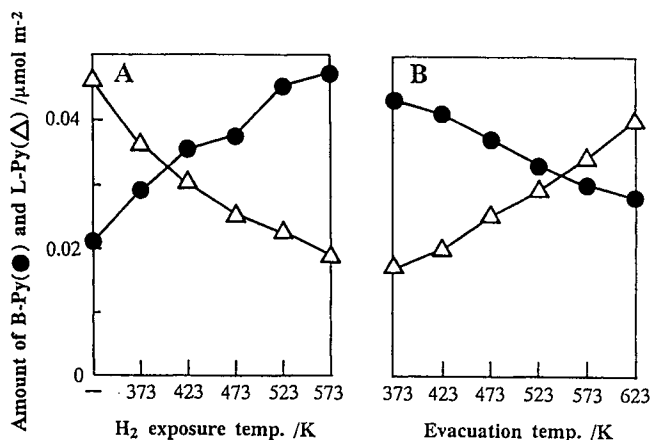


Fig. 2 The change in the amount of pyridine adsorbed on protonic sites and Lewis acid sites of Pt/$SO_4^{2-}$-$ZrO_2$ on (A) heating in the presence of hydrogen (500 Torr) and (B) subsequent evacuation.

6

oxygen atom nearby the Lewis acid site. The electron trapped at Lewis acid site reacts with a second hydrogen atom to form a bond of Lewis acid-H. The protons formed from molecular hydrogen disappear if gaseous hydrogen is removed from the system via the reversal steps.

It is to be noted that the formation and elimination of the surface protons require a high temperature. A step requiring a high energy barrier to proceed is involved in the formation and elimination of the surface protons.

## 2.3. Behavior of hydrogen on $Pt/SO_4^{2-}-ZrO_2$

### 2.3.1. TPD study of adsorbed hydrogen

In order to understand the behavior of hydrogen on $Pt/SO_4^{2-}-ZrO_2$, temperature programmed desorption (TPD) of adsorbed hydrogen was measured, in which temperature of hydrogen adsorption was varied[8]. Figure 3 shows the TPD plots. The amount of hydrogen desorbed from the surface strongly depended on the temperature of adsorption. The amount was larger as the adsorption temperature was higher. This result also indicate that a step requiring a high energy barrier to proceed is involved in the adsorption of hydrogen.

### 2.3.2. Sequential adsorption of $H_2$ and $D_2$

Hydrogen was first adsorbed at 423 K and briefly evacuated, and then deuterium was adsorbed at 423 K. TPD was then run[8]. The TPD plots for $H_2$, HD, and $D_2$ are shown in Fig. 4. Each peak appeared separately. If D and H were completely mixed on the surface, binomial distribution of $H_2$, HD, and $D_2$ would have been observed, and the desorption peaks for $H_2$, HD, and $D_2$ would have appeared at the same temperature. The results suggest that hydrogen molecule is dissociatively adsorbed on the platinum species to form hydrogen atoms which spillover onto the surface of $SO_4^{2-}-ZrO_2$ and undergo surface diffusion by the concentration gradient. A brief evacuation removes hydrogen from the platinum species and
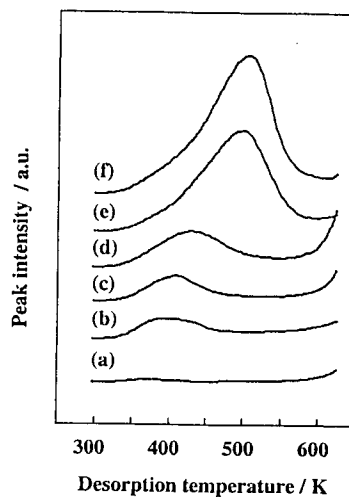


Fig. 3    TPD plots for hydrogen adsorbed on $Pt/SO_4^{2-}-ZrO_2$ at different temperatures: (a) 293 K, (b) 323 K, (c) 373 K, (d) 473 K, and (e) 523 K.
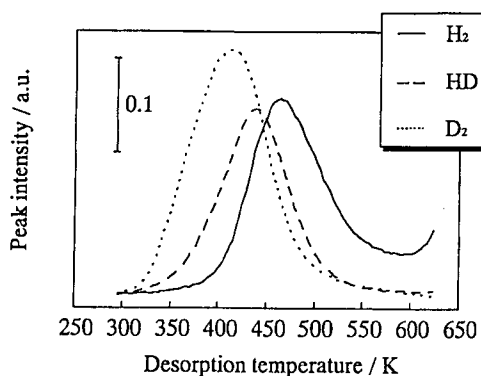


Fig. 4 TPD plots for sequential adsorption of $H_2$ and $D_2$ on $Pt/SO_4^{2-}-ZrO_2$. $H_2$ adsorbed at 523 K, evacuated at 373 K, $D_2$ adsorbed at 373 K.

nearby oxide region. Hydrogen located at a long distance from the platinum species does not easily diffuse back to the platinum species because of a reduced concentration gradient. Subsequent exposure to $D_2$ saturate the platinum species and the oxide region nearby the platinum species, resulting in the adsorbed H and D being spatially separated with D locating at a small distance from the platinum species. Consequently, it is expected that the order of desorption is $D_2$, HD, and $H_2$.

## 2.4. Kinetic Study of Hydrogen Adsorption on Pt/SO₄²⁻-ZrO₂

In Fig. 5 are shown the variations of hydrogen uptake on Pt/$SO_4^{2-}$-ZrO₂ as a function of time for different adsorption temperatures[9]. The rate and amount of hydrogen uptake increases as the temperature increases. The variations are classified into two temperature ranges; one for the temperature range 323 - 473 K, and the other 473 - 523 K. In the temperature range 323 - 473 K, the hydrogen uptake rate increases to a small extent with an increase in the temperature. In the temperature range 473 - 523 K, the rate increases much with an increase in the temperature. It is suggested that in the adsorption of hydrogen, a step requiring a high energy to proceed is involved. To cross over the energy barrier at an appropriate rate, a temperature above 473 K is required.

It should be emphasized that the hydrogen uptake continues more than 24 h when adsorption is carried out above 473 K. The hydrogen uptake reaches $2.5 \times 10^{20}$ atom/g cat in 24 h at 523 K. The number corresponds to H/Pt ratio of 16. Such a large value of the H/Pt ratio indicates the occurrence of hydrogen spillover onto the support followed by surface diffusion.

Adsorption of hydrogen on Pt/$SO_4^{2-}$-ZrO₂ involves the successive three steps; hydrogen dissociation on the platinum species, spillover of the adsorbed hydrogen atom onto the support, and surface diffusion of the spiltover hydrogen. To elucidate the slow step, kinetic analysis was performed.

In general, hydrogen adsorption on Pt is fast; adsorption occurs easily at room temperature. Therefore, this step should not be the rate controlling step for the
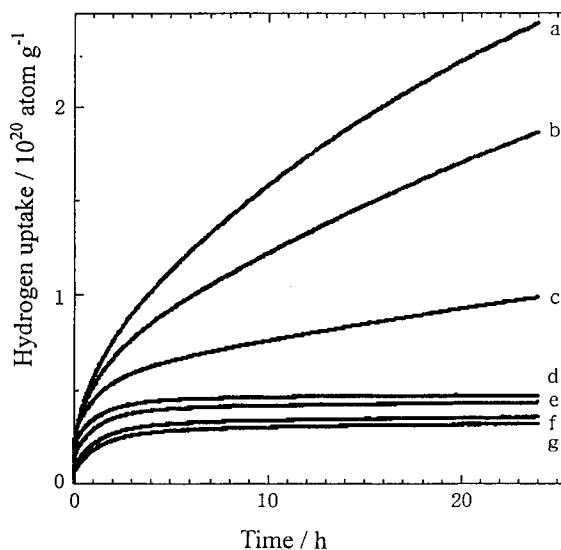


Fig. 5 Variation of hydrogen uptake on Pt/$SO_4^{2-}$-ZrO₂ as a function of time at different adsorption temperatures. (a) 523 K; (b) 513 K; (c) 493 K; (d) 473 K; (e) 423 K; (f) 373 K and (g) 323 K.

8

continuous hydrogen uptake observed above 473 K.

In the case where the spillover step is the rate controlling step, the rate of adsorption would be expressed by

$$dC/dt = k(C_e - C)$$ (1)

where $C$ represents the concentration of the spiltover hydrogen on the support and has the same value regardless of the distance from the Pt-support interface, and $C_e$ represents the concentration of the spiltover hydrogen on the support equilibrated with the hydrogen on the Pt site. Since the value $C_e$ is unknown, we applied different values for $C_e$ to find out whether a certain value of $C_e$ could be found to satisfy Eq. (1). We failed to find out a certain value of $C_e$ to satisfy Eq. (1) for different temperatures.

In the case where the surface diffusion is the rate controlling step, the rate of adsorption would be expressed by the equeation for Fick's second law.

$$\partial C/ \partial t = D/x \ (\partial / \partial x) \ ( x\partial C/\partial x)$$ (2)

where $C$, $x$, and $D$ represent a surface concentration of the spiltover hydrogen, a distance from the center of the platinum species, and a diffusion cefficient of the spiltover hydrogen, respectively. Introducing the boundary conditions and assuming $Dt/a^2$ being small yield the following equation.

$$M = 4\pi^{1/2}aC_0D^{1/2}t^{1/2}$$ (3)

where $M$, $a$, and $C_0$ represent the amount of the spiltover hydrogen, a radius of the platinum species, and the concentration of the spiltover hydrogen equilibrated with the hydrogen adsorbed on the Pt site, respectively.

Plots of $M$ versus $t^{1/2}$ for different adsorption temperatures are shown in Fig. 6. The plots for 513 and 523 K give straight lines over whole range of $t^{1/2}$. The plots for adsorption temperature of 473 and 493 K give straight lines in the initial 2.8 h. All plots have a common intercept of 1.5 x $10^{19}$ atom H/g cat. Equation (3) does not take into account the amount of hydrogen adsorbed on the sites other than those where surface diffusion takes place. The intercept is interpreted as the amount of hydrogen adsorbed on the Pt sites. The amount of hydrogen diffusing over the support is then expressed by the corrected $M' = M - 1.5$ x $10^{19}$. The slope of $M'$ versus $t^{1/2}$ is proportional to square root of diffusion constant $D$. By the variation of $D$ with the adsorption temperature, the
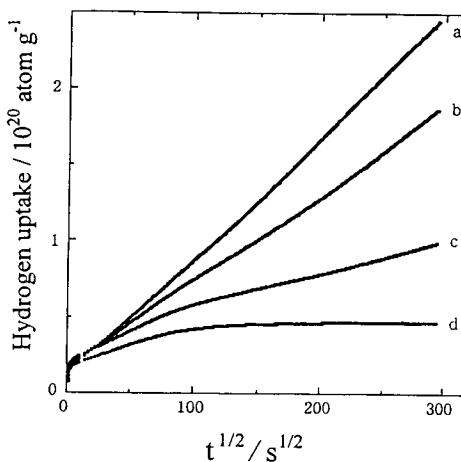


Fig.6　Plots of hydrogen uptake vs. square root of time for Pt/SO$_4^{2-}$-ZrO$_2$ at different temperatures. (a) 523 K; (b) 523 K; (c) 493 K; (d) 473 K.

activation energy for the surface diffusion was calculated to be 84 kJ/mol.

## 3. HYDROGEN EFFECTS ON Pt/WO$_3$-ZrO$_2$, Pt/H-ZSM5 AND Co Mo/SiO$_2$-Al$_2$O$_3$

### 3.1. Promotive effects of hydrogen on catalytic activity

The promotive effects of hydrogen on the catalytic activity were observed for catalysts other than Pt/SO$_4^{2-}$-ZrO$_2$ for several reactions[10].

In Fig. 7 are shown the activities of Co Mo/SiO$_2$-Al$_2$O$_3$ for n-hexane isomerization in the presence and absence of hydrogen. The activity is significantly higher in the presence of hydrogen than in the absence of hydrogen. The conversion is less than 10 % in a nitrogen stream, while the conversion is about 30 % in a hydrogen stream. The same hydrogen effect was observed for cumene cracking and toluene disproportionation over Co Mo/SiO$_2$-Al$_2$O$_3$.

Essentially the same promoting effects of hydrogen were observed for a physical mixture of Pt/SiO$_2$ and H-ZSM5, and Pt/WO$_3$-ZrO$_2$ for cumene cracking. In all cases, the catalytic activities of these catalysts for cumene cracking were higher in the presence of hydrogen than in the absence of hydrogen. An example is shown in Fig. 8 where the conversion of cumene cracking are plotted against pulse number when cumene was allowed to react over a mixture of Pt/SiO$_2$ and H-ZSM5. The conversions of H-ZSM5 alone are also plotted.

The physical mixture exhibited a high activity only in the presence of hydrogen. With H-ZSM5, the conversion
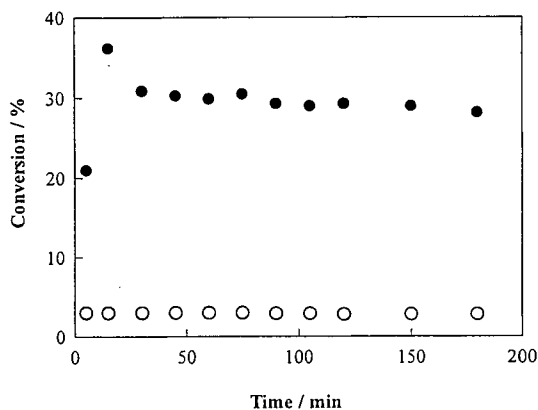


Fig. 7 n-Hexane isomerization over Co.Mo/SiO$_2$-Al$_2$O$_3$ at 693 K and 30 atom of hydrogen (●) and nitrogen(○).
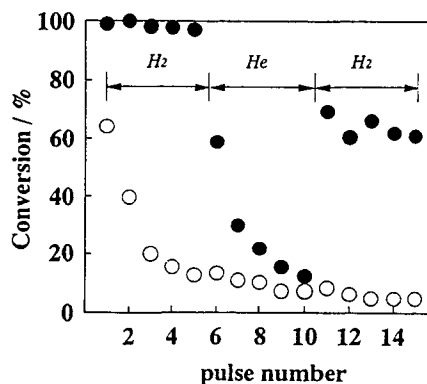


Fig. 8 Cumene cracking over H-ZSM5 and the physical mixture of H-ZSM5 and Pt/SiO$_2$ at 423 K in a pulse reactor.

10

rapidly decreased with the pulse number even in the presence of hydrogen. The conversion was not affected by the presence of hydrogen for H-ZSM5.

With $WO_3$-$ZrO_2$, the hydrogen effect was observed without Pt. It is suggested that molecular hydrogen can be activated by $WO_3$ on $ZrO_2$,

## 3.2. Kinetic study of hydrogen adsorption on Pt/$WO_3$-$ZrO_2$

Figure 9 shows the variation of hydrogen uptake on Pt/$WO_3$-$ZrO_2$ as a function of time. Hydrogen adsorption is faster on Pt/$WO_3$-$ZrO_2$ than on Pt/$SO_4^{2-}$-$ZrO_2$. Adsorption equilibrium was established within 30 h when the adsorption temperature was above 423 K. Kinetic analysis of the data for Pt/$WO_3$-$ZrO_2$ indicates that the rate controlling step is spillover step with activation energy of 21 kJ/mol. Therefore, surface diffusion of hydrogen is much faster on Pt/$WO_3$-$ZrO_2$ than on Pt/$SO_4^{2-}$-$ZrO_2$, though it is not clear what factor determines the rate of surface diffusion.

Unlike $SO_4^{2-}$-$ZrO_2$, $WO_3$-$ZrO_2$ is able to adsorbed hydrogen to a considerable extent even without Pt. Figure 10 shows hydrogen uptake on $WO_3$-$ZrO_2$ as a function of time. The rate of hydrogen uptake is slower on $WO_3$-$ZrO_2$ than on Pt/$WO_3$-$ZrO_2$. Hydrogen should be dissociatively adsorbed on $WO_3$ site.
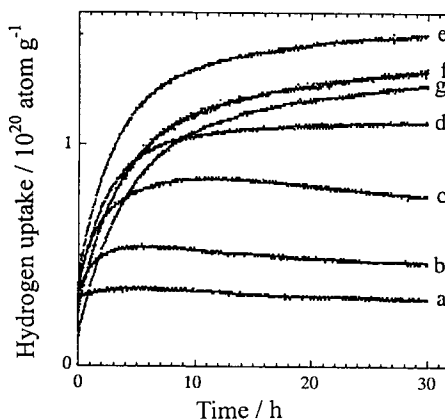


Fig. 9 Variation of hydrogen uptake on Pt/$WO_3$-$ZrO_2$ as a function of time at different adsorption temperatures. (a) 573 K; (b) 523 K; (c) 473 K; (d) 423 K; (e) 373 K; (f) 323 K and (g) 273 K.
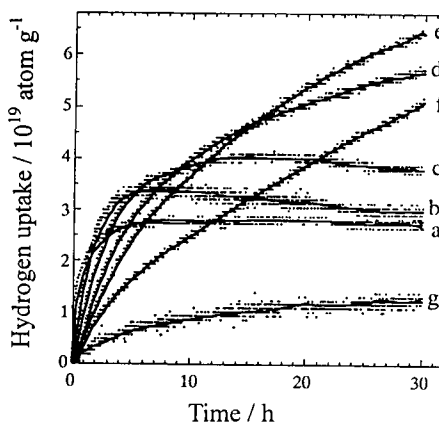


Fig. 10 Variation of hydrogen uptake on $WO_3$-$ZrO_2$ as a function of time at different adsorption temperatures. (a) 573 K; (b) 523 K; (c) 473 K; (d) 423 K; (e) 373 K (f) 323 K and (g) 273 K.

## 4. GENERAL MODEL

The hydrogen effects described above are rationalized by the formation of protonic acid sites from hydrogen molecules, though it is evident that hydrogen also plays a role other than as a source of protons. The schematic model for the formation of protonic acid sites is illustrated in Fig. 11. Hydrogen molecules are dissociatively adsorbed on the hydrogen activation center such as platinum and Co Mo species to form hydrogen atoms. The hydrogen atoms spillover onto the support, and undergo surface diffusion to Lewis acid sites, where the hydrogen atom releases an electron to become a proton. The proton may be stabilized on the O atom nearby the Lewis acid site. The electron trapped at the Lewis acid site may react with a second hydrogen atom to form a hydride which is stabilized on the Lewis acid site. As a whole, a hydrogen molecule converts into a proton and a hydride, and the Lewis acid site loses its function. The protonic acid sites thus formed act as catalytically active sites for acid-catalyzed reactions. We propose the concept *molecular hydrogen-originated protonic acid site* as a widely applicable acid site generation for solid acid catalysts.
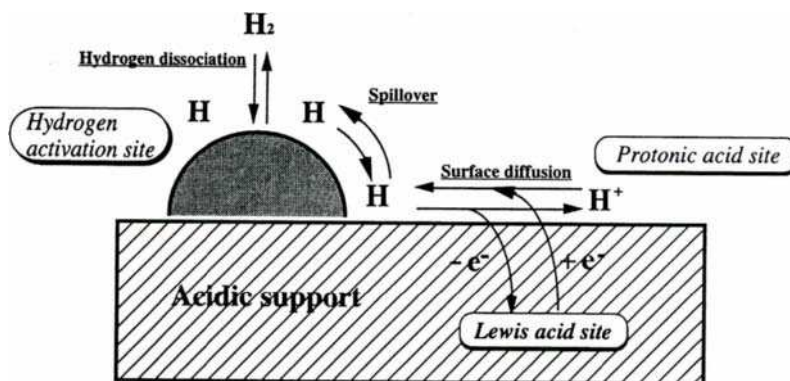


Fig. 11 General model for *molecular hydrogen-originated protonic acid site*

The concept of *molecular hydrogen-originated protonic acid site* is important in understanding the mechanisms of the reactions carried out in the presence of hydrogen. In a certain catalyst system, the concentration of the surface protons can be controlled by the hydrogen pressure and temperature. The number of active sites for acid-catalyzed reactions can be adjusted. The concept should be taken into account for the reactions carried out in the presence of hydrogen. Typical examples can be seen in the processes of petroleum refineries. There are several catalytic processes carried out in the presence of hydrogen such as hydrotreating, hydrocracking, hydroisomerization, and reforming. In these processes, acid-catalyzed reactions and acid site-assisted reactions are involved. So far, the acid sites intrinsically existing on the catalyst surfaces are considered to be

12

relevant to these reactions regardless of the presence and absence of hydrogen. However, it becomes clear that the *molecular hydrogen-originated protonic acid site* should be taken into account when active sites and mechanisms of these reactions are discussed. Indeed, the importance is stressed for the idea that there are such active sites which appear only in the reaction conditions [11].

## REFERENCES

[1] T. Baba and Y. Ono, Zeolites, 7 (1987) 292-294.
[2] T. Baba and Y. Ono, J. Phys. Chem., 100 (1996) 9064.
[3] X. Bai and W. M. H. Sachtler, J. Catal., 129 (1991) 121.
[4] T. Hosoi, T. Shimadzu, S. Ito, S. Baba, H. Takaoka, T. Imai and N. Yokoyama, Prep. Symp. Div. Petro. Chem. Am. Chem. Soc., Los Angels Meeting, (1988) p562.
[5] K. Ebitani, J. Konishi and H. Hattori, J. Catal., 130 (1991) 257.
[6] T. Shishido and H. Hattori, J. Catal., 161 (1996) 194.
[7] K. Ebitani, J. Tsuji, H. Hattori and H. Kita, J. Catal., 135 (1992) 609.
[8] T. Shishido and H. Hattori, Appl. Catal. A, 146 (1996) 157.
[9] N. Satoh. J.-i. Hayashi, and H. Hattori, Appl. Catal., A. 202 (2000) 207.
[10] T. Shishido, T. Nagase, K. Higo, J. Tsuji, and H. Hattori, Stud. Surf, Sci. Catal., 101 (1996) 523.
[11] B. Delmon, Bull. Soc. Chim. Belg., 104 (1995) 173.

# Spillover phenomena in stationary and non stationary hydrogen and syngas generation processes

P. Denton, E. Odier, C. Mirodatos

Institut de Recherches sur la Catalyse, CNRS,
2 avenue Albert Einstein, 69626 Villeurbanne Cédex, France

## 1. INTRODUCTION

Increasing energy demand for more efficient, cleaner and environmentally friendlier energy supply systems creates a new challenge for the scientific and technological community. Fuel cell technology emerges as the most promising technology to replace current combustion systems and conventional batteries, for all end use sectors. In particular, fuel cells using hydrogen are intrinsically clean. Moreover, in combination with conventional fuels such as natural gas, these cells have a large potential for energy savings and for reduction of pollutant emissions and green house gases (GHG), especially $CO_2$. Although natural gas is a non-renewable source, it is thought to be the fuel which, next to hydrogen, leads to the lowest $CO_2$ emissions.

On the other hand, natural gas also has to be considered as the major source of syngas $CO+H_2$, either for conventional chemical processes such as ammonia synthesis or for potential bulk production of clean fuels such as Fischer-Tropsch diesel and gasoline. Syngas production can combine steam/dry reforming and partial oxidation (see for instance the promising tri-reforming process proposed by Song in [1]). It may also lead to electricity generation with either integrated gasification combined cycles (IGCC)-type generators or fuel cells. A lot of research remains to be done in order to make these new or renewed technologies more cost-effective than existing processes, however.

For these systems aiming at direct or indirect transformation of natural gas into hydrogen, both the decomposition of methane into carbon and hydrogen and the oxidation of carbon into carbon oxides require numerous elementary steps and various active sites. Therefore, significant transfer processes from site to site are expected, depending on the catalytic phases and on the stationary or non stationary operating conditions. This paper focuses on these key elementary surface, bulk and spillover dynamics within the frame of this renewed field of hydrogen and syngas chemistry.

## 2. HYDROGEN PRODUCTION FROM METHANE CRACKING FOR FUEL CELL APPLICATIONS

### 2.1. General features of stationary and non stationary processes.

A first approach for producing hydrogen for fuel cell applications is to adapt the conventional existing processes in the production of $H_2$-rich gases : steam reforming, partial oxidation or autothermal reforming of light hydrocarbons, essentially natural gas [2]. However, their relative technological complexity may be costly in the final application. Because CO is a major co-product of $H_2$ generation, they must include, among others, downstream steps of purification (WGS, SELOX or PSA [3]) to remove the final residual CO and then reach the minimum of purity required by the most technologically advanced fuel cells, such as the PEMFC which are poisoned by more than 10 ppm CO in the hydrogen stream.

A new technology is the direct production of CO-free hydrogen by non-stationary catalytic decomposition of light hydrocarbons as suggested in references [4-5]. The decomposition of methane was first studied on Ni-based catalysts at temperatures above 600°C, in which case it is possible to produce $H_2$ with a stoichiometric ratio of almost 2 $H_2/CH_4$ during a few hours without overly rapid catalyst deactivation [6-8]. The relative stability of the catalyst could be related to the formation of filamentous carbon by carbide diffusion and extrusion out of the metal particles, without immediate poisoning by carbon encapsulation [5,9]. These high temperatures, however, render the deposited carbon highly stable (graphite-like). In addition, the need to regenerate the catalyst via oxidation presents serious drawbacks such as runaway (which may cause irreversible metal sintering and/or losses by vaporisation), hot spots and troublesome heat management. Finally, the resulting partial oxidation of the metal may lead to significant CO production during the following cracking period due to the stoichiometric reaction between metal oxide and carbonaceous adspecies [10].

To limit these drawbacks linked to the regeneration step, Choudhary and Goodman have recently proposed the stepwise steam reforming of methane [11,12]. In step I, methane is cracked into surface carbon and/or hydrocarbonaceous species [12].

$$CH_4 \rightarrow C_{ads} / [CH_n]_{ads} + \left(2 - \frac{n}{2}\right) H_2 \qquad \text{step I}$$
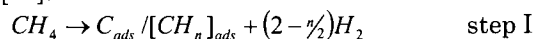
In step II the carbon and/or hydrocarbonaceous species react with water to regenerate the catalyst [12]. This constitutes the steam reforming step:

$$C_{ads} / [CH_n]_{ads} + H_2O \rightarrow CO_2 + \left(2 + \frac{n}{2}\right) H_2 \qquad \text{step II}$$
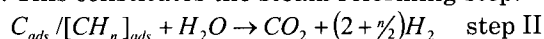
The authors have determined an optimum temperature ($\approx$400°C) which makes this cyclic process reversible. Increasing temperature favors step I (production of $H_2$) at the expense of step II (formation of graphitic surface carbon impossible to regenerate). Decreasing temperature renders the deposited carbon more easily removable by water in step II but at the expense of methane conversion in step I ($\approx$75%) [12]. At 400°C, $H_2$ is produced with less than 20 ppm CO, with between

1.0 to 1.3 mol/mol methane consumed and without catalyst deactivation after 20 reaction cycles. For each cycle, however, 10% of the deposited carbon is not regenerated and accumulates on the catalyst. Indeed, this constitutes a major drawback for long term applications such as commercial fuel cell systems.

For all of these concepts based on methane cracking followed by catalyst regeneration, the key goals are i) to improve the hydrogen yield during the methane cracking step and ii) to keep the cyclic process of carbon deposition/removal completely reversible.

On Ni-based catalysts with a neutral support like silica, carbon accumulates mostly into, onto or outside the metal phase under various highly heterogeneous forms such as surface and bulk carbide, encapsulating bi-dimensional veils, tri-dimensional aggregates or tubular filaments [13]. This polymorphous coke generation outlines the complexity of the related chemical and transfer processes : monomeric carbide diffusion, extrusion, polymerisation, graphitisation, aggregation, and so on.

Another option is to assist and control the accumulation of carbon by an active support, which may improve both the capacity and the quality of the transient storage, and therefore its reversibility. This bi-functionality of an active metallic phase (able to activate the gaseous hydrocarbon) deposited on an active support (able to store and release adsorbed carbonaceous species) requires tight interaction and reversible spillover/diffusion phenomena between the two components of the catalyst. These transfer phenomena may become rate-determining for the overall non stationary process and therefore have to be analysed in detail for any further evaluation.

## 2.2. Cyclic two-step process on Pt/CeO₂

A series of various bifunctional catalysts was prepared [14] and tested in a cyclic two-step process :

$$CH_4 \quad \rightarrow \quad C_{deposited\ on\ catalyst} + 2H_2 \qquad \text{reduction step I}$$

$$C^* + O_2 \rightarrow \quad CO_2 \qquad \text{oxidation step II}$$
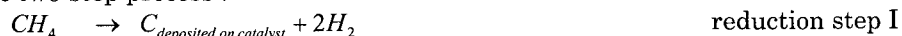
Among them, a Pt/CeO₂ catalyst was found to fulfill part of the process requirements, since it associates a noble metal active at low temperature and an active support well-known in three-way catalytic converters for its ability to buffer oxygen between reduction and oxidation [15]. Some experiments have attested that ceria does not stand up to overly high temperatures, which cause irreversible sintering (and therefore loss of surface area, an important factor for oxygen storage capacity and spillover properties) [16]. For the present study, however, a low temperature process is expected to be more efficient, since the rate of diffusion for the adspecies has to be comparable to the rate of carbon formation during the cracking step.

*Testing procedure.* The reaction was carried out under atmospheric pressure either in a tubular quartz micro-reactor (4 mm I.D.) or an *in situ* DRIFT (diffuse reflectance infrared spectroscopy) cell, as described in [14], to characterize the

surface of the working catalyst during the reaction. A typical experiment was performed at 400°C under flowing 20% $CH_4$ in inert gas, then pure inert gas (as a flush) and finally 10% $O_2$ in inert gas, all mixtures with a total flow rate of 50 ml/min (STP). The gas concentration at the reactor outlet was continuously monitored by on-line mass spectrometry. Before reaction the catalyst was reduced in-situ under hydrogen flow for 2 h at 400°C.

*Catalytic results.* Under forced nonsteady-state conditions, a reasonable methane conversion was obtained during the methane pulse (44%), leading to an average hydrogen yield of 18%. The remaining hydrogen extracted from methane was released as $H_2O$ essentially during the oxidation step. No CO was detected during methane cracking into $H_2$ or during the oxidative regeneration step, which was the prerequisite for the selection of this catalyst (see figure 1). Only a small $CO_2$ peak and a permanent trace release of water were detected during the methane pulse.
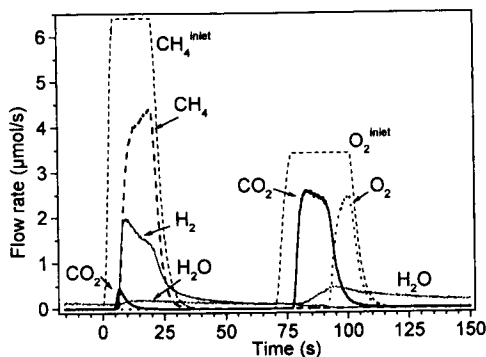


Figure 1: Inlet and outlet gas concentrations obtained over $Pt/CeO_2$ tested at 400°C by sequentially feeding a fixed bed reactor (4mm I.D.) with methane, then helium, then oxygen and so forth [14].

*In-situ DRIFTS study of $Pt/CeO_2$ under forced nonsteady-state conditions.*

Three IR spectra corresponding to each of the sequential steps described in Figure 1 are reported in Figure 2 and the main bands are assigned in Table 1 [17-19].

The main features reported in [14] can be summarized as follows :

i) When $CH_4$ is introduced into the cell, the decay of all OH bands reveals a progressive dehydroxylation of the ceria for several minutes. New bands due to platinum carbonyl species appear and grow rapidly (changing progressively from multibonded to polycarbonyl forms as attested by increasing C-O frequency), at the same time as formate, unidentate and bidentate carbonates on ceria. For the latter, the progressive increase and broadening of the associated bands indicate a growing concentration and heterogeneity. These reactions of carbon oxidation are followed by the reduction of ceria, which is proven by the progressive appearance of $Ce^{3+}$ sites.
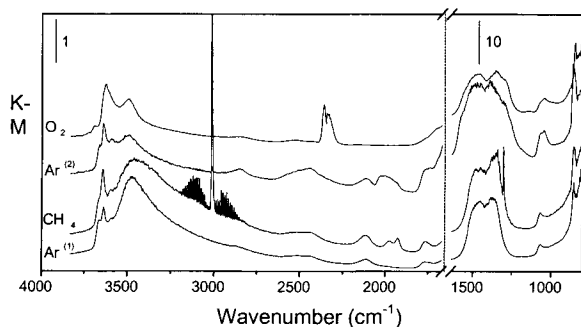
Figure 2: DRIFT spectra obtained at 400°C on Pt/CeO$_2$ (pre-reduced under H$_2$ flow at 400°C) during the following reaction cycle: Ar$^{(1)}$→CH$_4$→Ar$^{(2)}$→O$_2$ [14]

Table 1
Main IR bands observed during the sequential steps over Pt/CeO$_2$ at 400°C [14].

| 3690 cm$^{-1}$ | type I hydroxyl groups | Ce-OH |
|---|---|---|
| 3665 and 3640 cm$^{-1}$ | type II hydroxyl groups | H O / \ Ce Ce |
| c.a. 3480 cm$^{-1}$ | H-bonded hydroxyl groups | |
| 3200-2800, 1360-1250 cm$^{-1}$ | gaseous CH$_4$ | |
| 2390-2280 cm$^{-1}$ | gaseous CO$_2$ | |
| 2115 cm$^{-1}$ | Forbidden electronic transition on Ce$^{3+}$ $^2F_{5/2} \rightarrow {}^2F_{7/2}$ | |
| 2028-1928 cm$^{-1}$ | carbonyls on Pt | Pt-CO |
| 1070, 1380, 1460 cm$^{-1}$ | unidentate carbonates on ceria | Ce-O-C(=O)-O |
| 1300, 1560, 2850 cm$^{-1}$ | formate on ceria | Ce(O-)(O-)C—H |

ii) When CH$_4$ is flushed by Ar, most of the ceria adspecies (carbon-containing and hydroxyls) remain, while Pt carbonyl species are progressively removed.

iii) Upon switching to flowing O$_2$, the Pt carbonyl bands are quickly removed. The bands assigned to carbonates quickly decrease and then stabilize at lower levels than those of the originally reduced catalyst. The formate bands then start to decrease and ultimately disappear. The transient desorption of CO$_2$ is also demonstrated by the evolution of the characteristic rotation-vibration band centred at 2350 cm$^{-1}$. The type II OH groups disappear to the benefit of type I OH groups. This can be related to reoxidation of the ceria surface and to formate decomposition.

*Overall scheme of adspecies spillover*

From the IR study, it appears that in such a Pt/CeO$_2$ system, carbon is stored mainly as carbonyl, formate and carbonate species, and hydrogen is stored both as formate and hydroxyl groups. We now must determine by which chemical routes the gaseous methane is transformed into these adspecies accumulating both on the metal particles and on the support.

In CO oxidation on similar Pt/CeO$_2$ systems, the oxygen atoms provided by the reducible ceria are commonly assumed to spill over from the support to the metal to oxidize species adsorbed on the metal particles. Numerous indications are given about the role of lattice oxygen in ceria with platinum [20], the presence of linear or bridge carbonyls on platinum when CO$_2$ desorbs [18], and the role of Pt dispersion to increase the oxygen exchange between CO and CO$_2$ [21]. In these studies, the spillover process concerns only oxygen atoms mobile in and over ceria and exchangeable with Pt (mechanism described in figure 3), leading to oxidation or reduction according to the direction of the exchange.
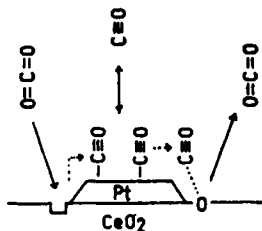


Figure 3 : Scheme of CO oxidation by spillover oxygen provided by the reducible ceria [20]

Other models concern water-gas shift [22] or steam reforming [23]. The latter is reported here as an example (where $\sigma$ represents an adsorption site on the metal):

$$CH_4 + \sigma = CH_{x,ads} + (4-x)H_{ads} \tag{1}$$

$$H_2O + Ce_3O_2 = 2CeO_2 + H_2 \tag{2}$$

$$2H_{ads} = H_2 + \sigma \tag{3}$$

$$CH_{x,ads} + 2CeO_2 = CO + \tfrac{x}{2}H_2 + Ce_2O_3 + \sigma \tag{4}$$
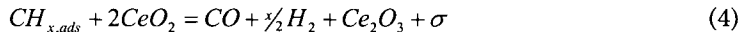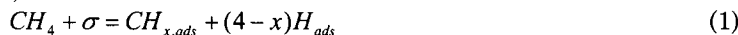
Reaction (4) suggests that ceria can be reduced by exchanging oxygen atoms directly with carbonaceous species issued from methane cracking on Pt. Reaction (1) corresponds to a group of elementary steps where x may vary within the range $1 \leq x \leq 4$. This partial dehydrogenation is indeed characteristic of methane decomposition on noble metals, which is recognized as less profound than over nickel [24]. This is directly proven by the specific patterns of H/D isotopic exchange reported for these metals : only single exchange (formation of CH$_3$D) for Pd, single to complete (formation of CH$_3$D and CD$_4$) for Pt and complete exchange (formation of CD$_4$) for Ni [25]. Reaction (4) could thus account for the sequential formation of formates and then of carbonates observed in our IR study. In fact,

according to Li et al. [18], formates are formed on partly reduced ceria while carbonates derive from CO adsorption on fully oxidized ceria.

The above model could apply for the present case of sequential methane cracking over $Pt/CeO_2$, except for reaction (2) which assumes that water is a reactant. This reaction assumes that ceria can react directly with the gas phase without platinum as a provider of reacting adspecies. The direct reactivity of ceria is generally described in terms of oxidation/reduction processes.

i) Ceria reduction is generally assumed to occur via reducing gases (CO, $H_2$, or hydrocarbon) activated over a noble metal phase in close contact with ceria [26,27]. In the absence of noble metal and at high temperature, however, the direct reduction of ceria by these reducing gases may also occur, either partially (at the surface) or totally (in the bulk). Thus, under hydrogen atmosphere, the reduction of $CeO_2$ remains restricted to the bulk formation of $Ce_2O_3$ according to Yao and Yu Yao [28]. Holmgren et al. [21] have shown that CO can react with ceria at 300°C, the uptake increasing linearly with the ceria surface area. Finally, a fresh sample of $CeO_2$ was found to be able to oxidize methane at 570°C [29].

ii) For ceria reoxidation, $H_2O$ is shown to form surface hydroxyl groups and $Ce^{4+}$ sites active for formate formation [18]. In contrast, the process of ceria oxidation by gaseous $O_2$ remains matter of debate, since there does not yet exist *in situ* surface spectroscopy able to identify the nature of activated surface species such as $O^-$, $O_2^-$ or $O_2^{--}$ [30]. Recently, the direct oxidation of ceria by $CO_2$ leading to the formation of residual carbonates was demonstrated [30].

Do all of these potential side reactions of ceria with the gas phase have to be considered in the present Pt/ceria system, or do the overall pathways only deal with the direct reaction of these gases with platinum, followed by spillover steps between metal and support?

To answer that question, the experimental transient outlet gas concentrations have been modelled by considering a comprehensive kinetic scheme that integrates the basic elementary steps revealed by the aforementioned IR study. In this scheme, summarized in Figure 4, the decomposition of methane on the
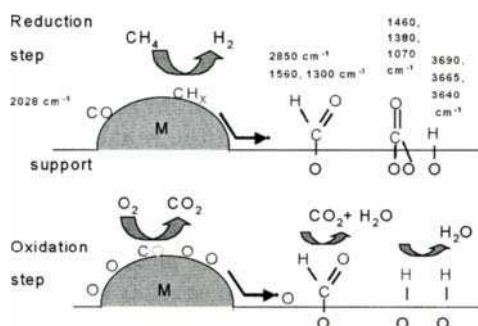


Figure 4 : Scheme of the two-step process over a catalyst which associates a noble metal dispersed on an active support [31], M = Pt, support = ceria

metal phase leads to the formation of hydrogen and to the storage of carbon as formates and carbonates on the support.

The corresponding elementary reactions can be proposed as follows, as discussed in a recent publication [31] :

$$CH_4 \text{ (g)} + Pt \rightleftharpoons CH_{x, Pt} + (4\text{-}x)H_{Pt} \rightleftharpoons C_{Pt} + 4H_{Pt} \qquad (5)$$

$$CH_4 \text{ (g)} + 4PtO \longrightarrow CO_2 + 2H_2O + 4Pt \qquad (6)$$

$$C_{Pt} + O_{Pt/supp} \longrightarrow CO_{Pt} \qquad (7)$$

$$CO_{Pt} + OH_{supp} \rightleftharpoons HCOO_{supp} \qquad (8)$$

$$2H_{Pt} \rightleftharpoons H_2 \text{ (g)} \qquad (9)$$

$$H_{Pt} + O_{supp} \rightleftharpoons OH_{supp} \qquad (10)$$
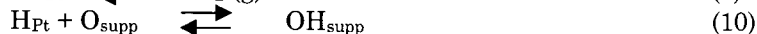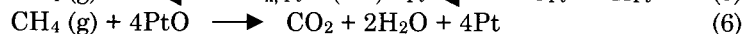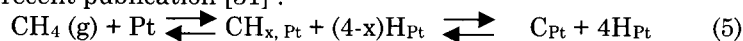
In this model, three kinetic steps describe the potential spillover processes between metal and support :

- Step 10 describes the formation of hydroxyls at the surface of the support. Under reducing atmosphere (methane), the hydrogen atoms provided by platinum (methane decomposition) react with the oxygen atoms available from the oxidized ceria. Since oxygen and hydrogen (and therefore hydroxyls) are very mobile at the ceria surface [32], the reaction is considered reversible and is assumed to occur at the metal-support interface.

- Step 8 is suggested by Li et al. [18], who consider that type I OH groups (corresponding to $Ce^{3+}$ or $Ce^{4+}$ linked to oxygen vacancies) are reactive enough to form formate adspecies with CO. Since no gaseous CO was formed, it can be deduced that adsorbed CO on Pt particles may rapidly react with ceria OH groups at the metal/support interface (or spill over onto the ceria surface) to produce the formate species which are detected very quickly after methane introduction.

- Step 7 is related to the formation of these CO adspecies following a process which remains unclear. First, the exact nature and composition of the carbonaceous deposits from methane cracking cannot be determined from DRIFT analysis (due to the overlapping C-H vibration from gaseous methane) and probably includes several degrees of hydrogen content, as indicated from the isotopic exchange experiments already mentioned. In addition, a complex dynamic formation of platinum carbonyls was revealed by the DRIFT study, suggesting the stepwise formation of multibonded species (1975 $cm^{-1}$), then of bridged bonded (1928 $cm^{-1}$), and finally of linear (2028 $cm^{-1}$) carbonyls, as expected from a metal surface progressively covered by accumulating CO (Figure 5). Step 7 must therefore be considered as an oversimplification of the actual elementary processes leading to CO formation. It is based on the reliable feature that a carbon atom comes from methane on Pt, and an oxygen atom is transferred directly or indirectly from ceria.

As written, this model assumes that before methane cracking starts, the platinum surface is essentially reduced and the ceria support is fully oxidized. Actually, a few oxidized Pt sites should also be considered to account for the fast and weak transient formation of $CO_2$ at the very beginning of $H_2$ production. This statement is related to the preceding process of catalyst regeneration during the

| Pt-CO (3) 2028 cm$^{-1}$: linear carbonyl |  |
| Pt-CO (2) 1975 cm$^{-1}$: bridged carbonyl |  |
| Pt-CO (1) 1928 cm$^{-1}$: multi-bonded carbonyl (edge and terrace sites) |  |
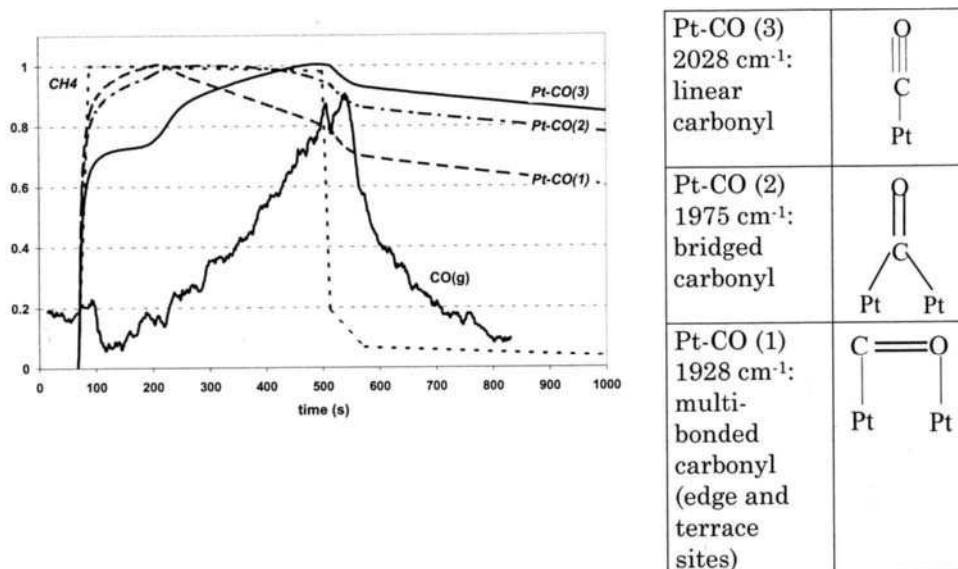
Figure 5 : Normalized changes in Pt-CO IR band intensities during the CH$_4$ step over Pt/CeO$_2$

oxidative regeneration step: gaseous oxygen chemisorbs dissociatively on platinum and then spills over onto the ceria support, both processes being fast according to Holmgren et al. [33].

The experimental data from Figure 1 are compared with the model curves in Figure 6. Adequate forms have been found for both methane and hydrogen curves (other products are not represented here). In particular, the long tailing of hydrogen desorption after the methane pulse is finished can be directly related to the reversibility of step 6.

As a conclusion of this first part dealing with hydrogen production under step transient conditions, it is clear that the simplified model described above cannot yet provide the true kinetic parameters related to the real adspecies. Further experimental and modelling studies are necessary if the elementary steps involved are to be described in more detail. Transient rsponses could be measured by the in situ IR technique and coupled with the model of the gas
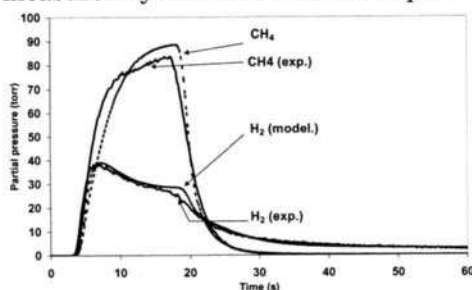


Figure 6: Outlet gas concentrations obtained during step I over a Pt/CeO$_2$ catalyst at 400°C compared with curves calculated according to the model.

phase. The introduction of diffusion reactions, for which the rates are beginning to be known for ceria [33], will give indications about the dispersion and the competition between adspecies.

## 3. SPILLOVER PHENOMENA DURING METHANE DRY REFORMING INTO SYNGAS

### 3.1. Case of nickel-based catalysts.

It is generally assumed that the active phase for $CO_2$ reforming of methane over nickel-based catalysts consists of metal particles coated with a layer of carbide-like nickel, $Ni_2C$ or $Ni_3C$, partly occupied by O atoms [13,35]. The carbon and oxygen atoms are respectively derived from methane cracking and from the dissociative adsorption of carbon dioxide on the metallic surface [34]. For silica supported catalysts, the support does not participate in the catalytic cycle. However, the metal/support interaction was found to control the nickel dispersion and morphology during the reduction period, which may indirectly affect the side reactions of coke formation [13]. In contrast, a major role of the support was generally postulated for other types of material, such as alumina or lanthana.

For lanthana, unique stability with time on stream was reported by Zhang et al. [35,36], while other formulae such as $Ni/Al_2O_3$, $Ni/CaO$ and $Ni/CaO/Al_2O_3$ presenting the same nickel loading (17 wt.%) continuously deactivated along the catalytic run.

In order to understand this specific behaviour of $Ni/La_2O_3$, a thorough study by high resolution transmission electron microscopy (TEM), *in situ* Diffuse Reflectance Infrared Fourier Transform spectroscopy (DRIFT), Steady State Isotopic Transient Kinetic Analysis (SSITKA) and Temporal Analysis of Products (TAP) was carried out on this catalyst as reported in [37].

The main features demonstrated were as follows :

i) As revealed by TEM/EDX, a thin layer (about 2 nm) decorating the nickel particles developed between the nickel and the lanthana phase after reduction. After a long period on stream (20 h), no major changes in catalyst morphology occurred, except that a few nickel particles were extracted from the lanthana support by carbon filaments.

ii) A pool of carbonate species (mostly dioxomonocarbonate $La_2O_2CO_3$) was directly and unambiguously revealed by isotopic transient DRIFT experiments under reaction conditions (700-800°C). Through modelling of the transient curves, it was calculated that about 300 $\mu mol/g_{cat}$ lanthanum oxide (or carbonate) decorated the nickel particles.

iii) As shown by the delay observed for the isotopic transients of gaseous CO in SSITKA experiments (Fig. 7), a much larger pool of CO precursors was found on the $Ni/La_2O_3$ than on a $Ni/SiO_2$ catalyst under similar operating conditions [34].
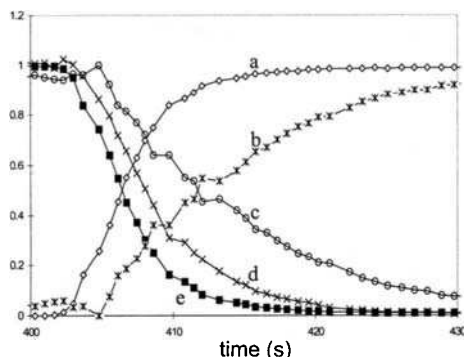
Figure 7. Normalized changes in isotopic concentration of the gas effluents after the $^{13}CO_2/^{12}CH_4/Ar/He$ to $^{12}CO_2/^{12}CH_4/Ar$ switch.
(a) $^{12}CO_2$; (b) $^{12}CO$; (c) $^{13}CO$; (d) He; (e) $^{13}CO_2$
Note that $CO_2$ curves superimposed with inert tracer He curves are not included for the sake of clarity [37].

For Ni/SiO$_2$, both CH$_4$ and CO$_2$ activations were assumed to occur directly on the metallic surface [34]. The measured accumulation of CO precursors was assigned to the carbon adspecies issued from methane cracking and to the oxygen adspecies issued from CO$_2$ dissociation into O and gaseous CO. The following scheme summarizes the related elementary steps :

$$CH_4 + Ni \rightleftharpoons NiC + 2\,H_2 \tag{11}$$
$$CO_2 + Ni \rightleftharpoons CO + NiO \tag{12}$$
$$NiC + NiO \longrightarrow CO + 2Ni \tag{13}$$
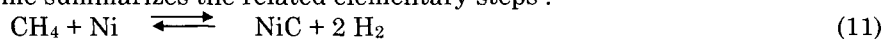
Step (11) was considered to be a fast step lumping together several elementary steps, largely reversible at 750°C and leading to the accumulation of dehydrogenated carbon monomers. Step (13) was assumed to be rate determining, in agreement with the absence of H/D isotopic effects [34].

For Ni/La$_2$O$_3$, such a mechanistic scheme could no longer apply, since a much larger accumulation of CO precursors was observed for a lower available surface of nickel [37]. A fairly good correspondence was found between the amount of CO precursors (225 μmol/g$_{cat}$) and the amount of lanthanum carbonates in equilibrium with the CO$_2$ atmosphere (300 μmol/g$_{cat}$). The storage of CO precursors outside the nickel surface, in the form of lanthanum carbonate, was therefore proposed. This led to the following mechanism:

$$CH_4 + Ni \longrightarrow NiC + 2\,H_2 \tag{14}$$
$$La_2O_2CO_3 + Ni \longrightarrow CO + NiO + La_2O_3 \tag{15}$$
$$NiC + NiO \longrightarrow CO + 2Ni \tag{16}$$
$$CO_2 + La_2O_3 \longrightarrow La_2O_2CO_3 \tag{17}$$
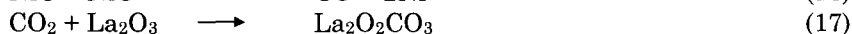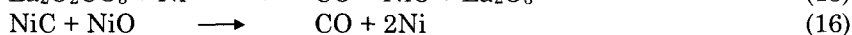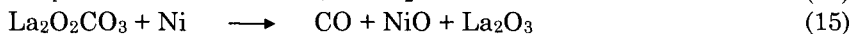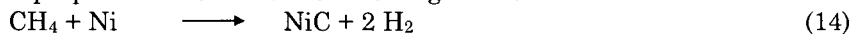
As such, step (15) represents a transfer of oxygen from the lanthanum carbonate adlayer to the Ni surface, which may be considered as a reacting intermediate spillover process slightly different from the usual concept as reported for Ni/SiO$_2$.

Steps (15,16) were found to be fast and solely controlled by the surface concentration of sites. Step (17), carbonate regeneration, was shown to be essentially irreversible under steady-state reaction conditions, since no accumulation of reversible CO$_2$ was detected by SSITKA (no delay between He and CO$_2$ responses in Fig. 7).

It was deduced from the above scheme that step (14), methane cracking, was now rate determining, unlike step (16) in the case of Ni/SiO₂, in agreement with the kinetic isotopic effect (KIE) observed earlier over the same Ni/La₂O₃ catalyst [38]. A plausible explanation for this specific mechanistic feature was that the decoration of nickel particles by the lanthana phase decreased the surface concentration of Ni sites available for cracking and release of H₂ molecules. Note that the spillover transfer in step (15) was fast enough to not limit the overall reaction rate. The close contact between the adlayer carbonate phase and the nickel particle may have facilitated that transfer.

This tight coating of nickel particles by the adlayer of lanthanum carbonate was also considered to account for the unique stability, namely coking resistance, of this catalyst. Due to the fast, continuous supply of oxygen atoms from the decomposition of the carbonate adlayer, the migration of carbon through the nickel particles and its further recombination as an encapsulating veil around the particle was assumed to be hindered.

Thus, in opposition to the "monofunctional" mechanism proposed for Ni/SiO₂, a "bifunctional" mechanism was proposed for Ni/La₂O₃, controlled by a spillover-like transfer between a thin overlayer of lanthana carbonate and the surface of nickel particles.

### 3.2. Case of noble metal-based catalysts.

Different types of spillover process were revealed in a similar kinetic study carried out over Ru-based catalysts [39]. Alumina, silica and high surface area graphite (HSAG) supports were used and their specific roles in the dry reforming process were analysed on the basis of transient responses obtained by both
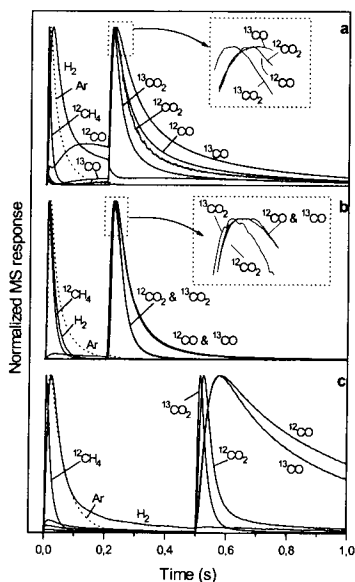


Figure 8 : Pump-probe TAP experiments, $^{12}CH_4$/Ar (9/1) followed by $^{13}CO_2$, on (a) Ru/Al₂O₃, (b) Ru/SiO₂ and (c) Ru/HSAG at 823 K.

SSITKA and TAP [40]. Typical TAP curves obtained after sequentially pulsing $^{12}CH_4$ and $^{13}CO_2$ are reported in Figure 8.

### Role of the ruthenium phase.

*Methane activation.* TAP results (Figure 8) showed that $H_2$ was formed on the $CH_4$ pulse regardless of the support, demonstrating that methane was activated on Ru. In addition, this activation was found to be irreversible, since no $^{12}CH_4$ was detected in SSITKA experiments upon switching from $^{12}CH_4$ to $^{13}CH_4$. This irreversible cracking could be considered as a specific property of noble metals, as reported in the first part of the present paper over Pt.

For at least one catalyst, namely $Ru/SiO_2$ (for which no support/spillover effect is expected), the selectivity of methane cracking to hydrogen is 100% during the TAP methane pulse. The methane cracking step can therefore be written as:

$$CH_4 + x\ Ru \longrightarrow Ru_{x-4}\text{-}C + 4\ Ru\text{-}H \tag{18}$$
$$2\ Ru\text{-}H \rightleftarrows 2\ Ru + H_2 \tag{19}$$

Again, step (18) represents a global reaction that does not exclude fast and step-wise intermediate dehydrogenation steps. From SSITKA, a steady-state accumulation of one active C for two Ru surface atoms was found for the most stable catalysts ($Ru/Al_2O_3$ and $Ru/HSAG$). Such $Ru_2C$ stoichiometry would be specific to ruthenium, in opposition to the $Ni_3C$ carbide stoichiometry reported in [34].

*Carbon dioxide activation.* The occurrence of the RWGS reaction, regardless of the type of support, showed that $CO_2$ was activated on Ru. In addition, under a $^{13}CH_4+^{12}CO_2$ reaction mixture, the four labelled and unlabelled CO and $CO_2$ species were produced, which demonstrated that the dissociation of $CO_2$ took place reversibly. Thus, the possible steps of carbon dioxide activation can be written as:

$$CO_2 + Ru \rightleftarrows Ru\text{-}CO_2 \tag{20}$$
$$Ru\text{-}CO_2 + Ru \rightleftarrows Ru\text{-}CO + Ru\text{-}O \tag{21}$$
$$Ru\text{-}CO + Ru \rightleftarrows Ru\text{-}C + Ru\text{-}O \tag{22}$$
$$Ru\text{-}CO \rightleftarrows CO + Ru \tag{23}$$
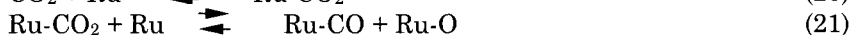
Here, no spillover transfer from the metal phase to the support is yet considered. However, considering the probable limited mobility of C and carbonyl adspecies, obvious surface oxygen transfer, and therefore diffusion parameters, should be considered for any process modelling. No surface accumulation of $CO_2$ was detected from the transient curves, indicating that step (21) is faster than step (20), both steps probably merging into only one kinetically significant step:

$$CO_2 + 2\ Ru \rightleftarrows Ru\text{-}CO + Ru\text{-}O \tag{24}$$
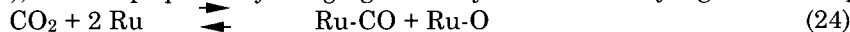
On $Ru/SiO_2$ and $Ru/HSAG$, all of these steps were found to be in fast equilibrium from the observed isotopic scrambling equilibrium. In contrast, for $Ru/Al_2O_3$, isotopic concentrations far from equilibrium were obtained, in agreement with the lesser extent of the RWGS reaction with respect to $Ru/SiO_2$

and Ru/HSAG. As will be discussed later, a significant spillover effect between alumina and ruthenium particles will have to be considered to account for such behaviour.

In TAP experiments, when pulsing $^{13}CO_2$ after $^{12}CH_4$ on $Ru/Al_2O_3$, $Ru/SiO_2$ and Ru/HSAG, $^{12}CO$ and $^{13}CO$ desorbed simultaneously (Figure 8 a,b,c). So, although according to the above scheme CO is formed both from $CO_2$ dissociation (step 24) and from surface carbon oxidation (reverse step 22), the desorption of CO (step 23) is the slowest step among equilibria (20 to 23). Step 23 must, however, be fast enough at this temperature to prevent the accumulation of large amounts of adsorbed CO. This CO would have been detected by *in situ* DRIFT spectroscopy. Note that on Ni catalysts, a marked difference in the two $^{12}CO$ and $^{13}CO$ TAP responses allowed us to conclude that the reverse step (22) of carbon oxidation limited the reforming process [40,41].

For $Ru/SiO_2$ and Ru/HSAG, no delay was observed between $CO_2$ and CO decays in SSITKA experiments, indicating that the oxygen coverage of ruthenium was low. Again, this supports the conclusion that steps (20 to 22) are fast.

On $Ru/Al_2O_3$, a significant $CO_2$ decay with respect to CO was found, which was ascribed to a support effect, as will be discussed later.

*$H_2O$ production.* In order to account for the side production of water, the following steps should be included in the mechanism for Ru particles supported on inert materials ($SiO_2$, HSAG):

$$Ru\text{-}O + Ru\text{-}H \rightleftharpoons Ru\text{-}OH + Ru \qquad (25)$$
$$2\,Ru\text{-}OH \rightleftharpoons Ru\text{-}O + Ru + H_2O \qquad (26)$$
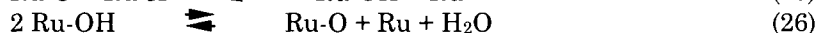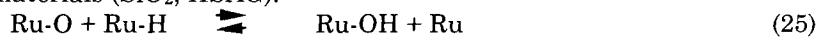
The combination of these steps with the previous ones leads to the overall RWGS equilibrium. Evidently, the $H_2$ selectivity of the reforming reaction depends directly on the stability and mobility of the Ru-O adspecies, which reacts competitively either with surface carbon (step 22) to form CO, or with surface hydrogen (step 25) to form water. For these RWGS steps, however, the rapidly achieved equilibria clearly indicated that no surface diffusion of oxygen or hydrogen species might have significantly limited the related rates. Again, the fast equilibria (25 and 26) were not expected to lead to a large accumulation of intermediates such as Ru-OH hydroxyls, which,in addition to the structural OH groups of the supports, would have been detected by *in situ* DRIFT.

### Role of the support

*Alumina.* In contrast to the other supports, $\gamma$-alumina was found to present a large concentration of basic to acidic hydroxyl groups under the reforming conditions, as demonstrated by *in situ* DRIFT (3765, 3715, 3685, 3670 $cm^{-1}$). A residual production of $H_2$ and CO was observed on $Ru/Al_2O_3$ when the reacting feed was switched to diluted methane at 823 K. In addition, a larger consumption of alumina OH groups was observed during the same transient sequence, by comparison to the consumption due to support dehydration under inert flow. Also, a long $H_2$ tailing and slow $^{12}CO$ desorption took place when the pulse of

$^{12}CH_4$ was introduced in TAP experiments (Figure 8 a). All of these results indicated that, in addition to the processes specifically related to the ruthenium phase, a continuous reverse spillover of OH groups from the alumina interface to the ruthenium surface took place as follows :

$$Al\text{-}OH + Ru \rightarrow RuOH + Al \tag{27}$$
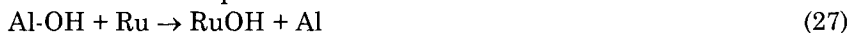
These OH groups provide through equilibrium (25) a continuous second source of i) H atoms that desorb as $H_2$ following step (19) and ii) O atoms that react with the carbon atoms generated by $CH_4$ dissociation, producing CO by the reverse steps (22 and 23).

Within this scheme, the TAP experiments (Figure 8a) can now fully be interpreted. First of all, the continuous flux of $^{12}CO$ observed after the $^{12}CH_4$ pulse arose from the oxidation of $^{12}C$ deposited after methane cracking, and was combined with the flux of $^{13}CO$ after the pulse of $^{13}CO_2$, the latter arising from $^{13}CO_2$ dissociation. Some $^{13}C$ formed from $^{13}CO$ dissociation (step 22) reacted with O from OH groups to give the slight flux of $^{13}CO$ also observed after the methane pulse. Second, the tailing pulse of $H_2$ observed after the methane pulse was comprised of the main flux coming directly from methane cracking (the narrow part of the pulse) and the hydrogen continuously fed by the reverse spillover of alumina OH groups (the tailing part). This tailing production of hydrogen decreased abruptly during the $CO_2$ pulse due to the large production of surface oxygen from $CO_2$ decomposition. This production of surface oxygen temporarily hindered OH dissociation over Ru (displacement of equilibrium 25).

This reverse spill-over of alumina OH groups was confirmed by observing that after a series of water vapour pulses at 823 K, the $H_2$ tailing as well as the continuous CO production were found to be markedly increased.

This continuous feeding of Ru-OH from alumina also explained the higher $H_2$ selectivity observed on alumina originated from the displacement toward the Ru-H species of equilibrium (25). This displacement also increased the surface concentration of Ru-O species. This, in turn, favoured CO formation at the expense of carbon polymerisation and further graphitisation, in agreement with the high stability observed on this catalyst [39].

A similar process of spillover between alumina and metal, but via migration of water molecules, was recently proposed by Wang et al. for the partial oxidation of methane over $Rh/Al_2O_3$ [42].

A second major property of alumina for $Ru/Al_2O_3$ was its strong, direct interaction with $CO_2$ similar to that observed for the $Ni/La_2O_3$ catalyst reported above. We note that :

i) a delay of $CO_2$ decay with respect to CO was observed in SSITKA, and

ii) the formation of carbonate and/or carboxylate under reaction conditions was observed by in situ DRIFT.

Such an interaction with alumina has been written as follows for bidentate carbonate and carboxylate, respectively :

$$2\ Al\text{-}OH + CO_2 \rightleftharpoons Al\text{-}O\text{-}CO\text{-}O\text{-}Al + H_2O \tag{28}$$

$$4\ Al\text{-}OH + 2\ CO_2 \rightleftharpoons 2\ Al\text{-}O\text{-}CO\text{-}OH + Al\text{-}O\text{-}Al + H_2O \tag{29}$$
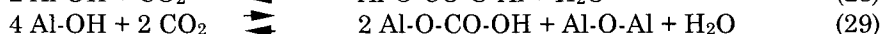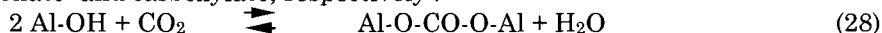
Note that the absence of decoration of alumina over the Ru particles prevented any direct transfer from the carbonate/carboxylate phases to the metal particles such as that which existed for the $Ni/La_2O_3$ system.

*Graphite.* The large $H_2$ tailing that followed the methane pulse in TAP (Figure 8c) and the very low $H_2$ selectivity (5%) on Ru/HSAG were well accounted for by the accumulation of hydrogen-rich $CH_x$ species over the graphite support and/or over the Ru phase. So, when the running catalyst was purged by He, these accumulated species decomposed into tailing gaseous hydrogen. Under the transient TAP conditions, the dehydrogenated support acted as a hydrogen trap via $CH_x$ entities (formed either directly from the reaction of gaseous hydrogen with surface carbon or from the spillover of $CH_x$ species from the Ru to the graphite surface). Under steady-state conditions, the spillover of $CH_x$ entities to the support and/or the availability of a second source of hydrogen at the Ru particles/support interface were assumed to hinder carbon graphitisation and explain the prominent stability of this catalyst [39].

*Silica.* As already stressed, no support effect was detected for silica, as expected from a relatively inert material with stable hydroxyl groups under steady-state or transient conditions. This led to a larger accumulation of surface carbon over the Ru phase and, therefore, to a marked trend toward polymerisation and graphitisation resulting in fast deactivation [39].

An improved reverse spillover effect was found in the similar case of Ru/MgO-HSAG [43]. Here, the magnesia located at the interface of Ru particles and the graphite surface was found to constitute a permanent source of oxygen atoms via the decomposition of carbonates and hydroxyl groups able to eliminate the toxic carbon species accumulating over the metal particles.

As a conclusion of this second part dealing with spillover phenomena in syngas generation, the kinetic behaviour of various Ni- and Ru-supported catalysts was shown to be determined essentially by the chemistry of the metallic phase. Advanced mechanistic schemes specific to the metal (noble or non-noble) were derived, with different rate-limiting steps and surface coverages of oxygen. Except with an inert silica support, however, major support effects were also found to contribute to the overall process, with prominent effects on catalyst stability. These supports effects include i) the transfer of oxygen from gaseous $CO_2$ to the Ni particles via a lanthanum carbonate adlayer decorating the metal particles ($Ni/La_2O_3$), and ii) the continuous reverse spillover of alumina hydroxyl groups, the accumulation of $CO_x$ species on the alumina surface ($Ru/Al_2O_3$) and of $CH_x$ species on the graphite (Ru/HSAG and Ru/MgO-HSAG).

## 4. CONCLUSION

Either for non steady-state or steady state processes, most of the catalytic systems related to this renewed field of hydrogen generation are shown to be strongly controlled by transfer/spillover phenomena between the active metal and support phases. From this combination of stoichiometric and catalytic steps, new reactor concepts may be proposed for small-to-large scale fuel cell application.

## REFERENCES

[1]   C. Song, Am. Chem. Soc., Div. Pet. Chem. Prep., 45 (2000) 159
[2]   M.A. Pena, J.P. Gomez, J.L.G. Fierro, App. Cat. A, 144 (1996) 7.
[3]   J. N. Armor, App. Cat., A 176 (1999) 159.
[4]   N.Z. Muradov, Energy Fuels, 12 (1998) 41.
[5]   T. Zhang, M. D. Amiridis, Appl. Catal. A, 167 (1998) 161.
[6]   T. Ishihara, Y. Miyashita, H. Iseda, Y. Takita, Chem. Lett., 2 (1995) 93.
[7]   K. Otsuka, T. Seino, S. Kobayashi, S. Takenaka, Chem. Lett., 11 (1999) 1179.
[8]   B. Monnerat, L. Kiwi-Minsker, A. Renken, 16th International Symposium on Chemical Reaction Engineering, 2000 Cracow, Powland.
[9]   J.-W. Snoeck, G.F. Froment, M. Fowles, J. Catal. 169 (1997) 240; J.-W. Snoeck, G.F. Froment, M. Fowles, J. Catal., 169 (1997) 250.
[10]  R. Aiello, J.E. Fiscus, H.C. Zur Loye, M.D. Amiridis, Appl. Catal. A 192 (2000) 227.
[11]  T.V. Choudhary, D.W. Goodman, Catal. Lett., 59 (1999) 93.
[12]  T.V. Choudhary, D.W. Goodman, J. Catal., 192 (2000) 316.
[13]  V.C.H. Kroll, H.M. Swaan, C. Mirodatos, J. Catal., 161 (1996) 409.
[14]  E. Odier, C. Marquez-Alvarez, Y. Schuurman, H.W. Zanthoff, C. Mirodatos, accepted for the 6th Natural Gas Conversion Symposium, Alaska, june 17-21 2001.
[15]  M. Shelef, R.W. MacCabe, Catal. Today, 62 (2000), vol 1, 35.
[16]  M. Boaro, C. de Leitenburg, G. Dolcetti, A. Trovarelli, J. Catal., 193 (2000) 338.
[17]  A. Laachir, V. Perrichon, A. Badri, J. Lamotte, E. Catherine, J.C. Lavalley, J. El Fallah, L. Hilaire, F. le Normand, E. Quéméré, G.N. Sauvion, O. Touret, J. Chem. Soc. Faraday Trans., 87 (1991) 1601.
[18]  C. Li, Y. Sakata, K. Domen, K. Maruya, T. Onishi, J. Chem. Soc. Faraday Trans., 85 (1989) 929 & 1451.

[19] J.A. Anderson, J. Chem. Soc. Faraday Trans., 88 (1992) 1197.

[20] T. Jin, T. Okuhara, G.J. Mains, J.M. White, J. Phys. Chem., 91 (1987) 3310.

[21] A. Holmgren, B. Andersson, D. Duprez, Appl. Catal., B, 22 (1999) 215.

[22] T. Bunluesin, R.J. Gorte, G. Graham, Appl. Catal.,, B 15 (1998), 107.

[23] R. Craciun, B. Shereck, R.J. Gorte, J. Catal. Lett. ,51 (1998), 149.

[24] A. Chak-Tong, N. Ching-Fai, L. Meng-Sheng, J. Catal., 185 (1999) 12.

[25] C. Mirodatos, V. Ducarme, H. Mozzanega, A. Holmen, J. Sanchez-Marcano, Q. Wu, G.A. Martin, "Natural Gas Conversion" (Holmen, A. et al. Eds), Studies in Surface Science and Catalysis, Elsevier, Amsterdam 61 (1991) 41.

[26] H. Cordatos, T. Bunluesin, J. Stubenrauch, J.M. Vohs, R.J. Gorte, J. Phys. Chem., 100 (1996) 785.

[27] E.S. Putna, T. Bunluesin, X.L. Fan, R.J. Gorte, J.M. Vohs, R.E. Lakis, T. Egami, Catal. Today, 50 (1999) 343.

[28] H.C. Yao, Y.F. Yu Yao, J. Catal., 86 (1984) 254.

[29] C. Bozo, N. Guilhaume, E. Garbowski, M. Primet, Catal. Today, 59 (2000) 33.

[30] Y. Madier, C. Descorme, A.M. Le Govic, D. Duprez, J. Phys. Chem., B 103 (1999) 50.

[31] E. Odier, Y. Schuurman, H. Zanthoff, C. Millet, C. Mirodatos, accepted for the 3rd International Symposium on Reaction kinetics and the development and operation of catalytic processes, Oostende, april 22-25 2001.

[32] D. Duprez, D. Martin, J. Barnier, Lett. Sc. Chim. 67 (1998) 14.

[33] A. Holmgren, D. Duprez, B. Andersson, J. Catal. 182 (1999) 441.

[34] V.C.H. Kroll, H.M. Swaan, S. Lacombe, C. Mirodatos, J. Catal., 164 (1996) 387.

[35] Z.L. Zhang, X.E. Verykios, Appl. Catal., 138 (1996) 109.

[36] Z.L. Zhang, X.E. Verykios, S.M. MacDonald, S. Affrosman, J.Phys. Chem., 100 (1996) 744; Z.L. Zhang, X.E. Verykios, J. Chem. Soc., Chem Com. (1995) 71.

[37] A.. Slagtern, Y. Schuurman, C. Leclercq, X. Verykios, C. Mirodatos, J. Catal., 172 (1997) 118.

[38] Z.L. Zhang, X.E. Verykios, 109; Catal. Lett., 38 (1996) 175.

[39] P. Ferreira-Aparicio, C. Márquez-Alvarez, I. Rodríguez-Ramos, Y. Schuurman, A. Guerrero-Ruiz, C. Mirodatos, J. Catal., 184 (1999) 202.

[40] Y. Schuurman, C. Marquez-Alvarez, V.C.H. Kroll, C. Mirodatos, Catalysis Today, 46 (1998) 107.

[41] Y. Schuurman, V.C.H. Kroll, P. Ferreira-Aparicio, C. Mirodatos, Catalysis Today 38 (1997) 129.

[42] D. Wang, O. Dewaele, A.M. de Groote, G.F. Froment, J. Catal., 159 (1996) 418.

[43] Y. Schuurman, C Mirodatos, P. Ferreira-Aparicio, I. Rodríguez-Ramos, A. Guerrero-Ruiz, Catal. Let., 66 (2000) 33.

# Involvement of support hydrogen in the $H_2$-$D_2$ isotopic exchange on sulfide catalysts

A. Scaffidi[a], L. Vivier[b], A. Travert[c], F. Maugé[c], S. Kasztelan[d], C. Scott[a] and G. Pérot[b]

[a]Centro de Catálisis Petróleo y Petroquímica – Escuela de Química
Facultad de Ciencias – Universidad Central de Venezuela
Apartado Postal 47102, Los Chaguaramos, Caracas 1020A, Venezuela
[b]Laboratoire de Catalyse en Chimie Organique UMR CNRS 6503
Faculté des Sciences – Université de Poitiers
40, avenue du Recteur Pineau, 86022 Poitiers Cedex, France
[c]Laboratoire de Catalyse et Spectrochimie UMR CNRS 6506
ISMRA – Université de Caen
6, boulevard du Maréchal Juin , 14050 Caen, France
[d]Institut Français du Pétrole
1 et 4, avenue de Bois Préau, 92852 Rueil-Malmaison Cedex, France

HD isotopic exchange experiments carried out over sulfided catalysts showed that part of the exchangeable hydrogen measured by isotopic dilution came from the support and depended on the pretreatment conditions. This hydrogen was essentially present as $H_2S$ adsorbed on the alumina support. $D_2$ (and $D_2S$) adsorption followed by FTIR confirmed the involvement of support hydrogen.

## 1. INTRODUCTION

Hydrodesulfurization and hydrodenitrogenation are industrially very important reactions which occur on sulfided $CoMo/Al_2O_3$ and $NiMo/Al_2O_3$ catalysts in the presence of hydrogen and hydrogen sulfide. These reactions involve various steps including hydrogenation and carbon-heteroatom bond cleavage, in which both hydrogen and hydrogen sulfide can play a role. To identify the mechanisms of these reactions, the process of adsorption (and of activation) of $H_2$ and of $H_2S$ must be well understood.

The isotopic exchange between $H_2$ and $D_2$ (and in particular the isotopic dilution of hydrogen in $D_2$) makes it possible to measure the amount of the hydrogen present on sulfides [1-3] and supported sulfides [4-8]. However, in the case of supported sulfides the amount of hydrogen preadsorbed on the solid measured by this method was much greater than on bulk sulfides, which is in accordance with results obtained by other methods [2,5,9-11].

The aim of this work was to demonstrate the contribution of the support to the amount of catalyst hydrogen which can be exchanged with gas phase hydrogen as well as to understand the process of the exchange phenomenon.

## 2. EXPERIMENTAL

### 2.1. Isotopic exchange reactions

The H-D isotopic exchange reaction between $H_2$ and $D_2$ was carried out at 80°C (NiMo catalysts) or 35°C (CoMo catalysts) in a 72 cm$^3$ recycling reactor. The NiMo/Al$_2$O$_3$ commercial catalyst contained 2.9 wt% NiO and 12.5 wt% MoO$_3$ deposited on alumina (230 m$^2$.g$^{-1}$). The catalyst was presulfided *in situ* with a flow of $H_2$ (90%) and $H_2S$ (10%) at 400°C for 15 hours. After sulfidation at 400°C, and before the H-D exchange reaction, the catalysts underwent two different pretreatments : they were either cooled down to 80°C in the presence of the sulfidation mixture (pretreatment **1**) or treated for 1h at different temperatures and cooled down to 80°C under helium (pretreatment **2**). The amount of desorbed $H_2S$ was measured by iodometry during pretreatment **2**. The reactants ($H_2$ plus $D_2$ ; 0.5 bar of each) were introduced into the reactor and the recycling pump was started.

Two series of sulfided Ni or Co promoted molybdenum on alumina catalysts were prepared by incipient wetness impregnation in order to have the same amount of Mo (8 wt %) and various loadings of Ni or Co. Their preparation and catalytic activity in the hydrodesulfurization of dibenzothiophene were reported elsewhere [12].

The $H_2$/HD/$D_2$ reaction mixture was analyzed by gas chromatography using a column of alumina impregnated with MnCl$_2$ and maintained at -196°C. The amount of exchangeable hydrogen on the catalyst was calculated by assuming that the H-D scrambling equilibrium was obtained at the end of the experiments and that H and D atoms were equally distributed in the gas phase and on the catalyst. All the details concerning the apparatus and procedure as well as the calculations were published elsewhere [6].

### 2.2. Dissociation of D$_2$ or D$_2$S followed by FTIR spectroscopy.

The catalyst was presulfided in the IR cell under dynamic conditions with a flow of $H_2$ (85%) and $H_2S$ (15%) at 400°C for 2.5 hours. After sulfidation the catalyst underwent a helium pretreatment for 1 hour at 400°C. Then, the temperature was decreased at 5°C.min$^{-1}$ down to 80°C for $D_2$ adsorption experiments. The exchange reaction with $D_2$ was carried out at 80°C with a flow of $D_2$ (50%) and He (50%) under atmospheric pressure. The dissociation of $D_2$ was followed *in situ* by IR spectroscopy ; the spectra were recorded with a Fourier Transform Magna IR spectrometer (Nicolet) with a resolution of 4 cm$^{-1}$.

## 3. RESULTS AND DISCUSSION

In a previous study on the isotopic exchange between $H_2$ and $D_2$ it was found that the reaction was much faster on the $NiMo/Al_2O_3$ catalyst than on its support, both of which had been sulfided and pretreated under the same conditions [6]. The isotopic exchange between $H_2$ and $D_2S$ indicated that both reactants have probably a common mode of dissociation involving the same catalytic centres as described in Eqs (1) and (2) [13, 14]. It was assumed that surface sulfur atoms and sulfur vacancies were involved in the heterolytic dissociation of hydrogen.

$$H_2 + \ast{-}V + \bullet{-}S^{2-} \rightleftharpoons \ast{-}H{-} + \bullet{-}SH{-} \qquad (1)$$

$$H_2S + \ast{-}V + \bullet{-}S^{2-} \rightleftharpoons \ast{-}SH{-} + \bullet{-}SH{-} \qquad (2)$$

Compared to the amount generally reported in the literature, the unexpected large amount of exchangeable hydrogen found on the sulfided $NiMo/Al_2O_3$ catalyst after pretreatment 1 (corresponding to a H/Mo atomic ratio around 3) was shown to be due to a large extent to hydrogen present on the support. The amount of exchangeable hydrogen present on the active phase represented less than about 10% of the total amount and the alumina support could be considered as an actual reservoir for hydrogen [7].

### 3.1. $H_2$-$D_2$ isotopic exchange on sulfided $NiMo/Al_2O_3$.

Considering that the exchange with the support alone was very slow, we supposed that the hydrogen of the support was exchanged through a spillover process with the gas phase hydrogen, which could only dissociate if the active phase was present. As expected, the amount of exchangeable hydrogen present on the catalyst depended on the pretreatment undergone by the catalyst before the exchange reactions. Different experiments carried out with a sulfided $NiMo/Al_2O_3$ catalyst showed that the rate of the formation of HD resulting from the $H_2$-$D_2$ exchange reaction increased (Fig. 1) while the amount of preadsorbed exchangeable hydrogen decreased with increasing pretreatment temperature (Fig. 2).

The amount of $H_2S$ desorbed during pretreatment 2 at different temperatures (Fig. 2) was measured by iodometry. It appeared that there was a good correlation between the amount of exchangeable hydrogen and the amount of titrated $H_2S$. Pretreatment 2 led to the desorption of a large amount of hydrogen essentially present at the surface as adsorbed $H_2S$ (about 75 %).
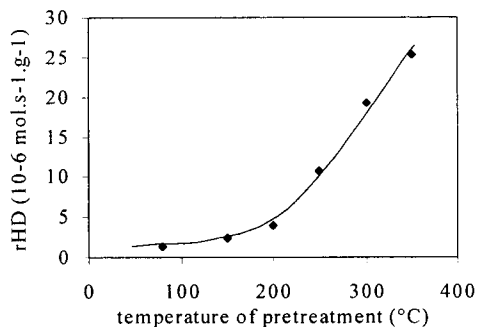
Fig. 1. Effect of the temperature of pretreatment under He on the rate of formation of HD by $H_2$-$D_2$ exchange on sulfided $NiMo/Al_2O_3$.
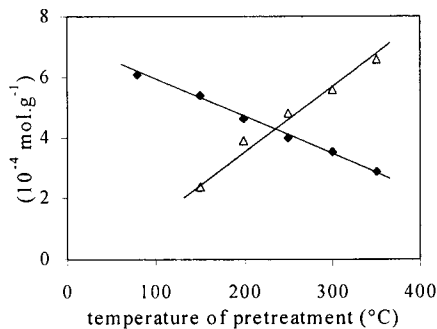
Fig. 2. Effect of the temperature of pretreatment under He on the amount of hydrogen preadsorbed on the surface of sulfided $NiMo/Al_2O_3$ (♦) and on the amount of desorbed $H_2S$ titrated by iodometry (△).

## 3.2. FTIR experiments on sulfided $NiMo/Al_2O_3$.

FTIR experiments confirmed the contribution of the hydrogen of the support (hydroxyl group of alumina) to the exchange with the deuterium in the gas phase. They proved also that the presence of the active phase was necessary for this exchange to occur. The disappearance of OH groups ($v = 3580$ $cm^{-1}$) accompanied by the formation of OD species ($v = 2640$ $cm^{-1}$) was observed in the case of $NiMo/Al_2O_3$ catalysts (Fig. 3) while OD bands were hardly detected on pure sulfided alumina under the same conditions (not shown).
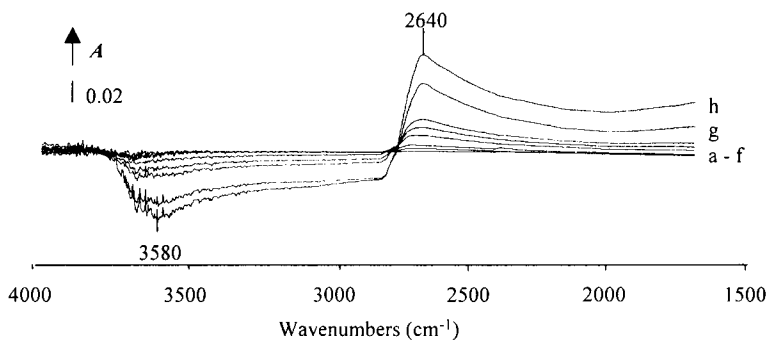


Fig. 3. Subtraction FTIR spectra of sulfided $NiMo/Al_2O_3$ under flowing $D_2$ at 80°C. Time of exposure : 0-1 min (a) ; 2 min (b) ; 3 min (c) ; 5 min (d) ; 10 min (e) ; 15 min (f) ; 60 min (g) ; 120 min (h). $A$ : absorbance.

The comparison of the number of OD which appeared with the number of OH which disappeared was not straightforward. There was, however, a linear correlation between the intensities of the two bands and no formation of new OD groups could be evidenced when the catalyst was in the presence of $D_2$.

This indicates that deuterium species resulting from the dissociation of $D_2$ on the active phase migrate by spillover to alumina to form OD groups while H species, initially present on the support as hydroxyl groups, follow the reverse route and desorb from the active phase as HD.

On the other hand, the formation of OD groups by dissociation of $D_2S$ on pure alumina was very fast, even at room temperature, thus showing the easiness of $D_2S$ (or $H_2S$) dissociation on alumina, even in the absence of the NiMo sulfide active phase. In a previous study [7], it was shown that the presence of $H_2O$ traces increased the rate of H-D exchange and it was concluded that $H_2S$ present in very small amounts could play the same role as water even if $H_2S$ inhibited the dissociation of $H_2$ ($D_2$) on the active phase when it was present in larger amounts. The exchange of hydrogen atoms between $H_2$ ($D_2$) and hydroxyl groups of alumina as well as the hydrogen isotopic exchange between $H_2$ and $D_2S$ are in favour of a heterolytic dissociation of $H_2$ on sulfide catalysts. In the H-D exchange process between $D_2$ in the gas phase and the hydroxyl groups of alumina, $H_2S$ could serve as a "shuttle molecule" to convey H (D) atoms between the support and the active phase as shown in the following scheme (reactions (3)-(9)) :

a) On the active phase :

$$D_{2(gas)} + Mo\square + MoS^{2-} \quad \rightarrow \quad MoD^- + MoS^{2-}D^+ \tag{3}$$

$$H_2S + Mo\square + MoS^{2-} \quad \rightarrow \quad MoSH^- + MoS^{2-}H^+ \tag{4}$$

$$MoSH^- + MoS^{2-}D^+ \quad \rightarrow \quad Mo\square + MoS^{2-} + HDS_{(gas)} \tag{5}$$

b) On the support :

$$HDS_{(gas)} + Al\square + AlO^{2-} \quad \rightarrow \quad AlSH^- + AlO^{2-}D^+ \tag{6}$$

$$AlSH^- + AlO^{2-}H_s^+ \quad \rightarrow \quad Al\square + AlO^{2-} + HH_sS_{(gas)} \tag{7}$$

c) On the active phase :

$$HH_sS_{(gas)} + Mo\square + MoS^{2-} \quad \rightarrow \quad MoSH^- + MoS^{2-}H_s^+ \tag{8}$$

$$MoD^- + MoS^{2-}H_s^+ \quad \rightarrow \quad Mo\square + MoS^{2-} + DH_{s(gas)} \tag{9}$$
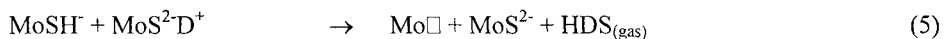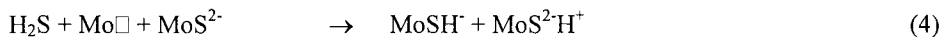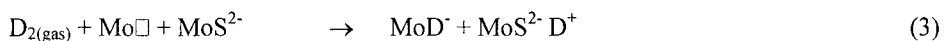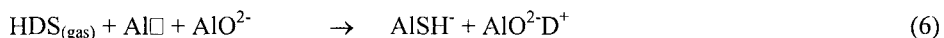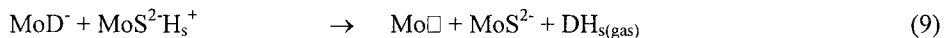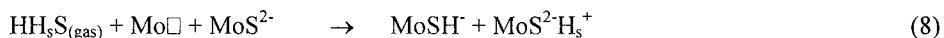
$D_2$ and $H_2S$ from the gas phase are heterolytically dissociated on the centers composed of a Mo vacancy and a sulfur anion (Eqs. (3) and (4)). Then the isotopic exchange and associative desorption of HDS can occur as shown in Eq. (5). Desorbed HDS can readsorb on the support (Eq. (6)), exchange $H^+$ with $H^+$ coming from the support (represented by $H_s^+$) and $HH_sS$ can eventually desorb (Eq. (7)). This new species will then adsorb on the active phase (Eq. (8)) and a HD species with a hydrogen atom coming from the support can desorb (Eq. (9)).

36

### 3.3. Promoter effect

The effect of promoters (Co or Ni) on both the amount of preadsorbed exchangeable hydrogen and the rate of H-D exchange between $H_2$ and $D_2$ was also examined. Two series of molybdenum catalysts promoted by nickel or cobalt were characterized by their activity in the hydrodesulfurization of dibenzothiophene [12]. Both series exhibited the expected synergy effect. In accordance with previous results reported in the literature [15 and references therein] the catalyst with a (promoter)/(promoter + molybdenum) atomic ratio of about 0.3 had an activity which was about 20 times higher than sulfided $Mo/Al_2O_3$ and was approximately the same as that of a commercial catalyst.
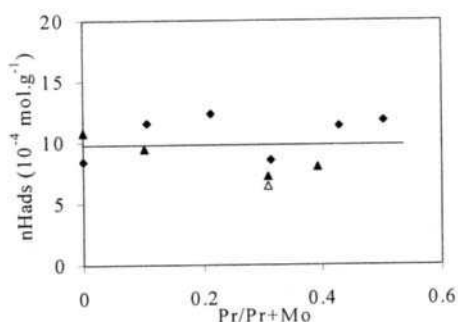


Fig. 4. Influence of promoter loadings on the amount of exchangeable hydrogen adsorbed on NiMo (▲) and CoMo (◆) catalysts after treatment **2** at 350°C. (△) commercial NiMo catalyst.
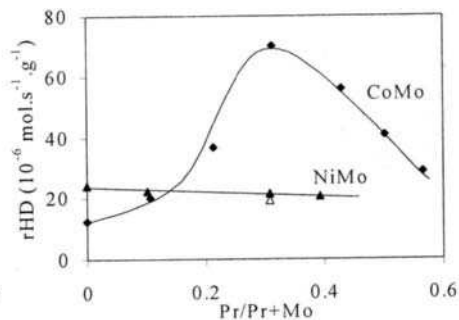
Fig. 5. Influence of promoter loadings on the initial rate of the $H_2$-$D_2$ exchange reaction on NiMo catalysts at 80°C (▲) and CoMo catalysts at 35°C (◆) after treatment **2** at 350°C. (△) commercial NiMo catalyst.
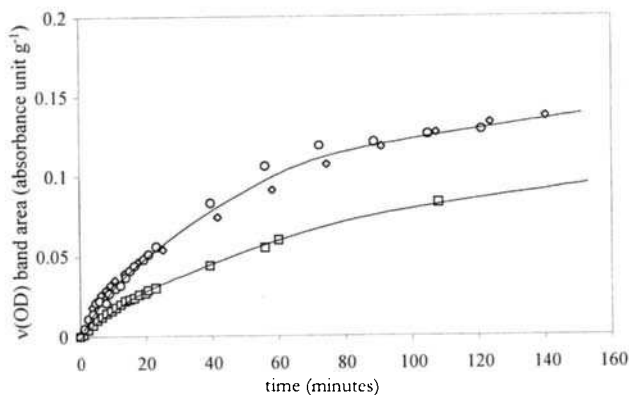


Fig. 6. Changes with time of the intensities of ν(OD) bands observed during exposure to $D_2$ of various catalysts : (□) $Mo/Al_2O_3$ ; (○) $NiMo/Al_2O_3$ (◇) ; $CoMo/Al_2O_3$.

As shown in Fig. 4 no promoting effect was obtained regarding the amount of preadsorbed exchangeable hydrogen with both series of catalysts after pretreatment **2** at 350°C. However, differences between the two series existed concerning the rate of the isotopic exchange between $H_2$ and $D_2$. With nickel, no promoting effect was observed whereas with cobalt a significant effect was obtained in particular after pretreatment **2** at 350°C (Fig. 5). A similar effect was obtained in the case of CoMo catalysts supported on carbon [16].

Fig. 6 shows that the rate of appearance of the bands corresponding to OD groups of the support was significantly greater with the promoted catalysts than with sulfided $Mo/Al_2O_3$. Moreover both promoters had quite similar effects.

The overall process of exchange of the hydrogen present on the support with hydrogen (deuterium) in the gas phase can be considered as involving three possible steps : i) the dissociation of $H_2$ ($D_2$) on the active sulfide phase ; ii) the transfer of H (or D) species between the active phase and the support and iii) the migration of H (or D) species on the surface of the support. As expected our experiments indicate that the rate-limiting step of the isotopic exchange of the hydrogen of the support is probably not the dissociation of $H_2$ ($D_2$) on the sulfide phase, otherwise both promoters would not have the same effect on the rate of appearance of the OD groups (Co has an effect on the rate of $H_2$-$D_2$ isotopic exchange on the sulfide while Ni has not). Consequently it can be assumed that the rate of exchange of the hydrogen of the support with the hydrogen (deuterium) of the gas phase is rather dependent on the faculty of migration of the hydrogen atoms on the support or on their transfer from the support to the active phase. Since both promoters have similar effects on the rate of exchange of support hydrogen, it can be supposed that they play a role in the transfer of H(D) atoms between the support and the active phase. Actually S atoms connected to promoter atoms at the edges of the slabs of molybdenum sulfide could help H(D) atoms to jump from the support to the sulfide phase (and vice versa), either because of their particular location [17-19] or because of their specific electronic properties (increased basicity for instance [12]). However, it was also shown that the presence of $H_2S$ could accelerate the exchange of the hydrogen of the OH groups of the support. This can be interpreted by supposing that adsorbed $H_2S$ increases the density of H atoms on the support (and hence makes their exchange easier) or that $H_2S$ would help to transport hydrogen (deuterium) atoms from the support to the sulfide phase through the gas phase (and vice versa) as shown in Eqs. (3)-(9). This would mean that at least part of the hydrogen of the support could be transferred to the sulfide phase by a process which should not be dependent on the promoter.

## 4. CONCLUSION

It was shown that part of the hydrogen present on the supported hydrotreating catalysts after sulfidation belonged to the support. Most of it was due to adsorbed $H_2S$.

It was also found that the presence of the active sulfide phase was necessary for the exchange of the support hydrogen (OH groups) with $D_2$ in the gas phase to occur. Ni or Co promoters had not the same effect on the rate of the isotopic exchange between $H_2$ and $D_2$

38

while they had similar effects on the rate of appearance of OD groups on the support when the catalysts were exposed to $D_2$ gas. Hence, it could be concluded that the exchange occurred through a spillover process in which the rate-limiting step was the migration of H (or D) atoms on the support or their transfer between the support and the sulfide phase.

REFERENCES

1. C.J. Wright, C. Sampson, D. Fraser, R.B. Moyes, P.B. Wells and C. Riekel, J.C.S. Faraday Trans. I 76 (1980) 1585.
2. T. Komatsu and W.K. Hall, J. Phys. Chem. 95 (1991) 9966.
3. T. Komatsu, and W.K. Hall, ibid. 96 (1992) 8131.
4. F.E. Massoth, J. Catal. 36 (1975) 164.
5. P. Sundberg, R.B. Moyes and J. Tomkinson, Bull. Soc. Chim. Belg. 100 (1991) 967.
6. C. Thomas, L. Vivier, J.L. Lemberton, S. Kasztelan and G. Pérot, J. Catal. 167 (1997) 1.
7. C. Thomas, L. Vivier, A. Travert, F. Maugé, S. Kasztelan and G. Pérot, J. Catal. 179 (1998) 495.
8. C. Thomas, L. Vivier, M. Lescanne, S. Kasztelan and G. Pérot, Catal. Lett. 58 (1999) 33.
9. J. Polz, H. Zeilinger, B. Müller and H. Knözinger, J. Catal. 120 (1989) 22.
10. L. Jalowiecki, J. Grimblot and J.P. Bonnelle, J. Catal. 126 (1990) 101.
11. S. Kasztelan and G.B. Mc Garvey, J. Catal. 147 (1994) 476.
12. J. Mijoin, V. Thévenin, N. Garcia Aguirre, H. Yuze, J. Wang, W.Z. Li, G. Pérot and J.L. Lemberton, Appl. Catal. A. General, 180 (1999) 95.
13. S. Kasztelan in "Symposium on Mechanism of HDS/HDN Reactions" Prep. Amer. Chem. Soc., Div. Petr. Chem., 38 (1993) 642.
14. S. Kasztelan and D. Guillaume, Ind. Eng. Chem. Res., 33 (1994) 203.
15. H. Topsoe, B.S. Clausen and F.E. Massoth, in "Hydrotreating Catalysis, Science and Technology" (J.R. Anderson and M. Boudard, edts) vol.11, Springer-Verlag,Berlin, 1996.
16. E.J.M. Hensen, G.M.H.J. Lardinois, V.H.J. De Beer, J.A.R. Van Veen and R.A. Van Santen, J. Catal., 187 (1999) 95.
17. L.S. Bysbov, J.K. Norskov, B.S. Clausen and H. Topsoe, J. Catal., 187 (1999) 109.
18. P. Raybaud, J. Hafner, G. Kresse, S. Kazstelan and H. Toulhoat, J. Catal., 190 (2000) 128.
19. J.V. Lauritsen, S. Helveg, E. Lægsgaard, I. Stensgaard, B.S. Clausen, H. Topsoe and F. Besenbacher, J. Catal.,197 (2001) 1.

# In-situ FTIR study of hydrogen spillover and reaction kinetics in hybrid catalysts

Azfar Hassan,[a] Kaoru Fujimoto,[b] Keiichi Tomishige,[b] Toshiaki Kusakari[b] and Asuka Akasaka [b]

[a] Center for Refining and Petrochemicals, Research Institute, King Fahd University of Petroleum and Minerals, Dhahran 31261, Saudi Arabia.

[b] Department of Applied Chemistry, School of Engineering, The University of Tokyo, Hongo, Bunkyo-ku, Tokyo 113-8656, Japan

An attempt is made to demonstrate that in hybrid catalysts there is a rapid molecular transfer between hydrogenation sites (which are the metals loaded on alumina) and the acid sites (zeolite)- the site of catalytic cracking. In this study a series of hybrid catalysts were prepared by loading metals Ni and W on $Al_2O_3$ and then physically mixing with H-USY to give the final catalysts. H-D Exchange (-OH + $D_2$) of the Bronsted acid site was carried out, that led to a complete description of interactions between spilt-over hydrogen and acid sites of the zeolite. The hybrid catalysts showed more H-D exchange as compared to USY zeolite alone. This was a clear demonstration of spill over. Amongst the hybrid catalysts, the bi-metallic hybrid catalyst (NiW) showed more exchange as compared to the mono metallic hybrid catalysts. This reflects on greater capacity of the bimetallic catalyst for the hydrogen spill over. The effect of spilt -over hydrogen on the catalytic activity for the hydrocracking of n-heptane was also investigated. n-heptane was cracked to form only two major products: propane and iso-butane. All hybrid catalysts showed high selectivity for the main products. NiW based hybrid catalyst showed excellent performance as a hydrocracking catalyst.

## 1. INTRODUCTION

Most of these hydrocracking catalysts are dual functional catalysts. They have hydrogenation-dehydrogenation function as well as acidic function. It is important that there should be a rapid molecular transfer between the acid site and hydrogenation site in order to avoid undesirable secondary reactions. This can be achieved by having the hydrogenation sites located in close proximity to the acid sites. The most predominant reaction mechanism for the hydrocracking of alkanes over a dual functional catalyst is as follows: (1) the dehydrogenation

of alkanes to olefin on the supported metal; (2) proton addition to the olefin to form carbenium ion on the acidic component; (3) -scission of the carbenium ion to form smaller carbenium ion and olefin on the acid component; (4) hydrogenation of the cracked olefin to alkanes on the supported metal [1].

Spillover phenomenon was first noticed in1960's by several groups. This phenomenon was defined at the 2nd International Symposium on Spillover as the migration of adsorbed species from one solid phase where it is easily adsorbed, to another solid phase, which is in contact with the first, where it was not directly adsorbed [4]. One can find many experimental evidences of hydrogen spillover in literature, especially by infrared spectroscopy [5-7] often being combined with H-D exchange and temperature programmed desorption [8,9]. There is a lot of discussion about the nature of spilt-over hydrogen species, such as H atoms, radicals, $H^+$ and $H^-$ ions, ion pairs, $H_3^+$ species or protons and electrons [10,11]. Thus, the elucidation of the nature of spilt-over hydrogen species is a matter of deep interest.

In this study a series of hybrid catalysts, containing Ni, and W supported on alumina, and then mixed with USY zeolite (H form) were prepared. The objective was to study the effect of metal type and the support content on the extent to which hydrogen spillover occurs in such hybrid catalysts and the role this hydrogen spill over plays in the stability of the catalyst during the high pressure hydrocracking of $n$-heptane.

## 2. EXPERIMENTAL

### 2.1. Catalyst Synthesis
Catalyst precursors were prepared by loading Ni and W on alumina ( -Al$_2$O$_3$). -Al$_2$O$_3$ was used in as-received form obtained from Aerosil, having a surface area of 100 m²/g. Ni was loaded as and NiO (8% by wt) of alumina; whereas W was loaded as WO$_3$ (12% by weight) of alumina. Nickel nitrate hexahydrate (Kanto Chemical Co, Japan), and ammonium metatungstate hydrate (Aldrich, USA) were used to load Ni and W respectively on alumina. Metal loading was carried out by impregnation method. Sequential impregnation was followed in cases where both metals were loaded. The support was calcined at 500°C for 2 h after the metal loading to give the catalyst precursor. About 5 g of the catalyst precursor was sulfided at 400 °C for 1 h to ensure complete sulfiding of the metal oxides. USY zeolite HSZ-330HUA (Tosoh Company, Japan) was obtained in H-form with a SiO$_2$/Al$_2$O$_3$ = 6.3. It was physically mixed in ratios of 1:1 and 9:1 by wt with metal sulfides loaded on Al$_2$O$_3$ to give a mixture; and then pressure molding (400 kg/cm²) the mixture to granules to 20/40 mesh. The details of these final catalysts are shown in Table 1.

### 2.2. H-D Exchange Study
The catalyst samples (100 mg), including USY were pressed to wafers under a pressure of 60 MPa. The wafer was then placed in a quartz-made *in situ* IR cell

Table 1
Composition of the hybrid catalysts

| Hybrid Catalyst | Metal(s) loaded/$Al_2O_3$ | | H-USY : Metal/$Al_2O_3$ |
|---|---|---|---|
| HC-1 | Ni | (sulfide form) | 9:1 |
| HC-2 | W | (sulfide form) | 9:1 |
| HC-3 | Ni-W | (sulfide form) | 9:1 |
| HC-4 | Ni | (sulfide form) | 1:1 |
| HC-5 | W | (sulfide form) | 1:1 |
| HC-6 | Ni-W | (sulfide form) | 1:1 |

with KBr windows and connected to the gas flow system. The sample was heated to 400 °C for 30 min under the flow of $H_2$. The temperature was then reduced to 300 °C. $H_2$ flow was stopped and $N_2$ was purged in for 10 min to remove traces of $H_2$. The flow of $N_2$ was reduced to 27 ml/min. After taking the initial spectra, $D_2$ was introduced along with $N_2$ to give a combined flow of 30 ml/min. FTIR spectra was then recorded at regular intervals. FTIR spectra were obtained by PROTÉGÉ 460 (Nicolet) with MCT detector. For the bimetallic catalyst D-H exchange study was also performed in a similar way described above.

## 2.3. n-Heptane hydrocracking

The hydrocracking of *n*-heptane was carried out in continuous flow type fixed bed reaction apparatus under pressurized conditions (1.1 MPa). The catalyst (0.5 g) was packed in the reactor. The reactor was a stainless steel tube with an inner diameter of 6 mm. *n*-Heptane was fed by a liquid pump at a rate of 150. The mole ratio of $H_2/C_7H_{16}$ in the feed was 9:1. W/F was kept at 2.0. Products were withdrawn in a gaseous state and were analyzed with an on line gas chromatograph (GC 353 from GL Sciences).

## 3. RESULTS AND DISCUSSION

### 3.1. H-D exchange on USY zeolite

Deuterium exchange with OH groups on USY zeolite was carried out using hybrid catalysts. The intensity of OH band around 3650 $cm^{-1}$ decreased and the band corresponding to OD groups appeared around 2680 $cm^{-1}$ with the passage of time. Similar pattern was observed for the hybrid catalysts. However the increase in the area of OD peak as a function of time was different for individual catalysts. Figure 1 shows a plot of change in the area of OD peak, as a function of time for the hybrid catalysts. The hybrid catalysts showed more H-D exchange as compared to USY zeolite alone. Amongst the hybrid catalysts, the bi-metallic hybrid catalyst (HC-3, showed more exchange as compared to the mono metallic hybrid catalysts. This reflects on greater capacity of the bimetallic catalyst for the hydrogen spillover.
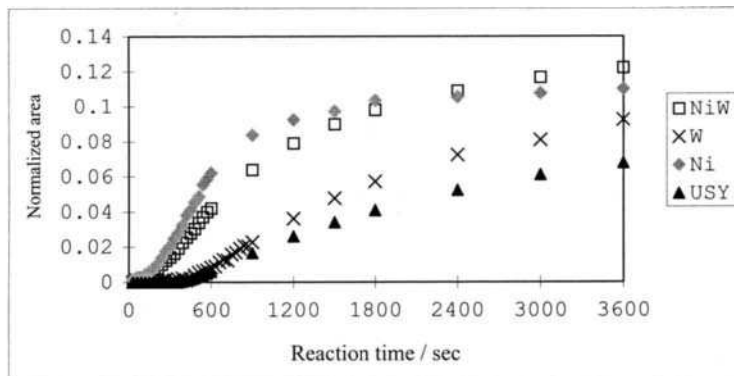
Fig. 1. Change in the area of OD peak as a function of time.

It can be noticed that USY alone has a long induction period as compared to the hybrid catalyst. This again reflects upon the slow H-D exchange rate of USY zeolite. The mono-metallic hybrid catalysts HC-1 (Ni) showed faster exchange as compared to HC-3 (Ni-W) catalysts.

D-H exchange studies were also carried out for the bimetallic hybrid catalyst, to see if there was any difference in the rates of H-D (H to D) and D-H (D to H) exchanges. The rates of the two dynamic processes were found to be nearly same in two cases (see Figure 2). This reflects upon the involvement of free radicals during the exchange process.
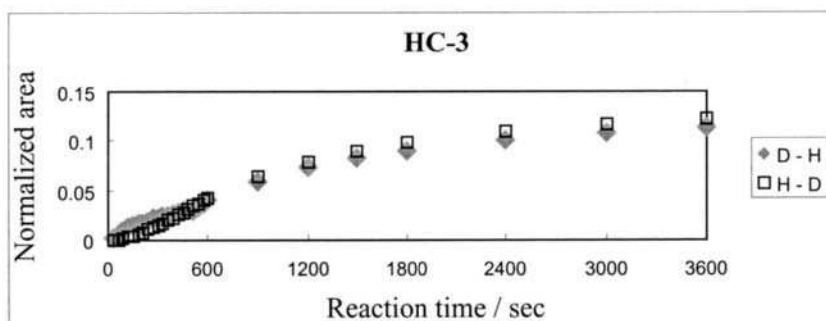


Fig. 2. H-D and D-H exchange study for HC-3 (NiW) catalyst

Hydrocracking of $n$-heptane was carried out using the hybrid catalysts (HC-4 to HC-6). The objective was to see the effect of hydrogen spill over upon catalyst performance for hydrocracking reactions. The activities of the hybrid catalysts are shown in Table 2 and Figure 3.

Table 2
Hydrocracking data of *n*-heptane by hybrid catalysts

| Catalyst | % Conversion of *n*-heptane | | | | |
|----------|-------|------|------|------|------|
| | Time (min) | | | | |
| | 55 | 95 | 135 | 175 | 215 |
| HC-4 | - | 88.5 | 98.9 | 98.2 | 89.4 |
| HC-5 | - | 87.5 | 64.3 | 42. 7 | 30.9 |
| HC-6 | 98.33 | 97.9 | 93.3 | 90.7 | 89.2 |

As evident from table 2 and the figure 3, out of the three hybrid catalysts HC-6 (that showed faster H-D exchange) also give higher conversion and stable activity as compared to W based catalyst (HC-5). Catalyst HC-5 deactivated very rapidly. Although it showed high activity initially, but slow spillover failed to prevent coke formation on the catalyst. Slight increase in the initial conversion rate of Ni is probably because of the incomplete reduction of Ni $^{2+}$ to the metallic state. Table 3 shows the TG/DTA results of the spent catalysts. The coke formation was high for the mono-metallic catalysts as compared to the bi-metallic catalyst. Because of effective hydrogen spillover the deactivation in HC-6 was gradual and less.
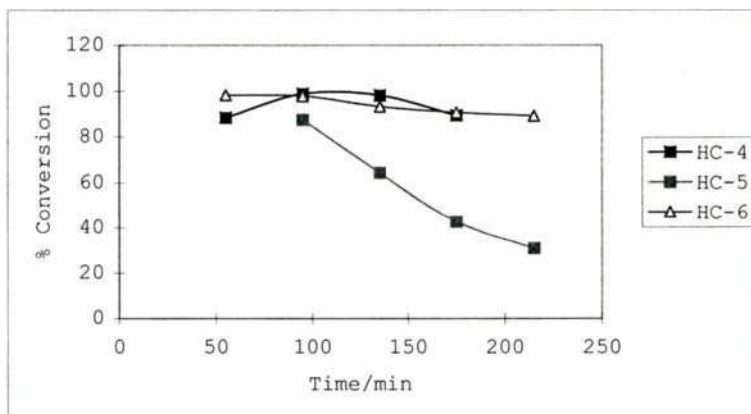


Fig 3. Hydrocracking activity of hybrid catalysts.

Figure 4 shows the selectivity of hydrocracking of $n$-heptane to the main products propane and *iso*-butane for these hybrid catalysts. It has been suggested that the formation of multibranched isomers from the feed and cracking are consecutive reactions [12]. As evident from the figure all hybrid catalysts showed high selectivity for the main products. As evident form Figure 3 the catalyst performance of the HC-6 (Ni-W based catalyst) appears to be the best amongst the three. The deactivation of the catalyst appears to be very slow.

Table 3
TG/DTA results of the spent catalysts

| S.No | Spent Catalyst | Reaction Time (min) | Wt % loss | |
|------|---------------|---------------------|-----------------|------------------|
|      |               |                     | (25 – 500 °C)   | (500-977 °C)     |
| 1    | HC-4          | 215                 | 6.2             | 3.9              |
| 2    | HC-5          | 215                 | 6.0             | 3.2              |
| 3    | HC-6          | 215                 | 4.0             | 9.7              |

Keeping in view the catalytic behavior of these hybrid catalysts, it can be safely concluded that the hydrocraking of $n$-heptane by these hybrid catalysts follows the same pathway as previously reported for dealuminated mordenite catalyst [13]. Because of the high energy barrier for -scission of mono branched carbenium ion to form primary carbenium ion, the cracking of $n$-heptane proceeds through a stage of formation of branched isomers, and then finally crack to form the two major products. The *iso-* butene, which is one of the pair of the primary cracked products, hydrogenates to *iso*-butane.over the catalyst in presence the of hydrogen. The hydride ion, which is formed as a counter ion of the proton during the spill over process, stabilizes C7 carbenium ions and the propyl- carbenium ions to give C7 isomers and propane respectively. Thus the oligomerization of the cracked fragments and consecutive cracking reactions are prevented in the hybrid system.

## 4. CONCLUSIONS

The hybrid catalysts, which were prepared by physically mixing H-USY and metal(s)/ $Al_2O_3$ demonstrated hydrogen spill over and as a consequence high hydrocracking activity. The bimetallic catalyst (Ni-W) showed higher exchange rate, and consequently higher cracking activity and greater catalytic stability than the mono-metallic hybrid catalysts.
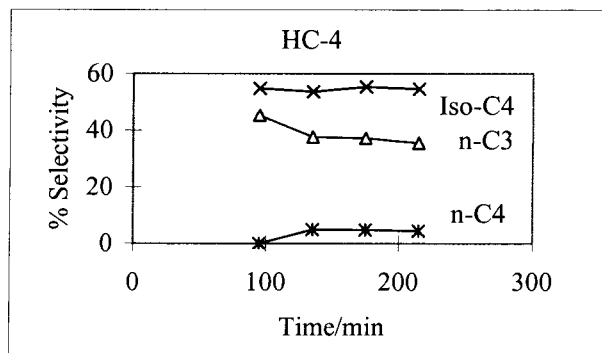
(a)
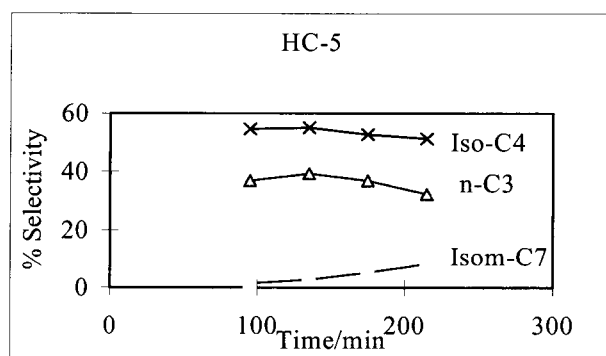


(b)
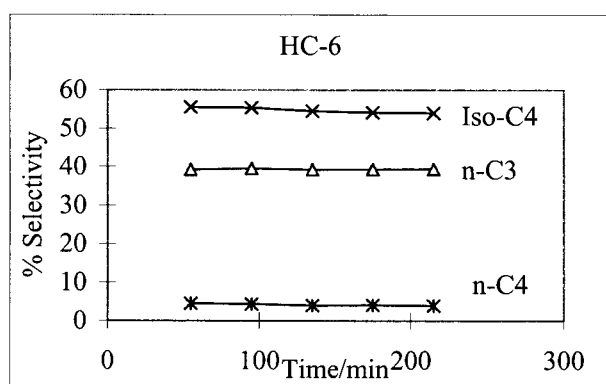


(c)

Fig 4. Product selectivity for hydrocracking of *n*-heptane using hybrid catalysts.

## Acknowledgement

## REFERENCES

1. B. S. Greensfelder, H. H. Voge and G. M. Good, Ind. Eng. Chem., 41 (1949) 2573.
2. K. Fujimoto, K. Maeda and K. Aimoto, Applied Catal., 91 (1992) 81.
3. I. Nakamura, R. Iwamoto and A. I. Ino, in "New Aspects of Spillover Effect in Catalysis" Elsevier, Amsterdam, 1993, pp. 77-84.
4. K. Fujimoto., Stud. Surf. Sci. Catal. 77 (1993) 9, and references cited therein.
5. M.G. Yang, I. Nakamura, and K. Fujimoto, Applied Catal., 144 (1996) 221.
6. R. Ueda, T. Kusakari, K. Tomishige and K. Fujimoto., Journal of Catalysis (in press).
7. R. Ueda, K. Tomishige and K. Fujimoto., Catalysis Letters, 57 (1999) 145.
8. R. Kramer and M. Andre, J. Catal., 58 (1979) 287.
9. J. M. Parera, E. M. Traffano, J. C. Musso and C. L. Pieck, Stud. Surf. Sci. Catal., 17(1983) 101.
10. W. C. Conner, G. M. Pajonk and S. J. Teichner, Adv. Catal. 34 (1986) 1.
11. U. Roland, T. Braunshweig and F. Roessner, J. Mol. Catal. A 127 (97) 61.
12. M. Steijins, G. Froment, P. Jacobs, J. Uytterhoeven and J. Weitkamp, Ind. Eng. Chem. Prod. Res. Dev., 20 (1981) 654.
13. I. Nakamura, K. Sunada and K. Fujimoto., Stud. Surf. Sci. Catal., 106 (1997) 361.

# H$_2$ Adsorption in Rhodium metal catalysts supported in oxides with different reducibility

C. Force [a], J.P. Belzunegu [a], J.Sanz [a].

[a]Instituto de Ciencia de Materiales de Madrid. Consejo Superior de Investigaciones Científicas (C.S.I.C).

Nuclear Magnetic Resonance has been used to monitor hydrogen spill-over in different rhodium metal supported catalysts. The detection of two lines in the NMR spectra allowed the differentiation of hydrogen adsorbed on Rh particles and on oxides used as supports. The study of intensities of these lines vs. pH$_2$ showed that hydrogen transferred to the support is favoured in metal catalysts supported on high hydroxylated reducible oxides. Spill-over depends on the area and nature of metal support interfaces, detecting some differences with the precursor metal salt used in catalyst preparation.

## 1. INTRODUCTION

There exist for a long time evidences that the catalytic behaviour of supported metal catalysts is affected by the incorporation of hydrogen into the support via spill-over processes[1], however, experimental evidences for this mechanism are not clear. In general, spill-over is produced when hydrogen dissociatively adsorbed on metals, spills over oxide supports that do not chemisorbs hydrogen in usual conditions [2]. In non-reducible oxides, Carter et al. in 1965 showed that spill-over, is enhanced by hydroxylated surfaces. In this work, authors showed that the proton exchange of OH⁻ groups of the support was accelerated by the spill-over of deuterium adsorbed on metal particles [3].

Spilt hydrogen is not necessary confined to the oxide surface and can penetrate into the bulk [4]. In particular, the amount of transferred hydrogen depends upon the nature of the support employed as hydrogen acceptor, and in general is more important in oxides capable to be reduced (TiO$_2$, CeO$_2$...). This fact makes difficult the differentiation of the spill-over from the bulk reduction of the support. On the other hand, the influence of parameters like specific area and nature on metal support interfaces [5] is difficult to be analysed in supported metal catalyst due to the heterogeneous diffusive character of this phenomenon. In particular, the speed of the process depends on the relative distance to the metal, decreasing considerably the rate of transference at long distances, and requiring long periods of time to be analysed [1].

In general, volumetric techniques commonly used to determinate the amount of hydrogen adsorbed on catalysts, are not able to separate the hydrogen adsorbed on the metal phase from that adsorbed on the support [6]. This fact makes that spectroscopic techniques like IR and $^1$H-NMR are more suitable to analyse this problem [7-9]. In particular, $^1$H-NMR

spectra of metal supported catalysts display two lines, one at the resonance frequency ascribed to OH groups of the support (line A), and other upfield shifted due to hydrogen adsorbed on metal particles (line B) [10]. The analysis of the intensity of the shifted line B, was used to estimate metal dispersions in $Rh/Al_2O_3$ catalyst [11].

In the actual work, we have analysed the non shifted line A $vs$. hydrogen pressure in metal catalysts supported on oxides with different reducibility ($SrTiO_3 < TiO_2 < CeO_2$), and from the obtained data, studied the evolution of OH groups at the support during hydrogen adsorption. The analysis of adsorption isotherms will permitted to deduce the conditions at which spill-over is produced.

## 2. SAMPLES

Rh supported catalysts were prepared by the incipient wetness impregnation of oxides of increasing reducibility ($SrTiO_3$, $TiO_2$ and $CeO_2$) with aqueous solutions of Rh (III) precursors salts, Rh $(NO_3)_3$, $Cl_3Rh$, (N and Cl samples). In the case of $Rh/SrTiO_3$ and $Rh/TiO_2$, the Rh loading was 2.5% and in $Rh/CeO_2$ catalysts 2%wt. In $Rh/CeO_2$ catalysts, two samples with different BET surface ($55m^2 \cdot g^{-1}$, and $10m^2 \cdot g^{-1}$) were used (HS and LS samples).

Rh metal dispersion values, can be deduced from intensity of NMR line B; by assuming H/Rh= 1:1 stoichiometry, (see table 1). From these values metal particles sizes have been estimated considering a semi-spherical shape.

Table 1
Surface area and metal dispersion of catalysts used in this work. Diameter of metal particles are calculated with expression given in ref 11.

| SAMPLE | Precursor salt | $S_{BET}$ $(m^2g^{-1})$ | Volumetric dispersion (%) | Diameter ($\phi$) ( Å) |
|---|---|---|---|---|
| Rh/SrTiO3 | $RhCl_3$ | 44 | 0.14 | 65 |
| Rh/TiO2 | $Rh(NO_3)_3$ | 50 | 0.11 | 82 |
| $Rh/CeO_2(N)(HS)$ | $Rh(NO_3)_3$ | 55 | 0.29 | 31 |
| $Rh/CeO_2(N)$ (LS) | $Rh(NO_3)_3$ | 10 | 0.33 | 27 |
| $Rh/CeO_2(Cl)(HS)$ | $RhCl_3$ | 55 | 0.5 | 18 |

Prior to NMR adsorption experiments, samples were submitted to a standard treatment consisting on an oxidation at 473K, a reduction at 673K, and an outgassing at 473K. After this treatment, $H_2$ adsorption was performed at increasing pressures.

$^1$H-NMR spectra were obtained in cells, directly connected to the volumetric apparatus that allow the hydrogen adsorption to be analysed in static and flow conditions.

NMR spectra were recorded at room temperature with a SXP 4/100 spectrometer equipped with an Aspect 2000 Fourier transform unit. The NMR frequency used was 67 MHz. The spectra were taken after $\pi/2$ pulse excitations (3.5$\mu$s), and the interval between successive accumulations (0.2 - 2 s) chosen to avoid saturation effects. The number of accumulations (300-500) was selected to maintain an appropriated signal to noise ratio (S/N=20). The quantitative analysis of intensities of the NMR lines was carried out by comparing their integrated intensities with that of a standard of mica in which the OH content is known.

## 3. RESULTS AND DISCUSSION

In previous works, it was shown that hydrogen adsorption on metal support catalysts depend on the nature of oxides used as supports. According to this fact, it has been first analysed the variation of lines A and B of $^1$H- NMR spectra $vs$. hydrogen pressure in Rh catalysts supported in a non-reducible oxide, Rh/SrTiO$_3$ (fig.1a). At very low pressures, the intensity of line A does not change appreciably, while the intensity (Ib) of line B increases significantly, indicating that hydrogen is adsorbed preferentially on the metal. A quantitative analysis of the intensity Ib $vs$ $p$H$_2$ showed the existence of two sites for hydrogen adsorption at the metal; at low pressures, hydrogen is preferentially adsorbed at stronger and well definite sites; however above 5 torr is adsorbed on weaker sites [12]. Adsorption at the second type increases considerably the mobility of hydrogen at the metal, favouring the transference of hydrogen to the support. This fact goes parallel with a faster increase of the line A, indicating that above 60 torr, hydrogen is preferentially retained at the support.
In order to analyse the influence of the catalysts oxidation on hydrogen adsorption, the Rh/SrTiO$_3$ catalyst was oxidized at 673 K, and then reduced at increasing temperatures, 373, 573 and 773 K (fig.1B). The decrease observed on the intensity Ia of the isotherm "b" with respect to that isotherm "a" is accompanied by an increase of the intensity Ib (not show in this work). Both observations are due to the reduction of oxidized metal particles detected with XPS; which produces H$_2$O, that is eliminated during outgassing treatments [13]. From this fact, it is reasonable to ascribe the important amount of hydrogen adsorbed in the sample
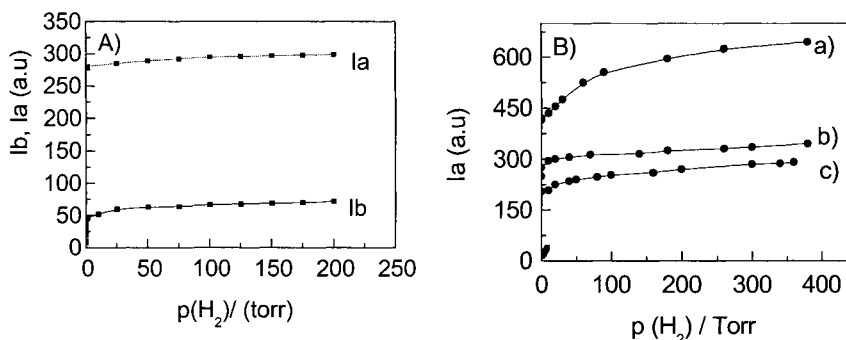


Fig 1: A) Plot of Ia and Ib $vs$. pH$_2$ in Rh/SrTiO$_3$. B) Intensity of line A against H$_2$ pressure for the Rh/SrTiO$_3$ catalyst oxidized at 673 and reduced in H$_2$ at: (a) 373 K; (b) 573 K; (c) 773 K.
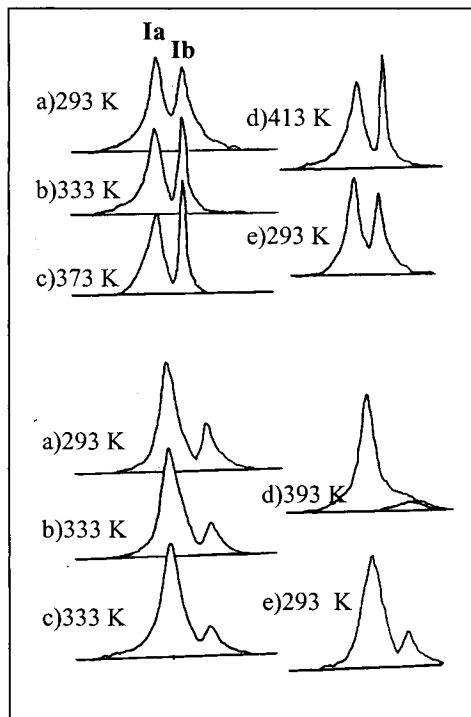
Fig 2 : Variation of $^1$H-NMR spectra in Rh/SrTiO$_3$ (top) and Rh/TiO$_2$ (below) catalysts submitted to 35 torr of hydrogen an heated at indicated temperatures. Spectra-e) are obtained after cooling of catalysts at

reduced at 373 K to hydrogen chemisorbed on surface oxygen atoms of oxidized particles (isotherm "a"). Once all Rh has been reduced [14], adsorption of hydrogen at the metal becomes preponderant; favouring at high pressures the hydrogen transference to the support (isotherm "b"). However, when support becomes dehydroxilated, this transference becomes less favourable (isotherm "c").

On the other hand, Bond. *et al.* showed that spill-over of hydrogen increases when the adsorption temperature exceeded 473 K [15]. To analyse this effect,$^1$H-NMR spectra of Rh/SrTiO$_3$ and Rh/TiO$_2$ samples exposed to 35 torr of hydrogen have been recorder at different temperatures (293-450 K) (fig. 2). In the case of Rh/SrTiO$_3$ sample, the increase of the temperature does not produce modifications on line A, but narrows considerably line B, indicating an increase of mobility of hydrogen adsorbed on the metal. When the sample is cooled, lines A and B recovers their starting values, indicating the spill-over is not important in this system.

In Rh/TiO$_2$ catalysts, the increase of temperature produced a decrease of line B and an increase of line A (spectra a-d). When the temperature is decreased, intensity Ib recovers its initial value, however, intensity of line A displays a higher intensity (e), indicating that part of hydrogen transferred to the support, has not been eliminated. Based in these facts, a most probable mechanism for spill-over in reducible oxides is proposed in the next scheme, in which hydrogen transferred as H$^+$ and e$^-$ favour the reduction of Ti$^{4+}$ cations (EPR) and the formation of OH groups (*scheme 2*). This fact makes that the amount of hydrogen transferred to the support should be enhanced in reducible oxides. When transferred H$^+$ and e$^-$ remains near each other, the outgassing of the sample produce the elimination through back- spill over mechanism of part of hydrogen spilt over the support. Hydrogen desorption is accompanied in this case by the oxidation of Ti$^{3+}$ to Ti$^{4+}$[16].

Spill-over and reduction mechanism of Rh/TiO₃ catalyst.

When the Rh/TiO$_2$ catalyst is reduced at increasing temperatures, hydrogen is consumed to eliminate oxygen atoms from the surface of the support, producing oxygen vacancies at the metal support interface (*scheme 3*) [17]. Dehydroxylation produced during the reduction of the catalyst decreases again the amount of hydrogen spilt-over at the support[9].

In Rh/CeO$_2$ catalysts, we have studied hydrogen adsorption on catalysts with similar metal loadings but different BET surfaces (50 and 10m$^2$ g$^{-1}$) [18]. In figure. 3 the evolution of the intensity Ia *vs.* hydrogen pressure is analysed for different Rh/CeO$_2$ catalysts. In all cases, intensity Ia is considerably higher than Ib, increasing quickly at low pressures and slowly at higher pressures. The increases of Ia is more important in samples HS (S$_{BET}$ 50m$^2$ g$^{-1}$) than in samples LS (S$_{BET}$ 10m$^2$ g$^{-1}$), indicating the existence of a more important amount of hydrogen transferred to the support in samples with higher surface area. In analysed samples the particles size is similar but the number of particles is higher in HS samples, indicating that spill-over depends on the extent of metal–support interface.



Fig 3: Variation of the intensity of lines A *vs.* H$_2$ pressure (torr) in Rh/CeO$_2$ (HS, LS) catalysts. Data concerning Ib in HS Rh/CeO$_2$ (N) sample are included for comparison.

In order to analyse the influence of chloride ions retained at the metal support interface, we have analysed the amount of hydrogen retained at the support in catalysts Rh/CeO$_2$ (55m$^2$· gr$^{-1}$) prepared from nitrate and chloride salts (fig 3). In both samples, the

line A increases much more than Ib; however intensity Ia in Cl-sample is slightly higher than in N-sample [19]. On the other hand, the decreases of the hydrogen spill-over reported in Rh/CeO$_2$ (Cl) [20], has not been observed here, indicating that the higher metal dispersion obtained in this work prevails over Cl$^-$ effect.

In figure 4, it is analysed H$_2$ adsorption in Rh/CeO$_2$ (N) catalyst oxidized at 673 K and reduced at increasing temperatures. In all cases, Ia increase quickly at low pressures, attains a plateau and increases again at higher pressures. The observed behaviour is similar to described for Rh/SrTiO$_3$ catalysts; however, some differences have been noted. Firstly, an easier reduction of metal particles is produced in Rh/CeO$_2$ at 373 K, which explain small differences observed in isotherms "a" and " b" of samples reduced at 373 and 573 K [21]. In all cases, the increase of line A is important indicating that spill-over is



**Fig 4**: Plot of intensity of line A *vs* hydrogen pressure in Rh/CeO$_2$-N (HS) catalyst, oxidized at 673 K and reduced in H$_2$ (150 torr) at a) 373, b) 573, c) 773 K.

considerable. Second, the intensity of Ia in isotherm "c" is appreciably lower than in isotherm "a" and "b" indicating that reductions at 773 K diminish the capacity of the support to adsorb H$_2$ in a much more extent that in Rh/SrTiO$_3$ catalyst. This fact suggest that reduction of the support could have a more important influence that dehydroxylation on hydrogen spill-over in reducible supports. In this case, the increase of the amount of electrons transferred to the support *(scheme II)* hinders the spill-over of hydrogen. At reduction temperature (Tr) > 473 K, the elimination of structural oxygen is favoured at the metal support interface, increasing again the amount of electrons retained by the support. Both facts causes the electron transference to be switched off, making possible that at higher reduction temperatures (Tr > 673 K) electron transference goes from the support to metal particles [22]. This transference is accompanied by a decrease on the intensity of NMR line B, indicating an important loss of hydrogen adsorption at metal particles. This effect, known as strong metal support interaction (SMSI), is favoured by the presence of oxygen vacancies at the metal-support interface. At this point, it is interesting to remark that the incorporation of chlorine into oxygen vacancies, producing cerium oxichloride specie (Ce$^{3+}$OCl) [23-25], that impedes electron exchanges between both phases. The great stability of these species, that remains after reductions at high temperatures, explains the difficulties reported to establish the metal-support interaction in Rh/CeO$_2$ (Cl) catalysts [11].

## 4. CONCLUSIONS

The use of $^1$H-NMR spectroscopy permit to differentiate hydrogen adsorbed on the metal from that adsorbed on the support; from the analysis of line A, associated with OH of the support, the spill-over of hydrogen has been monitored. In particular, it has been shown that this phenomenon depends upon area and nature on metal support interfaces, detecting some differences with the type precursor metal salt used on catalyst preparation. Dehydroxylation of the support surfaces decreases the amount of H spilt over the support.

Differences obtained on Rh catalyst supported on $SrTiO_3$, $TiO_2$ and $CeO_2$ showed that hydrogen spill-over is strongly dependent on the reducibility of the support. $^1$H-NMR experiments carried out at increasing temperatures showed that the hydrogen transference is considerably improved in reducible oxides, like $TiO_2$ and $CeO_2$; however, reduction of the support at 773 K decreases drastically the amount of hydrogen adsorbed on the metal (SMSI effect) and the extent of the hydrogen spill-over phenomenon.

### Acknowledgments

## REFERENCES

1. G. C. Bond, Spill-over and adsorbed species., Elsevier Science Published., (1983)1.
2. H.S. Taylor, Am.Rev.Chem., 5 (1967) 646.
3. J.L Carter, P.J. Lucchesi, P. Cornell, D.J.C. Yates, J.H.J. Shinfelt, Phys Chem., 69 (1965) 3070.
4. R. Kramer, M. André, J. Catal., 58 (1979) 287.
5. M. Dominique, D. Duprez. J.Phys Chem B, 101 (1997) 4428.
6. D.A. Dowen, C. Kemball. (Eds). Specialist Periodical Reports-Catalysts, Vol 3, The Chemical Society, London, Ch. 6 (1980) 136.
7. R. A. Dalla Betta, M.J. Boudart. J. Chem. Soc. Faraday Trans., 72 (1976) 1673.
8. T.H. Fang, J. P. Wey, W. C. Neely, S. D. Worley, J. Phys. Chem., 97 (1993) 5131.
9. J. P. Belzunegui, J.M. Rojo, J. Sanz. J. Chem..Soc..Faraday Trans., 85 (1989) 4287.
10. J. Sanz, J. M. Rojo. J. Phys Chem., 89 (1985) 4974.
11. C. Force, A. Ruiz Paniego, J. M. Guil, J. M. Gatica, C. López-Cartes, S. Bernal, J. Sanz. Langmuir., (2000). In press.
12. J.M. Rojo, J. P. Belzunegui, J. Sanz, J. M. Guil. J Phys Chem., 98 (1994) 13631.
13. J. P. Belzunegui. Doctoral Thesis., (1995).
14. A. Martínez-Arias, J. Soria, J. C. Conesa. J. Catal., 168 (1997) 364.
15. P. A. Sermon, G. C. Bond. Catal. Rev., 8 (1973) 211.
16. J. C. Conesa, J. Soria. J.Phys Chem., 86 (1985) 1392.

54

17. J. L. G. Fierro, J. Soria, J. Sanz, J. M. Rojo. J. Solid State Chemistry., 66 (1987) 154.
18. S. Bernal, F. J. Botana, J. J. Calvino, M.A. Cauqui, C.A Cifredo, A, Jorbacho, J. M. Pintado, J..M. Rodríguez Izquierdo. J. Phys Chem., 97 (1993) 4118.
19. C. Force, J. P. Belzunegui, J. Sanz, A. Martinez Arias, J. Soria. J. Catal., 197 (2001) 192.
20. S. Salasc, V. Perrinchon, M. Primet, M. Chevrier, F. Mathis, N. Moral. Catalysis Today, 50 (1999) 227.
21. J. P. Holgado. Doctoral Thesis (1996).
22. A. Pfau, J. Sanz, K. D. Schierbaum, W. Gopel, J. P. BelzuneguiJ. M. Rojo. Stud. Surf. Sci. Catal.. 40th Anniversary, (1996) 931.
23. F. Le Normand, L. Hilarie, K. Kili, G. Krill, G. Marie. J. Phys. Chem., 92 (1988) 2561.
24. A. Bradi, C. Binet, J. C. Lavalley. J. Phys Chem., 200 (1996) 8363.
25. S. Bernal, J. J. Calvino, C. A. Cifredo, J. M. Gatica, A. Perez-Omil, V. Laachir, V. Perrinchon. Stud. Surf. Sci. Catal. 96 (1995) 419.

# Hydrogen spillover on a carbon supported platinum fuel cell catalyst: a computational and inelastic neutron scattering study

A.J. Ramirez-Cuesta,[a,b] P.C.H. Mitchell,[b] S.F. Parker[c] J. Tomkinson[c] and D. Thompsett[d]

[a]Departamento de Fisica, Universidad Nacional de San Luis, 5700 San Luis, Argentina

[b]Department of Chemistry, University of Reading, Reading RG6 6AD UK

[c]ISIS Facility, Rutherford Appleton Laboratory, Chilton, Didcot OX11 OQX UK

[d]Johnson Matthey Technology Centre, Sonning Common, Reading, RG4 9NH UK

We are undertaking a study of hydrogen spillover using neutron scattering techniques allied with computer modelling. We report the direct observation of spillover hydrogen on a Pt/C fuel cell catalyst and a computational model of the interaction of spillover hydrogen with the catalyst support. Dihydrogen molecules dissociate on the Pt component of the catalyst and H atoms spillover onto the carbon support. The spillover H atoms comprise a mobile phase on the surface of the carbon characterised by a broad inelastic neutron scattering spectrum. A quantum mechanical calculation of the interaction energy of H atoms with the carbon surface shows that the energy differences between different potential binding sites are no more than a few kJ. Thus the spillover hydrogen is in the form of a layer on the carbon of weakly bound, mobile H atoms.

## 1. INTRODUCTION

Spillover of hydrogen is implicated in many catalytic reactions [1]. Most metal catalysts consist of metal particles supported on high surface oxide or carbon and many catalytic reactions including industrially important reactions involve hydrogen. The aim of our research is to obtain quantitative data on the nature of spillover hydrogen and on the energetics and kinetics of the spillover process. We report, using inelastic neutron scattering (INS), the direct observation of hydrogen atoms spilled over onto carbon from a Pt/C fuel cell catalyst, and a computational model of the spillover hydrogen.

The neutron is an ideal probe for the study of hydrogenous materials [2]. Neutrons are scattered by atomic nuclei. In incoherent scattering (which is the type of scattering here) the scattering is from a single centre and so there is no interference of scattered waves. A fraction of the neutrons loses energy by exciting vibrational modes of the scatterer; the INS spectrum is an energy loss spectrum. All molecular vibrations are neutron-active because the nuclear interactions are not subject to dipole or polarisability selection rules. All vibrations are therefore, in principle, observable. The scattering intensity is straightforwardly related to the concentration of the scatterer. Because the scattering cross section is much greater for hydrogen (80 barns) than for other elements (5 barns) motions involving hydrogen are

strongly emphasised in neutron spectroscopy. Subtraction of background spectra due, for example, to the containing vessel and the catalyst support is straightforward. We are thus able to obtain a complete vibrational spectrum of the substance over the range 16 to 8000 cm$^{-1}$ with a resolution of 1-2%.

## 2. EXPERIMENTAL

### 2.1. Catalyst and pre-treatment

The Pt/C catalyst was supplied by Johnson Matthey Technology Centre. It comprised 40 wt-% Pt on a carbon black support. The electrochemical surface area was 60 m$^2$ (g Pt)$^{-1}$. The catalyst was pelletted in an infrared KBr die (0.3 g catalyst under 0.2 tonnes) To remove superficial oxide and water the catalyst pellets (loaded into the cell used in the neutron scattering experiments, see below) were heated to constant mass in a flowing 10 vol.% H$_2$/He mixture at 373 K and evacuated to a constant 10$^{-5}$ mbar. The carbon support was treated in the same way.

### 2.2. The scattering cell and the detection of spillover hydrogen

To detect spillover H directly we used a *two component* technique. The first component is the Pt/C *catalyst*; the second component is the carbon *support* alone. The two components are in contact and so the spillover hydrogen has access to the carbon of *both* components. The experiment is so designed that neutrons are scattered only from the second component, the carbon support. We thus observe the spectrum of spillover hydrogen only. To achieve this the catalyst and support are contained by a specially designed circular steel cell, Fig. 1. The Pt/C catalyst pellets (3.79 g) were sliced in half and distributed around the inside of the cell. The cell was then filled with the carbon support (9.45 g), as a fine powder. The catalyst and support were pressed (10 tonnes) to ensure good contact. The catalyst was thus confined to an outer annular ring ca 1 cm wide and the carbon to a central disc of 5 cm diameter. The cell attached to a centre stick is lowered into the beam compartment of the TOSCA spectrometer and located so that the neutron beam (4.5 cm diameter) is scattered only from carbon disc. The cell, which is conveniently referred to as the *annular* cell, is equipped with inlet and outlet tubes to provide for evacuation and dihydrogen flow. The cell is equipped with a thermocouple and can be heated at any desired temperature in an oven or a furnace.
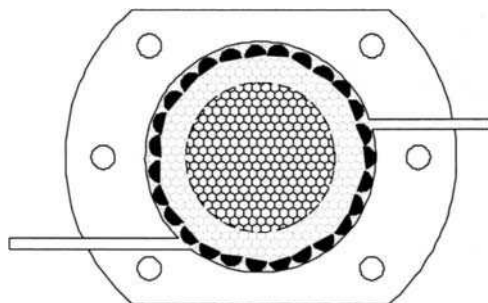


Fig. 1. The annular cell showing the location of the Pt/C catalyst pellets, the carbon disc and the neutron beam.

## 2.3. Dihydrogen dosing

The activated catalyst in the annular cell was attached to a steel vacuum line and dosed with pure dihydrogen (99.999%) from a 0.5 1 volume at 1 bar and at 473 K (to optimise the hydrogen spillover rate) for 36 h. The pressure change was measured during hydrogen uptake. Dosing was continued until there was no further pressure decrease, i.e. to equilibrium. A rapid initial hydrogen uptake (dead volume filling) was followed by a much slower uptake (100 ml of dihydrogen at atmospheric pressure) . The carbon support by itself, treated in the same way, did not take up dihydrogen.

## 2.4. Inelastic neutron scattering spectra

Inelastic neutron scattering (INS) spectra of the empty annular cell, the carbon support and the dihydrogen dosed catalyst were recorded on the TOSCA spectrometer at the ISIS pulsed neutron source at the Rutherford Appleton Laboratory, Chilton, UK[3]. TOSCA is a high resolution, broad range, inverse geometry spectrometer well suited to the spectroscopy of hydrogenous materials. It has an energy transfer range from 16 to 8000 cm$^{-1}$ and a resolution, $\Delta E/E \sim 2\%$. The spectra were recorded at ca 20 K to freeze the chemistry and to eliminate thermal broadening of the spectra. The spectra were analysed and converted to the conventional Scattering Law S($Q$,$\omega$) (S, intensity; Q, momentum transfer and; $\omega$, energy transfer) versus energy transfer (cm$^{-1}$).

## 2.5. Computational modelling of spillover hydrogen

The interaction of hydrogen atoms with an idealised graphite slab was modelled with the Crystal 98 program, which is a periodic hybrid Hartree Fock density functional theory code [4]. Details of the calculations are given in the results section.

## 3. RESULTS AND DISCUSSION

### 3.1. Inelastic neutron scattering spectra

The neutron scattering intensity is plotted versus neutron energy loss giving a spectrum that looks like an infrared or a Raman spectrum. The scattering law connects scattering intensity (S) with momentum transfer (Q) and the root mean square displacement of the scatterer

$$S(Q, n\omega_0) = \frac{\left(Q^2 U^2\right)^n}{n!} \cdot \exp\left(-Q^2 U^2\right)$$

Here n is an integer (1 for the fundamental, 2 for the first overtone, etc.); $Q$ is momentum; $\omega_0$ is the oscillator frequency; $U^2$ equals $\hbar/(2\mu\omega_0)$ where $\mu$ is the oscillator reduced mass. The INS spectrum is thus the amplitude-weighted vibrational density of states averaged over all Q space.

In Fig. 2 we show the INS spectrum of (a) carbon in the central region of the annular cell before hydrogen spillover, (b) the spectrum after hydrogen spillover. These spectra are *difference spectra*; we have subtracted the scattering of the annular cell and the undosed carbon support.

The spectrum of Fig. 2(a) was obtained by dosing the annular cell with hydrogen at 293 K for 1 min and then plunging the cell into liquid nitrogen to freeze the chemistry. In this

58

spectrum we see dihydrogen *molecules* as evidenced by the hydrogen rotor peak at 120 cm^{-1} (see the expanded scale in the inset) and the characteristic broad recoil feature. (Previously we have reported a thorough analysis of the dihydrogen rotational spectrum [5].)

The spectrum of Fig. 2(b) was obtained by dosing the annular cell with hydrogen at 473 K 36 h (cf. the Experimental section). We note the absence of molecular hydrogen (no INS peak at 120 cm^{-1}, contrast Fig. 2(a)) and the enhanced scattering towards higher energies. This scattering is attributed to mobile H atoms on the carbon surface[6], i.e. to spillover hydrogen. (Recall that this spectrum is a difference spectrum: we have already subtracted the scattering of the cell and the carbon support. The enhanced scattering, which we do not observe in Fig. 2(a) in spite of the $H_2$ molecules there present, is therefore due to hydrogen.
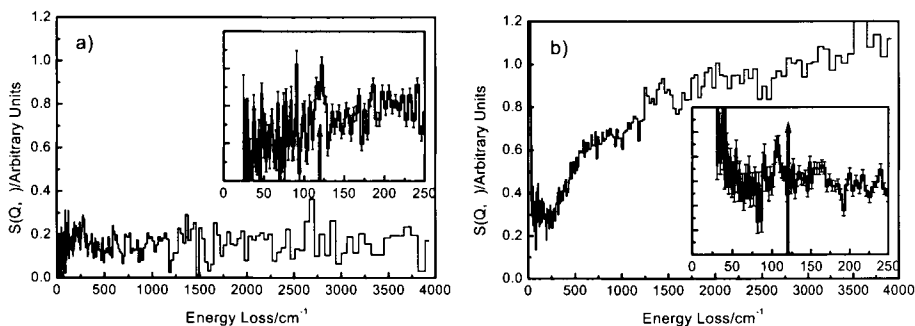


Fig. 2. INS spectra of the carbon component of the annular cell recorded at 20 K. Mass of Pt/C catalyst in the outer ring 3.79 g (not in the neutron beam). Mass of carbon in the central ring 9.45 g (in the neutron beam). (a) Dosed with hydrogen, 50 ml, at 293 K for 1 min and frozen in 1 $N_2$. (b) Dosed with hydrogen, 150 ml, held at 473 K for 36 h. The arrows show the position of the expected peak corresponding to the first rotational transition of the $H_2$ molecule at 120 cm^{-1}.

Other features of the spectrum of Fig. 2(b) are consistent with the presence of H atoms. The low frequency (< 100 cm^{-1}) lattice modes of carbon are enhanced (contrast Fig. 2(a)). We are seeing H atoms riding on the carbon atoms undergoing displacements: the H atom is behaving as a probe for the motions of the carbon atoms through its superior neutron scattering ability. Similarly we attribute the 107 cm^{-1} peak to a carbon motion probed by spillover H atoms.

### 3.2. Computational modelling

In Figure 3 we plot the interaction energies of hydrogen atoms approaching binding sites on an idealised graphite slab: top site, i.e. directly above a C atom; bridge site, i.e. at the mid point between two carbon atoms; hollow site, i.e. above the centre of the C-6 hexagon. The minima in the plots are at the maximum interaction energies. We see that the preferred hydrogen binding site is a top site. The interaction energies at the bridge site and the hollow site are smaller by 15 kJ/mol and their potential well is more diffuse. The results are consistent with those reported for H on coronene [7] We envisage a weakly bound and mobile precursor state of spilled over hydrogen atoms leading to a state of more strongly bound hydrogen atoms.
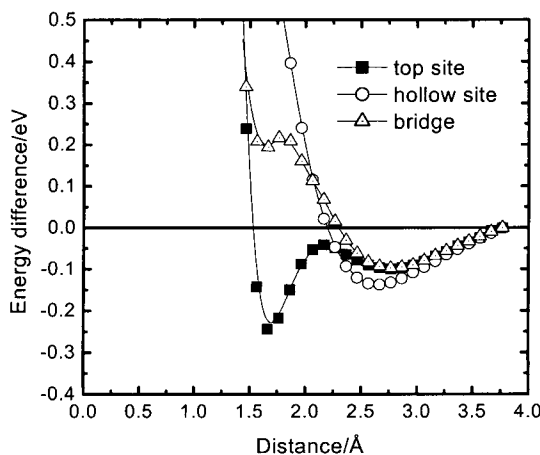
Fig. 3. Interaction of H atom with sites on graphite (see text): interaction energy vs the vertical height of H above the surface. Periodic calculation with CRYSTAL 98, 6-31 G basis, supercell (2x2)x2 unit cells.

## 4. CONCLUSIONS

We have through inelastic neutron scattering observed spillover hydrogen on a Pt/C fuel cell catalyst and have modelled with a periodic quantum mechanical code the interaction of hydrogen atoms at top, bridging and hollow sites on an idealised graphite slab. Dihydrogen molecules dissociate on the Pt component of the catalyst and H atoms spillover onto the carbon support. The spillover H atoms comprise a mobile phase on the surface of the carbon characterised by a broad inelastic neutron scattering spectrum. The quantum mechanical calculation of the interaction energy of H atoms with the carbon surface shows that the energy differences between different potential binding sites are no more than a few kJ. Thus the spillover hydrogen is in the form of a layer on the carbon of weakly bound, mobile H atoms.

### Acknowledgments

### REFERENCES

1.  G.M. Pajonk, Appl.Catal.A, 202 (2000) 157.
2.  P.C.H. Mitchell, Acta Physica Hungarica, 75 (1974) 131.
3.  Z.A.Bowden, M.Celli, F.Cilloco, D.Colognesi, R.J.Newport, S.F.Parker, F.P.Ricci, V.Rossi-Albertini, F.Sacchetti, J.Tomkinson, M.Zoppi, Physica B, 276-278 (2000) 98.

60

4. V.R.Saunders, R.Dovesi, C.Roetti, M.Causà, N.M.Harrison, R.Orlando, C.M.Zicovich-Wilson, CRYSTAL98 User's Manual, 1.0, University of Torino, Torino, 1999.
5. A.J. Ramirez-Cuesta, P.C.H. Mitchell, S.F. Parker, P.A. Barrett, Chem.Comm., (2000) 1257.
6. F.Fillaux, R.Papoular, A.Lautie, J.Tomkinson, Fuel, 74 (1995) 865.
7. L. Jeloaica, V. Sidis, Chem.Phys.Lett., 300 (1999) 157.

# TPR study of PdO catalysts supported on Ce$_x$Ti$_{1-x}$O$_2$ and Ce$_x$Y$_{1-x}$O$_{1.5+0.5x}$: effects of hydrogen spillover

Mengfei Luo, Wenjuan Shan, Pinliang Ying, Jiqing Lu and Can Li*

State Key Laboratory of Catalysis, Dalian Institute of Chemical Physics,
Chinese Academy of Sciences, Dalian 116023, China

Solid solutions, Ce$_x$Ti$_{1-x}$O$_2$ and Ce$_x$Y$_{1-x}$O$_{1.5-0.5x}$ were prepared by citrate sol-gel method, and characterized by XRD and TPR techniques. The structure of the solid solution depends on the Ce content. TPR results indicate that the addition of Y or Ti atoms into CeO$_2$ improves the reduction-oxidation behavior of CeO$_2$. The Ce$_x$Ti$_{1-x}$O$_2$ and Ce$_x$Y$_{1-x}$O$_{1.5+0.5x}$ supports are much easier to be reduced by hydrogen in the presence of palladium. This is attributed to the active hydrogen formed on Pd and then spillovers onto the Ce$_x$Ti$_{1-x}$O$_2$ and Ce$_x$Y$_{1-x}$O$_{1.5+0.5x}$ supports. The Ce$_x$Ti$_{1-x}$O$_2$ and Ce$_x$Y$_{1-x}$O$_{1.5+0.5x}$ mixed oxide-supported PdO catalysts show higher activities for CH$_4$ oxidation than PdO/CeO$_2$, PdO/Y$_2$O$_3$ and PdO/TiO$_2$ catalysts. The PdO/Ce$_{0.8}$Y$_{0.2}$O$_{1.90}$ catalyst is the most active one among all these catalysts.

## 1. INTRODUCTION

Ceria (CeO$_2$) has been extensively studied in recent years because of its wide applications in many aspects of chemistry. In catalysis, for example, CeO$_2$ has been used as an important component of automotive three-way catalysts (TWCs) for reducing the exhaust pollutants. The main roles of ceria in the three-way catalysis are to promote the noble metal dispersion [1], increase the thermal stability of the Al$_2$O$_3$ support [2,3], promote CO oxidation and water-gas shift reaction [4-6], and store/release oxygen as an oxygen reservoir [7-10]. Among these functions, the most important property of CeO$_2$ is to be used as an oxygen reservoir, which stores and releases oxygen via the changing between Ce$^{4+}$ and Ce$^{3+}$ under oxidizing and reducing conditions.

Among the CeO$_2$-containing solid solutions, special attention has been focused on the CeO$_2$-ZrO$_2$ solid solution, because this material has been found to be very important to the three-way catalyst for eliminating the exhaust gases. From reported results, the CeO$_2$-ZrO$_2$ solid solution shows enhanced thermal stability, redox, and catalytic properties compared to single ceria. The CeO$_2$-ZrO$_2$ mixed oxides have been demonstrated to be high structural stability and oxygen storage capability over a wide range of ceria content. Furthermore, we found that CeO$_2$-TiO$_2$ mixed oxides also show the high capacity of storage oxygen [11].

Spillover of hydrogen from metal particles, such as Pd and Pt, to metal oxides can lower the hydrogen reduction temperature of these oxides [12]. In this work, we investigate the

reduction properties and activity of methane combustion on $PdO/Ce_xTi_{1-x}O_2$ and $PdO/Ce_xY_{1-x}O_{1.5+0.5x}$ catalysts and it is found that the hydrogen spillover plays on important role in the redox process of the catalyst.

## 2. EXPERIMENTAL

### 2.1. Preparation of $Ce_xTi_{1-x}O_2$ and $Ce_xY_{1-x}O_{1.5-0.5x}$

$Ce_{0.2}Ti_{0.8}O_2$, $Ce_{0.5}Ti_{0.5}O_2$ and $Ce_{0.8}Ti_{0.2}O_2$ mixed oxide samples were prepared by sol-gel method. A solution of $Ti[O(CH_2)_3CH_3]_4$ and ethanol was added to another solution of $Ce(NO_3)_3$ and ethanol under stirring, the solution was slowly gelled after finishing the reaction between $Ti[O(CH_2)_3CH_3]_4$ and $H_2O$. The gel was dried at 100°C under stirring, then a yellow solid was obtained and calcined at 650°C for 4h.

$Ce_xY_{1-x}O_{1.5+0.5x}$ (x=0, 0.2, 0.4, 0.6, 0.8, 1) mixed oxides were prepared by evaporating an aqueous solution of mixed metal nitrates containing an equivalent amount of citric acid to obtain a gel. The gel, which was transparent and viscous, was dried in an oven at 100°C, then was calcined at 650°C for 4h.

### 2.2. Preparation of supported PdO catalysts

The supported PdO catalysts were prepared by the conventional wet impregnation method using oxide supports and an aqueous solution of $H_2PdCl_4$, The as-prepared sample wasdried overnight in an oven at 120°C and then heated in air at 650°C for 4h. The loading of Pd is estimated to be 0.75%wt.

### 2.3. Temperature-programmed reduction ($H_2$-TPR)

TPR of the mixed oxides was carried out using 10% $H_2$ in Ar as reducing agent. The rate of $H_2$ consumption during the reduction was detected by a thermal conductivity detector. The gas flow rate was 30 ml/min. The weight of sample was 25 mg, and the heating rate of TPR was 20°C/min. The water produced during TPR was trapped by a 5A molecular sieve. Quantitative calculations of the extent of reduction were performed by calibrating the apparatus for hydrogen consumption for reduction of CuO to Cu.

### 2.4. Activity measurement of methane combustion

Catalytic activity measurement was carried using a fixed bed reactor (i.d. 0.6 cm) with 150mg of catalyst. The total gas flow rate was set at 80 mL/min. The gas is consisted of 3% $CH_4$ and 8%$O_2$ in $N_2$. The product, $CO_2$, was analyzed by gas chromatography with Porapak Q columns operating at 50°C.

## 3. RESULTS AND DISCUSSION

### 3.1. $PdO/Ce_xTi_{1-x}O_2$ catalysts

Table 1 lists the phase composition of $Ce_xTi_{1-x}O_2$ mixed oxides on the basis of XRD

result[12]. From Table 1, it can be found that the structure of the mixed oxides changes with Ce/Ti ratio.

Table 1
Phase composition of $Ce_xTi_{1-x}O_2$ mixed oxides based on XRD[11]

| Sample | Phase composition |
|--------|-------------------|
| $TiO_2$ | Rutile and anatase |
| $Ce_{0.2}Ti_{0.8}O_2$ | Anatase and monoclinic |
| $Ce_{0.5}Ti_{0.5}O_2$ | Cubic and monoclinic |
| $Ce_{0.8}Ti_{0.2}O_2$ | Cubic |
| $CeO_2$ | Cubic |
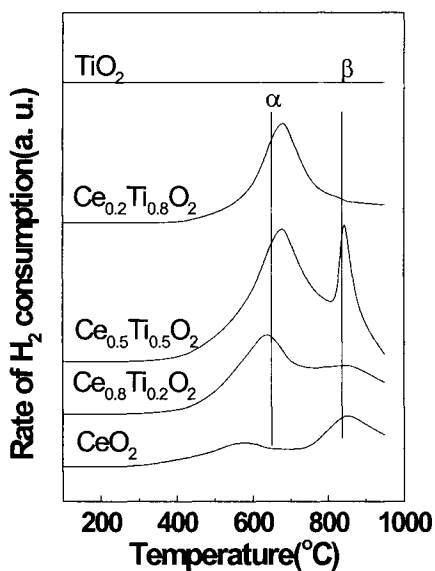


Fig.1. TPR profile of $Ce_xTi_{1-x}O_2$ samples ( x = 0, 0.2, 0.5, 0.8 and 1.0)
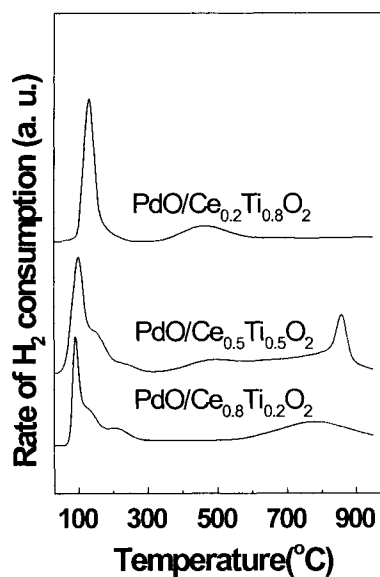
Fig.2. TPR profile of $PdO/Ce_{0.8}Ti_{0.2}O_2$, $PdO/Ce_{0.5}Ti_{0.5}O_2$ and $PdO/Ce_{0.2}Ti_{0.8}O_2$

Figure 1 shows the TPR profiles of the $CeO_2$, $Ce_{0.2}Ti_{0.8}O_2$, $Ce_{0.5}Ti_{0.5}O_2$, $Ce_{0.8}Ti_{0.2}O_2$ and $TiO_2$ samples. There are two reduction peaks at about 650°C and 850°C in the TPR profile for $CeO_2$, $Ce_{0.8}Ti_{0.2}O_2$ and $Ce_{0.5}Ti_{0.5}O_2$, while there is only one peak at 680°C for $Ce_{0.2}Ti_{0.8}O_2$. $TiO_2$ does not show evident reduction peak in the temperature range from 100 to 950°C. The amount of the $H_2$ consumption of $CeO_2$, $Ce_{0.8}Ti_{0.2}O_2$, $Ce_{0.5}Ti_{0.5}O_2$, and $Ce_{0.2}Ti_{0.8}O_2$ is 0.58, 1.43, 2.14 and 1.07 mmol/g, respectively. This indicates that the mixed oxides are easily reduced by

hydrogen than $CeO_2$ alone. Figure 2 shows the TPR profiles of $Ce_{0.2}Ti_{0.8}O_2$, $Ce_{0.5}Ti_{0.5}O_2$ and $Ce_{0.8}Ti_{0.2}O_2$ supported Pd catalysts. The amount of hydrogen consumption of low-temperature peak (<300°C) is 0.59, 1.02, 0.95 mmol/g for $PdO/Ce_{0.8}Ti_{0.2}O_2$, $PdO/Ce_{0.5}Ti_{0.5}O_2$ and $PdO/Ce_{0.2}Ti_{0.8}O_2$ catalysts, respectively. This is much larger than 0.06 mmol/g estimated for PdO reduction. The amount of hydrogen consumption of high-temperature peak (>300°C) is 1.01, 1.22 and 0.19 for $PdO/Ce_{0.8}Ti_{0.2}O_2$, $PdO/Ce_{0.5}Ti_{0.5}O_2$ and $PdO/Ce_{0.2}Ti_{0.8}O_2$ catalysts, respectively. But the total amount of hydrogen consumption of catalyst is close to those of their corresponding supports. Compared with Figure 1, it is found that the $\alpha$ peak of support does not appear in Figure 2. When the loading of Pd increases from 0.25% to 3.0%, the low-temperature peak shifts to lower temperatures, but the amount of hydrogen consumption remains unchanged. From results mentioned above, we believe that the low-temperature peak in Figure 2 is due to the reduction of PdO and part of $Ce^{4+}$. This indicates that the $Ce_xTi_{1-x}O_2$ support modified by PdO is easier to be reduced by hydrogen. This phenomenon can be explained as follows: PdO is easily reduced by $H_2$ to form Pd atom. Pd adsorbs $H_2$ and dissociates it into H atom, which then spillovers onto $Ce_xTi_{1-x}O_2$ support to promote its reduction [13], namely:

$$H_2 \xrightarrow{\quad Pd \quad} 2H_{SP} \quad (H_{SP}=\text{spillover H})$$

$$Ce^{4+}\text{-}O + 2H_{SP} \longrightarrow Ce^{3+} + H_2O$$
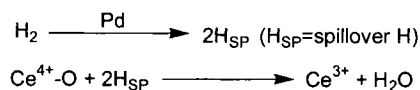
### 3.2. $PdO/Ce_xY_{1-x}O_{1.5+0.5x}$ catalysts

Figure 3 shows the TPR patterns of $Ce_xY_{1-x}O_{1.5+0.5x}$ mixed oxides calcined at 650°C. From the $Y_2O_3$ (211), (332), (431), and $CeO_2$ (440) diffraction peaks, it can be seen that only face-centered cubic phase is observed when the x>0.5, while only body-centered cubic phase is observed for $Ce_xY_{1-x}O_{1.5+0.5x}$ (x 0.5). Table 2 lists the changes in the lattice parameter of $Ce_xY_{1-x}O_{1.5+0.5x}$ mixed oxides. From Table 2, it can be seen that the lattice parameter decreases with increasing Y content. This means that the incorporation of $Y^{3+}$ ions into the ceria lattice when x>0.5, but that of $Ce^{4+}$ ions into $Y_2O_3$ lattice when x 0.5, can derive the solid solution of $Ce_xY_{1-x}O_{1.5+0.5x}$ because the radius of $Y^{3+}$ ions(0.092nm) is smaller than that of $Ce^{4+}$ ions(0.097nm).

Figure 4 shows the TPR profiles of the $Ce_xY_{1-x}O_{1.5+0.5x}$ solid solution. There are two reduction peaks at about 620°C ($\alpha$) and 770°C ($\beta$) in the TPR profile for $Ce_xY_{1-x}O_{1.5+0.5x}$ (x=0.9, 0.8, 0.6, 0.5, 0.3, and 0.2). $Y_2O_3$ does not show evident reduction peak in the temperature range from 100 to 950°C. The intensity of $\alpha$ peak increases with increasing Y content, while the intensity of $\beta$ peak decreases. This means that the presence of $Y_2O_3$ promotes the reduction of $CeO_2$ or $Y^{3+}$ ions weakens the Ce-O bond in the solid solution of $Ce_xY_{1-x}O_{1.5+0.5x}$ and make the $CeO_2$ component more easily reduced.

Figure 5 shows the TPR profiles of $PdO/Ce_xY_{1-x}O_{1.5+0.5x}$ catalysts. From Figure 5, it can be seen that there are three reduction peaks for $PdO/Y_2O_3$ catalyst. The $H_2$ consumption of two peaks ($\alpha$ and $\beta$) at lower temperatures is near 0.105 mmol/g expected for PdO reduction. We
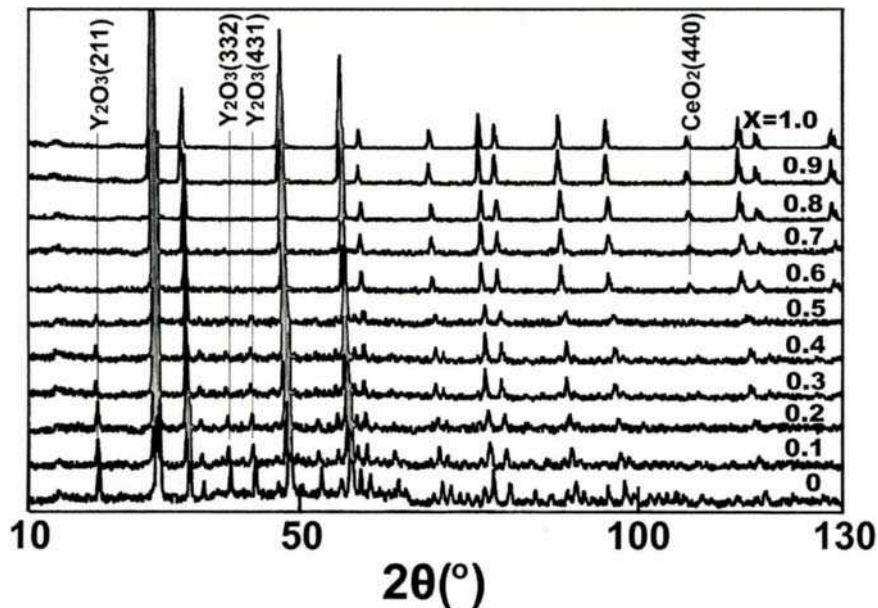
Fig. 3. XRD patterns of Ce-Y-O solid solution. x is Ce/(Ce+Y) mole ratio.

Table 2

Lattice parameter of $CeO_2$ phase (440) and $Y_2O_3$ phase (211) in $Ce_xY_{1-x}O_{1.5+0.5x}$

| Samples | $CeO_2$ (440)(nm) | $Y_2O_3$ (211)(nm) |
|---|---|---|
| $CeO_2$ | 0.5414 | |
| $Ce_{0.9}Y_{0.1}O_{1.95}$ | 0.5414 | |
| $Ce_{0.8}Y_{0.2}O_{1.90}$ | 0.5408 | |
| $Ce_{0.7}Y_{0.3}O_{1.85}$ | 0.5397 | |
| $Ce_{0.6}Y_{0.4}O_{1.80}$ | 0.5397 | |
| $Ce_{0.5}Y_{0.5}O_{1.75}$ | | 1.078 |
| $Ce_{0.4}Y_{0.6}O_{1.70}$ | | 1.074 |
| $Ce_{0.3}Y_{0.7}O_{1.65}$ | | 1.080 |
| $Ce_{0.2}Y_{0.8}O_{1.60}$ | | 1.076 |
| $Ce_{0.1}Y_{0.9}O_{1.55}$ | | 1.072 |
| $Y_2O_3$ | | 1.059 |

believe that the two peaks at lower temperatures are attributed to the reduction of the PdO precursor. The $\gamma_1$ peak is attributed to the reduction of $Y_2O_3$ support. For $Ce_xY_{1-x}O_{1.5+0.5x}$ (x=0.2,

0.4, 0.6, 0.8, and 0.9) supported PdO catalysts, the $H_2$ consumption of $\alpha$ and $\beta$ peaks is obviously higher than that expected for PdO reduction. The reason may be attributed to the concurrent reduction of surface $Ce^{4+}$ and/or $Y^{3+}$ ions, which occur at lower temperatures [14]. The $\gamma_1$ and $\gamma_2$ peaks are attributed to the reduction of the $Ce_xY_{1-x}O_{1.5+0.5x}$ support. In the presence of the Pd, the reduction of support becomes more facile. This indicates that the addition of the noble metal effectively promotes the reduction of $Ce_xY_{1-x}O_{1.5+0.5x}$ supports. This is attributed to the ability of the supported-metal (Pd) to activate $H_2$ and then hydrogen atoms spill the support [14]. In the absence of the metal, $H_2$ activation is difficult and may become the rate determining step. From Figure 5, it can be found that the different component in the supports affects the intensity of $\alpha$ peak for $PdO/Ce_xY_{1-x}O_{1.5+0.5x}$ catalysts, and the $PdO/Ce_{0.8}Y_{0.2}O_{1.90}$ catalyst shows the highest intensity of the $\alpha$ peak.
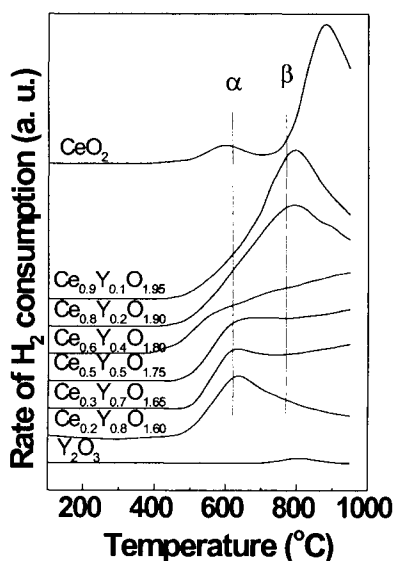


Fig. 4. TPR profiles of $Ce_xY_{1-x}O_{1.5+0.5x}$
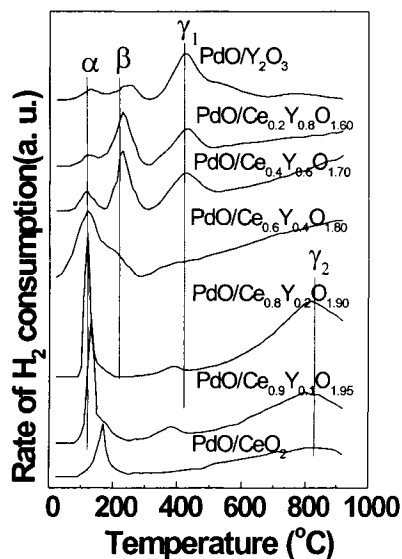
Fig. 5. TPR profiles of $PdO/Ce_xY_{1-x}O_{1.5+0.5x}$ catalysts

## 3.3. Catalytic activity for methane oxidation

Figures 6 and 7 show the light-off curves of the $PdO/Ce_xTi_{1-x}O_2$ and $PdO/Ce_xY_{1-x}O_{1.5+0.5x}$ catalysts for methane oxidation, respectively. It can be seen that the mixed-oxide-supported PdO catalysts are more active than the single-oxide-supported catalysts. For $PdO/Ce_xTi_{1-x}O_2$ catalysts, the $PdO/Ce_{0.8}Ti_{0.2}O_2$ is most active for methane oxidation, and $PdO/Ce_{0.8}Y_{0.2}O_{1.9}$ catalyst is most active among all $PdO/Ce_xY_{1-x}O_{1.5+0.5x}$ catalysts. The temperature of $T_{90}$ is only 400°C for $PdO/Ce_{0.8}Y_{0.2}O_{1.9}$. Compared the Figures 5 and 7 it can be found that the activity for methane oxidation is related to the intensity of $\alpha$ peak. It is interesting of that high activity of

mixed-oxide-supported PdO catalysts seem to be relevance to the abilities of hydrogen spillover.
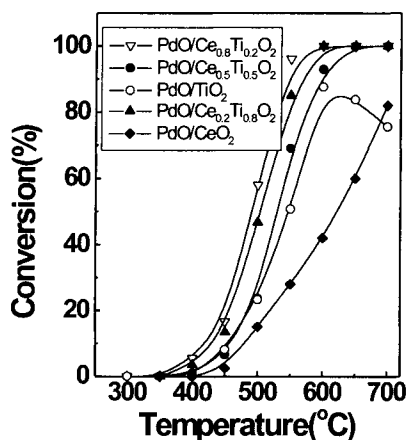


Fig. 6. Light-off curves of PdO/Ce$_x$Ti$_{1-x}$O$_2$ catalysts for methane oxidation
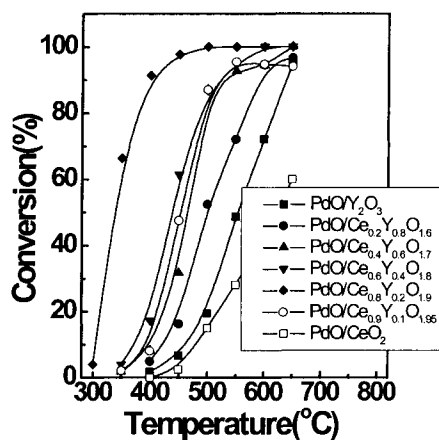
Fig. 7. Light-off curves of PdO/Ce$_x$Y$_{1-x}$O$_{1.5+0.5x}$ catalysts for methane oxidation

## 4. SUMMARY

The structure of the Ce$_x$Ti$_{1-x}$O$_2$ and Ce$_x$Y$_{1-x}$O$_{1.5-0.5x}$ mixed oxide materials depends on the Ce content. Addition of Y or Ti atoms into CeO$_2$ improves the reduction-oxidation behavior of CeO$_2$, which might be due to that the Y or Ti atoms weaken the Ce-O bond in the mixed oxides.

The Ce$_x$Ti$_{1-x}$O$_2$ and Ce$_x$Y$_{1+x}$O$_{1.5-0.5x}$ supports are much easier to be reduced by hydrogen in the presence of palladium. This is attributed to the active hydrogen formed on Pd and then spillovers onto the Ce$_x$Ti$_{1-x}$O$_2$ and Ce$_x$Y$_{1-x}$O$_{1.5-0.5x}$ supports.

Ce$_x$Ti$_{1-x}$O$_2$ and Ce$_x$Y$_{1-x}$O$_{1.5-0.5x}$ mixed oxide-supported PdO catalysts show higher activities for CH$_4$ oxidation than PdO/CeO$_2$, PdO/Y$_2$O$_3$ and PdO/TiO$_2$ catalysts, because the mixed oxides possess better redox property.

## ACKNOWLEDGMENTS

68

**REFERENCES**

1. F. L. Normand, K. Hilaire, K. Kili and G. Maire, J. Phys. Chem., 92(1988) 2561.
2. B. Harrison, A. F. Diwell and C. Hallett, Plat. Met. Rev., 32(1988) 73.
3. M. Ozawa and M. Kimura, J. Mater. Sci. Lett., 9(1990) 291.
4. J. G. Numan, H. J. Robota, M. J. Cohn and S. A. Bradley, J. Catal., 133(1992) 309.
5. C. Serre, F. Garin, G. Belot and G. Maire, J. Catal., 141(1993) 1.
6. M.-F. Luo, Z.-Y. Hou, X.-X. Yuan and X.-M Zheng,. Catal. Lett., 50(1998) 205.
7. S. Imamura, M. Shono, N. Okamoto, A. Hamada and S. Ishida,
   Appl. Catal. A, 142(1996) 279.
8. S. Kacimi, Jr. J. Barbier, R. Taha and D. Duprez, Catal. Lett., 22(1993) 343.
9. G. S. Zafiris and R. J. Gorte, J. Catal., 143(1993) 86.
10. C Padeste. N. W. Cant and D. L. Trimm, Catal. Lett., 18(1993) 305.
11. M.-F. Luo, J. Chen, L.-S. Chen, J. Lu, Z.-C. Feng and C. Li, Chem. Mater., 13(2001) 197.
12. W. C. Conner Jr and J. L. Falconer, Chem. Rev., 956(1995) 759
13. G. Xu, Y. Zhu, J. Ma, H. Yan and Y. Xie, Stud. Surf. Sci. Catal., 112(1997) 333.
14. P. Pornasiero, R. Di Monte, G. Ranga Rao, S. Meriani, A. Trovarelli and M. Graziani., J. Catal., 151(1995) 168.

# Comparison of Hydrogen Spillover Effect between Cumene Cracking and n-Pentane Hydroisomerization over Pt/SiO$_2$+H-Beta Using Pulse Reaction Method

Toshiaki Kusakari[a], Keiichi Tomishige[a] and Kaoru Fujimoto[a]

[a] Department of Applied Chemistry, School of Engineering, The University of Tokyo, 7-3-1, Hongo, Bunkyo-ku, Tokyo 113-8656, Japan

The effect of spilt-over hydrogen on the catalytic activity of physically mixed catalyst composed of Pt/SiO$_2$ and H-Beta for cumene hydrocracking and n-pentane hydroisomerization has been investigated by using pulse reaction method. The stable activity was observed under hydrogen atmosphere in two reactions over Pt/SiO$_2$ + H-Beta. Under this reaction condition, split-over hydrogen species is formed and inhibited the catalytic deactivation. The reaction order with respect to hydrogen in cumene cracking was negative. On the other hand, reaction order in n-pentane hydroisomerization was much dependent on the hydrogen pressure range. Under low hydrogen pressure, The positive effect of hydrogen on the catalytic activity in n-pentane hydroisomerization was observed.
*Key Words: hydrogen spillover; zeolite; bifunctional catalyst; physical mixture catalyst; cumene cracking; n-pentane hydroisomerization*

## 1. INTRODUCTION

It has been reported that hydrogen spillover phenomenon influences the catalytic properties in hydrocarbon conversion over bifunctional catalysts. This effect has been observed on zeolite supported metal catalysts and zeolite physically mixed with metal supported on silica (1-5). This effect was also observed on Pt/SiO$_2$ + SO$_4^{2-}$-ZrO$_2$ and Pt/SO$_4^{2-}$-ZrO$_2$ catalysts (6). The effects of hydrogen and reaction parameter were similar to each other. This indicates that the distance between metal and acid site does not affect so much. This can be because hydrogen spillover is rapid and long-range phenomenon.

Chemical state of spilt-over hydrogen species has been on the discussion, but it is suggested that the species can be $H^+$, $H^-$, ion pair, $H_3^+$ and so on (7-10). Hydrogen spills over from metal to acid catalyst as follows. At first, hydrogen molecule in the gas phase dissociates on metal surface, and then active hydrogen species spills over to the support surface, furthermore it diffuses toward the adjacent particles.

Our group has proposed the reaction mechanism of hydrocarbon conversion, which is involved in spilt-over hydrogen species. In this mechanism it is suggested that spilt-over $H^-$ species is supplied to the carbenium reaction intermediate to desorb as paraffin and spilt-over $H^+$ species regenerates a Brønsted acid site. The difference between the classical and hydrogen spillover mechanism is in the role of metal site and olefin. In the classical bifunctional mechanism, olefin is the reaction intermediate. However the polymerization of olefin on acid sites causes the catalytic deactivation in hydrogen spillover mechanism. Under hydrogen atmosphere, olefin formation was not detected generally. In addition, in the classical mechanism, dehydrogenation and hydrogenation is catalyzed by metal surface. On the other hand hydrogen dissociation and spillover is caused by metal surface. The interaction between metal and hydrocarbon molecule is not important in our proposed mechanism. Shishido and Hattori have reported that spilt-over hydrogen enhanced the catalytic activity of cumene cracking over $Pt/SO_4^{2-}$-$ZrO_2$ and inhibit its deactivation (11). It is explained that split-over hydrogen generates Brønsted acid site that is active for cumene cracking. Hosoi et al. also reported that $Pt/SO_4^{2-}$-$ZrO_2$ shows both the high catalytic activity and stability in n-pentane isomerization in hydrogen atmosphere (12). They explained that hydrogen removed coke by hydrogenation.

In this study, we investigated the effect of spilt-over hydrogen on the two reactions, cumene hydrocracking and n-pentane hydroisomerization over bifunctional catalyst from the standpoint of the spillover mechanism. Especially, we focused the interaction of spilt-over hydrogen species with acid sites.

## 2. EXPERIMENTAL

### 2.1 Catalyst Preparation

$Pt/SiO_2$ was prepared by impregnation method using a commercially available $SiO_2$ (Aerosil 380, BET 380 $m^2$ $g^{-1}$) with an aqueous solution of $H_2PtCl_6$ $6H_2O$ (Soekawa, Pt assay 37 %). After impregnation and the removal of water, the sample was dried at 393 K for 12 h, and was calcined at 723 K in air for 3 h. The loading of Pt was 2.5 wt%. $Pt/SiO_2$ and H-

zeolite physically mixed catalyst was prepared by grinding the mixture of Pt/SiO$_2$ and H-Beta (Tosoh, SiO$_2$/Al$_2$O$_3$=27, used mainly) or H-ZSM-5 (Tosoh, SiO$_2$/Al$_2$O$_3$=23.8) for 30 min. The amount of Pt/SiO$_2$ in catalyst was described as physical mixture ratio (described PMR in short) that was defined as below formula; PMR = (weight of Pt/SiO$_2$) / (total weight). Weight of H-Beta was fixed at 0.020 g. All catalysts were pressed, crushed and sieved and used as 420-820 μm granule for reaction.

### 2.2 Cumene Cracking and *n*-Pentane Hydroisomerization

Activity test was carried out in a microcatalytic pulse reaction system. Before reaction the catalysts were reduced in H$_2$ (50 cm$^3$ min$^{-1}$) at 523 K for 0.5 h and pretreated at 523 K for 1 h in H$_2$ stream. Reactions were carried out at following condition; reaction temperature 503 K on cumene cracking and 593 K on *n*-pentane hydroisomerization, reaction pressure 0.10 MPa, zeolite weight in catalyst 0.020 g, a dose of reactant 0.5 - 5.0 μl (cumene: 3.6-36, *n*-pentane: 4.4-44 μmol), flow rate 50 cm$^3$ min$^{-1}$, H$_2$:He = 4-x:x (x = 1-4). Reactant was introduced to the reactor with microsyringe every 20 and 10 min on cumene cracking and *n*-pentane
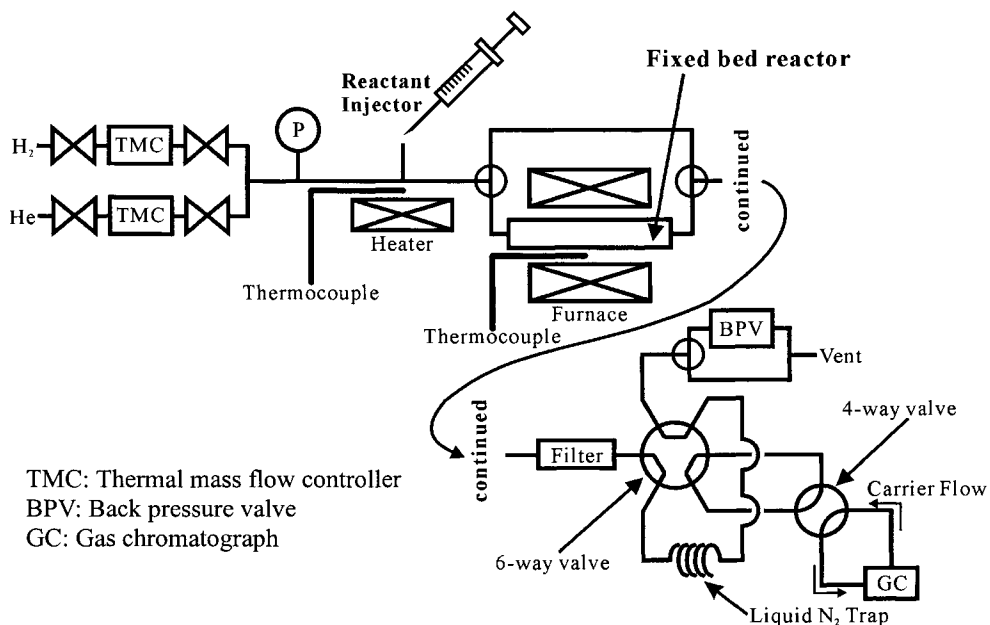


Fig. 1 Microcatalytic pulse reaction system
The line below the reactor is heated by ribbon heater.

hydroisomerization, respectively. The products were trapped at 77 K before being flash evaporated into GC capillary column (NEUTRABOND-1, GL Science) with FID detector. Figure 1 shows the scheme of microcatalytic pulse reaction system. For further analysis of products, GC capillary column (Shimadzu, PONA CBP-1) with FID detector was used.

## 3. RESULTS AND DISCUSSION

Figure 2(a) shows the effect of constituent of catalyst on cumene hydrocracking at 503 K under hydrogen or helium flowing. Major products were $C_3$ (propane and propene), and benzene and the minor are toluene, ethylbenzene, $n$-propylbenzene and dipropylbenzene and their hydrogenated compounds. Cumene cracking selectivity was about 80 mol%. The high and stable cracking activity was observed on $Pt/SiO_2$ + H-Beta catalyst under hydrogen flowing. In this case, hydrogen can spillover to zeolite from Pt. The cracking activity on $Pt/SiO_2$ + H-Beta catalyst under helium flowing was higher than that under hydrogen flowing. However, catalyst deactivation under helium flowing was observed. The behavior of the cracking activity on H-Beta catalyst under hydrogen flowing was very similar to that on
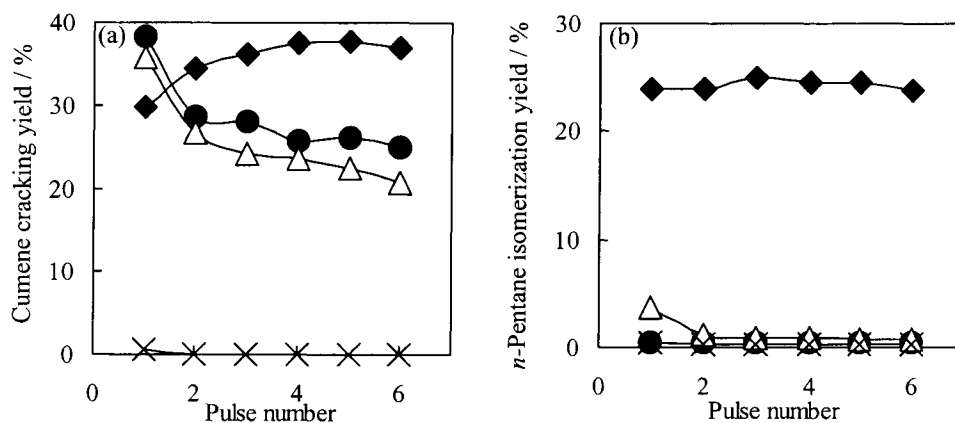


Fig. 2  Effect of effect of constituent of catalyst on cumene cracking (a)
and $n$-pentane hydroisomerization (b)
503 K(a), 593 K(b), 0.10 MPa, 50 cm$^3$ min$^{-1}$, $H_2$ or He flow
Cumene dose amount 1.0 μl (a: 7.2 μmol, b: 8.7 μmol)
: $Pt/SiO_2$ + H-Beta physically mixed catalyst in $H_2$ flow, 0.025 g, PMR 0.20
: $Pt/SiO_2$ + H-Beta physically mixed catalyst in He flow, 0.025 g, PMR 0.20
●: H-Beta (0.020 g) in $H_2$ flow
×: $Pt/SiO_2$ (0.020 g) in $H_2$ flow

Pt/SiO$_2$ + H-Beta catalyst under helium flowing. In these two cases, spilt-over hydrogen species cannot be formed. From these comparisons, the reaction behavior can be determined only H-Beta zeolite. Hydrogen doesn't affect the behavior on H-Beta zeolite. And Pt/SiO$_2$ does not affect the behavior on H-Beta zeolite without hydrogen flowing. In these results, the amount of cumene in one pulse is 7.2 μmol, and this corresponds to 29 % of the acid amount in H-Beta. Therefore, these results indicate the initial activity. Then Pt/SiO$_2$ exhibited no cracking activity under hydrogen flowing. The initial activity on Pt/SiO$_2$ + H-Beta under hydrogen flowing, Pt/SiO$_2$ + H-Beta under helium flowing, and H-Beta under hydrogen flowing was considerably similar to each other. Acidity can determine the catalytic activity on cumene cracking. On the other hand, the stability was different on these three catalysts. Hydrogen spillover is effective to maintain the acidity. At the same time, these results also indicated that hydrogen spillover did not enhance the activity of cumene cracking.

Figure 2(b) shows the results of $n$-pentane hydroisomerization at 593 K. Major product was *iso*-pentane and the biproducts (C$_2$, C$_3$ and *iso*-C$_6$) were detected. $n$-Pentane isomerization selectivity was about 65 mol%. The high and stable activity was observed over Pt/SiO$_2$ + H-Beta under hydrogen flowing. Pt/SiO$_2$ catalyst showed almost no activity under hydrogen flowing. These behaviors were also observed in cumene cracking. However, the activity of Pt/SiO$_2$ + H-Beta under helium flowing and H-beta under hydrogen flowing were much lower than that over Pt/SiO$_2$ + H-Beta under hydrogen flowing. This behavior was completely different from that in cumene cracking. It has been reported that the isomerization of $n$-paraffin proceeds in the bifunctional mechanism (13-15). In terms of the bifunctional mechanism, it is expected that the initial isomerization activity over Pt/SiO$_2$ + H-Beta under hydrogen flowing is similar to that under helium flowing, and olefin can be detected. However this is not true for these results. These results suggest that hydrogen spillover promotes $n$-pentane isomerization. From comparison between cumene cracking and hydroisomerization, the effect of hydrogen spillover on the activity is different.

Figures 3(a) and (b) show effects of hydrogen partial pressure and the dose amount on the catalytic activity over Pt/SiO$_2$ + H-Beta on cumene cracking and on $n$-pentane hydro-isomerization, respectively. As for hydrogen partial pressure, effect of hydrogen was negative in all the condition of dose amount in cumene cracking. In $n$-pentane hydroisomerization, the tendency was different. The dependence of the activity on hydrogen partial pressure is both positive and negative. In the case of smaller dose amount and higher hydrogen pressure, negative effect is observed. In the case of larger amount dose amount and lower hydrogen partial pressure, positive effect is observed.

Figures 4(a) and (b) show the effects of the amount of Pt/SiO$_2$ in Pt/SiO$_2$ + H-Beta and dose on the catalytic activity in cumene cracking and $n$-pentane hydroisomerization, respectively. In case of cumene cracking, the catalytic activity was decreased with the amount of Pt/SiO$_2$ and it was increased with dose amount. On the other hand, the effect of Pt/SiO$_2$ on the activity in $n$-pentane hydroisomerization was completely opposite to that in cumene cracking. The activity increased with the dose amount of 4.3-26 μmol in the all case of Pt/SiO$_2$ weight, but the activity was almost constant in the dose amount of 26-43 μmol in smaller amount of Pt/SiO$_2$. The effect of dose amount on the activity in isomerization was saturated.

Here, there is need to understand the meaning of controlling these reaction parameters; hydrogen partial pressure, physical mixture ratio and dose amount from the standpoint of spilt-over hydrogen species. Needless to say, hydrogen partial pressure affects directly the equilibrium amount and formation rate of spilt-over hydrogen species. Allowing that the platinum catalyzes hydrogen into spilt-over hydrogen species, the formation rate of spilt-over hydrogen species should be increased by increasing physical mixture ratio. And increase of dose amount reduces hydrogen partial pressure indirectly and gives negative effect to formation of spilt-over hydrogen species.
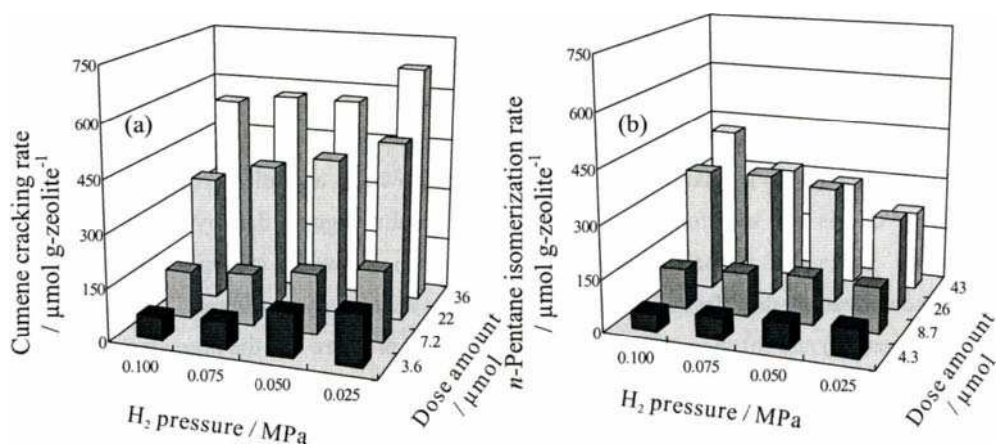


Fig. 3  Effect of H$_2$ partial pressure and dose amount on cumene cracking (a)
and $n$-pentane hydroisomerization (b)
503 K(a), 593 K(b), 0.10 MPa, 50 cm$^3$ min$^{-1}$, He Balance
Pt/SiO$_2$+H-Beta physically mixed catalyst 0.025 g, PMR 0.20

More spilt-over hydrogen species (higher hydrogen pressure and larger amount of Pt) decreases the catalytic activity. The positive effect of spilt-over hydrogen species on cumene cracking is the stabilization of catalytic activity (Fig. 2(a)). The positive effect of hydrogen spillover was clearly observed when dose amount was 26-43 μmol. This is not due to the inhibition of deactivation since our experimental method gives the initial activity on fresh surface. The mechanism of inhibition of deactivation is the supply of spilt-over hydride to the carbenium cation reaction intermediate on acidic site and its desorption as paraffin. The mechanism of the enhancement of the activity by spilt-over hydrogen species is not clear at present, however, it seems that spilt-over hydrogen species increase the acid strength. From the result of cumene cracking, the activity was determined by the presence of zeolite since cumene cracking proceeds on all the acid sites. However, the strong acid site on zeolite can take part in the $n$-pentane hydroisomerization because $n$-pentane has lower reactivity than cumene. It seems that the spilt-over hydrogen species can enhance the acid strength.
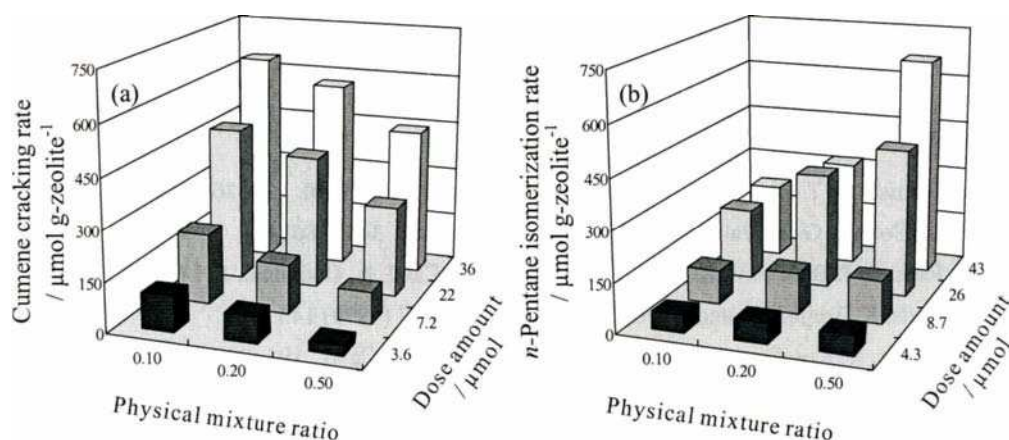


Fig. 4  Effect of physical mixture ratio and dose amount on cumene cracking (a)
and $n$-pentane hydroisomerization (b)
503 K(a), 593 K(b), 0.10 MPa, 50 cm$^3$ min$^{-1}$, H$_2$ 75 %, He Balance
Pt/SiO$_2$+H-Beta physically mixed catalyst, Weight of H-Beta 0.020 g
Physical mixture ratio = (weight of Pt/SiO$_2$) / (total weight)

## 4. CONCLUSION

In cumene cracking, The catalytic activity is determined by acidity in H-Beta, and not by hydrogen and metal. Hydrogen and metal can promote the catalytic stability drastically but higher hydrogen partial pressure and larger metal amount reduce the catalytic activity in cumene cracking. On the other hand, the catalytic activation in $n$-pentane hydroisomerization is enhanced by $Pt/SiO_2$ + H-Beta under hydrogen flowing. Furthermore, the dependencies of hydrogen partial pressure and metal amount were positive in the case of larger dose amount. From the results, it is suggested that hydrogen spillover enhance the acid strength.

## REFERENCES

1. K. Fujimoto, K. Maeda, and K. Aimoto, Appl. Catal. A General, 91 (1992) 81.

2. I. Nakamura, K. Sunada and K. Fujimoto, Stud. Surf. Sci. Catal., 105 (1997)1005.

3. I. Nakamura, K. Sunada, and K. Fujimoto, Stud. Surf. Sci. Catal., 106 (1997) 361.

4. A. Zhang, I. Nakamura, and K. Fujimoto, Stud. Surf. Sci. Catal., 106 (1997) 561.

5. A. Zhang, I. Nakamura, K. Aimoto and K. Fujimoto, Ind. Eng. Chem. Res., 34 (1997) 1074.

6. K. Tomishige, T. Okabe and K. Fujimoto, Appl. Catal. A General, 194 (2000) 393.

7. W. C. Conner, G. M. Pajonk and S.Teichner, Adv. Catal., 34 (1986) 1.

8. U. Roland, T. Braunshweigand F. Roessner, J. Mol. Catal. A: Chemical, 127 (1997) 61.

9. R. Ueda, K. Tomishige and K. Fujimoto, Catal. Lett., 57 (1999) 145.

10. R. Ueda, K. Kusakari, K. Tomishige and K. Fujimoto, J. Catal., 194 (2000) 14.

11. T. Shishido and H. Hattori, J. Catal., 161 (1996) 194.

12. T. Hosoi, T. Shimadzu, S. Ito, S. Baba, H. Takaoka, T. Imai, and N. Yokoyama, "Successful Design of Catalysts," Prepr. Symp. Div. Petr. Chem., Am. Chem. Soc., 562, p.99. Elsevier, Amsterdam, 1998

13. G. A. Mills, H. Heinemann, T. H. Milliken and A. G. Oblad, Ind. Eng. Chem., 45 (1953) 134.

14. P. B. Weisz and E. W. Swegler, Science, 126 (1957) 887.

15. H. Y. Chu, M. P. Rosynek and J. H. Lunsford, J. Catal., 178 (1998) 352.

# FTIR evidences of the reactivity of spilt-over stored hydrogen: Transformation of Lewis acid sites into Brönsted sites on Pt/ZrO$_2$ catalyst

Ruth L. Martins, Mariana M. V. M. Souza, Donato A. G. Aranda and Martin Schmal

NUCAT/PEQ/COPPE, Universidade Federal do Rio de Janeiro, C.P. 68502, 21945-970, Rio de Janeiro, Brazil

The reactivity of hydrogen species resulted from backspillover of H atoms stored in the support when Pt/ZrO$_2$ catalyst is reduced was shown even in the absence of H$_2$ in the gas phase. These species were able to create acidic hydroxyls and move pyridine chemisorbed on Lewis acid sites to the new Brönsted sites just formed, when the sample was heated in a closed system. Also piperidine chemisorbed on Lewis acid sites was dehydrogenated to pyridine when the sample was heated in a closed system, and the IR spectrum showed bands which were assigned to pyridine chemisorbed on Lewis and Brönsted sites. The reactivity of hydrogen spillover species was also observed by CO chemisorption experiments using FTIR and TPD techniques.

## 1. INTRODUCTION

Several authors reported many important phenomena assigned to hydrogen spilt-over in heterogeneous catalysis. They are relative to enhanced adsorption properties, enhanced isotopic exchange, promoting bulk changes, promoting strong metal-support interaction, etc. Concerning on influences about catalytic processes, it was also reported its activity in keeping clean catalyst surfaces, creating or regenerating selective sites through a remote control mechanism, improving activity and inhibiting deactivation, as observed in catalytic hydrogenation and dehydrogenation reactions [1].

A great effort has been made in characterizing the nature of spilt-over hydrogen species by reacting them with some probe molecules like CO, NO, D$_2$ and detecting the intermediates formed [2]. However, for characterizing the interaction of hydrogen spillover from metallic surface onto acidic surface, molecules like pyridine and piperidine are more suitable [3-6], as these bases are effective probes for determining surface acid sites and acidic properties.

In general, the experiments involving spilt-over hydrogen are carried out in the presence of H$_2$ in the gas phase as the spilt-over hydrogen stored on the support is considered to be poor in reactivity.

In the present work, it was shown, by using "in situ" Infrared Spectroscopy and pyridine adsorption, that the spilt-over hydrogen stored when the metallic catalyst was reduced, was able to transform Lewis acid sites into Brönsted sites on Pt/ZrO$_2$ catalyst. Also the reactivity of hydrogen species provided by backspillover was investigated using experiments of TPD of CO chemisorbed on the same catalyst.

## 2. EXPERIMENTAL

$ZrO_2$ support was obtained by calcination at 823 K for 2 h under flowing air of zirconium hydroxide (MEL Chemicals). The $Pt/ZrO_2$ catalyst was prepared by incipient wetness technique, using an aqueous solution of $H_2PtCl_6$ (Aldrich), followed by drying at 393 K for 16 h and calcination in air at 823 K for 2 h. The platinum content was around 1% (w/w), which was measured by atomic absorption spectrometry.

Infrared experiments were conducted using a Fourier transform spectrometer, Perkin Elmer 2000, and self supported wafers (9.8 mg $cm^{-2}$ thickness) by using a Pyrex cell with $CaF_2$ windows. During the sample pretreatment and gas adsorption the cell was attached to a vacuum glass system. The spectral domain was between 4000 and 1000 $cm^{-1}$ with a 4 $cm^{-1}$ resolution. The samples were reduced "in situ" with pure hydrogen at 573 K or 773 K for one hour, followed by evacuation up to $10^{-5}$ Torr at the same time and temperature. After cooling down to room temperature the infrared spectrum was recorded and used as background for the other adsorption experiments. The spectrum in the hydroxyl region was obtained by dividing the spectrum of reduced sample and the background of sample compartment. Adsorption studies were conducted by exposing the reduced wafers to 4 and 10 Torr of pyridine and piperidine, respectively, and for CO adsorption, to 30 Torr.

TPD was performed in a dynamic mode apparatus. First the catalyst was dried at 423 K for 30 min and reduced at 573 or 773 K for 1 h. After reduction the sample was purged with He during cooling down to room temperature. CO was admitted by injecting pulses until complete saturation of the catalyst surface was obtained. Desorption was performed by heating the catalysts at 20 K/min ramp up to 873 K in flowing helium. The effluent gas composition was monitored by a quadrupole mass spectrometer (Dycor MA100M- Ametek).

## 3. RESULTS AND DISCUSSION

### 3.1. Pyridine and Piperidine Adsorption

It is known that pyridine adsorbs on $Pt/ZrO_2$ catalyst only on Lewis acid sites and, in order to develop Brönsted acidity, it is necessary to incorporate sulfate ions to the oxide structure [7].

"In situ" Infrared experiments showed that, when $Pt/ZrO_2$ was reduced at 773 K under hydrogen flow, per one hour, followed by evacuation, at the same temperature, up to $10^{-5}$ Torr, the spilt-over hydrogen stored in the zirconia can transform, after pyridine chemisorption, Lewis acid sites into Brönsted acid sites while the temperature was raised up to 573 K (Figure 1).

As the migration of spilt-over hydrogen species to the lattice oxide oxygen corresponds to the slow step of the reaction, it was necessary to keep the experiment in a closed system, otherwise the spilt-over hydrogen migrates priority to the metal and desorbs as $H_2$, being pumped out by vacuum.

Spectrum (a) of the Figure 1 shows that, after pyridine chemisorption, bands at 1444 (vs), 1490 (w) and 1607 (s) $cm^{-1}$ appeared and were assigned to pyridine coordinated to Lewis acid sites on $ZrO_2$ surface. When the sample was heated, the hydrogen provided by backspillover (which was stored in the support) was activated, migrating probably first to the metal (but not desorbing as $H_2$, as the system was closed), and then returning to an $O^{2-}$ site in close neighborhood with the Lewis site where pyridine was adsorbed (spectrum (c)). The base was then moved to the new Brönsted site just formed, and a new band at 1540 $cm^{-1}$ was

created, besides the increase in intensity of the 1490 cm$^{-1}$ band, which also indicates the presence of Brönsted acid sites.

Figure 2 shows the IR spectra of pyridine adsorbed on $ZrO_2$ after the support has received the same pretreatment with $H_2$ gave to the Pt catalyst (spectrum (a)). As expected, after heating the support up to 573 K in a closed system no Brönsted acid sites were detected once no backspillover hydrogen species were formed due to the absence of $Pt^0$. It noteworthy that the acid sites on metallic catalyst are stronger than those on the support. On $Pt/ZrO_2$ catalyst pyridine remains chemisorbed up to 623 K (spectrum (b) in Figure 1).
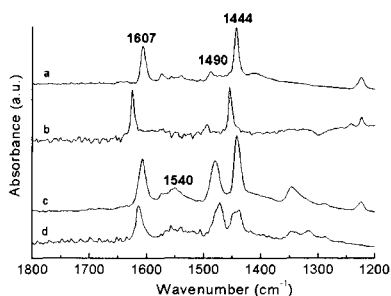


Figure 1. Pyridine chemisorption on $Pt/ZrO_2$ (a) at 423 K, vacuum up to 10$^{-5}$ Torr; (b) heating at 623 K in vacuum, (c) spectrum (a) heated at 573K in a closed system, (d) vacuum at 673 K.
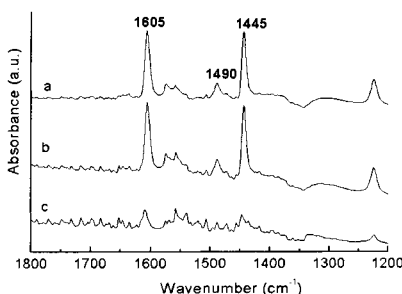
Figure 2. Pyridine chemisorption on $ZrO_2$ (a) at 423 K, vacuum up to 10$^{-5}$ Torr; (b) heating at 573 K in a closed system; (c) vacuum at 673 K.

Piperidine adsorbed on the same catalyst also showed interesting results. As $Pt/ZrO_2$ only exhibits Lewis acid sites, piperidine chemisorption showed the spectrum with the absence of the 1600 cm$^{-1}$ band attributed to piperidine chemisorbed on Brönsted sites (Figure 3). When the sample was heated up to 573 K, in a closed system, the asymmetric and symmetric stretching $CH_2$ vibration (2942 and 2862 cm$^{-1}$ respectively) diminished and new bands at 1485 and 1558 cm$^{-1}$ appeared, indicating that part of piperidine was dehydrogenated to pyridine and, at the same time, spilt-over hydrogen species create new Brönsted acid sites. The backspillover hydrogen, stored in the support when the sample is reduced, and the hydrogen provided by piperidine dehydrogenation are able to create protonic acid sites. Otherwise, pyridine can be hydrogenated to piperidine by the spilt-over hydrogen species, as shown for USY+Pt/SiO$_2$ hybrid catalyst [4] and Pt/ZSM-5 [5].

## 3.2. CO Adsorption

The CO desorption profiles of $Pt/ZrO_2$ catalyst are shown in Figure 4 for different reduction temperatures at 573 and 773 K. After reduction at 773 K no $H_2$ was observed and the $CO_2$ profile showed two peaks at 373 K and 513 K. After reduction at 573 K the $CO_2$ profile exhibited two distinctly regions: in the first one, it extends up to 500 K releasing only
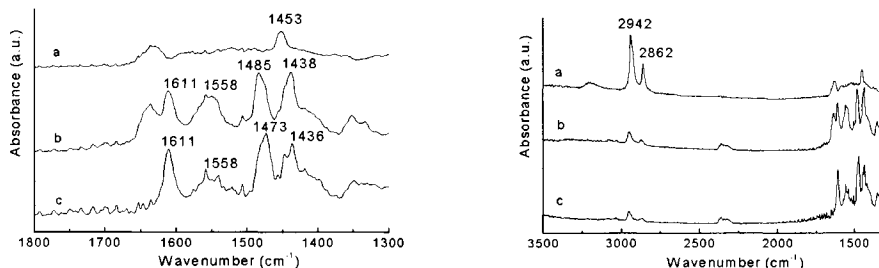
Figure 3. Piperidine chemisorption on $Pt/ZrO_2$ (a) at 423 K, vacuum up to $10^{-5}$ Torr; (b) heating at 573 K in a closed system; (c) vacuum at 673 K.

$CO_2$, while in the second region a maximum $CO_2$ desorption occurred at 550 K with simultaneous and symmetric formation of $H_2$.

$CO_2$ formation during TPD is generally attributed to the Boudouard reaction on metallic Pt ($2CO \rightarrow CO_2 + C$) [8]. The $CO_2$ profile of $Pt/ZrO_2$ catalyst reduced at 773 K could be related to this reaction, but it was ruled out as the total amount of $CO_2$ desorbed corresponded exactly to that of CO chemisorbed, as shown in Table 1. Instead it was proposed the reaction of CO with two different kinds of oxygen lattice of $ZrO_2$ (which were responsibly for the two $CO_2$ desorption regions), in the neighborhood of $Pt-ZrO_2$ interface: $CO(Pt^*) + [O](ZrO_x) \rightarrow CO_2$ ($Pt^*$ is the Pt surface active site and $ZrO_x$ is the reduced surface site).

Different desorption profiles were obtained for $Pt/ZrO_2$ reduced at 573 K where, aside the $CO_2$ desorption at two different temperatures, $H_2$ desorption was also observed. The origin of hydrogen desorption was suggested as provided by the reaction of CO with OH groups of $ZrO_2$ since oxide support was not completely dehydrated. This proposal was supported by analyzing the IR spectra of CO desorption at different temperatures on $Pt/ZrO_2$ catalyst reduced at 573 K, where OH consumption was observed (Figure 5). Also, according to Jackson *et al.* [9], the symmetric profiles of $CO_2$ and $H_2$ are ascribed to the surface reaction between carbon monoxide adsorbed on metallic surface and hydroxyls at the metal-support interface. Thus, the $CO_2$ desorption profile of sample reduced at 573 K includes the product of CO reaction with two different kinds of $O^{2-}$ sites on $ZrO_2$ (first peak) plus the product of CO reaction with OH groups close to the metal interface (second peak).

Table 1
Amounts of CO chemisorbed and $CO_2$ and $H_2$ released during thermal desorption on $Pt/ZrO_2$ catalyst ($\mu mol/g$).

| T reduction (K) | CO chemisorbed | $CO_2$ desorption | $H_2$ desorption |
|---|---|---|---|
| 773 | 16.7 | 16.9 | 0 |
| 573 | 38.2 | 37.2 | 45.2 |
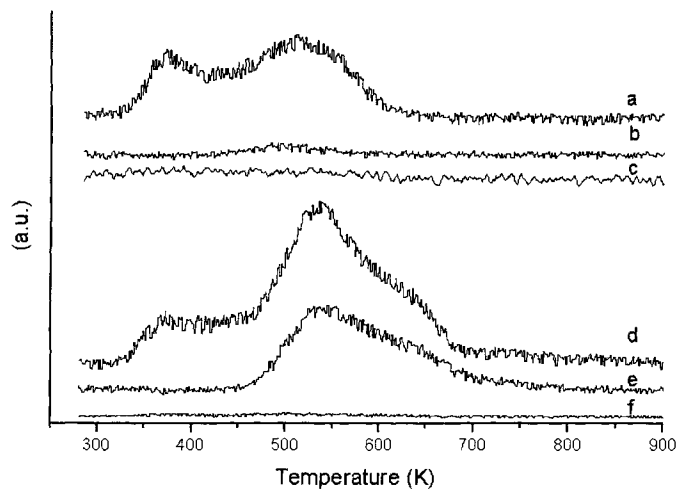
Figure 4. Desorption profiles, after CO adsorption on Pt/ZrO$_2$ catalyst reduced at 773 K: (a) CO$_2$, (b) H$_2$, (c) CO; reduced at 573 K: (d) CO$_2$, (e) H$_2$, (f) CO.

It can be seen in Figure 4 that H$_2$ profile of Pt/ZrO$_2$ reduced at 573 K can be decomposed into two peaks. The first peak was attributed to the reaction of CO with basic OH group on ZrO$_2$ (structural and formed by hydrogen species provided by backspillover) and the second peak to the migration of hydrogen backspillover species to Pt metallic particles followed by their desorption into the gas phase.
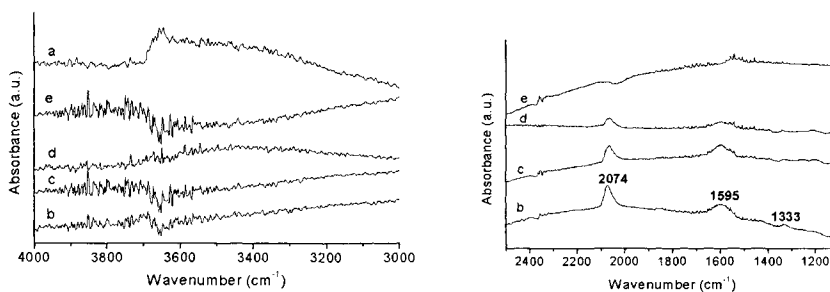


Figure 5. IR spectra of Pt/ZrO$_2$ (a) reduced at 573 K and after CO adsorption and treatment at vacuum at (b) 298 K, (c) 373 K, (d) 473 K and (e) 573 K.

Figures 5 and 6 represent the irreversible CO adsorption on $Pt/ZrO_2$ reduced at 573 and 773 K respectively. Spectra (a) in both Figures were obtained dividing the spectra of reduced samples by the background of the sample compartment. The other spectra in the same figures, concerning to CO adsorption, were taken by using as background the spectrum of the reduced sample.

In Figure 5, hydroxyl band at 3654 cm$^{-1}$ and a broad shoulder centered at 3515 cm$^{-1}$ are shown. After exposition to 30 Torr of CO (spectrum (b)) it was observed a slight consume of OH as suggested by the negative peak at 3654 cm$^{-1}$. At 473 K a slight increase of the hydroxyl bands was noted and coincidentally, that is the temperature where the $H_2$ desorption began during CO-TPD (Figure 4). Therefore, the origin of the new hydroxyls was attributed to hydrogen backspillover species interaction with $O^{2-}$ sites on the support. The formation of the new hydroxyl bands was not restricted to 473 K but were formed and consumed at the same time as CO was chemisorbed. The spectrum (b) in Figure 5 in the range of 2500-1100 cm$^{-1}$ supports these findings. Bands at 2074, 1595 and 1333 cm$^{-1}$ were assigned the first one to CO linearly bonded to $Pt^0$ particles and the others to CO interaction with basic hydroxyl of the support, forming acid carbonate (Scheme 1). As the temperature increases, CO linearly bonded species desorb, resulting in $CO_2$ formation by interaction with OH groups, as shown previously.
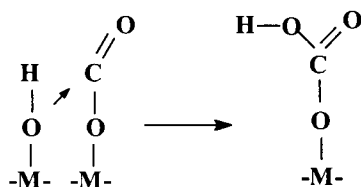


Scheme 1
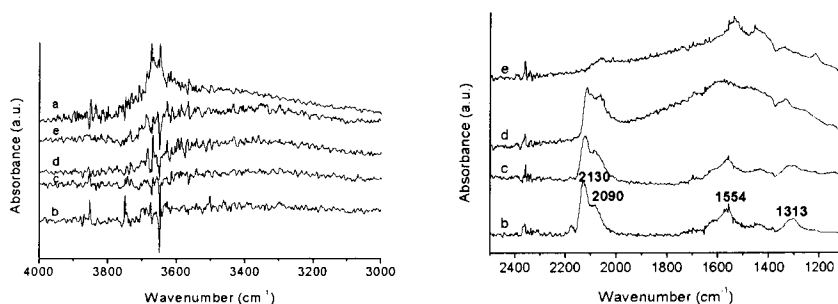


Figure 6. IR spectra of $Pt/ZrO_2$ (a) reduced at 773 K and after CO adsorption and treatment at vacuum at (b) 298 K, (c) 373 K, (d) 473 K and (e) 573 K.

Hydroxyl bands at 3650 cm$^{-1}$ are also observed in the spectrum of $Pt/ZrO_2$ catalyst reduced at 773 K. As in the sample reduced at 573 K, acid carbonate species absorbing at

1554 and 1313 cm$^{-1}$ were observed and attributed to CO reaction with basic OH groups on ZrO$_2$. However, the thermal treatment at 773 K in H$_2$ flow resulted in a surface on which the platinum atoms are in close interaction with the support, being more resistant to reduction. In fact, bands at 2130 and 2090 cm$^{-1}$ were assigned as CO bonded to Pt oxidized and partially oxidized states. These findings support the absence of H$_2$ desorption in the CO-TPD experiments but not ruled out the spillover phenomenon. Pt reduced species are still present, as shown by the presence of the band at 2090 cm$^{-1}$ after CO chemisorption and hydrogen spillover was observed not only by the slight increase in the OH bands (spectra (d) and (e), Figure 6), but also when pyridine and piperidine were chemisorbed followed by heating in a closed system.

## 4. CONCLUSIONS

FTIR spectroscopy provided excellent means to investigate hydrogen backspillover interaction with the support, aside of the metal-support interaction effect, oxidation state of metal atoms and nature of adsorbed species.

Pt/ZrO$_2$ catalyst reduced at different temperatures resulted in different surfaces with distinct properties. When the catalyst was treated at 773 K in the presence of hydrogen, the Pt particles became in close interaction with the support and the reduction process was incomplete. As a consequence, CO chemisorption showed bands of CO bonded to Pt oxidized particles and also linearly bonded to Pt$^\circ$ particles. When pyridine was chemisorbed on this surface, Lewis acid sites were transformed into Brönsted acid sites, as the sample was heated in a closed system. Hydrogen spillover species, which were stored in the support when the sample was reduced, were then activated and migrated toward O$^{2-}$ ions in close neighborhood with Lewis acid sites. Pyridine coordinated to Lewis acid sites moved toward the new hydroxyls just created, and bands due to Brönsted acid sites were observed. If the sample was heated in vacuum the hydrogen backspillover species migrate preferentially to the metal particles and then desorb as H$_2$ since the interaction with the O$^{2-}$ ions are slower then their migration toward the metal. Piperidine chemisorbed on the same surface was dehydrogenated as the sample was heated in a closed system and at the same time the pyridine just formed was chemisorbed on Lewis and Brönsted acid sites. The formation of the Brönsted acid sites was explained by interaction of hydrogen species, provided by the dehydrogenation and the backspillover processes, with the O$^{2-}$ ions in close neighborhood with Lewis acid sites.

When Pt/ZrO$_2$ catalyst was heated at 573 K in the presence of H$_2$ no metal-support interaction was observed and the reduction process was completed. CO chemisorption on this surface provided a band at 2074 cm$^{-1}$ assigned to CO linearly bonded to Pt$^\circ$ particles. As the reduction was completed, more hydrogen spillover species were formed and could migrate back to the metal, being detected as H$_2$ during TPD of CO.

The findings resulted from the present set of experiments support the idea of the reactivity of spillover species stored in the support when the samples are reduced. Pyridine chemisorbed on Lewis sites moves to new Brönsted sites created by hydrogen backspillover species even in the absence of H$_2$ in the gas phase. Also H$_2$ desorption was detected by performing the CO-TPD experiment, when the sample was reduced at 573 K.

84

## REFERENCES

1. W.C. Conner, S.J. Teichner and G.M. Pajonk, Adv. Catal., 34 (1986) 1.
2. W.C. Conner and J.L. Falconer, Chem. Rev., 95 (1995) 759.
3. A. Zhang, I. Nakamura and K. Fujimoto, Ind. Eng. Chem. Research, 34 (1995) 1074.
4. Y. Fan, I. Nakamura and K. Fujimoto in "Spillover and Migration of Surface Species on Catalysts", Stud. Surf. Sci. Catal., 112 (1997) 319.
5. A. Zhang, I. Nakamura and K. Fujimoto, J. Catal., 168 (1997) 328.
6. H. Hattori in "New Aspects of Spillover Effect in Catalysis", Stud. Surf. Sci. Catal., 77 (1993) 69.
7. T. Tanaka, K. Ebitani, H. Hattori and S.Yoshida in "New Aspects of Spillover Effect in Catalysis", Stud. Surf. Sci. Catal., 77 (1993) 285.
8. K. Foger and J.R. Anderson, Applic. of Surf. Sci., 2 (1979) 335.
9. S.D. Jackson, B.M. Glanville, J. Willis, G.D. McLellan, G. Webb, R.B. Moyes, S. Simpson, P.B. Wells and R. Whyman, J. Catal., 139 (1993) 207.

# Hydrogen spillover in $H_2$ oxidation on Pd-Ti$^{3+}$/TiO$_2$

V.V. Gorodetskii[a], A.V. Matveev[b]

[a]Boreskov Institute of Catalysis, Novosibirsk 630090, Russia.

[b]Novosibirsk State University, Novosibirsk 630090, Russia.

A dual-site mechanism of $H_2$ dissociation on the Pd particles and then migration $H_{ads}$ across the TiO$_x$ surface to the active sites with the $O_2^{\delta-}{}_{ads}$ species have been studied on the defects of Ti$^{3+}$-$\square_O$/TiO$_2$ and Pd-Ti$^{3+}$-$\square_O$/TiO$_2$ types with XPS, UPS, TDS, mass-spectrometry and pre-adsorbed oxygen photodesorption techniques. The effect of spillover phenomena ($H_{ads}$/Pd $\rightarrow$ $O_{2ads}$/Ti$^{3+}$/TiO$_2$) on the overall rate of $H_2$ oxidation have been studied as well. The role of defects (Ti$^{3+}$ sites) in the adsorption centres formation, their stabilization by the palladium particles and then defects participation in $H_2$ + $O_2$ reaction have been studied on the TiO$_x$ surface. The results obtained with $H_2$ + $O_{ads}$ reaction over Pd (110) single crystal surface have been compared. A series of activity sets: Ti$^{3+}$/TiO$_2$ $\ll$ Pd $\sim$ Pd-Ti$^{3+}$/TiO$_2$ have been determined. Through the hydrogen spillover from Pd to Ti$^{3+}$/TiO$_2$ $H_2$ oxidation proceeds on two sites of the Pd- model catalysts in can occur: on Pd particles and on the Ti$^{3+}$/TiO$_2$ support.

## 1. INTRODUCTION

The metal modifying effect on the active centres properties in the supported metal catalysts is known to be realized by: (i) strong metal support interaction (SMSI) [1]; (ii) orientation of metal crystallites surface structure [2]; (iii) defects formation on metal and support [3]; (iv) metal $\leftrightarrow$ support spillover phenomena [4]. Two main mechanisms – for instance an electron transfer from Ti$^{3+}$ to Pt [5] and encapsulation of the Pd particles by supported titanium oxide species [6] – have been proposed to explain the modifying effect of catalytic properties induced by SMSI. Spillover phenomena involve the transfer of hydrogen atoms from the metal particles (Pt, Pd) to the support of a bifunctional catalyst. As a rule, the stoichiometric oxide surface (TiO$_2$) is supposed to be catalytically inactive, whereas the supported metals (Pt, Pd) present a highly active part of the catalytic system. Reduction of the TiO$_2$ surface by ion-sputtering or vacuum-heating leads to the formation of the Ti$^{3+}$-$\square_O$ type defects ($\square_O$ is an oxygen vacancy), which are responsible for the molecularly adsorbed O$_2$ species [7-9]. Spillover of oxygen was found as a precursor state on the oxide support in $H_2$ oxidation in Pd/SiO$_2$ system [10].

In this work, the role of defects (Ti$^{3+}$ sites) in the adsorption centres formation, their stabilization by the palladium particles and then defects participation in $H_2$ + $O_2$ reaction have been studied on the TiO$_x$ surface. The O$_2$ adsorption and the reaction of $O_2^{\delta-}{}_{ads}$ molecular state as well as an $O_{ads}$ atomic state with $H_2$ have been studied on the defects of Ti$^{3+}$-$\square_O$/TiO$_2$ and Pd-Ti$^{3+}$-$\square_O$/TiO$_2$ types with XPS, UPS, TDS, mass-spectrometry and photodesorption

techniques. The effect of spillover phenomena ($H_{ads}/Pd \rightarrow O_{2ads}/Ti^{3+}/TiO_2$) on the overall rate of $H_2$ oxidation have been studied as well. The results obtained with $H_2$ oxidation over Pd (110) surface have been compared.

## 2. EXPERIMENTAL

The UPS (He I) and XPS (MgKα) measurements were carried out in a VG ESCA-3 UHV photoelectron spectrometer equipped with QMS. The Pd-$Ti^{3+}$-$\Box_O$/$TiO_2$ model system was prepared by a successive vacuum evaporation of palladium onto a flat thin oxide layer ($Ti^{3+}/TiO_2$) formed on the clean titanium foil ($Ar^+$ etching) upon oxygen adsorption of $10^3$ ML (T = 900 K, $P(O_2) = 10^{-2}$ torr), and reduction by heating in vacuum at T ~ 700 K [7]. The photoelectron spectrum of the surface shows titanium, oxygen and palladium lines only. According to XPS (Pd $3d_{5/2}$) and TDS ($H_{ads}/Pd/TiO_x$) data the $\theta_{Pd}$ value is O.3 ML (1ML = $1.10^{15}$ at/cm$^2$). The experimental setup for $H_2$ and $O_2$ study on the Pd(110) surface is described in Ref. [11].

The thermal (TDS) and photodesorption (PhDS) measurements were accomplished. The catalytic activity of Pd/$TiO_x$ system at $H_2$ oxidation was studied in a separate all-glass ultrahigh vacuum 1.5 L apparatus at pressure < $10^{-10}$ torr. Reaction gases such as $H_2$ and $O_2$ of the highest purity were introduced with a flow rate of ~ 1.5 L s$^{-1}$, and controlled by the omegatrone mass-spectrometer. The rate measurements of the $H_2$ + $O_2$ reaction were described in Ref. [12]. Ti (7 cm$^2$) and Pd foil surfaces were cleaned by $Ar^+$ etching as described elsewhere [7]. The preparation regime and the amount of the Pd deposited were the same as in the case of the Pd-$Ti^{3+}$-$\Box_O$/$TiO_2$ sample prepared under the XPS and hydrogen TDS control. A low pressure Hg lamp with a set of interference filters was used as the photon source at PhDS studies. The flux intensity with hv > 3 eV through the optical quartz window to the sample was $4 \times 10^{15}$/cm$^2$ s [7].

## 3. RESULTS AND DISCUSSION

### 3.1. The effect of oxygen vacancies $Ti^{3+}$- $\Box_O$ /$TiO_2$ on $O_2$ adsorption

According to the XPS data, the reduction in the thin oxide layer ($TiO_2$/Ti, ~ 300 Å) with heating in vacuum at 700 K leads to appearance of the state Ti $2P_{3/2}$ with the binding energy $E_B = 457.5$ eV and formation of the oxygen vacancy defects sites, (Fig. 1). The
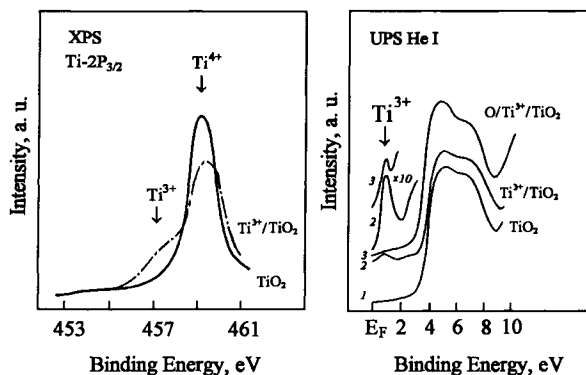


Fig. 1. Ti $2p_{1/2}$ XPS spectra of the $TiO_2$/Ti thin layer taken after annealing in UHV at T ~ 700 K.

Fig. 2. Changes in UV spectra caused by reduction of the $TiO_2$ thin layer (1) at 700 K (2) and oxygen adsorption on the $Ti^{3+}/TiO_2$ surface at 300 K (3), exposure $10^3$ L.

reduction of the oxide layer occurs due to the titanium diffusion on the surface and oxygen one into the metal. The surface layer containing the $Ti^{3+}$-$\square_O$ defects are detected by UV photoemission as the state 0.8 eV below the Fermi level in the forbidden region, (Fig. 2). The oxygen vacancy defect sites are the active sites in $O_2$ dissociative adsorption and can be eliminated by oxygen adsorption at 300 K.

Therefore, a low temperature study of adsorption and reactions at defect sites is necessary for detailed understanding the catalytic properties of $TiO_x$ surfaces. Two molecular $\gamma$- and $\alpha$- states of the adsorbed oxygen (100 K) with $T_{des} \sim$ 140 and $\sim$ 240 K were found on such surface by TDS, (Fig. 3). The molecular character of $\gamma$- and $\alpha$- states was determined by
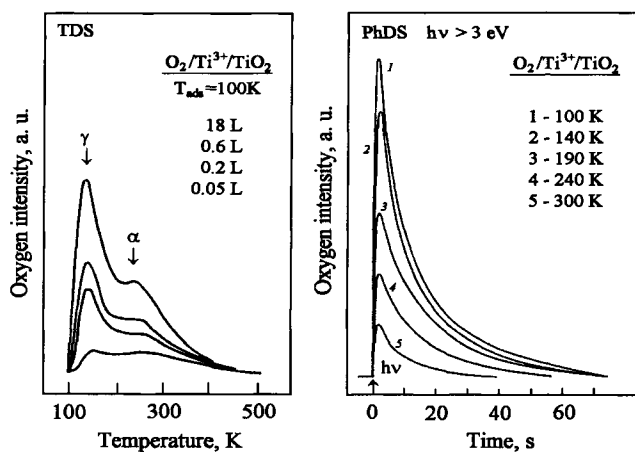


Fig. 3. TD spectra obtained after $O_2$ adsorption at 100 K.

Fig. 4. Oxygen photodesorption yield from $Ti^{3+}/TiO_2$ (18 L, 100 K) as a function of annealing temperatures. Annealing time at $T_a$ corresponds to 120 s.

means of isotopes. At the UV irradiation of the surface with light of 2.8<hv<3.4 eV the sharp photodesorption of $O_2$-peak was found to occur only from $\alpha$ - species as a result of reaction between holes ($p^+$) and $\alpha$-$O_2^{\delta-}{}_{ads}$. The photosensitive oxygen state concentration is about $10^{-2}$ ML. Figure 4 presents the photodesorption spectra for the $O_2{}_{ads}$ layer at different stages of the thermal annealing from 100 to 300 K. The initial photodesorption of $O_2$-peak dramatically decreases as a result of thermal desorption and dissociation of $\alpha$-$O_2^{\delta-}{}_{ads}$ state with a simultaneous oxidation of the $Ti^{3+}$ sites at T < 300 K.

### 3.2. The effect of Pd particles on the $Ti^{3+}$- $\square_O$ /$TiO_2$ surface at $O_2$ adsorption

Strong interaction of supported palladium particles with electron donor defects ($Ti^{3+}$-$\square_O$) over the oxide layer has been found to lead to the stabilization of these defects with respect to oxidation by oxygen [7]. According to the XPS data, from the initial coverages $\theta_{Pd}$ = 0.06 ÷ 0.3 ML there is an increase of the Pd $3d_{5/2}$ и Pd $3d_{3/2}$ lines intensity with their simultaneous shift by 0.5 eV to the smaller binding energy $E_b$, (Fig. 5, curves 1- 4). After 700 K annealing (curves 5), the state of palladium on the model catalyst is $E_b$ (Pd $3d_{5/2}$) = 335.5 eV and in the neighbourhood as for the bulk metal. The $Ti^{3+}$ spectral regions are presented in Fig. 5 (XPS Ti $2p_{3/2}$) and Fig. 6 (UPS He I). The Pd deposition is accompanied by diminution of the $Ti^{3+}$ sites intensity as a result of electron density transfer from the $Ti^{3+}$-$\square_O$ electron donor defects to metal [13].
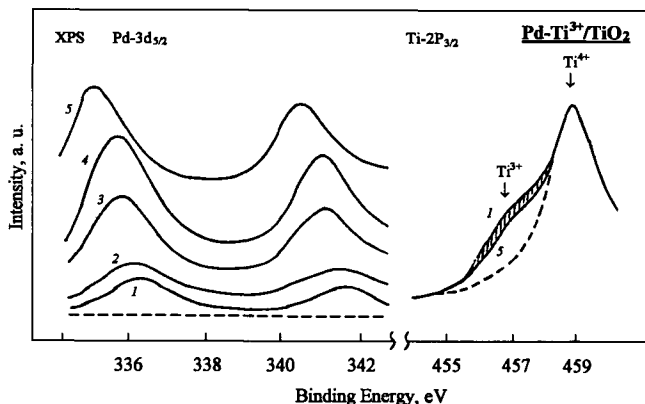
Fig. 5. Pd $3d_{5/2}$ (a) and Ti $2p_{1/2}$ XPS spectra of the Pd/T$_i^{3+}$/TiO$_2$ system as a function of Pd thickness ($\theta_{Pd}$ (1-4): 0.06, 0.08, 0.24, 0.3 ML), recorded at 300 K. The upper curve show Pd $3d_{5/2}$ spectra after annealing for 120 s at T = 700 K.

According to the UPS spectra with $E_b \sim 2.8$ eV, the state of palladium at $\theta \sim 0.1$ ML is characteristic for electron emission from $d^9$- state of single metal atoms supported on the oxide surface [14]. The analysis of difference UPS spectra shows the change of line width at half peak intensity from 1.6 eV (0.1 ML) up to 2.5 eV (0.3 ML), that is caused by increasing of the Pd particles size. Heat-up at 700 K is accompanied by electron photoemission near the Fermi level (Curve 5), indicating the particles formation (< 20 Å) with properties close to the bulk metal [2].
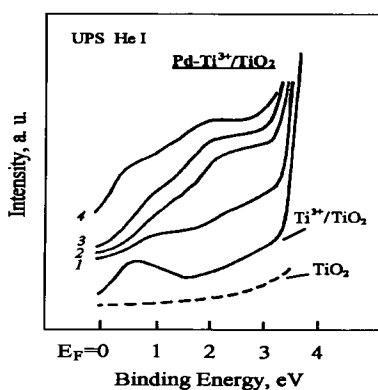




Fig. 6. UP valence band spectra of Ti$^{3+}$/TiO$_2$ surfaces after stepwise evaporation of Pd at 300 K with increasing of Pd coverages $\theta_{Pd}$:1-0.08, 2-0.24, 3-0.3 ML. The latter is determined from corresponding XPS intensities. The upper curve (4) shows the valence band spectra after annealing for 120 s at T = 700 K.
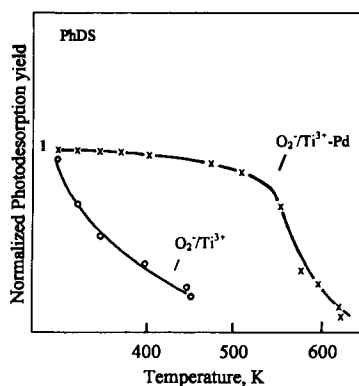
Fig. 7. Normalized oxygen photodesorption yield from the O$_2^-$ $_{ads}$/Ti$^{3+}$/TiO$_2$ and O$_2^-$$_{ads}$/Ti$^{3+}$-Pd/TiO$_2$ surfaces (18 L, 100 K) as a function of annealing temperatures in UHV. Annealing time at $T_a$ corresponds to 180 s.

### 3.3. $H_2$ oxidation on palladium

Results of $O_2$ adsorption and $H_{ads} + O_{ads}$ reaction on Pd(110) are shown in Fig. 8. TDS study indicates two states: from the atomic oxygen recombination (820 K) and associated with the desorption from the subsurface oxygen layer (740 K) [15]. Interaction of the O/Pd(110) atomic oxygen layer with hydrogen was determined to be accompanied by water molecules formation with a desorption peaks at T ~ 220 and ~ 260 K.
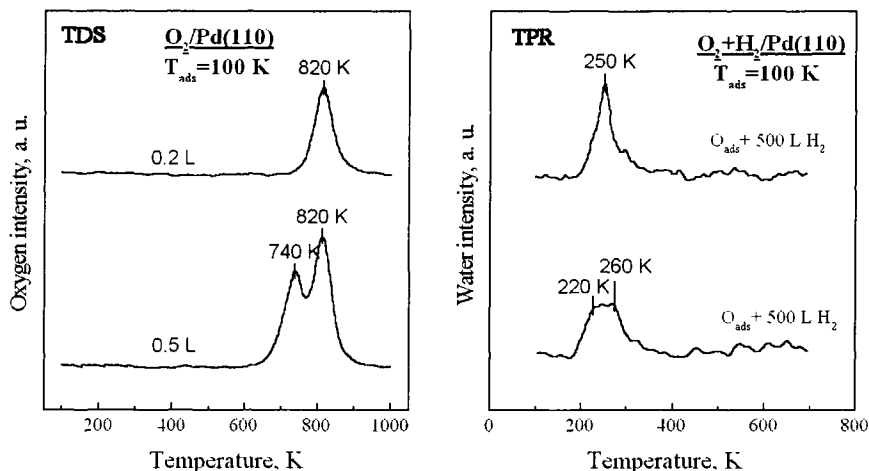


Fig. 8. Series of TD spectra of oxygen (a) and TPR spectra of the $H_2O$ molecules formation (b) during $H_{ads} + O_{ads}$ reaction on the Pd(110) surface obtained after low temperature $O_2$ and $H_2$ adsorption.

### 3.4. The hydrogen spillover effect on $H_2$ oxidation over Pd-$Ti^{3+}$/$TiO_2$

One might expect that in Pd-$Ti^{3+}$/$TiO_2$ system owing to electron transfer ($Ti^{3+} \rightarrow$ Pd) the conversion of $Ti^{3+}$ electron donor defects to oxidized $Ti^{4+}$ ions, accompanied by the losses of the $TiO_x$ oxide surface to oxygen adsorption ability in $O_2^-_{ads}$ state could be possible. However, the data presented in Fig. 9 a (Curve 1) show that the sharp photodesorption of $O_2$-peak (~ $10^{-2}$ ML) proceeds from oxygen adlayer (150 K) by the UV irradiation, as in Fig. 4. The threshold energy for the $O_2$ photodesorption was at hν ~ 3.0 eV, corresponding to the band-gap of the bulk rutile $TiO_2$, (Fig. 11). Apparently there is a possibility of a reversible electron transition Pd $\rightarrow$ $Ti^{3+}$ $\rightarrow$ $O_{2ads}$ with the $O_2^-_{ads}$ anion – radical state formation. The similar reversible electron transition is typical for the metal - complex compounds at replacement of the electron - donor ligands by electron - acceptor ligands [16]. The $O_2^-_{ads}$ state at the palladium particles presence is much more stable and exists up to temperatures ~ 550 K, (Fig. 7). The increase in defect stability to the oxidation is stipulated by electron - acceptor properties of Pd particles diminishing the electron density on the $Ti^{3+}$-$\square_O$ defects due to SMSI effect [1]. Since at Pd presence the transfer of the second electron on $O_2^-_{ads}$ is sharply impeded, then the defect oxidation in direction: $O_2 \xrightarrow{e-} O_2^- \xrightarrow{e-} O_2^{2-} \rightarrow 2O^- \xrightarrow{e-} 2O^{2-}_{i}$, accompanying by nonreversible disappearance of oxygen vacancies -$\square_O$ is unlikely.

Fig. 9 shows a set of curves for the isothermal reaction of $H_2$ with pre-adsorbed oxygen at 150 K over the $Pd$-$Ti^{3+}$/$TiO_2$ surface. The $O_2^-{}_{ads}$-state photodesorption is used as a test for spillover studies. The reacted oxygen molecules are determined by the difference of the photo peak areas for initial concentration (Curve 1) and after reaction (Curves 2-4).
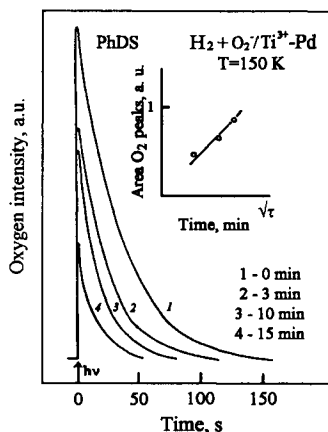


Fig. 9. (a) Oxygen photodesorption yield from $Pd$/$Ti^{3+}$/$TiO_2$ (18 L, 100 K) as a function of $H_2$ + $O_2^-{}_{ads}$ reaction at 150 K and $P(H_2) = 10^{-7}$ torr. 1) Initial spectra after $O_2$ adsorption at 100 K, 20 L. (2-4) Reaction time: 2) 3 min; 3) 10 min; 4) 15 min. (b) Rectification of difference square of curves 1-4.
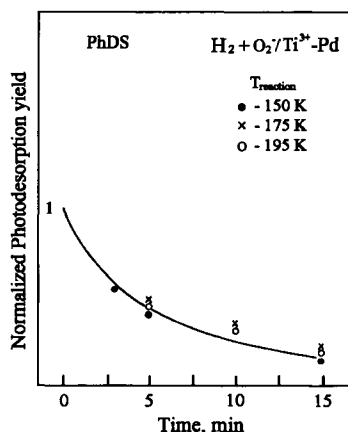
Fig. 10. Normalized oxygen photodesorption yield from $O_2^-$ $_{ads}$/$Ti^{3+}$-$Pd$/$TiO_2$ surfaces (18 L, 100 K) as a function of $H_2$ + $O_2^-{}_{ads}$ reaction temperature, $P(H_2) = 10^{-7}$ torr.

The reaction proceeds only at the palladium ($\theta_{Pd}$ =0.3 ML) presence with the constant diminution of photo-peak intensity in time. Rectification in co-ordinates: the concentration of the reacted oxygen ($O_2$ peak area) as a function of time ($\sqrt{t}$), indicates the diffusion availability associated with the hydrogen migration from $Pd$ onto the $TiO_x$ surface.

The hydrogen atoms transfer from metal to the support is considered to be the limiting stage in spillover phenomena [1]. $H_2O$ molecules formation in the $H_2$ oxidation can proceed through the intermediates such as $HO_2^*$ radical [17]. The interaction of $\alpha$-$O_2^{\delta-}{}_{ads}$ molecular layer with hydrogen over $Pd$/$Ti^{3+}$/$TiO_2$ surfaces in the temperature interval of 150-195 K is characterized by an activation energy close to zero, (Fig. 10). This reaction seems to involve the "protonate" hydrogen atoms ($H^+$/$TiO_x$) as a result of the spillover effect: - $H_{ads}$ atoms diffusion from $Pd$ particles on the $TiO_x$ surface [1]. The $\alpha$-$O_2^{\delta-}{}_{ads}$ molecular state on the $TiO_x$ surface appears to be non reactive to hydrogen due to the absence of centres required for the $H_2$ dissociative adsorption.

It has been found that the low temperature $H_2$ oxidation on palladium (T<300 K) results from the high reactivity of $H_{ads}$ and $O_{ads}$ atomic species, (Fig. 8). The study of the catalytic activity at 300 K as a function of $O_2$ pressure in the reaction mixture has shown a positive first reaction order of the oxygen concentration, (Fig. 12). Under the steady state
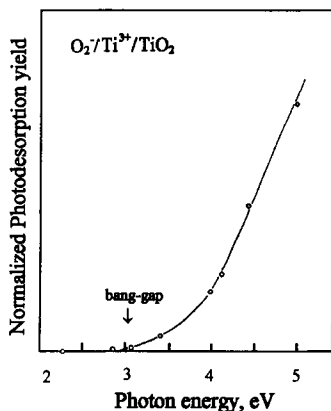
Fig. 11. The photon energy dependence of the oxygen photodesorption rate from Pd-$Ti^{3+}/TiO_2$ (18 L, 100 K). The photodesorption yield has been normalized to the photon flux at each photon energy.
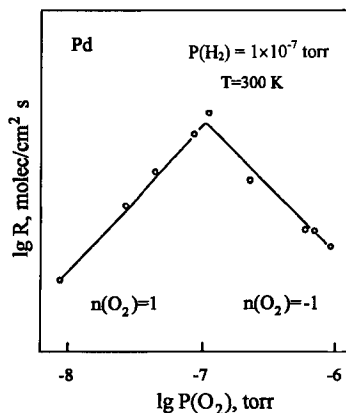
Fig. 12. Reaction orders of hydrogen oxidation with respect to $O_2$ on Pd at 300 K: lg W (molec. $O_2/cm^2$ s) vs. lg $P(O_2)$ (torr) at $P(H_2) = 1\times10^{-7}$ torr.

reaction conditions at $P(H_2):P(O_2) = 2:1$ the Pd surface is covered by hydrogen. Therefore, the rate of $H_2$ oxidation on the $Pd/TiO_x$ system should include the rate on Pd particles and the contribution of spillover phenomena ($H_{ads}/Pd \rightarrow O_{2ads}/Ti^{3+}/TiO_2$) on the overall rate.

The specific catalytic activity of Pd-$Ti^{3+}/TiO_2$ system at UV irradiation (+ hv (– $\alpha$-$O_2^{\delta-}{}_{ads}$ state)) is equal to $9.2\times10^{11}$ molecules $H_2O/cm^2$·s at the following reaction conditions: T = 220 K, P = $1.5\times10^{-7}$ torr ($H_2:O_2 = 2:1$). In the dark (– hv (+ $\alpha$-$O_2^{\delta-}{}_{ads}$ state)) the reaction rate increases up to $1.0\times10^{12}$ molecules $H_2O/cm^2$·s and approaches the specific catalytic activity of polycrystalline Pd wire [18]. A series of activity sets: $Ti^{3+}/TiO_2 \ll Pd \sim Pd/Ti^{3+}/TiO_2$ have been determined.

## The mechanism of $H_2 + O_2$ /Pd-$Ti^{3+}/TiO_2$ reaction with participation of spillover effect

### $H_2$ oxidation on Pd crystallites

1. $O_{2gas} + 2* \rightarrow 2 O_{ads}$
2. $H_{2gas} + 2* \rightarrow 2 H_{ads}$
3. $H_{ads} + O_{ads} \rightarrow OH_{ads} + *$
4. $H_{ads} + OH_{ads} \rightarrow H_2O_{ads} + *$
5. $H_2O_{ads} \rightarrow H_2O_{gas} + *$

### Spillover effect in $H_2$ oxidation on $Ti^{3+}/TiO_2$

6. $H_{ads}$ (Pd) $\xrightarrow{spillover}$ $H_{ads}$ ($TiO_2$) + (Pd)
7. $H_{ads}$ ($TiO_2$) $\xrightarrow{protonation}$ $H^+$ ($TiO_2$) + $e^-$ (Pd)
8. $O_{2gas} + (Ti^{3+}) \rightarrow O_2^{\delta-}{}_{ads}$ ($Ti^{3+}$)
9. $2H^+$ ($TiO_2$) + $O_2^{\delta-}{}_{ads}$ ($Ti^{3+}$) $\rightarrow [H_2O_2]^*{}_{ads} \rightarrow$
   $\rightarrow OH_{ads}$ ($TiO_2$) + $OH_{ads}$ ($Ti^{3+}$)
10. $H^+$ ($TiO_2$) + $OH_{ads}$ ($TiO_2$) $\rightarrow H_2O_{gas} + 2(TiO_2)$
11. $H^+$ ($TiO_2$) + $OH_{ads}$ ($Ti^{3+}$) $\rightarrow H_2O_{gas} + (Ti^{3+}) + (TiO_2)$

## 4. CONCLUSIONS

Partially-reduced titanium supports are particularly interesting in oxidation catalysis, because their surfaces reveal the additional oxidation activity due to an oxygen species associated with titanium oxide directly involved in the oxidation. The deposition of Pd particles with the size < 20 Å on the $TiO_x$ surface leads to: (i) stabilization of surface defects $Ti^{3+}$ (SMSI) with respect to oxidation; (ii) increase of thermal stability of the $\alpha$-$O_2{}^{\delta-}_{ads}$ state up to $T_{des} \sim 550$ K. One of the important functions of Pd crystallites in $H_2$ oxidation is to atomize hydrogen and oxygen molecules and then supply the $H_{ads}$ atoms with $O_{2ads}/Ti^{3+}/TiO_2$ throught spillover phenomena. $H_2$+$O_2$ reaction on Pd-$Ti^{3+}/TiO_2$ model catalysts is *spillover sensitive*. The combination of metallic (Pd) and ionic sites ($Ti^{3+}$) provides the catalyst with molecular oxygen storage capacity. Two different parallel reactions through the atomic and molecular oxygen states in $H_2$ oxidation were found to proceed.

**Acknowledgement**

## REFERENCES

1. S.J. Tauster, S.C. Fung and R.L. Garten, J. Am. Chem. Soc., 100 (1978) 170
2. C.R. Henry, Surface Science Reports, 31 (1998) 231
3. D.I. Kochubey, S.N. Pavlova, B.N. Novgorodov, G.N. Kryukova and V.A. Sadikov, J. Catal., 161 (1996) 500
4. W. Curtis Conner, Jr., G.M. Pajonk and S.J. Teichner, Adv. Catal., 34 (1986) 1
5. S.C. Fung, J. Catal., 76 (1982) 225
6. T. Suzuki and R. Souda, Surf. Sci., 448 (2000) 33
7. M.Yu. Smirnov, K.I. Zamaraev and V. V. Gorodetskii, Poverhnost, 5 (1991) 21[In Russian]
8. G. Lu, A. Linsebigier and J. T. Yates, Jr., J. Chem. Phys., 102 (1995) 4657
9. M.A. Henderson, W. S. Epling, C.L. Perkins, C.H.F. Peden and U. Diebold, J. Phys. Chem. B, 103 (1999) 5328
10. M. Eriksson and L.-G. Petersson, Surf. Sci., 311 (1994) 139
11. V.V. Gorodetskii, A.V. Matveev, P.D. Cobden and B.E. Nieuwenhuys, J. Molec. Catal. A: Chemical 158 (2000) 155
12. V.V. Gorodetskii, G.I. Panov, V.A. Sobyanin and N.N. Bulgakov, React. Kinet. Katal. Lett., 9 (1978) 239
13. J.A. Horsley, J. Amer. Chem. Soc., 101 (1979) 2870
14. M.G. Mason, L.J. Gerenser and S.-T. Lee, Phys. Rev. Lett., 39 (1977) 288
15. J.-W. He and P.R. Norton, Surf. Sci., 204 (1988) 26
16. J.S. Valentino, Chem. Rev., 75 (1973) 235
17. H.D. Gesser and L. Krucznski, J. Phys. Chem., 88 (1984) 2751
18. V.V. Gorodetskii, V.A. Sobyanin, A.R. Cholach and M.Yu. Smirnov, in: Proc. 8th Int. Congr. on Catalysis, W. Berlin, 1986, p. III-323

# HYDROISOMERIZATION OF C$_6$–C$_{14}$ n-ALKANES OVER HYBRID CATALYSTS

T.V. Vasina[a], O.V. Masloboishchikova[a], E.G. Khelkovskaya-Sergeeva[a], L.M. Kustov[a], and J.I. Houzvicka[b]

[a]N.D. Zelinsky Institute of Organic Chemistry, Russian Academy of Sciences, Moscow, Leninsky prosp. 47, 117334 Russia, E-mail: lmk@ioc.ac.ru

[b]Haldor Topsøe A/S, Nymollevej 55, P.O. Box 213, DK-2800, Lyngby, Denmark

Various hybrid catalysts prepared by mechanically mixing Pt(Pd) promoted oxides (Al$_2$O$_3$, SiO$_2$) and an acidic component (RE-FAU, H-Beta zeolites and SO$_4$/ZrO$_2$ solid superacid) were studied in C$_6$–C$_{14}$ n-alkane skeletal isomerization. The hybrid catalysts exhibited high activity and selectivity in paraffin isomerization. The enhancement in the activity of hybrid catalysts as compared to individual components was rationalized in terms of spillover of reactive species between metal promoted oxide systems and acidic sites.

## 1. INTRODUCTION

The efficiency of bifunctional catalysts in hydrocarbon transformations (skeletal isomerization, aromatization, disproportionation, etc.) is determined by the proper combination of the metallic and acidic functions [1—3]. However, the direct interaction between acid sites and metal species may influence both the acidic properties of the acid sites and the dehydrogenation activity of the metal, thus decreasing the catalytic activity of the catalytic systems in the target process [4]. It is now well established that the presence of the Broensted acid sites in the vicinity of the metal nanoparticles, for instance, in zeolites or sulfated oxides results in the formation of an adduct in which the metal particle demonstrates pronounced electron deficiency or a cationic character [5], i.e., the metallic properties in such an adduct are somewhat suppressed. Such a metal particle exhibits the catalytic properties in hydrocarbon transformations, which are significantly different from those of the neutral particles of the same size and morphology. On the contrary, the direct interaction between the metal particle and the acid sites causes a weakening of the strength of Broensted sites [6], thus modifying their activity in acid-type reactions or stages of the complex process occurring on a bifunctional catalyst. Hence, by separating spatially the metal and acidic functions, one can change, in particular increase the stability and activity of bifunctional catalytic systems. The use of hybrid catalytic systems prepared by physically mixing two separate components is a simple and very attractive way to enhance the performance of catalysts [7—10].

The hydrogen spillover plays very important role in catalysis by hybrid catalysts [11, 12]. The catalytic performance of such hybrid catalysts is strongly dependent on

the efficiency of the exchange of hydrogen between the gas phase and active sites of two separate heterogeneous active phases. The hydrogen spillover is also important for the regeneration of Broensted acid sites (BAS) and stabilization of the intermediate carbonium ions [13, 14]. The activity of some hybrid systems in n-pentane isomerization was studied in [15—17].

The main purpose of the present study was to elucidate the activity of various types of hybrid catalysts in the skeletal isomerization of $C_6$–$C_{14}$ linear alkanes and to unravel the role of the acidity and spillover effects in these systems.

## 2. EXPERIMENTAL

γ-Alumina (specific surface area, 180 $m^2$/g), silica (specific surface area, 450 $m^2$/g, acidic forms of zeolites (RE-FAU, H-Beta), and solid superacid, sulfated zirconia containing 5 wt. % $SO_4$, were used for the preparation of metal-containing catalysts and hybrid systems. The contents of rare-earth element concentrate in RE-FAU-1, RE-FAU-2 and RE-FAU-3 zeolites were 8.8, 12.2, and 15 wt. %, respectively. Platinum and palladium were supported from aqueous solutions of $H_2PtCl_6$ and $PdCl_2$, respectively. The metal loadings were 0.5 or 1.0 wt. %. Prior to catalytic tests, the metal-containing catalysts were calcined in an air flow at 400°C and then reduced in a hydrogen flow at 300°C for 1 h.

The hybrid systems were prepared by mechanically mixing the metal-promoted oxides (0.5%Pt/$Al_2O_3$, 1%Pt/$Al_2O_3$, 0.5%Pd/$Al_2O_3$, 1%Pt/$SiO_2$) and the acidic component (RE-FAU and H-Beta zeolites, 5%$SO_4$/$ZrO_2$ oxide system). The mass ratio of the components in the mixture was 1 : 1. The activity of Pt-promoted systems, including Pt/$Al_2O_3$, Pt/RE-FAU, and Pt/H-Beta systems, and Pt-free catalysts, including RE-FAU, H-Beta, and $SO_4$/$ZrO_2$ catalysts, was also studied for comparison.

Catalytic testing in $n$-$C_6$–$C_{14}$ alkane isomerization was performed in a flow unit at 190–360°C, LHSV = 1 $h^{-1}$, $P$ = 0.1 MPa, and $H_2$ : hydrocarbon ratio = (6–10) : 1 (mol). The reaction products were analyzed by gas-liquid chromatography on packed and capillary columns.

## 3. RESULTS AND DISCUSSION
### 3.1. n-Hexane Isomerization
The influence of the specific characteristics of the catalytic system on the performance in n-hexane isomerization was studied by varying the nature and the concentration of the metal and acidity of the oxide component as well as the nature of the acidic component.

The results of testing of hybrid catalysts in n-hexane isomerization are shown in Table 1 and Fig. 1. The oxide catalysts (0.5-1.0%Pt/$Al_2O_3$, 0.5%Pd/$Al_2O_3$, 0.5%Pt/$SiO_2$) and acidic systems (RE-FAU and H-Beta zeolites, 5%$SO_4$/$ZrO_2$ superacid) containing no metals exhibit low activity in n-hexane isomerization under conditions chosen for testing.

Thus, the 0.5%Pt/$Al_2O_3$ catalyst used for the preparation of hybrid catalysts shows a relatively low activity and selectivity in *n*-hexane isomerization. The isohexanes yield is below 20% and the selectivity is only 35–50%. The main reactions of hydrocarbon

Table 1.
Isomerization of n-hexane on hybrid catalysts
(catalyst loading 2 c.c., LHSV = 1 h$^{-1}$, P = 0.1 MPa, H$_2$ : CH = 6 : 1 mol./mol.)

| Catalyst | T, °C | Conversion % | Selectivity, % | Yields*, wt. % | | |
|---|---|---|---|---|---|---|
| | | | | iso-C$_6$H$_{14}$ | | C$_1$- |
| | | | | DMB | MP | C$_5$ |
| RE-FAU-3 | 300 | 18.8 | 40.4 | 1.2 | 6.4 | 11.2 |
| 0.5%Pt/Al$_2$O$_3$ | 300 | 13.8 | 38.4 | - | 5.3 | 6.6 |
| 0.5%Pt/Al$_2$O$_3$ + RE-FAU-1 | 360 | 42.1 | 93.1 | 4.2 | 35.0 | 1.7 |
| | 300 | 73.1 | 72.0 | 10.0 | 42.6 | 18.2 |
| 0.5%Pd/Al$_2$O$_3$ + RE-FAU-1 | 300 | 35.7 | 98.9 | 3.8 | 31.5 | 0.4 |
| 0.5%Pt/Al$_2$O$_3$ + RE-FAU-3 | 300 | 76.6 | 88.4 | 15.3 | 52.4 | 8.4 |
| 1%Pt/Al$_2$O$_3$ + RE-FAU-3 | 280 | 77.9 | 87.2 | 16.3 | 51.6 | 9.5 |
| 0.5%Pt/RE-FAU-3 | 300 | 80.2 | 93.1 | 19.6 | 55.1 | 5.5 |
| 1%Pt/Al$_2$O$_3$ + H-Beta | 240 | 56.1 | 95.9 | 7.9 | 45.9 | 2.0 |
| | 260 | 74.1 | 89.3 | 12.3 | 53.9 | 7.6 |
| 1%Pt/SiO$_2$ + H-Beta | 300 | 58.1 | 69.9 | 6.2 | 34.4 | 17.5 |
| 0.5%Pt/H-Beta | 250 | 75.9 | 91.2 | 11.3 | 57.9 | 6.7 |
| H-Beta | 260 | 12.5 | 48.0 | 0.7 | 5.1 | 6.7 |
| | 420 | 48.2 | 6.0 | 0.5 | 2.4 | 43.2 |
| 1%Pt/Al$_2$O$_3$+5%SO$_4$/ZrO$_2$ | 280 | 76.7 | 88.1 | 12.9 | 54.7 | 8.6 |
| | 220 | 15.6 | 96.1 | 1.4 | 13.6 | 0.6 |
| 5%SO$_4$/ZrO$_2$ | 220 | 3.0 | 86.7 | 0.1 | 2.5 | 0.4 |

*The cumulative yields of other products are up to 2.1 wt. %;
DMB – dimethylbutanes, MP - methylpentanes

conversion are cracking or hydrocracking (hydrogenolysis) with the formation of C$_1$–C$_5$ hydrocarbons, dehydrogenation, and dehydrocyclization. These reactions became predominant at elevated temperatures, and their contribution leads to a significant decrease in the selectivity of isomerization (Table 1 and Fig. 1). Similarly, the activity of the purely acidic catalysts used as a second component is low and the n-hexane conversion does not exceed 10-15% in the low-temperature region of testing conditions.

The combination of metal-promoted oxide and zeolite components in the Pt/Al$_2$O$_3$ + RE-FAU hybrid system leads to an increase in the activity and selectivity of isomerization as compared with the individual componens of the hybrid system. The catalytic activity of the 0.5%Pt/Al$_2$O$_3$ + RE-FAU-3 hybrid system is only slightly lower than the activity of the 0.5%Pt/RE-FAU-3 catalyst (Table 1 and Fig. 1).

An increase in the acidity of RE-FAU by increasing the Na for RE exchange degree (from 8.8 up to 15 wt.% RE) leads to the growth of the isohexanes yields from 52.6 to 67.7%. The selectivity remains relatively high (72–88%). Simultaneously, the temperature of the maximum activity under the conditions chosen in this study

Legend (top):
— ■ — □ — 0.5% Pt/Al₂O₃
— ▲ — △ — 0.5% Pt/Al₂O₃ + RE-FAU-3
— ▼ — ▽ — 1% Pt/Al₂O₃ + RE-FAU-3
— ● — ○ — 0.5% Pt/RE-FAU-3

— ▲ — △ — 0.5% Pt/Al₂O₃ + RE-FAU-1
— ● — ○ — 0.5% Pd/Al₂O₃ + RE-FAU-1
— ■ — □ — 0.5% Pt/Al₂O₃
— ◆ — ◇ — 0.5% Pd/Al₂O₃
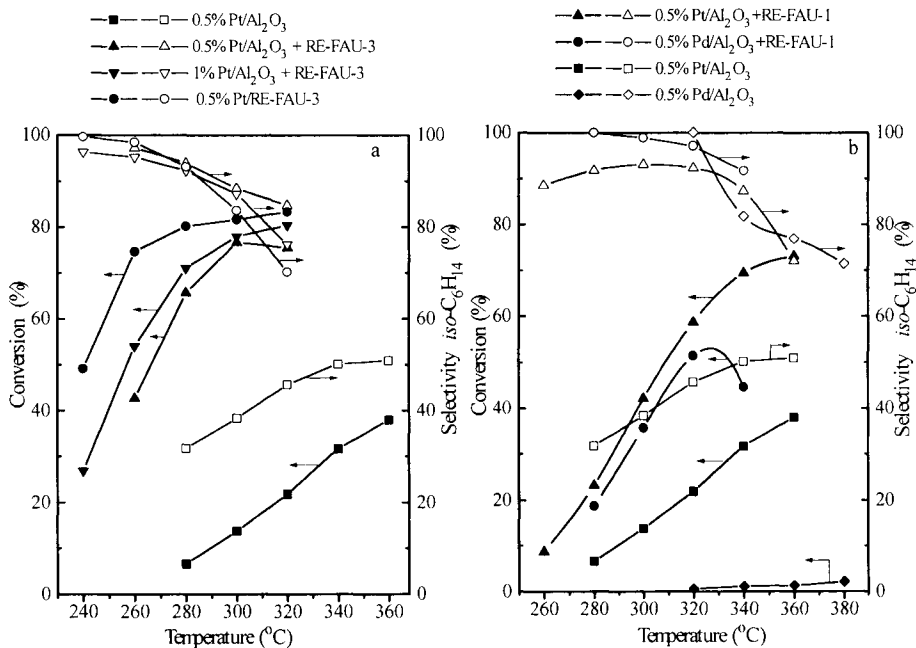
Fig. 1. Performance of dual-function zeolite and hybrid catalysts in n-hexane isomerization

decreases from 360 to 300°C. The total yield of isohexanes as well as the yield of monobranched products were not lower than those for the single-component Pt-zeolite promoted catalyst. However, the yield of dibranched alkanes on the hybrid catalyst was slightly lower. This seems to be the result of the decreasing rate of the consecutuve reactions leading to the formation of dibranched paraffins via intermediate formation of the monobranched hydrocarbons. On the other hand, this may be accounted for by the twice lower concentration of acid sites in the hybrid catalyst "diluted" with weakly acidic alumina.

The influence of the nature of acidic components on the performance of the hybrid catalysts is also illustrated in Table 1. The nature of the acidic component was varied in the wide range, and the activity was found to diminish in the following order:

$SO_4/ZrO_2 > H\text{-Beta} \geq RE\text{-FAU-3} > RE\text{-FAU-1}$.

An increase in the acidity of the acidic component leads to a decrease in the optimal temperature of the reaction from 360°C to 260°C in the following order:

$Pt/Al_2O_3 + RE\text{-FAU-1} > Pt/Al_2O_3 + RE\text{-FAU-3} > Pt/Al_2O_3 + SO_4/ZrO_4 > Pt/Al_2O_3 + H\text{-Beta}$.
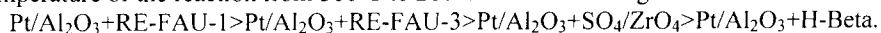
An increase in the concentration of Pt in the $Pt/Al_2O_3$ system from 0.5 to 1.0% does not significantly influence the catalytic activity of the hybrid system (Table 1). This result indicates that the concentration of platinum sufficient for efficient catalytic

transformation of n-hexane is below 0.5%. When palladium was used instead of platinum as the active metal, the isohexane yield diminished. However, the isohexane selectivity on the Pd-catalyst (97-98%) is higher as compared with the Pt-promoted system (93%). The weaker dehydrogenation activity of Pd compared to Pt could be the reason behind the decrease in the catalytic activity of the Pd-containing hybrid system. The enhancement of the activity of the hybrid catalysts as compared to individual $Pt/Al_2O_3$ and acidic catalysts can be explained by a spillover effect on metal-promoted hybrid systems combining the acidic and dehydrogenating properties. It can be suggested that spillover of hydrogen is very important for the stabilization of intermediate carbenium or carbonium ions.

The overal acidity of the oxide in the composition of the metal-containing component of the hybrid catalyst is also an important characteristic necessary to achieve the maximum activity. When silica was used as a support for platinum in the metal-bearing component of the hybrid catalyst, instead of alumina, the catalytic activity in n-hexane isomerization somewhat decreased (Table 1). The total isohexane yield and the yield of dibranched isomers dropped to 34.4 and 6.2%, respectively. This effect can be explained by decreasing dispersion of the supported metal in the $Pt/SiO_2$ system as compared to $Pt/Al_2O_3$. In general, the metal dispersion is a function of the acid-base properties of the support, which stabilizes the supported metal particles.

The close performances of the hybrid catalyst (in which the dehydrogenating and acidic functions are spatially separated) and metal-containing acid catalysts (with acid and metal centers located in close vicinity) indicate that the step of hydrogen and hydrocarbon species spillover is not a limiting step in the n-alkane conversion on the hybrid catalysts. It means that the spillover of the reactive species (migration from the metal particle to the acid site) occurs with a high rate.

### 3.2. n-Octane isomerization

The characteristics of the performance of the monocomponent Pt-free RE-FAU and $Pt/Al_2O_3$ and Pt/RE-FAU catalysts, as well as hybrid $Pt/Al_2O_3$ + Pt/RE-FAU system in n-octane isomerization are presented in Table 2 and Fig. 2.

Table 2.
Isomerization of n-octane on hybrid catalysts
(catalyst loading 2 c.c., LHSV = 1 $h^{-1}$, P = 0.1 MPa, $H_2$ : n-octane = 10 : 1 mol/mol)

| Catalyst | T (°C) | Conver- sion (%) | Selecti vity (%) | Yield of products (wt. %) | | | |
|---|---|---|---|---|---|---|---|
| | | | | $C_1$-$C_4$ | $C_5$-$C_7$ | iso-$C_8H_{18}$ | Other products |
| 1%Pt/Al₂O₃ | 280 | 3.3 | 27.3 | - | 0.4 | 0.9 | 2.0 |
| | 380 | 36.5 | 18.6 | 2.8 | 3.8 | 6.8 | 23.1 |
| 1%Pt/Al₂O₃ + RE-FAU | 280 | 77.4 | 79.8 | 10.1 | 4.4 | 61.8 | 1.1 |
| 0.5%Pt/RE-FAU | 230 | 80.5 | 79.3 | 12.3 | 4.4 | 63.8 | - |
| RE-FAU | 280 | 18.1 | 22.1 | 9.5 | 4.3 | 4.0 | 0.3 |

The activity of the Pt-free RE-FAU and $Pt/Al_2O_3$ systems was very low. The isooctanes yield was below 5% and the selectivity was 22–27%. The hydrocracking, dehydrogenation, and dehydrocyclization are the main side reactions. However, the hybrid system is characterized by the high activity and selectivity in $n$-octane isomerization. The isooctanes yield at 280°C is 61.8% and the selectivity is 79.8%. These data are close to the results obtained for the monocomponent Pt/RE-FAU catalyst. But the optimal reaction temperature for the hybrid system is 50° higher. Again, this can be explained by the twofold decrease in the concentration of acid sites in the hybrid catalyst as compared to the conventional dual-function catalyst (Pt/zeolite).
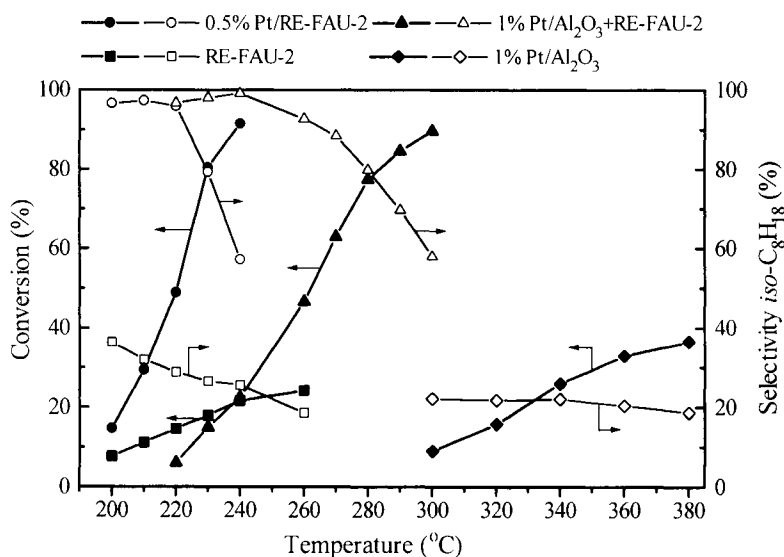


Fig. 2. Temperature dependences of the activity and selectivity of hybrid and reference catalysts in n-octane isomerization.

### 3.3. n-Tetradecane isomerization

Isomerization of still heavier hydrocarbon feedstock is by far more complicated problem as compared to isomerization of $C_6$-$C_8$ paraffins. Therefore, it was a challenging task to test the dual-function zeolite catalysts in skeletal isomerization of $C_{14}$ n-alkane. The same hybrid and reference catalytic systems as those tested in $C_6$-$C_8$ paraffin isomerization were studied in $n$-tetradecane isomerization (Table 3).

The behavior of the RE-FAU + $Al_2O_3$ and $Pt/Al_2O_3$ systems is similar to that observed in the isomerization of $n$-hexane and $n$-octane. The activity of the hybrid system was close to the activity of the monocomponent Pt/RE-FAU catalyst. The isomer yields were 40.3 and 47.6%, respectively, and the selectivity in both cases was

close to 84%, although the content of platinum in the hybrid catalyst was 2 times lower, as well as the concentration of the acid sites.

Table 3.
Isomerization of n-tetradecane on hybrid catalysts
(catalyst loading 2 c.c., LHSV = 1 h$^{-1}$, P = 0.1 MPa, H$_2$ : CH = 10 : 1 mol./mol.)

| Catalyst | T (°C) | Conver-sion (%) | Selectivity to iso-$C_{14}H_{30}$ (%) | Yield of products (wt. %) | | |
|---|---|---|---|---|---|---|
| | | | | $C_1$-$C_4$ | $C_5$-$C_{13}$ | iso-$C_{14}H_{30}$ |
| 0.5%Pt/Al$_2$O$_3$ | 230 | 1.0 | 70.0 | - | 0.3 | 0.7 |
| 0.5%Pt/Al$_2$O$_3$ + RE-FAU | 220 | 48.0 | 84.4 | 1.0 | 6.5 | 40.5 |
| 0.5%Pt/RE-FAU | 200 | 56.7 | 84.0 | 2.2 | 6.9 | 47.6 |
| RE-FAU + Al$_2$O$_3$ | 220 | 8.8 | 45.5 | - | 4.8 | 4.0 |

The performances of the hybrid catalysts and the individual components of hybrid catalysts are compared in the optimal conditions in Fig. 3. These data clearly show the effect of synergism between the metal-containing component and the acidic component of the hybrid catalyst in n-paraffin isomerization.
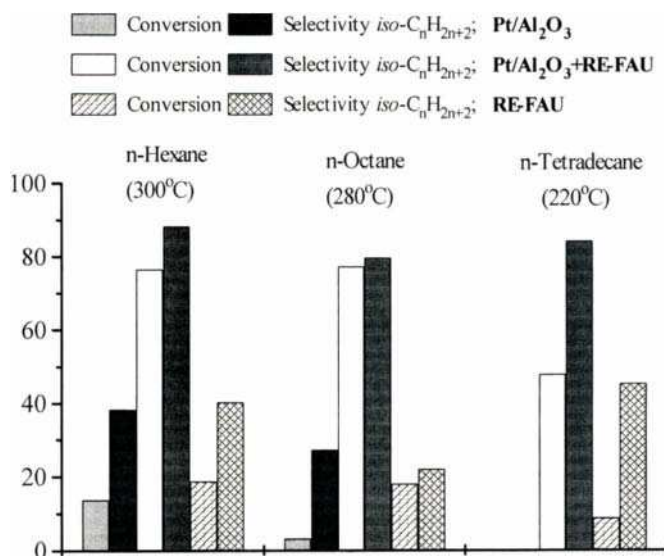


Fig. 3. Comparison of the hybrid catalyst with the components in terms of the activity and selectivity in isomerization of three different substrates (n-$C_6H_{14}$, n-$C_8H_{18}$, n-$C_{14}H_{30}$).

## 4. CONCLUSIONS

Thus, it was shown that the hybrid catalysts are very active in $C_6$–$C_{14}$ $n$-alkane isomerization. The catalytic properties of the systems depend on the contribution of acidic and dehydrogenating properties of the system, which is mediated by spillover of reactive species, in particular hydrogen and hydrocarbon moieties (carbocations). The concentration of the metal (Pt) in $Al_2O_3$ does not significantly influence the catalytic activity of the hybrid systems. The total acidity of the hybrid system is a very important factor. The limiting step of the process seems to be the conversion of surface species on BAS of catalyst, whereas the step of hydrogen and hydrocarbon species spillover is not a limiting step in the n-alkane conversion on the hybrid catalysts. It was demonstrated that the spillover of the reactive species (migration from the metal particle to the acid site) occurs with a high rate.

## 5. REFERENCES

1. N.S. Gnep, J.Y. Doyemet, and M. Guisnet, J. Mol. Catal., 45 (1998) 261.
2. I. Nakamura, A. Zhang, and K. Fujimoto, Stud. Surf. Sci. Catal., 94 (1995) 464.
3. I. Nakamura and K. Fujimoto, Stud. Surf. Sci. Catal., 100 (1996) 235.
4. A.Yu. Stakheev and L.M. Kustov, Appl. Catal., A: General, 188 (1999) 3.
5. W.M.H.Sachtler and Z.C. Zhang, Adv. Catal., 39 (1993) 129.
6. A.Yu. Stakheev and L.M. Kustov, submitted to North American Catalysis Society Meeting, Toronto, 2001.
7. W.C. Conner and J.L. Falconer, Chem. Rev., (1995) 95.
8. P.A. Sermon and G.C. Bond, Catal. Rev., 8 (1973) 211.
9. J.M. Sinfelt and P.J. Lucchesi, J. Am. Chem. Soc., 85 (1963) 3365.
10. P.A. Sermon and G.C. Bond, J. Chem. Soc., Faraday Trans., 75(1) (1980) 889.
11. M.G. Yang, I. Nakamura, and K. Fujimoto, Appl. Catal., A, 127 (1995) 115.
12. H. Horrori, H.T. Shischido, J. Tsuji et. al., Science and Technology in Catalysis, 1994.
13. I. Nakamura, A. Zhang, and K. Fujimoto, Stud. Surf. Sci. Catal., 109 (1997) 325.
14. A.H. Zhang, I. Nakamura, and K. Fujimoto, J. Catal., 168 (1997) 328.
15. K. Fujimoto, K. Maeda, and K. Aimoto, Appl. Catal., A, 91(2) (1992) 81.
16. J.G. Santiesteban, J.C. Vartuli, S. Han et al., J. Catal., 168 (1997), 431.
17. J.G. Santiesteban, D.C. Calabro, W.S. Borghard et. al., J. Catal, 183 (1999) 314.

101

# Hydrogen spillover on supported TiO₂ films doped by platinum particles

D.V. Malevich[*], A.F. Masez, V.G. Matys and I.M. Zharskii

Department of Chemistry, Technology of Electrochemical Manufacture and Materials of Electronic Technique, Belarussian State Technological University 220630 Minsk, Belarus

Cyclic voltammetry was performed on supported titanium oxide coatings doped by platinum particles. The electrodes were prepared by thermal decomposition of $H_2PtCl_6$ + $TiCl_3$ mixture. Hydrogen adsorption and spillover were investigated at different temperatures and potential sweep rates. Quantity of adsorbed hydrogen moles, which transfers onto support was about $10^{-8}$ - $10^{-9}$ moles per 1 $cm^2$ of geometric area. The diffusion coefficients of hydrogen were found to be of the order of $10^{-11}$ $cm^2$ $s^{-1}$.

## 1. INTRODUCTION

Supported platinum particles are used very frequently as electrocatalysts in fuel cells, gas evolution, electrosynthesis, sewage waters treatment etc. Usually, two kinds of such electrode materials are used: immediately fixed particles on the support surface and oxide coatings doped by platinum. There are a number of such materials synthesis methods: thermal decomposition of substances on the surface of electrode matrix [1-3], thermal treatment of oxides powder and platinum particles mixture [4], ion implantation into supported oxide films [5], electroplating – electrooxidation procedure [6-7] etc. Frequently, relative electrochemical process rate on doped films is higher than on smooth or platinized platinum electrode [8-10] as well as on pure support or oxide film. Such synergetic effect can be explained by the following phenomena:

(i) interaction between particles and support (film or substrate). This results in activating of support in zone of platinum/support interface [11];

(ii) spillover effect [12], i.e. transfer of adsorbed particles onto support and participation of semiconductor film in the electrochemical processes.

Researches of such effects have high interest for systems "platinum particles – oxides of high-melting metals (Ti, Ta, Nb etc.)". There are three reasons for such interests at least:

(i) essential difference in Fermi levels of platinum and these oxides. This results in appearance of considerable contact potential and strong metal – support interaction;

(ii) spillover – effect often promotes the electrochemical processes carrying out on the surface of semiconductors, i.e. it activates these oxides and results in appearance of new mechanisms of reactions;

(iii) such oxides correspond to metals which are used very frequently as bases of dimensionally stable anodes and other supported electrode materials.

[*]Corresponding author. Present address: Dept. of Chemistry and Biochemistry, University of Guelph, Guelph, N1G 2W1, ON, Canada. E-mail: dmalevic@uoguelph.ca

In this paper, we focus on the transfer of adsorbed hydrogen onto support from underpotential deposited (UPD) layer. Investigations of these layers are carried out very frequently in spillover researches because this gives a possibility to use very convenient and informative method of cyclic voltammetry and reach data base of UPD-layers behavior on polycrystalline and monocrystalline pure electrodes. This paper concerns the hydrogen spillover on supported titanium oxide coatings doped by platinum particles.

## 2. EXPERIMENTAL

The titanium oxide coatings doped by platinum were deposited onto titanium foil with geometric area 1 cm$^2$. The Ti-base was etched in NaF-H$_2$SO$_4$ solution to remove residual oxide for 2-3 minutes. Solution for coatings deposition was prepared with highly pure H$_2$PtCl$_6$ and TiCl$_3$. These substances were dissolved in ethanol, the concentrations of both were 10 mM. Fixed quantity of solution was applied by drop pipette onto the prepared metal surface in 5 sequential layers, each being dried for 10-20 min on air at room conditions and heated at 723 K for 2-3 min in muffle furnace (air atmosphere). After deposition of 5 layers the samples were finally heated at 723 K for 30 minutes. Total platinum weight was about 5 g·cm$^{-2}$.

After films had been deposited, the samples were washed in triply-distilled water and before the experiment, they were heated in the electrolyte at maximal experimental temperature for 6 hours.

Electrochemical experiments were carried out in glass electrochemical cell (Pyrex) with water jacket, Pt wire counter electrode in separated compartment and Ag/AgCl/KCl saturated reference electrode (SSE). Compartment of reference electrode was separated with wetted and closed tap and Luggin capillary. Temperature was held with U-2 thermostat and was controlled within ± 0.5 K.

The solution for electrochemical experiments was 0.05 M H$_2$SO$_4$. It was prepared from high-pure acid and triply distilled water. Before the experiments pure nitrogen was bubbled through the main compartment for 6 hours to remove oxygen from electrolyte.

A potentiostat type PI 50-1.1 connected with IBM-80386 (40 MHz) computer was used. The experimental voltammetric data was analyzed with the aid of software Origin 4.1 (Microcal Software, Inc.).

## 3. RESULTS AND DISCUSSION

Figures 1 and 2 show cyclic voltammograms (CV) for the electrodes for different potential sweep rates and for different temperatures (5$^{th}$ scan was recorded). These CV demonstrate that hydrogen desorption peak bit shifts towards more positive potentials upon the potential sweep rate increase. There is no clear separation of desorption plots on partial peaks in comparison with hydrogen UPD desorption profile on pure platinum electrode [13]. But asymmetric form of these plots may be explained by the presence of partial hydrogen desorption peaks, which corresponding to different energies of H-Pt bonds.

The form of desorption peak for potential sweep rate $v \leq 0.050$ V s$^{-1}$ inessentialy depends on the temperature but adsorption currents grow with the increasing of temperature (see fig.2). The charges spent on adsorption ($Q_{ads}$) and on ionization of adsorbed hydrogen ($Q_{des}$) were defined for each voltammogram.

j, mA cm$^{-2}$



j, mA cm$^{-2}$
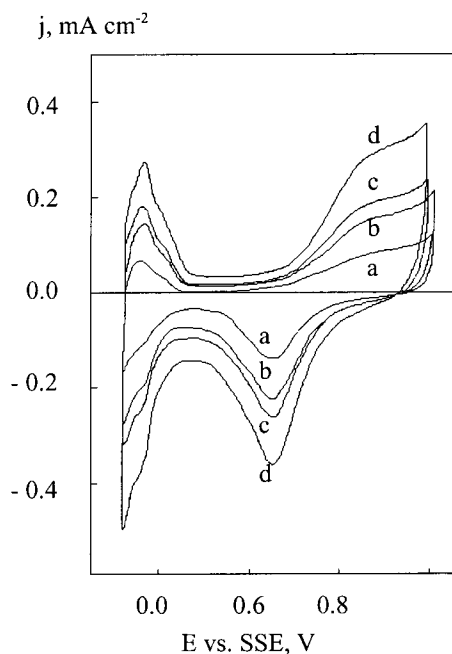


Fig. 1. Cyclic voltammograms for potential sweep rates 0.010 (a), 0.020 (b), 0.025 (c) and 0.040 (d) V s$^{-1}$. Temperature – 291 K.
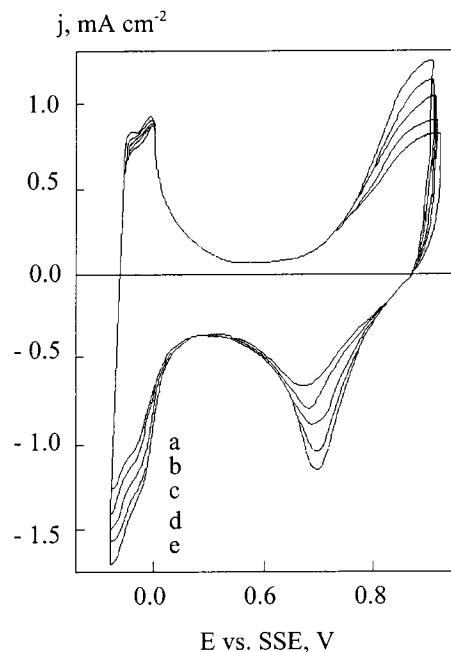
Fig. 2. Cyclic voltammograms for temperature 287 (a), 295 (b), 305 (c), 316 (d) and 326 (e) K. Potential sweep rate – 0.100 V s$^{-1}$.

These parameters were calculated by integrating the cathodic and the anodic parts of voltammograms at potentials ranging -0.17 – 0.13 V (SSE). These limits correspond to maximal ($\theta \approx 1$) [14] and minimal ($\theta \approx 0$) hydrogen coverage. Potential 0.13 V has been chosen because it corresponds to minimal cathodic current on CV curves.

For potential sweep rate $v \leq 0.050$ V s$^{-1}$ the value of $Q_{ads}$ groves with $v$ decreasing when $Q_{des}$ inessentialy depends on $v$ (Fig 3). Using these $Q_{des}$ values we determined electrochemically active area of platinum as 5.50 ÷ 7.31 cm$^2$ per 1 cm$^2$ of geometric area, assuming 0.21 mC·cm$^{-2}$ for H monolayer on polycrystalline platinum electrode [15, 16]. It is near the value of 6.67 cm$^2$ per 1 cm$^2$ of geometric area, defined by desorption of copper UPD-monolayer deposited in 5·10$^{-5}$ M CuSO$_4$ [17] (this experiment was carried out after voltammetry in hydrogen adsorption-desorption potentials region).

When potential sweep rate is 0.05 – 0.20 V s$^{-1}$, the values of $Q_{ads}$ and $Q_{des}$ are almost the same (especially at low temperature), but $Q_{des}$ has a plateau at $v < 0.05$ V s$^{-1}$ when $Q_{ads}$ groves with $v$ decreasing. Schematically it is showed on fig. 4. So, when $v < 0.05$ V s$^{-1}$, the values of $Q_{ads}$ are more than $Q_{des}$. Taking into account that dissolved oxygen was removed, we can suggest that part of adsorbed hydrogen transfers onto titanium oxide acceptor (spillover effect).
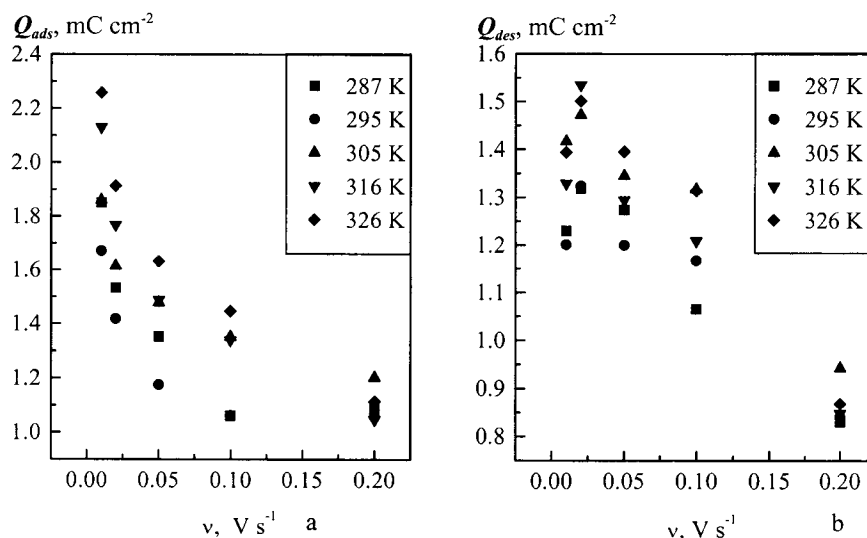
Fig. 3. Adsorption (a) and desorption (b) charges vs. potential sweep rate. Values are given per geometric area.

For platinum particles supported by Pt-plate, where spillover has not been observed, hydrogen adsorption charge is a function of potential sweep rate. In particular, the value of $Q_H/Q_O$ increases with $v$ dropping [18] ($Q_H$ and $Q_O$ are the charges of hydrogen and oxygen adsorption, $Q_O$ is often used for supported catalysts area estimation [19] because oxygen spillover is much slower, but it occurs for such type of materials [20]). In our experiments, we did not see any essential changes of $Q_O$, so, shape of $Q_H/Q_O$ - $v$ function is the same as for Pt/Pt electrode. Probably, such shape can be explained by adsorption kinetic restrictions, which may occur at high potential sweep rates.

On a base of these results we can make two conclusions. Firstly, hydrogen spillover is inessential during desorption process. That can be concluded taking into account closeness of electrochemically active areas estimated by copper underpotential deposition and hydrogen desorption when $v < 0.050$ V s$^{-1}$. We can conclude that chemical potential of H-atoms adsorbed on Pt is higher than on TiO$_x$, at least when coverage is close to 1, because hydrogen transfers from Pt. Hydrogen atoms concentration decreases during the desorption process and this results in essential spillover slowing due to the drop of chemical potential gradient over Pt/TiO$_x$ interface. Secondly, spillover rate is essentially lower than adsorption rate. When potential sweep rate is high, essential amount of H-atoms can not transfer over Pt/TiO$_x$ interface within short adsorption period because low diffusion rate. In this case, the values of $Q_{ads}$ and $Q_{des}$ coincide. Contrary, when potential sweep rate is low, spillover results in transfer of adsorbed hydrogen from Pt surface and free Pt sites can be occupied by new H-atoms. This results in $Q_{ads}$ increasing.
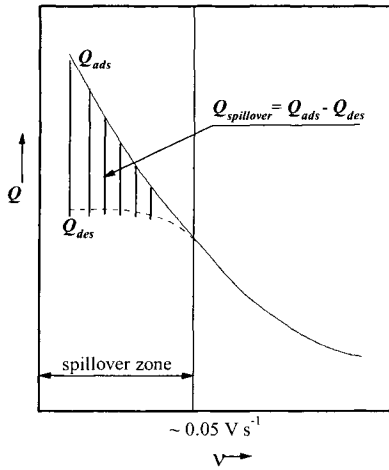
Fig. 4. Common shapes of $Q_{ads}$ $(Q_{des})$ - $v$ dependences.
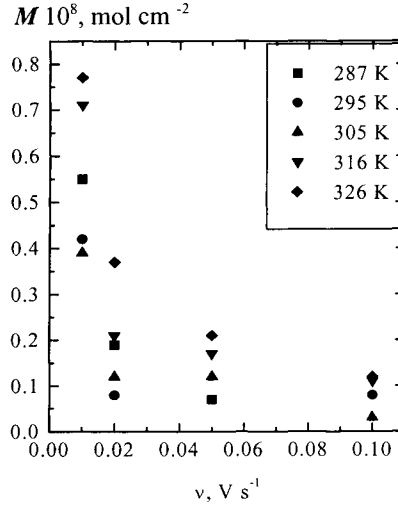
Fig. 5. Quantity of transferred hydrogen vs. potential sweep rate. Values are given per geometric area.

Quantity of moles of adsorbed hydrogen, which is transferring onto $TiO_x$ within one potential cycle, can be recalculated as

$$M = \frac{(Q_{ads} - Q_{des})n}{Q' N_A} \tag{1}$$

where $n$ is the surface concentration of hydrogen atoms in monolayer adsorbed on smooth Pt ($n = 1.13 \cdot 10^{15}$ cm$^{-2}$); $Q'$ is the charges of hydrogen monolayer ionization ($Q' = 0.21$ mC·cm$^{-2}$); $N_A$ is the Avagadro constant ($N_A = 6.02 \cdot 10^{23}$, mol$^{-1}$).

Dependence of $M$ vs. potential sweep rate for experimental samples is showed on fig. 5. The data may be use for recalculation of adsorbed hydrogen diffusion coefficients.

Quantity of adsorbed hydrogen moles, which is transferring onto support within of time t, can be recalculated as [21]

$$m = C_H \cdot I_o \cdot \sqrt{\cdot D_H \cdot t} \tag{2}$$

where $C_H$ is the concentration of adsorbed hydrogen on the Pt surface, mol cm$^{-2}$; $I_o$ is the summarized perimeter of platinum particles, cm$^{-1}$ (all parameters are given per 1 cm$^2$ of geometric area); $D_H$ is the coefficient of adsorbed hydrogen diffusion on the surface of support, cm$^2$ s$^{-1}$. The current value of $C_H$ is

$$C_H = C_{max} \Theta \tag{3}$$

where $\Theta$ is the coverage of platinum surface by adsorbed hydrogen; $C_{max}$ is the concentration of adsorbed hydrogen at $\Theta = 1$, mol cm$^{-2}$

The values of $C_{max}$ as well as other parameters must be recalculated per 1 cm$^2$ of geometric area

$$C_{max} = \frac{n \cdot S_r}{A \cdot S_g} \tag{4}$$

where $S_r$ and $S_g$ are the electrochemically active (real) and geometric areas, cm$^2$.

The values of $\Theta$ can be determined by Temkin's isotherm equation

$$\Theta = A + \frac{lnP_H}{f} \tag{5}$$

where $P_H$ is the hydrogen pressure, atm; $f$ is the surface heterogeneity parameter; $A$ – constant.

For determination of $lnP_H$ which correspond to different values of potential we can use the Nernst's equation (for simplification equation we assumed that $a_{H+} \approx C_{H+} = 0.1$ M)

$$E = \frac{RT}{2F} ln \frac{a_H^2}{P_H} = -\frac{RT}{2F}(2 + lnP_H ) \tag{6}$$

Had summarized (5) and (6) we obtained

$$\Theta = A - \frac{2EF}{fRT} - \frac{2}{f} \tag{7}$$

We assumed that $t=0$ at $E=E^*$, where $E^*$ is the potential at $\Theta=0$ ($E^*=0.13$ V). Then, for uniform change of potential in hydrogen adsorption region ($-0.17 \leq E \leq 0.13$) current value of t can be recalculated as

$$t = \frac{E^* - E}{v} \tag{8}$$

Putting (3), (7) and (8) in (2) leads to

$$m = ( A - \frac{2}{f} - \frac{2EF}{fRT} )C_{max}I_o\sqrt{\pi D_H \frac{E^* - E}{v}} \tag{9}$$

Then, quantity of adsorbed hydrogen moles which is transferred onto support at potential changing from $E_1= E^*$ to $E_2= -0.17$ V can be recalculated as

$$M = \int_{E_1}^{E_2}((A - \frac{2}{f} - \frac{2EF}{fRT})C_{max}I_o\sqrt{\pi D_H \frac{E-E^*}{v}} )dE \tag{10}$$

For simplification of (10) we marked some fragments this equation as

$$b_1 = A - \frac{2}{f}, \; b_2 = \frac{2F}{fRT}, \; b_3 = C_{max}I_o, \; b_4 = \frac{\pi D_H E^*}{v}, \; b_5 = \frac{\pi D_H}{v}$$

Then, decision of (10) is

$$M=b_1b_3\left[-\frac{2}{3b_5}(b_4-b_5E)^{3/2}\right]_{E_1}^{E_2}+\frac{2b_2b_3}{3b_5}\left(\left[E(b_4-b_5E)^{3/2}\right]_{E_1}^{E_2}+\frac{2}{5b_5}\left[(b_4-b_5E)^{5/2}\right]_{E_1}^{E_2}\right)(11)$$

Substituted $b_1...b_5$ and simplified the equation we obtained

$$M=\frac{2}{3}C_{max}I_o\sqrt{\frac{\pi D_H}{v}}\left[\frac{2F}{fRT}(E_2(E^*-E_2)^{3/2})+\frac{4F}{5fRT}(E^*-E_2)^{5/2}-(A-\frac{2}{f})(E^*-E_2)^{3/2}\right](12)$$

We assumed that $k$ particles with form of hemisphere and diameter $d$ are on the $TiO_2$ film surface , than

$$I_o=k\pi d=\frac{2S_r}{\pi d^2}\pi D=\frac{2S_r}{d} \qquad (13)$$

Using $d=0.25\cdot10^{-4}$ cm [20] we recalculated the value $I_o=5,336\cdot10^5$ cm. The parameters $A$ and $f$ were recalculated from initial isotherms of hydrogen adsorption on (Pt-$TiO_2$)/Ti electrode [22] (Table 1). Using these parameters and values $M$ (see. fig. 3) we recalculated, firstly, the coefficients $b_1...b_5$, and, after, the values of $D_H$ from equation (12) (see. tab. 1). Values of $M$ at potential sweep rate region $0.01\div0.05$ $V\cdot s^{-1}$ where $Q_{des}$ corresponds to electrochemically active area obtained by copper underpotential deposition have been used.

Table 1.
Diffusion coefficients and parameters used for calculation

| Temperature, K | $A$ | $f$ | $D_H\cdot10^{11}$, $cm^2\cdot s^{-1}$ |
|---|---|---|---|
| 295 | 1.06 | 13.77 | 2.1 |
| 305 | 1.03 | 14.48 | 3.9 |
| 316 | 0.96 | 14.90 | 6.6 |

The obtained values of $D_H$ exceed diffusion coefficients for non electrochemical oxide catalysts [23]. For example, $D_H$ is about $10^{-16}$ for $WO_3$, $10^{-13}$ for $MoO_3$ [24], $10^{-14}$ $cm^2\cdot s^{-1}$ for $SiO_2$ [25] if temperature less than 100°C. Only if temperature is about 400°C this coefficient achieves the value of $10^{-11}\div10^{-12}$ $sm^2\cdot s^{-1}$ [26]. These values are defined at permanent coverage, whereas table 1 contains the average values when $\Theta$ is changing between 0 and 1. Although $D_H$ should not be a function of coverage, altering of the lateral interaction in adsorbed layer occurs when coverage is changing and that can cause a difference in hydrogen diffusion coefficients determined at permanent and non-permanent coverage conditions.

108

**REFERENCES**

1   D. V. Malevich, V.B. Drozdovich and I. M. Zharskii, Russian. J. Electrochem., 33 (1997) 331.
2.  K. Tammevseski, T. Tenno, A. Rosental, P. Talonen, L.-S. Johansson and L. Niinisto, J. Electrochem. Soc., 146 (1999) 669.
3.  G. Foti, C. Mousty, K. Novy, Ch. Comninellis and V. Red, Electrochim. Acta, 30 (2000) 147.
4.  L. He, H.E. Franzen and D.C. Johnson, J. Appl. Electrochem., 26 (1996) 785.
5.  C. Zhang, J. Yang and Z. Wu, Mater. Sci. Ing. B, 68 (2000) 138.
6.  W. Schmicler and U. Stimming, Thin Solid Films, 75 (1981) 331.
7.  M. J. Esplandiu, L. B. Avalle and V. A. Macagno, Electrochim. Acta, 40 (1995) 2587.
8.  Yu. V. Telepnya, D. M. Shub, P. A. Zhdan and E. V. Kasatkin, Sov. Electrochem. 26 (1990) 88.
9.  D. V. Malevich, V. B. Drozdovich and I. M. Zharskii, Russian J. Electrochem., 52 (1996) 1298.
10. V. S. Bagotzky, L. S. Kanevsky, and V. Sh. Planker, Electrochim. Acta, 18 (1973) 473.
11. L.N. Kulikova, V.N. Fateev, V.P. Pakhomov, G.F. Potapova and E.V. Kasatkin, Sov. Electrochem. 26 (1990) 942.
12. V. S. Bagotzky and A. M. Skundin, Electrochim. Acta, 29 (1984) 757.
13. A. Zolfaghari, M. Chayer and G. Jerkiewicz, J. Electrochem. Soc., 144 (1997) 3034.
14. S. Gilman, Electroanalytical chemistry, A. J. Bard (eds.), Arnold, London, 1967.
15. G. Jerkiewicz and J.J. Borodzinski, J. Chem. Soc., Faraday Trans. 90 (1994) 3669.
16. B.E. Conway and L. Bai, J. Electroanal. Chem., 198 (1986) 149.
17. S. A. S. Machado, A. A. Tanaka and E. R. Gonzales, Electrochim. Acta., 36 (1991) 1325.
18. T. Kessler, A.M. Castro Luna, W.E. Triaca and A.J. Arvia, J. Appl. Electrochem., 16 (1986) 693
19  S. Trasatti and O.A. Petrii, Pure Appl. Chem., 63 (1991) 711.
20. H. Lin, J. Molecular Catal. A, 144 (1999) 189
21. R. Cramer and M. Andre, J. Catal., 58 (1979) 287.
22. D. V. Malevich, V. B. Drozdovich and I. M. Zharskii, Stud. Surf. Sci. Catal., 112 (1997) 359.
23. V.V. Rozanov. and O.V. Krylov, Russian Chem. Rev., 66 (1997) 107.
24. P.A. Sermon and G.C. Bond, J. Chem Soc., Faraday Trans., 72 (1976) 730.
25. T. Fleisch and R. Abermann, J. Catal., 50 (1977) 278.
26. D. Martin and D. Duprez, Stud. Surf. Sci. Catal., 77( 1993) 201.

# Future research on spillover

Bernard Delmon

Université catholique de Louvain
Place Croix du Sud 2/17, B-1348  Louvain-la-Neuve, Belgium

Recent progress makes possible new research on spillover processes (SO). Three essential characteristics of the SO phenomenon will be examined, namely:
1/ Mobility of a species ($S_p$) from phase D (donor) to phase A (acceptor);
2/ Species $S_p$ is normally not present on A;
3/ Species $S_p$ causes or facilitates a specific reaction (R);
   A fourth section will speculate on a few possible consequences in catalysis.

## 1. INTRODUCTION

Spillover species ($S_p$) possess very special chemical properties. SO phenomena can therefore explain many results. The concept can be used for inventing more efficient catalysts and  more selective processes. To evaluate the potential impact of spillover, it is necessary to consider the facts that determine its specificity. SO implies surface mobility of a species $S_p$ *from a first phase* (for convenience: donor D) *to a second phase* (acceptor A) where this species is normally not present. It also involves *some reaction of this species on, or with* A. When conspicuous effects are observed, neither just *mobility on one surface* nor *the existence of two phases* in a catalyst are sufficient for proving the occurrence of SO processes. For example, in our CO oxidation experiments using Cu(111) on the Pt(111) surface, the reaction occurred at the Cu/Pt border, where O was present. The mobility of CO on Pt allowed the reaction to proceed at this interface, a CO-depleted zone appeared on the Pt side and progressively expanded as a reaction front on Pt [1]. No species seemed to cross the border between phases. Spillover was not at stake. Conversely, U. Roland et al. investigated a zeolite receiving spillover hydrogen ($H_{SO}$) produced by Pt deposited on an adjacent phase. They detected a Hall effect, thus proving mobility [2]. The reactivity of $H_{SO}$ present in zeolites has been demonstrated by many investigators. In such cases, a full SO process takes place.

A close workshop symposium organized in Namur in 1976 concluded that the SO phenomenon did not open any practical prospect (but was very exciting). This occurred at about the same time as it was discovered that spillover species ($H_{SO}$ and $O_{SO}$) promoted coke elimination, leading, in particular, to the introduction of a small amount of noble metals in industrial cracking catalysts. Actually, the discovery of spillover had been made when observing that $H_{SO}$ reacted with the surface of an oxide to initiate reduction. No much later than 1976, the phenomenon that G. Pajonk named the "catalysis of catalytic processes", namely the creation of catalytic sites by spillover species (a reaction with a surface!), was discovered. Also $O_{SO}$, besides $H_{SO}$, attracted interest. The perspectives then became more exciting than the conclusions of the meeting in Namur. The objective of this small contribution

is to help point to perhaps undetected possibilities that spillover offers. The nature and reactivity of $S_p$ species are central to the discussion. This dictates the plan and serves as a background for the presentation.

## 2. MOBILITY

Returning to the initial remarks, a first crucial aspect is *mobility*. The fact that a D phase modifies a phenomenon occurring on A is not sufficient to prove spillover. The occurrence of part of a reaction on A and transfer from D to A of an intermediate species is rightly mentioned as an alternative (bifunctional catalysis). It can be suspected that critical remarks concerning experimental data presented during this Conference will sometimes raise doubts on explanations based on SO. Full proofs equivalent to those of U. Roland et al. with deuterium are not frequent. Using Infrared Spectroscopy and a magnetic field, they observed an effect that exists only when charged particles move, namely the Hall effect [2].

Proving that a given species is mobile implies that this species can be unequivocally identified. An equally important demand is to have marks ("milestones") in space, in order precisely to locate signals or images. Ideally, they should be as directly visible as in a microscope. In the design of the corresponding experiments, it is essential to remember that SO is *a dynamic process*. The $S_p$ species only moves when driven by some *chemical potential gradient*. There must be a source and a sink. This implies an isotope exchange or the flow of $S_p$ from D to A where it is destroyed or consumed.

### 2.1. Creation of a concentration gradient

Much hope rests on surface science techniques for identifying moving species and proving that they are mobile. Recent experiments of G. Ertl and his group using near field microscopy showed oxygen atoms diffusing on a surface after the impact of $O_2$ on this surface. This experiment could in principle be extrapolated to a sample containing two different surface phases. One of the main difficulties in surface science is to create a concentration gradient. The main reason is that measurements should take place at low or very low pressures, thereby diminishing the dissociation rate of the molecule giving the $S_p$ species. The difficulty is to establish, permanently or transitorily, a concentration gradient on the observed surface. Fortunately, special devices permit to direct a flow of precursors of $S_p$ (molecules) on a localized region on the surface. The gradient would be created between this region (D) and the "sink", i.e. the A surface where either a chemical reaction takes place or from where $S_p$ could escape in some way. The dissociation (or reaction) rates differ very much from surface to surface. It is therefore possible in principle to use pulse techniques for differently "loading" or "unloading" D and A, and creating a transient gradient. One of the difficulties presently is the relatively large time needed to change experimental conditions in a high vacuum chamber. A light beam could deplete a given region by laser-induced desorption, thus creating the sink. Additional hope rests on the use of the so-called environmental scanning microscope, where pressures are not so critically low as in present surface science experiments.

### 2.2. Identification of the moving species

The identification of the spillover species remains a problem. The use of isotopes and/or sensitive spectroscopy techniques gives a direct answer in some cases. More elaborate strategies are often necessary. The group of D. Duprez associated the use of isotopes with the dynamics of adsorption-desorption (of H or O), as summarized recently in the case of oxygen

[3]. The increasing sophistication of pulse techniques (more precise pulse shaping) and devices inspired from the TAP technique (in particular very sensitive and rapid analysis methods) allows the detection of SO. The source can be the small reservoir that the surface of D constitute. The sink would be A from which species $S_p$ desorbs or the product of a reaction of $S_p$ with a co-reactant. This is typically the strategy to be used for evaluating the respective capacity of ceria and $CeO_2$-$ZrO_2$ solutions to provide $O_{SO}$ to an oxidation catalyst.

Proving the mobility of OH groups is still a problem. The difficulty resides in the detection of a signal exclusively originating from OH, and not from O or from H atoms jumping from oxygens to oxygens. The consequence is that comprehensive experimental approaches must be taken. Several physico-chemical techniques must complement each other. The cooperative work coordinated by the organizers of this conference on the dry reforming of methane shows promising perspectives [4].

## 2.3. Localization

Visual (microscopic) evidences are still lacking for the demonstrating the mobility of O, OH, or other atoms or chemical groups because their mobility is lower than that of H, and the distance at which they move is smaller. A possibility now exists using labeled O, provided D and A particles are sufficiently large (>10$\mu$m). For that purpose, Raman confocal measurements or laser induced desorption with MS are adequate techniques. In "surface science" experiments, Photo-Electron Emission Microscopy (PEEM) can also be used, with presently the same level of spatial resolution (a few $\mu$m). This was used by the group of X.H. Bao for showing oxygen spillover from noble metals to silver in the catalytic decomposition of NOx in the presence of oxygen [5].

Spillover involves two different surfaces. Critical is therefore the mutual position of D and A. Nanolithography permits the unambiguous positioning of phases suspected to be D or A. The fabrication of nanomaterials composed of two kinds of phases or surfaces will provide ideal samples for proving spillover with certainty. Microreactors exploiting the corresponding technologies, namely nanolithography and finely localized detection of reactions, and the use of combinatorial approaches will permit the detection of new SO effects. Near Field Microscopies (STM, AFM, AFM with functionalized tips) are also potentially able to prove the existence of SO.

## 3. NATURE OF SPILLOVER SPECIES

This section concerns the chemical state of the $S_p$ species (as opposed to the element(s) H, O, OH from which it is formed). This state, i.e. neutral, or charged, etc., explains its preferential formation on D, the possibility of migration to A, and the reactivity on A. Quite logically, the nature, more precisely the electronic state of the SO species, has been inferred from mechanistic considerations [6-8]. Nevertheless more direct approaches are needed, in particular to validate such mechanisms.

### 3.1. Electronic state of the SO species

The SO species are almost necessarily bound to surfaces by strong bonds. They possess a reactivity which is distinct (often higher) than the same element naturally present on this surface. Is their electronic state accessible? Classical theories describe the electronic structure of boundary electronic layers at surfaces and the corresponding adsorbates. They can be

adapted to SO, in parallel with experiments. The use of isotopes, as emphasized in the call for papers of 5ICSP, will bring much, provided that adequate techniques for the identification of the chemical state of the corresponding elements are available. The proof of U. Roland et al. that $S_p$ hydrogen is electrically charged [2] shows that there are ways for identifying $S_p$, especially hydride ion and proton (as evoked by K. Fujimoto et al.[6,7] or ourselves [9]). In spite of the likely weakness of signals of NMR, ESR, these with increased sensitivity, in addition to Raman and IR, and grazing angle diffusion experiments could provide information. The measurement of surface potential is also possible (Y. Barbaux and B. Grzybowska). Identification of $S_p$ by specific co-reactants is a further possibility.

Theoretical chemistry could bring much. $S_p$ species are very simple, presumably single atoms of simple electronic structure (charged or neutral), or groups of atoms (OH). The difficulty with SO is the choice of a common origin for energy. Can this problem be solved by combining different theoretical approaches? Much can be expected from theoretical chemistry, using models where potential SO species are *added* to the surface of a representative cluster.

### 3.2. "Non-Faradaic Electrochemical Modification of Catalytic Activity" (NEMCA)

New developments may come from a comparison with the "NEMCA" species described by C.G. Vayenas (but using new experimental arrangements) and from the determination of the chemical potential of $S_p$. NEMCA corresponds to an enhancement of the catalytic performances when hydrogen or oxygen are "pushed" by an electric field to catalytic surfaces. A direct interpretation would be that the reaction partner thus "pushed" would be in a different electronic state. But this explanation is not compatible with the very low amount of NEMCA species compared to reaction stoichiometry, a feature also characterizing the Remote Control (RC). A more acceptable explanation would be that a polarization of some surface structure by the NEMCA (or the SO) species would facilitate dissociative chemisorption of hydrogen or oxygen and/or some concerted chemical mechanism. The similitude between NEMCA and RC suggests that an increase of the free energy of the surface species could explain the enhancement effects. The NEMCA effect could suggest that the *enthalpy* part is mainly responsible for the free energy increase. Considering NEMCA and RC together, it seems more likely that the increase of the *chemical potential*, via the surface concentration term, explains the higher reactivity of the surface species. Potentiometric measurements (M. Estenfelder and H.-G. Lintz [10]) can give access to this quantity. Essential in this line of research is a quantitative comparison of NEMCA and Remote Control.

### 3.3. Interconversion of SO species.

There is no difficulty in considering that a H or O ion can jump from one to another oxide surface. But there are also many experimental evidences of H spillover from a *metal* to an *oxide*. The chemical bond on these two surfaces cannot be identical. It is also known that $H_{SO}$ is chemically similar to atomic hydrogen and E. Baumgarten and L. Maschke give excellent experimental evidences of hydrogen "spillover" through the gas phase [11]. Could the chemical nature of $H_{SO}$ be deduced from these facts? F.Keren and A.Soffer demonstrated the interconversion of $H_{SO}$ in *dry* conditions to a proton *solvated in water* [12]. This implies a considerable change in the chemical nature of mobile species. Incidentally, would this suggest the possibility to acidify an aqueous solution by injecting $H_{SO}$ by dissociation of high pressure $H_2$, thus avoiding contaminating anions? These phenomena are intriguing. They unfortunately might contribute to increase the skepticism of colleagues who are not convinced by the role of

spillover. Conversely, the clarification of the corresponding problems would constitute a great scientific achievement and open new perspectives on the practical level. Could spectroscopic techniques provide the useful information?

## 4. CHEMICAL EFFECT OF $S_p$ SPECIES

The major scientific challenge concerning SO is certainly to understand the reactivity of $S_p$ on A. Typically, why is $O_{SO}$ on oxides different from the oxygen species normally present (on A)? The reason must be a difference in chemical potential. Is this due to the *concentration* or to the *standard energy term.* Probably both! Electrochemistry can give a global answer, but the special reactivity of $S_p$ with both *solid surfaces* and *adsorbed species* can help refine the conclusion. These aspects are often linked to each other.

### 4.1. SO species in catalytic reactions
For example, let us take the case of hydrocracking processes. This has been recently discussed in a very clear way [13]. The cooperation between a metal (often a noble metal) or a sulfide, one the one hand, and zeolites, on the other hand, is explained by the intervention of $H_{SO}$. As protons are quite generally supposed to play a crucial role in these reactions, this $H_{SO}$ species is supposed to be positively charged. This guess however raises the problem of respecting a balance of charges between the neutral molecular hydrogen introduced in the system through the metal and the protons reacting with hydrocarbons in the zeolite pores. It seems necessary to suppose that both protons and hydride ions are present and cooperate (K. Fujimoto et al.[6,7], F. Roessner and U. Roland [14] or ourselves [9]). Experiments prove the validity of these mechanisms. The frequently advanced hypothesis of a *creation* of acidic sites by protons appears therefore as an independent problem. According to these new mechanisms, $H_{SO}$ species react with adsorbed molecules, but not with the catalyst surface.

Could refinements in selective oxidation mechanisms allow similar progress concerning $O_{SO}$? The oxides active alone or mixed together in selective oxidation have semi-conducting properties, especially in the special oxidation state they acquire under the reaction conditions. Charge compensation is easy. The surface can be exclusively populated with oxygen atoms carrying one or two electronic charges or, more probably, fractional charges determined by the electronic interactions with the metal atom in the catalysts and the presence of hydrogen atoms in certain (or many) cases. This will certainly be clarified when more studies will be conducted really *in situ,* namely in the real reaction conditions ("*in operandi*").

### 4.2. Reaction of SO species with surfaces; creation of catalytically active features.
Classical examples of reaction of $S_p$ with surfaces dealt with the initiation of solid state processes (reductions, formation of suboxides, etc.). The surface and bulk of catalytic solids are also modified by SO. This necessarily has an impact on the overall catalytic process.

One example deals with that. $MoS_2$, together with promoters (Co, Ni), is present in the majority of hydrotreating catalysts. X. Chu and L.D. Schmidt showed that the presence of the Co or Ni accelerated the attack of hydrogen on the edges of $MoS_2$ [15], where the catalytically active sites are situated. This observation shows that $H_{SO}$ can remove sulfur atoms and consequently modify the coordination of Mo sites. This supports one of the hypotheses of the Remote Control, namely the creation of active site by SO species. We could use an ab-inito approach for calculating the electronic structure of the edge atoms of both very small (7 Mo

atoms) [16] and larger clusters of MoS$_2$, the latter being completely representative in shape and structure of crystallites observed in industrial catalysts [17]. In addition to giving support to the attribution of specific activities to the various Mo edge sites, the results provided indications concerning their genesis by removal of S atoms. For some of them, this removal demands a highly reactive form of hydrogen [17], e.g. atomic H or a proton, namely species supposed to correspond to H$_{SO}$. This example suggests the potential of an approach considering different facets of the action of SO processes together with other aspects: theoretical chemistry (or preferably?) physico-chemical characterizations, as on ref. 4 or 19, to cite only articles mentioned at other places in this paper.

Another case of special interest is the creation of Brönsted sites in zeolites or silica-aluminas. The situation here is complicated by the fact that H$_{SO}$ in highly reducing conditions can open Si-O-Al bonds [18], but also remove coke deposits poisoning the acidic sites. An increase of the reaction rate could therefore correspond either to the formation of new Brönsted sites or the removing of coke precursors poisoning such sites. This uncertainty deserves discussions during this Conference.

### 4.3. Identification of SO species on the basis of reaction mechanisms

It is clearly difficult to improve our knowledge concerning SO species on the sole basis of catalytic reaction mechanisms. This explains the controversies and also some exaggerated skepticism as regards the existence of the SO phenomenon. This is perhaps harmful to the development of research in this area and more generally to the development of catalytic sciences. In a future oriented attitude, it is however possible to imagine guidelines. This cannot be discussed in detail here. Essentially, the previous sections present a sort of checklist providing guidelines for strengthening the belief that SO processes occur.

There is no doubt that, in spite of the tradition of organic chemistry to offer several different concepts concerning mechanisms, conclusions concerning the intervention or not of SO processes are able to generate the most fruitful ideas and also suggest novel applications of the corresponding concepts. Physically separating D from A in experimental arrangements gives convincing evidences, even if the catalytic performances of such catalysts or arrangements are poor compared to those of conventionally prepared catalysts. Special attention should be given to the absence of mutual contamination by elements entering in the composition of D or A. This is a constant matter of dispute. Conspicuous effects cannot all be explained by spillover, or exclusively by an electronic effect, or by contamination. Contamination is clearly another possibility. But to be fair, the discussion should show that the hypothesis of contamination is based on as many experimental proofs as that of spillover. Signals of metals detected by most techniques are stronger than those of H, D, O or OH. Experimental proofs should be easier to collect. Arguments based on the reasoning that contaminating metals are so active that an undetectable amount must explain catalytic effects deserve proofs, for avoiding their belonging to alchemy. Another argument is that the contaminating elements move forth to the other phase under the reaction conditions and swiftly back immediately afterward!

### 5. NEW CATALYSTS, NEW PROCESSES

Spillover processes have been definitely proven to play the crucial role in reactions the mechanism of which had been a puzzle for many years. These are important industrial

processes like methanol synthesis. This is excellently indicated in a recent article [19]. A new discovery concerning the role of NEMCA in ammonia synthesis [20] suggests other interventions. Not neglecting future discoveries, can we discern directions in which a rational use of the unique characteristics of SO could help develop new catalyst or new processes?

## 5.1. Catalyst formulation and preparation

In the domains where the role of SO is well documented, few efforts have been made so far to optimize the proximity between D and A. Progress in catalyst preparation along with already known approaches could further enhance catalyst efficiency. For example (based on our recent work) this could be particularly useful for making uniform throughout the catalyst the reconstruction of oxides, thus leading to optimal selectivity. Small particle size, maximization of the D-A contacts (using all sorts of interactions), grafting of A on D or vice-versa, avoiding mutual encapsulation, etc. are guidelines that have already been used. The development of nanomaterials, micelles and surface science opens unlimited perspectives.

## 5.2. Benefit to take from the nature and different diffusion path of $S_p$ to reaction site

New ideas could be generated from the remark that $S_p$, a species with unusual reactivity, has access to the active sites through a path distinct from that of the co-reactants. This would lead to the concept of a "nanomembrane" or nanoreactors conceptually similar to biological membranes, but standing relatively high temperatures. Examples are:
- to allow the production of $S_p$ on sites normally poisoned in the reaction conditions. The encapsulation of D, for example in a zeolite of pores so narrow that the poison could not have access to D, could achieve the goal, as shown by C. Song [21]. Ion exchange in small pore zeolites is routinely achieved and the widely used concept of "ship-in-the-bottle" led to many successful strategies for encapsulating elaborate catalytic materials. This could be a donor.
- to use the somehow symmetric strategy, a sort of "trap and kill strategy". This would be to adsorb selectively the molecules supposed to react with $S_p$ in very specific adsorbent-catalysts A (e.g. taking advantage of some molecular recognition). The strategy would then be to "irrigate" this trap with $S_p$. This possibility might be particularly attracting for eliminating pollutants. $H_{SO}$ and $O_{SO}$ are known to penetrate in pores and remove coke. They could achieve the same kind of reaction with adsorbates. This mechanism does not seem to have been mentioned explicitly, but empirical achievements perhaps correspond to this strategy.
- to imitate the macroscopic membranes using the NEMCA effect, namely establishing a flow of $S_p$ through an adequate microporous wall. It is actually possible that this has been achieved through a rational or empirical approach but not identified as due to spillover.

Japanese scientists have published intriguing results showing the beneficial role of *hydrogen* in selective *oxidations*. An obvious temptation (or wish of safety!) would be to avoid the direct contact of oxygen and hydrogen. But the Tosoh Co. accepts this dangerous cohabitation in the industrial oxidation of benzene to phenol!

## 5.3 New kinetic models, new reactors

This last example leads to speculate on new ideas that the existence of SO phenomena could generate for the benefit of chemical engineering. We already reviewed kinetic models based on SO mechanisms. New ones are created (e.g. by N. Satoh, J.i. Hayashi and H.Hattori

116

[22]). New catalysts designed for maximising the effect of SO and these kinetic models are dictating new operation conditions and the design of new reactors.

## 6 . PERSPECTIVES

Advances in many fields of chemical and physical science and new discoveries concerning spillover make that the perspectives opened by this phenomenon become more precise. It will be increasingly more difficult to advance alternative explanations based on incomplete investigations or *a priori* interpretations based on old-fashioned views. It is hoped that this short communication will bring a few useful additions to the articles assembled P. Grange in Appl.Catal. A, vol. 202, no 2. I personally thank the contributing authors of this issue for the very stimulating proof they gave that spillover is an essential ingredient in the development of catalysis.

## REFERENCES

1. M. Kolodzejczyk, R.E.R. Colen, M. Berdau, B. Delmon and J.H. Block, Surf. Sci. 375 (1997) 235.
2. U. Roland, H. Winkler, H. Bauch and K.-H. Steinberg, J. Chem. Soc., Faraday Trans., 87 (1991) 3921.
3. C. Descorme and D. Duprez, Appl. Catal. A, 202 (2000) 231.
4. P. Ferreira-Aparicio, I. Rodriguez-Ramos, J.A. Anderson and A. Guerrero-Ruiz, Appl. Catal. A 202 (2000) 183.
5. W.X. Huang, J.W. Teng, T.X. Cai and X.H. Bao, 12th International Congress on Catalysis (A. Corma, F.V. Melo, S. Mendioroz and J.L.G. Garcia-Fierro, eds.), Elsevier, Amsterdam, vol.B, 2000, 1409-1414.
6. K. Fujimoto, in B. Delmon, G.F. Froment and P. Grange (eds.) Hydrotreatment and Hydrocracking of Oil Fractions, Elsevier, Amstedam, 1999, pp. 37-49;
7. R. Ueda, T. Kusakari, K. Tomishige and K. Fujimoto, J. Catal., 194 (2000) 14.
8. T. Inui, Y. Ono, Y. Takagi and J.-B. Kim, Appl. Catal. A, 202 (2000) 215.
9. A.M. Stumbo, P. Grange and B. Delmon, in G.F. Froment, B. Delmon and P. Grange (eds.), Elsevier, Amsterdam, 1997, pp. 225-233.
10. M. Estenfelder and H.G. Lintz, Appl. Catal. A, 202 (200) 223.
11. E. Baumgarten and L. Maschke, Appl. Catal. A, 202 (2000) 171.
12. E. Keren and A.Soffer, J. Catal., 50 (1997) 43.
13. G.M. Pajonk, Appl. Catal. A, 202 (2000) 157.
14. F. Roessner and U.Roland, J. Molec. Catal., 112 (1996) 401.
15. X. Chu and L.D. Schmidt, J. Catal., 144 (1993) 77.
16. Y.-W. Li, X.-Y. Pang and B. Delmon, J. Molec. Catal., *in press*
17. Y.-W. Li, X.-Y. Pang and B. Delmon, J. Phys. Chem., 104 (2000) 11375.
18. A.M. Stumbo, P. Grange and B. Delmon, Catal. Lett., 31 (1995) 173.
19. H. Kalies, N. Pinto, G.M. Pajonk and D. Bianchi, Appl. Catal. A, 202 (2000) 197.
20. G. Marnellos, S. Zisekas and M. Stoukides, J. Catal., 193 (2000) 80.
21. C. Song, ChemTech, March 1999, 26.
22. N. Satoh, J.i. Hayashi and H. Hattori, 202 (2000) 207.

# Oxygen transfer in the partial oxidation of propene on multi-component oxidic catalysts. A Solid Electrolyt Potentiometry aided study

H.-G. Lintz and M. Köhler

Institut für Chemische Verfahrenstechnik, Universität Karlsruhe, D-76128 Karlsruhe, Germany

Two single oxides – bismuth tungstate and iron cobalt molybdate – and a mixture of both have been investigated in situ through the determination of their oxygen activity with solid electrolyte potentiometry (SEP). The variation of the oxygen activity in the solid catalysts was followed as a function of the gas composition in the partial oxidation of propene to acrolein. At both single oxides the oxygen activity strongly decreases with the acrolein content, thus showing a higher reductive potential and therefore a lower stability of the partially oxidized intermediate than the original hydrocarbon. By contrast, an opposite evolution is observed using the mixture of the single oxides. In that case the values of the oxygen activity are lower at high propene concentrations than in the presence of acrolein, illustrating a higher stability of the latter and the selective efficiency of the mixed catalyst, and thus confirm the results of the kinetic investigation. The remarkable synergy may be explained by an oxygen transfer between the two single oxides.

## 1. INTRODUCTION

Multicomponent oxidic catalysts are commonly used in the partial oxidation of organic compounds [1]. The efficiency of such catalysts and the synergetic efects observed on mixtures of defined oxidic phases raise the question of their origin. Among the different explanations proposed the concept of the remote control is based on the spill-over of oxygen from one oxide (donor phase) to another (acceptor phase) [2].

The availability and transfer of oxygen is a function of the phase composition of the catalyst, ist oxidation state. To characterize the oxidation state of a solid, Carl Wagner [3] proposed the measurement of ist oxygen activity by a potentiometry (SEP), as it is based on the use of an oxygen ion conducting solid electrolyte. The method can be applied in situ under reaction conditions and thus allows the combined kinetic and potentiometric investigation of reactions on oxidic catalysts.

We have already made such measurements in the partial oxidation of acrolein on a multicomponent catalyst, maisdnly based on Mo, V and Cu [4,5]. The aim of the present investigation is the study of the partial oxidation of propene to acrolein on a catalyst consisting of bismuth tungstate and iron cobalt molybdate. In this system a strong synergy effect had been observed between both single oxides in the analogous partial oxidation of i-butene to methacrolein [6]. The combined kinetic and potentiometric study should therefore give insight in the nature of the interaction of different oxidic phases in such reactions.

## 2. EXPERIMENTAL

The preparation of the multicomponent catalyst and the two singular oxides is described elsewhere [7,8]. To study the oxygen activity of the catalyst as a function of the gas composition the concentration profiles in the gas phase developed along a tubular fixed bed reactor were used through axially distributed local sampling (Fig.1).
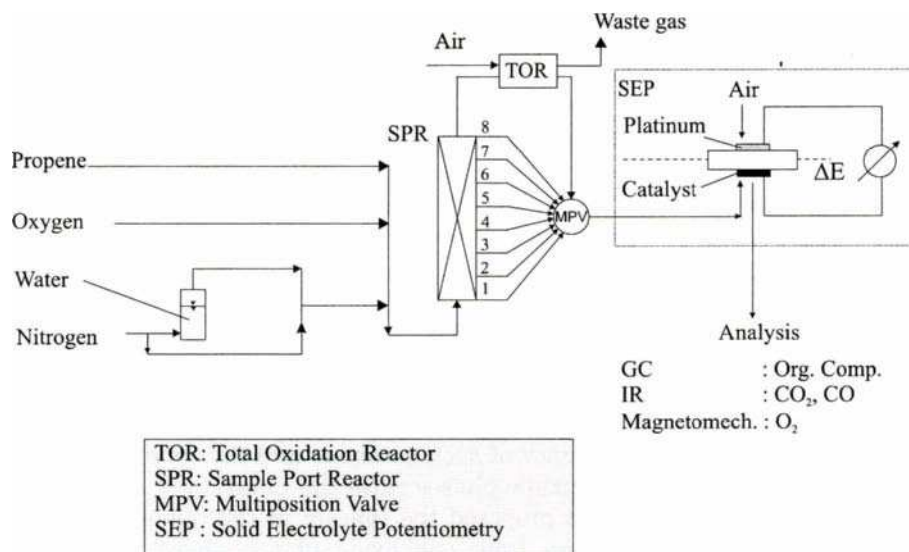


Fig. 1. Schematic diagram of the experimental setup.

The experimental set up can be divined into two parts, the fixed bed reactor for kinetic measurements and the development of the concentration profile and a second device for the solid electrolyte potentiometry.

The tubular reactor (length 1.5 m, diameter 15 mm) is filled with about 200g of sherical egg-shell catalyst containing the multicomponent oxide as active compound. It can be considered as an isothermally operated plug-flow reactor. In

steady state a well defined constant profile of the gas phase concentration is built up along ist axis. The local composition is analyzed by sampling at 8 different locations and is measured as a function of the modified residence time $t_{m,z}$ which is defined by the ratio of the mass of the catalytically active oxide $m_{C,z}$ between the reactor inlet and the sample port z and the volume flow $\dot{V}$ through the reactor:

$$t_{m,z} = \frac{m_{C,z}}{\dot{V}} \tag{1}$$

The composition of the carbon containing compounds at the port z is quantified by using a normalized concentration of the species i:

$$y_{i,z} = \frac{\dot{n}_{i,z} \cdot \varepsilon_i}{\dot{n}_{C\,Pr\,opene,in} \cdot \varepsilon_{C\,Pr\,opene,in}} \tag{2}$$

with    $\varepsilon_i$: Number of carbon atoms in molecule i

$\dot{n}_i$: Molar flow rate; $[\dot{n}_i] = mol \cdot s^{-1}$

In case of the reaction products $y_{i,z}$ represents the yield.

SEP is based on the use of an ion-conducting solid as the electrolyte consisting of yttria (8.5 − wt%) stabilized zirconia. Two porous electrodes of a galvanic cell are separated gas-tight by the solid electrolyte. The catalyst electrode is exposed to the reacting gas mixture; the second electrode is in contact with a given value of the oxygen partial pressure as reference. The measurement of the potential difference between these two electrodes $\Delta E$ results in the value of the oxygen activity in the catalyst, which is operationally defined by this method:

$$a_O^2 = p_{O_2}^{Ref.} \cdot exp\left(-\frac{4 \cdot F \cdot \Delta E}{R \cdot T}\right) \tag{3}$$

with        F:    Faraday constant; $F = 96486\ A \cdot s \cdot mol^{-1}$
            R:    Gas constant; $R = 8.3147\ J \cdot mol^{-1} \cdot K^{-1}$
            T:    Temperature; $[T] = K$
            $p_{O_2}^{Ref.}$:  Oxygen partial pressure at the reference side; $[p_{O_2}^{Ref.}] = bar$

The reactant mixture leaving the fixed bed reactor passes through a multicomposition valve over the catalyst electrode of the galvanic cell used in SEP measurements prior to analysis of the gas composition. Because of the small amount of catalyst on the electrode the propene conversion in the galvanic cell was kept below 10%. Thus the oxygen activity of the catalyst electrode is characteristic for the oxidation state of the catalyst in contact with a gas phase the composition of which is determined by ist value at the corresponding sampling port of the tubular reactor.

## 3. RESULTS AND DISCUSSION

Let us start with the case wheere the fixed bed and the catalytic electrode contain the same active compound. Then the combination of the tubular reactor and the galvanic cell allows the simultaneous determination of both the concentration and activity profiles along the reactor axis as the catalytic electrode "sees" the same gas phase composition as the egg-shell catalyst. Typical results are represented in Fig. 2. The normalized concentrations $Y_i$ (left ordinate), the oxygen partial pressure and the oxygen activity at the multicomponent catalyst (right ordinate) are plotted against the modified residence time $t_m$.

The values of the oxygen activity are always at least 12 orders of magnitude lower than the oxygen partial pressure of the corresponding gas phase over the catalyst. This clearly indicates a partially reduced state of the catalyst rather than an equilibrium between the oxygen in the catalyst and the surrounding gas phase since in the latter case the oxygen activity should equal the oxygen partial pressure.
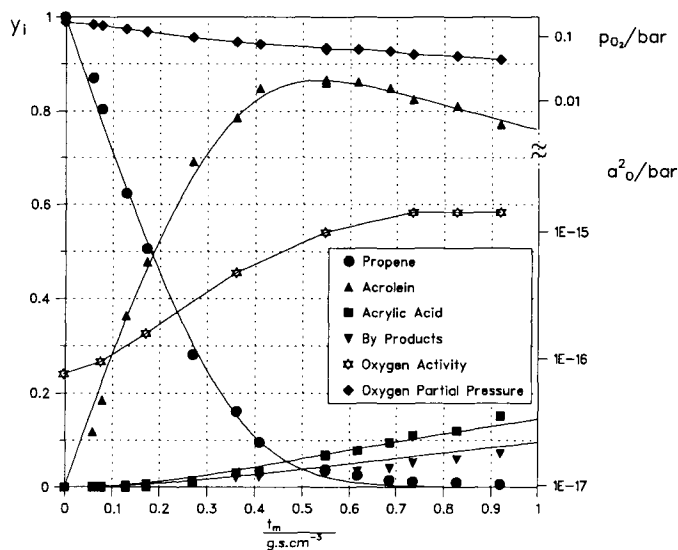


Fig. 2. Product distribution (left axis), oxygen activity of the mixture and oxygen partial pressure (right axis) as a function of the modified residence time at 360°C, 1.5 bar, $x_{Propene,in} = 0.06$, $x_{O_2,in} = 0.11$, $x_{H_2O,in} = 0.12$ in propane.

The evolution of the oxygen activity along the fixed bed reactor shows no discontinuity, indicating the absence of any sharp phase transition. The values start at $7.6 \cdot 10^{-17}$ bar under the initial propene concentration and reach a constant level of $1.4 \cdot 10^{-14}$ at a propene converion of 99%. This evolution may be

explained as follows: with increasing residence time propene is converted to acrolein, acrylic acid and by-products ($CO_2$, CO, acetic acid etc.). It has been verified that propene is a stronger reducing agent than acrolein and acrylic acid in the case of the multicomponent catalyst. Thus the oxygen activity increases steadily with decreasing propene concentration.

After complete propene conversion acrolein and acrylic acid are the main oxygen acceptors in the gas phase. The reduction potential of acrolein is stronger than that of acrylic acid. Therefore the influence of the still decreasing oxygen partial pressure is compensated by the further conversion of acrolein to acrylic acid and this leads to an apparently constant level of the oxygen activity for high values of the residence time ($T_m > 0.7$ g · s/cm$^3$).

It is easily seen from Fig. 2 that under operating conditions the oxygen activity at the catalyst, is not only determined by the oxygen partial pressure in the gas phase. It results from the rates of oxygen transfer to and from the solid. The higher the rate of oxygen transfer from the catalyst to an oxygen acceptor in the gas phase the lower is the resulting value of the oxygen activity at the solid. A high reuctive power of such an organic oxygen acceptor thus means a high reactivity at the catalyst surface. By contrast, the lower its reductive power the higher is the stability of the organic intermediate formed under analogous conditions, that is high selectivity of ist formation. Therefore the results of the potentiometric measurements – low value of the oxygen activity in propene containing mixtures and higher values under acrolein – are consistant with the high selectivity of the acrolein formation observed in the kinetic investigation.

But what about the roll of the two single oxides in the multicomponent catalyst? The study of the partial oxidation of i-butene had shown [6] that both the activity in the oxidation of the olefin and the selective formation of the unsaturated aldehyde are rather low in the case of bismuth tungstate or of iron cobalt molybdate alone. Mixtures of both compounds, however, led to a high synergy effect. Analogous, unpublished, results were obtained in the propene oxidation on the same catalysts. The results hab been explained by oxygen transfer from one oxide to the other but the respective rolls of both phases couldn't be determined by the kinetic measurements alone.

In the present study both single oxides wege equally investigated by SEP and the oxygen activity was determined as a function of the gas phase composition. In such measurements the same concentration profiles were adjusted in the tubular reactor as before but the catalyst electrodes in the galvanic cell consited of the single oxides. Thus the modified residence time remains a measure of the gas phase composition. In Fig. 3 the results are therefore plotted against $t_m$, comparing the oxygen activities obtained under identical conditions.

At both single oxides the oxygen activity strongly degreases with the acrolein content, thus showing a higher reductive potential and therefore a lower stability of the partially oxidized intermediate than of the original hydrocarbon. Once more the results are consistent with the kinetic data.

Independenly of the gas phase composition, iron cobalt molybdate always shows higher values of the oxygen activity than bismuth tungstate.

The synergy between the two single oxides may be explained by an oxygen transfer. The activity gradient is the driving force in the transfer of oxygen from the richer oxide to the poorer one. Thus iron cobalt molybdate may be considered as an oxygen donor in the reaction studied (Fig. 4). The same conclusions had been published in the case of iron cobalt molybdate/bismuth molybdate catalysts [9,10].
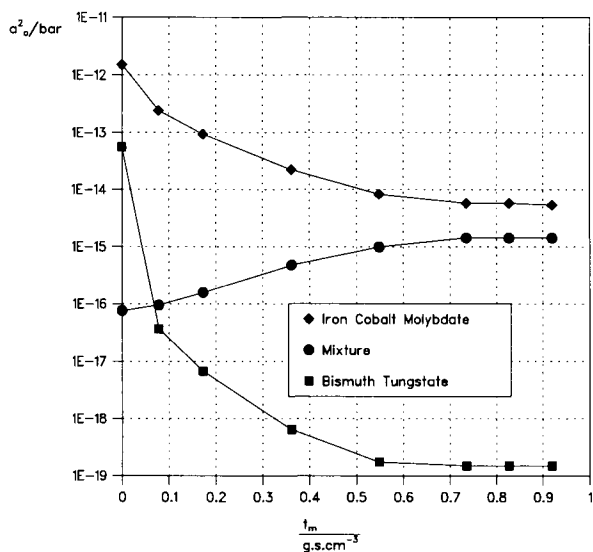


Fig. 3. The course of the oxygen activity in different oxidic catalysts for gas phase composition fixed by the concentration profiles given in Fig. 2 at 360°C, 1.5 bar, $x_{Propene,in} = 0.06$, $x_{O_2,in} = 0.11$, $x_{H_2O,in} = 0.12$ in propane.
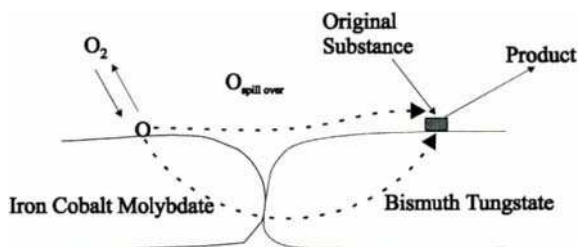


Fig. 4. Oxygen transfer in a mixture of bismuth tungstate and iron cobalt molybdate in the partial oxidation of propene

Due to the potential difference at the single oxides a mixed potential should be obtained at the multicomponent ctalyst containing both compounds. As in the case of the acrolein oxidation catalyst [4] we may expect that this mixed potential and thus the derived oxygen activity lie in between the values characteristic of the single oxides. Fig. 3 illustrates that this is generally true but for the results measured in the initial gas mixture containing merely propene as oxygen acceptor. In fact, the results represented in Fig. 3 are steady state values and by contrast to the former work [4], the multicomponent catalyst shows a pronounced induction period of up to 50 h if one uses the as prepared catalyst (Fig. 5) in contact with the same gas phase composition as schown before.
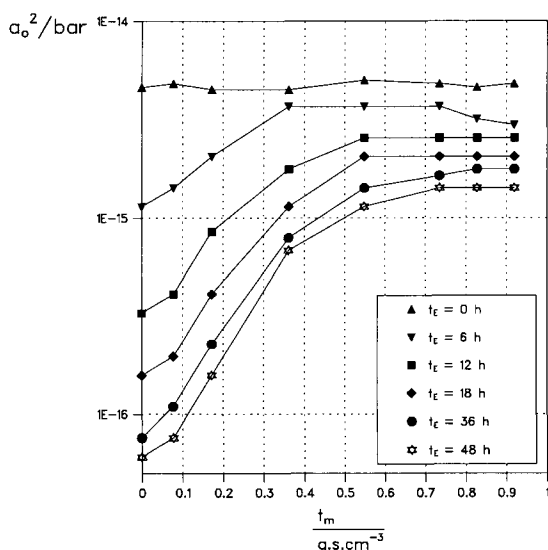


Fig. 5. Oxygen activity induction period of the mixture at 360°C, 1.5 bar, $x_{Propene,in}$ = 006, $x_{O_2,in}$ = 0.11, $x_{H_2O,in}$ = 0.12 in propane

During the induction period the variation of the oxygen activity as a function of the gas phase composition is completely altered illustrating the strong interaction between reactant concentrations and catalyst composition.

Thus one may speculate on the mechanism of the oxygen transfer and the real nature of the mixed catalyst. In fact, one has to remind that SEP remains a global method and doesn't quantify an oxygen content of the solid nor a surface coverage even if it seems that there is a characteristic relation between the oxygen activity and the total oxygen consumption in the reactive system [5,8]. However, the mixed potential is dependent on both the gas phase composition and the geometry of the device. As the former is kept constant in the present

case, the variations represented on Fig. 5 should indicate a local evolution of the catalyst.

It is interesting to note that during the induction period the catalytic activity of the multicomponent oxide remains constant whereas the selectivity to acrolein is increasing and the formation of $CO_x$ simultaneously cut in half. This is consistent with the hypothesis that during that period the oxygen transfer between both single phases is intensified without a variation of the relative proprtions of their surfaces.

The results of the combined kinetic and potentiometric investigation are therefore consistent with the hypothesis that the observed synergy in the multicomponent oxide is due to the transfer of oxygen from the molybdate to the tungstate, even if we cannot totally exclude the wetting of one oxidic phase by the other [1] as an alternative explanation.

## 4. CONCLUSIONS

Considering the observed influences of catalyst preparation and the working conditions together with the analogy with the partial oxidation of i-butene studied in detail on the same catalyst [6], we still believe in the spill-over of oxygen as the reason behind the remarkable synergy reported. The SEP measurements clearly identify the iron cobalt molybdate as the donor phase and the bismuth tungstate as the acceptor phase for the transferred oxyde, the oxygen activity gradient between both phases being the driving force of this transfer.

## REFERENCES

1. J. Haber, Stud. Surf. Sci. Catal. 72 (1992) 271
   B. Grzybowska-Swierkosz, Topics in Catal. 11/12 (2000) 23
2. B. Delmon and L.T. Wenig, Appl. Catal. A 81 (1992) 141
3. C. Wagner, Adv. Catal. 21 (1970) 323
4. M. Estenfelder and H.-G. Lintz, Appl. Catal. A 202 (2000) 223
5. M. Estenfelder and H.-G. Lintz, J. Catal. 195 (2000) 38
6. S. Breiter and H.-G. Lintz, Chem. Eng. Sci. 50 (1995) 785
7. BASF, European Patent 0 575 897 (1993)
8. M. Köhler, Thesis, Karlsruhe 2001
9. Y. Moro-Oka, D.H. He and W. Veda, Stud. Surf. Sci. Catal. 67 (1991) 57

10. J.M.M. Millet, H. Ponceblanc, G. Goudurier, J.M. Herrmann and J.C. Védrine, J. Catal. 142 (1993) 381

# Oxygen storage and oxygen mobility on ceria and ceria-zirconia supported noble metals

S. Bedrane, C. Descorme* and D. Duprez

Laboratoire de Catalyse en Chimie Organique (LACCO) – UMR CNRS 6503 – Poitiers University – 40, avenue du Recteur Pineau – 86022 POITIERS CEDEX

Four $CeO_2$ and $Ce_{0.63}Zr_{0.37}O_2$-supported rhodium and iridium catalysts were fully characterized by XRD, $N_2$ adsorption at 77K, TEM and $H_2$ chemisorption. Both the oxygen storage capacity (OSC) and the activity in the $^{18}O/^{16}O$ isotopic homoexchange reaction were measured on fresh and aged-catalysts. Interestingly, Ir was found to be responsible for the largest OSC enhancement. For all catalysts, large metal particles were shown to be more reactive. Looking at oxygen activation on metal particles, Ir and Rh appear to behave differently. Ir catalysts activity in the homoexchange reaction was found to be independent on the underlying support. On the opposite, a comparison between OSC and isotopic homoexchange results evidenced a strong metal/support interaction in the case of Rh catalysts.

## 1. INTRODUCTION

In the past decades, many studies have been performed in the field of environmental catalysis. Evolution towards stricter regulations on automotive pollution control implied an optimization of Three-Way Catalysts (TWC) which operate under transient conditions. One key parameter is the oxygen storage. Cerium-zirconium solid solutions were shown to be good candidates with enlarged Oxygen-Storage Capacity (OSC) and improved redox properties [1-6]. However, only a few studies have been devoted to understand oxygen storage processes . This paper deals with the study of $CeO_2$ and $Ce_xZr_{1-x}O_2$-supported Rh and Ir catalysts. The influence of both the metal particle morphology and the oxide structure on oxygen migration processes are investigated on the basis of OSC measurements and Isotopic Exchange experiments.

## 2. EXPERIMENTAL

Cerium-based oxides ($CeO_2$ and $Ce_{0.63}Zr_{0.37}O_2$) were directly supplied by Rhodia Rare Earths (La Rochelle, France) after pre-calcination at 900 °C for 6 hours. Catalysts were prepared by incipient wetness impregnation using metal precursor solutions ($Rh(NO_3)_3$ in water and $Ir[CH(COCH_3)_2]_3$ in toluene). Samples were dried at 120°C for 24 h and finally

---

* Corresponding author : claude.descorme@univ-poitiers.fr , Tel: +335 49 45 39 97, Fax: +335 49 45 34 99.

pretreated under flowing air or hydrogen (30 $cm^3.min^{-1}$) at 500 °C (ramp rate : 0.5 °C.min$^{-1}$) for 4 h. Metal loading was either 1 wt-% Rh or 2 wt-% Ir to have the same percentage of metal atoms for all catalysts - around 100 micromoles of metal atoms per gram of catalyst. Furthermore, to analyze the influence of metal particle size, all catalysts were aged at different temperatures and under various conditions.

The oxides structure was characterized by XRD using a Siemens D5005 diffractometer. Crystalline phases were identified by comparison of experimental diffractograms with ICDD files. The average crystallite size was estimated from the Scherrer relation. Surface areas were measured by $N_2$ adsorption at −196 °C (single point method) using a Micromeritics Flowsorb II apparatus.

Metal dispersion was calculated from $H_2$ chemisorption experiments. These measurements were carried out under optimized conditions to prevent hydrogen spillover onto the support [7]. Transmission Electron Microscopy (TEM) direct observations and Energy Dispersive X-Rays (EDX) analysis were carried out on a CM 120 Philips microscope.

Oxygen storage capacity (OSC) measurements, according to the method developed by Yao et al. [8], were carried out on an home-made system described earlier [9,10]. To investigate oxygen activation, $^{16}O/^{18}O$ isotopic exchange experiments were also carried out on an home-made apparatus [11-13]. Masses m/e=32, 34 and 36, characteristic of the three different oxygen isotopomers ($^{16}O_2$, $^{16}O^{18}O$, $^{18}O_2$), are monitored continuously. The evolution of the partial pressure of $^{16}O_2$, $^{16}O^{18}O$, $^{18}O_2$ may be followed as a function of time and temperature. The homoexchange reaction rate is calculated from the initial slope of the curve $P(^{16}O^{18}O)$ vs. time.

## 3. RESULTS AND DISCUSSIONS

### 3.1. Structural characterizations

The main structural characteristics of the materials under study are summarized in Table 1. Oxide particles size was estimated from the XRD pattern and the dispersion of the metal was calculated based on $H_2$ chemisorption measurements.

From XRD characterizations, $CeO_2$ was confirmed to be cubic with a fluorite-type structure. Lattice parameter a for $CeO_2$ was calculated to be 5.4113 Å. Furthermore, a contraction of the unit cell is evidenced upon substitution of Ce cations by Zr cations. As a result, lattice parameter a for $Ce_{0.63}Zr_{0.37}O_2$ mixed oxide decreases down to 5.3044 Å. Additionally, $Ce_{0.63}Zr_{0.37}O_2$ is shown to be a purely monophasic solid solution.

Table 1
Main characteristics of bare oxides and supported Rh and Ir catalysts.

| | Oxides | | Rh dispersion (%) | | Ir dispersion (%) | |
|---|---|---|---|---|---|---|
| | $S_{BET}$ ($m^2.g^{-1}$) | Particle size (Å) | Fresh | Aged | Fresh | Aged |
| $CeO_2$ | 24 | 195 | 88 | 5 | 38 | 3 |
| $Ce_{0.63}Zr_{0.37}O_2$ | 39 | 66 | 62 | 14 | 29 | 2 |

Looking at surface areas, one may conclude that $Ce_{0.63}Zr_{0.37}O_2$ exhibits a high thermal stability. In fact, the surface area of $Ce_{0.63}Zr_{0.37}O_2$, after calcination at 900°C (as supplied), was measured to be about twice the one of pure ceria.

Finally, the metal dispersion was accessed from both $H_2$ chemisorption measurements and TEM observations. For Ir catalysts, a stoichiometry of 3 H atoms chemisorbed per surface iridium atom was considered [14]. On fresh samples, the metallic phase was shown to be well-dispersed with an average particle size of about 10 Å for fresh Rh-catalysts and around 30 Å for fresh Ir-catalysts. After severe aging under appropriate conditions, catalysts dispersion decreases drastically. In fact, only the results obtained on fresh and highly sintered catalysts will be presented in this paper. Aging conditions were adjusted, depending on the metal and the support, in order to obtain a strong decrease of the metal dispersion. $Rh/CeO_2$ was aged under $H_2$ at 800°C for 4 hours and the metal dispersion decreases down to 5%. For $Rh/Ce_{0.63}Zr_{0.37}O_2$ aging was carried out under dry air at 900°C for 4 hours. In that case, the dispersion also decreases to 14%. Nevertheless, a comparison between the two Rh-catalysts - considering both initial and final dispersions - seems to show that Rh would be more stable on $Ce_{0.63}Zr_{0.37}O_2$ than on $CeO_2$ even under more severe temperature conditions. On the other hand, Ir-based catalysts were aged under air at 700°C for 4 hours. In both cases, the metal dispersion falls down to a few percents. Looking at initial Ir dispersions and aging conditions, one may conclude that the interaction between iridium and ceria-based supports is weak.

## 3.2. Oxygen Storage Capacity

From earlier OSC measurements carried out at 400°C, it was concluded that OSC is strongly enhanced by both the introduction of zirconium in the ceria framework and the presence of noble metal particles at the oxides surface [10, 15]. In fact, it was shown that the OSC at 400°C is multiplied by a factor of 4 between $CeO_2$ and $Ce_{0.63}Zr_{0.37}O_2$. Furthermore OSC at 400°C is respectively multiplied by a factor of 6 and 5 in the presence of rhodium particles at the surface of ceria and ceria-zirconia.

Moreover, the influence of temperature on the OSC was evaluated for the four catalysts ($Rh/CeO_2$, $Rh/Ce_{0.63}Zr_{0.37}O_2$, $Ir/CeO_2$ and $Ir/Ce_{0.63}Zr_{0.37}O_2$). In fact, such a study had already been carried out on bare oxides. It was demonstrated that oxygen storage is almost restricted to the surface for ceria while bulk oxygen atoms do participate to oxygen storage in the case of the mixed oxide [7]. In the case of ceria, OSC reaches a maximum corresponding to the number of reducible surface atoms. On the opposite, for ceria-zirconia mixed oxides, the participation of bulk oxygen atoms is characterized by an exponential increase of the OSC with temperature. Nevertheless, this kind of study had never been extended to metal supported catalysts. The first results are presented on Figure 1. These results evidenced that OSC is larger for Ir-based catalysts than for Rh catalysts in the whole temperature range from 200 to 500°C. Additionally, OSC for ceria-supported catalysts was shown to vary slightly with temperature and to reach a maximum after full reduction of the surface. In this case, OSC appears to be limited by surface diffusion. On the opposite, for ceria-zirconia supported catalysts, OSC is multiplied by a factor of 3 to 4 - depending on the metal - between 200 and 500°C. Bulk reduction is then responsible for such a large increase of the OSC. In that case, oxygen storage would be limited by bulk diffusion.
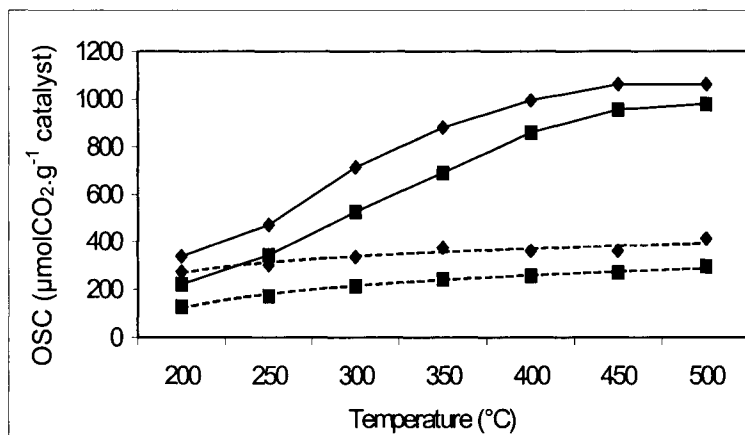
Figure 1 - Evolution of the oxygen storage capacity (OSC) as a function of temperature. Effect of the metal (♦: Ir catalysts and ■: Rh catalysts) and the support ($CeO_2$ : dotted lines and $Ce_{0.63}Zr_{0.37}O_2$ : full lines).

The different contributions to the OSC (metal, surface, bulk) and the number of oxygen layers involved in oxygen storage (NL) are summarized in Table 2. These figures confirm that oxygen storage is restricted to the surface for ceria-supported catalysts while it involves bulk oxygen atoms in the case of $Ce_{0.63}Zr_{0.37}O_2$-based catalysts.

Table 2
Experimental and theoretical OSC.

|  | $OSC_{metal}$[1] | $OSC_{surface}$[1] | $OSC_{max.}$[1,2] | $OSC_{exp.}$[3] | NL[4] |
|---|---|---|---|---|---|
| $Rh/CeO_2$ | 115 | 143 | 3000 | 296 | 1.1 |
| $Rh/Ce_{0.63}Zr_{0.37}O_2$ | 128 | 159 | 2160 | 980 | 3.4 |
| $Ir/CeO_2$ | 266 | 143 | 3100 | 413 | 1.0 |
| $Ir/Ce_{0.63}Zr_{0.37}O_2$ | 308 | 159 | 2300 | 1062 | 2.3 |

[1] expressed in micromole of oxygen atoms per gram of catalyst ($\mu molOat.g^{-1}$catalyst)
[2] corresponds to the participation from both the metal particles and the oxide bulk [10]
[3] expressed in micromole of $CO_2$ molecules per gram of catalyst ($\mu molCO_2.g^{-1}$catalyst)
[4] number of oxygen layer involved in the oxygen storage process

In the presence of noble metal particles, oxygen storage is now limited by the oxygen diffusion either at the surface or in the bulk of the oxide. In fact, due to the metal, oxygen activation is fast. In this case, metal particles act as portholes for the subsequent migration and storage of oxygen on the support. As a result OSC should depend not only on the oxide but

also on the quality of the interface between the metal and the support. The influence of both parameters will be checked.

As shown just before, the role of the metal particles is crucial for the oxygen storage process. To check the influence of metal particle size, the OSC of aged catalysts was measured under the same conditions as for fresh catalysts (Figure 1). Figures 2 and 3 clearly exemplify the decrease of the OSC (expressed per gram of catalyst) upon aging. For all catalysts, OSC appears to be reduced by a constant amount in almost the whole range of temperature. This observation could indicate that some "active" sites have been irreversibly lost upon aging.

Again, Rh-catalysts - which undergo the highest metal sintering upon high temperature aging - are the most sensitive if one consider the OSC decrease. It is known from Table 1 that the metal dispersion drastically decreases upon aging, nevertheless we could check that the OSC does not vary linearly with the metal dispersion.

Furthermore, the general trends of the evolution of the OSC as a function of temperature discussed for fresh catalysts do not appear to be modified in the case of aged catalysts. Surface diffusion is rate limiting in the case of ceria-supported catalysts while bulk diffusion governs the whole oxygen storage process for ceria-zirconia supported catalysts. Generally speaking, activation energies would be almost the same but the number and/or the accessibility of "active" sites would be lower.
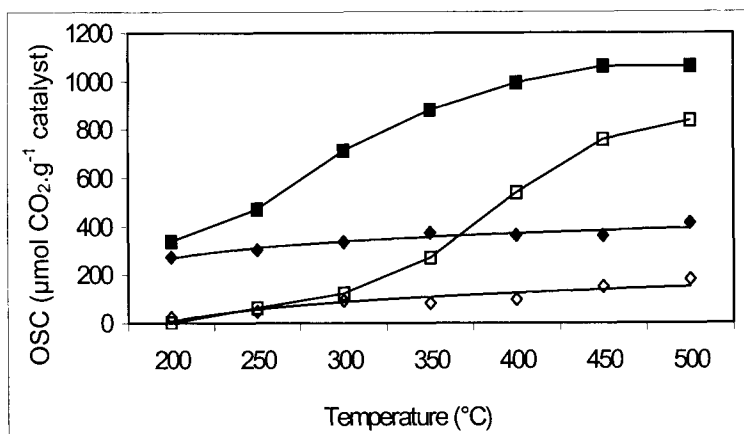


Figure 2 – Influence of aging on the oxygen storage capacity (OSC) of $Ir/CeO_2$ (♦) and $Ir/Ce_{0.63}Zr_{0.37}O_2$ (■) catalysts (fresh catalysts : closed symbols and aged catalysts: open symbols). OSC is expressed in micromole of $CO_2$ produced per gram of catalyst.
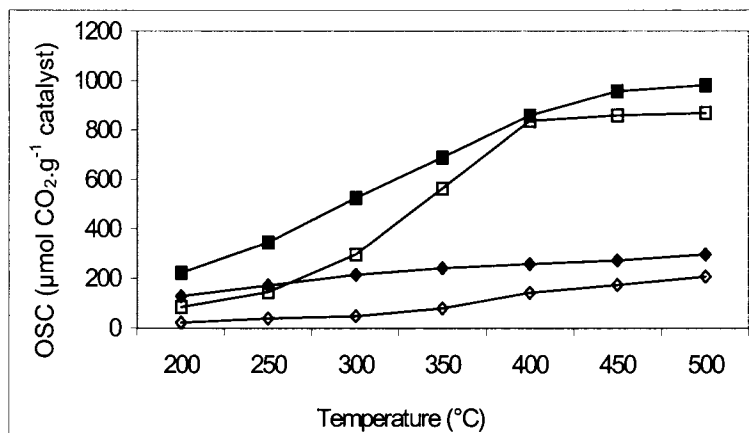
Figure 3 – Influence of aging on the oxygen storage capacity (OSC) of $Rh/CeO_2$ ($\blacklozenge$) and Rh/$Ce_{0.63}Zr_{0.37}O_2$ ($\blacksquare$) catalysts (fresh catalysts : closed symbols and aged catalysts: open symbols).

To go even further, OSC were also expressed as a function of the metal surface area derived from $H_2$ chemisorption experiments (Table 3).

Table 3
Influence of aging on OSC expressed per gram of catalyst and per $m^2$ of metal.

| | OSC at 500 °C ($\mu$mol $CO_2$.$g^{-1}$ catalyst)[1] | | OSC at 500 °C ($\mu$mol $CO_2$.$m^{-2}$ metal)[1] | |
|---|---|---|---|---|
| | Fresh | Aged | Fresh | Aged |
| $Rh/CeO_2$ | 296 | 208 | 96 | 1190 |
| $Rh/Ce_{0.63}Zr_{0.37}O_2$ | 980 | 867 | 405 | 1590 |
| $Ir/CeO_2$ | 413 | 180 | 175 | 970 |
| $Ir/Ce_{0.63}Zr_{0.37}O_2$ | 1062 | 837 | 511 | 5840 |

[1] amount of $CO_2$ produced after the first CO pulse under alternating CO and $O_2$ pulses.

This table shows that the amount of $CO_2$ produced by $m^2$ of metal is much larger for aged catalysts than in the case of fresh catalysts. In fact, the OSC at 500 °C for the aged-$Rh/CeO_2$ catalyst is 12 times larger than the OSC of the fresh catalyst. Such an enhancement of the OSC upon sintering of the metallic phase would indicate either that large particles are more active as portholes for the subsequent migration of the oxygen or that the metal/oxide

interface has been modified in such a way that the oxygen transfer from the metal particle to the support is more efficient.

### 3.3. $^{18}O/^{16}O$ Isotopic Homoexchange

Metal particles play a major role in the oxygen storage process. In fact, it was shown earlier that metal particles could act as portholes for the subsequent migration and storage of oxygen species on the support. $^{18}O/^{16}O$ isotopic homoexchange was used to study oxygen activation on metal particles. The reactivity of each catalysts was tested to estimate the efficiency of the metallic phase in the oxygen activation process. The influence of particle size and the effect of the support on the performances of the metal for oxygen activation was checked. The reaction rate (Re), expressed in atoms of oxygen exchanged per $nm^2$ of metal and per second, can be calculated from the rate of formation of $^{18}O^{16}O$ [16].

The results obtained for fresh catalysts are reported in Figure 4. Above 300°C, $Rh/CeO_2$ is more active than $Rh/Ce_{0.63}Zr_{0.37}O_2$, $Ir/Ce_{0.63}Zr_{0.37}O_2$ and $Ir/CeO_2$ respectively. Both Ir-catalysts exhibit the same activity. As expected, no effect of the support could be evidenced. On the opposite, it appears that $Rh/Ce_{0.63}Zr_{0.37}O_2$ is more active than $Rh/CeO_2$ below 300 °C and vice versa. This difference could be attributed either to a support effect or to the influence of particles size. In the case of Rh-catalysts, Descorme et al. [16] reported only a small effect of the support. In fact, these authors showed that the equilibration rate varied slightly depending on the oxide used as a support (alumina, silica, ceria, zirconia,...).
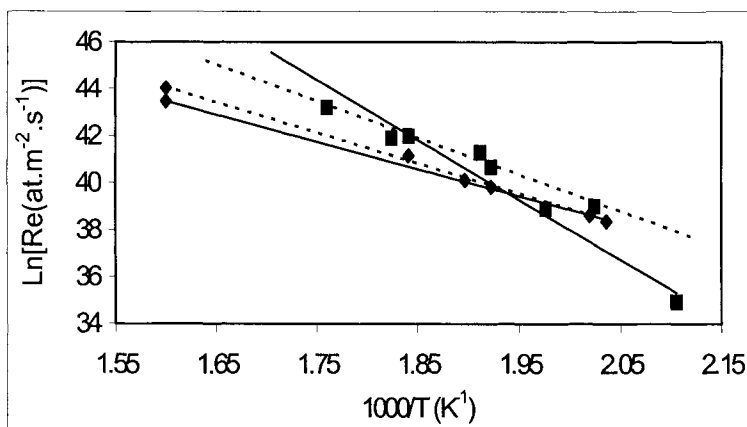


Figure 4 : Evolution as a function of temperature of the homoexchange reaction rate on Ir ($\blacklozenge$) and Rh catalysts ($\blacksquare$) - ($CeO_2$ : full lines and $Ce_{0.63}Zr_{0.37}O_2$ : dotted lines). Re is expressed in atom of oxygen exchanged per second and per $m^2$ of metal.

To check the influence of metal particle size, the reactivity of both fresh and sintered catalysts was compared. Figures 5 and 6 clearly evidence the two different behaviors between Ir and Rh catalysts. Above 250°C, aged Ir-catalysts are more active than fresh Ir-catalysts (Figure 5). On the opposite, both Rh catalysts deactivate upon aging (Figure 6).

Figure 5 : Evolution as a function of temperature of the homoexchange reaction rate (Re) on Ir/CeO$_2$ (■) and Ir/Ce$_{0.63}$Zr$_{0.37}$O$_2$ (♦) catalysts (fresh catalysts: closed symbols and aged catalysts: open symbols). Re is expressed in atom of oxygen exchanged per second and per m$^2$ of metal.
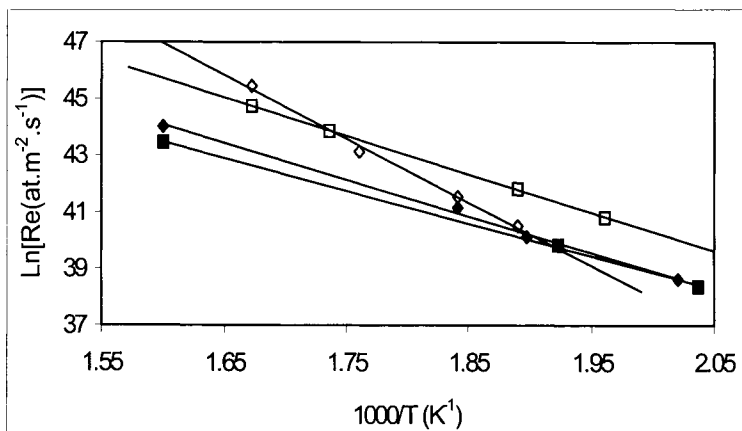


Figure 6 : Evolution as a function of temperature of the homoexchange reaction rate (Re) on Rh/CeO$_2$ (■) and Rh/Ce$_{0.63}$Zr$_{0.37}$O$_2$ (♦) catalysts (fresh catalysts: closed symbols and aged catalysts: open symbols). Re is expressed in atom of oxygen exchanged per second and per m$^2$ of metal.
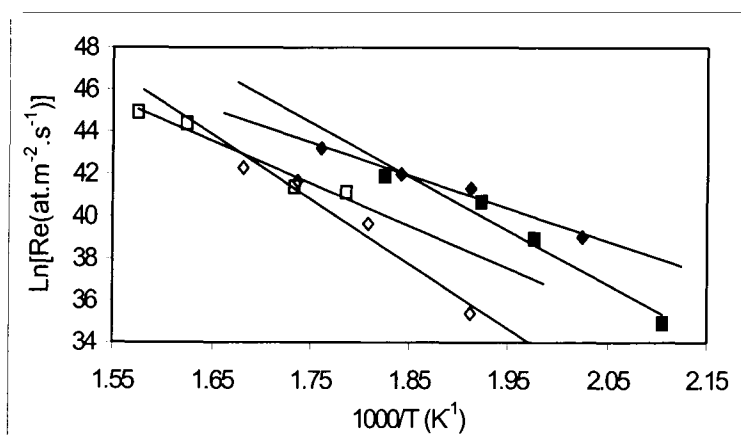
To compare the influence of all these parameters, equilibration rates measured at 300°C are reported in Table 5. Equilibration rates were expressed in oxygen atom exchanged per second and per $m^2$ of metal.

Table 5
Equilibration rate of fresh and aged Rh and Ir catalysts at 300°C.

| | Re (O at.m$^{-2}_{metal}$.s$^{-1}$) | |
|---|---|---|
| | Fresh | Aged |
| Rh/CeO$_2$ | $2.18 \times 10^{19}$ | $1.20 \times 10^{18}$ |
| Rh/Ce$_{0.63}$Zr$_{0.37}$O$_2$ | $8.29 \times 10^{18}$ | $5.97 \times 10^{17}$ |
| Ir/CeO$_2$ | $1.42 \times 10^{18}$ | $1.01 \times 10^{19}$ |
| Ir/Ce$_{0.63}$Zr$_{0.37}$O$_2$ | $2.13 \times 10^{18}$ | $9.45 \times 10^{18}$ |

Looking at Rh catalysts, one can immediately see a large decrease of the reactivity upon aging. Homoexchange reaction rates are respectively divided by a factor of 18 and 14 for Rh/CeO$_2$ and Rh/Ce$_{0.63}$Zr$_{0.37}$O$_2$ after aging. In agreement with earlier studies [17], this result evidence the influence of Rh particle size on oxygen activation. In fact, it had been shown that the homoexchange reaction rate on Rh/Al$_2$O$_3$ catalysts at 300°C is divided by a factor of 3 when the dispersion decreases from 87 to 8%. Oxygen homoexchange is faster on small Rh particles.

Nevertheless, the influence of Rh particle size is not the only influencing parameter. Whatever the catalyst state - fresh or aged - Rh activity is also influenced by the support (Figure 6). In fact, comparing equally dispersed metal supported catalysts, R. Taha [17] measured an homoexchange reaction rate of $6 \times 10^{18}$ at.m$^{-2}_{metal}$.s$^{-1}$ on Rh/Al$_2$O$_3$ (D=87%) while we measured (in this study) a rate of $2.18 \times 10^{19}$ at.m$^{-2}_{metal}$.s$^{-1}$ on Rh/CeO$_2$ (D=88%). Additionally, deactivation upon aging also appears to depend on the support. In fact, deactivation is much more important in the case of ceria-supported catalysts than for ceria-zirconia and alumina supported catalysts. As a conclusion, homoexchange must be considered as support-sensitive. Any modification of the metal/oxide interface greatly influences the oxygen activation on the catalyst.

On the opposite, in the case of iridium catalysts, effect of the support appears to be negligible ($1.42 \times 10^{18}$ at.m$^{-2}_{metal}$.s$^{-1}$ on Ir/CeO$_2$ vs. $2.13 \times 10^{18}$ at.m$^{-2}_{metal}$.s$^{-1}$ on Ir/Ce$_{0.63}$Zr$_{0.37}$O$_2$). Oxygen activation on Ir particles is not influenced by the support. Ir interaction with the support is weak and the metal properties are not influenced by the underlying oxide. Looking at particle size effect, homoexchange is faster on large Ir particles ($1.01 \times 10^{19}$ at.m$^{-2}_{metal}$.s$^{-1}$ for Ir/CeO$_2$ aged catalyst vs. $1.42 \times 10^{18}$ at.m$^{-2}_{metal}$.s$^{-1}$ for the fresh one). This type of behavior had already been reported in the case of Pt/Al$_2$O$_3$ catalysts [18]. The weakness of the interaction between Ir and the support is also exemplified by the low Ir dispersion on fresh catalysts compared to Rh-catalysts.

134

## 4. CONCLUSIONS

Supported rhodium and iridium catalysts were shown to be very efficient for oxygen activation and storage. Total OSC is respectively multiplied by a factor of 6 and 9 in the presence of Rh and Ir particles on the support. OSC, expressed per gram of catalyst, decreases upon aging for all samples. Nevertheless, large metal particles were shown to be more active.

Looking at oxygen activation on metal particles, two different behaviors were evidenced. $^{18}O/^{16}O$ homoexchange is faster on small Rh particles while large Ir particles are more reactive. It was further proposed that metal particles act as portholes for the subsequent migration and storage of oxygen on the support. Indeed, in the case of Ir catalysts, large Ir particles are more efficient to activate oxygen and OSC for sintered catalysts is larger. However, in the case of Rh catalysts, oxygen activation is faster on small particles while oxygen storage is promoted on large particles. In that case, the morphology of rhodium particles is not the only influencing parameter. In fact, a strong metal/support interaction would be responsible for the modifications of oxygen storage on rhodium catalysts.

**Acknowledgment**

**REFERENCES**

1    P. Fornasiero, G. Balducci, J. Kaspar, M. Graziani, Catal. Today, 29 (1996) 47
2    P. Fornasiero, G. Balducci, R. Di Monte, J. Kaspar, V. Sergo, G. Gubitosa, A. Ferrero, M. Graziani, J. Catal., 164 (1996) 173
3    A. Trovarelli, F. Zamar, J. Catal., 169 (1997) 490
4    G. Vlaic, P. Fornasiero, S. Geremia, J. Kaspar, J. Catal., 168 (1997) 380
5    D. Terribile, A. Trovarelli, J. Llorca, Catal. Today, 43 (1998) 79
6    G. Vlaic, R. Di Monte, P. Fornasiero, E. Fonda, J. Kaspar, M. Graziani, Stud. Surf. Sci. Catal., 116 (1998) 185
7    Y. Madier, Ph-D Thesis, Poitiers University (1999)
8    S. Kacimi, J. Barbier Jr., R. Taha, D. Duprez, Catal. Lett., 22 (1993) 343
9    Y. Madier, C. Descorme, A.M. Le Govic, D. Duprez, J. Phys. Chem. B, 103 (1999) 10999
10   H.C. Yao, Y.F. Yu Yao, J. Catal., 86 (1984) 254
11   D. Duprez, Stud. Surf. Sci. Catal., 112 (1997) 13
12   D. Martin, D. Duprez, J. Phys. Chem., 100 (1996) 9429
13   A. Holmgren, D. Duprez, B. Andersson, J. Catal., 182 (1999) 441
14   S. Bedrane, C. Descorme, D. Duprez, submitted for publication in J. Catal.
15   P. Fornasiero, J. Kaspar, V. Sergo and M. Graziani, J. Catal., 182 (1999) 56
16   C. Descorme, D. Duprez, Appl. Catal. A, 202 (2000) 231
17   R. Taha, Ph-D Thesis, Poitiers University (1994)
18   R. Taha, D. Duprez, J. Chim. Phys., 92 (1995) 1506

# Surface mobility and redox properties: Study of Pt/CeO$_2$-ZrO$_2$ catalysts

Toshitaka Tanabe[a]#, Akihiko Suda[a], Claude Descorme[b], Daniel Duprez[b], Hirofumi Shinjoh[a] and Masahiro Sugiura[a]

[a]*Applied Catalysis Div. Toyota Central R&D Labs., Inc. 480-1192, Nagakute Aichi, JAPAN*
*#To whom correspondence should be addressed, e-mail : t-tanabe@mosk.tytlabs.co.jp,*
*Tel : +81-561-63-5283, Fax : +81-561-63-6150*

[b] *LACCO, UMR CNRS 6503, Poitiers University, 40 avenue du Recteur Pineau, 86022 Poitiers, FRANCE*

Structural characterizations and dynamic OSC measurements were performed on three Pt/CeO$_2$-ZrO$_2$ (Pt/CZ). The catalyst supports were prepared by 1) precipitation-oxidation (CZ-O), 2) high energy ball milling (CZ-D), 3) precipitation and high temperature reduction (CZ-R). XRD and TEM-EDX results revealed that the homogeneity of Zr introduction into CeO$_2$ framework is in the order of CZ-R > CZ-D > CZ-O. Among all the catalysts, Pt/CZ-R showed both the highest OSCC under cyclic transient reaction conditions and the highest reactivity in the isotopic exchange reaction. An atomically homogeneous introduction of Zr ions into CeO$_2$ framework enhance the reactivity and the mobility of oxygen in CZ oxides. Some kinetic data concerning oxygen storage and the thermal stability of Pt/CZ at high temperature are also discussed.

## 1. INTRODUCTION

Ceria is one of the most important materials in automotive three way catalyst (TWC). One of the main role of ceria is to store and release oxygen under transient conditions to insure a stoichiometric atmosphere in the automotive catalyst. This oxygen buffering capacity improves the catalytic activity of the automotive catalyst. The amount of oxygen that an oxide may store and release is the so called Oxygen Storage Capacity

(OSC, OSCC) [1]. Oxygen storage was shown to be closely related to oxygen mobility in the catalysts. Improvement of OSC of ceria is one of the key technology to develop high efficiency TWC. In modern automotive catalyst, $CeO_2$-$ZrO_2$ mixed oxides are nowadays used as a promoter in stead of ceria. Addition of $ZrO_2$ to $CeO_2$ improves the oxygen storage capacity of ceria as well as its thermal stability [2]. The fast part of oxygen storage capacity (OSC) is known to be important for catalytic reaction under fluctuating operating conditions. To evaluate the fast part of oxygen storage capacity, determining OSC kinetics is important. This study presents the redox behavior of the three different Pt/CZ catalysts and the some kinetic data concerning oxygen storage.

## 2. EXPERIMENTAL

Three different types of $CeO_2$-$ZrO_2$ (Ce:Zr=1:1 molar ratio) were synthesized. The first one (referred as CZ-O) was prepared by precipitation of $Zr(OH)_4$ on a fine ceria powder (Anan Kasei Co., Ltd., 99.9 % purity, specific surface area :120 $m^2$/g) using the hydrolysis of $ZrO(NO_3)_2$ with aqueous $NH_3$. The solid was dried at 90°C and calcined at 500°C for 5 hours in air. The second one (referred as CZ-R) was prepared via the same procedure as the previous one, except that the oxide was first reduced at 1200°C for 4 hours by CO and further re-oxidized at 500°C for 3 hours in air. The third one (referred as CZ-D) was prepared by the mechano-chemical reaction of $CeO_2$ and $ZrO_2$ powder with high energy ball milling [3]. Pt/CZ catalysts were prepared by conventional impregnation using $Pt(NH_3)_2(NO_2)_2$ as platinum precursor and calcination at 500°C for 3 hours in air. Using the same preparation route, a Pt/$\gamma$-$Al_2O_3$ catalyst ($\gamma$-$Al_2O_3$ Nikki Universal Co., Ltd., specific surface area : 140 $m^2$/g) was also prepared to serve as a reference.

Cyclic transient reactions were performed to measure OSC of the Pt/CZ catalysts. A schematic of the experimental setup is shown in Figure 1. At a given temperature, the reactor was alternatively fed every 180 seconds with 2 % of CO in $N_2$ or 1 % of $O_2$ in $N_2$. Total flow rate was 5 l/min. and 1.0 g of catalyst was used. $CO_2$ concentration at the outlet was measured using a BEX-5000 (Best Instruments Co., Ltd.) gas analysis system. OSC and OSCC were calculated by integration of $CO_2$ concentration over time. The catalytic activity of the catalysts was investigated using simulated exhaust gas conditions with oscillations of the gas feed composition around the stoichiometry ($\lambda$=1.00±0.04, 0.25 Hz). XRD patterns of $CeO_2$-$ZrO_2$ were collected using a RINT2200 (Rigaku Co., Ltd.) diffractometer with Cu-K$\alpha$ radiation (1.5406 Å). XRD was used to characterize the crystalline phase of $CeO_2$-$ZrO_2$ supports. To obtain structural information a FE-TEM
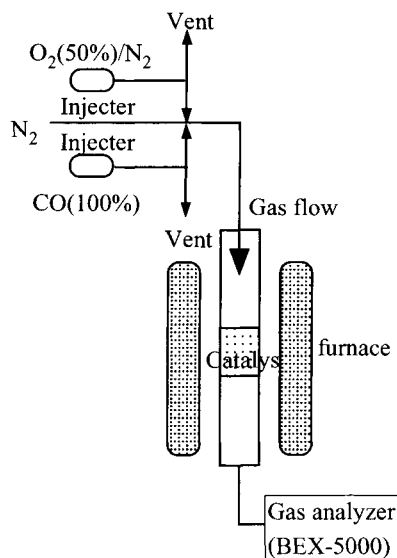
Fig. 1 Schematic of experimental setup for reactivity measurements under transient reaction conditions.

(Hitachi 2000H) microscope was also used. The Ce/Zr atomic ratio in $CeO_2$-$ZrO_2$ crystallites was determined by EDX analysis during TEM observations. The analysis spot diameter is 2nm. Specific surface areas (SSA) were determined by $N_2$ adsorption (one point BET method) using a Micro Sorb 4232II (Micro Data Co., Ltd.). Aging tests under various atmospheres were also performed to evaluate the thermal stability of Pt/CZ catalysts. Samples were heated under flowing gas at 1000°C for 5 hours. Four different conditions were used : cyclic reduction (10% CO in $N_2$) and oxidation (5% $O_2$ in $N_2$) in the presence of 3% $H_2O$. 2) cyclic reduction (10% CO in $N_2$) and oxidation (5% $O_2$ in $N_2$) in the absence of water. 3) reduction (10% CO in $N_2$) in the presence of 3% $H_2O$. 4) oxidation (5% $O_2$ in $N_2$) in the absence of water. In the case of aged catalysts, Pt particles size was determined from the FWMH of the Pt (311) diffraction peak using the Sherrer equation. Isotopic Exchange reactions study was used to estimate the reactivity and the mobility of surface and bulk oxygen atoms in $CeO_2$-$ZrO_2$ supports. Experimental setup was fully described in a previous paper [4].

## 3. RESULTS AND DISCUSSIONS

### 3.1 Structural characterizations of $CeO_2$-$ZrO_2$ supports

Structural properties concerning $CeO_2$-$ZrO_2$ solids are presented in Table 1. From XRD results (Figure 2), CZ-O was shown to be a mixture of a cubic $CeO_2$ phase and a tetragonal $ZrO_2$ phase. CZ-D and CZ-R were shown to be monophasic $Ce_{0.5}Zr_{0.5}O_2$ solid solution with a cubic structure. After high temperature reduction, $CeO_2$-$ZrO_2$ oxide transforms into a pyrochlore-type $Ce_2Zr_2O_{7+\delta}$ phase with $\delta<0.07$ [5]. In such a phase Ce and Zr ions are distributed in an ordered arrangement. $\kappa$-$Ce_{0.5}Zr_{0.5}O_2$ was obtained by mild oxidation of the pyrochlore-type structure. In that last structure, Ce ions and Zr ions have similar arrangement to that of pyrochlore-type structure [5]. XRD pattern of CZ-R almost corresponds to $\kappa$-$Ce_{0.5}Zr_{0.5}O_2$. This result indicates that Zr ions were homogeneously substituted in the $CeO_2$ lattice. CZ-D was also found to have a cubic phase structure. It shows that CZ solid solutions may easily be prepared by high energy ball milling [3]. In the case of CZ-D, due to peak broadening, it is difficult to estimate how homogeneous the introduction of Zr ions is. Peak broadening could originate either from the small particle size or from a non-homogeneous solid solution. Figure 3 shows the Ce/Zr atomic ratio determined by EDX
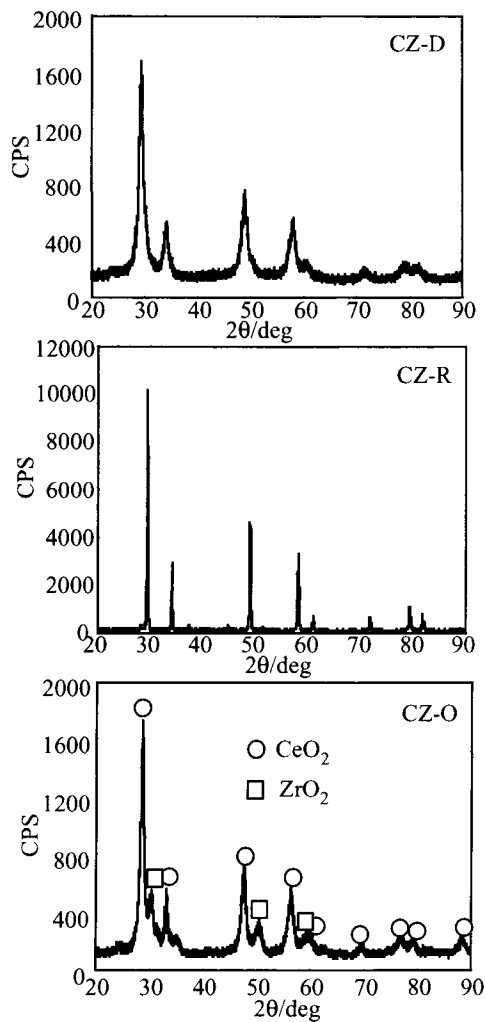


Fig. 2  X-Ray Diffraction patterns of the $CeO_2$-$ZrO_2$ supports

Table 1  Structural propeties of $CeO_2$-$ZrO_2$ supports

| | structure | lattice parameter/nm | $SSA$/m$^2$·g$^{-1}$ |
|---|---|---|---|
| CZ-O | cubic+tetragonal | 0.541(CeO2), 0.513, 0.509(ZrO2) | 129 |
| CZ-D | cubic | 0.526 | 58 |
| CZ-R | cubic | 0.527 | 3 |
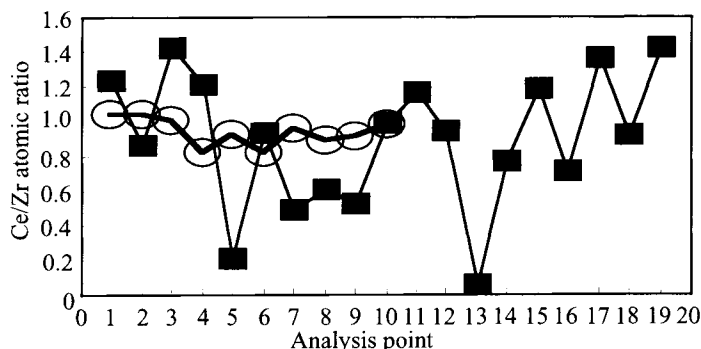


Fig. 3  Ce/Zr atomic ratio in Pt/ $CeO_2$-$ZrO_2$
determined by EDX ○ Pt/CZ-R, ■ Pt/CZ-D

analysis during TEM observations. Although the Ce/Zr ratio for CZ-R is almost constant at 1.0, this ratio varies between 0.2 and 1.4 for CZ-D. This result means that the distribution of Zr ions into $CeO_2$ framework in CZ-D is not as homogeneous as in CZ-R. To summarize, the homogeneity of Zr introduction into the $CeO_2$ framework decreases as follows : CZ-R > CZ-D > CZ-O.

### 3.2 Dynamic OSC measurements on Pt/CZ catalysts.

Figure 4 shows the temperature dependence of OSCC for the different catalysts. Above 300°C, Pt/CZ-R has the highest OSCC which reaches a maximum around 400°C. This maximum value corresponds to the total amount of reducible oxygen atoms in CZ oxide. This means that all Ce ions in Pt/CZ-R were reduced to $Ce^{3+}$ (bulk reduction). Pt/CZ-D has the second highest OSCC and Pt/CZ-O has the lowest one. It is well known that the introduction of Zr ions into $CeO_2$ framework enhances the reducibility of $CeO_2$ [2]. CZ-R was found to be a homogeneous solid solution of $Ce_{0.5}Zr_{0.5}O_2$. So, an atomically homogeneous introduction of Zr ions would be responsible for high OSCC value. CZ-O was found to be a mixture of $CeO_2$ and $ZrO_2$. This means that only a few Zr ions were introduced into the $CeO_2$ framework. This could explain the low OSCC value of Pt/CZ-O.

140

In the case of CZ-D, looking at the OSCC values, the level of Zr introduction into the $CeO_2$ framework in CZ-D should be somewhere in between CZ-R and CZ-O. This estimation is in good agreement with XRD and TEM-EDX results. So, the OSCC of these catalysts would vary with the homogeneity of Zr introduction into $CeO_2$ framework.

The number of the surface oxygen atoms was estimated from the specific surface area of CZ [6]. The number of surface oxygen atoms should be ca. 3 $\mu mol/m^2$ for CZ-D,
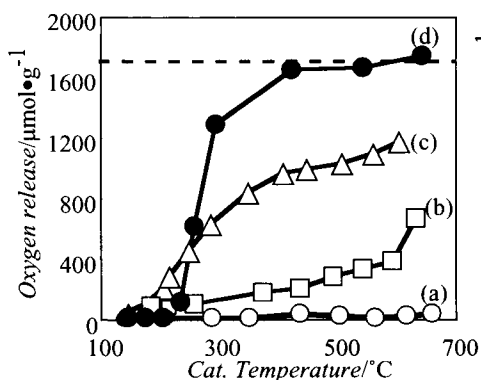


Fig.4 Temperature dependence of oxygen storage capacity. (a) Pt/$\gamma$-$Al_2O_3$, (b) Pt/CZ-O, (c) Pt/CZ-D, (d) Pt/CZ-R. The dashed line indicates the total amount of reducible oxygen atoms in Pt/CZ catalysts.
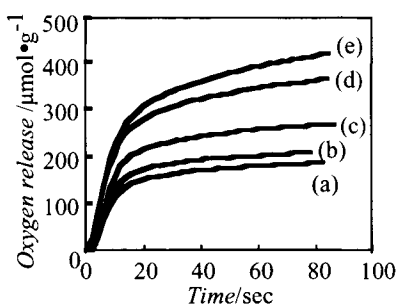
Fig.5.1 Time dependence of oxygen release from Pt/CZ-O under transient reaction conditions. (a)368°C, (b)430°C, (c)488°C, (d)589°C, (e)632°C
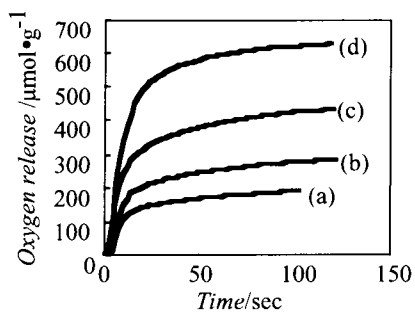
Fig.5.2 Time dependence of oxygen release from Pt/CZ-D under transient reaction conditions. (a)203°C, (b)216°C, (c)246°C, (d)284°C
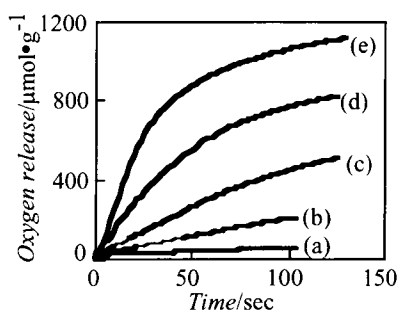
Fig.5.3 Time dependence of oxygen release from Pt/CZ-R under transient reaction conditions. (a) 229°C, (b) 245°C, (c)258°C, (d)272°C, (e)289°C

CZ-R and CZ-O. The experimental values were 530 $\mu$mol/m$^2$, 15.5 $\mu$mol/m$^2$ and 1.7 $\mu$mol/m$^2$ for Pt/CZ-R, Pt/CZ-D and Pt/CZ-O respectively. So, the reduction of Pt/CZ-O is restricted at the surface. In Pt/CZ-D, reduction proceeds up to the ca. 5 layers from the surface. Of course, in Pt/CZ-R, all bulk oxygen atoms do participate in the redox process.

Under real automotive catalyst operating conditions, the composition of the exhaust gas oscillates at a frequency in the order of 0.1 Hz to 10 Hz. Thus, the fast part of OSCC (OSC) is important to contribute in the catalytic reaction. To estimate the fast part of OSC of Pt/CZ catalysts, the initial rate of oxygen release under transient reaction condition was calculated. Figure 5 shows the time dependence of the oxygen release at different temperature. The initial rate of oxygen release was estimated from the initial slope of the different curves. Temperature range was selected so that the maximum CO conversion was below 30% to exclude any diffusion problems. The evolution of the initial rate for oxygen release is presented in Figure 6 (Arrhenius coordinates). The initial rate for oxygen release from Pt/CZ-D was the highest in the whole temperature range from 200°C to 300°C. This result indicates that oxygen atoms close to the surface readily contribute to the OSC even at low temperature. The apparent activation energy for oxygen release (Table 2) was estimated from Figure 6. Apparent activation energy for Pt/CZ-R was about 100 kJ/mol. This value is close to the activation energy of oxygen hopping in the stabilized ZrO$_2$ [7]. For Pt/CZ-R, which has a very low specific surface area, bulk oxygen contributes the OSC. Then the activation energy measured for Pt/CZ-R would reflect the energy for oxygen hopping in the bulk of CZ-R oxide. The apparent activation energy of Pt/CZ-D and Pt/CZ-O are much lower than that of Pt/CZ-R. In these cases, reduction is restricted to the surface or to the sub-surface of these oxides. Activation energy would then reflect the energy required for oxygen migration at the surface or subsurface of such CZ oxides.

Figure 7 shows the conversion of CO at 200°C under simulated automotive exhaust gas conditions over Pt/CZ catalysts. Pt/CZ-D catalyst showed the highest activity among the catalysts. The order in activity is well correlated with the order in the initial rate of oxygen release at 200°C (Fig. 6). This result indicates that the initial rate of oxygen release (OSC) would be best parameter to be measured if one wants to get some insights about the catalytic activity under "real" operating conditions.

Oxygen migration process in CZ oxide was also studied using Isotopic Exchange reactions. Homoexchange and Heteroexchange reactions were performed on three Pt/CZ catalysts. Figure 8 shows the temperature dependence of the heteroexchange rate on the three Pt/CZ catalysts (Arrhenius coordinates). The activity of Pt/CZ-R in the heteroexchange reaction was the highest among the three catalysts. The activity of Pt/CZ-D and Pt/CZ-O was almost the same. This results would indicate that the mobility and the reactivity of oxygen atoms in Pt/CZ-R are the highest among the three catalysts. Those

142



Fig.2 Apparent activation energy for oxygen release from Pt/CZ catalysts

|          | $E/kJmol^{-1}$ |
|----------|----------------|
| Pt/CZ-O  | 11             |
| Pt/CZ-D  | 32             |
| Pt/CZ-R  | 103            |
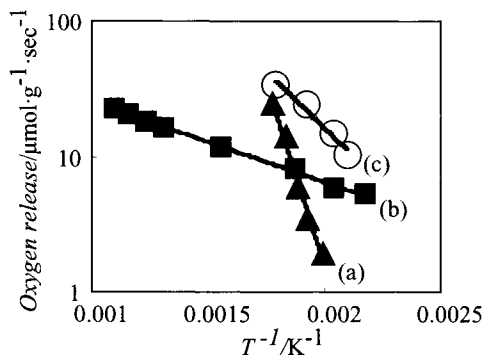
Fig.6 Evolution of the initial rate for oxygen release from Pt/CZ catalysts as a function of temperature (Arrhenius coordinates). (a)Pt/CZ-R, (b)Pt/CZ-O, (c)Pt/CZ-D
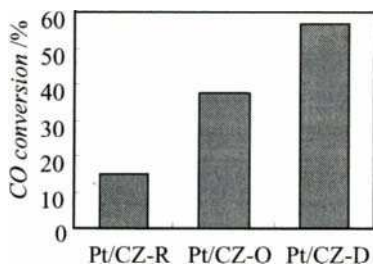


Fig. 7 CO conversion at 200°C in the simulated exhaust reaction oscillating around the stoichimetric condition ($\lambda=1.00\pm0.04$, 0.25Hz).
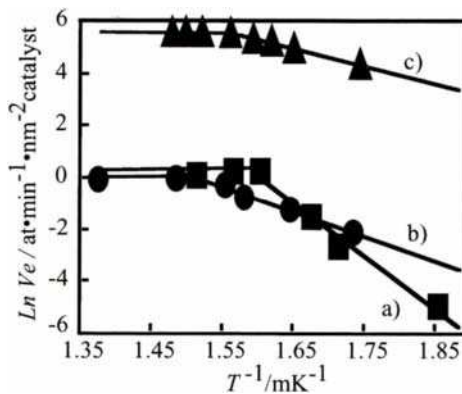


Fig. 8 $^{16}O/^{18}O$ heteroexchange reaction rate over Pt/CZ catalysts. Ve is the amount of exchanged oxygen atoms per minute and per $nm^2$ of catalyst a) Pt/CZ-O, b) Pt/CZ-D and c) Pt/CZ-R

observations are in good agreement with OSC values and structural characteristics. A homogeneous introduction of Zr ions into $CeO_2$ framework enhance the reducibility (OSCC) and the mobility of oxygen in $CeO_2$-$ZrO_2$ oxides.

Thermal stability of $CeO_2$-$ZrO_2$ at high temperature is also very important for automotive applications. Figure 9 shows the OSCC at 500°C of aged catalysts. The OSCC of Pt/CZ-R was the highest among all catalysts whatever the aging conditions. Although, it was reported that the presence of $H_2O$ accelerates the OSCC decrease [8], in our case, redox aging in the absence of water was the most severe aging treatment. No correlation could be found between Pt particle size and the OSCC decrease for aged catalysts. Considering thermal stability, this result shows that the nature of the oxide is more important than Pt particle size.
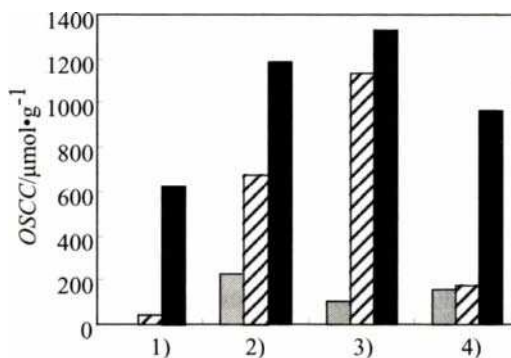


Fig. 9 OSCC at 500°C of Pt/CZ catalysts after aging tests. Catalysts were aged at 1000°C for 5 hours 1)cyclic reduction and oxidation in the absence of water, 2)cyclic reduction and oxidation in the presence of water, 3)reduction in the presence of water and 4) oxidation in the absence of water. ▨ Pt/CZ-O, ◪ Pt/CZ-D, ■ Pt/CZ-R

## 4.CONCLUSIONS

High temperature reduction of $CeO_2$-$ZrO_2$(CZ) oxides is responsible for the atomically homogeneous introduction of Zr into $CeO_2$ framework. Homogeneity of Zr introduction appears to govern the OSCC of Pt/CZ catalysts. Oxide homogeneity also favors a high mobility and reactivity of oxygen atoms in CZ oxides as evidence by Isotopic Exchange. Comparing oxygen release measurements (OSC) and reactivity results obtained under "real" operating conditions, it appears that a simple measurement of the initial rate rate for oxygen release gives some diretc information about the catalyst state - active or inactive. Pt/CZ catalysts aging under different atmospheres showed that the influence on thermal stability and OSCC of the nature of the oxide is more important than the Pt particles size.

144

**REFERENCES**

[1] H. C. Yao and Y. F. Yu Yao, J. Catal., **86**, 254 (1984)

[2] M. Ozawa, M. Kimura and A. Isogai, J. Alloys and Compd., **193**, 73 (1993)

[3] A. Suda, T. Kandori, Y. Ukyo, H. Sobukawa and M. Sugiura, J. Cera. Soc. Jpn., **108(5)**, 473 (2000)

[4] D. Martin and D. Duprez, J. Phys. Chem., **100**, 9429 (1996)

[5] T. Omata, H. Kishimoto, S. O. Y. Matsuo, N. Ohtori and N. Umesaki, J. Solid State Chem., **147**, 573 (1999)

[6] Y. Madier, C. Descorme, A. M. Le Govic and D. Duprez, J. Phys. Chem., **103**, 10999 (1999)

[7] J. F. Baumard and P. Abelard, Adv. in Ceramics,**12**, 555 (1984)

[8] R. Taha, D. Duprez, N. Mouaddib-Moral and C. Gauthier, Stud. Surf. Sci. Catal. **116**, 549 (1998)

145

# A rational strategy to design performant multiphasic oxide catalysts based on the cooperation between phases via spillover oxygen: the Bi-V-Sb-O system

E.M. Gaigneaux*, F. Englebert and P. Ruiz

Unité de catalyse et chimie des matériaux divisés, Université catholique de Louvain, Croix du Sud 2/17, B-1348 Louvain-la-Neuve, Belgium.

We describe a rational strategy directed to the elaboration of more performant formulations of multiphasic oxide systems used in selective oxidation processes. The strategy consists mainly in the systematic detection of the phases present in the systems, precising those with beneficial influences on the performance, and in their identification as spillover oxygen donor and/or acceptor during the reaction. The strategy is illustrated in the case of the $Bi_4V_{2-x}Sb_xO_{11-\mu}$ system used in the oxidation of propene to acrolein. Based on the remote control theory, the key to obtain the most performant $Bi_4V_{2-x}Sb_xO_{11-\mu}$ formulations is to promote the simultaneous formation of $BiSbO_4$, $Bi_{1.33}V_2O_6$ and $Bi_{13}V_5SbO_{34}$ during the synthesis and their stabilization under the conditions of the catalytic reaction. Another aspect is to avoid the formation of $BiVO_4$ in the synthesis and during the reaction.

## 1. INTRODUCTION AND OBJECTIVES

A possible origin of the high performance of multiphasic catalysts in selective oxidation processes is the cooperation between the oxide phases present in their formulations [1]. Our laboratory has previously demonstrated that for several catalytic systems, such cooperation is due to the action of spillover oxygen (Oso) as described in the remote control theory [2]. Precisely, via the migration of Oso species that they produce, phases playing the role of Oso donors succeed to modulate the superficial characteristics of phases playing the role of Oso acceptors during the catalytic reaction, so improving the activity and selectivity of the acceptor phases, and thus of the whole system.

The objective of this work is to show that to follow a rational strategy directed to identify systematically the Oso donor and/or Oso acceptor role of each oxide present in multiphasic systems is a powerful approach to design more performant catalysts. This strategy consists in:

---

i) identifying the oxide phases present in the fresh multiphasic system,
ii) synthesizing separately, with the highest purities as possible, the phases identified in i),
iii) preparing for each of the phases synthesized in ii) a physical mixture with a typical Oso donor and with a typical Oso acceptor,
iv) measuring the catalytic performance of all the pure oxide phases and mixtures prepared,
v) characterizing the catalysts after the reaction and particularly detecting new compounds having possibly formed under the conditions of reaction,
vi) performing steps ii) to vi) with each new compound possibly detected, and this, until no additional modification of the samples during the reaction is found,
vii) assigning a Oso donor and/or a Oso acceptor character to each of the phases investigated,
viii) stating the rules leading to the most performant combinations of the phases investigated.

This contribution illustrates the use of the strategy described above in the case of the $Bi_4V_{2-x}Sb_xO_{11-\mu}$ system. Depending on x and $\mu$, the system contains several oxide phases as $Bi_{13}V_5SbO_{34}$, $Bi_{1.33}V_2O_6$, $BiSbO_4$, $Bi_4V_2O_{11}$, $BiVO_4$ and $Bi_2O_3$. The main ones were synthesized by solid-state reactions and their behaviors under the conditions of reaction were investigated following the steps ii) to vii) of the strategy. For the mixtures, the Oso donor selected was $\alpha$-$Sb_2O_4$. As Oso acceptors, $MoO_3$ and $SnO_2$ were selected. The oxidation of propene to acrolein was used as the probe catalytic reaction. Characterization of the catalysts was done by X-ray diffraction, specific area measurements, photoemitted electron spectroscopy, Raman spectroscopy and environmental electron microscopy.

## 2. EXPERIMENTAL

### 2.1. Preparation of the samples
The syntheses of the samples investigated are described at adequate places in the text.

### 2.2. Catalytic activity measurements
The selective oxidation of propene was performed at atmopsheric pressure in a continuous fixed bed microreactor. Depending on the samples, the reaction was run at 653 K, 673 K and/or at 733 K. The composition of the gas feed was propene : $O_2$ : He = 1 : 2 : 7 by volume. The total gas flow was 30 mL min$^{-1}$. In all cases, the tests were performed with 1 g of catalyst previously conditioned to pellets with a granulometry between 500 and 800 $\mu$m.

### 2.3. Characterization
Powder X-ray diffraction (XRD) was performed with a Kristalloflex Siemens D5000 diffractometer using the $K_{\alpha1,2}$ radiation of Cu ($\lambda$=1.5418 Å) and equipped with a

secondary curved graphite monochromator. The analyses were done in the continuous coupled $\theta/2\theta$ reflection mode. Two-$\theta$ angles were scanned between $10°$ and $80°$ at a rate of $0.4°$ min$^{-1}$.

Specific areas were measured with a Micromeritics ASAP 2010 equipment. Analyses were based on the adsorption isotherm of Kr at 77 K for P/P° values from 0.05 to 0.30.

X-ray photoelectron spectroscopy (XPS) was performed with a X probe SSX-100/206 ESCA equipment from Fisons Surface Science Instruments using the monochromatized Al K$_{1,2}$ radiation (1486.6 eV). Charge neutralization was achieved using an electron flood-gun adjusted at 8 eV and placing a Ni grid 3.0 mm above the sample. Binding energy values were referred to the $\underline{C}$-(C,H) contribution of the C1s peak fixed at 284.8 eV. In addition to C1s, Bi4f, Sb3d, V2p and O1s bands were recorded. No other elements were detected. Quantification of the element proportions at the surface was done by using a Shirley baseline and Wagner sensibility factors [3].

Environmental scanning electron microscopy was done with a Philips XL30 ESEM-FEG microscope using a field emission gun. Samples were analyzed without any coating. Observations were made either with a secondary electron detector (high vacuum in the cell, accelerating voltage of 4 kV), a backscattered electron detector (ca. 0.3 Torr of water in the cell, accelerating voltage of 10 to 25 kV) or a gaseous secondary electron (0.4 Torr to 4 Torr of water in the cell, accelerating voltage of 25 kV).

Raman spectroscopy was performed with a Dilor spectrometer using a Ar/He laser ($\lambda$ = 632 nm) at a power of 18 mW. Analyses were done between 100 and 1500 cm$^{-1}$.

## 3. RESULTS AND DISCUSSION

### 3.1. Synthesis and characterization of the $Bi_4V_{2-x}Sb_xO_{11-\mu}$ samples

Five $Bi_4V_{2-x}Sb_xO_{11-\mu}$ samples, with x = 0, 0.08, 0.3, 1 and 1.7, were prepared following exactly the procedure described by Aghabozorg et al [4]. The synthesis consisted in the calcination in air at 1073 K during 18 hours of a homogeneous mixture of $Bi_2O_3$ (Aldrich, 99.9%), $V_2O_5$ (Aldrich, 99%) and $Sb_2O_3$ (UCB, >98%) obtained by "ball-milling" adequate stoichiometric quantities of the 3 oxides together.

Table 1 shows, as a function of x (i.e. the quantity of Sb in the empirical formula), the phases detected by XRD for our $Bi_4V_{2-x}Sb_xO_{11-\mu}$ samples. Corresponding specific area values are also shown. Aghabozorg et al claimed that 1° regardless of the value of x, $Bi_4V_{2-x}Sb_xO_{11}$ samples always contain $Bi_4V_2O_{11}$, 2° a second phase appears for values of x superior to 0.3 but it remained unidentified, and thus 3° the $Bi_4V_{2-x}Sb_xO_{11-\mu}$ system should better be regarded as a monophasic one. The XRD patterns obtained for our samples were identical to those reported by Aghabozorg et al. However, the careful interpretation of the patterns revealed very clearly that our samples corresponded to several different crystalline phases and combinations of them. The phases found were $Bi_4V_2O_{11}$, $BiVO_4$, $Bi_{13}V_5SbO_{34}$, $Bi_{1.33}V_2O_6$, $BiSbO_4$ and $Bi_2O_3$.

Table 1
Phases detected in the X-ray diffractograms and specific area values of our $Bi_4V_{2-x}Sb_xO_{11-\mu}$ samples as a function of the quantity of Sb in the empirical formula

| x | Empirical formula | Phases detected | Specific area ($m^2 g^{-1}$) |
|---|---|---|---|
| 0 | $Bi_4V_2O_{11}$ | $Bi_4V_2O_{11}$ | 0.27 |
| 0.08 | $Bi_4V_{1.92}Sb_{0.08}O_{11-\mu}$ | $Bi_4V_2O_{11}$, $BiVO_4$ | 0.32 |
| 0.3 | $Bi_4V_{1.7}Sb_{0.3}O_{11-\mu}$ | $Bi_{13}V_5SbO_{34}$ | 0.55 |
| 1 | $Bi_4VSbO_{11-\mu}$ | $Bi_{1.33}V_2O_6$, $BiSbO_4$ | 0.63 |
| 1.7 | $Bi_4V_{0.3}Sb_{1.7}O_{11-\mu}$ | $Bi_{1.33}V_2O_6$, $BiSbO_4$, $Bi_2O_3$ | 0.64 |

## 3.2. Investigation of the catalytic behavior of $BiSbO_4$, $Bi_{1.33}V_2O_6$ and $Bi_{13}V_5SbO_{34}$

To find the guidelines leading to the optimization of its formulation, it turns out unquestionably from section 3.1 that the $Bi_4V_{2-x}Sb_xO_{11-\mu}$ system should be considered as a multiphasic one. In the following, we therefore synthesized separately with the highest purities as possible the phases found in the different $Bi_4V_{2-x}Sb_xO_{11-\mu}$ samples. We then tested their individual performance in the oxidation of propene to acrolein and checked their stability under the conditions of reaction. A crucial line concerned the determination of the tendency for each of the phases to play as a spillover oxygen (Oso) donor, or as a spillover oxygen acceptor, in the system. To do so, we prepared physical mixtures of each of the phases found in the $Bi_4V_{2-x}Sb_xO_{11-\mu}$ system with a typical Oso donor, namely $\alpha$-$Sb_2O_4$ [2], and with a typical Oso acceptor, namely $MoO_3$ or $SnO_2$ [2]. We then tested the performance of the mixtures to detect eventual synergetic effects between the phases mixed together, and finally we checked the stability of the mixtures during the reaction, in particular to evaluate the tendency of the phases mixed together to undergo mutual contamination.

As Sb is frequently incorporated in oxidation catalysts in significant amount, we restricted our investigation to the phases detected for the $Bi_4V_{2-x}Sb_xO_{11-\mu}$ samples with values of x higher than 0.08. Pure $Bi_2O_3$ was not investigated in this work since, as such, it is well known not to be an active phase in the oxidation of propene to acrolein [5,6].

### 3.2.1. Synthesis of $BiSbO_4$, $Bi_{1.33}V_2O_6$, $Bi_{13}V_5SbO_{34}$ and $BiVO_4$

$BiSbO_4$ was prepared as described by Nedil'ko and Sych [7] by calcination in air at 1173 K during 20 hours of an equimolar mixture of $Bi_2O_3$ (Aldrich, 99.9%) and $Sb_2O_3$ (UCB, 99.9%) previously ground together in an agate mortar.

$Bi_{1.33}V_2O_6$ was prepared as described by Ramanan et al [8] by the solid-state reaction of a mixture of $Bi_2O_3$ (Aldrich, 99.9%), $V_2O_3$ (Aldrich, 99%) and $V_2O_5$ (Aldrich, 99%) with 1.33 : 1 : 1 molar proportions. After that the mixture was evacuated in a silica tube down to $10^{-4}$ Torr, the tube was sealed and then maintained at 1173 K during 7 days.

$Bi_{13}V_5SbO_{34}$ was prepared by calcining in air at 1073 K during 18 hours a mixture of $Bi_2O_3$ (Aldrich 99.9%), $V_2O_5$ (Aldrich, 99%) and $Sb_2O_3$ (UCB, 98%) with 13.3

: 6.5 : 1 molar proportions obtained by "ball-milling" adequate quantities of the 3 oxides together.

From XRD analyses, it turned out that $BiSbO_4$ and $Bi_{13}V_5SbO_{34}$ were monophasic solids. By contrast, for $Bi_{1.33}V_2O_6$, $BiVO_4$ was detected in addition to the desired compound. Therefore, it was also required to synthesize $BiVO_4$ as a pure phase and to evaluate its behavior during catalysis. Aghabozorg et al did not mention the presence of $BiVO_4$ in their samples [8].

$BiVO_4$ was prepared by mixing an equimolar quantity of $NH_4VO_3$ (Merck, 99%), dissolved at 373 K in distilled water and then complexed with an equivalent amount of citric acid (Merck, 99%), with $BiONO_3.H_2O$ (Merck, 99%), dissolved and complexed identically, then concentrating the resulting solution under vacuum at 313 K, drying it under vacuum at 353 K overnight, decomposing the obtained solid at 573 K in air during 16 hours, and finally calcining it in air at 773 K during 16 hours. XRD showed that $BiVO_4$ was obtained as a monophasic solid.

### 3.2.2. Preparation of the physical mixtures with α-$Sb_2O_4$, $MoO_3$ and $SnO_2$

α-$Sb_2O_4$ was obtained by calcination at 773 K in air during 20 hours of $Sb_2O_3$ (Aldrich, 99%).

$MoO_3$ was prepared from an aqueous solution of ammonium heptamolybdate dihydrate (Merck, 99%) complexed with the equivalent amount of oxalic acid dihydrate (Janssen Chimica, 99%) and stirred at 313 K until being limpid. The water was removed under reduced pressure, and the obtained solid was thereafter dried at 353 K during 20 hours, decomposed at 573 K during 20 hours and finally calcined at 673 K during 20 hours in air.

$SnO_2$ was synthesized by neutralizing with $NH_3$ (Janssen Chimica, 25 wt% in water) a limpid aqueous solution of $SnCl_2$ (UCB, p.a.) acidified with HCl (Janssen Chimica). The tin hydroxide precipitate was then washed with water until complete removal of $Cl^-$ anions then dried at 383 K during 20 hours, calcined at 873 K during 8 hours and finally at 1173 K during 16 hours in air.

Physical mixtures of $BiSbO_4$, $Bi_{1.33}V_2O_6$ or $Bi_{13}V_5SbO_{34}$ with α-$Sb_2O_4$, $MoO_3$ or $SnO_2$ were prepared by interdispersing 2 g of both of the oxides to combine in 400 mL of n-pentane (Aldrich, 98%) using an ultra-turrax mixer (6000 rpm, 10 min) and ultrasounds (10 min), before the resulting solid was dried under vacuum at 308 K, then in air at 353 K overnight. As a reference sample, a mixture of $MoO_3$ and α-$Sb_2O_4$ was also prepared. To make the comparison with the mixtures rigorous, the pure oxides also received the "physical mixing" procedure before being used in the catalytic reaction.

### 3.2.3. Performance of $BiSbO_4$, $Bi_{1.33}V_2O_6$ or $Bi_{13}V_5SbO_{34}$ and of the mixtures with α-$Sb_2O_4$, $MoO_3$ or $SnO_2$ in the oxidation of propene to acrolein

Table 2 shows the catalytic performances of $BiSbO_4$, $Bi_{1.33}V_2O_6$, $Bi_{13}V_5SbO_{34}$ and $BiVO_4$ and of the mixtures with α-$Sb_2O_4$, $MoO_3$ or $SnO_2$ in the oxidation of propene to acrolein.

Table 2
Conversion of propene (C), yield in acrolein (Y) and selectivity to acrolein (S) obtained at 673 K and/or 733 K for $BiVO_4$, $BiSbO_4$, $Bi_{1.33}V_2O_6$, $Bi_{13}V_5SbO_{34}$, $\alpha-Sb_2O_4$, $MoO_3$, $SnO_2$ and their physical mixtures. For the mixtures, figures in parentheses correspond to the mass-averaged performances calculated as if the phases in the mixtures behaved independently of each other (i.e. as if no synergy effect happened), and assuming a reaction order of zero

| Catalysts | T° (K) | C (%) | | Y (%) | | S (%) | |
|---|---|---|---|---|---|---|---|
| $BiSbO_4$ | 673/733 | 0/6.5 | | 0/0 | | 0/0 | |
| $Bi_{13}V_5SbO_{34}$ | 673/733 | 0/5.3 | | 0/0 | | 0/0 | |
| $Bi_{1.33}V_2O_6$ | 673/733 | 2.6/16.4 | | 2.4/4.1 | | 92.3/25.0 | |
| $BiVO_4$ | 653 | 36.0 | | 0 | | 0 | |
| | | | | | | | |
| $\alpha-Sb_2O_4$ | 673/733 | 0/2.6 | | 0/0 | | 0/0 | |
| $MoO_3$ | 673 | 19.8 | | 2.6 | | 13.0 | |
| $SnO_2$ | 673 | 14.0 | | 3.6 | | 26.0 | |
| | | | | | | | |
| $MoO_3 + \alpha-Sb_2O_4$ | 673 | 4.2 | (9.9) | 2.0 | (1.3) | 47.6 | (13.1) |
| | | | | | | | |
| $BiSbO_4 + \alpha-Sb_2O_4$ | 733 | 0.3 | (4.6) | 0.0 | (0) | 0.0 | (0) |
| $BiSbO_4 + MoO_3$ | 673 | 17.9 | (9.9) | 15.5 | (1.3) | 86.0 | (13.1) |
| $BiSbO_4 + SnO_2$ | 673 | 14.8 | (7.0) | 4.0 | (1.8) | 27.0 | (25.7) |
| | | | | | | | |
| $Bi_{13}V_5SbO_{34} + \alpha-Sb_2O_4$ | 733 | 1.3 | (4.0) | 0.0 | (0) | 0.0 | (0) |
| $Bi_{13}V_5SbO_{34} + MoO_3$ | 673 | 21.2 | (9.9) | 6.9 | (1.3) | 32 | (13.1) |
| $Bi_{1.33}V_2O_6 + \alpha-Sb_2O_4$ | 733 | 9.1 | (12.3) | 4.5 | (2.8) | 49.4 | (22.8) |
| $Bi_{1.33}V_2O_6 + MoO_3$ | 673 | 6.5 | (11.2) | 4.0 | (2.5) | 61.5 | (22.3) |

BiSbO$_4$ and Bi$_{13}$V$_5$SbO$_{34}$ were active only at 733 K and completely non selective to acrolein. On the contrary, Bi$_{1.33}$V$_2$O$_6$ succeeded to convert propene. The selectivity to acrolein was particularly high at 673 K. BiVO$_4$ was the most active, succeeding to considerably convert propene from 653 K, but it was completely non selective to acrolein and yielded exclusively secondary oxidation products.

Mixtures of BiSbO$_4$ and α-Sb$_2$O$_4$ and of Bi$_{13}$V$_5$SbO$_{34}$ and α-Sb$_2$O$_4$ led to conversions of propene lower than those expected if no cooperation between phases happened, while the mixtures remained completely non selective to acrolein. This shows clearly that BiSbO$_4$ and Bi$_{13}$V$_5$SbO$_{34}$ do not present any tendency to work synergetically with α-Sb$_2$O$_4$ to produce acrolein. For all the other mixtures, synergetic effects (i.e. measured performances superior to those expected if no cooperation happened), in some cases dramatic, were observed. For the mixture of BiSbO$_4$ with MoO$_3$, the synergy corresponded to increases by 556% of the selectivity to acrolein and by 1093% of the yield in acrolein with respect to performances expected if the phases had behaved independently in the reaction. The corresponding values were 5% and 122% for the mixture of BiSbO$_4$ with SnO$_2$, 144% and 430% for the mixture of

$Bi_{13}V_5SbO_{34}$ with $MoO_3$, 116% and 60% for the mixture of $Bi_{1.33}V_2O_6$ with $\alpha$-$Sb_2O_4$, 176% and 60% for the mixture of $Bi_{1.33}V_2O_6$ with $MoO_3$.

### 3.2.4. Stability of $BiSbO_4$, $Bi_{1.33}V_2O_6$ or $Bi_{13}V_5SbO_{34}$ and of their mixtures during the oxidation of propene to acrolein

In general, taking into account the results from all the characterization techniques, most of the samples investigated were stable under the conditions used for the oxidation of propene to acrolein. Most of the different pure oxides had identical characteristics before and after the catalytic reaction. Also, most of the mixtures gave identical characterization results before and after the oxidation of propene. Finally, the global tendency was that the oxides behaved exactly in the same way when reacted alone and in mixtures.

However, some exceptions to these rules were found. *For the mixture of $BiSbO_4$ and $MoO_3$*, while the XPS Sb/Bi atomic percentage ratio remained similar before and after reaction (as it did also for pure $BiSbO_4$), Sb/Mo and Bi/Mo ratios were significantly lower for the tested sample (Table 3). Additionally, although pure $BiSbO_4$ had identical Raman spectra before and after reaction, several Raman bands corresponding to $BiSbO_4$ in the mixture (135, 156, 390 and 446 cm$^{-1}$) had significantly lost intensity after reaction with respect to the bands of $MoO_3$ (284, 666, 821 and 991 cm$^{-1}$). (Fig.1) Also, while no clear  difference was observed between fresh and used crystals of pure $BiSbO_4$, ESEM showed that, for the used mixture with $MoO_3$, $BiSbO_4$ crystals had their surface decorated with tiny particles (Fig.2).

XPS V/Bi atomic percentage ratio remained identical before and after reaction for pure $Bi_{13}V_5SbO_{34}$, but *for the mixture of $Bi_{13}V_5SbO_{34}$ and $MoO_3$*, V/Bi ratio was higher after reaction by about 40% than before, Bi/Mo ratio was lower after reaction by about 30%, and V/Mo ratio remained essentially unchanged before and after oxidation of propene (Table 3).

Table 3
Main XPS atomic percentage ratios for $BiSbO_4$, $Bi_{13}V_5SbO_{34}$ and their mixtures with $MoO_3$ before and after use in the oxidation of propene

|  |  | Sb/Bi | Sb/Mo | Bi/Mo |
|---|---|---|---|---|
| $BiSbO_4$ | before reaction | 0.74 | - | - |
|  | after reaction | 0.83 | - | - |
| $BiSbO_4/MoO_3$ | before reaction | 0.86 | 0.17 | 0.20 |
|  | after reaction | 0.77 | 0.10 | 0.12 |
|  |  | V/Bi | V/Mo | Bi/Mo |
| $Bi_{13}V_5SbO_{34}$ | before reaction | 0.27 | - | - |
|  | after reaction | 0.27 | - | - |
| $Bi_{13}V_5SbO_{34}/MoO_3$ | before reaction | 0.23 | 0.03 | 0.14 |
|  | after reaction | 0.39 | 0.04 | 0.09 |
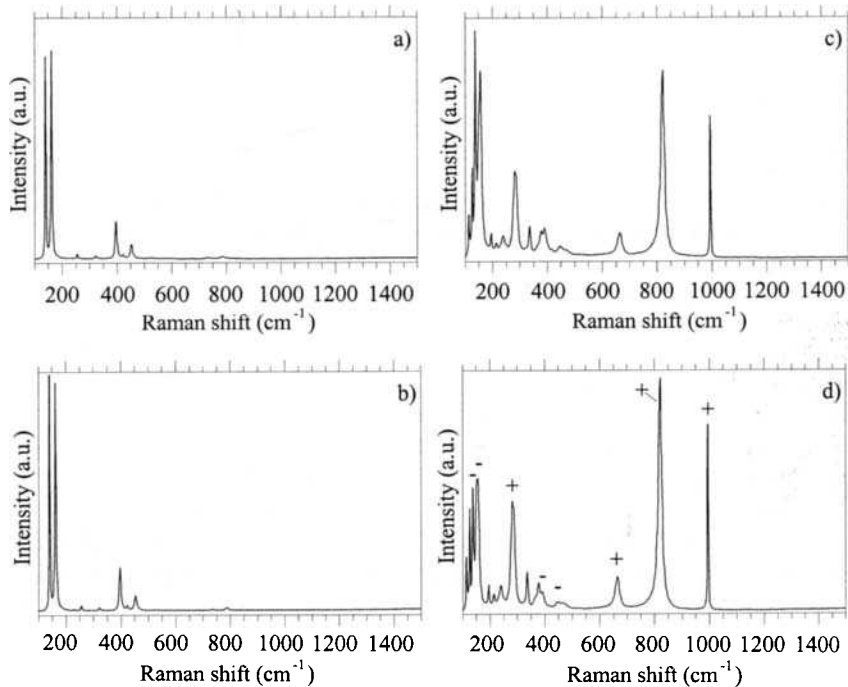
Figure 1. Laser Raman spectra for a) pure $BiSbO_4$ before reaction and b) after reaction, and for c) the mixture of $BiSbO_4$ and $MoO_3$ before reaction and d) after reaction. The - point to the peaks of $BiSbO_4$ which lost intensity after reaction; the + point to the peaks of $MoO_3$ which gain intensity after reaction.
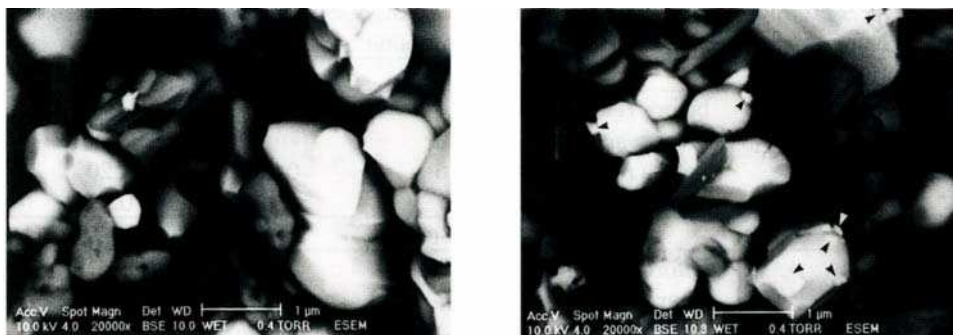


Figure 2. ESEM micrographs of left) the mixture of $BiSbO_4$ and $MoO_3$ before reaction, and right) after reaction. Arrows indicate the tiny particles decorating $BiSbO_4$ crystals after reaction.
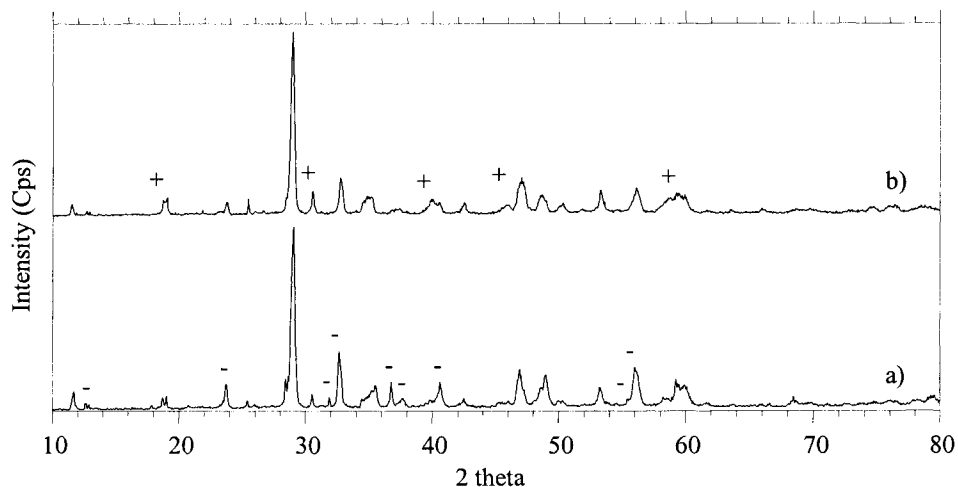
Figure 3. XRD patterns for $Bi_{1.33}V_2O_{11}$ a) before and b) after being used as catalyst in the oxidation of propene. The - point to the peaks of $Bi_{1.33}V_2O_6$ which had lost intensity after reaction; the + point to the peaks of $BiVO_4$ which had gained intensity after reaction.
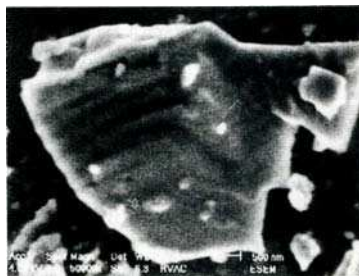


Figure 4. ESEM micrograph of a crystal of $Bi_{1.33}V_2O_6$ with the streaked morphology acquired during the catalytic reaction.

The case of the samples involving $Bi_{1.33}V_2O_6$ also deserves a special comment. Several XRD peaks of pure $Bi_{1.33}V_2O_6$ (12.8°, 23.8°, 32.1°, 32.6°, 36.9°, 37.6°, 40.8°, 55.6° and 56°) had smaller intensities after reaction than before, while intensities of the peaks corresponding to $BiVO_4$ (18.8°, 30.5°, 40°, 46.1° and 59.5°) were increased after oxidation of propene (Fig.3). The likely recrystallization of pure $Bi_{1.33}V_2O_6$ to $BiVO_4$ under the conditions of catalytic reaction was also suggested by ESEM which showed a very peculiar streaked morphology for the used $Bi_{1.33}V_2O_6$ crystals (Fig.4). Such streaked morphology was not observed for the fresh $Bi_{1.33}V_2O_6$ sample. There was no indication from XRD that the recrystallization did not happen during reaction with the *mixtures of $Bi_{1.33}V_2O_6$ and $MoO_3$, and of $Bi_{1.33}V_2O_6$ and $\alpha$-$Sb_2O_4$.*

### 3.2.5. Origin of the synergetic effects observed with the physical mixtures

Clearly, the cooperation between the phases present in the catalysts through a migration of spillover oxygen plays an important role in the selective oxidation of propene on $Bi_4V_{2-x}Sb_xO_{11-\mu}$ system. In all cases, no other phases than those present

in the fresh catalysts were found after the catalytic reaction, meaning that the formation of a new more performant compound from the phases mixed together is not acceptable to account for the observed synergetic effects.

However, for the mixtures of $BiSbO_4$ and $MoO_3$, and of $Bi_{13}V_5SbO_{34}$ and $MoO_3$, the differences observed for the XPS atomic percentage ratios before and after reaction could be interpreted as a strong indication of a possible mutual contamination between oxides under the conditions of reaction. The variations of the XPS Bi/Mo ratio observed in the case of the mixture of $BiSbO_4$ and $MoO_3$ could result from the formation during the reaction of a bismuth molybdate compound covering the $BiSbO_4$ crystals. This hypothesis must however be discarded 1° as peaks typical of mixed Bi-Mo oxides were never observed in the Raman spectra of the used mixture of $BiSbO_4$ and $MoO_3$ and also 2° as the Sb/Bi ratio remained unchanged so discarding the possibility that the crystals of $BiSbO_4$ are covered by a compound containing Bi but no Sb (which would have resulted in a decrease of the Sb/Bi ratio). Thus, the decrease of the XPS Sb/Mo and Bi/Mo ratios must rather be correlated with a deposition of $MoO_3$ particles at the surface of $BiSbO_4$ crystals during the reaction. The hypothesis is actually supported by ESEM which showed the presence of particles at the surface of the used crystals, and by the higher relative intensities after reaction of the Raman peaks of $MoO_3$. Although not proven unambiguously, a similar deposition of $MoO_3$ particles should also very likely be considered for the mixture of $Bi_{13}V_5SbO_{34}$ and $MoO_3$.

On one hand, as such $MoO_3$ deposition could correspond to an increase of the surface developed by active $MoO_3$ crystallites, the phenomenon could have led to some improved activities for the catalysts. Such improvement was actually observed through the synergetic effects on the conversion of propene for the mixtures. However, on the other hand, with the deposition of $MoO_3$ particles on $BiSbO_4$ and $Bi_{13}V_5SbO_{34}$ crystals, the selectivities to acrolein for the mixtures of $BiSbO_4$ and $MoO_3$ and of $Bi_{13}V_5SbO_{34}$ and $MoO_3$ should thus be close to that obtained with pure $MoO_3$, but not higher. As the selectivities observed for both mixtures are far above that of pure $MoO_3$, they thus cannot be accounted by the simple deposition of $MoO_3$ particles on $BiSbO_4$ and $Bi_{13}V_5SbO_{34}$. Moreover, synergetic effects were detected between $SnO_2$ and $BiSbO_4$. At the quite low reaction temperature used, $SnO_2$ could not undergo a sublimation-deposition on $BiSbO_4$. This is a positive argument supporting that the synergy between $BiSbO_4$ and $MoO_3$ does not originate from the decoration of $BiSbO_4$ crystals by $MoO_3$, but that $BiSbO_4$ is able to improve "at distance" the performance of active phases remaining separate during the reaction.

$Bi_{1,33}V_2O_6$ had a clear tendency to recrystallize to $BiVO_4$ when it was reacted alone and likely also when it was used in mixtures with $\alpha$-$Sb_2O_4$ or $MoO_3$. In this work, pure $BiVO_4$ turned to be very active, namely more active than $Bi_{1.33}V_2O_6$, but completely non selective to acrolein. $BiVO_4$ was indeed reported to be active in ammoxidation processes [9]. And arguments indeed support that $BiVO_4$ preferentially achieves the non selective oxidation of hydrocarbons: first, the selectivity to acrolein of pure $Bi_{1,33}V_2O_6$ dropped very dramatically when increasing the temperature of reaction from 673 K to 733 K, i.e. when the formation of $BiVO_4$ is promoted; second, $BiVO_4$ was shown in the literature to perform methane oxidation and to produce

considerable amount of $CO_x$ in the oxidative dehydrogenation of propane at relatively low temperatures [10,11].

The fact that $Bi_{1.33}V_2O_6$ shows a high selectivity (92.3%) in spite of the presence of $BiVO_4$, suggests that $Bi_{1.33}V_2O_6$ succeeds to inhibit the non selective properties of $BiVO_4$. This is supported by the results obtained for the mixture of $Bi_{1.33}V_2O_6$ and $MoO_3$. In this case, a very high selectivity to acrolein (61.5%) was obtained, while pure $MoO_3$ is not selective. The inhibition of the non selective sites accounts for the lower conversion in both mixtures, as it does also for the mixtures of $MoO_3$ and $\alpha$-$Sb_2O_4$. These results thus show that 1) the formation of $BiVO_4$ should be avoided, and that 2) the synergetic effects observed in the mixtures of $Bi_{1.33}V_2O_6$ and $\alpha$-$Sb_2O_4$ and of $Bi_{1.33}V_2O_6$ and $MoO_3$ are due to cooperation "at distance" between the phases mixed together. Another argument supporting that the formation of $BiVO_4$ should be avoided is that it was shown to rapidly decompose within reduction-oxidation cycles and to have its surface rapidly covered by inactive metallic Bi [12].

### 3.2.6. Spillover oxygen donor and/or acceptor character of the phases investigated

It is clear that the remote control mechanism via the migration of Oso operates in the multiphasic $Bi_4V_{2-x}Sb_xO_{11-\mu}$ system. $BiSbO_4$ and $Bi_{13}V_5SbO_{34}$ are typical Oso donors, because they induced synergetic effects in mixtures with $MoO_3$ and $SnO_2$ (i.e. with typical Oso acceptors) but not in mixtures with a typical Oso donor like $\alpha$-$Sb_2O_4$. $Bi_{1.33}V_2O_6$ possesses a dual Oso acceptor-donor character, as it induced synergetic effects with both $MoO_3$ and $\alpha$-$Sb_2O_4$. Additionally, $BiSbO_4$ is a more powerful Oso donor than $\alpha$-$Sb_2O_4$ because $BiSbO_4$ induced more intense synergetic effects in mixture with $MoO_3$ than those observed for the mixture of $MoO_3$ and $\alpha$-$Sb_2O_4$.

### 4. CONCLUSION

Though they are very weakly active in the reaction, $BiSbO_4$ and $Bi_{13}V_5SbO_{34}$ are crucial components in the $Bi_4V_{2-x}Sb_xO_{11-\mu}$ system as they prove to be excellent Oso donors able to improve "at distance" the performance of active phases used in their presence. $Bi_{1.33}V_2O_6$ also plays an important role because it is active and selective, because its selectivity can be successfully improved under the action of a phase with a Oso donor character, and finally because it succeeds to improve the selectivity of Oso acceptor phases.

The conclusion is that the catalytic performance of the $Bi_4V_{2-x}Sb_xO_{11-\mu}$ system is directly related to the simultaneous presence of $BiSbO_4$, $Bi_{1.33}V_2O_6$ and $Bi_{13}V_5SbO_{34}$. Hence, more performant $Bi_4V_{2-x}Sb_xO_{11-\mu}$ catalysts should be obtained by applying synthesis methods promoting the simultaneous segregation of these phases from the precursor, optimizing the number and the quality of contacts between them, and avoiding the formation of non selective phases as $BiVO_4$ and $Bi_2O_3$.

156

## Acknowledgment

## REFERENCES

1.   B. Delmon, P. Ruiz, S.R.G. Carrazan, S. Korili, M.A. Vicente Rodriguez and Z. Sobalik. Stud. Surf. Sci. Catal., 100 (1996) 1.
2.   L.T. Weng and B. Delmon. Appl. Catal. A, 81 (1992) 141.
3.   C.D. Wagner, L.E. Davis, M.V. Zeller, J.A. Taylor, R.H. Raymond and L.H. Gale. Surf. Interf. Anal., 3 (1981) 211.
4.   H.R. Aghabozorg, W.R. Flavell and B.H. Sakakini. J. Catal., 1667 (1997) 164.
5.   M. El Jamal, M.D. Forissier, G. Coudurier and J.C. Vedrine, in: Proceedings of the Ninth International Congress on Catalysis, Vol. 4, Calgary, Canada, 1988, p. 1617.
6.   L. Moens, P. Ruiz, B. Delmon and M. Devillers. Catal. Lett., 46 (1997) 93.
7.   S.A. Nedil'ko and A.M. Sych. Inorg. Mater., 12 (1976) 1652.
8.   A. Ramanan, J. Gopalakrishan and C. Rao. J. Solid State Chem., 60 (1985) 376.
9.   M.-D. Lee, W.-S. Chen and H.-P Chiang. Appl. Catal. A, 101 (1993) 269.
10.  A. Corma, J.M. Lopez-Nieto, N. Paredes, M. Perez, Y. Shen, H. Cao and S.L. Suib. Stud. Surf. Sci. Catal., 72 (1992) 213.
11.  A. Cherrak, R. Hubaut, Y. Barbaux and G. Mairesse. Catal. Lett., 15 (1992) 377.
12.  W. Ueda, C.-L. Chen, K. Asakawa, Y. Moro-Oka and T. Ikawa. J. Catal., 101 (1986) 369.

157

# Synergy in Sn-Mo-Ti-O catalysts in the dehydrogenation of isopropanol to acetone

S.R.G. Carrazán, M. Jiménez, C. Martín and V. Rives*

Departamento de Química Inorgánica, Universidad de Salamanca, 37008-Salamanca, Spain

$SnO_2/MoO_3/TiO_2$ catalysts prepared by mechanically mixing $SnO_2$ and $MoO_3/TiO_2$ have been characterised by different techniques, SEM, XRD, TPR and FT-IR assessment of surface acidity; reconstruction of the (100) face (selective for oxidation processes) of $MoO_3$ at expense of the non-selective (010) face has been found. This face is responsible for the increase in the selectivity of isopropanol oxidation to acetone observed on this catalyst respect to that observed on binary $MoO_3/TiO_2$ catalysts.

## 1. INTRODUCTION

Biphasic $MoO_3$-$SnO_2$ catalysts have been studied in oxidation of alcohols and olefins [1-7]. The synergetic cooperations occurring between these phases in these reactions have been attributed to different origins, such as nature and mobility of lattice oxygen, changes in surface acidity, remote control mechanism, etc. In the oxidation of methanol to methyl formate, Ai [8] attributes these synergy effects to the distribution of acidic and basic sites on the catalyst surface, but no additional description of the surface is given, so the phases present, nor the active sites, could be identified. Weng and Wolf [9] put in evidence the difficulty in determining the absolute purity of the phases present in these type of systems. Their XPS studies showed broad and low intensity bands in the Sn XPS spectra probably due to the interaction between $MoO_3$ and $SnO_2$ by formation of $SnMoO_4$ species, although the assignment of the interaction to Sn-Mo species was only speculative. (No Sn-Mo compounds have been prepared).

$SnO_2$, with an acidity between that of $MoO_3$ and that of $TiO_2$, is useless as an oxidation catalysts by itself because of its low activity. However, mixed oxides systems combining $SnO_2$ with other metal oxides are effective for certain oxidation reaction; nevertheless, the role played by the second (or even third) component has not definitively been established.

Actually, introduction of a large specific surface area support (i.e., $TiO_2$) to these systems has proved to be useful to avoid excessive sintering of the particles during thermal treatment. The final description of this system might correspond to a complex catalyst which architecture is difficult to determine. In order to understand the catalytic performance of this catalyst, it is necessary to carry out a detailed, systematic, study of the possible cooperative effects between the different phases existing in the whole system.

The present communication deals with the physicochemical transformations occurring in a $SnO_2/MoO_3/TiO_2$ catalyst prepared by mechanically mixing $SnO_2$ and $MoO_3/TiO_2$; the catalysts have been tested by FTIR spectroscopy in the oxidative dehydrogenation of isopropanol to acetone.

## 2. EXPERIMENTAL

Mo-Ti-O catalysts were prepared by impregnation of the titania support (Degussa P25, ca. 50 % anatase) with an aqueous solution of ammonium heptamolybdate (AHM); the relative amounts of AHM and titania were chosen to obtain, after calcination at 500 °C (sample M-500) or 700 °C (sample M-700) for 3 h, solids with 2 monolayer of $MoO_3$ which corresponds to 8.8 mol $MoO_3$/mol$TiO_2$, taking into account the specific surface area of the original, unloaded titania support (ca. 50 m$^2$/g) and the area covered by one molecule of $MoO_3$, 15x10$^4$ pm$^2$ [10], that is, in this case we speak of a "geometrical" monolayer [11]. With this, one monolayer equals 4.4 mol $MoO_3$/mol $TiO_2$ (or 7.96 g $MoO_3$/100 g $TiO_2$). The Sn-Mo-Ti-O catalyst (sample MS-700) was obtained by manually grinding $SnO_2$ and Mo-Ti-O (sample M-500) [weight $MoO_3$/$SnO_2$ ratio=1] in an agate mortar for 5 min, and further calcination at 700 °C for 3h. All calcinations were carried out at open air.

Characterisation, before and after reaction, has been accomplished by powder X-ray diffraction (PXRD, Siemens D500 with Cu Kα radiation), Scanning Electron Microscopy (SEM, Digital Scanning Microscope Zeiss DSM 940), Temperature-programmed Reduction (TPR/TPD 2900 from Micromeritics), specific surface area ($S_{BET}$, Gemini instrument from Micromeritics) monitoring, and surface acidity assessment by FT-IR monitoring of pyridine adsorption using specially designed high vacuum cells with $CaF_2$ windows and self-supported disc of sample (1 cm diameter and 10-20 mg).

The reactivity of samples M-700 and MS-700 in isopropanol decomposition has been studied by FTIR spectroscopy in the same system above described to study pyridine adsorption. Isopropanol and pyridine were adsorbed at room temperature on samples previously outgassed *in situ* at 400 °C for 2h.

## 3. RESULTS AND DISCUSSION

### 3.1. Specific surface area

The specific surface areas of the pure oxides, $TiO_2$, $MoO_3$ (obtained by calcination of AHM at 500 °C under the same experimental conditions used to prepare the catalysts) and $SnO_2$, and of the mixed oxides catalysts prepared, are given in Table 1.

Table 1
Summary of specific surface areas ($S_{BET}$) and TPR results

| Sample | $S_{BET}$(m$^2$/g) | $(H_2)$exp/$(H_2)$calc* |
|---|---|---|
| $TiO_2$ | 50 | - |
| $MoO_3$ | 6 | 0.45 |
| $SnO_2$ | 4 | 1.00 |
| M-500 | 43 | 0.94 |
| M-700 | 14 | 0.95 |
| M-700(at)† | not measured | 0.74 |
| MS-700 | 26 | 0.97 |
| MS-700(at) | not measured | 0.95 |

*[experimental]/[calculated] ($Mo^{6+}$→$Mo^0$ and $Sn^{4+}$→$Sn^0$) $H_2$ consumption. †at = after test.

Decrease in $S_{BET}$ from 43 to 14 m²/g on going from sample M-500 to sample M-700 is mainly due for the rutilisation of the titania support as the calcination temperature is increased, as concluded from their PXRD diagrams. However, if calcination is performed even at the same temperature (700 °C), but after incorporation of $SnO_2$, rutilisation is somewhat hindered, thus accounting for the lower decrease in the specific surface area of the sample MS-700, 26 m²/g, and sample M-700, 14 m²/g.

### 3.2. X-ray difraction

The highest dispersion capacity of Mo-Ti-O samples prepared by impregnation of $TiO_2$ with different AHM content as determined from quantitative PXRD measurements of residual crystalline $MoO_3$ corresponds to 3.1 mol $MoO_3$/100 mol $TiO_2$, that is, 0.70 geometrical monolayers [12]. In the case of the catalyst with 2 monolayer of $MoO_3$, that is 8.8 mol $MoO_3$/100 mol $TiO_2$ (15.92 g $MoO_3$/100 g $TiO_2$), the surplus of $MoO_3$ over 3.1 mol $MoO_3$/100 mol $TiO_2$, appears as crystalline $MoO_3$, molybdite (equivalent to 5.7 mol $MoO_3$/100 mol $TiO_2$ or 10.32 g $MoO_3$ /100 g $TiO_2$).

The difractograms of samples M-700 and MS-700 before and after test are shown in
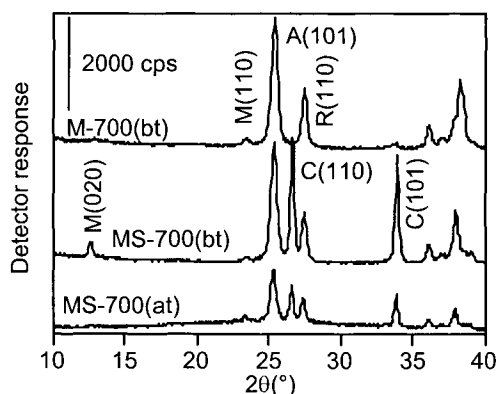


Fig. 1. PXRD difractograms of samples M-700 and MS-700, before (bt) and after test (at). A=anatase, R= rutile, C= casiterite and M= molybdite.

Figure 1. These diagrams indicate the lack of any crystalline Sn-Mo-O phase in catalyst MS-700. In addition to intense peaks due to titania support (both anatase an rutile), peaks due to molybdite-$MoO_3$ are recorded at 3.81 Å (110 planes) and 6.93 Å (020 planes), for both samples, together with diffraction peaks due to $SnO_2$ (casiterite) for sample MS-700. However, it is worth noting that the relative intensities of the peaks due to (110) and (020) planes of $MoO_3$ are inverted for sample MS-700 with respect to their intensities in pure molybdite and in sample M-700; this evidences some sort of interaction with the $SnO_2$ phase, thus giving rise to a preferential orientation of (020) planes.

No change is observed in the difractogram of the sample M-700 after the catalytic tests, but for catalyst MS-700 the line due to (020) planes has completely vanished. This result evidences the role of tin oxide on the changes occurring to the molybdenum-containing phases.

### 3.3. Scanning electron microscopy (SEM)

SEM micrographs of fresh, untested samples M-700 and MS-700 catalysts are observed in Figure 2. Comparison of both micrographs reveals modifications occurring in the molybdenum oxide crystallites after incorporating $SnO_2$.



Fig.2. SEM micrographs of catalysts M-700 (left) and MS-700 (right) before test.

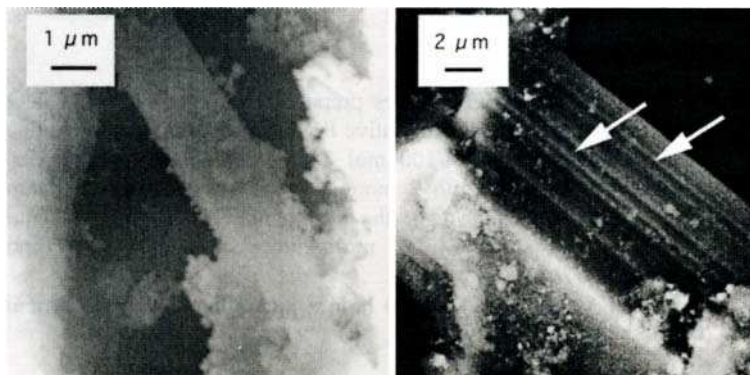The edges between the (010) basal face and the (100) lateral faces, which exhibits a sharp intersection in catalyst M-700 (and also in pure $MoO_3$, molybdite) acquired a facetted structure, by developing (100) steps on the (010) faces in catalyst MS-700.

This phenomenon is more pronounced on catalyst MS-700 after test.

### 3.4 Temperature-programmed Reduction

Reduction maxima in the TPR profiles of samples M-700 and MS-700 are recorded at different temperatures, indicating a different reducibility of the species existing in these samples because of the presence of tin compounds. A maximum at 500 °C is ascribed in the profile for M-700 to reduction of dispersed polymolybdate species, while those at 612 and 872 °C are due to reduction of dispersed and crystalline $MoO_3$, respectively [13]. The low temperature (437 °C) maximum recorded for sample MS-700 is ascribed to reduction of dispersed molybdate/polymolybdate species, the broad feature at ca. 630-720 °C to reduction of $SnO_2$, and that at 768 °C to reduction of crystalline $MoO_3$, which is at a lower temperature in the presence than in the absence of $SnO_2$. Hydrogen consumption during TPR studies, determined from the reduction profiles in the 200-900 °C temperature range, are coincident for samples M-700 and MS-700, within experimental error, with those calculated assuming total reduction of starting $Mo^{6+}$ and $Sn^{4+}$ species to $Mo^0$ and $Sn^0$, respectively. A lower (ca. 20%) $H_2$ consumption is observed for the M-700 sample after test, while for the tested MS-700 sample such a decrease in reduction amounts only 2-3%, suggesting that the Sn-free catalyst is heavily reduced by isopropanol, while catalyst MS-700 is not. For bulk $MoO_3$ the simultaneous sublimation along the TPR experiments leads to experimental values lower than the expected ones.

### 3.5 Surface acidity

Adsorption of pyridine (py) at room temperature on sample M-700 and outgassing at this same temperature gives rise to bands in the FT-IR spectrum (Fig. 3) at 1609, 1575, 1488, and
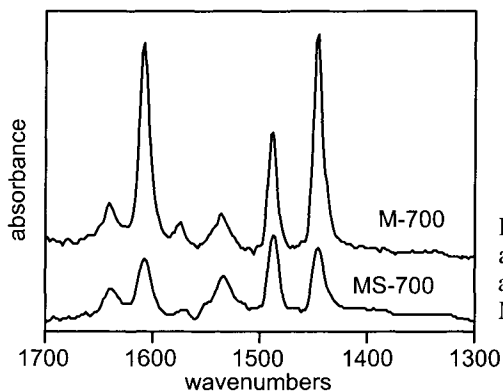


Fig. 3. FT-IR spectra recorded after adsorption and outgassing of pyridine at room temperature on samples M-700 and MS-700.

1446 cm$^{-1}$, which can be ascribed to modes 8a, 8b,19a, and 19b, respectively, of py adsorbed on surface Lewis acid sites; the bands at 1638 and 1537 cm$^{-1}$ are originated by modes 8a and 19b of pyridinium species, indicating the presence of surface Brönsted acid sites. A similar spectrum is recorded for sample MS-700, but in this case the relative intensity of the bands due to py adsorbed on surface Brönsted acid sites, with respect to those corresponding to adsorption on Lewis acid sites, is larger than for sample M-700. It should be noted that both types of surface acid sites are relatively strong in both samples, as py is not completely removed even after outgassing the samples at 400 °C.

### 3.6. Reactivity

FT-IR spectra have been recorded after adsorption of isopropanol (ISP) at room temperature, and outgassing or without outgassing the gas phase.

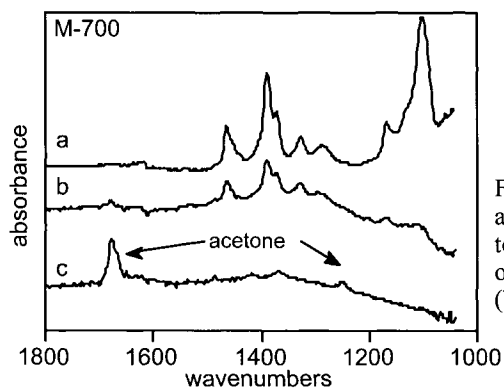In the first case, Fig. 4, adsorption of ISP at room temperature on sample M-700, and



Fig. 4. FT-IR spectra recorded after adsorption of isopropanol at room temperature on sample M-700 and outgassing at (a) room temperature, (b) 100 °C, and (c) 200 °C.

outgassing at this same temperature gives rise to a spectrum with bands characteristic of isopropoxide species at 2977 and 2884 cm$^{-1}$ (not shown) due to $\nu(CH_3)$, 1464, 1390, and 1375 (shoulder) cm$^{-1}$ due to $\delta(CH_3)$, 1325 cm$^{-1}$ due to out-of-plane $\delta(CH)$, and 1164, 1129, and 1104 cm$^{-1}$ due to coupled $\nu(C-C)/\nu(C-O)$, as a result of the dissociative adsorption of the alcohol. After heating at 200 °C two new, medium intensity bands (which were already ill defined in the spectrum recorded after heating at 100 °C) are recorded at 1675 and 1252 cm$^{-1}$, characteristic of $\nu(C=O)$ and $\nu(C-C-C)$ species of acetone, coordinated to surface Lewis acid sites. Simultaneously with development of this band, the intensity of those due to the isopropoxide species decrease. All species are easily removed after outgassing the sample above 200 °C.

A similar spectrum is recorded upon adsorption of ISP, under the same experimental conditions, on sample MS-700, Fig. 5. However, it should be noticed that in this case the presence of the carbonyl species is already detected at 100 °C, bands due to modes $\nu(C=O)$ and $\nu(C-C-C)$ being detected at 1679 and 1245 cm$^{-1}$, respectively. All bands are removed after outgassing at 200 °C, and in no case the presence of carboxylate species could be detected.

In the second case (spectra recorded without outgassing of the gas phase), adsorption of
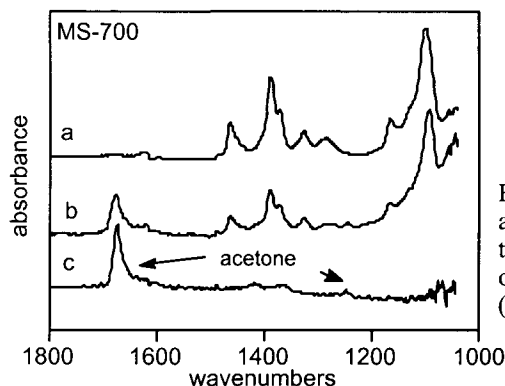


Fig. 5. FT-IR spectra recorded after adsorption of isopropanol at room temperature on sample MS-700 and outgassing at (a) room temperature, (b) 100 °C, and (c) 200 °C.

ISP at room temperature on samples M-700 and MS-700 gives rise to a FT-IR spectrum, Fig. 6, with bands at 2977, 2884 (not shown), 1465, 1386, 1372, 1250, 1159, 1130 (shoulder), and 1085 cm$^{-1}$, previously ascribed to the presence of isopropoxide species, although in this case the simultaneous presence of molecularly adsorbed, undissociated ISP is also evidenced by the $\delta(OH)$ band at 1250 cm$^{-1}$. Heating sample MS-700 at 100 °C, or sample M-700 at 200 °C gives rise to developing of new bands, Fig. 6. The bands at 3090, 3013 (not shown), and 1660 cm$^{-1}$ are characteristic of modes $\nu_{as}(=CH_2)$, $\nu(=CH)$ and $\nu(C=C)$ of propene; intense bands at 1742 and 1215 cm$^{-1}$ can be ascribed to modes $\nu(C=O)$ and $\nu(C-C-C)$ of acetone, respectively. As the bands are only very slightly shifted for both species, we should conclude that interaction with the surface should be rather weak. A concomitant increase of the intensities of the bands (especially those of acetone) is observed with the heating temperature, while those of isopropoxide and the molecular species decrease.

We have also studied the adsorption of ISP on samples where pyridine had been previously adsorbed, without removing the basic molecule. The spectra recorded are rather different from
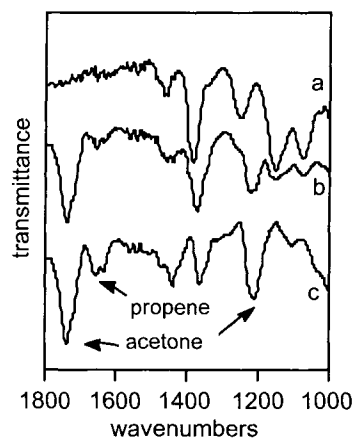


Fig. 6. FT-IR spectra recorded after adsorption of isopropanol on (a) samples M-700 and MS-700 at room temperature, (b) sample M-700 and 200 °C, and (c) sample MS-700 and 100 °C.

those previously reported, and formation of propene and acetone does not take place at low temperature, only above 300 °C a weak band at 1736 cm$^{-1}$ due to $v(C=O)$ of acetone is recorded. Similar results were obtained if the surface had been previously reduced with $H_2$; only at 300 °C weak bands due to propene and acetone were recorded.

These results suggest that both oxidative dehydrogenation of ISP to acetone, and dehydration to yield propene take place via intermediate formation of surface isopropoxide species, which are readily removed at rather low temperatures. Carbonyl species are formed via abstraction of the H atom from the alkoxide, and remains weakly coordinated to surface Lewis acid sites, being removed easily without formation of carboxylate species. Formation of acetone involves reduction of $Mo^{6+}$ species. Altogether, surface acid sites are necessary for both oxidation and dehydration of isopropanol, red-ox centers being also necessary for oxidative dehydrogenation.

## 4. CONCLUSIONS

The rather large selectivity shown by these systems is mainly due to (i) the easy reduction of the active species, as evidenced by the TPR results, and to (ii) the surface acid properties (presence of Lewis and Brönsted acid sites).

As these properties are very similar in both samples (M-700 and MS-700), which also show similar specific surface areas and nature of the active phase (new Mo-Sn-O phases have not been detected), the increase in the selectivity for acetone formation shown by catalyst MS-700 can be due to two facts: (i) developing of selective sites on $MoO_3$ through structural changes induced by $SnO_2$; it is well established that the (010) basal face and (100) lateral face of $MoO_3$ crystallites exhibit different catalytic properties, total and partial oxidation, respectively; reconstruction of $MoO_3$ crystallites only takes place in the presence of $SnO_2$, as previously observed for $MoO_3/\alpha-Sb_2O_4$ [14], ie., $SnO_2$ must be favouring oxygen spill-over

164

to "regenerate" oxygen sites on $MoO_3$ by the selective coordination of Mo atoms, typical of (100) face, at the expense of the non-selective ones of the (010) face. Alternatively, (ii)such a behaviour can be due to an effective cooperation between $MoO_3$ and $SnO_2$, thus stabilizing the active sites in a highly oxidated state [15], probably by oxygen spillover.

## Acknowledgments

## REFERENCES

1. S. Tan, Y. Moro-Oka and A. Ozaki, J. Catal. 17 (1970) 132.
2. M. Ai, J. Catal. 40 (1975) 327.
3. Y. Okamoto, K. Oh-Hiraki, T. Imanaka and S. Teranishi, J. Catal. 71 (1981) 99.
4. D. Herla, M. Sc. Thesis, Université Louvaine-la-Neuve, Belgium (1994).
5. M. Ai, J. Catal. 4 (1975) 318.
6. B. M. Reddy, K. Narsimha, C. Sivaraj and P. K. Rao, Appl. Catal. 55 (1989) L1.
7. D. Martin, P. Kaur, D. Duprez, E. Gaigneaux, P. Ruiz and B. Delmon, Catal. Today, 32 (1996) 329.
8. M. Ai, J. Catal., 83 (1983) 141.
9. T. Weng and E.E. Wolf, Appl. Catal . A: General, 96 (1993) 383.
10. T. Fransen, D.C. Van Berge and P. Mars in "Preparation of Catalysts", edited by B. Delmon, P.A. Jacobs and G. Poncelet (Elsevier, Amsterdam, 1984) p 405.
11. G. Bond, S. Flamerz and R. Shukri, Faraday Discuss. Chem. Soc., 87 (1989) 65.
12. M. Del Arco, S. R. G. Carrazán, C. Martín and V. Rives, J. Mat. Sci., 31 (1996) 1561.
13. M. Del Arco, S. R. G. Carrazán, C. Martín, I. Martín, V. Rives and P. Malet, J. Mater. Chem., 3 (1993) 1313.
14. E. M. Gaigneaux, P. Ruiz and B. Delmon, Catal. Today, 32 (1996) 37.
15. L. T. Weng and B. Delmon, Appl. Catal. A: General, 81 (1992) 141.

# On some catalytic reactions recently revisited by H₂, O₂ and NO spillover

GM Pajonk

Laboratoire d'Applications de la Chimie à l'Environnement. UMR 5634 Université Claude Bernard Lyon 1-CNRS. 43 boulevard du 11 novembre 1918. 69622 Villeurbanne France

## Introduction

Many catalytic reactions of industrial interest were, very recently, reinvestigated with the help of spillover concepts. They include: the synthesis of methanol, the water gas shift reaction, the Fischer-Tropsch synthesis, the hydrogenation of acetic acid, the isomerization of butane on sulphated Pt-zirconia, the role of $H_2$ spillover in the reduction of oxide systems-zeolite composite catalysts, and some CO and NO oxidation reactions, many $NO_x$ conversions in environmental catalysis.

This review is intended to contribute an improved understanding of complex reactions,(some of them very often and directly concern the "layman"), especially their reaction mechanisms. A large span of examples will be discussed in order to point out clearer ideas, on the role and consequences induced by the participation of a spillover phenomenon during the course of a catalytic reaction.

The choice of these selected reactions is twofold: first they are of industrial interest, if not directly industrial applications by themselves, like the methanol and water-gas shift reactions for instance, and second, in all cases they can be associated with at least what Boudart (1) recently named "model catalysts" in the sense that the necessary reductionism method used to study them at the laboratory scale, can help for understanding the many complex phenomena accompanying the reaction dynamics of catalytic systems. Spillover is one of these category of complex phenomena able, paradoxically, to simplify the description of such complicated catalytic industrial working applications.

Other reactions, especially selective oxidation as well as some acid catalyzed reactions were already discussed in relation with spillover processes in another paper (2 and references therein).

### Methanol synthesis and water-gas shift reactions

The synthesis of methanol from $CO, CO_2$ and $H_2$ mixtures represents a case history in the development of industrial chemistry since it was the second time a high pressure economical process was put into work after the well known synthesis of ammonia. Since the sixties, the low pressure-low temperature process is based on copper on alumina and zinc oxide systems (3). Up to now there is still a controversy on the different roles played by the $Cu^0$ or the $Cu^+$ surface species and the influence of the ZnO component of the multiphasic industrial catalysts. The recent review published by Spencer gives an account of the different cases where hydrogen spillover is invoked to explain the synergy encountered between copper and

zinc oxide (3 and references therein). For instance the evidence of a hydrogen spillover intervention was established from both kinetics and NMR studies. It has been shown that in the case of high pressure conditions (around 50 bars), high hydrogen to carbon monoxide and dioxide ratios (80/10/10 for example) and low conversions (high space velocities) there was no synergy effect detected during the reaction. These conditions are typically those used by ICI units. But in the reverse conditions i.e.; low pressure (10 bars), low hydrogen to carbon monoxide and dioxide (2/1 and 3/1 respectively) and high conversions close to the equilibrium values, a synergy effect was recorded which depended upon the composition of the support, especially in ZnO. The experimental results in that case were explained with the help of a hydrogen spillover from ZnO to Cu surface zerovalent atoms. However, in both experimental conditions, it was assumed that the same rate determining step was involved, hydrogenolysis of a formate species and its subsequent hydrogenation due to the hydrogen spilling atoms.

Other copper based catalysts containing either simply zirconia or under the form of the well known high temperature superconductor $YBa_2Cu_3O_7$ (noted here YBaCuO) were recently depicted by Jung and Bell and Gao and Au respectively (4,5). Jung and Bell have found that with $CO_2$ as a reactant, two forms of spillover occurred from a unique donor Cu metal towards the acceptor zirconia: a hydrogen one and formate species one (detected by FTIR means). The first one being the most important one and of an order of magnitude faster than the methanol synthesis rate itself measured by the hydrogenation of the methoxy moieties, thus it was not a rate determining step during the reaction. The second work was performed with carbon dioxide with the YBaCuO catalyst which once reduced by hydrogen displayed oxygen vacancies where $CO_2$ adsorbed, consuming the trapped electrons and re-oxidising $Cu^+$ into $Cu^{2+}$ ions. Quite the same intermediates species as above described were identified using FTIR and FT-Raman spectroscopies, among them the formate and methoxy groups. Here it was assumed that hydrogen spillover was provided through the $Cu^+$ as the donor phase to oxygen or carbon containing adsorbed species formed from the adsorbed carbon dioxide.

It is clear that the general discussion about the methanol synthesis is not yet finished , the problems of the role of the Cu metal and/or $Cu^+$ as well as that of ZnO still are subject of dispute. However the concept of spillover (chiefly that of hydrogen) has cast some light on the participation of Cu species in the presence of ZnO, indeed one must remember that while pure Cu is active in the synthesis, its combination with ZnO leads to a much more interesting catalytic system in terms of resistance to sintering and to poisons.

The low temperature water gas-shift (and also the reverse water gas-shift) reaction was studied on a series of two gold containing catalysts by Boccuzzi et al. (6). The authors prepared gold supported on titania and $Fe_2O_3$ and they first checked that gold-free titania was quite completely inactive whatever the reaction temperatures used while pure iron oxide showed activity only at high reaction temperatures. Hydrogen chemisorptions evaluated by FTIR showed that on both supported solids, a reduction of their supports-$Ti^{4+} \rightarrow Ti^{3+}$ and $Fe^{3+} \rightarrow Fe^{2+}$ respectively-took place through the finely dispersed gold particles or clusters. Spilled over hydrogen created some additional reduced cation sites of adsorption on the supports for the adsorption of CO. Beside hydrogen spillover created some so-called active OH groups. The main result was that both supported gold on titania and gold on iron oxide exhibited the same activity for the water-gas-shift even at low reaction temperatures. A redox system, analogous to that already described in the case of copper based catalysts, seemed to account for all the results obtained with the two types of catalysts.

## Fischer-Tropsch catalysis

In order to produce liquid hydrocarbons ( the so-called synthetic fuels for instance) from the synthesis mixture, namely $CO + H_2$ two great families of Fischer-Tropsch catalysts are principally described in the literature : supported  cobalt and supported iron systems. Very selective catalysts are needed giving as low methane and carbon dioxide yields as possible.

Sun et al. (7) have described  the preparation of a series of cobalt supported by silica catalysts using two different precursors: Co II nitrate (designed by N) and Co II acetate (designed by A) which were either co-impregnated or stepwise impregnated using the aqueous incipient wetness procedure and then reduced by hydrogen in TPR experiments. Different N/A weight ratios catalysts were also prepared. They discovered that the degrees of reduction of their cobalt salts were in excess to the ones calculated for all the catalysts prepared  with the two precursors. They also found that using the acetate without adjoining the nitrate resulted in a very poor reducibility. Using a mixture  $H_2/CO=2$  the N/A catalysts were found to be more active then either the N or the A ones without changing the selectivity into $CH_4$ and  $CO_2$ from one catalyst to another, the mean values of the $\alpha$ coefficient being 0.85. To interpret their experimental results the authors proposed a mechanism of reduction based on the easy reduction of the N salt (in weak interaction with the support)  into Co zero-valent which further acted as a donor phase for the production of spilled over hydrogen atoms which reduced the A salt, assumed to be in strong interaction with the support, with high efficiency this time. As a result of the spillover action, very reduced Co  as well as finely divided Co- particles  in the range of 10 nm, could be obtained for the Fischer-Tropsch synthesis.

Iron  based catalysts are very attractive for the Fischer- Tropsch synthesis as well for the water-gas shift. Sun and Datye (8) recently showed that  $Fe_2O_3$ (hematite), supported on silica and unsupported  but both containing some copper oxide CuO as a dope, could be reduced into $Fe_3O_4$ (magnetite) and Fe, due to the  easy reduction of the copper oxide into copper metal which served as spilled over hydrogen donor centres to reduce the hematite into magnetite and Fe. Without the copper dope it was much more difficult to reduce the hematite into magnetite. Moreover the  better results  obtained from $H_2$ or CO-TPR experiments were recorded with the more intimate mixing of hematite with copper oxide.

It is then clear that using  hydrogen spillover permits to fabricate more easily more efficient Fischer-Tropsch catalytic compounds.

## Acetic acid hydrogenation

It is well known that, industrially, it would be very desirable to synthesise oxygenated organic molecules such as aldehydes, alcools, esters from cheap carboxylic acids according to Rachmady and  Vannice (9). For instance acetic acetic can be hydrogenated into acetaldehyde in a selective way, and therefore can serve as a model. The authors have used supported platinum on four different oxides : silica, titania, hematite and η-alumina. The more active and selective catalyst was platinum on titania and with the exception of silica, a synergy between Pt and its support was always detected which could be explained according two concepts: the first one invoked was a support effect-metal support interaction-while the second one was the participation of hydrogen spillover from the metal to the support where the acid is adsorbed and hydrogenated. This mechanism is conceived as a long range effect,

the resulting catalytic properties of which add to those specifically pertaining to platinum alone. The authors strongly favoured this last hypothesis i.e; the intervention of hydrogen spillover to explain the synergy they observed during the hydrogenation of acetic acid.

It seems interesting to mention here two other papers dealing with hydrogenation of aromatic molecules, benzene (10) and toluene (11), on acidic supported Pt or Pd concluding to a reaction mechanism involving first the adsorption of the aromatics on the acidic support and their subsequent hydrogenation by spilled over hydrogen provided by the noble metals. Concerning the hydrogenation of benzene, Wang et al. (10) used a Pt on Y zeolite system, concluded that the more metallic sites the higher the hydrogen spillover concentration, and as a final result the more cyclohexane obtained while the more acid sites the more methylcyclopentane formed.

Kalies et al. (12) have shown by FTIR, that with zirconia from the one hand, and Pt supported by zirconia from the other, the reactivity of the formate species adsorbed on the oxide and coming from the reaction between CO and $H_2$ can be very different. The catalyst contained 0.5% in weight of Pt and was analogous to the one already described by Kalies et al (13), it showed a very poor dispersion of the metal, roughly 4% only. This meant that the surface of Pt-free zirconia is a major characteristic of the surface composition of the catalyst. On pure zirconia, the formate species could not be hydrogenated at all in the presence of dihydrogen, while in the presence of the supported catalyst it reacted to yield adsorbed methoxy groups and finally methane, probably involving two spillover steps: one dealing with hydrogen from Pt to zirconia and another concerning the methoxy groups spilling from zirconia to the metal (site transfer phenomenon). Indeed, the very poor Pt dispersion indicated that the surface presumably was constituted by large clusters of metal unevenly situated at the surface of the zirconia, hence hydrogen adatoms had to spill from the metal to the oxide to react with the formate and/or carbonate adsorbed species.

Spillover participation to a catalytic reaction is not always positive as demonstrated by Praserthdam et al. (14) for the selective hydrogenation of acetylene into ethylene on Pd-Ag deposited on γ-alumina. Indeed they identified two sites responsible for the conversion of ethylene into ethane, thus decreasing the selectivity of their catalyst. One of these is located on the Pd particles while the second one is on the alumina where ethylene is transformed into ethane by spilled over hydrogen coming from platinum across carbonaceous species adsorbed at the surface and playing the well known role of a bridge for hydrogen spillover.

**Normal butane isomerization**

The reaction of isomerisation of normal paraffin is of paramount importance for gasoline production of high octane numbers. Hydrogen is added to the reactants to suppress the formation of olefinic polymerisation and to diminish the amount of carbonaceaous species which can form as side products. Sulphated zirconia associated with platinum constitutes a model catalyst while n-butane plays the role of a model molecule.

Two types of catalysts were studied: Pt impregnated sulphated zirconia, and physical mixtures of sulphated zirconia and Pt on silica. Tomishige et al. (15) have made studies with both kinds of catalysts, first they disclosed with the chemisorption of hydrogen a $H_{ads}/Pt$ ratio of 8 instead of 1 as expected with a metal dispersion of 100%, obviously hydrogen spillover was the cause of this behaviour. Second they proposed that dihydrogen was dissociated in an homogeneous fashion by platinum into hydrogen atoms which then spills over to the sulphated zirconia and convert into a proton at a Lewis centre and thereafter is stabilised by

an nearby oxygen atom on one hand, on the second hand they can be simultaneously converted into a hydride species by capture of an electron at a Lewis acid site according to the scheme recalled by Satoh et al. (16). These two hydrogen species coexisting only in the presence of molecular hydrogen. Hydrogen spillover was thought responsible of two main results: regeneration of Bronsted acid sites and addition of the hydride species on the carbenium ion leading to the formation of isobutane through a mono-molecular mechanism. At low temperature a high partial pressure of hydrogen exerted a negative effect on the catalyst activity by favouring too much the hydride formation trough the spillover process. In conclusion the authors claimed that the proximity of the two parts of the composite catalysts was not an important condition for the isomerization reaction. Satoh et al. (16) measured the quantities of hydrogen adsorbed by platinum free sulphated zirconia and platinum supported on the sulphated oxide, they found values of $1.42 \ 10^{17}$ and $6.46 \ 10^{19}$ H-atoms per g catalyst respectively. The last value gave a H/Pt much higher than one and represented the evidence of the spillover process taking place on the metal supported catalyst. In their paper the authors quantified the rate hydrogen adsorption and found that the rate of spillover was the limiting step of the adsorption reaction.

Thus in conclusion hydrogen spillover can be involved in the additional creation of new acid sites (protonic ones) favouring the isomerisation reaction while in certain conditions it can be detrimental towards the activity of the multiphasic catalyst, an observation already discussed by the author in a previous review (17).

## H-spillover and reduction of oxides-zeolite systems

In a series of four recent papers Sachtler and his coworkers (18-21) have studied the reduction by hydrogen of physical mixtures containing hematite and various metal loaded zeolites. The metals used were Ni, Co, Pt, Rh and Pd in association with Na-ZSM5 and Na-mordenite. Their main and fundamental results were that unless the metal (noble or transition ones) containing zeolites have not been submitted to a high temperature calcination treatment, no hydrogen spillover effect was evidenced and consequently no reduction of hematite into magnetite occurred. It was only after such a treatment that the iron oxide could be reduced by hydrogen spillover. This meant, according to the authors, that mobile noble or transition-metal oxides had first to be built inside the channels of the zeolites by the calcination treatment and thereafter had to migrate out of the zeolites, to be converted into a donor phase permitting hydrogen, thereafter, to spill towards the hematite and finally reduce it. By analogy with multiphasic -selective oxidation of hydrocarbons catalysts-(2), a kind of remote control concept can also explained the above results.

These experiments showed that under the conditions used, there was no hydrogen spillover capabilities into the channels of the zeolites. Spillover proceeded only outside the zeolites, once hydrogen had reduced the noble or transition-metal oxides they initially contained in their respective porosities.

## CO and NO$_x$ catalytic conversions in environmental chemistry

Three Way Exhaust Catalysts (TWC) are now commonly used at an "industrial scale" in the sense that many hundreds of million of cars are equipped with such devices for NO$_x$, CO and unburned gasoline abatements, respectively. They consist mainly of bi-metallic noble metals (Pt-Rh for instance) associated with alumina plus ceria and/or ceria-zirconia. The role

of the ceria ion pairs $Ce^{3+}/Ce^{4+}$ has been well identified as the redox system responsible for the Oxygen Storage Capacity (OSC) exhibited by the TWC.

A thorough study of the redox properties of ceria-zirconia solid solutions (mixed oxides) loaded with Rh, Pt or Pd was published by Fornasiero et al. (22) which underlined the role of the noble metal and zirconia on the surface properties using temperature programmed techniques. Hydrogen spillover was evidenced in relation with the reducibility of the $Ce^{4+}$ ions which are involved in the OSC. Ex-chloride and ex-nitrate supported Rh on the same type of mixed oxides, Ce-Zr-O, were evaluated for their redox properties at high or low-temperatures redox recycling treatments (23-24). For both experimental conditions the detrimental influence of chloride residues on the extent of hydrogen spillover was disclosed in good agreement with more ancient published results and decreased the extent of the formation of vacancies. In addition high temperature treatments, by decreasing the amount of OH groups on which hydrogen can spill, gave the same effect then the presence of the chloride species. These results have very important consequences at the industrial stage because chloride precursors are widely used for the synthesis of these TWCs. This points out, that in order to obtain the most catalytic efficient systems, at the industry scale, it is absolutely necessary to get rid of Cl or to select other chloride-free chemicals.

Descorme et al. (25) recently studied the mechanism of the OSC on metal free Ce-Zr-O by FTIR and established that the migration of oxygen, once activated at the surface under the form of dissociated oxygen anions (involving superoxide and peroxide ions), diffused in the bulk of the solid through the oxygen vacancies.

A beautiful, very convincing and parallel work has been done by Bennett et al. (26) and Bowker et al. (27) on the redox properties of titania in the presence and in the absence of Pd using the Scanning Tunnelling Microscope (STM). A new type of SMSI effect ( Strong Metal Support Interaction ) could be detected, which here occurred in oxidizing and not in a reducing set of experimental conditions (28). Clearly this SMSI effect is detrimental to a kind of OSC of titania, an OSC similar to that exhibited by ceria containing exhaust car catalysts, since for titania it encapsulated the Pd nanoparticles. With the help of this elegant technique, the authors were able to "see in-situ" the very images of the spillover of oxygen atoms from the palladium metal to its $TiO_2$ surroundings : indeed new layers of titania were observed to grow, they were formed by the reaction of spilled over atoms of oxygen and interstitial $Ti^{3+}$ cations diffusing to the surface of the catalyst. A STM movie or this surface chemistry can be seen at web-site: www.njp.org. Though the bulk crystalline structure of titania is different from that of ceria (rutile versus fluorite), their comparable variable degrees of oxidation-reduction, $4^+/3^+$, are thought to be responsible for the two OSC they exhibit.

Oxygen spillover was also advocated by Inui et al. (29) for the oxidation of CO at low temperature, by Cu-zeolite A, containing or not a tiny amount of Rh, for fuel cell systems developed on the basis of the steam reforming processes, delivering hydrogen, carbon dioxide and a few ppm of carbon monoxide which must be selectively oxidised leaving hydrogen intact, of course. When Rh was added to the copper catalyst, its activity was greatly enhanced and attributed to oxygen spillover which participates in the redox properties of copper.

The last example of this paper on spillover, is that of the migration of $NO_x$ species, under the conditions of lean burn or diesel-engines, from the metal to the support as in the case of Pt-alumina, and its reduction into $N_2$ by a mixture of propene and oxygen and published by Arena et al. (30) and constituting a reaction model. Using DRIFT and transient experiments, the authors showed that the $NO_x$ moieties formed at the Pt surface inhibited the total oxidation of the hydrocarbons in favour of a selective oxidation reaction and yielded a mixture of

acrolein and acrylic acid, which finally selectively reduced the $NO_x$ species at low temperature. However, at higher reaction temperatures, the $NO_x$ migrated much more rapidly from Pt to alumina, and it ensued the total combustion of the hydrocarbon due to the free access to the platinum oxidized surface sites, and the formation of $NO_2$ on the alumina surface.

## Conclusions

This series of very recent results adds to the already vast amount of studies dedicated to spillover phenomena. Model reactions for industrial applications as well as applied reactions are now widely concerned by spillover which generally speaking is quite always beneficial and may play or not, the rate determining step, but it can even exert detrimental effects as discussed above in two cases. Some semi-detailed reaction networks including the role of spillover were formerly published by the author (31).

Because of the possibility of experiencing sometime, negative effects, it appears necessary to make investigations to look for the possibility of a "bad spillover" effect among all the plausible causes of these bad effects. It appears necessary to disclose if it is, at least, one of these kinds of causes, and then to suppress it as much as possible by appropriate chemical and/or physical treatments.

## REFERENCES

1. M Boudart, Topics in Catal. 13 (2000) 147
2. GM Pajonk, Appl. Catal. A :General. 202 (2000) 157
3. MS Spencer, Topics in Catal. 8 (1999) 259
4. KD Jung and AT Bell, J.Catal. 193 (2000) 207
5. LZ Gao and CT Au, J. Catal. 189 (2000) 1
6. F Boccuzzi, A Chiorino, M Manzoli, D Andreeva and T Tabakova, J. Catal. 188 (1999) 176
7. S Sun, N Tsubaki and K Fujimoto, Appl. Catal. A :General. 202 (2000) 121
8. Y Jin and AK Datye, J. Catal. 196 (2000) 8
9. W Rachmady and MA Vannice, J. Catal. 192 (2000) 322
10. J Wang, Q Li and J Yao, Appl. Catal. A :General. 184 (1999) 181
11. J Chupin, NS Gnep, S Lacombe and M Guisnet, Appl. Catal. A :General. 206 (2000) 43
12. H Kalies, N Pinto, GM Pajonk and D Bianchi, Appl. Catal. A :General. 202 (2000) 197
13. H Kalies, D Bianchi and GM Pajonk, Stud. Surf. Sci and Catal. 112 (1997) 81
14. P Praserthdam, S Phanatasri and J Meksikarin, Catal. Today. 63 (2000) 209
15. K Tomishige, A Okabe and K Fujimoto, Appl. Catal. A :General. 194-5 (2000) 383
16. N Satoh, J Hayashi and H Hattori, Appl. Catal. A :General. 202 (2000) 207
17. GM Pajonk in : Proceedings of the 2$^{nd}$ International Conference on Spillover, KH Steinberg ed., 1989, p1. Leipzig FRG.
18. OE Lebedeva, WA Chiou and WMH Sacthler, J. Catal. 188 (2000) 365
19. HY Liu, G Frohlich and WMH Sachtler, Topics in Catal. 10 (2000) 49
20. OE Lebedova, WA Chiou and WMH Sachtler, Catal. Lett. 66 (2000) 189
21. OE Lebedova and WMH Sachtler, J. Catal. 191 (2000) 364
22. P Fornasiero, J Kaspar, V Sergo and M Graziani, J. Catal. 182 (1999) 56

23. P fornasiero, N Hickey, J Kaspar, C Dossi, D Gava and M Graziani, J. Catal. 189 (2000) 326

24. P Fornasiero, N Hickey, J Kaspar, T Montini and M Graziani, J.Catal. 189 (2000) 339

25. C Descorme, Y Madier and D Duprez, J. Catal. 196 (2000) 167

26. RA Bennett, P Stone and M Bowker, Faraday Discuss. 114 (1999) 267

27. M Bowker, RA Bennett, A Dickinson, D Jame , R Smith and P Stone, 3rd International Symposium : Reaction kinetics and the development of operation of catalytic processes. Ostende, Belgium. April 22-25, 2001

28. M Bowker, LJ Bowker, RA Bennett, P Stone and A Ramirez-Cuesta, J. Molec. Catal. A : Chemical. 163 (2000) 221

29. T Inui, Y Ono, Y Tagaki and JB Kim, Appl. Catal. A :General. 202 (2000) 215

30. GE Arena, A Bianchini, G Centi and F Vazzena, Stud. Surf. Sci. and Catal. 130 (2000) 1301

31. GM Pajonk, in : G Ertl, H Knozinger and H Weitkamp (Eds.), Handbook of Heterogeneous Catalysis, VCH, New York, 1997, p 1064

# SURFACE DIFFUSION MODELLING: TRANSFER MATRIX APPROACH

A.V. Myshlyavtsev

Tuvinian Institute for Exploration of the Natural Recourses of the Siberian Branch of the Russian Academy of Science, Kyzyl, Tuva, 667007, Russia

The transfer matrix technique is shown to be very effective for studies of two-dimensional systems with various lattices. In particular, transfer matrix method can be used for simulation of the surface diffusion. The results obtained for square and honeycomb lattices are briefly discussed. The transfer matrix method seems to be the best addition to the Monte Carlo simulations.

## 1. INTRODUCTION

Surface diffusion is of considerable intrinsic interest and is also important for understanding the mechanism of surface reactions, ranging from the simplest, like recombination of adsorbed particles on surfaces to the complex processes encountered in heterogeneous catalysis [1,2]. The most direct way to describe diffusion is the molecular dynamics simulation, but this method at finite coverages take a lot of computer time.

It is well known that diffusion of chemisorbed particles occurs, as a rule, via jumps between nearest- neighbor sites and can be rather accurately described in the frameworks of the transitient state theory and lattice-gas model. Customarily, the lattice-gas models take into account lateral interactions only between nonactivated particles. However, it is obviously that the effect of the lateral interaction of an activated complex with its environment on surface diffusion can be strong for adsorbed particles with hard core [3,4].

Phenomenologically, diffusion is described by Fick's laws

$$J = -D\nabla c; \qquad \frac{\partial c}{\partial t} = div J; \qquad (1)$$

where $D$ is the chemical diffusion coefficient and $c$ is the concentration.

We will assume that surface diffusion occurs via activated jumps of particles to nearest-neighbor sites. In the framework of the lattice gas model, the chemical diffusion coefficient can be expressed as

$$D = a^2\Gamma \frac{z\,\theta}{4\,T} \frac{\partial\mu}{\partial\theta}, \qquad (2)$$

where $a$ is the lattice spacing, $z$ the number of the nearest-neighbor sites, $\mu$ the chemical potential of adparticles, $\Gamma$ the rate of jumps to one of the nearest-neighbor sites,

$$\Gamma = \nu \exp\!\left(- E_a^0 \, / \, T\right)\sum P_{A0,i} \exp\!\left[-\left(\varepsilon_i^* - \varepsilon_i\right)\!/ T\right] ,$$ (3)

$\nu$ and $E_a^0$ are the Arrhenius parameters for diffusion at low coverages, $P_{A0,i}$ the probability that a particle $A$ has an empty nearest neighbor site (with the environment being marked by the index $i$) and $\varepsilon_i\!\left(\varepsilon_i^*\right)$ the lateral interaction of a particle $A$ (an activated complex $A^*$) with its environment; the Boltzman constant is set to unity. The strict kinetic derivation of Eqs. (2) and (3) has been given in ref. [5].

To calculate the chemical diffusion coefficient the cluster approximation [2] or Monte Carlo simulation [6-8] are usually employed. This problem was shown can be also solved by the transfer matrix technique [9,10]. The latter approach is very effective especially for system with site blocking. Let us consider the main principles of the transfer matrix technique.

## 2. TRANSFER MATRIX TECHNIQUE

The transfer matrix method (TMM) is the one of the most powerful methods of the contemporary theoretical physics. This method yields an accurate solution for the one-dimensional lattice-gas model, i.e. allows to calculate the exact value of the grand partition function [11]. This technique can also be used very effectively to solve two-dimensional problem, for example to calculate phase diagrams of adsorbed overlayers [12].

Applications of TMM to simulation the rate processes with participation of adsorbed particles was offered by author [13]. In particular, TMM has been used to describe thermal desorption spectra [13,14], the effect of surface reconstruction on the apparent Arrhenius parameters for desorption [15,16] and the coverage dependence of the chemical diffusion coefficient [9,10].

To describe rate processes one should, however calculate not only thermodynamic values but also the probabilities of various arrangements of particles. For simplicity, let us consider adsorption on a square lattice with nearest-neighbor lateral interactions. The thermodynamic Hamiltonian corresponding to this model can be represented as

$$H_{eff} = \sum_{i,j} \varepsilon\!\left(n_{i,j} n_{i+1,j} + n_{i,j} n_{i,j+1}\right) - \sum_{i,j} \mu n_{i,j}$$ (4)

where $n_{i,j}$ is the occupation number of site $(i,j)$, $\varepsilon$ the energy of the nearest – neighbor lateral interactions, $\mu$ the chemical potential.

The grand partition function for the model under consideration can be calculated as follows.

The infinite square lattice is replaced by the strip of finite width $M$ along the X direction and infinite along the Y direction. The periodic boundary conditions are usually introduced along the X direction. It is rather obviously, that the two-dimensional model is reduced to the one-dimensional one with nearest-neighbor lateral interactions. The number of the site states for this new model is equal to $2^M$ (in general case this number is equal to $p^M$, where $p$ is the number of the site states for original model). Thus, the transfer matrix technique can be applied to the studies of the two-dimensional lattice-gas models as a powerful numerical

method. The reduced two-dimensional square lattice with periodic boundary conditions for $M$ = 4 is shown in Fig. 1. The possible states of the new site for $p = 2$ is shown in Fig. 2.
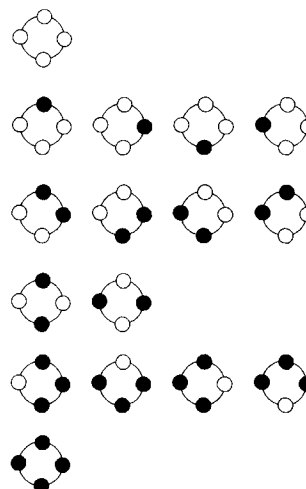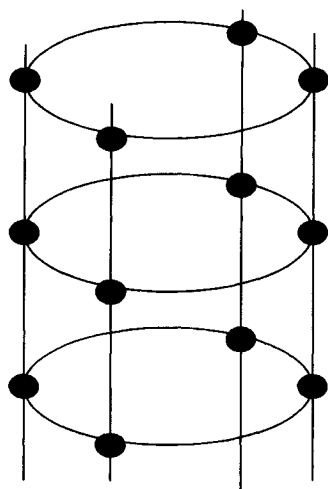


Fig. 1. The reduced square lattice for $M = 4$.



Fig. 2. The possible states of the new site for $M = 4$ and $p = 2$.

One of the most important advantages of the TMM is the possibility to calculate not only the grand partition function but also the probabilities of various arrangements of particles. The latter feature is very useful for surface diffusion and other rate processes modeling.

For model under consideration the transfer matrix elements can be written in the following form

$$T_{kl} = \exp\left[-\left(0.5u_k + 0.5u_l + v_{k,l}\right)/T\right] \tag{5}$$

where

$$u_k = \varepsilon \sum_{i=1}^{i=M} n_i^k n_{i+1}^k - \mu \sum_{i=1}^{i=M} n_i^k \tag{6}$$

$$v_{k,l} = \varepsilon \sum_{i=1}^{i=M} n_{i+1}^k n_i^l \tag{7}$$

Physically the terms $u_k$ and $u_l$ describe rings (new sites) in states $k$ and $l$ respectively and $v_{k,l}$ describes the interaction between nearest rings in states $k$ and $l$.

The main formulae of the TMM is

$$\Omega = -\frac{T}{M} \ln \lambda_{\max} \tag{8}$$

where $\Omega$ is the grand potential per one lattice site, $\lambda_{\max}$ is the largest in magnitude eigenvalue of the transfer matrix.

The general expression for the probabilities of various arrangements of adsorbed particles can be written as

$$P_{k_1 k_2 \ldots k_n} = \frac{s_{k_1, l} T_{k_1 k_2} T_{k_2 k_3} \ldots T_{k_{n-1} k_n} s_{k_n, r}}{\lambda_{\max}^{n-1} \sum_l s_{l,l} s_{l,r}} \tag{9}$$

where $s_{l,l} / s_{l,r}$ are the appropriate components of the left/right eigenvectors corresponding to the largest in magnitude eigenvalue of the transfer matrix.

The accuracy of data obtained by TMM depends on $M$ and of course on the concrete problem studied. Experience shows that TMM often yields very good results for kinetic simulations already at small $M$ like $M = 4$ or 6.

## 3. CHEMICAL DIFFUSION COEFFICIENT FOR SQUARE AND HONEYCOMB LATTICES

According to Fick's first law (1), the diffusion flux of particles is determined by the concentration gradient of these particles and the chemical diffusion coefficient. This coefficient on solid surfaces is often strongly dependent on coverage due to lateral interaction between diffusing particles. Coverage dependence of the chemical diffusion coefficient can be obtained in the framework of the lattice-gas models. These models were widely used to explore the effect of lateral interactions between adsorbed particles on the coverage dependence of the diffusion coefficient. As it was outlined in Section 2 the transfer matrix method is one of the best one for studies of the lattice-gas models. In particular, the coverage dependence of the chemical diffusion coefficient can be effectively obtained by TMM. Let us briefly discuss the results for square and honeycomb lattices.

### 3.1. Square lattice

As an example of the employing of the transfer matrix technique we will consider the singularities in the coverage dependence of the chemical diffusion coefficient in the critical vicinity of the continuous phase transitions in adsorbed overlayers. With decreasing temperature, the lateral interactions in the ground state result in the formation of ordered phases in adsorbed overlayers. The simplest phase diagram occurs for a square lattice if one takes into account only the nearest-neighbor repulsion between adsorbed particles. This lattice-gas model and related transfer matrix have been described in Section 2. As it is easily seen from Eqs. (2), (3), the coverage dependence of the chemical diffusion coefficient is defined by two factors, namely $\Gamma$ and $(\theta/T)(\partial\mu/\partial\theta)$. The first of them is kinetic, and the second one is thermodynamic. The thermodynamic analysis shows that the jump rate $\Gamma$ is smooth at critical coverages. On the other hand, the thermodynamic factor proportional to the derivative $\partial\mu/\partial\theta$ may have anomalies at critical coverages. To emphasize the physical

background of these anomalies we recall that according to statistical physics the thermodynamic factor can be represented as

$$\frac{\theta}{T}\frac{\partial\mu}{\partial\theta} = \frac{\langle N\rangle}{\langle(\delta N)^2\rangle},$$

(10)

where $\langle(\delta N)^2\rangle$ is the mean square number fluctuation. At critical coverages, fluctuations are well developed. This fact results in a cusplike minimum at critical coverage.

These conclusions were verified by the transfer matrix technique and Monte Carlo simulations. The jump rate dependence obtained by TMM on coverage is shown in Fig. 3. It
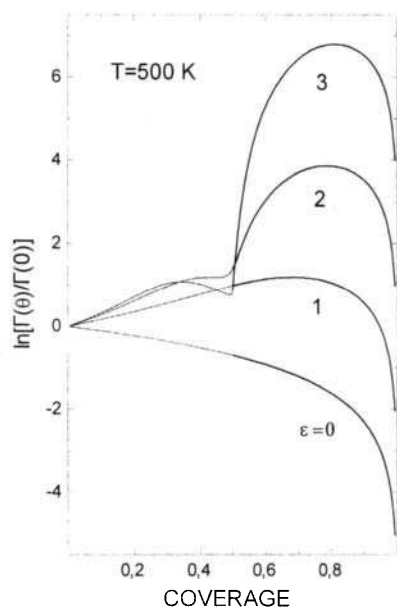


Fig. 3. The jump rate as a function of coverage for model with nearest-neighbor lateral interactions. The energies of the lateral interactions in kcal/mol are shown in figure.
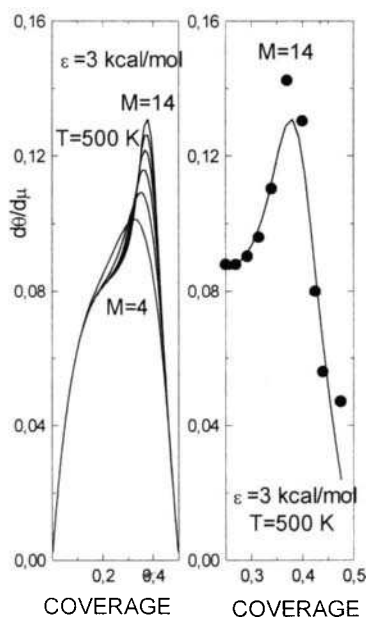
Fig. 4. Derivative $\partial\theta/\partial\mu$ as a function of coverage. The filled circles were obtained by Monte Carlo method for the 32×32 lattice.

should be noticed that the value of the jump rate at fixed coverage weakly depends on $M$ and curves are smooth near critical coverages. This is in agreement with the results of the thermodynamic analysis. The same dependencies have been also obtained by the cluster variation method [17].

The derivative $\partial\theta/\partial\mu$ as a function of coverage obtained by TMM and Monte Carlo method is shown in Fig. 4 [10]. The anomalies of one yield the corresponding anomalies of

178

the chemical diffusion coefficient. As it was shown earlier the chemical diffusion coefficient goes to zero at critical coverages and the singular part of the diffusion coefficient can be represented in the following form [18]

$$D \propto |\theta - \theta_c|^{\alpha/(1-\alpha)} \tag{11}$$

where $\alpha$ is the specific-heat exponent at fixed coverage and $\theta_c$ is the critical coverage at fixed temperature. Equation (11) is correct at $\alpha > 0$. For $\alpha = 0$ (the Ising case) the theory yields

$$D \propto 1/|\ln|\theta - \theta_c|| \tag{12}$$

It should be noticed that for systems encountered in surface science $\alpha \geq 0$. The model under consideration belongs to Ising universality class with $\alpha = 0$. The numerical results presented in Fig. 4. show that the maximum of the derivative $\partial\theta/\partial\mu$ (this maximum corresponds to the phase transition point) increases with increasing $M$. The asymptotic behavior of the maximum value of $\partial\theta/\partial\mu$ is expected to be given by

$$(\partial\theta/\partial\mu)_{max} = a + bM^{\gamma} \tag{13}$$

Our calculations indicate that $\gamma \approx 0.2$. It means that the derivative $\partial\theta/\partial\mu$ should be infinite at the critical coverage. Accordingly, the chemical diffusion coefficient should be equal to zero. Thus, the numerical results verify the thermodynamic analysis [10]. We have obtained analogous results for the hard hexagon model. In particular, our calculations yield $\gamma \approx 0.42$.

Note, the computer resources employed to obtain the TMM data presented in Fig. 4. were *much* lower compared to those used to get the Monte Carlo results.

### 3.2. Honeycomb lattice

In general, the honeycomb lattice is less investigated than the square lattice. At the same time, there are a lot of real systems with the honeycomb lattice. We will bear in the mind one of these systems, namely H/Ni(111). The hydrogen atoms are placed on the hollow sites of the Ni(111) [19]. The nearest-neighbor lateral repulsion is very strong (more than 20 kcal/mol) and at not very high temperatures we may assume that this interaction is infinite.

Thus, we will consider the honeycomb lattice-gas model with infinite nearest-neighbor repulsion. We also take into account the next-nearest-neighbor lateral interactions in the ground state and infinite nearest-neighbor repulsion in the activated state. The latter interaction has not an effect on the thermodynamic properties but as we will see below one has a strong impact on the coverage dependence of the chemical diffusion coefficient. As it was shown earlier the next-nearest-neighbor lateral interaction is also repulsion for system under consideration. The existence of two kinds of the competing lateral interactions yields the complex phase diagram. For given model, there are two ordered structure, namely (2×2) and (1×1) at $\theta = 0.25$ and $\theta = \theta_{max} = 0.5$ respectively [19]. However, our results indicate that, at the least, one ordered phase exists besides those. This new phase completes at $\theta = 0.375$ and has more complex elementary cell.
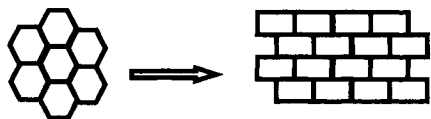
Fig. 5. The transformation of the honeycomb lattice to the rectangular lattice.
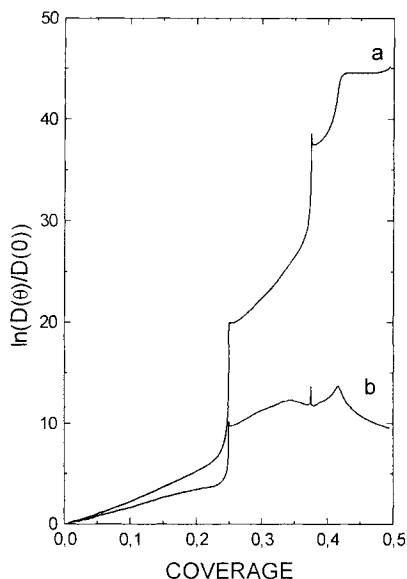
The employing of the transfer matrix method for the honeycomb lattice is more complex than for the square lattice. The first step is the transformation of the honeycomb lattice to the rectangular one. This step is shown in Fig. 5. Note, the lattice should be divided into even and odd rows as the transfer matrix "even-odd" is distinguished from the transfer matrix "odd-even". Equations (2) and (3) were used for calculation of the coverage dependence of the chemical diffusion coefficient. The main expressions of the transfer matrix method given in Section 2. also stay valid.

The results obtained by the transfer matrix method are shown in Fig. 6. The sharp peaks at $\theta = 0.25$ and $\theta = 0.375$ respect to "ideal" ordered structures which take place for our model. The more smooth maximum nearly $\theta \approx 0.41$ on curve "b" has another origin and directly connects with the infinite lateral repulsion in the activated state. The chemical diffusion coefficient tends to infinity at $\theta \to \theta_{max}$ if we do not take into account the lateral interaction in the activated state and tends to zero at $\theta \to \theta_{max}$ in the opposite case. The curves presented in Fig. 6. Demonstrate that site bloking is a significant effect which needs to be considered in the interpretation of diffusion experiments on surfaces.



Fig. 6. Chemical diffusion coefficient as function of the coverage calculated at T=500 K, $\varepsilon_{nnn}$=5 kcal/mol. (a) without lateral interactions in the activated state; (b) with infinite lateral interactions in the activated state.

*The results obtained allow us to conclude that the transfer matrix approach is very effective for studies of the chemical diffusion coefficient for two-dimensional lattice-gas models with ordered structures and site blocking.*

*It should be noticed that the transfer matrix method is exact for semi-infinite lattices and seems to be the best addition to the Monte Carlo simulations.*

## REFERENCES

1. R. Gomer, Rep. Prog. Phys., 53 (1990) 917
2. V.P. Zhdanov, Elementary Physicochemical Processes on Solid Surfaces, Plenum, New York,1991.
3. V.P. Zhdanov, Surf. Sci. 257 (1991) 63

180

4. J.T. Goldstein, G. Ehrlich, Surf. Sci. 420 (1999) 1.
5. V.P. Zhdanov, Surf. Sci., 149 (1985) L13.
6. C. Uebing and R. Gomer, J. Chem. Phys. 95 (1991) 7648.
7. C. Uebing and R. Gomer, Surf. Sci., 317 (1994) 165.
8. C. Uebing and R. Gomer, Surf. Sci., 381 (1997) 33.
9. A.V. Myshlyavtsev and V.P. Zhdanov, Surf. Sci., 291 (1993) 145.
10. A.V. Myshlyavtsev, A.A. Stepanov, C. Uebing and V.P. Zhdanov, Phys. Rev. B, 52 (1995) 5977.
11. R.J. Baxter, Exactly Solved Models in Statistical Mechanics, Academic, London, 1982.
12. N.C. Bartlet, T.L. Einstein and L.D. Roelofs, Phys. Rev. B, 34 (1986) 1616.
13. A.V. Myshlyavtsev and V.P. Zhdanov, Chem. Phys. Lett., 162 (1989) 43.
14. A.V. Myshlyavtsev and V.P. Zhdanov, Langmuir, 9 (1993) 1290.
15. A.V. Myshlyavtsev and V.P. Zhdanov, J. Chem. Phys., 92 (1990) 3909.
16. A.V. Myshlyavtsev and M.D. Myshlyavtseva, Phys. Low-Dim. Struct., N 9/10(1998) 55.
17. A. Danani, R. Ferrando, E. Scalas and M. Torri, Surf. Sci., 409 (1998) 117.
18. M. S. Veshchunov, Phys. Lett. A., 169 (1992) 483.
19. K. Nagai, Surf. Sci., 136 (1984) L14.

# A simple model to describe electrochemical promotion of catalysis

Ian S. Metcalfe[*]

School of Chemical Engineering, University of Edinburgh, Edinburgh EH9 3JL, UK

A simple model to describe the reversible electrochemical promotion of supported metal catalysts has been formulated. This model is derived from first principles and allows for the presence of two forms of catalyst surface oxygen, one ionic and one neutral. Both forms of surface oxygen are able to undergo charge-transfer reactions with the solid-electrolyte ion-conducting support. The ionic oxygen is assumed to be the only ion present with a significant surface coverage and, as such, dictates the properties of the catalyst surface double layer. Using this basis thermodynamic relationships governing the chemical potentials of the catalyst surface oxygen species are derived for the case of equilibrium between ions in the support and on the surface of the catalyst. By considering a simple reaction mechanism that involves a charged transition state and accounting for the effect of long-range electrostatic interactions it is possible to express reaction rates as a function of applied overpotential.

## 1. INTRODUCTION

It has been shown by Vayenas and co-workers that when an active catalyst, in the form of an electrode in a solid-electrolyte electrochemical cell, has small currents of ions supplied to it or removed from it, there can be a dramatic change in the activity of the catalyst. Such an effect has been termed the non-Faradaic electrochemical modification of catalytic activity (NEMCA). Electrochemical promotion, or NEMCA, has been observed for over 50 catalytic reactions (a number of reviews exist [1, 2, 3]) performed over a number of metal catalysts with differing supports [4] including oxygen-ion conductors, sodium-ion conductors, proton conductors and fluorine-ion conductors. Electrochemical promotion has also been observed in the case of a titania mixed ionic-conducting and electronic-conducting support [5]. The effect has been explained in terms of a modification of the work function of the electrode catalyst as a result of changes in the electrode overpotential; these changes in the work function have been confirmed by the use of a Kelvin probe [6]. It has been found that [6],

$$\eta = \Delta\Phi \tag{1}$$

where $\eta$ is the applied overpotential and $\Delta\Phi$ is the change in electron extraction potential of the catalyst. Any imposed overpotential is reflected in a change in the macroscopically determined work function (determined with a Kelvin probe and equal to $e\Delta\Phi$ where $e$ is the charge on an electron). It has been postulated that the work function of the catalyst is changed by an electrochemically induced oxygen species, much less reactive and more ionic than

[*] Present address: Department of Chemical Engineering, UMIST, PO Box 88, Manchester, M60 1QD, UK

chemisorbed oxygen, which spills over the catalyst surface. This change in work function modifies the kinetic behaviour of the catalyst and, in general, the new reaction rate, $R$, can be related to the overpotential by an equation of the form [e.g. 1],

$$\ln\frac{R}{R^0} = \alpha\frac{e(\Delta\Phi - \Delta\Phi*)}{kT} \qquad (2)$$

where $k$ is the Boltzmann constant, $R^0$ is the open-circuit reaction rate and $\alpha$ and $\Delta\Phi*$ are empirically determined constants.

In other work Metcalfe and co-workers [7, 8, 9] have studied the behaviour of a platinum electrode both in air and under reaction conditions. They found that the change in electron extraction potential was related to the overpotential (within the range of investigation), however, the two were not equal, with

$$\Delta\Phi = \xi\eta \qquad (3)$$

where $\xi$ depends upon operating conditions and electrode morphology. As with the work of Vayenas, reaction rate modifications were observed and obeyed Equation (2). Imbihl et al. [10] investigated the variation of extraction potential with applied overpotential for electrodes prepared in their own laboratory and electrodes prepared in the laboratory of Vayenas and coworkers in Patras. They did indeed find Equation (1) to be valid for the Patras electrodes but found that their own electrodes showed no change in extraction potential under similar conditions.

The purpose of this paper is to derive from first principles a framework for understanding and interpreting catalytic behaviour in the presence of ionic spillover from a support to a metal catalyst. As an example, a metal supported on an oxygen-ion-conducting support will be considered. The characteristics associated with reaction rate modification will then be predicted by using transition state theory and considering the role of long-range electrostatic interactions in the absence of any short-range effects.

## 2. THERMODYNAMIC CONSIDERATIONS

Let us consider a working electrochemical cell consisting of metal electrodes deposited upon an oxygen-ion conducting support. The electrochemical potential of electrons associated with either metal electrode, $\bar{\mu}_e$, can be related to the inner or Galvani potential of the electrode, $\phi$, and the chemical potential of the electrons, $\mu_e$,

$$\bar{\mu}_e = \mu_e - e\phi \qquad (4)$$

This potential can be split into a surface potential, $\chi$, and an outer potential or Volta potential, $\Psi$,

$$\phi = \chi + \Psi \qquad (5)$$

The work function, $e\Phi$, where $\Phi$ is the electron extraction potential, is defined by,

$$e\Phi = -\mu_e + e\chi \tag{6}$$

If an adsorbate, such as oxygen, is introduced onto the metal surface electron exchange with the metal may occur. As oxygen is electrophilic, there will be a tendency for electrons to be donated from the metal to the surface oxygen. Here, for the purposes of illustration, we will consider only two adsorbed oxygen species, neutral $O$ atoms and $O^{2-}$ oxygen ions, to have significant coverages. We will assume that adsorbed ionic oxygen is in equilibrium with the oxygen ions of the support as a result of fast spillover processes,

$$\bar{\mu}_{O^{2-},\text{supp}} = \bar{\mu}_{O^{2-}} \tag{7}$$

where $\bar{\mu}_{O^{2-},\text{supp}}$ is the electrochemical potential of the oxygen ions associated with the support and $\bar{\mu}_{O^{2-}}$ is the electrochemical potential of the oxygen ions on the catalyst surface.

The energy required to remove an electron from the metal and hold it on the surface in the form of an oxygen ion depends upon the surface potential barrier, $\chi$, and any lateral interactions between the ions (or more correctly dipoles), $V_{lat,O^{2-}}$. We can relate the potential of electrons associated with the metal, $\phi$, to the potential of electrons associated with the oxygen ions, $\phi_{O^{2-}}$,

$$\phi = \phi_{O^{2-}} + \chi + V_{lat,O^{2-}} \tag{8}$$

provided that electrons must cross the entire surface potential barrier on creation or destruction of an $O^{2-}$ ion (this is true if $O^{2-}$ ions are the only ions present in significant amounts).

Hence the electrochemical potential of surface oxygen ions is given by,

$$\frac{1}{2}\bar{\mu}_{O^{2-}} = \frac{1}{2}\mu_{O^{2-}} + e\chi + eV_{lat,O^{2-}} - e\phi \tag{9}$$

Consider the case of the electrode potential being measured relative to a fixed-potential reference electrode. On polarisation of the cell, the electrochemical potential of oxygen ions cannot be modified because of equilibrium with the support,

$$e\eta = \frac{1}{2}\Delta\mu_{O^{2-}} + e\Delta\chi + e\Delta V_{lat,O^{2-}} \tag{10}$$

and the electrode overpotential is equal to the change in electrode potential. To proceed further we need to investigate how each of the terms of the right-hand side of Equation (10) depend on the coverage of oxygen ions.

For a Langmuir adsorption isotherm (i.e. no lateral interactions - as lateral interactions are accounted for elsewhere in Equation (10) - and similar energetics for all sites), it can easily be shown that [11],

184

$$\Delta\mu_{O^{2-}} = kT \ln \frac{\theta_{O^{2-}}}{\theta_*} \frac{\theta_*^0}{\theta_{O^{2-}}^0}$$ (11)

where the superscript '0' is used to represent an initial catalyst state, $\theta_i$ is the coverage of the $i$th species and * refers to vacant sites.

We may express changes in the surface potential in terms of changes in ionic coverage through the Helmholtz Equation. As doubly-charged oxygen ions are the only ions with any appreciable coverage,

$$e\Delta\chi = \frac{(\sigma - \sigma^0)\mu}{2\varepsilon_0} = \frac{Ne\mu}{\varepsilon_0}\left(\theta_{O^{2-}} - \theta_{O^{2-}}^0\right)$$ (12)

where $N$ is the density of surface sites, $\sigma$ is the surface charge density, $\varepsilon_0$ is the vacuum permittivity and $\mu$ is the dipole moment of the oxygen ion.

We take account of the potential energy of an ion (or more correctly a dipole) as a result of lateral interaction with all other surface ions or dipoles. By considering a hexagonal array of oxygen ions, with $a_{O^{2-}}$ being the separation distance of the dipole charges for the oxygen ion (assumed to be much less than the distance between individual dipoles) and $r_{O^{2-}}$ being the effective ionic radius of the oxygen ion, we can show from simple electrostatic arguments that the lateral interaction potential between ions is given by [11],

$$e\Delta V_{lat,O^{2-}} = \frac{Ne\mu}{\varepsilon_0} \frac{\pi\sqrt{3}}{16} \frac{a_{O^{2-}}}{r_{O^{2-}}}\left(\theta_{O^{2-}}^{3/2} - \theta_{O^{2-}}^{0\ 3/2}\right)$$ (13)

We may proceed with a very simplistic analysis. If coverages of oxygen ions are neither very low or very high (i.e. intermediate coverages) such that logarithmic terms in the expression for oxygen-ion chemical potential can be neglected relative to other terms in Equation (10), then,

$$\Delta\mu_{O^{2-}} \approx 0$$ (14)

In addition, if oxygen-ion coverages are low enough that lateral dipole-dipole interactions can be ignored, Equation (10) becomes,

$$e\eta \approx e\Delta\chi$$ (15)

and we recover the one-to-one relationship between applied overpotential and change in surface potential that has been found experimentally by Vayenas and coworkers [6]. However, we note here that this relationship is not generally applicable but is only valid if there is equilibrium between oxygen ions in the electrolyte support and on the catalyst surface, intermediate oxygen-ion coverages and no lateral interaction between surface ions.

## 3. REACTION RATE MODIFICATION

Let us consider a reaction between adsorbed surface species,

$$A + B \rightarrow C \hspace{4cm} \text{(Reaction 1)}$$

where either $A$ or $B$ could be atomic surface oxygen but do not need to be. Vayenas [e.g. 1], has suggested that the surface reaction rate may depend upon a rate-determining step involving electron transfer between the catalyst and an adsorbed reactant, in this case either $A$ or $B$. Here we use this idea of the importance of electron transfer to or from the reactants to develop a simple reaction rate model based on transition state theory. Oxygen ion supply or removal from the surface is considered to modify equilibria involving electron supply or removal by altering the surface potential of the catalyst and modifying the potential of electrons associated with the surface $O/O^{2-}$ redox couple, hence only long-range electrostatic interactions are invoked to describe rate modification.

Reaction 1 can proceed in the absence of charge transfer with the catalyst or other adsorbates, through the following fundamental steps. The reactants are in equilibrium with a reactive transition state, $AB$,

$$A + B \Leftrightarrow AB \hspace{4cm} \text{(Reaction 2)}$$

with the rate of decomposition of the transition state into the product being the rate-determining step,

$$AB \rightarrow C \hspace{4cm} \text{(Reaction 3)}$$
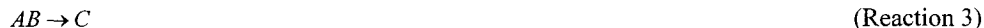
Now let us consider a reaction proceeding through a negatively-charged transition state. We explain the modified reaction rate in terms of a modification in the coverage of the charged transition state formed by the reaction of $A^-$ with $B$, $A^-B$, or of $A$ with $B^-$, $AB^-$ (we restate our assumption that the coverage of such charged transition states is much lower than that of oxygen ions and therefore their effect on the properties of the surface double layer may be neglected). There are two sources of electrons for the modification of reaction rate, the catalyst and adsorbed oxygen ions themselves. (Vayenas and coworkers have defined an electrophilic reaction as one promoted by a greater availability of electrons from the metal catalyst as determined by the surface potential. Note that a negatively-charged transition state is formally different from an electrophilic reaction because of the possibility of electron donation from the adsorbed $O/O^{2-}$ redox couple as well as the metal). For the purposes of illustration let us suppose that the species $A$ equilibrates with electrons from the catalyst to form $A^-$ while the species $B$ equilibrates with surface oxygen ions to form the species $B^-$. Hence we have two reaction schemes,

$$A + e^- \Leftrightarrow A^- \hspace{4cm} \text{(Reaction 4)}$$

$$A^- + B \Leftrightarrow A^-B \hspace{4cm} \text{(Reaction 5)}$$

$$A^-B \rightarrow C + e^- \hspace{4cm} \text{(Reaction 6)}$$

186

and,

$$B + \frac{1}{2}O^{2-} \Leftrightarrow B^- + \frac{1}{2}O \qquad \text{(Reaction 7)}$$

$$A + B^- \Leftrightarrow AB^- \qquad \text{(Reaction 8)}$$

$$AB^- \rightarrow C + e^-_{surf} \qquad \text{(Reaction 9)}$$

$$e^-_{surf} + \frac{1}{2}O \rightarrow \frac{1}{2}O^{2-} \qquad \text{(Reaction 10)}$$
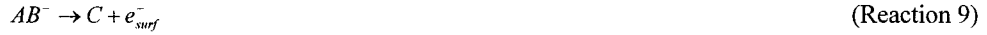
where $e^-_{surf}$ is an electron associated with the metal surface rather than the metal bulk. (Here we consider $A^-B$ and $AB^-$ to have distinct chemical identities, however, we could equally well consider them to be chemically identical but analysis would be much more complex in this case as the transition state could not be in equilibrium with all of the reactants under closed-circuit operation.)

We now consider how coverages of $A^-B$ and $AB^-$ depend upon overpotential. Provided that the chemical potentials of surface $A$, $B$ and neutral oxygen are not modified, i.e. gas-phase chemical potentials are constant (differential reactor operation) and there are fast adsorption and desorption processes, we can show that [12],

$$\Delta\mu_{A^-B} = e\Delta\phi_{A^-B} - e\Delta\phi \qquad (16)$$

where $\phi_{A^-B}$ is the potential of electrons associated with the $A^-B$ species. After Equation (11), the change in the chemical potential of $A^-B$ is given by,

$$\Delta\mu_{A^-B} = kT \ln \frac{\theta_{A^-B}}{\theta_*} \frac{\theta_*^0}{\theta_{A^-B}^0} \qquad (17)$$

However, the change in potential difference between electrons associated with the $A^-B$ species and the metal depends upon changes in the surface potential and changes in the potential associated with lateral interactions. To form the $A^-B$ species an electron need not cross the entire double-layer formed by the ionic oxygen dipoles provided that the charge separation for the $A^-B$ species is less than that for the ionic oxygen. As the lateral interaction potential of a surface $A^-B$ dipole depends linearly on the separation distance of the dipole charges, $a_{A^-B}$, the average electric field experienced by the dipole within the double layer is approximately constant [12] and,

$$e\Delta\phi_{A^-B} - e\Delta\phi = -\frac{a_{A^-B}}{a_{O^{2-}}} \left( e\Delta\chi + e\Delta V_{lat,O^{2-}} \right) \qquad (18)$$

Using Equations (10), (16), (17) and (18),

$$eΔ\phi_{A^-B} - eΔ\phi = kT \ln \frac{\theta_{A^-B}}{\theta_{A^-B}^0} \frac{\theta_*^0}{\theta_*} = -\frac{a_{A^-B}}{a_{O^{2-}}} \left( e\eta - \frac{1}{2} Δ\mu_{O^{2-}} \right) \tag{19}$$

The rate of Reaction 6 is proportional to the coverage of the $A^-B$ species and if Equation (14) is valid, and the coverage of vacant sites is approximately constant, we obtain, using Equation (19),

$$r_6 = r_6^0 \frac{\theta_{A^-B}}{\theta_{A^-B}^0} \approx r_6^0 \exp\left\{ -\frac{a_{A^-B}}{a_{O^{2-}}} \frac{e\eta}{kT} \right\} \tag{20}$$

We may consider the modification of the rate of Reaction 9 in a similar manner, obtaining,

$$r_9 = r_9^0 \frac{\theta_{AB^-}}{\theta_{AB^-}^0} \approx r_9^0 \exp\left\{ \frac{a_{O^{2-}} - a_{AB^-}}{a_{O^{2-}}} \frac{e\eta}{kT} \right\} \tag{21}$$

Any reactions which do not depend upon charge transfer with the metal or the oxygen redox couple, i.e. take place between neutral adsorbed species, will be unaffected by electrode polarisation.

For a negatively-charged transition state at negative overpotentials Reaction 6 may dominate as a result of the reduced surface potential and the increased ease of donation of electrons from the metal. At positive overpotentials Reaction 9 may dominate as a result of electron donation from oxygen ions through Reaction 7. Figure 1 shows the approximate form of the rate versus overpotential behaviour with the reactions requiring electron transfer being much slower than the reaction which does not require electron transfer under open-circuit conditions. Reaction rate increases at both positive and negative overpotentials as a result of electron donation from the $O/O^{2-}$ redox couple and the metal. Note that the position in the double layer of the charge associated with the transition state influences the kinetic behaviour.

For reactions involving positively-charged transition states a similar analysis may be performed. However, it can be shown [12] that once more the reaction rate will eventually increase for both large positive and negative overpotentials. Importantly, this overpotential-reaction rate behaviour for both negatively- and positively-charged transition states is similar to that observed in many experimental studies [e.g. 1, 2] where reaction rate is seen to increase both at positive overpotentials and negative overpotentials.
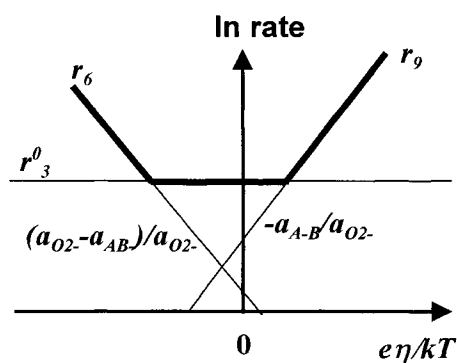


Fig. 1. Schematic of rate versus overpotential in the case of a negatively-charged transition

188

## 4. CONCLUSIONS

A simple model to describe the reversible electrochemical promotion of supported catalysts has been formulated. This model is derived from first principles and allows for the presence of two forms of surface oxygen, one ionic and one neutral. The ionic oxygen is assumed to be the only ion present with a significant surface coverage and, as such, dictates the properties of the catalyst surface double layer. Using this basis thermodynamic relationships governing the chemical potentials of the catalyst surface oxygen species are derived. It is shown that the catalyst surface potential will change by an amount equal to the applied overpotential for a system satisfying the following conditions, equilibrium between oxygen ions in the electrolyte support and on the catalyst surface, intermediate oxygen-ion coverages and no lateral interaction between surface ions. By considering a simple reaction mechanism that involves a charged transition state and accounting for the effect of long-range electrostatic interactions it is possible to express reaction rates as a function of applied overpotential. Electron donation and acceptance from the metal catalyst and the surface $O/O^{2-}$ redox couple are both considered. It is shown that under certain conditions reaction rates are predicted to increase on application of both negative and positive overpotentials (for both positively-charged and negatively-charged transition states) in agreement with many experimental studies [e.g. 1, 2].

## 5. REFERENCES

[1]     C. G. Vayenas, S. Bebelis, I. V. Yentekakis and H. -G. Lintz, Catalysis Today **11**, 303-442 (1992).
[2]     C. G. Vayenas, M. M. Jaksic, S. Bebelis and S. G. Neophytides, in 'Modern Aspects of Electrochemistry' (P. Horsman, B. E. Conway and R. E. White, Eds), Volume 29, p. 57, Plenum Press, New York, 1996.
[3]     C. G. Vayenas and S. G. Neophytides, in 'Catalysis', Volume 12, Chapter 6, The Royal Society of Chemistry, Cambridge 1996.
[4]     S. Bebelis, M. Makri, A. Buekenhoudt, J. Luyten, S. Brosda, P. Petrolekas, C. Pliangos and C. G. Vayenas, Solid State Ionics, **129**, 33-46 (2000).
[5]     C. G. Vayenas, S. Bebelis and S. Ladas, Nature (London) **343**, 625 (1990).
[6]     C. Pliangos, I. V. Yentekakis, S. Ladas and C. G. Vayenas, J. Catal. **159**, 189 (1996).
[7]     D. A. Emery, P. H. Middleton and I. S. Metcalfe, Surf. Sci. **405**, 308-315 (1998).
[8]     D. A. Emery, R. J. C. Luke, P. H. Middleton and I. S. Metcalfe, J. Electrochem. Soc. **146**, 2188-2193 (1999).
[9]     D. A. Emery, P. H. Middleton and I. S. Metcalfe, J.Electrochem. Soc. **146**, 2194-2198 (1999).
[10]    J. Poppe, S. Völkening, A. Schaak, E. Schütz,, J. Janek and R. Imbihl, Phys. Chem. Chem. Phys. **1**, 5242 (1999).
[11]    I. S. Metcalfe, J. Catal. (accepted).
[12]    I. S. Metcalfe, J. Catal. (accepted).

# Electronic Processes in Hydrogen Spillover

Jean-Marie HERRMANN

Laboratoire de Photocatalyse, Catalyse et Environnement (CNRS,IFOS), Ecole Centrale de Lyon, BP 163 , 69131 Ecully-cedex (France) ; e-mail : jean-marie.herrmann@ec-lyon.fr

H spillover has been put in evidence by electrical conductivity measurements on metal catalysts deposited on semiconductor oxides through the experimental law : $\sigma = a\, P_{H2}^{1/2} + b$ , whose coefficients a and b could be explicited : slope a is proportional to the metal dispersion and the ordinate at the origin b to the relative electron enrichment of the metal. A similar law exists under illumination for photoconductivity and accounts for the bifunctional character of $M/TiO_2$ photocatalysts. Various examples of catalytic reactions involving spilt over hydrogen are presented, especially in photocatalysis, since it operates at room temperature. These reaction concern Alkane-Deuterium Isotopic Exchange (ADIE), alcohol photocatalytic dehydrogenation, photocatalytic hydrogen transfer from alcohols to unsaturated compounds and eventually *in situ* photocatalytic $H_{0.93}MoO_3$ bronze formation.

## 1. INTRODUCTION

The electrical conductivity of a n-type semiconductor powder can be written as: $\sigma = A\,[e^-]$, where $[e^-]$ is the concentration of quasi-free electrons and A is a textural parameter which depends on the compression of the powder and on the number and quality of contact points between particles (1). In a biphasic sample, the overall conductivity of the solid becomes governed by the more conducting component above a certain percentage, called the percolation threshold (2). It corresponds to a minimum relative amount above which the electrical conductivity can be established through preferential paths along the sample constituted exclusively by the more conductive minority phase. It has been estimated to be close to 40% for a mixture of oxides of similar texture (particle size and shape) (3). Such a "surface percolation threshold" problem has been previously analysed for titania-deposited Pt (1,4). For $Pt/TiO_2$ catalysts with metal loadings as high as 10 wt%, one could have expected an increase of conductivity because of a possible improvement of the surface conductivity and of the quality of the intergranular contact points. Actually, the reverse was observed with a decrease in conductivity (4) or in photoconductivity (5) when Pt% was increased from 0 to 10%. This was explained by an electron transfer from titania to Pt, induced by the alignment of the Fermi levels of both phases. These two examples illustrate the fact that in a supported catalyst the electrical conductivity is mainly that of the support, which is in electronic interaction (i) with the supported phase, presently a metal, and (ii) the reactant phase.

Therefore, electrical conductivity is a precious tool for detecting species spilt over from a solid phase to another one as examplified by the various following examples, provided that the support is not an insulator. All the supports tested such as titania, ceria, zinc oxide, were n-type semiconductors (6).

## 2. EXPERIMENTAL

### 2.1. Catalysts preparation and characterization

The various deposited metal catalysts were prepared by the impregnation method, followed by drying, reduction by hydrogen at 480 °C, unless otherwise stated. The metal deposits were characterized by hydrogen chemisorption, $H_2$-$O_2$ titrations and electron microscopy.

### 2.2. Electrical conductivity measurements

The catalyst was placed between two platinum electrodes where it was slightly compressed (1kgf/cm$^2$ i.e. ca. 10$^5$ Pa) to ensure (i) good electrical contacts between the grains without modifying the texture and (ii) a full gas-solid interaction at all the surface. To control the temperature, both electrodes were soldered to thermocouples whose wires were also used, when short-circuited, to determine the electrical conductivity $\sigma$ of the powder sample by the given formula :

$$\sigma = \frac{1}{R} \times \frac{t}{S}$$

where $R$ is the electrical resistance measured with an ohmmeter (Kontron, Model DMM 4021) for $1 \leq R \leq 2 \times 10^6$ ohm and with a teraohmmeter (Guildline Instruments Model 9520) for $10^6 \leq R \leq 10^{14}$ ohm and where $t/S$ is the geometrical factor including the thickness $t$ (ca. 4.5 mm) and the cross sectional area $S$ of the circular electrodes whose diameter is equal to 1.00 cm. A general description of this static cell has been given elsewhere (1).

## 3. RESULTS

### 3.1. Spillover in conventional heterogeneous catalysis

#### 3.1.1. Hydrogen chemisorption at room temperature.

The electrical conductivity of a metal catalyst supported on a semiconductor oxide increases with the hydrogen pressure at room temperature, which can be accounted for by the following steps and equations :

- dissociative chemisorption of $H_2$ on the metal:

$$H_2(g) + 2M_s \Leftrightarrow 2 M_s - H \tag{1}$$
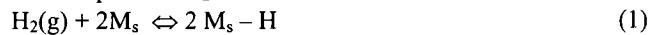
- H atoms spillover on the oxide as protons:

$$M_s - H + O^{2-}{}_S \Leftrightarrow M_s + OH^-{}_S + e^- \tag{2}$$
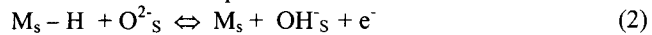
- electron transfer from the support to the metal due to the alignment of the Fermi levels of the metal and of the reduced semiconductor oxide support:

$$e^- + M \Leftrightarrow e^-{}_M \tag{3}$$

If steady state is applied to eqs (1-3), one gets :

$$d[e^-]/dt = k_2 [M_S - H] [O_S^{2-}] + k_{-3}[e^-{}_M] - k_{-2} [e^-] [M_S] [OH_S^-] - k_3 [e^-] [M] = 0$$

There results :

$$\sigma \propto [e^-] = \frac{k_{-3}[e^-{}_M]}{k_3[M] + k_{-2}[M_S][OH_S^-]} + \frac{k_2 K_1[M_S][O_S^{2-}]}{k_3[M] + k_{-2}[M_S][OH_S^-]} \times \sqrt{P_{H_2}} \tag{4}$$
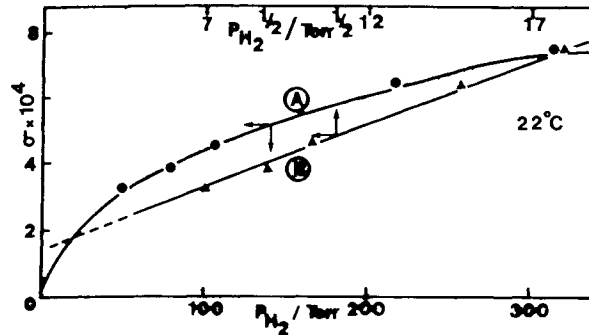
Fig.1.Electrical conductivity isotherm $\sigma = f(P_{H2}^{1/2})$ (curve A) and its linear transform $\sigma = a\,P_{H2}^{1/2} + b$.

This expression is of the form:
$$\sigma = a\,P_{H2}^{1/2} + b \qquad (5)$$
in agreement with the linear transform of Fig.1. Parameters a and b have a common denominator. If the second term of the denominator, $k_{-2}[M_S]\,[OH_S^-]$, which is relative to hydrogen reverse spillover (eq.-2) can be neglected, and if $[O_S^{2-}]$ can be considered as constant (great excess), therefore eq ( 4) becomes :

$$\sigma \propto [e^-] = \frac{k'_2\,K_1[M_S]}{k_3[M]} \times \sqrt{P_{H_2}} + \frac{[e^-_M]}{K_3[M]} \qquad \text{with} = k'_2 = k_2\,[O_S^{2-}] \qquad (6)$$

In the above relationship $\sigma = a\,P_{H2}^{1/2} + b$ (eq.5), it can be recognized that a contains the metal dispersion $D = [M_S]/[M]$ and b contains a factor $\varepsilon = [e^-_M]/M$, defined as the electron enrichment of the metal. Therefore, the linear transform of the hydrogen isotherm $\sigma = f(P_{H2}^{1/2})$ has the following mathematical expression

$$\sigma = (k'_2\,k_I/k_3)\,D\,P_{H2}^{1/2} + K_3^{-1}\,([e^-_M]/[M]) = \alpha\,D\,P_{H2}^{1/2} + \beta\,\varepsilon \qquad (7)$$

This theoretical equation is quite general for oxide-supposited noble metals and has been duely observed on Pt, Rh, Ni / TiO₂ ; Pd/ZnO... For instance, the electron enrichment $\varepsilon = [e^-_M]/[M]$ of a 5 wt % Pt/TiO₂ was varied by increasing the reduction temperature $T_R$ from 473 K to 773 K : the dispersion did not changed and a remained constant, whereas $b = K_3^{-1}\,\varepsilon$ was seriously affected as indicated in Table 1.

*Consequences of H spillover for the determination of metal dispersion by chemisorption.*

Hydrogen spill over is directly connected to hydrogen chemisorption, for which two types of sites have been observed depending on their heat of adsorption : a strong and irreversible one with an enthalpy equal to -22 kcal/mol H₂ (-92 kJ/mol) and a weak one with $\Delta H = -9$ kcal/mol H₂ (i.e. -37.7 kJ/mol), both values having been measured by calorimetry.

Hydrogen spillover would originate from the weak adsorption sites, which are necessarily located at the metal-support perimeter. By contrast, oxygen adsorption is very exothermic and irreversible ($\Delta H_{(ads)} = -72$ kcal/mol H₂ (-301 kJ/mol). This explains why the amounts of

hydrogen chemisorbed determined for metal dispersion measurement, are always found larger than those of oxygen in the same reference surface state.

In conclusion, $H_2$ spillover was confirmed by the linear isotherm $\sigma = f(P_{H2}^{1/2})$ whose slope is proportional to the metal dispersion and the ordinate at the origin to the relative electron enrichment of the metal. Spilt over hydrogen is in its protonic form, already detected by NMR (8). Such a catalytic system can be considered as an hydrogen sensor.

Table 1
Linear isotherm $\sigma = a \, P_{H2}^{1/2} + b$ : variations of the slope a (a $= (k_2' \, K_I/k_3)$ D) and of the ordinate at the origin b (b $= K_{-3} \, \varepsilon$) for different pretreatments affecting $\sigma$.

| Pretreatment | $a = \partial\sigma / \partial(P_{H2}^{1/2}]$ (proportional to metal dispersion D) in $ohm^- \, cm^{-1} \, torr^{-1/2}$ | $b = K_{-3} \, \varepsilon$ $\varepsilon = [e^-_M] / [M]$ |
|---|---|---|
| Reduction at $T_R = 473$ K ($P_{H2} = 250$ Torr) | $4.0 \times 10^{-5}$ | $4.5 \times 10^{-5}$ |
| Reduction at $T_R = 773$ K first $H_2$ adsorption | $6.9 \times 10^{-5}$ | $2.0 \times 10^{-3}$ |
| Reduction at $T_R = 773$ K second $H_2$ adsorption (after $O_2$ adsorption) | $5.4 \times 10^{-5}$ | $0.96 \times 10^{-3}$ |

### 3.1.2. H spillover in Weak ($T_R=200°C$) and Strong ($T_R=500°C$) Metal Support Interactions

Hydrogen spillover occurs at both reduction temperatures, thus catalyzing the surface reduction of the support with the formation of singly ionized anionic vacancies, whose existence is demonstrated by the law : $\sigma = kP_{O2}^{-1/4}$ with a formation enthalpy of +81 kcal/mol. The SMSI state is destroyed either by gaseous oxygen ($\Delta H = -81$ kcal/mol) or by oxygen-containing molecules such as $H_2O$ ($\Delta H = -23$ kcal/mol). The higher $T_R$ induces a higher reduction, i.e. a higher conductivity but simultaneously a higher electron transfer to the metal. All $\sigma$ measurements were in agreement with eqs (4-5)

### 3.2. Reactivity of spilt over hydrogen in bifunctional photocatalysis

Spilt over hydrogen plays an important role in *bifunctional photocatalysis* on near-UV irradiated bifunctional metal/titania photocatalysts as further examplified, because photocatalysis does occur at room temperature, in « Chimie Douce » conditions, in which the conventional activation of the catalyst by phonons have been replaced by a non-conventional activation by photons.

### 3.2.1. Hydrogen spillover on UV-irradiated M/TiO$_2$ (M = Pt, Rh, Ni)

Hydrogen chemisorption on UV-irradiated $M/TiO_2$ photocatalysts is not perturbed by the photons since it is essentially a thermodynamic process, independent of UV-irradiation. However, titania becomes photoconductor whose electrical photoconductivity $\sigma$ originates from the absorption of efficient photons, i.e. with an energy $h\nu \geq$ band gap energy $E_G$ of the solid (presently, for titania : $E_G = 3.2$ eV $\Leftrightarrow \lambda < 400$ nm).

$$(TiO_2) + h\nu \rightarrow e^- + p^+ \tag{8}$$

The generation rate of electrons G is equal to :

$$G = \alpha\Phi \, , \qquad \text{with } \alpha = \text{absorbance and } \Phi = \text{radiant flux} \tag{9}$$

If steady state is applied to eqs (1-3 and 7), one gets :

$$d[e^-]/dt = \alpha\Phi + k_2 [M_S - H] [O_S^{2-}] + k_{-3}[e^-_M] - k_{-2} [e^-] [M_S] [OH_S^-] - k_3 [e^-] [M] = 0 \tag{10}$$

and :

$$\sigma \propto [e^-] = \frac{k'_2 K_1 [M_S]}{k_3 [M]} \times \sqrt{P_{H_2}} + \frac{[e^-_M] + \alpha\Phi}{K_3 [M]} \qquad \text{with } = k'_2 = k_2 [O_S^{2-}] \tag{11}$$

It can be seen that $\sigma$ varies proportionally to $\Phi$ and $P_{H2}^{1/2}$ and conversely to the metal content [M], which was experimentally checked by the hyperbolic relationship $\sigma = f([M])$

### 3.2.2. Alkane-Deuterium Isotopic Exchange (ADIE)

This test-reaction of academic interest is typical for metal catalysts. It was performed at T < -10°C for eliminating any thermal activity of Pt/TiO$_2$. The selectivity was 100 % in primary H atoms exchanged by deuterium

$$C_nH_{2n+2} + D_2 \rightarrow C_{n-1}H_{2n-1}-CH_2D + HD \tag{12}$$

This reaction can be decomposed in an eight elementary step mechanism in which direct and reverse H spillovers play a capital role. This is illustrated for propane in Fig.2. First, D$_2$ dissociatively chemisorbs on Pt and deuterates all the OH surface groups of titania by direct D-spillover and reverse H-spillover:

$$D_2(g) + 2 Pt_s \Leftrightarrow 2 Pt_s-D \tag{13}$$

$$Pt_s-D + OH_S \Leftrightarrow Pt_s-H + OD_S$$

Such a deuteration has been experimentally confirmed by IR spectroscopy. The activation mode includes the action of OD° radicals formed by the neutralization of OD⁻ surface species by photoholes $p^+$ :

$$OD^- + p+ \rightarrow OD°$$
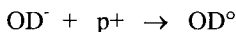
OD° radicals attack the alkane molecules, generating mono-exchanged R-D molecules and atomic H° radicals, which join Pt particles by reverse spill over. Once in contact with Pt$_S$, H atoms are evolved in the gas phase as HD and mainly as H$_2$ molecules. The amount of H$_2$ molecules formed, which is much higher than that of HD expected from the stoichiometry of reaction (11), confirms that labile and mobile hydrogen species are those of the metal-support interface perimeter, which plays the role of a gate to spillover with weak adsorption sites having an adsorption enthalpy equal to –9 kcal/mol, indicated in §1.1.

194
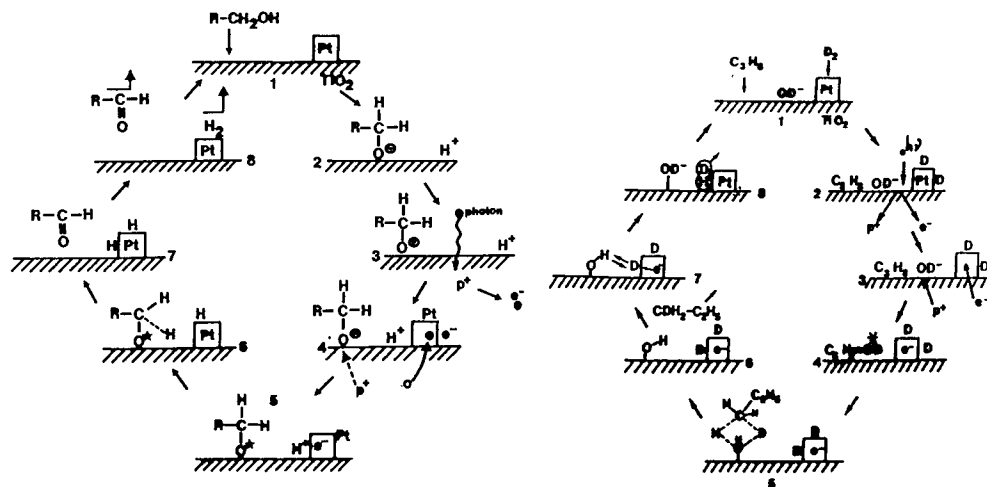


Fig. 2 (right) Photocatalytic alkane-deuterium isotopic exchange. Illustration of the 8-step cyclic mechanism of mono-deutero-exchange. Case study of propane

Fig.3 (left) 8-step cyclic mechanism of alcohol photocatalytic dehydrogenation

### 3.2.3. Alcohol photocatalytic dehydrogenation by reverse spillover.

UV-irradiated $M/TiO_2$ photocatalysts can dehydrogenate primary and secondary alcohols into their corresponding aldehydes and ketons and gaseous dihydrogen. The reaction mechanism is a eight-step process, illustrated in Fig.3. First, alcohols dissociatively adsorb as protons and alcoholate $RO^-$ species. $RO^-$ are neutralized by photoholes $p^+$ into $RO^\circ$ radicals. These radicals lose one H atom, which, by reverse spillover, joins the metal particles and recombine into gaseous di-hydrogen. The protons initially formed during the adsorption are attracted by the same negatively charged metal particles, which plays the role of nanocathodes. The process depends on the amount of metal, the optimum catalyst (0.5 wt% Pt), corresponding to one or two metal crystallites per titania particle. Up to 1000 catalytic cycles operating on the same sites have been observed without any loss of activiy. The bi-functional nature of this reaction with metal particles playing the role of electron traps (eqs.(3) and (10)) which avoid electron-hole recombination, enables the obtention of high quantum yields $\rho$, $\rho$ being defined as the ratio of the reaction rate r in molecules/s to the photonic flux $\varphi$ in photons/s. A value as high as 40% was obtained for $\rho$ in the dehydrogenation of methanol.

It has to be noted that naked titania alone is able to generate $H_2$ but the process is not catalytic. It is rather stoichiometric and ceases when the initial pool of active sites have been exhausted. The photocatalytic alcohol dehydrogenetion requires a (noble) metal co-catalyst, necessary (i) to attract photogenerated $H^\circ$ atoms by reverse spillover, (ii) to recombine them into dihydrogen and (iii) to evolve them from the weak adsorption sites from the metal-support perimeter.

### 3.2.4. Photocatalytic hydrogen transfer from alcohols to unsaturated compounds.

The hydrogen produced according to § 2.3 by alcohol dehydrogenation can be *in situ* « re-invested » by saturating some C=C double bonds present, either in the initial alcoholic

reactant molecule (intramolecular hydrogen transfer) or in other co-reactant ones (intermolecular hydrogen transfer) (9).

**Intramolecular hydrogenation :**

The photocatalytic dehydrogenation of pure liquid allyl alcohol in absence of oxygen (air) generates acrolein and $H_2$ :

$$CH_2=CH-CH_2OH \rightarrow CH_2=CH-CHO + H_2$$
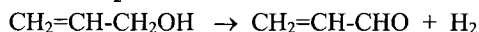
The hydrogen atoms which are gathered at the surface of Pt before evolution as dihydrogen in the gas phase can be consumed before desorption by the double bond >C=C< interacting with Pt and adsorbing on it.

$$>C=C< + H_2 \rightarrow -CH_2-CH_2-$$
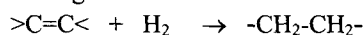
The main reaction is propanol formation because of the high concentration of pure liquid allyl alcohol ($C_0 = 14.70$ mol/L).

$$CH_2=CH-CH_2OH + H_2 \rightarrow CH_3-CH_2-CHOH$$
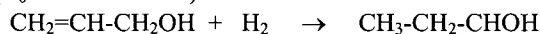
However, when conversion increases, acrolein becomes converted to propanal :

$$CH_2=CH-CHO + H_2 \rightarrow CH_3-CH_2-CHO$$
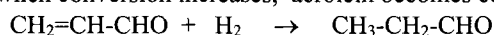
Similarly, cinnamyl alcohol can be dehydrogenated into cinnalmaldehyde

$$C_6H_5-CH=CH-CH_2OH \rightarrow C_6H_5-CH=CH-CHO + H_2$$
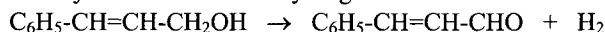
and hydrogen can subsequently hydrogenate the double bond :

$$>C=C< + H_2 \rightarrow 3\text{-phenyl-propanol} + \text{phenyl-3-propanal}$$
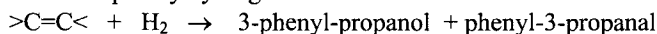
A too remote double bond remains unsaturated. For instance, citronellol gives 100% citronellal

$$(CH_3)_2>C=CH-CH_2-CH_2-CH(CH_3)-CH_2-CH_2OH \rightarrow$$
$$(CH_3)_2>C=CH-CH_2-CH_2-CH(CH_3)-CH_2-CHO + H_2$$
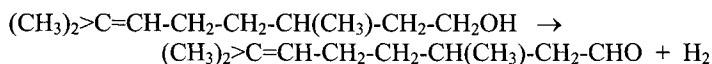
with the same dehydrogenation rate as that of tetrahydrogeraniol, its saturated homologue

$$(CH_3)_2>CH-CH_2-CH_2-CH_2-CH(CH_3)-CH_2-CH_2OH$$
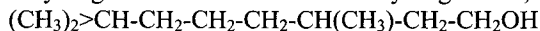
**Intermolecular transfer :**

Hydrogen can be transmitted to an unsaturated compound introduced in the medium. For instance, $H_2$ can be transferred from allyl alcohol to tolane to form cis-stilbene.

$$CH_2=CH-CH_2OH \rightarrow CH_2=CH-CHO + H_2$$
$$\varphi\text{-CH}\equiv\text{CH-}\varphi \text{ (tolane)} + H_2 \rightarrow \varphi\text{-CH}_2=\text{CH-}\varphi \text{ (cis-stilbene)}$$
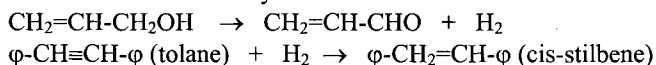
### 3.2.5. *In situ* photocatalytic $H_{0.93}MoO_3$ bronze formation

As mentioned in§2.3, $H_2$ can beproduced by naked photoactive support, but in a limited amount, corresponding to the stoichiometric threshold.

When adding $MoO_3$, which is « not photo-insensitive », to a UV-irradiated alcoholic suspension of $Pt/TiO_2$, $H_2$ is evolved according to the process detailed in § 2.3. Dehydrogenation being photocatalytic, it occurs mainly on titania but also, in a much minor extent on molybdena. Reverse hydrogen spillover from titania to Pt enables the recombination of two H atoms in di-hydrogen on the metal surface before evolution of $H_2$ in the head space on the photoreactor. Simultaneously, atomic hydrogen is spilt over from molybdena to titania from which it is evolved as $H_2$ via its transfer to Pt (Fig.4).

By contrast, *in absence of Pt*, H atoms, mainly photogenerated on titania, cannot be evolved as $H_2$ from the metal. There results a spontaneous generation of H atom, mainly on titania since titania is hundred times more active than molybdena. A large difference in concentrations [H] is built up, which induces a high concentration gradient between the particles of both oxides. This gradient acts as a driving force, which induces a spontaneous hydrogen spillover from titania to molybdena particles, when they are in temporary contact
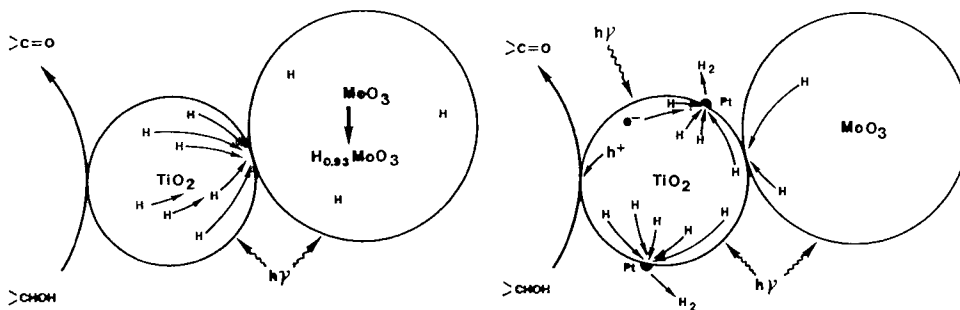
196



Fig.4 (left) : $H_{0.93}MoO_3$ bronze formation by transfer of photocatalytically generated hydrogen from titania to molybdena.

Fig.5 (right) : Inhibition of $H_{0.93}MoO_3$ bronze formation by the evolution through the « platinum gate » of hydrogen photocatalytically generated mainly on titania and eventually on molybdena.

inside the suspension. The accumulation of H atoms at the surface of $MoO_3$ favors their dissolution into the molybdena lattice, thus forming a hydrogen bronze, identified as the $H_{0.93}MO_3$ phase. The reaction mechanism of the photocatalytic $H_{0.93}MoO_3$ bronze formation is illustrated by Fig.4. This reaction constitutes an original « hexaphasic gas-solid-solid-solid-liquid-light » catalytic system, in which the last but not the least phase is constituted by the « electromagnetic phase ».

## 4. CONCLUSION

Electrical and photo-electrical conductivity measurements have clearly demonstrated the existence of dissociated hydrogen spillover. The role of both direct and reverse hydrogen spillover has been underlined in various cases of chemisorption, catalysis and photocatalysis. It clearly appears that hydrogen spillover is more evident in biphasic photocatalysis than in conventional catalysis essentially because photocatalysis operates *at room temperature.*

## REFERENCES

1  J.M. Herrmann, in "Catalyst Characterization, Physical Techniques for Solid Materials", ed. B. Imelik and J.C. Védrine, Plenum Press, New York, Chap. 20, p. 559 (1994).

2  A.Ovenston and J.R. Walls and references therein, J. Phys. D. Appl. Phys., 18 (1985)1850.

3  A.Ammi, D.Bideau,J.P. Treoadec, F.Ropital and G.Thomas, Solid State Commun, 55 (1985) 1.

4  J.M.Herrmann, J.Catal., 118 (1982) 43.

5  J.Disdier, J.M.Herrrmann and P.Pichat, J.Chem. Soc. Faraday Trans.I, 1983,79,651.

6  O.Krylov in " Catalysis by Non-Metals ", Acad . Press , (New-York), 1970.

7  T.Uchijima, J.M.Herrmann, Y.Inoue, R.L.Burwell, J.B.Buttand J.B.Cohen, J.Catal., 50 (1977) 464.

8  T.M.Apple, P.Gajardo and C.Dybowski, J.Catal., 68 (1981)103.

9  P.Pichat, J.Disdier, M.N.Mozzanega and J.M.Herrmann, Dechema, Vol.III, 1984, p.487.

# Spillover-modified catalysis: Experimental rules and mathematical modeling

C. Vayenas and S. Brosda

Department of Chemical Engineering, University of Patras, 26500 Patras, Greece

Electrochemical and conventional promotion are closely related since the former is due to electrochemically controlled migration (backspillover) of promoting ionic species on metal catalyst surfaces. In both cases the promoting species alter the catalyst surface work function $\Phi$. Here we develop simple and rigorous rules which describe the dependence of catalytic rates on catalyst work function. These rules are in very good agreement with the electrochemical and conventional promotion literature. These experimentally derived rules also follow from a mathematical model which takes into account lateral electrostatic adsorbate interactions.

## 1. INTRODUCTION

The use of several surface sensitive techniques including work function measurements [1], XPS [2], TPD [3], STM [4] and AC impedance spectroscopy [5] has established [6-8] that the effect of electrochemical promotion or Non-faradaic electrochemical modification of catalytic activity (NEMCA effect) [1, 6-12] is due to electrochemically controlled backspillover of promoting ions ($O^{2-}$, $Na^+$, $H^+$, etc) from the solid electrolyte support onto the gas exposed catalyst surface. The same techniques have established that ion spillover-backspillover is a real phenomenon taking place over enormous (~mm) atomic distances and that the backspillover ions migrating onto the catalyst surface establish there an overall neutral double layer (Fig. 1) which affects the chemisorptive bond strength of reactants and intermediates and thus influences catalytic activity and selectivity in a dramatic manner [7,8].

In this paper we use the conclusive experimental evidence proving the existence of the back-spillover-formed double layer on catalyst surfaces interfaced with solid electrolytes and present for the first time a rigorous mathematical model, based on isotherms which account explicitly for the electrostatic interaction between the adsorbates and the electric field of the double layer. The model describes all aspects of electrochemical, but also classical, promotion, in a semiquantitative manner. In particular the model accounts for:

(i)     The observed linear variation in heats of adsorption with work function change.

(ii)     The four main types of kinetic behaviour observed upon changing the catalyst potential $U_{WR}$ and work function $\Phi$ ($\Delta\Phi=e\Delta U_{WR}$
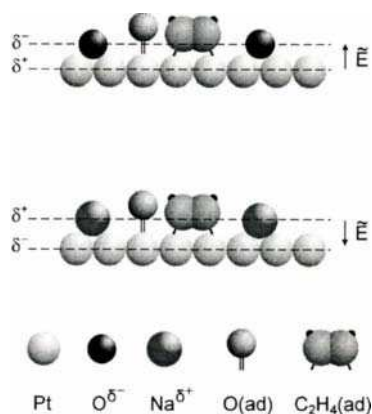


Fig. 1: Schematic of the double layer during $C_2H_4$ oxidation on Pt promoted by $O^{\delta-}$ and $Na^{\delta+}$.

[1,7,14,15]) and thus the coverage of the promoting backspillover ions: electrophobic, electrophilic, volcano type and inverted volcano type behaviour [7,8].

Denoting by D and A the electron donor and electron acceptor reactant, respectively, the model describes the rate dependence on dimensionless catalyst potential or work function $\Pi(=\Delta\Phi/k_bT)$ on the basis of only four parameters which are:

a) The two adsorption coefficients $k_D$ and $k_A$, which quantify the chemisorptive bond strength of D and A at the point of zero charge on the catalyst surface [15].

b) The two partial charge transfer parameters $\lambda_D$ (>0) and $\lambda_A$ (<0) which describe the electron donicity of the reactants. The values of $\lambda_D$ and $\lambda_A$ are considered fixed except for the case of very weak adsorption ($k_Dp_D$, $k_Ap_A < 10^{-2}$) where $\lambda_D$ and $\lambda_A$ are assumed to vanish in the potential range of repulsive interactions ($\Pi <0$ and $\Pi>0$ respectively). This means that in the region of low coverages ($\theta_D$, $\theta_A < 10^{-2}$) repulsive interactions are neglected. All four parameters are amenable to direct experimental measurement.

The backspillover-formed double layer model of catalysis is compared with experimental results obtained over the last few years with more than 70 electrochemically and classically promoted catalytic reactions [7,8,13,16].

## 2. PROMOTIONAL RULES

Table 1 classifies all published electrochemical promotion studies on the basis of the observed global r vs $\Phi$ (or $\Pi$) behaviour and also provides the kinetic order of each reaction with respect to the partial pressures $p_D$ and $p_A$. The rules of electrochemical and classical promotion follow directly from Table 1: For example, all purely electrophobic reactions are positive order in D and zero or negative order in A. All purely electrophilic reactions are positive order in A and zero or negative order in D. Volcano-type reactions are always positive order in one reactant and purely negative order in the other. Inverted volcano-type reactions are positive order in both reactants. Thus the following promotional rules can be formulated:

### 2.1 Electrophobic reactions

Inspection of Table 1 shows the following rule for electrophobic reactions:

*Rule G1:* A reaction exhibits purely electrophobic behaviour ($(\partial r/\partial\Phi)_{p_A,p_D} > 0$) when the kinetics are positive order in the electron donor (D) reactant and negative or zero order in the electron acceptor (A) reactant. Table 1 provides 21 such examples. There appear to be no exceptions. Two typical examples are shown in Figure 2(a) and 3(a). An equivalent formulation of rule G1 is the following:

*Rule G1':* A reaction exhibits purely electrophobic behaviour ($(\partial r/\partial \Phi)_{p_A,p_D} > 0$) when the electron acceptor reactant (A) is much more strongly adsorbed on the catalyst surface than the electron donor reactant (D). In the context of Langmuir-Hinshelwood type kinetics the latter can be expressed as:

$$k_Ap_A >> k_Dp_D \Rightarrow (\partial r/\partial \Phi)_{p_A,p_D} > 0 \tag{1}$$

where $k_A$, $k_D$ are the adsorption equilibrium constants of A and D on the catalyst surface.

### 2.2 Electrophilic reactions

Inspection of Table 1 shows the following rule for electrophilic reactions:

*Rule G2:* A reaction exhibits purely electrophilic behaviour ($(\partial r/\partial \Phi)_{p_A,p_D} < 0$) when the kinetics are positive order in the electron acceptor (A) reactant and negative or zero order in

**Table 1**

Classification of Electrochemical Promotion studies on the basis of global r vs. be h aviour.

A. Purely electrophobic reactions

| Reactants (D) | (A) | Catalyst | Solid Electrolyte | $p_A/p_D$ | T (°C) | Kinetics in D $\partial r/\partial p_D)$ | Kinetics in A $\partial r/\partial p_A$ | Rule | Ref |
|---|---|---|---|---|---|---|---|---|---|
| $C_2H_4$ | $O_2$ | Pt | $ZrO_2(Y_2O_3)$ | 12-16 | 260-450 | + | 0 | G1 | (7) |
| $C_2H_4$ | $O_2$ | Pt | $\beta''-Al_2O_3$ | 238 | 180-300 | + | 0 | G1 | (7) |
| $C_2H_4$ | $O_2$ | Pt | $TiO_2$ | 3.5-12 | 450-600 | + | 0 | G1 | (7) |
| $C_2H_4$ | $O_2$ | Rh | $ZrO_2(Y_2O_3)$ | 0.05-2.6 | 250-400 | + | 0 | G1 | (7) |
| $C_2H_4$ | $O_2$ | Ag | $ZrO_2(Y_2O_3)$ | 0.2-1.1 | 320-470 | + | 0 | G1 | (7) |
| $C_2H_4$ | $O_2$ | $IrO_2$ | $ZrO_2(Y_2O_3)$ | 300 | 350-400 | + | 0 | G1 | (7) |
| $C_2H_4$ | $O_2$ | $RuO_2$ | $ZrO_2(Y_2O_3)$ | 155 | 240-500 | + | ≤0 | G1 | (13) |
| CO | $O_2$ | Pt | $CaF_2$ | 11-17 | 500-700 | + | 0 | G1 | (7) |
| CO | $O_2$ | Pd | $ZrO_2(Y_2O_3)$ | 500 | 400-550 | ? | ? | ? | (7) |
| $CH_4$ | $O_2$ | Pd | $ZrO_2(Y_2O_3)$ | 0.2-4.8 | 380-440 | + | 0 | G1 | (13) |
| $C_3H_6$ | $O_2$ | Ag | $ZrO_2(Y_2O_3)$ | 20-120 | 320-420 | + | ≤0 | G1 | (7) |
| $CH_4$ | $O_2$ | Ag | $ZrO_2(Y_2O_3)$ | 0.02-2 | 650-850 | + | 0 | G1 | (7) |
| $C_6H_6$ | $H_2$ | Pt | $\beta''-Al_2O_3$ | 0.02-0.12 | 100-150 | ≥0 | ~0 | G1 | (7) |
| $C_2H_2$ | $H_2$ | Pt | $\beta''-Al_2O_3$ | 1.7-9 | 100-300 | ? | ? | ? | (13) |
| $H_2$ | $CO_2$ | Rh | $ZrO_2(Y_2O_3)$ | 0.03-0.7 | 300-450 | + | 0 | G1 | (7) |
| $H_2$ | $C_2H_2$, $C_2H_4$ | Pd | $\beta''-Al_2O_3$ | 0.1-5.9# | 70-100 | ≥0 | 0 | G1 | (13) |
| $H_2S$ | - | Pt | $ZrO_2(Y_2O_3)$ | --- | 600-750 | ? | | ? | (7) |
| $CH_4$ | - | Ag | $SrCe_{0.95}Yb_{0.05}O_3$ | --- | 750 | ? | | ? | (7) |
| $NH_3$ | - | Fe | $CaZr_{0.9}In_{0.1}O_{3-a}$ | 4-12kPa | 530-600 | + | | G1 | (13) |
| $NH_3$ | - | Fe | $K_2YZr(PO_4)_3$ | 4-12kPa | 500-700 | + | | G1 | (13) |
| $CH_4$ | $H_2O$ | Ni | $ZrO_2(Y_2O_3)$ | 0.05-3.5 | 600-900 | + | ≤0 | G1 | (7) |

(#) $p_D = p_{C_2H_2} + p_{C_2H_4}$

B. Purely electrophilic reactions

| Reactants (D) | (A) | Catalyst | Solid Electrolyte | $p_A/p_D$ | T (°C) | Kinetics in D $(\partial r/\partial p_D)_\Phi$ | Kinetics in A $(\partial r/\partial p_A)_\Phi$ | Rule | Ref |
|---|---|---|---|---|---|---|---|---|---|
| $C_2H_4$ | $O_2$ | Pt | $CaZr_{0.9}In_{0.1}O_{3-a}$ | 4.8 | 385-470 | - | + | G2 | (13) |
| $C_2H_4$ | $O_2$ | Pt | $CeO_2$ | 1.6-3.7 | 500 | - | + | G2 | (13) |
| $C_2H_4$ | $O_2$ | Pt | YZTi10 | 3 | 400-475 | ? | ? | ? | (13) |
| $C_2H_4$ | $O_2$ | Ag | $\beta''-Al_2O_3$ | 0.3-0.4 | 240-280 | - | + | G2 | (13) |
| CO | $O_2$ | Ag | $\beta''-Al_2O_3$ | 0.1-10 | 360-420 | 0 | + | G2 | (7) |
| $C_3H_6$ | $O_2$ | Pt | $ZrO_2(Y_2O_3)$ | 0.9-55 | 350-480 | ≤0 | + | G2 | (7) |
| $CH_3OH$ | $O_2$ | Ag | $ZrO_2(Y_2O_3)$ | 0-2 | 500 | ? | + | G2 | (13) |
| $CH_4$ | $O_2$ | Au | $ZrO_2(Y_2O_3)$ | 0.1-0.7 | 700-750 | 0 | + | G2 | (7) |
| $H_2$ | $N_2$ | Fe | $CaZr_{0.9}In_{0.1}O_{3-a}$ | 0-3 | 440 | ? | ? | ? | (13) |
| $H_2$ | $C_2H_4$ | Ni | $CsHSO_4$ | 1 | 150-170 | ? | ? | ? | (7) |
| | $CH_3OH$ | Pt | $ZrO_2(Y_2O_3)$ | --- | 400-500 | | ? | ? | (7) |
| | $CH_3OH$ | Ag | $ZrO_2(Y_2O_3)$ | 0-6 kPa | 550-750 | | + | G2 | (7) |
| $C_2H_4$ | NO | Pt | $ZrO_2(Y_2O_3)$ | 0.2-10 | 380-500 | 0 | + | G2 | (13) |
| $C_2H_4$ | NO | Pt | $\beta''-Al_2O_3$ | 0.1-1.1 | 280-400 | ? | ? | ? | (7) |
| CO | NO | Pt | $\beta''-Al_2O_3$ | 0.3-5 | 320-400 | ≤0 | + | G2 | (13) |
| CO | NO | Pd | $ZrO_2(Y_2O_3)$ | 0.5-6.5 | 320-480 | ~0 | + | G2 | (13) |
| CO | $N_2O$ | Pd | $ZrO_2(Y_2O_3)$ | 2-50 | 440 | - | + | G2 | (13) |
| | $1-C_4H_8$ | Pd | Nafion | --- | 70 | | ? | G2 | (13) |

**Table 1**

Classification of Electrochemical Promotion studies on the basis of global r vs. $\Phi$ behaviour.

C. Volcano type reactions

| Reactants (D) | (A) | Catalyst | Solid Electrolyte | $p_A/p_D$ | T (°C) | Kinetics in D $(\partial r/\partial p_D)_\Phi$ | Kinetics in A $(\partial r/\partial p_A)_\Phi$ | Rule | Ref |
|---|---|---|---|---|---|---|---|---|---|
| $C_2H_4$ | $O_2$ | Pt | $Na_3Zr_2Si_2PO_{12}$ | 1.3-3.8 | 430 | - | + | G3 | (13) |
| CO | $O_2$ | Pt | $ZrO_2(Y_2O_3)$ | 0.2-55 | 468-558 | + | - | G3 | (7) |
| CO | $O_2$ | Pt | $\beta''-Al_2O_3$ | 0.5-20 | 300-450 | - | + | G3 | (7) |
| $H_2$ | $O_2$ | Pt | $H_2O - 0.1N$ KOH | 0.3-3 | 25-50 | + | - | G1 | (7) |
| $H_2$ | $O_2$ | Pt | Nafion | 0.2-5 | 25 | + | - | G3 | (7) |
| $SO_2$ | $O_2$ | Pt | $V_2O_5-K_2S_2O_7$ | 1.8 | 350-450 | ? | ? | ? | (13) |
| $C_3H_6$ | NO | Pt | $\beta''-Al_2O_3$ | 2-70 | 375 | - | + | G3 | (13) |
| $H_2$ | NO | Pt | $\beta''-Al_2O_3$ | 0.3-6 | 360-400 | - | + | G3 | (13) |

D. Inverted Volcano reactions

| Reactants (D) | (A) | Catalyst | Solid Electrolyte | $p_A/p_D$ | T (°C) | Kinetics in D $(\partial r/\partial p_D)_\Phi$ | Kinetics in A $(\partial r/\partial p_A)_\Phi$ | Rule | Ref |
|---|---|---|---|---|---|---|---|---|---|
| $C_2H_4$ | $O_2$ | Pt | $TiO_2$ | 0.2-0.3# | 450-600 | + | + | G4 | (7) |
| $C_3H_6$ | $O_2$ | Pt | YZTi10 | 5 | 400-500 | ? | ? | ? | (13) |
| CO | $O_2$ | Ag | $ZrO_2(Y_2O_3)$ | 0.6-14 | 350-450 | + | + | G4 | (7) |
| CO | $O_2$ | Ag-Pd alloy | $ZrO_2(Y_2O_3)$ | 3.5-12.5 | 450-500 | + | + | G4 | (13) |
| CO | $O_2$ | Au | $ZrO_2(Y_2O_3)$ | 3-53 | 450-600 | + | $\geq 0$ | G4 | (7) |
| $C_2H_6$ | $O_2$ | Pt | $ZrO_2(Y_2O_3)$ | 0.06-7 | 270-500 | + | + | G4 | (7) |
| $CH_4$ | $O_2$ | Pt | $ZrO_2(Y_2O_3)$ | 0.02-7 | 600-750 | + | + | G4 | (7) |
| $CH_3OH$ | $O_2$ | Pt | $ZrO_2(Y_2O_3)$ | 3-45 | 300-500 | + | ? | ? | (7) |
| $H_2$ | $CO_2$ | Pd | $ZrO_2(Y_2O_3)$ | 0.2-1.1 | 500-590 | + | + | G4 | (7) |
| $C_3H_6$ | $NO,O_2$ | Rh | $ZrO_2(Y_2O_3)$ | 0.08-8$ | 250-450 | + | NO: + $O_2$: 0 | G4 | (13) |
| CO | $NO,O_2$ | Rh | $ZrO_2(Y_2O_3)$ | 0.33$ | 250-450 | + | NO: + $O_2$: 0 | G4 | (13) |

($): $p_A/p_D$ is the ratio $p_{NO}/p_{C_3H_6}$ and $p_{NO}/p_{CO}$. The $p_{O_2}$ range is between $0 - 6$ kPa.

(#): low $p_A$, $p_D$ region

(?): no data available

the electron donor (D) reactant. Table 1 provides 18 such examples and no exceptions. Some typical examples are shown in Figure 2(b) and 3(b). An equivalent formulation of rule G2 is the following:

*Rule G2':* A reaction exhibits purely electrophilic behaviour $((\partial r/\partial \Phi)_{p_A,p_D} < 0)$ when the electron donor reactant (D) is much more strongly adsorbed on the catalyst surface than the electron acceptor reactant (A). In the context of Langmuir-Hinshelwood type kinetics the latter can be expressed as:

$$k_A p_A \ll k_D p_D \Rightarrow (\partial r/\partial \Phi)_{p_A,p_D} < 0 \qquad (2)$$

**2.3 Volcano-type reactions**

Inspection of Table 1 shows that reactions exhibiting volcano-type (maximum type) behaviour with respect to $\Phi$ are those where the kinetics also exhibit a maximum with respect

to A and D so that the rate is always positive order in A or D and at the same time negative (not zero) order in D or A respectively. Thus the following rule is derived:

*Rule G3:* A reaction exhibits volcano-type behaviour when both the electron donor D and electron acceptor A are strongly adsorbed on the catalyst surface. Table 1 provides 8 such examples and no exceptions. Some typical examples are shown in Figure 2(c) and 3(c). In the context of Langmuir-Hinshelwood type kinetics, Rule G3 can be expressed as:

$$k_A p_A, k_D p_D \gg 1 \Rightarrow \begin{cases} (\partial r / \partial \Phi)_{p_A, p_D} > 0; \ \Phi < \Phi_M \\ (\partial r / \partial \Phi)_{p_A, p_D} = 0; \ \Phi = \Phi_M \\ (\partial r / \partial \Phi)_{p_A, p_D} < 0; \ \Phi > \Phi_M \end{cases} \quad (3)$$

where $\Phi_M$ is the work function value at the rate maximum (volcano-maximum).
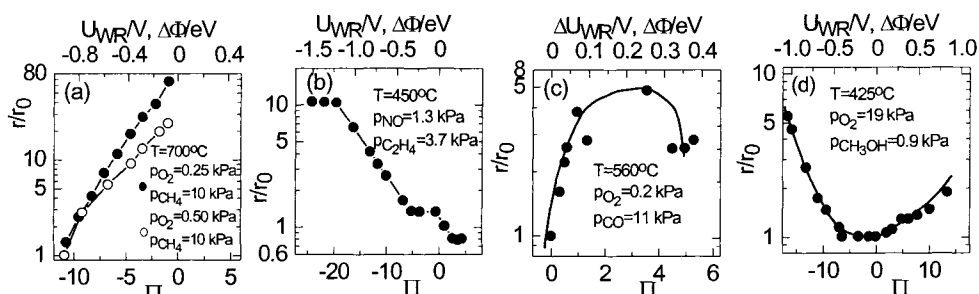


Fig. 2: Examples of the four types of electrochemical promotion behaviour: (a) purely electrophobic, (b) purely electrophilic, (c) volcano-type (d) inverted volcano-type. Effect of catalyst potential $U_{WR}$, work function $\Phi$ change (vs I=0) and dimensionless catalyst work function $\Pi = \Delta\Phi/k_b T$ on the rates of: (a) $CH_4$ oxidation on Pt films deposited on YSZ for high (20:1 and 40:1) $CH_4$ to $O_2$ feed ratios. (b) NO reduction by $C_2H_4$ on Pt films deposited on YSZ. (c) CO oxidation on Pt films deposited on YSZ. (d) $CH_3OH$ oxidative dehydrogenation to $H_2CO$ on Pt films deposited on YSZ [7, 13].
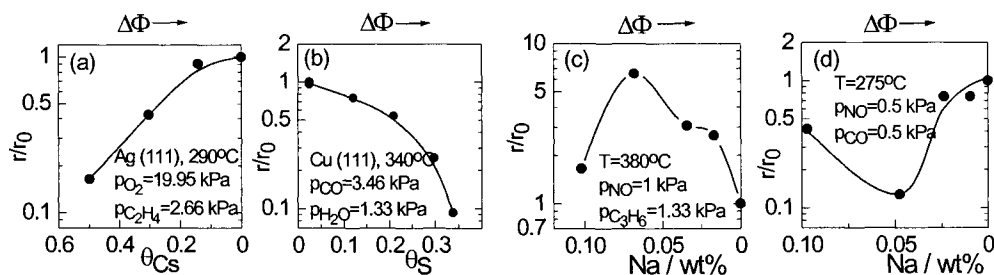


Fig. 3: Examples of the four types of classical promotion behaviour: (a) purely electrophobic, (b) purely electrophilic, (c) volcano-type, (d) inverted volcano-type. Effect of decreasing electropositive (a,c,d) or increasing electronegative (b) promoter coverage and of concomitant $\Delta\Phi$ change on the rates of: (a) $C_2H_4$ epoxidation on Cs-promoted Ag(111). (b) Water-gas shift reaction on S-poisoned Cu(111). (c) NO reduction by $C_3H_6$ on Na-promoted Pd supported on 8 mol%$Y_2O_3$ stabilized zirconia (YSZ). (d) NO reduction CO on Na-promoted 0.5 wt% Rh supported on $TiO_2$(4%$WO_3$) [13].

## 2.4 Inverted volcano (minimum) type reactions

Inspection of Table 1 shows the following rule for inverted volcano type reactions:

*Rule G4:* A reaction exhibits inverted volcano (minimum rate) type behaviour when the kinetics are positive order in both the electron acceptor (A) and electron donor (D) reactant.

Table 1 provides 11 such examples and no exceptions. Some typical examples are shown in Figure 2(d) and 3(d). In the context of Langmuir-Hinshelwood type kinetics, Rule G4 can be expressed as:

$$k_A p_A, k_D p_D \ll 1 \Rightarrow \begin{cases} (\partial r / \partial \Phi)_{p_A, p_D} < 0 ; & \Phi < \Phi_m \\ (\partial r / \partial \Phi)_{p_A, p_D} = 0 ; & \Phi = \Phi_m \\ (\partial r / \partial \Phi)_{p_A, p_D} > 0 ; & \Phi > \Phi_m \end{cases} \qquad (4)$$

where $\Phi_m$ is the work function value at the rate minimum.

## 3. MATHEMATICAL MODELING

The Langmuir isotherm approach does not take into account the electrostatic interaction between the dipole of the adsorbate and the field of the double layer [14]. In order to account explicitly for this interaction one can write the adsorption equilibrium in the form:
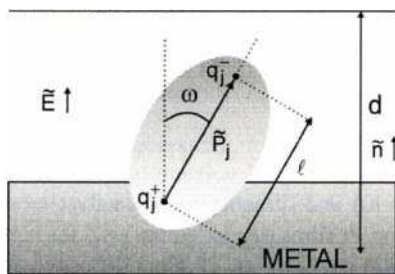


Fig. 4: Schematic of a dipole in an electric field.

$$S_j(g) \leftrightarrow S_j^{\lambda_j^\dagger} - \lambda_j e^- \qquad (5)$$

where the partial charge transfer parameter $\lambda_j$ is the net number of electrons donated by the adsorbate to the metal during chemisorptive bond formation. The rhs of Eq. (5) represents the overall neutral dipole adsorbate formed on the catalyst surface and accounts explicitly for partial charge transfer between the adsorbate and the metal (Fig. 4). The quantity $\lambda_j$ is zero for a truly covalent chemisorptive bond, positive for an electron donor adsorbate and negative for an electron acceptor adsorbate. The partial electron transfer parameter $\lambda_j$ is directly related to the dipole moment, $P_j$, of adsorbed j via:

$$P_j = -q_j \cdot \ell / 2 = -\lambda_j e \, \ell / 2 \qquad (6)$$

where $\ell$ is the distance between the centers of the positive and negative charges in the adsorbed dipole.

The modified electrochemical Langmuir isotherm obtained from the above physical model is:

$$\theta_j / (1 - \theta_j) = k_j p_j \exp(-\lambda_j \Pi) \qquad (7)$$

which is consistent with the frequently observed linear variation of heats of adsorption with $\Delta\Phi$ [14,16,17]

$$\Delta H_{ad,j} = \Delta H_{ad,j}^o + (\lambda_j / 2) \, \Delta\Phi \qquad (8)$$

We thus consider an arbitrary catalytic reaction between an electron donor D ($\lambda_D > 0$) and an electron acceptor A ($\lambda_A < 0$):

D + A →products $\qquad$ (9)

and also assume that adsorbed D and A are in equilibrium with gaseous D and A respectively $(\mu_D(g) = \bar{\mu}_D(ad), \; \mu_A(g) = \bar{\mu}_A(ad))$ and that product adsorption is relatively weak and their desorption fast, so that the reaction between adsorbed D and A is rate limiting.

We start by noting that when D and A coadsorb, their adsorption isotherms are given by:

$$\theta_D/\theta_v = k_D p_D \exp(\lambda_D \Pi) \; ; \; \theta_D/\theta_v = k_A p_A \exp(\lambda_A \Pi) \qquad (10)$$

where $\theta_v$ is the coverage of vacant sites on the catalyst surface. Combining with Eqs. (7) and (10) one obtains:

$$\theta_D = \frac{k_D p_D \exp(\lambda_D \Pi)}{1 + k_D p_D \exp(\lambda_D \Pi) + k_A p_A \exp(\lambda_A \Pi)} \qquad (11)$$

$$\theta_A = \frac{k_A p_A \exp(\lambda_A \Pi)}{1 + k_D p_D \exp(\lambda_D \Pi) + k_A p_A \exp(\lambda_A \Pi)} \qquad (12)$$

$$r = k_R \theta_D \theta_A \qquad (13)$$

where the surface reaction rate constant $k_R$ can in general be expressed as:

$$k_R = k_R^o \exp(\lambda_R \Pi) \qquad (14)$$

Since little is presently known, experimentally or theoretically, about the parameter $\lambda_R$ and its possible relationship to $\lambda_D$ and $\lambda_A$ we have set it equal to zero and have attempted to derive
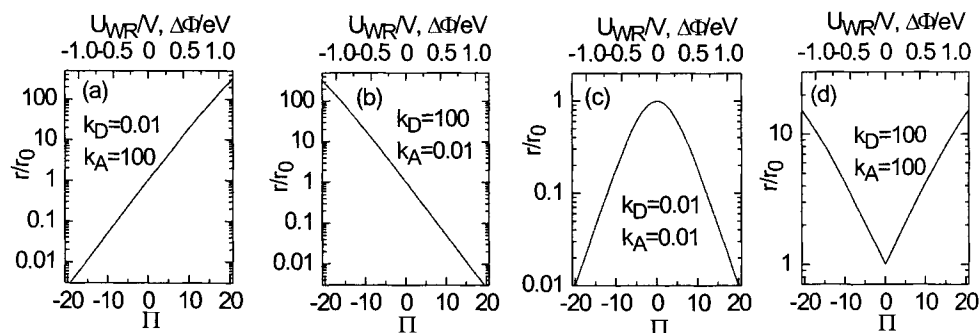


Fig. 5: Model predicted electrochemical promotion behaviour (a) for electrophobic (b) electrophilic (c) volcano-type and (d) inverted volcano-type reaction, parameter: $\lambda_D = 0.15$, $\lambda_A = -0.15$, $p_D = 1$, $p_A = 1$, adsorption coefficients $k_D$ and $k_A$ given in the figure

all global promotional rules in terms of only four parameters, $k_D$, $k_A$, $\lambda_D$ and $\lambda_A$. As shown in Figure 5 the above simple mathematical model of Eqs. (11 to 13) is in excellent qualitative agreement with experiment as shown for all four main reaction types. Figure 5 shows how the model predicts the type of r vs $\Phi$ global behaviour for fixed $\lambda_D$ and $\lambda_A$, $p_D$ and $p_A$, by just varying the adsorption equilibrium constants $k_D$ and $k_A$. It describes in a semiquantitative manner all electrochemical promotion studies up to date and nicely predicts the experimentally observed global electrochemical and classical promotion rules G1 to G4.

204

## 4. CONCLUSIONS

Careful classification and examination of the electrochemical promotion and classical promotion literature has revealed four simple and rigorous experimental rules (G1 to G4) which enable one to predict the rate vs work function, $\Phi$, behaviour of catalytic reactions (electrophobic, electrophilic, volcano, inverted volcano) on the basis of the rate dependence on the reactants partial pressures on the unpromoted surface. The rate vs $\Phi$ dependence traces, generally, the rate vs $p_D$ dependence.

The rules presented here allow one to make some very clear predictions. Although we have found no exceptions in more than 70 cases, it will be interesting to compare these rules with more catalytic systems where the r vs $p_A$, $p_D$ and $\Phi$ dependence is studied in detail.

## REFERENCES

1.  C.G. Vayenas, S. Bebelis and S. Ladas, *Nature* (London) **343**, 625 (1990)
2.  S. Ladas, S. Kennou, S. Bebelis and C.G. Vayenas, *J. Phys. Chem.* **99**, 8845 (1993)
3.  S. Neophytides and C.G. Vayenas, *J. Phys. Chem.* **99**, 17063 (1995)
4.  M. Makri, C.G. Vayenas, S. Bebelis, K.H. Besocke and C. Cavalca, *Surface Science* **369**, 351 (1996)
5.  D. Kek, M. Mogensen, S. Pejovnik in: S. Hocevar et al. (Eds.) *Proc 3$^{rd}$ Intl. Symp. Electrocatal.*, Portoroz, Slovenia, 1999, pp 257-261
6.  C.G. Vayenas, R.M. Lambert, S. Ladas, S, Bebelis, S. Neophytides, M.S. Tikhov, N.C. Filkin, M. Makri, D. Tsiplakides, C. Cavalca and F. Besocke, *Studies in Surface Science and Catalysis*, **112**, 39 (1999)
7.  C.G. Vayenas, M.M. Jaksic, S.I. Bebelis, and S.G. Neophytides, in *Modern Aspects of Electrochemistry*, J. O'M. Bockris, B.E. Conway and R.E. White, Editors, Vol. 29, pp.57-202, Plenum (1996)
8.  C.G. Vayenas and I.V. Yentekakis in *Handbook of Heterogeneous Catalysis*, G. Ertl, H. Knoezinger and J. Weitcamp eds., Vol. 3, pp. 1310-1325, Wiley-VCH, Weinheim (1997)
9.  T.I. Politova, V.A. Sobyanin and V.D. Belyaev, *Reac. Kinet. Catal. Lett.* **41**, **321** (1990)
10.  I.R. Harkness, and R.M. Lambert, *J.Catal.* **152**, 211 (1995)
11.  C. Cavalca and G. Haller, *J.Catal.*, **177**, 389 (1998)
12.  E. Varkaraki, J. Nicole, E. Plattner, Ch. Comninellis and C.G. Vayenas, *J. Appl. Electrochemistry* **25**, 978 (1995)
13.  C.G. Vayenas, S. Brosda and C. Pliangos, *J. Catal.*, submitted, (2001).
14.  C.G. Vayenas, S. Bebelis, C. Pliangos, S. Brosda and D. Tsiplakides, in *"The Electrochemical Activation of Catalysis"*, in press, Plenum Press, 2001; references therein.
15.  C. G. Vayenas, and D. Tsiplakides, *Surf. Sci.* **467**, 23 (2000).
16.  M. Kiskinova, in *"Poisoning and Promotion in Catalysis based on Surface Science Concepts and Experiments"*, Studies in Surface Science and Catalysis, Vol. 70. Elsevier, Amsterdam, 1992; references therein.
17.  S. Neophytides, D. Tsiplakides, and C.G. Vayenas, *J. Catal.* **178**, 414-428 (1998).

# Spillover effect for the oxidation of H₂S in the presence of ammonia and water

Dae-Won Park[a], Byung-Kook Park[a], Dae-Kwang Park[a] and Hee-Chul Woo[b]

[a] Department of Chemical Engineering, Pusan National University, Pusan, 609-735, Korea

[b] Department of Chemical Engineering, Pukyung National University, Pusan, 608-739, Korea

The selective oxidation of hydrogen sulfide containing excess water and ammonia was studied over vanadium oxide based catalysts. The investigation was focused on the phase cooperation between $V_2O_5$ and $\alpha$-$Sb_2O_4$ in the reaction. Strong synergistic phenomenon in catalytic activity was observed for the mechanically mixed catalyst of $V_2O_5$ and $\alpha$-$Sb_2O_4$. Temperature programmed reduction (TPR) and oxidation (TPO) and XPS analyses were carried out to explain this synergistic effect by oxygen spillover over the boundary between $\alpha$-$Sb_2O_4$ and $V_2O_5$.

## 1. INTRODUCTION

Hydrogen sulfide released from stationary source is usually removed by the well-known Claus process [1,2]. The Claus process consists of two steps; thermal oxidation and catalytic reaction. In the thermal oxidation step, one-third of the hydrogen sulfide is first burned with air to sulfur dioxide in a waste heat furnace ($H_2S+O_2 \rightarrow SO_2 + H_2O$). In the subsequent catalytic reaction step, unconverted $H_2S$ and $SO_2$ are reacted in a 2/1 ratio to elemental sulfur ($2H_2S + SO_2 \leftrightarrow 3/n\ S_n + 2H_2O$) over an $Al_2O_3$ catalyst. However, due to thermodynamic limitations, typically 3 to 5% $H_2S$ is not converted into sulfur. As the legal regulation has been tightened, it is necessary to further treat the residual gas of the Claus installation, the so-called tail gas.

Various commercial tail gas treatment (TGT) processes have been developed. Conventional Claus TGT processes involved a hydrogen sulfide absorption step, in which a tail gas containing unreacted hydrogen sulfide is introduced into an alkaline solution bath. The most attractive process that has been recently developed is Modop (Mobil Direct Oxidation Process) process [3-5] or Super Claus Process [6-8], both of which are based on direct oxidation of $H_2S$ to elemental sulfur.

In our previous works [9,10], we reported very high activity of $TiO_2$ and $V_2O_5$ catalysts in the selective oxidation of hydrogen sulfide to elemental sulfur. Some binary metal oxides, such as Bi-V-O [11] or Fe-Cr-O [12] have also been reported as catalysts for the gas phase conversion of $H_2S$ to sulfur. Recently Li et al. [13,14] reported V-Mo, V-Bi, V-Mg, Fe-Sn and Fe-Sb mixed oxide catalyst system. However,

it was difficult to isolate the role of each metal oxide since they used coprecipitated mixed oxide catalysts where solid solution can exist. The role of $\alpha$-Sb$_2$O$_4$ in the phase cooperation of binary mixed oxide system has been widely studied and very well reviewed by Delmon et al. [15]. Mechanical mixture of two pure metal oxides can offer many informations about the phase cooperation. Although vanadium-antimony catalyst is recently studied for the oxidation of hydrogen sulfide to elemental sulfur [16], no information is available about the use of this catalyst system for the selective oxidation of H$_2$S containing NH$_3$ and excess water. The mixed gas of H$_2$S, NH$_3$ and water vapor is released from steel smelting process where the H$_2$S from coke oven is generally scrubbed and concentrated using aqueous ammonia solution. The concentrated H$_2$S is separated from the solution and transferred to the Claus plant. However, the separation of H$_2$S from the solution is not perfect and the remaining aqueous ammonia stream contains about 2% H$_2$S which in turn causes the SO$_X$ emission problem during incineration. We reported a new vapor phase catalytic process for the selective conversion of H$_2$S in the stream containing both of ammonia and water [10]. V$_2$O$_5$/SiO$_2$, Fe$_2$O$_3$/SiO$_2$ and Co$_3$O$_4$/SiO$_2$ catalysts showed good catalytic activities in the selective oxidation of the H$_2$S to ammonium thiosulfate (ATS) and elemental sulfur.

In this study, mechanical mixtures of V$_2$O$_5$ and $\alpha$-Sb$_2$O$_4$ are used to further investigate the reaction paths and the role of each metal oxide in the selective oxidation of H$_2$S to ATS and elemental sulfur. Solid state modifications of the mixtures during the catalytic reaction tests are verified by the characterization of the catalysts before and after the test using XRD and XPS. Temperature programmed techniques (TPR and TPO) are used to elucidate the phase cooperation mechanism in this reaction by spillover oxygen.

## 2. EXPERIMENTAL

### 2.1. Catalyst preparation

$\alpha$-Sb$_2$O$_4$ (1.37 m$^2$/g) was produced by calcination of Sb$_2$O$_3$ (Merck, analytical purity) in air at 500°C for 20h. The mechanical mixture catalysts were prepared according to the literature [15]. The pure V$_2$O$_5$ and $\alpha$-Sb$_2$O$_4$ were dispersed in n-pentane (Merck, analytical purity). The suspension was stirred in an ultrasonic vibrator (Brasonic 32) during 10min. n-Pentane was evaporated with agitation at 25°C under vacuum. The remaining n-pentane was removed by drying in air at 80°C for 20h. The sample was designated as V$_2$O$_5$+Sb$_2$O$_4$ (x:y) where x and y represents the weight ratio of V$_2$O$_5$ and Sb$_2$O$_4$, respectively.

### 2.2. Reaction test

Reaction tests were carried out in a continuous flow fixed-bed reactor. The reactor was made of a Pyrex® tube with an I.D. of 1 inch. A condenser was attached at the effluent side of the reactor, and its temperature was constantly maintained at 110°C to condense only solid products (sulfur + ammonium thiosulfate). A line filter was installed after the condenser to trap any solid mist which had not been captured by the condenser. From the condenser up to gas chromatography, all the lines and fittings were heated above 120°C to prevent condensation of water vapor. The flow rate of gas was controlled by a mass flow controller (Brooks MFC 5850E). Water vapor was

introduced to the reactant stream using an evaporator filled with small glass beads, and its amount was controlled by a syringe pump. The reaction test was performed after stabilization of catalyst in the stream of reactant mixtures for about 4h.

The content of effluent gas was analyzed by a gas chromatography (HP 5890) equipped with a thermal conductivity detector and a 6 ft Porapak T column (80-100 mesh) at 100°C. The exit gas from the analyzer was passed through a trap containing a concentrated NaOH solution and vented out to a hood. The conversion of $H_2S$ and the selectivity to $SO_2$ are defined as follows:

$$\text{Conversion of } H_2S \ (X) = \frac{[H_2S]_{inlet} - [H_2S]_{outlet}}{[H_2S]_{inlet}} \times 100 \ (\%)$$

$$\text{Selectivity to } SO_2 \ (S) = \frac{[SO_2]_{outlet}}{[H_2S]_{inlet} - [H_2S]_{outlet}} \times 100 \ (\%)$$

## 2.3. Characterization of catalysts

The surface area of the individual oxides and their mechanical mixtures was measured by $N_2$ adsorption method using the BET technique (Micromeritics ASAP 2000). The phase analysis was performed by X-ray diffraction crystallography with Cu-Kα radiation (Rigaku, DMAX 2400). The 2θ range between 5 and 90° was scanned at a rate of 2°/min. Identification of the phases was carried out by using JCPDS data base. XPS analyses were performed with a X-ray photoelectron spectrometer (VG, ESCALAB 220) with monochromatic Al-Kα radiation. The samples were pressed into self-supporting wafers without any binder followed by a pretreatment at an ultrahigh vacuum. The binding energies were calculated using the C1s band as reference (284.6 eV). The recorded spectra were decomposed using a least squares fitting routine program. The element atomic concentration on the surface were calculated from the relative intensities of decomposed peaks using different sensitivity factors supplied by the manufacturer. $V2p_{3/2}$ and $Sb3d_{3/2}$ were used for the calculation of V and Sb, respectively. In order to investigate the phase cooperation mechanism, TPR was carried out. Before reduction, samples were pretreated by heating under air flow from 25°C to 450°C at 10°C/min. Reduction was achieved under a $H_2/N_2$ gas mixture (10 vol.% $H_2$). Gas flow was 20cc/min and temperature program was from 25°C to 700°C at heating rate of 10°C/min. The amount of consumed $H_2$ was detected by mass spectroscopy (VG Quadrupole). After TPR experiment, the same sample was instantly tested in TPO under 2.5 vol.% $O_2$ with helium gas balance.

## 3. RESULTS AND DISCUSSION

### 3.1. Catalytic activity of the mechanical mixture ($V_2O_5 + Sb_2O_4$)

Five different mechanical mixture catalysts of $V_2O_5$ and $Sb_2O_4$ are used to study the phase cooperation phenomena with reactant composition of 5%vol. $H_2S$, 2.5%vol. $O_2$, 10vol.% $NH_3$, 60% $H_2O$ and the balance helium. The weight ratios of $V_2O_5 / Sb_2O_4$ were 1/0, 3/1, 1/1, 1/3, 0/1. Figure 1 shows the $H_2S$ conversion and $SO_2$ selectivity as a function of mass ratio ($V_2O_5/(V_2O_5+Sb_2O_4)$) at 280°C with GHSV of 12,000 $h^{-1}$. Pure $Sb_2O_4$ shows low conversion of $H_2S$ (about 43%). Considering the $H_2S$
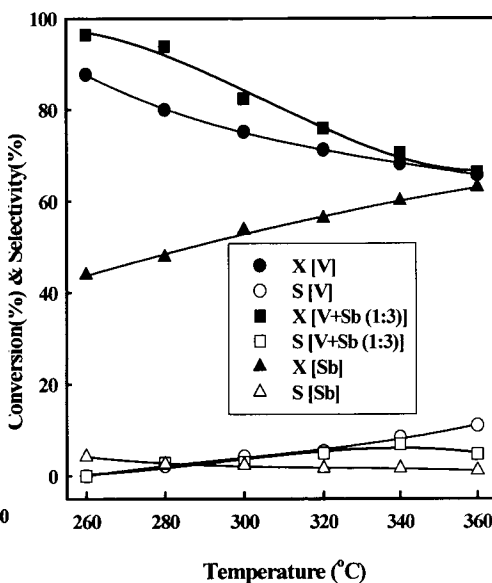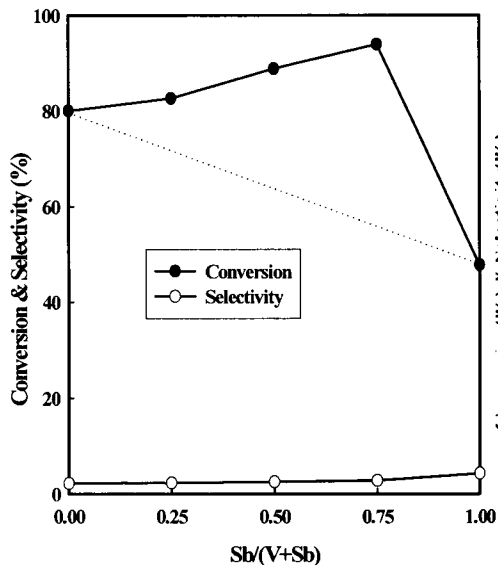
Fig. 1. Conversion of H₂S and selectivity to SO₂ for V₂O₅+Sb₂O₄ mechanical mixture catalysts at 280°C (5% H₂S, 2.5% O₂, 10% NH₃, 60%H₂O; GHSV=12,000 h⁻¹).

Fig. 2. Conversion of H₂S and selectivity SO₂ for V₂O₅, V₂O₅+Sb₂O₄(1:3) and Sb₂O₄ catalysts at various temperatures(5vol.% H₂S, 2.5vol.% O₂, 10 vol.% NH₃, 60vol.% H₂O, GHSV=12,000 h⁻¹).

conversion of 38% at 280°C for the blank test, pure $Sb_2O_4$ had not practically played any significant catalytic role on this reaction. This low activity of antimony oxide should be due to the fact that $Sb_2O_4$ could not be reoxidized by gaseous oxygen [16]. However, the addition of $V_2O_5$ into $Sb_2O_4$ greatly increased $H_2S$ conversion. All the mechanical mixture catalysts ($V_2O_5+Sb_2O_4$) show higher $H_2S$ conversion than the arithmetic average conversion (expressed as dotted line in Figure 1) of pure $V_2O_5$ and pure $Sb_2O_4$; a strong synergy exists between $V_2O_5$ and $Sb_2O_4$. However, it was not easy to find any synergistic effect for the $SO_2$ selectivity because the $SO_2$ selectivities were very low for all the catalysts.

Since maximum $H_2S$ conversion was obtained with $V_2O_5+Sb_2O_4$ (1:3) catalyst, temperature dependence of the $H_2S$ conversion and $SO_2$ selectivity for this mechanical mixture catalyst and pure $V_2O_5$ and $Sb_2O_4$ is shown in Figure 2. The $H_2S$ conversion for $V_2O_5$ and the mixture catalysts decreased with temperature. It is consistent to the previously estimated equilibrium calculations reported by Chun [17] since the selective oxidation contains several reaction steps including the reverse Claus reaction. The opposite temperature dependence of the $H_2S$ conversion for $Sb_2O_4$ suggests again that $Sb_2O_4$ does not participate directly to the catalytic oxidation of $H_2S$. On the whole temperature ranges, 260°C - 360°C, the mixture catalyst exhibits higher $H_2S$ conversion than pure $V_2O_5$ and pure $Sb_2O_4$. Thus, the synergy for the mixture catalyst was confirmed over wide temperature ranges. The $SO_2$ selectivity for the mixture catalyst is also lower than pure $V_2O_5$ itself.

## 3.2. Phase cooperation

The synergistic effect observed in mixed oxide catalysts are generally known [15] to be from the three main reasons: (1) formation of new active phase by reaction between two phases, (2) increase of surface area, (3) formation of mobile oxygen species and some chemical action of the latter (remote control mechanism). In order to understand the phase cooperation for $V_2O_5+Sb_2O_4$ catalyst, the first possibility was verified by XRD method. The X-ray diffraction patterns of $V_2O_5+Sb_2O_4$ (1:3) catalyst are presented in Figure 3. Fresh catalyst shows only characteristic peaks of $V_2O_5$ and $Sb_2O_4$. The spent catalyst, used for 8 h for the reaction, shows the existence of reduced phase of $V_2O_5$ like $VO_2$. Part of $Sb_2O_4$ was also sulfided to $Sb_2S_3$. However, no new phase (principally $V_xSb_{1-x}O_y$ ) detectable by XRD was generated during the catalytic tests. Vanadium antimonate ($VSbO_4$) is reported to be one of the most active phase in coprecipitated V-Sb-O mixed oxide catalyst used in several reactions, like propane ammoxidation [18-20] and oxidation of hydrogen sulfide to elemental sulfur [16,21].

Secondly, BET surface areas of the fresh and used $V_2O_5+Sb_2O_4$ (1:3) catalyst were measured and they were 2.4 and 1.9 $m^2/g$, respectively. The surface area of the fresh catalyst was nearly the same as the arithmetic average value of pure $V_2O_5$(5.4 $m^2/g$) and $Sb_2O_4$ (1.4 $m^2/g$). The decrease in surface area of spent catalyst may be due to the increase of grain size. Therefore, the above two possibilities can be excluded to explain the increase of $H_2S$ conversion in this study. These two phenomena are
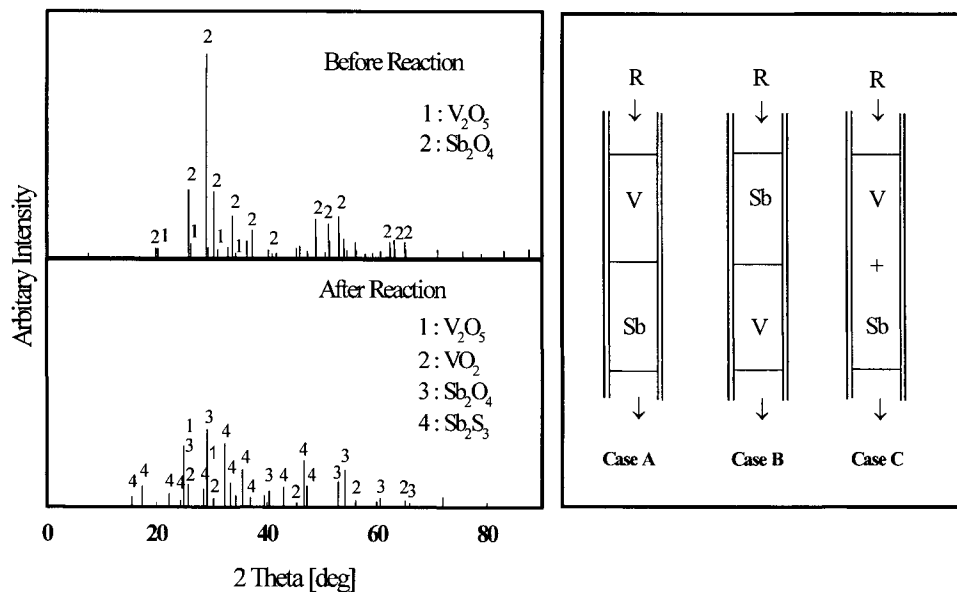


Fig. 3. XRD patterns of $V_2O_5+Sb_2O_4$(1:3) catalyst before and after reaction.

Fig. 4. Three types of two-bed operation for the $H_2S$ oxidation (V= $V_2O_5$, Sb= $Sb_2O_4$, R= reactant mixture).

Table 1
Conversion of H$_2$S and selectivity to SO$_2$ for different two-bed operations at 260°C

| Cases in Fig.7. | Conversion of H$_2$S (%) | Selectivity to SO$_2$ (%) |
|---|---|---|
| A ( V$_2$O$_5$ → Sb$_2$O$_4$ ) | 72.3 | 0 |
| B ( Sb$_2$O$_4$ → V$_2$O$_5$ ) | 77.2 | 0 |
| C ( V$_2$O$_5$ + Sb$_2$O$_4$ ) | 80.9 | 0 |

Reactant composition = H$_2$S/O$_2$/NH$_3$/H$_2$O =5/2.5/5/60, V$_2$O$_5$= 0.75g, Sb$_2$O$_4$ = 0.75g , GHSV = 4,000h$^{-1}$, reaction time

generally accepted to be not evident to describe synergistic effect in mechanically mixed catalysts [15].

The role of mobile oxygen species is extensively studied to explain phase cooperation in mechanically mixed catalysts. Delmon et al. [15] reviewed remote control effects of two phases in several selective oxidation catalysts. This remote control mechanism supposes that a mobile oxygen species (spillover oxygen) is formed from O$_2$ on one of the phases and migrates onto the surface of the other, where it creates and/or regenerates the catalytic centers. They also reported Sb$_2$O$_4$ could be a strong donor of mobile oxygen species. An attempt to verify the existence of the synergistic effect by the remote control mechanism is to test the H$_2$S oxidation in two-bed operation modes as shown in Figure 4. In case A, the reactant mixture is first contacted with V$_2$O$_5$ then Sb$_2$O$_4$ before it comes out of the reactor. The case B is the reverse order of case A. In case C, the uniform mixtures of V$_2$O$_5$ and Sb$_2$O$_4$ are placed together in the reactor. The H$_2$S conversion at three different operations are summarized in Table 1. The operation in case A shows lower H$_2$S conversion than case B and case C. One conclusion can be drawn from this result that Sb$_2$O$_4$ is the controlling (donor) phase and that V$_2$O$_5$ is controlled (acceptor) phase for the spillover oxygen.

In order to identify the real nature of this phase cooperation in V$_2$O$_5$+Sb$_2$O$_4$ catalyst, TPR and TPO techniques are used in this study. Comparative temperature programmed reduction
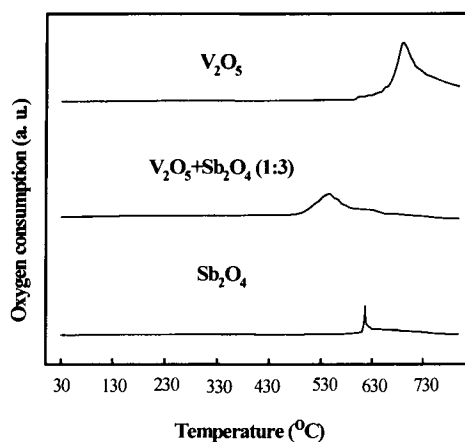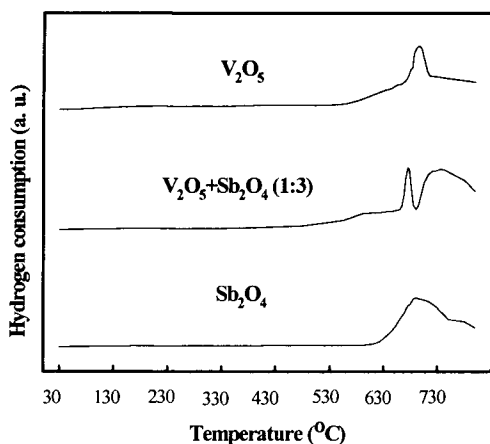


Fig. 5. TPR profiles for V$_2$O$_5$, V$_2$O$_5$+Sb$_2$O$_4$ (1:3) and Sb$_2$O$_4$ catalysts.

Fig. 6. TPO profiles for V$_2$O$_5$, V$_2$O$_5$+Sb$_2$O$_4$ (1:3) and Sb$_2$O$_4$ catalysts.

Table 2
Relative percentage of different oxidation states of vanadium from XPS analyses for catalysts before and after reaction

| Catalyst | V(Area %) | | |
|---|---|---|---|
| | V(5+) | V(4+) | V(3+) |
| BE (eV) | 517.2 | 516.9 | 514.3 |
| fresh $V_2O_5$ | 100 | - | - |
| used $V_2O_5$ | 81.9 | 13.6 | 4.5 |
| fresh $V_2O_5 + Sb_2O_4$ (1:3) | 100 | - | - |
| used $V_2O_5 + Sb_2O_4$ (1:3) | 89.3 | 10.7 | - |

Reactant composition = $H_2S/O_2/NH_3/H_2O$ =5/2.5/5/60, GHSV = 12,000h$^{-1}$, T= 260°C, reaction time = 4h.

(TPR) and the following temperature programmed oxidation (TPO) are carried out for $V_2O_5$, $Sb_2O_4$ and $V_2O_5+Sb_2O_4$ (1:3), and the results are shown in Figure 5 and 6. The reducibility of catalysts was first measured using TPR method with hydrogen as a reductant. For the mixture catalyst, hydrogen consumption started from 480°C, lower than that in the case of pure $Sb_2O_4$ (600°C) and $V_2O_5$(540°C). In the subsequent TPO experiment, the mixture catalyst showed better reoxidation property than pure $V_2O_5$ and pure $Sb_2O_4$. The maximum peak of $O_2$ consumption for the $V_2O_5+Sb_2O_4$ (1:3) was 540°C, much lower than $V_2O_5$ ($T_{max}$ = 680°C) and $Sb_2O_4$ ($T_{max}$ = 610°C).

Since $Sb_2O_4$ had practically no catalytic activity on $H_2S$ oxidation, the increase of $H_2S$ conversion in $V_2O_5+Sb_2O_4$ mixture will be from the capacity of $Sb_2O_4$ for reoxidizing reduced phases of $V_2O_5$ catalyst during the reaction. XPS analysis results in Table 2 supported the reoxidizing capacity of $Sb_2O_4$. Vanadium in fresh pure $V_2O_5$ was only $V^{5+}$. After the reaction test $V^{5+}$ and $V^{4+}$ was observed, in addition V was strongly reduced to $V^{3+}$. For the mixture catalyst of $V_2O_5+Sb_2O_4$, the reduction of vanadium was less severe and no $V^{3+}$ signal was detected. However, $Sb3d_{3/2}$ (540.3 eV) binding energy did not show any appreciable change after the reaction test.

In the context of the remote control mechanism, the role of the controlling phase ($\alpha$-$Sb_2O_4$, producing spillover oxygen) and that of the controlled phase ($V_2O_5$, giving catalytic site for oxidation of hydrogen sulfide) can be distinguished. As $Sb_2O_4$ is very difficult to be reoxidized by gaseous oxygen to $Sb^{5+}$ oxide [20], direct adsorption of $O_2$ on $Sb_2O_4$ will be less probable. The possible explanation for the synergistic effect of $V_2O_5+Sb_2O_4$ mixture catalyst will be the following sequence of redox process. Since $Sb_2O_4$ is a p-type semiconductor [22], electron transfer can occur from $V_2O_5$ to $Sb_2O_4$ at the boundary of these two metal oxides. Then, oxygen vacancy can be formed and it will promote the dissociative adsorption of $O_2$. The oxygen ion $O^{2-}$ spills over the boundary between $Sb_2O_4$ and $V_2O_5$. Therefore, the partially reduced $V_2O_{5-x}$ can be reoxidized and participate to the increase of catalytic activity.

$$Sb^{4+} + 2e \rightarrow Sb^{2+} \qquad (1)$$
$$Sb^{4+} + 1/2O_2 \rightarrow Sb^{4+} + O^{2-} \qquad (2)$$
$$V_2O_{5-x} + xO^{2-} \rightarrow V_2O_5 + 2xe \qquad (3)$$

## 4. CONCLUSION

The selective oxidation of hydrogen sulfide in the presence of excess water and ammonia was investigated in this study. Hydrogen sulfide was successfully converted into harmless ammonium thiosulfate and elemental sulfur without considerable emission of sulfur dioxide. Mechanical mixture catalyst of $V_2O_5+Sb_2O_4$ showed good synergistic effect for the $H_2S$ oxidation. The phase cooperation between $Sb_2O_4$ and $V_2O_5$ was explained by redox mechanism and oxygen spillover between their boundaries.

## ACKNOWLEDGEMENTS

## REFERENCES

1. J. A. Lagos, J. Borsboom, P.H. Bezben, Oil and Gas J. 10 (1988) 68.
2. J. Wieckowska, Catalysis Today. 24 (1995) 105.
3. T. Chopin, J. L. Hebrand, E.Quemere, Ep 422999 (1990).
4. R. Kettner, N. Liermann, Oil and Gas J. 11 (1983) 63.
5. R. Kettner, T. Lubcke, N. Liermann, EP 78690 (1982)
6. P. J. Brink, J. W. Geus, US Patent 4818740 (1989)
7. P. J. Brink, J. W. Geus, EP 409353 (1990)
8. R. J. A. M. Terorde, P. J. Brink, L. M. Visser, A. J. Dillen, Catalysis Today 17 (1993) 217.
9. S. W. Chun, J. Y. Jang, D. W. Park, H. C. Woo, J. S. Chung, Appl. Catal. B 16 (1998) 235.
10. D. W. Park, S. W. Chun, J. Y. Jang, H. S. Kim, H. C. Woo, J. S. Chung, Catalysis Today, 44 (1998) 73.
11. R. H. Haas, J. W. Ward, US Patent 4528277 (1985)
12. P. J. Brink, J. W. Geus, US Patent 5286697 (1994).
13. K. T. Li, M. Y. Huang, W. D. Cheng, Ind. Eng. Chem. Res. 35 (1996) 621.
14. K. T. Li, C. S. Yen, N. S. Shyu, Appl. Catal. A 156 (1997) 117.
15. L. T. Weng, B. Delmon, Appl. Catal. A 81 (1992) 141.
16. K. T. Li and N. S. Shyu, Ind. Eng. Chem. Res. 36 (1997) 1480.
17. S. W. Chun, Ph. D. Thesis, Pusan National University, Pusan, Korea (1998).
18. R. Catani, G. Centi, F. Trifiro, R. Grosselli, Ind. Eng. Chem. Res. 31 (1992) 107.
19. R. Nilsson, T. Lindlad, A. Anderson, J. of Catal. 148 (1994) 501.
20. G. Centi, S. Perathoner, Appl. Catal. A 124 (1995) 317.
21. K. T. Li, T. Y. Chien, Catal. Lett. 57 (1997) 77.
22. G. W. Godin, C. C. McCain, E. A. Porter, Proc. 4th Int. Cong. Catal. 1 (1997) 271.

# Compensation effects in the liquid-phase regioselective hydrogenation of functionalized alkenes on supported rhodium catalysts

F. M. Bautista, J. M. Campelo, A. Garcia, D. Luna,[*] J. M. Marinas and A. A. Romero

Department of Organic Chemistry, Córdoba University, Campus de Rabanales, Edificio C-3; E-14014 Córdoba, Spain[**]

The liquid-phase selective hydrogenation of sixteen functionalized alkene substrates was carried out at low hydrogen pressures and temperature range 293-323 K, on four different rhodium 1 wt % supported catalysts. Two different amorphous $AlPO_4$ (Al/P = 1) and an $AlPO_4/SiO_2$ (20:80 wt%) system, as well as a natural Sepiolite were used as metal supports. The reaction rates were a function of both the substituent group of olefinic double bond as well as of the Rh catalyst support. Valuable information about hydrogenation mechanism was also obtained from several "isokinetic parameters" calculated from the existence of a "compensation effect" between ln A and Ea from the Arhenius equation (as well as between $\Delta S^{\neq}$ and $\Delta H^{\neq}$ from the Eyring equation).

## 1. INTRODUCTION

Supported rhodium catalysts are industrially important in several processes such as carbon monoxide hydrogenation [1], reduction of nitrogen monoxide in automobile exhaust gas [2] and hydroformylation of olefins. Besides, these catalysts are now investigated in several processes, such as heterogeneous benzene combustion [3] or methane reforming with carbon dioxide [4]. Liquid-phase hydrogenation reactions are also a very important application of these catalysts in the industrial production of so called "fine chemicals" [5-7]. In this respect, among all the components of group VIII metals, Rh is the most active metal for hydrogenation of olefins but its use is limited by its high cost [7]. However, the choice of more active catalysts makes it possible to operate at lower temperature, obtaining higher selectivities due to the milder reaction conditions as well as to use lower amount of catalysts. Thus, the synthesis and characterization of very well dispersed rhodium catalyst are studied extensively because the catalytic properties of supported rhodium catalysts are strongly affected by the nature of the inorganic support as well as by the preparation method [8,9]. Consequently, the subject of a great part of current research in catalysis by metals is the study of metal-support interaction effects. In this connection, the activity and selectivity of catalysts towards the hydrogenation of different polyfunctional molecules is interesting in many respects. In order to expand the results obtained in previous works on supported rhodium catalysts [10-17], in the present paper, we study the liquid-phase hydrogenation of sixteen functionalized alkene substrates on 1 wt% $Rh/AlPO_4$ and Rh/Sepiolite catalysts.

[*] E-mail: qo1lumad@uco.es

## 2. EXPERIMENTAL

Catalysts containing 1 wt% rhodium were prepared by impregnation of the supports to incipient wetness with aqueous rhodium (III) trichloride hydrate (Merck) and reduced at 473 K in hydrogen stream (200 ml/min) for 10 min [10-17]. As supports were used two different amorphous $AlPO_4$ (Al/P = 1) and an $AlPO_4/SiO_2$ (20:80 wt%) system, all they obtained according to a sol-gel method [10-16], as well as a natural Sepiolite from Vallecas (Madrid), supplied by Tolsa S.A., with chemical analysis: $SiO_2$ 62.0, MgO 23.9, $Al_2O_3$ 1.7, $Fe_2O_3$, 0.5, CaO 0.5, $K_2O$ 0.6 and $Na_2O$ 0.3% [16,17]. The former $AlPO_4$ supports were obtained by precipitation of aluminum orthophosphate, from an aqueous solution of aluminum chloride and phosphoric acid, with ammonia $AlPO_4$-A or propylene oxide $AlPO_4$-P [12-15]. For the $AlPO_4/SiO_2$ support the precipitation of $AlPO_4$ was carried out on commercial silica (Merck, Kieselgel 60, 70-230 mesh) [10,11]. Before metal impregnation, the supports, 200-250 mesh size, were calcined at 920 K for 3 h. Table 1 collects textural properties of supports (surface area, $S_{BET}$, pore volume, V, and main pore diameter, d) obtained by nitrogen adsorption [11,18,19] as well as the surface basicity and acidity of supports determined by a spectrophotometric method that allows titration of the amount of irreversible adsorbed pyridine (PY, $pK_a$ = 5.25) and benzoic acid (BA, $pK_a$ = 4.19) [18,19]. Metal surface area, $S_{Rh}$, and volume mean diameter, $D_{Rh}$, obtained from TEM measurements using a Philips EM-300 [10-12] and assuming a spherical geometry are also shown in Table 1.

According to the procedure previously described [11-18], catalytic activity measurements were developed in a low pressure hydrogenator (Parr Instruments Co., model 3911). hydrogenation runs were accomplished with 25 ml of 1 M methanolic solution of different substrates with catalyst amounts between 0.02-0.5 g, under initial hydrogen pressures in the interval 0.3-0.7 MPa and temperatures in the studied range 293-323 K. The pure alkenes were used as supplied by Merck, p.a., after distillation under reduce pressure and low temperature and passage through alumina at room temperature. Methanol (p.a. 99%, Scharlau) and hydrogen (99.999%, SEO) was used without further purification. The analysis of reaction products were performed on a HP-5720 gas chromatograph equipped with an FID and using a stainless-steel column packed with 5% squalene on Chromosorb GAW-DMCS 80/100 at 313-358 K. The only products always detected were those corresponding to the hydrogenation of the carbon-carbon double bond. The initial reaction rates were obtained from a least-square fit to the slopes of the plots of the initially linear decrease in hydrogen pressure vs. reaction time. Since these plots were always practically linear until 70-90% conversion, the determination of initial rates was straightforward. The relative error from at least three repetitive measurements was about 6%.

## 3. RESULTS AND DISCUSSION

Several hydrogenation runs, performed at various agitation regimes and with different amounts of catalysts, showed the absence of external diffusion control above 200 strokes/min. According to results previously obtained [11-14,16-18], the internal diffusion was excluded by using catalysts with an enough small grain diameter, so that the kinetic

Table 1
Textural and acid-base properties of different supports, as well as volume mean diameters and metal surface areas of 1 wt % rhodium supported catalysts.

| Support | $S_{BET}$ $(m^2/g)$ | V $(ml/g)$ | d $(nm)$ | Acidity vs PY $(\mu mol/g)$ | Basicity vs BA $(\mu mol/g)$ | $D_{Rh}$ $(nm)$ | $S_{Rh}$ $(m^2/g_{Rh})$ |
|---|---|---|---|---|---|---|---|
| $AlPO_4$-A | 156 | 0.68 | 3.6 | 190 | 200 | 4.2 | 115 |
| $AlPO_4$-P | 228 | 0.94 | 2.5 | 227 | 166 | 5.4 | 90 |
| $AlPO_4$-$SiO_2$ | 327 | 0.46 | 3.0 | 380 | 70 | 4.0 | 121 |
| Sepiolite | 203 | 0.54 | 5.3 | 31 | 174 | 5.0 | 97 |

data obtained under the present experimental conditions are free from transport influences. Besides, hydrogenation rates for all substrates studied were first order in initial hydrogen pressure in the studied interval 0.3-0.7 MPa, and zero order in the substrate concentration (in the studied range 0.4-2 M), for all catalysts. Similar results were obtained with these catalysts in the liquid phase hydrogenation of cycloalkenes [11] styrene [12] and benzylidene ketones [17]. However, in the hydrogenation of $\alpha,\beta$-unsaturated alcohols [14] and 1-alkenes [16] the reactions order in the substrate concentrations was lower than zero (about -0.5). In all cases, the zero reaction orders (or lower than zero but higher than -1) in the substrate concentration could be accounted for by a slow reaction (or dissociative adsorption) of hydrogen molecules directly from the gas phase on the surface complex formed by the adsorption of the olefinic double bond on Rh surface active sites, according to the Langmuir-Hinshelwood-Hougen-Watson adsorption model [20]. Accordingly, the kinetic equation for the systems under study can be written as:

$$r = dC/dt = N_T\, r_0 K_{H2}\, p_{H2} \tag{1}$$

where $N_T$ is the number of active sites, $K_{H2}$ the adsorption constant of $H_2$ molecules, $r_0$ is the reaction rate constant and $p_{H2}$ is the hydrogen pressure. For the rate constant of the rate-determining step, the Eyring equation, that evaluates the temperature dependence of reaction rate in terms of transition-state theory, let us obtain the enthalpy, $\Delta H^{\neq}$, and entropy, $\Delta S^{\neq}$, components:

$$r_0 = (kT/h)\, \exp(\Delta S^{\neq}/R - \Delta H^{\neq}/RT) = K_0\, \exp(-E_a/RT) \tag{2}$$

where $k$ and $h$ are the Boltzmann's and Plank's constants. Similarly, the values of the apparent activation energies, $E_a$ and the corresponding Arrhenius constant values, ln A can be obtained from the initial reaction rates, in the temperature range studied, and collected in Table 2, where reaction rates, $r_0$ (mol/min $g_{Rh}$), are always considered for an amount of catalyst containing 1 g of supported Rh. These values can be easily transformed into areal rates as well as into turnover numbers, but taking into account the very similar values in $D_{Rh}$ (and consequently in $S_{Rh}$) in Table 1, the direct use of $r_0$ values in Table 2, probably do not significantly affects the activation parameters obtained in Tables 3-6, for different catalysts and substrates.

On the other hand, based on these activation parameters (ln A, $E_a$, $\Delta H^{\neq}$ and $\Delta S^{\neq}$)

Table 2

Support influence on hydrogenation rates, $r_O$, (mol/min $g_{Rh}$) at different temperatures, T (°K), obtained with 1 wt% Rh catalysts on different supports, under standard operation conditions.

| Entry | Substrate | T | $AlPO_4$-A | $AlPO_4$-P | $AlPO_4$-$SiO_2$ | Sepiolite |
|---|---|---|---|---|---|---|
| 1 | $CH_2=CH-OCH_2CH_3$ | 293 | 2.40 | 1.06 | 3.20 | 2.49 |
|  | (ethyl vinyl ether) | 303 | 3.25 | 1.53 | 4.20 | 3.58 |
|  |  | 313 | 4.50 | 2.39 | 5.40 | 5.34 |
|  |  | 323 | 5.75 | 3.28 | 6.90 | 8.07 |
| 2 | $CH_2=CH-CO-CH_3$ | 293 | 0.46 | 0.14 | 1.30 | 0.92 |
|  | (methyl vinyl ketone) | 303 | 0.67 | 0.23 | 1.70 | 1.57 |
|  |  | 313 | 0.91 | 0.39 | 2.10 | 2.19 |
|  |  | 323 | 1.22 | 0.69 | 2.50 | 2.86 |
| 3 | $CH_2=CH-COOH$ | 293 | 1.50 | 0.61 | 2.20 | 2.22 |
|  | (acrylic acid) | 303 | 2.10 | 0.87 | 2.70 | 3.02 |
|  |  | 313 | 2.70 | 1.26 | 3.30 | 3.58 |
|  |  | 323 | 3.60 | 1.74 | 4.00 | 4.57 |
| 4 | $CH_2=CH-COOCH_2CH_3$ | 293 | 3.08 | 2.74 | 9.50 | 6.10 |
|  | (ethyl acrylate) | 303 | 4.19 | 4.70 | 13.70 | 8.80 |
|  |  | 313 | 6.28 | 7.48 | 19.50 | 12.60 |
|  |  | 323 | 8.90 | 13.02 | 26.60 | 18.60 |
| 5 | $CH_2=CH-CO-NH_2$ | 293 | 0.82 | 0.56 | 1.05 | 1.05 |
|  | (acrylamide) | 303 | 1.04 | 0.71 | 1.30 | 1.52 |
|  |  | 313 | 1.46 | 0.97 | 1.50 | 1.89 |
|  |  | 323 | 1.76 | 1.30 | 1.80 | 2.89 |
| 6 | $CH_2=CH-O-CO-CH_3$ | 293 | 0.44 | 0.78 | 0.84 | 0.50 |
|  | (vinyl acetate) | 303 | 0.60 | 1.04 | 1.06 | 0.69 |
|  |  | 313 | 0.81 | 1.55 | 1.32 | 0.91 |
|  |  | 323 | 1.07 | 1.87 | 1.64 | 1.21 |
| 7 | $CH_2=CH-CH_2-O-CO-CH_3$ | 293 | 0.52 | 0.95 | 1.70 | 0.74 |
|  | (allyl acetate) | 303 | 0.78 | 1.25 | 2.60 | 1.39 |
|  |  | 313 | 1.04 | 1.56 | 3.90 | 2.12 |
|  |  | 323 | 1.50 | 1.96 | 5.40 | 2.93 |
| 8 | $CH_2=CH-C_5H_4N$ | 293 | 0.50 | 0.21 | 0.65 | 0.43 |
|  | (4-vinylpyridine) | 303 | 0.65 | 0.35 | 0.89 | 0.75 |
|  |  | 313 | 0.91 | 0.58 | 1.20 | 1.07 |
|  |  | 323 | 1.20 | 0.73 | 1.60 | 1.40 |
| 9 | $CH_2=CH-NC_4H_6O$ | 293 | 1.11 | 3.56 | 6.50 | 6.60 |
|  | (1-vinyl-2-pyrrolidone) | 303 | 1.98 | 5.10 | 9.10 | 9.70 |
|  |  | 313 | 3.23 | 8.06 | 11.70 | 14.00 |
|  |  | 323 | 4.31 | 10.00 | 16.00 | 19.00 |
| 10 | $C_6H_5-CH=CH-CO-CH_3$ | 293 | 0.39 | 0.25 | 0.65 | 0.52 |
|  | (trans-benzylideneacetone) | 303 | 0.53 | 0.35 | 0.88 | 0.70 |
|  |  | 313 | 0.74 | 0.53 | 1.20 | 0.89 |
|  |  | 323 | 1.18 | 0.73 | 1.50 | 1.15 |
| 11 | $C_6H_5-CH=CH-COOH$ | 293 | 0.52 | 0.21 | 0.73 | 0.40 |
|  | (trans-cinnamic acid) | 303 | 0.81 | 0.33 | 1.00 | 0.51 |
|  |  | 313 | 1.07 | 0.48 | 1.40 | 0.57 |
|  |  | 323 | 1.60 | 0.66 | 1.80 | 0.69 |
| 12 | $C_6H_5-CH=CH-COO-CH_3$ | 293 | 0.37 | 0.22 | 0.47 | 0.24 |
|  | (methyl trans-cinnamate) | 303 | 0.58 | 0.38 | 0.64 | 0.37 |
|  |  | 313 | 0.77 | 0.53 | 0.89 | 0.48 |
|  |  | 323 | 1.06 | 0.80 | 1.04 | 0.67 |

Table 3
Activation parameters: $E_a$ (KJ/mol), ln A (mol/min $g_{Rh}$), $\Delta H^{\neq}$ (KJ/mol) and $\Delta S^{\neq}$ (J/mol °K), obtained from reaction rates in Table 2 with the Rh/AlPO$_4$-A catalyst. Uncertainties are determined by standard deviations.

| Entry | Substrate | $E_a$ | Ln A | $\Delta H^{\neq}$ | $\Delta S^{\neq}$ |
|---|---|---|---|---|---|
| 1 | $CH_2=CH-OCH_2CH_3$ | 23.2 ± 0.7 | 10.4 ± 0.3 | 20.6 ± 0.6 | -167.0 ± 2.1 |
| 2 | $CH_2=CH-CO-CH_3$ | 25.5 ± 0.8 | 9.7 ± 0.2 | 22.9 ± 0.6 | -173.0 ± 2.0 |
| 3 | $CH_2=CH-COOH$ | 22.7 ± 0.7 | 9.7 ± 0.3 | 20.1 ± 0.7 | -172.7 ± 2.0 |
| 4 | $CH_2=CH-COOCH_2CH_3$ | 28.2 ± 1.4 | 12.7 ± 0.5 | 25.6 ± 1.4 | -148.2 ± 4.5 |
| 5 | $CH_2=CH-CO-NH_2$ | 20.7 ± 1.5 | 8.3 ± 0.6 | 18.2 ± 1.4 | -184.5 ± 4.7 |
| 6 | $CH_2=CH-O-CO-CH_3$ | 23.3 ± 0.1 | 8.8 ± 0.1 | 20.8 ± 0.1 | -180.7 ± 0.3 |
| 7 | $CH_2=CH-CH_2-O-CO-CH_3$ | 27.3 ± 1.1 | 10.6 ± 0.4 | 24.7 ± 1.1 | -165.8 ± 3.5 |
| 8 | $CH_2=CH-C_5H_4N$ | 23.3 ± 1.0 | 8.8 ± 0.4 | 20.7 ± 1.0 | -179.9 ± 3.2 |
| 9 | $CH_2=CH-NC_4H_6O$ | 36.0 ± 2.9 | 15.0 ± 1.2 | 33.4 ± 3.0 | -129.4 ± 9.7 |
| 10 | $C_6H_5-CH=CH-CO-CH_3$ | 28.7 ± 2.7 | 10.8 ± 1.0 | 26.1 ± 2.6 | -163.9 ± 8.5 |
| 11 | $C_6H_5-CH=CH-COOH$ | 28.7 ± 1.6 | 11.2 ± 0.6 | 26.2 ± 1.6 | -160.8 ± 5.2 |
| 12 | $C_6H_5-CH=CH-COO-CH_3$ | 27.1 ± 1.5 | 10.2 ± 0.6 | 24.6 ± 1.6 | -168.9 ± 5.1 |

Table 4
Activation parameters: $E_a$ (KJ/mol), ln A (mol/min $g_{Rh}$), $\Delta H^{\neq}$ (KJ/mol) and $\Delta S^{\neq}$ (J/mol °K), obtained from reaction rates in Table 2 with the Rh/AlPO$_4$-P catalyst. Uncertainties are determined by standard deviations.

| Entry | Substrate | $E_a$ | ln A | $\Delta H^{\neq}$ | $\Delta S^{\neq}$ |
|---|---|---|---|---|---|
| 1 | $CH_2=CH-OCH_2CH_3$ | 30.1 ± 1.2 | 12.4 ± 0.5 | 27.6 ± 1.2 | -150.1 ± 3.8 |
| 2 | $CH_2=CH-CO-CH_3$ | 41.4 ± 1.7 | 15.0 ± 0.7 | 39.2 ± 1.8 | -127.7 ± 5.7 |
| 3 | $CH_2=CH-COOH$ | 27.8 ± 0.5 | 10.9 ± 0.2 | 25.1 ± 0.4 | -163.3 ± 1.3 |
| 4 | $CH_2=CH-COOCH_2CH_3$ | 40.4 ± 1.3 | 17.6 ± 0.5 | 37.9 ± 1.3 | -107.3 ± 4.3 |
| 5 | $CH_2=CH-CO-NH_2$ | 22.4 ± 1.3 | 8.6 ± 0.5 | 19.7 ± 1.2 | -182.5 ± 4.1 |
| 6 | $CH_2=CH-O-CO-CH_3$ | 23.7 ± 2.0 | 9.5 ± 0.8 | 21.3 ± 2.0 | -174.3 ± 6.4 |
| 7 | $CH_2=CH-CH_2-O-CO-CH_3$ | 19.0 ± 0.3 | 7.7 ± 0.1 | 16.3 ± 0.4 | -189.5 ± 1.3 |
| 8 | $CH_2=CH-C_5H_4N$ | 33.1 ± 3.3 | 12.1 ± 1.3 | 31.0 ± 3.2 | -151.8 ± 9.5 |
| 9 | $CH_2=CH-NC_4H_6O$ | 28.0 ± 2.3 | 12.8 ± 0.9 | 25.5 ± 2.3 | -147.2 ± 7.4 |
| 10 | $C_6H_5-CH=CH-CO-CH_3$ | 28.0 ± 1.0 | 10.1 ± 0.4 | 26.0 ± 1.0 | -167.7 ± 3.4 |
| 11 | $C_6H_5-CH=CH-COOH$ | 30.1 ± 1.5 | 10.8 ± 0.6 | 27.5 ± 1.1 | -163.8 ± 3.5 |
| 12 | $C_6H_5-CH=CH-COO-CH_3$ | 33.2 ± 2.0 | 12.1 ± 0.8 | 30.6 ±1.9 | -152.7 ± 6.2 |

collected in Tables 3-6, a series of common isokinetic parameters can be obtained due to the existence of a relationship between the kinetic parameters, $\Delta H^{\neq}$ and $\Delta S^{\neq}$, as well as between ln A and $E_a$, (as it is shown in Fig. 1) according to the most habitual expression of the "compensation effect" or "isokinetic relationship" [21-23]:

$$\ln A = \ln \alpha + E_a/\theta R \qquad (3)$$

$$\Delta G^{\neq} = \theta R \ln K^{\neq} = \Delta H^{\neq} - \theta \Delta S^{\neq} \qquad (4)$$

Thus, several isokinetic parameters of catalysts (and substrates) are obtained: $\theta$, isokinetic temperature at which identical values of reaction rate constant, $\alpha$; the equilibrium

Table 5

Activation parameters: $E_a$ (KJ/mol), ln A (mol/min $g_{Rh}$), $\Delta H^{\neq}$ (KJ/mol) and $\Delta S^{\neq}$ (J/mol °K), obtained from reaction rates in Table 2 with the $Rh/AlPO_4-SiO_2$ catalyst. Uncertainties are determined by standard deviations.

| Entry | Substrate | $E_a$ | ln A | $\Delta H^{\neq}$ | $\Delta S^{\neq}$ |
|---|---|---|---|---|---|
| 1 | $CH_2=CH-OCH_2CH_3$ | 20.1 ± 0.1 | 9.4 ± 0.1 | 17.6 ± 0.2 | -175.2 ± 0.3 |
| 2 | $CH_2=CH-CO-CH_3$ | 17.1 ± 0.8 | 7.3 ± 0.3 | 14.6 ± 0.9 | -192.7 ± 2.8 |
| 3 | $CH_2=CH-COOH$ | 15.7 ± 0.2 | 7.2 ± 0.1 | 13.1 ± 0.1 | -193.4 ± 0.5 |
| 4 | $CH_2=CH-COOCH_2CH_3$ | 27.1 ± 0.2 | 13.4 ± 0.1 | 24.5 ± 0.2 | -142.3 ± 0.8 |
| 5 | $CH_2=CH-CO-NH_2$ | 13.9 ± 0.6 | 5.8 ± 0.2 | 11.3 ± 0.6 | -205.7 ± 2.0 |
| 6 | $CH_2=CH-O-CO-CH_3$ | 17.5 ± 0.2 | 7.0 ± 0.1 | 15.0 ± 0.2 | -195.2 ± 0.5 |
| 7 | $CH_2=CH-CH_2-O-CO-CH_3$ | 30.5 ± 0.7 | 13.1 ± 0.3 | 28.0 ± 0.7 | -144.9 ± 2.4 |
| 8 | $CH_2=CH-C_5H_4N$ | 23.6 ± 0.2 | 9.3 ± 0.1 | 21.1 ± 0.1 | -176.5 ± 0.4 |
| 9 | $CH_2=CH-NC_4H_6O$ | 23.3 ± 0.8 | 11.4 ± 0.3 | 20.7 ± 0.8 | -158.6 ± 2.7 |
| 10 | $C_6H_5-CH=CH-CO-CH_3$ | 22.2 ± 0.8 | 8.7 ± 0.3 | 19.7 ± 0.8 | -181.2 ± 2.5 |
| 11 | $C_6H_5-CH=CH-COOH$ | 24.0 ± 0.7 | 9.5 ± 0.3 | 21.4 ± 0.7 | -174.3 ± 2.2 |
| 12 | $C_6H_5-CH=CH-COO-CH_3$ | 19.6 ± 2.9 | 7.3 ± 1.1 | 18.9 ± 1.9 | -186.6 ± 6.0 |

constant of the activated complexes, $K^{\neq}$ and their activation free energies, $\Delta G^{\neq}$. They are also shown in Tables 7 and 8. So, although the compensation effect is usually represented by Eqn. (3), it also may be obtained from the entropy-enthalpy relationship (4) indicating the existence of a linear free-energy relationship (LFER), exhibiting the same $\Delta G^{\neq}$ value for any set of reactions of the same type and mechanism. This constraint on $\Delta G^{\neq}$ is what allows us to determine the set of isokinetic parameters closely associated with the substrates (Table 7), and another set exclusively related to the catalysts (Table 8). Besides, from Eqns. (2) and (3) and from Eqns. (2) and (4), the Arhenius and Eyring can be expressed:

$$r_0 = \alpha \exp[(E_a/R)(1/\theta - 1/T)] = (kT/h) \exp[(\Delta H^{\neq}/R)(1/\theta - 1/T) + \ln K] \qquad (5)$$

On the basis of these results, $\alpha_S$, $\theta_S$ and ln $K_S$ values in Table 7 may account for the different influence of substituents of olefinic double bond on the catalytic activity at different temperatures, in the hydrogenation of substrates with every studied catalyst. Besides, the values of $\alpha_C$, $\theta_C$ and ln $K_C$ can explain, better than $D_{Rh}$ (or $S_{Rh}$), the most usual sequence obtained in the hydrogenation of most substrates for different catalysts: $Rh/AlPO_4-SiO_2 > Rh/Sepiolite > Rh/AlPO_4-A \geq Rh/AlPO_4-P$, as well as the different sequences obtained by the combined influence of temperature, the activation parameters, $E_a$ (or $\Delta H^{\neq}$), collected in Tables 3-6, and the isokinetic parameters $\alpha_C$, $\theta_C$ and ln $K_C$ in Table 8. It is also easy to see in Eqn (5) how at reaction temperatures below $\theta_C$, substrates with the lowest $E_a$ exhibit the highest reaction rates, whereas above $\theta_C$ the inverse is true.

Furthermore, if a compensation effect holds for a reaction series, exhibiting similar isokinetic parameters, a single common interaction mechanism, through a common transition state, can be expected [21-23]. Besides, the relative low values of $\Delta S^{\neq}$ (negative) for all substrates and catalysts (Tables 3-6) indicate that, on going from the ground state to the transition state, an extensive restriction in degrees of freedom must be considered. On the

Table 6

Activation parameters: $E_a$ (KJ/mol), ln A (mol/min $g_{Rh}$), $\Delta H^{\neq}$ (KJ/mol) and $\Delta S^{\neq}$ (J/mol °K), obtained from reaction rates in Table 2 with the Rh/Sepiolite catalyst. Uncertainties are determined by standard deviations.

| Entry | Substrate | $E_a$ | ln A | $\Delta H^{\neq}$ | $\Delta S^{\neq}$ |
|---|---|---|---|---|---|
| 1 | $CH_2=CH\text{-}OCH_2CH_3$ | $30.9 \pm 1.3$ | $13.6 \pm 0.5$ | $28.3 \pm 1.2$ | $-140.8 \pm 4.0$ |
| 2 | $CH_2=CH\text{-}CO\text{-}CH_3$ | $29.5 \pm 2.7$ | $12.1 \pm 1.1$ | $27.0 \pm 2.8$ | $-153.0 \pm 9.3$ |
| 3 | $CH_2=CH\text{-}COOH$ | $18.4 \pm 1.2$ | $8.4 \pm 0.5$ | $15.9 \pm 1.3$ | $-183.9 \pm 4.1$ |
| 4 | $CH_2=CH\text{-}COOCH_2CH_3$ | $29.1 \pm 0.2$ | $13.8 \pm 0.4$ | $26.6 \pm 0.9$ | $-139.2 \pm 2.9$ |
| 5 | $CH_2=CH\text{-}CO\text{-}NH_2$ | $25.6 \pm 2.3$ | $10.5 \pm 0.9$ | $23.0 \pm 2.3$ | $-168.9 \pm 7.5$ |
| 6 | $CH_2=CH\text{-}O\text{-}CO\text{-}CH_3$ | $22.9 \pm 0.3$ | $8.7 \pm 0.1$ | $20.5 \pm 0.3$ | $-180.6 \pm 0.9$ |
| 7 | $CH_2=CH\text{-}CH_2\text{-}O\text{-}CO\text{-}CH_3$ | $36.1 \pm 3.2$ | $14.6 \pm 1.3$ | $33.4 \pm 3.4$ | $-132.8 \pm 9.9$ |
| 8 | $CH_2=CH\text{-}C_5H_4N$ | $30.7 \pm 2.9$ | $11.8 \pm 1.1$ | $28.2 \pm 3.0$ | $-154.9 \pm 9.9$ |
| 9 | $CH_2=CH\text{-}NC_4H_6O$ | $27.9 \pm 0.5$ | $13.3 \pm 0.2$ | $25.3 \pm 0.5$ | $-142.6 \pm 1.7$ |
| 10 | $C_6H_5\text{-}CH=CH\text{-}CO\text{-}CH_3$ | $20.6 \pm 0.5$ | $7.8 \pm 0.2$ | $18.1 \pm 0.4$ | $-188.5 \pm 1.3$ |
| 11 | $C_6H_5\text{-}CH=CH\text{-}COOH$ | $13.7 \pm 1.2$ | $4.7 \pm 0.5$ | $11.2 \pm 1.2$ | $-214.0 \pm 4.0$ |
| 12 | $C_6H_5\text{-}CH=CH\text{-}COO\text{-}CH_3$ | $26.3 \pm 1.7$ | $9.4 \pm 0.7$ | $23.8 \pm 1.5$ | $-175.3 \pm 5.0$ |
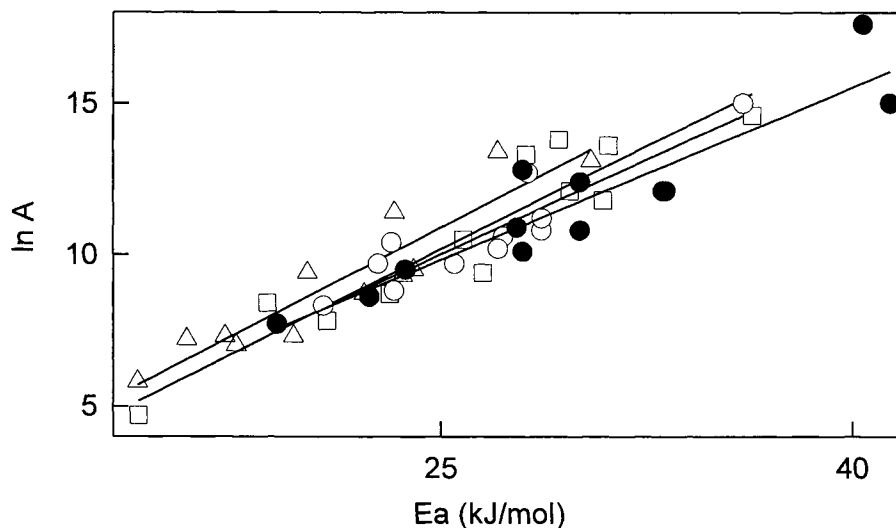


Figure 1. Compensation effects between ln A and $E_a$ for different catalysts: (O) Rh/AlPO$_4$-A; (●) Rh/AlPO$_4$-P; Rh/AlPO$_4$-SiO$_2$ (△) and (□) Rh/Sepiolite.

other hand, the zero reaction orders in the substrate concentration and first order in hydrogen is accounted for by a slow reaction (or dissociative adsorption) of hydrogen molecules, directly from the gas phase, on the surface complex formed by the adsorption of

220

## 1°- Two successive adsorption steps:
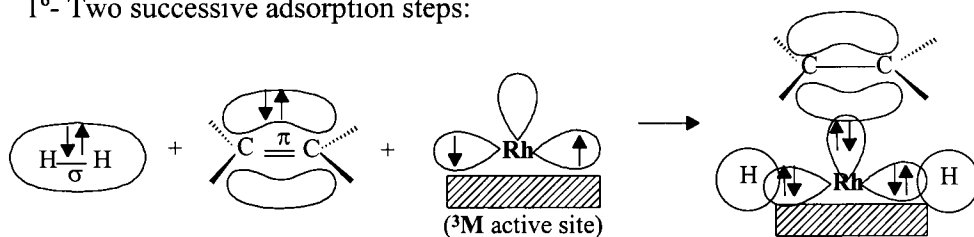


## 2°- Concerted desorption step:
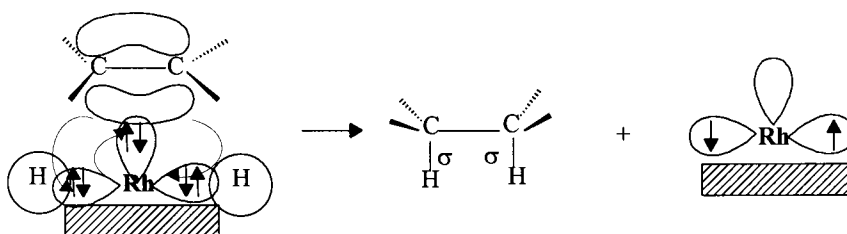


Figure 2. Reaction mechanism of the liquid-phase hydrogenation of alkene double bonds on supported rhodium catalysts.

Table 7

Isokinetic parameters of different substrates: $\alpha$ (mol/ s $g_{Rh}$) and $\theta_S{}^a$ (°K) are obtained from the representation of ln A *vs.* $E_a$, as well as $\theta_S{}^b$ (°K), $\Delta G_S{}^{\neq}$ (KJ/mol) and ln $K_S{}^{\neq}$ from the representation of $\Delta H^{\neq}$ *vs.* $\Delta S^{\neq}$. Uncertainties are determined by standard deviations.

| Entry | Substrate | $\alpha$ | $\theta_S{}^a$ | $\theta_S{}^b$ | $\Delta G_S{}^{\neq}$ | ln $K_S{}^{\neq}$ |
|-------|-----------|----------|---------------|---------------|----------------------|-------------------|
| 1 | $CH_2=CH\text{-}OCH_2CH_3$ | $10.0 \pm 0.6$ | $343 \pm 21$ | $328 \pm 45$ | $75.5 \pm 7.1$ | $-27.7 \pm 0.4$ |
| 2 | $CH_2=CH\text{-}CO\text{-}CH_3$ | $6.4 \pm 0.5$ | $372 \pm 30$ | $364 \pm 37$ | $84.8 \pm 6.1$ | $-28.0 \pm 0.3$ |
| 3 | $CH_2=CH\text{-}COOH$ | $15.1 \pm 1.4$ | $401 \pm 37$ | $395 \pm 36$ | $89.0 \pm 6.5$ | $-27.1 \pm 0.3$ |
| 4 | $CH_2=CH\text{-}COOCH_2CH_3$ | $32.1 \pm 0.8$ | $345 \pm 19$ | $330 \pm 49$ | $73.0 \pm 6.7$ | $-26.6 \pm 0.4$ |
| 5 | $CH_2=CH\text{-}CO\text{-}NH_2$ | $1.2 \pm 0.8$ | $306 \pm 23$ | $298 \pm 33$ | $73.1 \pm 6.1$ | $-29.5 \pm 0.3$ |
| 6 | $CH_2=CH\text{-}O\text{-}CO\text{-}CH_3$ | $2.4 \pm 0.1$ | $346 \pm 16$ | $324 \pm 58$ | $78.6 \pm 9.7$ | $-29.2 \pm 0.5$ |
| 7 | $CH_2=CH\text{-}CH_2\text{-}O\text{-}CO\text{-}CH_3$ | $0.8 \pm 0.1$ | $291 \pm 21$ | $283 \pm 33$ | $70.4 \pm 5.3$ | $-29.9 \pm 0.3$ |
| 8 | $CH_2=CH\text{-}C_5H_4N$ | $3.5 \pm 0.3$ | $360 \pm 27$ | $351 \pm 37$ | $83.5 \pm 6.1$ | $-28.6 \pm 0.3$ |
| 9 | $CH_2=CH\text{-}NC_4H_6O$ | $218.5 \pm 11,7$ | $448 \pm 24$ | $428 \pm 66$ | $88.0 \pm 9.6$ | $-24.7 \pm 0.6$ |
| 10 | $C_6H_5\text{-}CH=CH\text{-}CO\text{-}CH_3$ | $0.7 \pm 0.1$ | $313 \pm 51$ | $308 \pm 15$ | $76.8 \pm 2.8$ | $-30.0 \pm 0.1$ |
| 11 | $C_6H_5\text{-}CH=CH\text{-}COOH$ | $0.7 \pm 0.1$ | $306 \pm 21$ | $296 \pm 36.$ | $74.4 \pm 6.5$ | $-30.2 \pm 0.3$ |
| 12 | $C_6H_5\text{-}CH=CH\text{-}COO\text{-}CH_3$ | $1.3 \pm 0.1$ | $337 \pm 39$ | $359 \pm 46$ | $86.1 \pm 8.0$ | $-28.8 \pm 0.4$ |

Table 8

Isokinetic parameters of different 1 wt% Rh supported catalysts: $\alpha$ (mol/ s $g_{Rh}$) and $\theta_C^a$ (°K) are obtained from the representation of ln A $vs.$ $E_a$, as well as $\theta_C^b$ (°K), $\Delta G_C^{\neq}$ (KJ/mol) and $lnK_C^{\neq}$ from the representation of $\Delta H^{\neq}$ $vs.$ $\Delta S^{\neq}$. Uncertainties are determined by standard deviations.

| Catalyst | $\alpha$ | $\theta_C^a$ | $\theta_C^b$ | $\Delta G_C^{\neq}$ | $Ln\ K_C^{\neq}$ |
|---|---|---|---|---|---|
| Rh/AlPO$_4$-A | 0.66 ± 0.03 | 289 ± 12 | 245 ± 18 | 64.4 ± 3.3 | -31.6 ± 0.2 |
| Rh/AlPO$_4$-P | 1.40 ± 0.05 | 317 ± 35 | 275 ± 10 | 70.4 ± 1.6 | -30.8 ± 0.1 |
| Rh/AlPO$_4$-SiO$_2$ | 0.44 ± 0.03 | 257 ± 19 | 223 ± 17 | 58.4 ± 3.0 | -31.5 ± 0.1 |
| Rh/Sepiolite | 0.35 ± 0.04 | 266 ± 33 | 233 ± 8 | 61.8 ± 1.3 | -31.9 ± 0.1 |

the olefinic double bond on Rh surface active sites [20]. Consequently, the reaction mechanism must be interpreted within the context of a $cis$-concerted mechanism, close similar to that previously obtained, with supported Rh catalysts, in the liquid phase hydrogenation of cycloalkenes [11]styrene [12], benzylidene ketones [17], $\alpha,\beta$-unsaturated alcohols [14] and 1-alkenes [16]. In such $cis$-concerted mechanism, according to Fig. 2, the slowest step is the concerted desorption reaction, after stabilization and immobilization, of both reactant molecules on the rhodium-surface $^3M$ active sites. These $^3M$ (corners or kinks) sites are considered to work like an organometallic complex (Ph$_3$P)$_2$RhCl, in the homogeneous hydrogenation of olefinic double bond [24,25], where (on the three coordinative insaturations) it is possible simultaneously adsorb the alkene $\Pi$-bond (through a transfer $\Pi$-complex) and two hydrogen atoms (through a dissociative $\sigma$-bond adsorption and breaking). The transfer of the two hydrogen atoms to the double bond through a concerted process, where the interaction with the catalysts removes the symmetry restrictions imposed by the Woodward-Hoffmann rules, leads directly to the functionalized alkane formation [26]. Consequently, here we have the classical steps postulated by Horiuty and Polanyi [27], however, in the present case we exclude any intermediate half-hydrogenated state, which is also considered to be the limiting step in reactions at relatively low hydrogen pressures [28], as well as any hydrogen atom migration on metal (or support) surfaces.

**REFERENCES**

1    M.Te, E.E. Lowenthal and H.C. Foley, Chem. Eng. Sci., 49 (1994) 4851.
2    M. Shelef and G.W. Graham, Catal. Rev. Sci. Eng., 36 (1994) 433.
3    M.E. Viste, K.D. Gibson and S. J. Sibener, J. Catal., 191 (2000) 237.
4    P. Ferreira-Aparicio, M. Fernandez-García, I. Rodriguez-Ramos and A. Guerrero-Ruiz, Stud. Surf. Sci. Catal., 130 (2000) 3675.
5    Y.A. Ryndin, C.C. Santini, D. Prat and J. M. Basset, J. Catal., 190 (2000) 364.
6    D.H. Holm, C.C. Hill and A.H. Conner, In. Eng. Chem. Res., 34 (1995) 3392.
7    F. Cavani and F. Trifiro, Catal. Today, 34 (1997) 269.
8    G.L. Haller and D.E. Resasco, Adv. Catal., 36 (1989) 173.
9    M.C.J. Bradfor, M.A. Vannice, Appl. Catal. A, 142 (1996) 97.
10   J.M. Campelo, A. García, D. Luna and J.M. Marinas, Colloids Surfaces, 5 (1982) 227.
11   J.M. Campelo, A. García, D. Luna and J.M. Marinas, Appl. Catal., 10 (1984) 1.

12 J.A. Cabello, J.M. Campelo, A. García, D. Luna and J.M. Marinas, J. Catal., 94 (1985) 1.

13 J.A. Cabello, J.M. Campelo, A. García, D. Luna and J.M. Marinas, J. Org. Chem., 51 (1986) 1786

14 J.M. Campelo, A. García, D. Luna and J.M. Marinas, J. Catal., 113 (1988) 172.

15 F.M. Bautista, J.M. Campelo, A. García, D. Luna and J.M. Marinas, Bull. Chem.Soc. Jpn., 62 (1989) 3670.

16 J.A. Cabello, J.M. Campelo, A. García, D. Luna and J.M. Marinas, J. Catal., 78 (1993) 249.

17 A.Cabello, J.M. Campelo, A. García, D. Luna and J.M. Marinas, J. Mol. Catal., 67 (1991) 217.

18 F.M. Bautista, J.M. Campelo, A. García, D. Luna, J.M. Marinas and R.A. Quiros, Catal. Lett.,52 (1998) 205.

19 F.M. Bautista, J.M. Campelo, A. García, D. Luna, J.M. Marinas, and R.A. Quiros, Catal. Lett.,60 (1999) 229.

20 F. Kapteijn, J.A. Moulijn and R.A. van Santen, Stud. Surf. Sci. Catal., 79 (1993) 69.

21 A. Corma, F. Llopis, J.B. Monton and S. Weller, J. Catal, 142 (1993) 97.

22 E. Grinwald and C. Steel, J. Am. Chem. Soc., 117 (1995) 5687.

23 J.J. Roney, Catal. Lett., 50 (1998) 15.

24 R.L. Agustine, R.W. Warner and M.J. Melnick, J. Org. Chem., 49 (1984) 4853.

25 S.A. Jackson, P.AM. Hodges, M. Poliakoff, J.J. Turner and F.W. Grevels, J. Am. Chem. Soc., 112 (1990) 1221.

26 R. Ponec, Collect. Czech. Chem. Commun., 51 (1986) 1843.

27 I. Horiuty and M. Polanyi, Trans. Faraday Soc., 30 (1934) 1164.

28 H.O. House, in "Modern Synthetic Reactions", pp. 20, Benjamin Cummings, Menlo Park, CA, 1972.

223

# NMR relaxation of chloroform adsorbed over alkali-exchanged FAU type zeolites

M. Sánchez-Sánchez, A. Vidal-Moya and T. Blasco*

Instituto de Tecnología Química (UPV-CSIC), Universidad Politécnica de Valencia, Avda. de los Naranjos s/n, 46022-Valencia, Spain.

We have measured the $^1$H and $^{13}$C NMR longitudinal relaxation times ($T_1$) of $CHCl_3$ and $^{13}CHCl_3$, respectively, adsorbed over alkali exchanged zeolites of type FAU. Our results suggest that the mobility of the adsorbed molecules at room temperature depends on the zeolite basicity. Moreover, $^1$H to $^{13}$C cross polarisation (CP) experiments of the adsorbed chloroform show that the optimum contact time at which the maximum signal intensity is observed depends on the host zeolite.

## 1. INTRODUCTION

Alkali exchanged zeolites possess basic properties attributed to the Lewis basic framework oxygen. Therefore, this property is related to the negative charge density on the oxygen atoms, which will depend on the chemical composition and the zeolite structure [1]. The basic strength of zeolites increases with the framework aluminum content, and for a given Si/Al ratio, with decreasing the electronegativity of the alkaline cation which are compensating the framework charges [1]. These observations are supported by the average negative charge on the oxygen atoms calculated by the method of Sanderson [1].

The most common methods used to characterise zeolites basicity are based on the use of infrared probe molecules, such us chloroform [1], whereas nuclear magnetic resonance (NMR) spectroscopy has been scarcely applied. Recently, it has been shown that the $^1$H NMR chemical shift of chloroform adsorbed over zeolites X and Y is a measure of the intrinsic basicity [2, 3]. Also, the $^{13}$C chemical shift of adsorbed $^{13}CHCl_3$ has been reported to depend on the mean negative charge over the framework oxygen [3]. In the present work, we have measured the $^1$H and $^{13}$C NMR longitudinal relaxation times ($T_1$) as well as the $^1$H to $^{13}$C cross polarisation experiments of chloroform adsorbed over alkali exchanged zeolites of type FAU. The results obtained suggest that besides the $^1$H and $^{13}$C chemical shifts, also the $T_1$ and the $^1$H to $^{13}$C cross polarisation behaviour of adsorbed chloroform are influenced by the interaction with the zeolite host.

## 2. EXPERIMENTAL

Zeolites NaX (13X, Aldrich) and NaY (CBV 100, PQ) were commercially available. Partially exchanged zeolites LiNaY, KNaY, CsNaY and LiNaX, KNaX, CsNaX were prepared from commercial NaY and NaX, respectively, by chemical exchange methods as described previously [3]. The chemical compositions of the samples are summarised in table 1. The Si/Al ratio was determined by $^{29}Si$ magic angle spinning (MAS) NMR to be 1.23 for zeolites Y and 2.50 for zeolites X. In order to reduce the concentration on iron, the most common paramagnetic impurity, zeolite NaY1 was synthesised in the laboratory using sodium aluminate ($NaO_2.Al_2O_3$, Carlo Erba) and zeolite NaY2 from metallic pure aluminum metal (99.999 % STREM) as aluminum sources. The Si/Al ratio as measured by NMR was 2.3 for NaY1.

The experimental procedure to adsorb chloroform was as follow: the samples were introduced into glass inserts and degassed at 673 K for 12 h until a final pressure $10^{-5}$ kPa. Then, zeolites were contacted with the vapour pressure of $CHCl_3$ (or $^{13}CHCl_3$) at room temperature for 5 min followed by degassing 30 min at the same temperature. The glass inserts were sealed while immersed in liquid nitrogen, and the amount of adsorbed chloroform was estimated from the integration of the $^1H$ MAS NMR signals.

Solid state $^1H$ and $^{13}C$ MAS NMR spectra were recorded with a Varian VXR-S 400-WB spectrometer, using an RT CP/MAS Varian probe with 7 mm silicon nitride rotors spinning at 5 KHz. Some experiments were carried out at variable temperature with a 5 mm VT CP/MAS Varian probe. The $^1H$ spectra were acquired using $\pi/2$ rad pulses of 5 $\mu$s and recycle delay of 5 s. $^{13}C$ Bloch decay spectra with high power proton decoupling were recorded using 7 $\mu$s $\pi/2$ rad pulses and delays of 5 s. $^1H$ to $^{13}C$ MAS NMR spectra were carried out using $\pi/2$ rad pulses of 7 $\mu$s for protons and a recycle time of 5 s. Conventional inversion recovery pulse sequence was used to measure the longitudinal relaxation times.

Table 1
Chemical composition of the zeolites and the amount of adsorbed chloroform

| Zeolite | Na$^+$/u.c.[a] | M$^+$/u.c.[a] | Mol./u.c.[b] | Fe (ppm)[c] |
|---------|------------|-----------|-----------|------------|
| LiNaY | 31 | 24 | 22 | 265 |
| NaY | 55 | - | 26 | 248 |
| KNaY | 13 | 42 | 36 | 246 |
| CsNaY | 17 | 37 | 23 | - |
| LiNaX | 29 | 57 | 31 | - |
| NaX | 85 | - | 35 | 252 |
| KNaX | 20 | 66 | 40 | - |
| CsNaX | 33 | 53 | 27 | 204 |

[a] Number of Na$^+$ and M$^+$ (M+ = Li, Na, Cs) cations per unit cell. [b] Number of molecules of chloroform adsorbed per unit cell. [c] Iron content expressed in ppm.

## 3. RESULTS AND DISCUSSION

Figure 1 shows some typical ^{1}H MAS NMR spectra of chloroform adsorbed over alkali exchanged zeolites of type FAU. The spectra consist of a peak originated by the proton of the adsorbed $CHCl_3$ molecule which progressively shifts to low field as the zeolite basicity increases [3]. This shift can be understood by the polarisation of the $CHCl_3$ molecule through hydrogen bonding with highly nucleophilic framework oxygen atoms. The peak position shows a good correlation with the zeolite electronegativity as calculated by the method of Sanderson, which indicates that chloroform can be used as a probe molecule to characterise zeolite basicity by ^{1}H NMR [3]. Characteristic ^{13}C MAS NMR with proton decoupling signals of adsorbed [13]$CHCl_3$ are shown in figure 2. The ^{13}C chemical shift also depends on the basicity of the zeolite framework [3]. As previously reported for the samples studied here, the zeolite basic strength increases in the order: LiNaY < NaY < KNaY < LiNaX < CsNaY < NaX < KNaX < CsNaY [3].

The evolution of the ^{1}H NMR signal with the acquisition temperature is illustrated in figure 3 for samples NaY. As it can be observed, the line width increases as the temperature is lowered, whereas at room temperature, it is only slightly affected by spinning the samples above 3 kHz. These properties and the absence of spinning side bands are characteristic of highly mobile
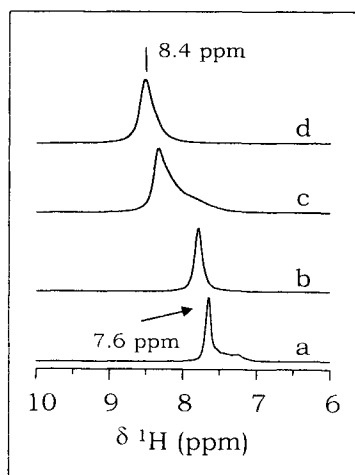


Figure 1: ^{1}H MAS NMR spectra of clhoroform adsorbed on a) LiNaY, b) NaY, c) NaX and d) CsNaX
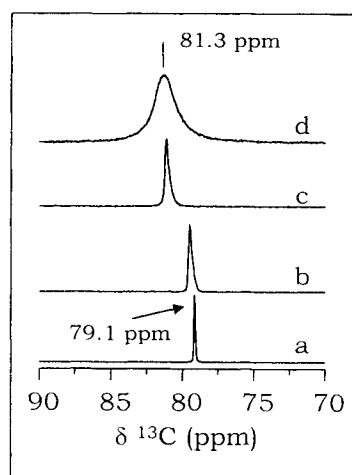
Figure 2: Proton decoupled[13]C MAS NMR spectra of chloroform adsorbed on a) LiNaY, b) NaY, c) NaX and d) CsNaX

chloroform molecules [4]. Accordingly, rapid exchange among sites with different basicity will lead to an average chemical shift, which makes not possible to discriminate sites with different basic strength. The investigations on the chloroform-zeolite system are expanded studying the longitudinal relaxation and cross polarisation dynamics behaviours of chloroform on zeolites with the FAU type structure.

It is known, that the ^{1}H NMR longitudinal relaxation time of adsorbed molecules is controlled by the presence of paramagnetic impurities being iron the most common one in commercial zeolites [5]. Usually, the longitudinal proton spin relaxation rate is controlled by the proton-proton magnetic interactions and by the proton-electron interaction with paramagnetic species [5, 6]. This latter often predominates, since the electron magnetic moment is around three orders of magnitude higher than that of proton [5, 6]. In the simplest case, the longitudinal relaxation rate is described by the following expression:

$$\frac{1}{T_1} = \frac{1}{15} \frac{mN_s}{N} \frac{\gamma_1^2 \mu_S^2}{r_{IS}^6} \frac{6\tau_c}{1+(\omega_1 \tau_c)^2} \tag{1}$$

where $\gamma_1$ is the proton magnetogyric ratio, $\omega_1$ the proton Larmor frequency, $\mu_S$ the magnetic moment of the paramagnetic ion, and $r_{IS}$ the proton-ion distance. The factor $mN_s/N$ is the probability of the proton-electron interaction to take place; $N$ is the total number of protons, $m$ is the number of molecules interacting with the paramagnetic ion and $N_s$ the number of interacting protons per molecule. $\tau_c$ the proton-electron correlation time of the molecule, which has several contributions and is a function of the temperature [5, 6]. However, also the proton-proton interactions play a role in the relaxation behaviour of the adsorbed molecules, which also depends
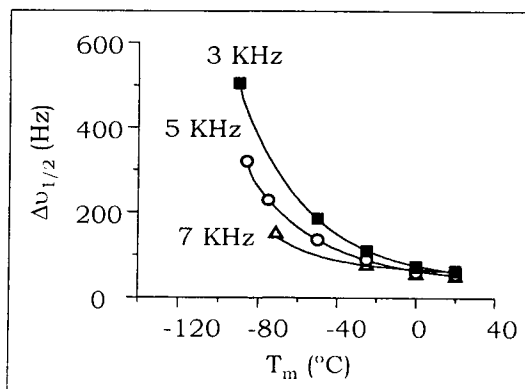


Figure 3: Evolution of the half height linewidth of the ^{1}H NMR signals of chloroform adsorbed over zeolite NaY with the measurement temperature ($T_m$) and the spinning rate

on a correlation time characterising the fluctuation in the distances of the nuclei involved [5, 6]. If rapid exchange is produced among the adsorbed molecules experiencing both types of interactions, the overall longitudinal relaxation time is given by:

$$\frac{1}{T_1} = \frac{1}{T_1^{p-e}} + \frac{1}{T_1^{p-p}}$$

(2)

To estimate the influence of the iron impurity content on the $^1H$ $T_1$ relaxation time of $CHCl_3$ adsorbed on the commercial zeolites and those derived from them, we studied the samples NaY1 and NaY2, with a lower Fe concentration. Representative results are summarised in table 2. Comparison of the $^1H$ $T_1$ of chloroform adsorbed on NaY zeolites shows that the $T_1$ is more than one order of magnitude longer when the Fe content is decreased below 100 ppm. For commercial zeolites NaY and NaX with similar iron concentration, a much longer $T_1$ is measured for NaX, suggesting that other contribution have an effect on the relaxation time. This is further confirmed for zeolites X. The $^1H$ $T_1$ of chloroform adsorbed over CsNaX is one order of magnitude longer than that measured for NaX, which cannot be explained only by the different concentration of paramagnetic impurities (table 2).

The longitudinal $^1H$ and $^{13}C$ relaxation times of the zeolites studied here are represented in figure 4 against the $^{13}C$ chemical shift, which depends on the zeolite basicity [3]. The tendency observed in figure 4 is that, at room temperature, both the $^{13}C$ and $^1H$ $T_1$ increase as the intrinsic framework basicity of the zeolite increases, which is specially evident for $^{13}C$. Although more dispersed values are obtained for $^1H$ even when they are represented against the framework electronegativity (not shown), the general trend is also preserved. Zeolite NaX is marked in figure 4 because it gives shorter $T_1$ values than expected. The results shown in figure 4 suggest that although the interaction with the paramagnetic impurities is the main longitudinal relaxation mechanism of chloroform, the host-guest interactions also affects the room temperature $T_1$ relaxation time, probably by modifying the mobility of the guest molecules, and therefore their correlation times.

Table 2: $^1H$ NMR longitudinal relaxation time ($T_1$) and iron content for some characteristic samples.

| Zeolite | Fe (ppm) | $^1H$ $T_1$ (s) |
|---------|----------|-----------------|
| NaY     | 248      | 0.045           |
| NaY1    | 169      | 0.17            |
| NaY2    | < 100    | 1.26            |
| KNaY    | 246      | 0.4             |
| NaX     | 252      | 0.17            |
| CsNaX   | 204      | 1.4             |
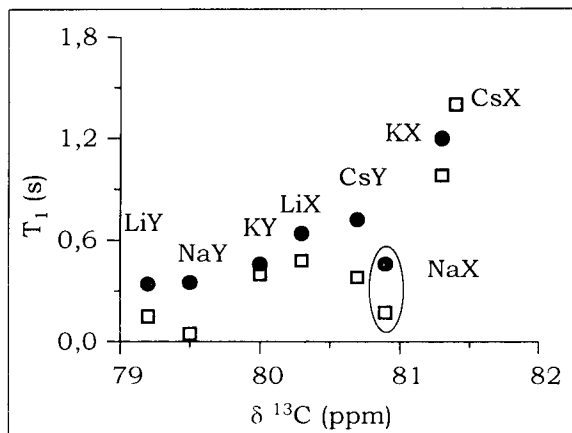
Figure 4: Longitudinal relaxation times ($T_1$) of $^1H$ (squares) and $^{13}C$ (circles) MAS NMR signals against the $^{13}C$ chemical shift of chloroform adsorbed over the alkali exchanged zeolites indicated in the figure.

An alternative explanation for the variation of the $T_1$ values could be the changes in the accessibility of the paramagnetic ions in the zeolites, either by modifications on the iron distribution or by changes in the extraframework cation population. Regarding the first hypothesis, different iron species not equally exposed have been observed in commercial zeolites [7]. However we start from the same parent zeolite, and we do not expect any important modification during the cation exchange process. On the other hand, changes in the nature and concentration of extraframework cations could screen in some way the paramagnetic impurities, therefore decreasing its exposure to the chloroform molecules, which can only enter the supercage. In this case a sharp change would be expected by changing from Y to X zeolites because the higher population of supercage cations in the latter. However, although we cannot completely rule out both contributions to the $T_1$ variations, the evolution shown in figure 4 points out toward an influence of the zeolite basicity, and therefore of the host-guest interaction. Anyhow, variable temperature measurements are required to get definite conclusions.

We also carried out $^1H$ to $^{13}C$ CP/MAS NMR at variable contact time. The results obtained are represented in figure 5. The contact time for which a maximum intensity is obtained depends on the zeolite. We must note that the position of the maximum depends on the number of adsorbed molecules, which changes for the different chloroform-zeolite systems studied here (see table 1). For instance, we observed that for zeolite LiNaY, the maximum was shifted to 6 and 3 ms as the chloroform amount decreased to 16 and 8 molecules per unit cell, respectively. However, the results shown in figure 5 cannot be explained by the different chloroform content in the samples; the zeolite CsNaX with the highest number of molecules gives the maximum intensity at very short ($\approx$ 0.5 ms) contact times. The understanding of the cross polarisation dynamics of a system requires some knowledge of the
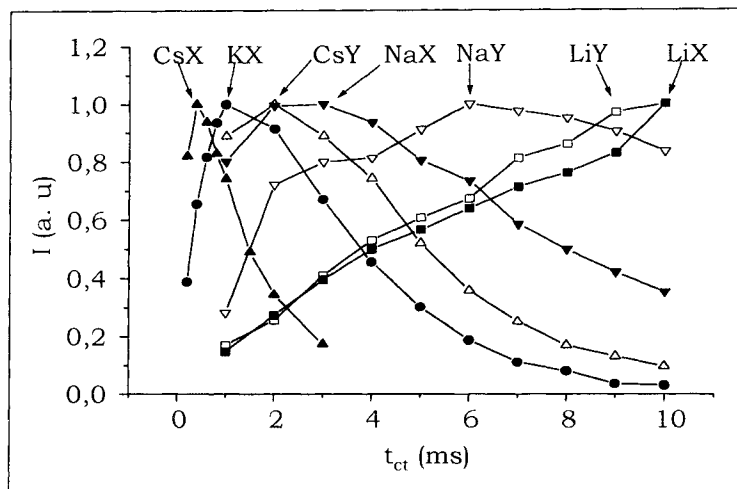
Figure 5: Evolution of the intensity (arbitrary units) of the ^{1}H to ^{13}C MAS NMR signals of chloroform adsorbed over the alkali exchanged zeolites indicated in the figure.

cross relaxation time constant ($T_{CH}$) and the relaxation times (usually the [1]H $T_{1\rho}$,) which governs the build up and decay of the signal intensity as a function of the contact time [8]. A detailed study is out of the scope of this contribution, but our results suggest that as a general trend, the contact time which gives the maximum intensity (figure 5) depends on the Si/Al molar ratio, being usually shorter for X than for Y zeolites, and specially, on the nature of the alkali cation. This latter observation could be related to the interaction of the chlorine atoms of the chloroform molecule with the supercage cations as suggested by theoretical calculations [9, 10]. Although it is speculative, this direct interaction with cations could affect some of the parameters involved in the cross polarisation of chloroform.

We are aware that a more detailed investigation on the longitudinal relaxation mechanisms (doing variable temperature measurements), and on the cross polarisation dynamics (by determining experimentally some time constants) are required to reach definite conclusions. However, the results presented here suggest that besides the ^{1}H and ^{13}C chemical shifts, other parameters such as the longitudinal relaxation time and the ^{1}H to ^{13}C cross polarisation dynamics of chloroform adsorbed on alkali zeolites of FAU type reflects the existence of host-guests interactions.

**ACKNOWLEDGEMENTS**

**REFERENCES**

(1) D. Barthomeuf, Chem. Rev., 95 (1995) 537.

(2) E. Bosch, S. Huber, J. Weitkamp and H. Knözinger, Phys. Chem. Chem. Phys., 1 (1999) 579.

(3) M. Sánchez-Sánchez, T. Blasco and F. Rey, Phys. Chem. Chem. Phys., 1 (1999) 4529.

(4) T. Baba, N. Komatsu, Y. Ono, H. Sugisawa, J. Phys. Chem. B 102 (1998) 804.

(5) H. Winkler, B. Bierner and V. Bosacek, Zeolites 9 (1989) 293.

(6) H. Pfeiffer, NMR Basic Principles and Progress, vol. 7, Springer, New Yourk, 1972, p. 53.

(7) E. G. Derouane, M. Megstdagh and L. Vielvoye, J. Catal. 25 (1972) 223.

(8) T. H. Walter, G. L. Turner and E. Oldfield, J. Magn. Reson. 76 (1988) 106.

(9) C. F. Mellot, A. K. Cheetham, S. Harms, S. Savitz, R. J. Gorte and A. L. Myers, J. Am. Chem. Soc., 120 (1998) 5788.

(10)   C. F. Mellot, A. M. Davidson, J. Eckert and A. K. Cheetham, J. Phys. Chem. B 102 (1998) 2530.

# Simultaneous isomerization of n-heptane and hydrogenation of benzene over bimetallic PtMe/Beta catalysts in the absence and presence of sulfur

M.A. Arribas, V. Fornés and A. Martínez

Instituto de Tecnología Química. Avenida de los Naranjos S/N 46022 Valencia. Spain.
Phone : +34-96 3877808. Fax: +34 963877809. E-mail: amart@itq.upv.es

Bifunctional bimetallic PtMe/Beta catalysts (Me= Pd, Ir, Ru) have been prepared and studied for the simultaneous isomerization of n-heptane and hydrogenation of benzene. In the absence of sulfur, PtPd samples were less selective to iso-$C_7$ than PtIr and PtRu. The extent of cracking increased with the Pd concentration in PtPd/Beta. The conversion of benzene was 100% for all catalysts. In the presence of 200 ppm sulfur, the n-$C_7$ conversion decreased while the cracking selectivity increased. The relative decrease of activity was lower for PtPd catalysts, suggesting a higher sulfur resistance as compared to PtIr and PtRu. Benzene conversion was much less affected by sulfur, but there was a loss of activity for isomerization of cyclohexane into methylcyclopentane. The better sulfur resistance of PtPd samples may arise from a stabilization of partially charged $Pt^{\delta+}$ species by interaction with Pd, which could be associated with a lower reducibility of $Pt^{2+}$ to $Pt^0$ in presence of Pd, as observed by TPR.

## 1. INTRODUCTION

Owing to environmental concerns, new legislation has been introduced to limit the amount of aromatics (and particularly of benzene) in gasoline. Reduction of benzene has a negative impact on gasoline octane which need to be compensated by increasing the contribution of high-octane aromatic-free components, such as isoparaffins, in the gasoline pool.

An interesting alternative for eliminating benzene while minimizing the octane loss would be to carry out, in a single catalytic step, the hydrogenation of benzene to cyclohexane and its isomerization to methylcyclopentane, with a higher octane, and the isomerization of n-$C_6$ and n-$C_7$ paraffins that are the benzene precursors in the reformer naphtha feeds (1). Unfortunately, the amount of benzene and $C_{7+}$ n-paraffins that can be introduced in commercial n-$C_5$/n-$C_6$ isomerization units using Pt/Mordenite catalysts is very limited. In fact, it has been shown that addition of significant amounts of benzene reduced the isomerization efficiency of Pt/Mordenite catalysts (2), whereas in presence of $C_{7+}$ paraffins the gas yield increased to undesired limits owing to an extensive cracking of the $C_{7+}$ isoparaffins (3).

Recently, we have shown that both Pt/Beta and Pt/WO$_x$-ZrO$_2$ catalysts are active and selective for the isomerization of n-$C_7$ in the presence of 25 wt% of benzene with total conversion of the aromatic under typical hydroisomerization conditions (4). Although Pt/Beta displayed a higher sulfur resistance than Pt/WO$_x$-ZrO$_2$, the isomerization activity of Pt/Beta catalysts was, however, decreased to some extent in the presence of 200 ppm sulfur in the n-$C_7$/benzene feed (4). A further benefit in isomerization selectivity and sulfur resistance was observed when decreasing the crystal size of the Beta zeolite by favoring metal dispersion and enhancing the diffusion of the branched isomers (5).

Besides changing the support characteristics, the sulfur resistance can also be varied by acting directly on the metallic function of the bifunctional catalyst. In this sense, it has been reported the good sulfur tolerance displayed by bimetallic PtPd-supported catalysts for both aromatics hydrogenation (6, 7) and n-paraffin isomerization (8) processes.

In this work we have prepared a series of bimetallic PtMe/Beta catalysts (Me = Pd, Ir, Ru) and studied their catalytic performance for the simultaneous isomerization of n-$C_7$ and hydrogenation of benzene both in the absence and in the presence of sulfur (200ppm).

## 2. EXPERIMENTAL

### 2.1 Preparation of the catalyst

A commercial HBeta zeolite obtained from PQ Corp. (acid form, Si/Al = 12) was used as support without further treatments. Bimetallic catalysts were prepared by co-impregnating (incipient wetness method) the HBeta zeolite with a 0.2 N HCl solution containing the required amounts of the corresponding metal precursors (Pt=$H_2Cl_6$Pt, Ir= $H_2Cl_6$Ir, Ru= $RuCl_3$, and Pd= $PdCl_2$). The total metal content in the catalysts was kept constant to 1 wt%. The Me/(Me+Pt) atomic ratio was 0.5 for PtRu and PtIr, and 0.5, 0.6 and 0.8 for PtPd. This ratio is given in parenthesis after the metal in the nomenclature of the catalysts. Monometallic samples (Me/Beta, Me = Pt, Pd, Ir, Ru) were also prepared by impregnation with the above precursors for comparison purposes. The metal content in the monometallic samples was also 1 wt%. After impregnation the samples were dried at 100°C and finally calcined at 500°C for 3 hours.

### 2.2 Characterization techniques

The relative crystallinity of the PtMe/Beta samples was calculated by X-ray diffraction (Phillips X`PERT, Cukα radiation) by comparing the area peak at ca. 2θ = 22° with that for the starting HBeta zeolite (100% crystallinity).

The textural properties of the catalysts were determined from $N_2$-adsorption-desorption isotherms at 77 K in a ASAP-2000 equipment (Micromeritics).

The acidity of the samples was measured by infrared spectroscopy with adsorption of pyridine and desorption at different temperatures as described in (9) using a Nicolet 710 FTIR apparatus.

$H_2$ chemisorption measurements were carried out in a ASAP 2010 equipment (Micromeritics) after reducing the catalysts at 400°C for 2 h in hydrogen. The stoichiometry of $H_{irrev}$ to Me was assumed to be unity.

Temperature-programmed reduction (TPR) of the PtMe/Beta catalysts was performed in a TPD/TPR 2900 equipment (Micromeritis) using a TCD. Before the measurements, the sample (about 0.5 grams) was placed in a quartz cell and pre-treated in Ar flow (30 cm$^3$/min) at 25 °C for 30 minutes. Then, the sample was heated from room temperature up to 900 °C at a heating rate of 10 °C/min while flowing a mixture of 10 vol % $H_2$ in Ar through the sample. The amount of $H_2$ consumed was determined using CuO as a reference.

### 2.3 Catalytic experiments

The experiments were performed in a continuous fixed-bed stainless steel reactor. Three grams of catalysts were crushed and sieved to a particle size of 0.25-0.42 mm diameter and diluted with CSi (0.59-0.89 mm particle size) to a constant bed volume of 10 cm$^3$. Then the catalyst was reduced in a $H_2$ flow (300 ml/min) at 450°C and atmospheric pressure for 2

hours. The conversion of a n-heptane/benzene mixture (25 wt% in benzene) was carried out at 30 bar total pressure, $H_2$/hydrocarbon molar ratio of 10, WHSV of 3 $h^{-1}$ and temperature in the 240-270 °C range. The reactor effluent was depressurized, vaporized at 170°C and analyzed on line at regular intervals in a gas chromatograph (Varian 3800) equipped with a capillary column (Petrocol DH 50.2, 50mx0.2mm) and a FID.

For the sulfur resistance experiments, 200 ppm of S were added as 2-methylthiophene to the n-$C_7$/benzene feed.

## 3. RESULTS AND DISCUSSION

### 3.1 Characterization of catalysts

The HBeta zeolite used as support presented a B.E.T. area of 599 $m^2$/g and a micropore volume of 0.17 $cm^3$/g. The concentration of Brönsted and Lewis acid sites was estimated by IR-pyridine using the molar extinction coefficients given by Emeis (10). The values obtained for the HBeta support at different desorption temperatures are shown in Table 1. The area B.E.T., relative crystallinity, and acidity of Beta zeolite were seen to remain almost unaltered after metal impregnation.

Table 1
Acidity of HBeta support

| $T_{desorption}$ | Acidity ($\mu$mol/g) | |
|---|---|---|
| °C | Brönsted | Lewis |
| 250 | 46 | 49 |
| 350 | 27 | 41 |
| 400 | 15 | 42 |

The metal content and the $H_{irr}$/Me ratio obtained from hydrogen chemisorption experiments on PtMe/Beta catalysts are presented in Table 2. As observed in Table 2, for catalysts prepared with Me/(Me+Pt)= 0.5 highest $H_{irr}$/Me ratios were obtained for PtPd/Beta. PtIr/Beta presented a somewhat lower hydrogen uptake, while PtRu/Beta showed the lowest $H_{irr}$/Me ratio. Therefore, according to the $H_{irr}$/Me values the metal dispersion should increase in the following order: PtRu < PtIr ≤ PtPd. In the case of PtPd samples, no significant differences in dispersion were observed when varying the Pd/Pt ratio.

Table 2
Metal composition and $H_2$ chemisorption results for bimetallic PtMe/Beta catalysts

| Catalysts | Me/(Me+Pt) atomic ratio | Pt, %wt | Me, % wt | $H_{irr}$/Me ratio |
|---|---|---|---|---|
| PtRu(0.5)/Beta | 0.5 | 0.658 | 0.341 | 0.060 |
| PtIr(0.5)/Beta | 0.5 | 0.504 | 0.495 | 0.138 |
| PtPd(0.8)/Beta | 0.8 | 0.379 | 0.621 | 0.154 |
| PtPd(0.6)/Beta | 0.6 | 0.524 | 0.476 | 0.156 |
| PtPd(0.5)/Beta | 0.5 | 0.648 | 0.352 | 0.148 |

The temperature programmed reduction (TPR) curves for monometallic samples (1%wt metal content) are shown in Figure 1. Pt/Beta sample showed two main reduction peaks in the low temperature range with maxima at about 105 °C and 138 °C, and a small peak at ca 230 °C. Besides those peaks, a signal at ca 380 °C can also be observed in Fig. 1 for Pt/Beta. The low temperature peaks can be ascribed to the reduction of $Pt^{4+}$ to $Pt^{2+}$ (11), while the high temperature peak probably corresponds to the reduction of $Pt^{2+}$ to $Pt^0$ (4).
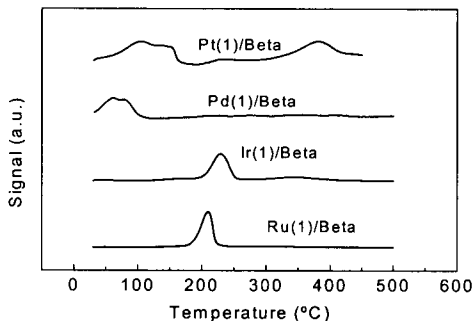
Figure 1. Temperature programmed reduction of monometallic samples.
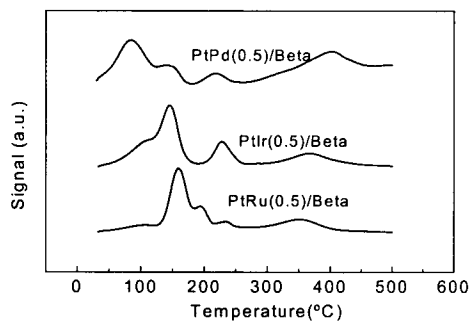
Figure 2. Temperature programmed reduction of bimetallic PtMe/Beta [Me/(Me+Pt)=0.5].

Palladium in monometallic Pd/Beta is reduced at very low temperature, with a maximum signal at ca. 70°C-80°C. On the other hand, Ir and Ru supported on zeolite HBeta showed clear and sharp reduction peaks with maxima at ca. 210°C and 230°C, respectively (Fig. 1).

The temperature reduction profiles for the bimetallic samples are shown in Figure 2. At first sight, it becomes evident that the reduction profiles can not be explained by the simple addition of the individual contribution of the two metals, thus suggesting some kind of interaction between the metallic particles. In the low temperature region, PtPd sample showed reduction peaks at ca 80, 140, and 230°C. The peak at ca 80°C can arise from a contribution of both Pd and Pt, while the peaks at 140 and 230°C are clearly attributed to Pt reduction (see TPR of Pt/Beta in Fig. 1). For PtIr sample, an increase of the relative intensity of the Pt reduction peak at ca 140°C with respect to that at 105°C can be observed in Fig. 2. The TPR of PtIr also showed a reduction feature at 230°C that was observed for both monometallic Pt and Ir samples (Fig. 1). In the case of PtRu, the low temperature Pt reduction peak at ca 105°C almost disappeared while that at 140°C shifted to higher reduction temperatures (ca 160°C). The presence of Pt in the bimetallic PtRu catalyst slightly increased the reducibility of Ru species, as suggested by the decrease of the Ru reduction temperature from 210°C to 195°C. Moreover, the high temperature reduction peak of Pt observed at 380°C in the monometallic sample (reduction of $Pt^{2+}$ to $Pt^{0}$) was also affected by the presence of a second metal in bimetallic catalysts. Thus, the reduction temperature increased from 345°C for PtRu to 365°C for PtIr and to 405°C for PtPd (Fig. 2). That is, Ir and Ru increased the reducibility of these species with respect to the monometallic sample, while the contrary was observed for Pd. It can be speculated from these results that the higher reduction temperature observed for PtPd can arise from a stabilization of positively charged $Pt^{\delta+}$ species by the presence of Pd in bimetallic PtPd/Beta catalyst.

### 3.1 Catalytic experiments
#### 3.1.1 Experiments in the absence of sulfur
The conversion of n-heptane on the different bimetallic samples prepared with a Me/(Me+Pt) ratio of 0.5 is presented in Fig. 3. There were only subtle differences in activity, as could be expected, since all catalysts showed similar textural and acidic properties.
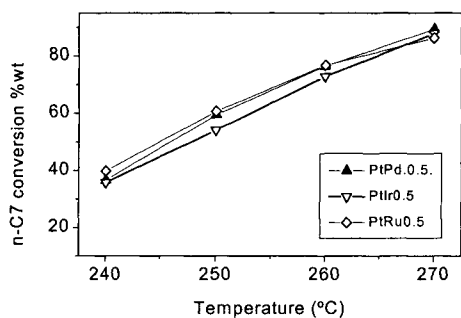
Figure 3. Conversion of n-C$_7$ as a function of reaction temperature for PtMe/Beta catalysts with Me/(Pt+Me)= 0.5.
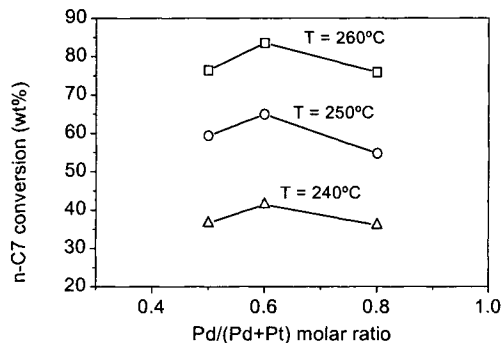
Figure 4. Influence of Pd concentration on n-C$_7$ conversion for PtPd/Beta samples.

Anyway, PtIr(0.5)/Beta catalyst gave a slightly lower conversion, particularly at intermediate temperatures (250-260°C). When the concentration of Pd in bimetallic PtPd was varied, a maximum in activity was obtained for the catalyst with a Pd/(Pt+Pd) atomic ratio of 0.6, irrespective of the reaction temperature (Fig. 4).

The selectivity to iso-heptanes is plotted in Fig. 5 as a function of n-C$_7$ conversion. As observed, isomerization selectivities above 80% were obtained for PtIr and PtRu catalysts for n-C$_7$ conversions of up to ca 75%. Lower selectivities to iso-heptanes were observed, however, for PtPd catalysts. Furthermore, the selectivity to iso-C$_7$ decreased when increasing the concentration of Pd in PtPd samples. The higher hydrocracking activity of PtPd samples indicated a missbalance between the hydrogenating and the acidic functions of the bifunctional catalysts. Taking into account the TPR results discussed before, it could be speculated that the missbalance could be caused by the formation of less reducible Pt particles (probably partially charged Pt$^{\delta+}$ species) interacting with Pd in the bimetallic PtPd sample. Blomsma et al. (12) also found a decrease of the isomerization selectivity for PdPt/Beta catalysts when increasing the Pd/(Pt+Pd) ratio above 0.4.

On the other hand, the conversion of benzene present in the feed (25 wt%) was 100% for all catalysts in the whole range of temperatures studied. The selectivity to hydrogenated products (CH + MCP) was high (above 95%) for all catalysts with Me/Pt= 1, but was somewhat lower for the PtPd samples with higher Pd concentrations. This is in agreement with a higher hydrocracking activity of PdPt during n-C$_7$ isomerization, as discussed above. As commented in the introduction, to maximize product octane hydrogenation of benzene should be accompanied by the isomerization of CH into the higher octane MCP. Figure 6 compares the MCP/CH ratio at constant reaction temperature (250°C) for the bimetallic samples. As observed, higher MCP/CH ratios were obtained for PtPd, with a maximum for the catalyst with Pd/(Pt+Pd)= 0.6.
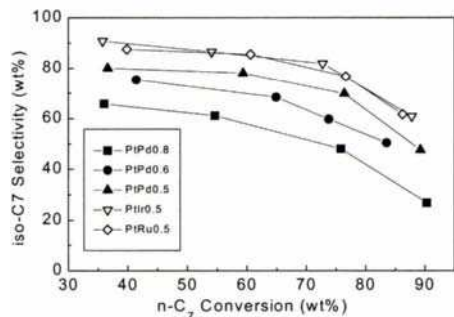
Figure 5. Selectivity to iso-$C_7$ as a function of n-$C_7$ conversion.
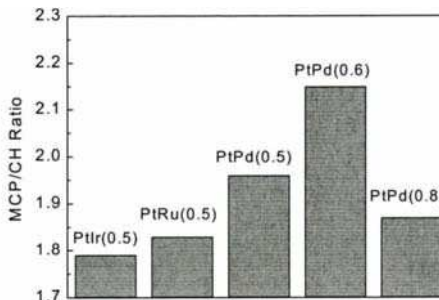
Figure 6. MCP/CH ratio obtained at 250°C for PtMe/Beta catalysts.

### 3.2.2 Experiments in the presence of 200 ppm of S

Results in Fig. 7 show the change of n-heptane conversion with time on stream (T.O.S.) in the presence of 200 ppm sulfur in the n-$C_7$/benzene feed. As observed, the n-heptane conversion initially decreased on all PtMe/Beta catalysts, and tended to reach a pseudo-stationary state at larger T.O.S. The decrease of activity of PtMe/Beta catalysts in the presence of S can be ascribed to a partial deactivation of acid sites by coke precursors whose formation becomes favored by a loss of the hydrogenating properties of the metal sites poisoned by sulfur. It is known that the sulfur resistance of noble metals (Pt, Pd) is increased by supporting them on an acid support, such as zeolite (13). In the case of the PtMe/Beta catalysts studied here, we used the same support for all metals, and therefore, the differences in sulfur resistance should arise from a modification of the electronic properties caused by mutual interaction between the two metals. The relative change of conversion ($X_S/X_0$) for the isomerization of n-heptane and the hydrogenation of benzene in the presence of S is given in Table 3. As observed, a higher



Figure 7. Change of n-$C_7$ conversion with time on stream in the presence of 200 ppm S for the bimetallic PtMe/Beta catalysts. Experiments performed at 260°C except for PtPd(0.6), for which a T=255°C was used. Same symbols as in Fig. 5.

relative loss of activity for n-$C_7$ conversion occurred for the PtIr and PtRu catalysts as compared to PtPd samples. It has to be noted the relatively high deactivation of PtIr, which retained only 35% of its initial activity after the addition of S. The better sulfur resistance of

PtPd/Beta samples might be related with a stabilization of electron-deficient Pt$^{\delta+}$ species by interaction with Pd particles, as it has been described in the literature (6, 8) and inferred from the TPR results discussed here. It has to be considered also that PtIr and PtRu catalysts presented the lowest $H_2$ chemisorption capacity (Table 2), suggesting a lower metal dispersion.

Table 3
Relative change of n-heptane and benzene conversions in the presence of 200 ppm of sulfur. Reaction conditions : WHSV = 3.1 h-1, $H_2$/feed = 10 mol/mol, P = 30 bar, T = 260°C (except for PtPd(0.6), for which a T= 255°C was used).

| | Relative conversions* | |
|---|---|---|
| Catalysts | Xs/Xo)n-heptane | Xs/Xo)benzene |
| PtPd(0.8)/Beta | 0.79 | 0.72 |
| PtPd(0.6)/Beta | 0.67 | 0.98 |
| PtPd(0.5)/Beta | 0.70 | 0.99 |
| PtIr(0.5)/Beta | 0.35 | 0.97 |
| PtRu(0.5)/Beta | 0.57 | 1.00 |

*Xs and Xo are the conversions in the presence and absence of sulfur, respectively.

By contrast, all catalysts displayed high benzene conversions in the range of T.O.S. studied (ca 6 h on stream). In this case, the largest deactivation was observed for the PtPd sample with the highest Pd concentration. Curiously, we found a clear relationship between the residual hydrogenation activity in the presence of S and the absolute Pt content in the bimetallic catalysts (Table 2). This can be related with a stronger hydrogenation ability of Pt as compared to the other metals (13, 14).

The above results also indicate that the acidic function of the bifunctional PtMe/Beta catalysts becomes more affected by the presence of S than the hydrogenating function.
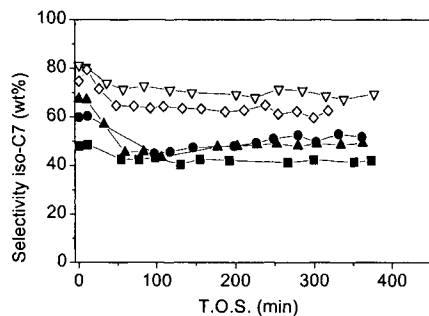


Figure 8. Effect of sulfur addition on iso-C$_7$ selectivity for PtMe/Beta catalysts. Symbols as in Fig. 5.
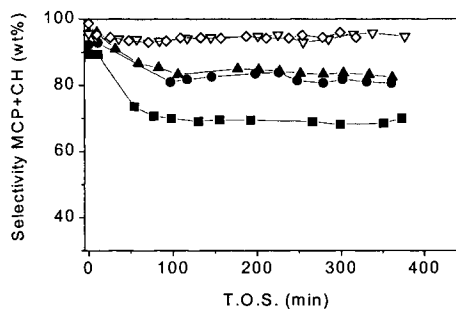
Figure 9. Change of selectivity to CH + MCP with the addition of sulfur for PtMe/Beta samples. Symbols as in Fig. 5.

For all catalysts studied, the decrease of n-heptane conversion observed in the presence of S was accompanied by a loss of isomerization selectivity in favor of cracking products (Fig. 8). Similarly, the selectivity to hydrogenated products (CH + MCP) also decreased with the addition of 200 ppm sulfur to the n-$C_7$/benzene feed, as observed in Fig. 9. The decrease of CH+MCP selectivity was also paralleled by a decrease of the MCP/CH ratio, that is, by a loss of activity for isomerization of cyclohexane. The higher hydrocracking activity observed for both n-$C_7$ and benzene conversion products results from a lower hydrogenating ability of the metal centers which are deactivated by sulfur. This hinders the desorption of the intermediate carbocations, which remain adsorbed on the acid sites of the zeolite for a longer time increasing the probability to undergo consecutive cracking reactions.

As it was previously observed in the experiments performed in the absence of sulfur, PtPd catalysts also displayed the lowest selectivity to iso-$C_7$ and (CH+MCP) in the presence of sulfur. Moreover, results in Figs. 8 and 9 show that the cracking selectivity increased with increasing the Pd content, as it occurred in the sulfur-free experiments.

## Acknowledgments

## REFERENCES

1. J. Hancsok and A. Hollo, Petroleum and Coal, 39 (1997) 4.
2. J-K Chen, A.M. Martin and V.T. John, J.Catal., 111 (1998) 425.
3. K. Chao, H. Wu and L. Leu, Appl. Catal. A, 143 (1996) 223.
4. M.A. Arribas, F. Márquez and A. Martínez, J.Catal., 190 (2000) 309.
5. M.A. Arribas and A. Martínez, Catal. Today, (2001) in press.
6. T.B. Lin, C.A. Jan and J.R. Chang, Ind. Eng. Chem. Res., 34 (1995) 4284.
7. H. Yasuda, T. Sato and Y. Yoshimura, Catal. Today, 50 (1999) 63.
8. J.K. Lee and H.K. Rhee, J. Catal., 177 (1998) 208.
9. A. Corma, V. Fornés, A. Martínez and A.V. Orchillés, ACS Symp. Ser.,368 (1998) 542.
10. C.A. Emeis, J. Catal., 141 (1993) 347.
11. G. Larsen, E. Lotero and R.D. Parra, Stud. Surf. Sci. Catal., 101 (1996) 543.
12. E. Blomsma, J.A. Martens and P.A. Jacobs, J.Catal.,165 (1997) 241.
13. Stanislaus and Cooper Cat. Rev. Sci. Eng. 36 (1994) 75.
14. M. Koussathana, D. Vamvouka, H. Economou and X. Verkios, Appl. Catal., 77 (1991) 283.

# CH$_4$ and CO$_2$ transformations initiated by hydrogen-accumulated systems. Role of spillover and lattice bound hydrogen

M.V.Tsodikov[a], V.Ya.Kugel[a], F.A.Yandieva[a], E.V.Slivinskii[a], I.I.Moiseev[b], G.Colón[c], M.C.Hidalgo[c] and J.A.Navío[c*]

[a] A.V.Topchiev Institute of Petrochemical Synthesis RAS, 117912, Leninskii prosp. 29, 117912, Moscow, Russian Federation.

[b] A.V. Kurnakov Institute of General and Inorganic Chemistry RAS, 117912, Leninskii prosp. 31, 117912, Moscow, Russian_Federation.

[c]Instituto de Ciencia de Materiales de Sevilla. C/ Américo Vespucio, s/n, 41092-Sevilla, Spain.

In this paper the stoichiometric reaction of methane is reported over a hydrogen-accumulated system (based on a high porosity titanium impregnated with 0,5% Ni and titanium chips in a ratio 5:1) giving rise to ethylene and ethane as well as propylene and propane at 450$^0$C and pressure 10 atm. At the same time, results related to methane and carbon dioxide transformations, initiated by the hydrogen-accumulated systems, are analyzed in context of the role of the spillover phenomena and lattice bound hydrogen during these processes.

## 1. INTRODUCTION

Methane and carbon dioxide are the most naturally abundant building blocks of C$_1$ –chemistry. Utilization of these components of natural gas and a great quantity of industrial waste is a challenging task. Activation of these substrates under mild conditions constitutes one of the main objectives pursued by numerous researches [1-3].

Methane is the most stable representative of aliphatic hydrocarbons [4,5]. Activation energy of C-H cleavage constitutes 320±20 kJ/mol [4]. According to thermodynamic data, the shift to the side of cracking methane product formation is achievable only above 1100$^0$C.

Oxidation of hydrogen atoms with an appropriate oxidant or their chemical occlusion by a strong absorbing system makes stripping off the methane molecule thermodynamically more favorable.

In this paper we report a stoichiometric reaction between methane and a hydrogen-accumulated system (high porosity titanium impregnated 0,5% Ni and titanium chips prepared in a ratio 5:1) (1) giving rise to ethylene and ethane as well as propylene and propane at 450$^0$C and 10 atm pressure [6] (see section 3.1). Results related to methane and carbon dioxide transformations, initiated by hydrogen-accumulated systems, are also reported and

---

* corresponding author: navio@cica.es

analyzed in context of the role of the spillover phenomena and lattice bound hydrogen during these processes.

Cyclohexane dehydrogenation in the presence of $CO_2$, and $CO_2$ in CO reduction are processes discussed in section **3.2**.

## 2. EXPERIMENTAL

The conversion of methane and $CO_2$ was carried out in a flow-circulated type of home-installed set-up with summary volume – 0,7 l. For methane conversion a catalytic run was used at $450^0C$ and 10 atm of methane for 56 h in a closed-circulating system. Also, separate methane thermodesorption was performed in the presence of the planning and nickel-titanium system at the same temperature and pressure. For this purpose methane was charged into the system with a catalytic bed and circulated at room temperature for 2 h. Then, methane was exchanged for Ar and the temperature was raised to $450^0C$ in the regime of circulation. At this temperature gaseous samples were taken out for "on-line" analysis.

Reactions of $CO_2$ in the presence of intermetallic hydride [$TiFe_{0,95}Zr_{0,03}Mo_{0,02}$]$H_x$ (2) were studied at $430^0C$ and initial pressure of 10-12 atm by using the same closed home-installed set-up equipped with a system allowing the introduction of liquid reactant (cyclohexane) into a catalytic bed. The reaction vessel was charged with 60 g of the intermetallic alloy $TiFe_{0,95}Zr_{0,03}Mo_{0,02}$ prepared by a high temperature alloying method. Another catalytic system (6,3 g) was commercial $Pt/Al_2O_3$ (3) processed in the form of granules sizes 1,5 – 2 mm.. Catalyst (4) was prepared by carefully mixing 60 g of intermetallic (2) and 6,3 g of commercial $Pt/Al_2O_3$ (3).

In order to characterize the hydrogen capacity and structure peculiarity of intermetallic (2), the intermetallic alloy TiFe, widely used as a traditional hydrogen storage material, was prepared by the same method [7].

Every catalytic system containing intermetallic (2) underwent standard activation: systems were treated by $H_2$ flow at $100^0C$, P=1 atm for 10-14 h. Then the reactor was cooled to 25-$30^0C$ under $H_2$ circulation and then filled with $H_2$ at a pressure of 130 atm. Activation temperature ($T_a$) and the time of $H_2$ absorption depends on the sample nature: for the sample (2) $T_a = 60-75^0C$ and $t_a \sim 120$ min., while that for sample(4) $T_a \sim 35-40^0C$ and $t_a \sim 30$ min. For the system TiFe the temperature and the time of absorption were $90-100^0C$ and 24 h, respectively [8]. An initial $H_2$ uptake took place, at a period when the fast pressure drop was observed. The amount of absorbed $H_2$ was measured by using high sensitive manometer set-up.

For the sample (2), Ar replaced hydrogen atmosphere, and then, the temperature was raised linearly to $430°C$. Then the catalytic set-up kept at this temperature until complete hydrogen release from intermetallic alloy (2) and equilibrium between gas atmosphere and the catalytic sample is achieved. The amount of $H_2$ evolved was measured by using a high – precise manometer. In order to study $CO_2$ reduction over intermetallic hydride, Ar was replaced by $CO_2$ at initial pressure of 10 atm. The $CO_2$ reactions were studied at $430^0C$, 10 atm and the turnover number of gas circulation of $5,0$ l h$^{-1}$. Fresh portions of $CO_2$ were added to the reaction vessel several times until $CO_2$ reaction with hydrogen was completed (each new $CO_2$ loading was preceded by Ar circulation). For the catalysts **2, 3, 4** after the above mentioned $CO_2$ reduction was completed, the reaction of $CO_2$ reduction coupled with cyclohexane dehydrogenation was studied. For this purpose a new portion of $CO_2$ was replenished to the gas phase and liquid cyclohexane was added drop by drop to the catalytic bed with an hourly

space velocity of 0,08-0,1 h$^{-1}$ over 2-3h. For catalytic runs using of Pt/Al$_2$O$_3$ catalyst, gaseous H$_2$ and CO$_2$ placed in the ratio of 1/1 was added to the reactor simultaneously. The total duration of catalytic runs for the catalysts **2**, **3** and **4** was 227, 67 and 277 h, respectively; 8 and 14 cycles of CO$_2$ hydrogenation, Ar and fresh carbon dioxide replacing were carried out with using (**2**) and (**4**) catalytic systems.

Gaseous products were analyzed by "on-line" chromatography using an LKhM – 8MD setup supplied with computer control and program "Ekohrom". The content of hydrocarbons was determined with the use of helium as a carrier gas in a column packed with α-Al$_2$O$_3$ (0,25-0,50 mm fraction), modified by 5% squalane and a flame-ionization detector. The composition of gas contained H$_2$, CO, CH$_4$ and CO$_2$ analyzed with the use of Ar as a carrier gas in a column packed with coal granules (0,25-0,50 mm SKT) and the TC detector. Composition consisting of high - porosity titanium (14 g) impregnated by 0,4% Ni in the form of cylindrical pellets 10 mm long and 5 mm in diameter and titanium planning (5,3 g) made of high – purity titanium. This catalytic composition was thermally activated at 850$^0$C in vacuum (10$^{-5}$ T) before charging into a reactor.

X-Ray powder diffraction of heterogeneous system have been studied using Dron-3M diffractometer with filtered Cu K$_\alpha$ radiation. The samples selected for study were prepared in Ar and were protected by amorphous polymer film.

Laser (ML-2) and scanning high temperature mass spectroscopy (VIMS MS-7201) were used to study the composition of the surface of heterogeneous components.

## 3. RESULTS AND DISCUSSION

### 3.1. Methane transformation

As mentioned above two types of the titanium-content contacts were used for methane conversions: porous titanium with 0,5% Ni impregnated on the surface (Ni/Ti) and titanium chips (see experimental).

The experiments on methane thermodesorption study showed that the massive titanium chips themselves were not able to activate methane. At the same time the thermodesorption of absorbates from the surface of the porous Ni/Ti contact in Ar showed that the system absorbed 0,63 cm$^3$ of methane; in the desorption products, the methane conversion into C$_2$, C$_3$ hydrocarbon at 450$^0$C was 25 wt.%, among which: ethane –7%, ethylene – 16% and propane – 2%.

In the presence of the mixing composition consisting of porous Ni/Ti combined with titanium chips a small methane conversion (0,1%) into ethane and ethylene was observed even at 350$^0$C. At 450$^0$C conversion of methane reached 4,7% wt. Data on the composition of methane conversion products formed after continuous circulation of the gas mixture during 56 h are reported in Table 1. As can be seen, the methane conversion into alkane-alkene fraction increases monotonically over a circulation period of 22 h and reach 20 % wt. At the end of this period the olefin content reaches 68-73%, with ethylene content accounting for 50-55% (Table 1). Practically no hydrogen was observed in the gas phase, from the circulation of methane through the catalytic composition during this time.

The activity and selectivity of the heterogeneous system changed after 22 h of methane circulation: the amount of methane increased again and the content of higher hydrocarbons decreased. After 56 h of running operation, the gas composition was not changed, which is probably due to the loss of catalytic activity. Such unusual changes in the system dynamics

242

were accompanied by a certain decrease in the selectivity of the olefins formation and increase in the content of $C_2$, $C_3$ alkanes (Table 1).

Chromatographic data showed that, within the accuracy range of the method, the content of hydrogen during the first 22 h of operation was $\leq 0,1$ vol. % and increased to 0,1 vol.% at the time 56 h.

Table 1
Methane conversion and the composition of the products its transformation
(T= 450$^0$C, P= 10 atm.)

| Time, h | 1 | 5 | 22 | 28 | 50 | 56 |
|---|---|---|---|---|---|---|
| Composition wt % | | | | | | |
| $CH_4$ | 95,3 | 85,3 | 79,8 | 80,1 | 86,5 | 87,3 |
| $C_2H_4$ | 2,5 | 8,2 | 10,0 | 10,8 | 8,4 | 5,8 |
| $C_2H_6$ | 1,9 | 3,0 | 4,8 | 4,4 | 4,1 | 5,1 |
| $C_3H_6$ | 0,1 | 2,5 | 3,1 | 2,1 | 0,4 | 0,7 |
| $C_3H_8$ | 0,2 | 0,4 | 0,4 | 0,3 | 0,2 | 0,3 |
| $C_4H_8$ | <0,1 | 0,4 | 1,3 | 1,7 | 0,2 | 0,4 |
| $C_4H_{10}$ | <0,1 | 0,2 | 0,6 | 0,6 | 0,2 | 0,3 |

The set of identified products can be rationalized to methylene and methyl radicals formed from methane and coordinated on the Ni/Ti surface (Scheme 1).

The recombination of these radicals gives rise to higher hydrocarbons identified in the gas phase. The transformation of methane was found to be accompanied by considerable changes in the titanium reagents itself. Visually the color of the reaction mixture changed from brown for the starting porous titanium and typical metallic color for the planning to dark violet for both components. X-Ray diffractograms for initial titanium porous system (Fig.1) display typical interplane distances for metallic titanium with d(A) = 2,24; 2,34, 255 [12]. The same picture was observed for initial titanium chips. For titanium chips after reaction around 50 % of metallic phase transferred to hydride phase, TiH$_2$ (d =1,31; 2,20; 2,53) [13]. At the same time, for the porous Ni/Ti system only a shift of reflections in the range $0,45 - 0,47^0$ associated with the metal titanium phase was observed. This is evidence for the formation of a interstitial solid solution of hydrogen in the framework of porous titanium material during decomposition of methane.

Highly sensitive laser mass-spectroscopy showed the averaged probes of the solids contained 0,0095% (titanium chips) and 0,0021 wt.% (porous nickel-containing titanium) of carbon before experimenting with methane. After 56 h of reaction, the content of carbon on the surface of the porous system and the metal ships increased to 0,058 and 0,487-wt.%, respectively.

**Scheme 1**

$$CH_4 \xrightarrow{-2[H]} [CH_2]$$
$$CH_4 \xrightarrow{-[H]} [CH_3]$$
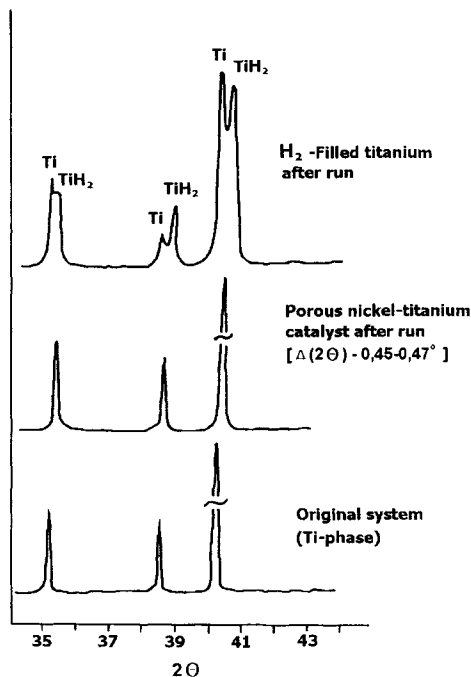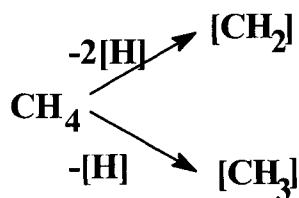


Fig. 1. X-ray diffraction patterns exhibited by the indicated samples.

On the base of kinetic data combined with X-Ray data of the heterogeneous systems phase transformations we can propose the role of hydrogen spillover involved in methane conversion. In fact, the recombination possibility of the active methane derived intermediates forming the higher hydrocarbons can be realized only due to [H] transfer trapped in the porous of the Ni-Ti system to titanium chips.

Since the major product of methane transformation is ethylene it can be assumed that the methylene surface species were formed. With respect to Scheme 2 with phase transformations of the planning and porous titanium, the most probable mechanism of methane transformation including mechanism of hydrogen spillover is presented:

**Scheme 2**

$$xCH_4 + S_{Ni-Ti} \rightarrow xCH_2 + S_{Ni-Ti}[2H]_{chemisorbed} \qquad (1a)$$
$$S_{Ni-Ti} + [2H]_{spillover} \rightarrow Ti[2H]_{chemisorbed} \qquad (1b)$$
$$Ti[2H]_{absorption} \rightarrow TiH_2 \qquad (1c)$$
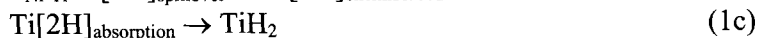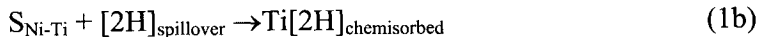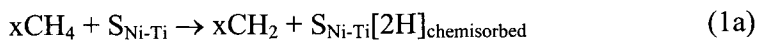
In accordance with this scheme it can be proposed also that during the first 22 h $r_{Ia} \approx r_{Ib}$, $r_{Ia}$ and $r_{Ib}$ being the rates of active surface species formation and hydrogen spillover to titanium planning, respectively.

As has been determined by the use of mass-spectroscopy study the carbon and hydrocarbon fragments were accumulated on the heterogeneous systems surface during methane conversion. It could be the result of methane and formed hydrocarbon dehydrogenation. It is known that the rate of the higher molecular hydrocarbon dehydrogenation is more than that of methane. Probably this is the main reason for the increasing content of methane in the gaseous phase after 28 h of the process.

An alternative explanation of this tendency could be an interaction of active surface carbon with active hydrogen on the nickel-titanium system surface. Also, we can not exclude that the decreasing of the hydrogen spillover stripping off of active surface blocking by adsorbed hydrocarbon fragments to titanium planning was the main reason for completely termination of methane conversion.

### 3.2. CO$_2$ transformations

The reaction of methane conversion could be considered as a part of a catalytic cycle if an oxidative process is added. Carbon dioxide seems to be an attractive oxidant, since the reduction of carbon dioxide to CO is industrially important [3]. For instance, the following reaction set could be of interest:

$$CH_4 \rightarrow C_2H_6 + [2H]$$
$$\underline{[2H] + CO_2 \rightarrow CO + H_2O}$$
$$CH_4 + CO_2 \rightarrow CO + H_2O + C_2H_6 \qquad (1)$$
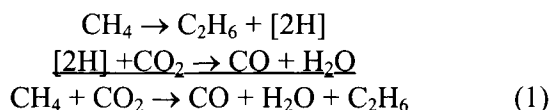
Where [H] is the hydrogen dissolved in the lattice matrix of the hydrogen-accumulating system.

However the reaction 1 ($\Delta G^0_{298} = +51,766$ kcal/mol) is allowed at elevated temperatures only when a Ti-content catalyst is not inert toward CO$_2$. Moreover, any hydrogen-accumulating system is expected to be destroyed because oxidation by carbon dioxide. Another reason preventing system 1 to be converted into a catalyst is a strong Ti-H bond ($\Delta G^0_{298} = -129$ kJ/mol) [8,9]. This makes system 1 not a perspective for achievement of the goal. This is why another hydrogen-accumulated system, TiFe$_{0,95}$Zr$_{0,03}$Mo$_{0,02}$ (2), having an essentially weaker binding energy of absorbed hydrogen (-49 kJ/mol) [7,9] in comparison with metallic titanium, was chosen as an alternative catalyst. Cyclohexane was chosen as the substrate instead of methane to reduce the thermodynamic restrictions.

To improve the dehydrogenation activity of the catalytic system we added to intermetallic 2 the catalyst 3 (Pt/Al$_2$O$_3$) (see experimental section). Firstly, we have studied the single CO$_2$ conversion over the hydride intermetallic 2, as well as over catalyst 3 and over a mixing composition consisting of hydride form of 2 and 3 (contact 4).

It was established that one mol of intermetallic absorbed around 1 mol H$_2$. The experiment on thermodesorption of hydrogen at leaner increasing of temperature in closed setup system showed that $\sim 0,85 - 0,82$ moles of hydrogen was eliminated from the structure of the intermetallic in Ar at increasing of temperature to $430^0$ C. The $0,15 - 0,18$ moles of H$_2$ remained in the intermetallic structure is denoted as strong-bonded H$_2$ (SBH).

The intermetallic containing the strong-bonded hydrogen has the ability to selective $CO_2$ reduction to CO. For intermetallic hydride $[Int]H_{0,34}$ during 1-st hour of $CO_2$ reaction with the strongly bonded hydrogen, at most CO and $C_1$-$C_5$ hydrocarbons were formed. The following results have been obtained: overall $CO_2$ conversion W=60% and selectivity of CO formation S=80%. At the end of the second hour of reaction the conversion reached the top value W= 100%, while the selectivity significantly decreased up to 50%. After refreshing the reactor with a new portion of $CO_2$, conversion (W) showed the value 22% while the selectivity ($S_{co}$) increase to ~ 100% .

In the presence of the mixing composition named (4) the highest selectivity S (CO) up to 97-100% was reached at conversion $CO_2$ W= 70% in fist cycle of carbon dioxide hydrogenation.

Table 2 report data related with selectivity to CO formation in the presence of intermetallic alone, alumina-platinum catalyst and hybrid system consisting of hydride intermetallic mixing with $Pt/Al_2O_3$ catalyst at $430^0C$. It can be seen that over hydride form of (2) and (4), an initial rate of $CO_2$ hydrogenation by a level of magnitude higher then that for catalyst (3). Moreover, for the catalysts (2) and (4), for which the role of SBH is especially important, the time of 40% conversion of $CO_2$ achievement, by two order of magnitude smaller that for the catalyst (3). It should be noted that the gas composition formed from $CO_2$ in the presence of hydrogen-accumulating systems is extremely different from gas composition obtained over $Pt/Al_2O_3$. The selectivity in CO formation was 51 and 98% during first cycle over (2) and (4) system. At the same time using a traditional hydrogenation process regime, the catalytic runs over $Pt/Al_2O_3$ (sample 3) were carried out at 10 atm and $T=430^0C$ with the gaseous mixture of $H_2$ and $CO_2$ placed in the ratio 1:1. An analysis of the reactor effluent showed that the total $CO_2$ conversion took the value W=40% with the selectivity of CO formation not exceeding 15-18%. Except CO, as the main reaction product, the reaction yielded also $C_1$- $C_4$ hydrocarbons where methane prevailed (Table2).

Table 2
The rate of $CO_2$ transformation, the selectivity in CO formation and the composition of the gas-products.

| System | Time to reach 40-45% $CO_2$ conversion, h | Started rate of $CO_2$ transformation, $mmol \times [g\ h]^{-1}$ | Selectivity in CO formation, % mol | Gas-products composition, % mol | | | |
|---|---|---|---|---|---|---|---|
| | | | | CO | $C_1$ | $C_2$-$C_4$ | $C_2$ |
| $[Int]H_x$ (1): | | | | | | | |
| $350\ ^0C$ | - | 3,5 | 98 | 36,6 | 0,16 | | 11,9 |
| $430\ ^0C$ | 0,25 | 3,3 | 51 | 45,5 | 4,5 | 3,2 | 16,7 |
| $[Int]H_x$ + $Pt/Al_2O_3$ (3), $430^0C$ | 0,25 | 3,7 | 99 | 99 | - | - | 0,16 |
| $Pt/Al_2O_3$ (2), $430^0C$ | 23 | 0,34 | 17,7 | 7,3 | 16,8 | 3,6 | 2,7 |

Fig.2 shows typical kinetic curves for $CO_2$ conversion over the sample (4). As can be seen, the rate of $CO_2$ conversion per one cycle is decreased as far as CO is accumulated in the products. While the CO kinetic curves show the maximum yield of hydrocarbons following a weak induction period is increased with decreasing the CO concentration. All these facts might support the conclusion on the sequence character of the hydrogenation process:

$$CO_2 \rightarrow CO \rightarrow C_1 - C_4$$
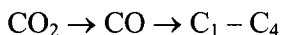
As for the retardation mechanism of $CO_2$ conversion, we suggest two possible reasons. Firstly, because the main component of the catalyst (2) is iron, an appearance of stable carbonyl complexes of iron on active surface sites may reduce $CO_2$ chemisorption. Secondly, the diffusion of SBH trough lattice (2) to the surface may become a rate controlling step of the entire process.

In the combined catalytic run on the $CO_2$ reduction and cyclohexane dehydrogenation, catalysts 2-4 were used after complete extraction of the SBH species. During the dehydrogenation process the concentration of molecular $H_2$ in the gas phase significantly increased, this being accompanied by an essential increase of $CO_2$ hydrogenation over catalysts (2) and (4).
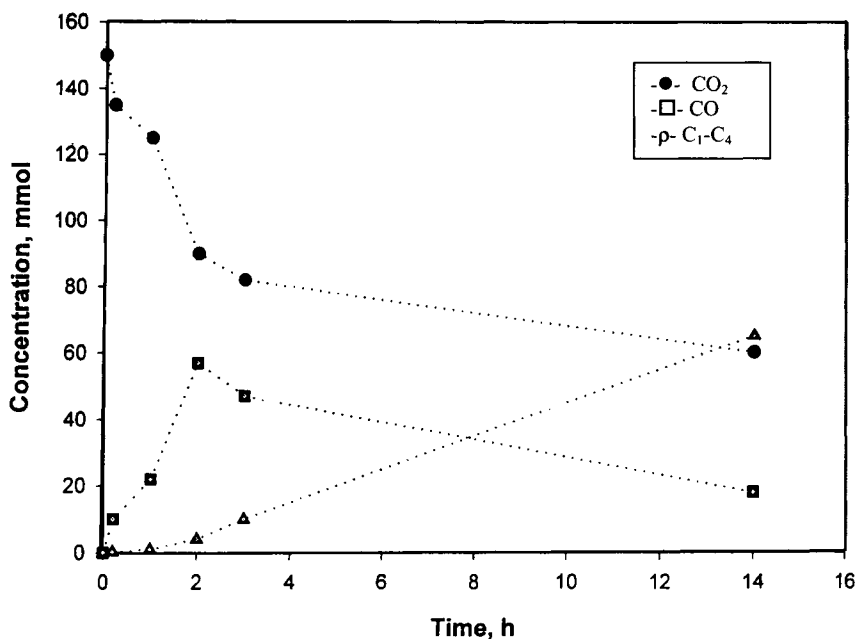


Fig. 2. Kinetic profiles of the indicated molecules during the $CO_2$ conversion over catalyst named (4) [$P_{started}$=10 atm; T=430°].

Table 3 shows that for catalyst (2) the conversion of cyclohexane does not exceed 2,5%, while the cyclohexane conversion reaches 98 and 49% over catalysts (3) and (4), respectively. By prolonging the circulation of the gaseous products over the catalyst (2) and (4), and even after the cyclohexane feeding process was over, the $CO_2$ and CO hydrogenation yielding hydrocarbons is still continuing. The latter means that at least part of the $H_2$ obtained via cyclohexane dehydrogenation was absorbed by the intermetallic hydride. As a result, after exchange of the reaction products with the fresh $CO_2$ the selectivity of CO formation again reaches 99-100% while an overall conversion was 20%. It should be noted that in the presence of catalyst (3) $CO_2$ hydrogenation is low even at high cyclohexane conversion.

Table 3
Dehydrogenation of cyclohexane in the presence $CO_2$
($T=430^0C$; $P_{started}=10$ atm; specific velocity – 0,08-0,12 $h^{-1}$)

| System | Conversion of cyclohexane, % mol | Selectivity in benzene formation % mol | Amount of $H_2$ consumed on $CO_2$ hydrogenation from cyclohexane, % mol |
|---|---|---|---|
| $[Int]H_x$ | 2,5 | 68,8 | 50 |
| $[Int]H_x + Pt/Al_2O_3$ | 49 | 92,3 | 58,5 |
| $Pt/Al_2O_3$ | 97 | 85,8 | 25 |

Fig.3 report the X-Ray results of initial intermetallic as well as hydride forms of intermetallic (2) with different degree of $H_2$ saturation. The main reflexes of the initial intermetallic system is the same that for the known cubic TiFe system (Fig.3 a) [10]. The deviation of this pattern from the structure of TiFe is the existence of two minor reflexes at angles $2\theta = 40,5$; $41,75^0$ (d, A =2,22; 2,16).

Existence of these reflexes can be the reason for tetragonal distortion of the structure as a result of doping by Zr and Mo modified components. For the sample having the maximum amount of absorbed hydrogen (x=2) a dramatic changing of structure was observed. This sample is a multiphase system mainly consist of cubic $[Int]H_{1,93}$; orthorhombic $[Int]H$ and a little quantity of metallic Fe phases (Fig.3 b) [11]. The cubic $[Int]H_{1,93}$ is the dominate phase in this distribution. For the sample having 0,5 moles $H_2$ the distribution changes and orthorhombic $[Int]H$ became a dominant phase. Apart from this phase the samples have a smaller quantity of $[Int]H_{1,93}$ and Fe. Additional cubic $[Int]H_{0,06}$ occurs in the phase composition (see Fig.3 c) [12]. Sample d) was obtained after the weak bonded hydrogen was extracted from the structure by heating of the intermetallic hydride in Ar at $430^0C$. For this sample the reflexes on the pattern relate to $[Int]H_{0,06}$ phase [12]. On the balance basis, in this sample can exist around 0,17 moles of $H_2$ absorbed by the structure. But in accordance with X-ray study determination for $[Int]H_{0,06}$ phase the quantity of absorbed hydrogen could not exceed 0,06 moles of $H_2$. This misbalance permits the conclusion that the system contained other quantities of the absorbed hydrogen dissolved in the intermetallic structure. The misbalanced quantity of hydrogen was extracted from the structure during the heat treatment in Ar at temperature range $700-920^0C$. At least in the structure of sample e), obtained after long-term $CO_2$ hydrogenation, along side with the main reflexes related to cubic TiFe

248

structure, the minor reflexes characterizing the tetragonal motive of structure ($d, A = 2,16$; $2,21$) appeared again. It should be noted that the main reflexes of the cubic structure were considerably wider compared to the shape of the initial intermetallic (see Fig.3 e). This evidence is a probe for the destruction of the intermetallic structure following by its crushing after processes of absorption- desorption of hydrogen.

1-[Int]

2-[Int]H$_{1,93}$ (cub)

3-$\alpha$-Fe

4-[Int]H (orthorhombic)

5-[Int]H$_{0,06}$ (cubic)

6-[Int]H$_{0,06-x}$ (cubic)
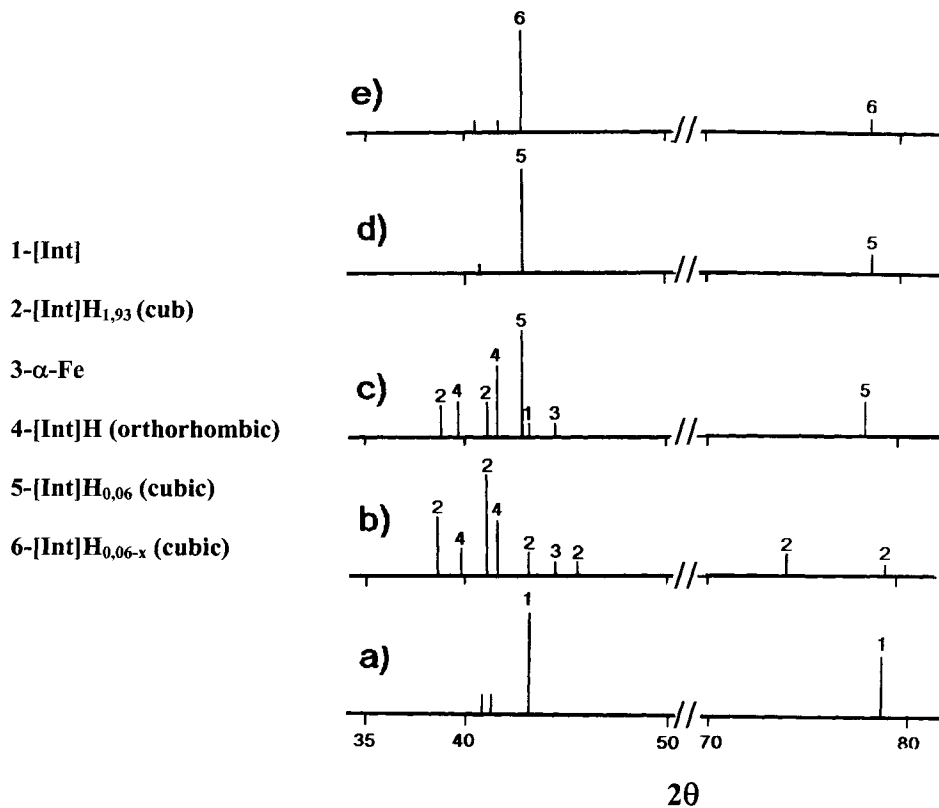


Fig. 3. X-ray patterns of the original intermetallic [Int] $TiFeZr_{0,3}Mo_{0,02}$ (a) and its hydride forms [Int]H$_x$, where x=2 (b), 1 (c), 0,5 (d) and <0,06 (e).

## 4. CONCLUSIONS

Our experiments showed cyclohexane undergoing dehydrogenation smoothly, giving rise to benzene at $430^0C$ in the presence of catalyst 2. The second step of the catalytic process was found to proceed rather non-selective with catalyst (2) giving rise to hydrocarbons besides the goal product, carbon dioxide. This obstacle made us add a traditional catalyst $Pd/Al_2O_3$ (3) to catalytic system (2). It was expected that dihydrogen evolved by the cyclohexane

dehydrogenation would be used to reduce $CO_2$ to CO with the catalyst $Pt/Al_2O_3$. In fact, hydrogen transferred from catalyst (2) to catalyst (3) via a spillover mechanism instead of gaseous dihydrogen was found to be involved in the high selective $CO_2$ reduction to CO. It is known that the process of $H_2$ absorption by intermetallic deal to destroy the structure being accompanied by its crushing after first cycle of absorption [15]. As a result the initial grains of alloy have been charged in the reactor, transforming in the dust mass can be strew the cylindrical grains of $Pt/Al_2O_3$ catalyst. By this way it can be estimated a contact between two type of catalysts leading the formation of channels for hydrogen transfer from the intermetallic system to the surface of the $Pt/Al_2O_3$ catalyst.

The intermetallic hydride contains two forms of hydride hydrogen having different abilities in catalytic $CO_2$ transformation. Hydride phases such as cubic $[Int]H_{1,93}$ and orthorhombic structure $[Int]H$ have a weakly bound hydrogen which easy evolved from the structure by heating up to $430^0C$. Hydrogen contained in cubic phase $[Int]H_{0,06}$ as well as hydrogen distributed in the framework of intermetallic more strong bound with crystal cell. The existence of SBH in the framework of the intermetallic does not deal with remarkable changes of the structure. Only some changes relate with intensity of reflexes close to the initial system while the weakly bound hydrogen in the hydride phases deal with full reconstruction of the structure.

It was estimated that the original cubic intermetallic (2) was characterised by microdistortion of the structure probably due to insertion of the modified component such as Zr and Mo, in comparison with known cubic TiFe intermetallic. Such a deviation of the structure can be attested by the existence of surface and volume defects and, as a consequence, by decreasing the framework packing density. Probably SBH absorbed by the structure strongly interacts with titanium atoms of the framework. Disordered hydride clusters [Ti-H] influence only some changes of the reflex intensity on the patterns. The energy of hydride bonds in these hydride-titanium clusters is more than the energy of bonds in determined hydride phases of intermetallic. It is clear that the destruction of that bonds is being accompanied by extracting of $H_2$ which is observed only during heating at high temperatures more than $700^0C$ in Ar. At the same time SBH evolved easy enough from the structure of intermetallic consuming on reaction of $CO_2$ reduction.

The high selectivity can be explain by the strong interaction of the partially negative charge of SBH with partially positive carbon in chemisorbed dioxide on the surface of intermetallic:
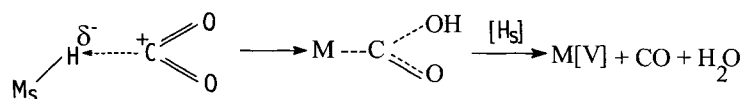


Where M =Ti.

As result of such a $CO_2$ reduction, the vacancy burns in the surrounding of titanium. Probably the affinity of this vacancy to hydrogen is sufficiently high. The latter could be reason for the SBH transport to surface:
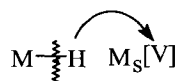
**REFERENCES**

1. J.M.Fox., Catal.Rev.-Sci.Eng. V.35, N 2 (1993) 169.
2. P.G.Jessop, T.Ikarida, and R. Noyori, Chem.Rev., 95 (1995) 259
3. O.V.Krylov, A.Kh.Mamedov, Russ.Chem.Rev., 64, 9 (1995) 877.
4. A.E.Shilov, and G.B.Shulpin. Activatsiya i katalyticheskie reaktsii uglevodorodov (Activation and Catalytic Reaction of Hydrocarbon), Moscow: Nauka, 1995.
5. D.Stull, E.Westrum, and G. Sinke "The Chemical Thermodinamics of Organic Compouds, New-York:Wiley, 1969.
6. M.V.Tsodikov, Ye.V.Slivinskii, V.P.Mordovin, O.V.Bukhtenko, G.Colón, M.C.Hidalgo and J.A.Navío, Chem.Commun., (1999) 943.
7. Patent (The Netherlands) N 7513159 (1977).
8. V.I.Micheeva, Gidridi perehodnykh metallov (Transition – Metal Hydrides), Moscow: Akad. Nauk SSSR, 1960.
9. G.Alefeld and J.Volkl (eds.), Hydrogen in metals, II Application – Oriented Properties Topics and Applied Physics Springer – Verlag; Berlin – Heidelberg – New York, 1978, V.29, 430 p.
10. JCPDS-ICDD Copyright -1995 (card 05-0682i).
11. JCPDS-ICDD Copyright -1995 (card 09-0371).
12. JCPDS-ICDD Copyright -1995 Card 19-636.
13. JCPDS-ICDD Copyright -1995 Cards: 26-805; 33-514; 6-696.
14. JCPDS-ICDD Copyright -1995 Card 42-919.
15. G.K.Shenoy, B.D.Dunlap, P.J.Vicarro, and D.Niarchos, Mössbauer Spectroscopy and its Application, 1981, V.23, 501-52.

# Effect of hydrogen spillover in hydrogenolysis and cracking of butane on Co-niobia-silica catalysts

F. Tiu[a], V. Părvulescu[b], P. Grange[c] and V. I. Părvulescu[a]

[a]-University of Bucharest, Department of Chemical Technology and Catalysis, B-dul Regina Elisabeta 4-12, Bucharest 70346, Romania, E-mail: V_PARVULESCU@chim.upb.ro.

[b]- Institute of Physical Chemistry of Romanian Academy of Sciences, Splaiul Independentei 213, Bucharest, Romania.

[c]- Universite Catholique de Louvain, Unite de Catalyse et Chimie des Materiaux Divises, Place Croix du Sud 2/17, 1348 Louvain-la-Neuve, Belgium, E-mail: grange@cata.ucl.ac.be.

A series of Co-Nb$_2$O$_5$-SiO$_2$, Co-SiO$_2$ and Co-Nb$_2$O$_5$ catalysts with 10 wt.% Co and 10 wt.% niobium oxide were prepared following three sol-gel procedures: colloidal, polymeric, and an intermediate one. Impregnated mixed oxides and oxides were also prepared, as well as physical mixtures of impregnated oxides in order to obtain information about the existence of the spillover species. These catalysts were investigated using several techniques: N$_2$ adsorption and desorption curves at 77 K, XRD, FTIR and XPS. H$_2$-chemisorption, H$_2$-TPR and H$_2$/D$_2$ exchange were used to prove the existence of the spillover effect. The activity of these catalysts was evaluated in hydrogenolysis and cracking of butane. Their increased stability in hydrogen was associated to a scavenger effect, enhanced by the spillover species.

## 1. INTRODUCTION

The contribution of hydrogen spillover in acid-catalyzed reactions has been demonstrated by several authors [1, 2]. In a recent paper, Pajonk [3] has showed that hydrogen-spillover species may influence these reactions in two ways: static, by creation of acid sites like for silica and dynamically, by direct intervention of these sites in the catalytic reaction. Hence, silica activated by H-spillover may be transformed into an acid catalyst able to yield hydrogenolysis and cracking of various hydrocarbons [4]. The deposition of an active species like a Group 8 metal helps this process. Therefore most hydrogen spillover studies have been investigated on supported metal catalysts with metal particle size in the range 1-10 nm [5].

Niobia is different on silica. Depending on the temperature of calcination, it may act as a strong acid catalyst or support. In addition, silica and niobia have a complete immiscibility in all compositions in that range [6]. According to Tanabe, niobia-silica mixed oxides will exhibit an increased acidity caused by the imbalance along Si-O-Nb linkages [7]. The deposition of a metal on such surfaces may lead to very effective bifunctional catalysts in reactions like isomerization of alkanes. Previous research in hydrogenolysis of butane on Co-niobia and Co-silica-niobia catalysts [8, 9] revealed some specific characteristics of these materials. Some these could be the consequence of the spillover effect.

The aim of this study was to bring evidence about the existence of hydrogen spillover species in mixed niobia-silica oxides and bifunctional cobalt-niobia-silica catalysts. Another issue was to elucidate the contribution of these species in improving the catalyst stability, and for such purpose they were tested in hydrogenolysis of butane which is known as a reaction that deactivates the catalysts very rapidly [10]. To evidence these effects physical mixtures of Co-SiO$_2$ with niobia and of Co-Nb$_2$O$_5$ with silica were considered.

## 2. EXPERIMENTAL

The preparation of the catalysts was made following several sol-gel routes: i) colloidal (designated as #A), ii) polymeric (designated as #B), and iii) an intermediate procedure between the colloidal and polymeric sol-gel method (designated as #C). The main difference between these procedures is the nature of the precursors: the colloidal one started from NbCl$_5$ and SiCl$_4$, the polymeric one from niobium pentaethoxide and tetraethyl-orthosilicate, and the procedure iii) from the same precursors as for i), but these were dissolved in a mixture of anhydrous ethanol with CCl$_4$. Cobalt was added to these catalysts during the gellation step as a solution of Co(NO$_3$)$_2$. For comparison, samples obtained via classical incipient wetness impregnation of mixed oxides prepared via the same procedures i) – iii) were synthesized as well (designated as #D). All these procedures have been exhaustively described elsewhere [11]. Samples containing 10 wt.% Co and 10 wt.% niobium oxide (expressed as Nb$_2$O$_5$) were obtained. Separately, pure niobia and silica were prepared following both the colloidal and polymeric procedures for niobia, and only the polymeric procedure for silica. The deposition of cobalt on these oxides was carried out via incipient wetness impregnation. The amount of Co was the same, i. e. 10 wt.%.

The characterization of the resulting catalysts was performed using several techniques. N$_2$ adsorption and desorption curves at 77 K were recorded using a Micromeritics ASAP 2001 apparatus. H$_2$-chemisorption measurements were carried out using a Micromeritics ASAP 2010C apparatus using a procedure we reported elsewhere [9]. The amount of metal considered in the calculation was that determined by O$_2$ titration performed in TPO conditions on catalysts reduced at 723 K, using a Micromeritics Pulse Chemisorb 2705 apparatus and a 5% O$_2$ in He gas mixture (50 ml min$^{-1}$). Typical experiments were carried out at 723 K with a ramp of 10 K min$^{-1}$. Reduced cobalt was determined assuming that at 773 K Co is converted to Co$_3$O$_4$ [26], an assumption that was confirmed by XRD and XPS analyses. H$_2$-TPR experiments were carried out with a TPD/TPR 2705 instrument, 027 Pulse Chem Sorb option (Micromeritics). Ar was preferred over nitrogen as a diluent in order to avoid the possible formation of nitrides suspected by several authors. In order to avoid the effect of the operating variables on the shape of the TPR profile and temperature of maximum reduction (TM), values of the characteristic K and P numbers between 55 and 140 s, and 20 K, respectively, were calculated according to the empirical equations of Monti and Baiker [12] and Malet and Caballero [13], namely, $K = S_o/V*C_o$ and $P = \beta K$, where $S_o$ is the amount of reducible species (in µmol), $V*$ is the total flow rate of the reducing gas mixture (in cm$^3$ (STP) s$^{-1}$), $C_o$ is the hydrogen concentration in the gas mixture (in µmol cm$^{-3}$), and $\beta$ is the heating rate (in K s$^{-1}$). All the experiments were carried out with a constant flow rate $V* = 0.79$ cm$^3$ (STP) s$^{-1}$, and hydrogen concentration $C_o = 2.05$ µmol cm$^{-3}$. H$_2$ consumption was obtained from the integrated peak area relative to the calibration curve. The TPR profiles were normalized to the amount of Co. The XPS spectra were recorded using a SSI X probe FISONS spectrometer

(SSX-100/206) with monochromated Al-Kα radiation. The spectrometer energy scale was calibrated using the Au4f$_{7/2}$ peak (binding energy 84.0 eV). For the calculation of the binding energies, the C1s peak of the C-(C,H) component of adventitious carbon at 284.8 eV was used as an internal standard. The peaks assigned to Co$_{3p}$, Nb$_{3d}$, Si$_{2p}$, and O1s levels were analysed. XRD patterns were recorded with a SIEMENS D-5000 diffractometer operated at 40kV and 50 mA and equipped with variable slit, diffracted beam monochromator and scintillation counter. The diffractograms were recorded between 2 and 80° 2θ at a scanning speed of 0.50° 2θ min$^{-1}$, using Cu-Kα radiation (l = 1.5418 Å). OH and OD groups were FTIR followed using a Brucker IFS88 instrument. Deuterium exchange measurements were carried out in a home-made apparatus. The reaction was carried out in a 70 cm$^3$ recycling reactor. The composition of H$_2$/D$_2$ before and during the reaction was monitored by gas chromatography.

The catalytic tests in butane hydrogenolysis and cracking were carried out in a quartz microreactor, at atmospheric pressure and H$_2$:butane or N$_2$:butane = 10:1 ratio. The exit of the reactor was connected on-line to a Carlo-Erba gas chromatograph. The reaction was monitored using the reactant concentration and conversion was expressed as a percentage of the total carbon fed to the reactor.

## 3. RESULTS

### 3. 1. Structure and textural characteristics

Table 1 compiles the textural characteristics (BET surface areas and pore size diameter) of the investigated catalysts. The samples denoted by B, namely using the polymeric sol-gel procedure, exhibit the higher surface areas. XRD patterns showed peaks due to Co, Co$_3$O$_4$, Nb$_2$O$_5$, CoNb$_2$O$_6$, and SiO$_2$.

### 3. 2. H$_2$-TPR

H$_2$-TPR profiles of the investigated catalysts are given in Fig. 1. These profiles show two peaks in the low temperature range due to the reduction of Co (one prominent, which may be associated with the reduction of Co$^{3+}$ to Co$^{2+}$, and an additional one, very close to the first due to the reduction of Co$^{2+}$ to Co$^0$), and a peak at high temperatures, due to the reduction of niobia. Co-SiO$_2$ prepared following the polymeric route (Fig. 1.b) exhibits only a very weak peak. This may correspond to less accessible Co caused by the formation of silica. However, XRD did not detected silicate phases. For Co-Nb$_2$O$_5$ the peaks are more evident, showing that Co is more reducible in these catalysts. The hydrogen consumed for all Co-Nb$_2$O$_5$-SiO$_2$ catalysts is much higher. The impregnated catalysts seem to be even more reducible (Fig. 1b). The advanced reduction of Co has as a direct consequence the reduction of niobia. The position of these peaks and their relative areas depend on the preparation route. The order of the reducibility is A > B > C, which corresponds to the degree of immobilization of Co in the oxide matrix.
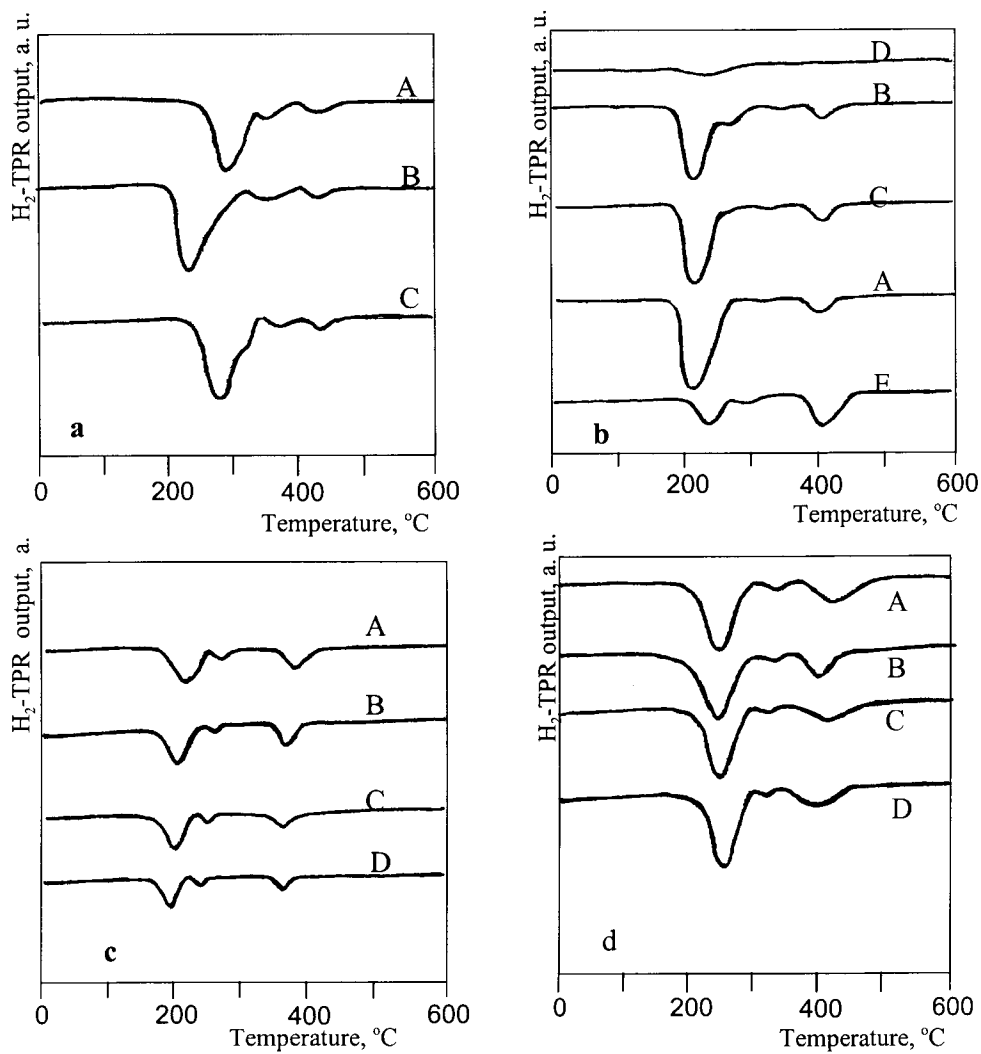
Figure 1. $H_2$-TPR profiles of the investigated catalysts: a) sol-gel prepared Co-$Nb_2O_5$-$SiO_2$ catalysts; b) A-C: Co impregnated $Nb_2O_5$-$SiO_2$ catalysts, D: Co-$SiO_2$-B, E: Co $Nb_2O_5$-B; c: physical mixtures of Co-$SiO_2$ with $Nb_2O_5$. A: A+B, B: B+A, C: B+B, D: A+A; d: physical mixtures of Co-$Nb_2O_5$ with $SiO_2$ A: A+A, B: B+A, C: A+B, D: B+B.

Physical mixtures of Co-SiO$_2$ with Nb$_2$O$_5$, and of Co-Nb$_2$O$_5$ with SiO$_2$ showed a different behavior, the first ones being more reduced. In all these samples the reduction of Co is superior to that observed for Co-SiO$_2$. The way in which the oxides were synthesized is again important. For both mixtures a more advanced reduction of niobia and Co occurs for oxides prepared by the colloidal route. H$_2$-TPR experiments carried out with successive beds of these mixtures separated by a quartz layer showed the same behavior as that of pure components.

Table 1
Textural measurements

| Catalyst | Surface area m$^2$ g$^{-1}$ | Pore size nm | Catalyst | Surface area m$^2$ g$^{-1}$ | Pore size nm |
|---|---|---|---|---|---|
| Co-Nb$_2$O$_5$-SiO$_2$-A | 96 | 2.1 | Co-SiO$_2$-C | 273 | 2.3 |
| Co-Nb$_2$O$_5$-SiO$_2$-B | 180 | 2.0 | Co-Nb$_2$O$_5$-A | 72 | 3.1 |
| Co-Nb$_2$O$_5$-SiO$_2$-C | 105 | 3.2 | Co-Nb$_2$O$_5$-B | 91 | 3.0 |
| Co-Nb$_2$O$_5$-SiO$_2$-A$^D$ | 43 | 4.6 | Co-Nb$_2$O$_5$-C | 85 | 2.9 |
| Co-Nb$_2$O$_5$-SiO$_2$-B$^D$ | 57 | 4.5 | SiO$_2$-A | 489 | 1.8 |
| Co-Nb$_2$O$_5$-SiO$_2$-C$^D$ | 48 | 4.7 | SiO$_2$-B | 568 | 1.9 |
| Co-SiO$_2$-A | 243 | 2.4 | Nb$_2$O$_5$-A | 134 | 2.5 |
| Co-SiO$_2$-B | 292 | 2.3 | Nb$_2$O$_5$-B | 168 | 2.5 |

$^D$-impregnated samples

### 3. 3. Hydrogen chemisorption

H$_2$-uptake data are given in Table 2. All the investigated samples were calcined under the same conditions. These data show differences in the H$_2$-uptake with the chemical composition and preparation procedure. Thus, Co supported on mixed oxides prepared via the polymeric sol-gel procedure, even by impregnation of these, exhibit higher H$_2$-uptake than the samples obtained via other procedures. For the other catalysts, the procedure A led to higher H$_2$-uptakes.

Table 2.
Hydrogen chemisorption and H/D exchange data

| Catalyst | H$_2$-uptake $\mu_{mole}$/g | H/D exchange 10$^8$mole HD/gs | Catalyst | H$_2$-uptake $\mu_{mole}$/g | H/D exchange 10$^8$mole HD/gs |
|---|---|---|---|---|---|
| Co-Nb$_2$O$_5$-SiO$_2$-A | 20.4 | 18.1 | Co-SiO$_2$-C | 11.8 | 6.7 |
| Co-Nb$_2$O$_5$-SiO$_2$-B | 22.6 | 14.0 | Co-Nb$_2$O$_5$-A | 13.3 | 9.4 |
| Co-Nb$_2$O$_5$-SiO$_2$-C | 18.7 | 16.2 | Co-Nb$_2$O$_5$-B | 12.5 | 7.0 |
| Co-Nb$_2$O$_5$-SiO$_2$-A$^D$ | 15.1 | 12.6 | Co-Nb$_2$O$_5$-C | 13.1 | 8.2 |
| Co-Nb$_2$O$_5$-SiO$_2$-B$^D$ | 16.9 | 13.5 | SiO$_2$-A | 0 | 0.2 |
| Co-Nb$_2$O$_5$-SiO$_2$-C$^D$ | 15.8 | 12.9 | SiO$_2$-B | 0 | 0.3 |
| Co-SiO$_2$-A | 12.1 | 7.1 | Nb$_2$O$_5$-A | 0 | 1.5 |
| Co-SiO$_2$-B | 11.7 | 6.2 | Nb$_2$O$_5$-B | 0 | 1.5 |

$^D$-impregnated samples

The low values obtained for silica may be associated to the formation of large metal agglomerates which is not unusual for this support. In addition, as it was shown from $H_2$-TPR data, these catalysts were less reducible. The values obtained for niobia, which are also low, may be theoretically assigned to a suppression of the hydrogen adsorption on Co due to a strong interaction of this with niobia. But, for temperatures at which these samples were treated, such a possibility is rather small. A suppression of the hydrogen adsorption as a consequence of a direct interaction of reduced metallic sites with the acidic OH groups in the close proximity is also less probable [14], considering the higher uptakes obtained for Co supported on mixed oxides. To explain the results obtained on these catalysts one may consider the contribution of hydrogen spillover. The mixed oxides contain very acid OH groups [9], which may facilitate at the temperatures at which these measurements were carried out, a spillover of hydrogen from cobalt to support. The acidity of these mixed oxides is higher than that of niobia. Cobalt deposition by impregnation blocks partially the acid sites of mixed silica-niobia oxides, and also leads to higher metal particles that those resulting from direct introduction in the sol-gel process.

### 3. 4. Deuterium exchange

There is much evidence that hydrogen chemisoption on cobalt is a kinetically activated process, and therefore the amount of adsorbed hydrogen can be smaller than that corresponding to one hydrogen per metal atom. On the other hand, Duprez has shown that the increase of the temperature exchange may suppress the hydrogen spillover [15]. Therefore these experiments were carried out at 370 K. In addition, both hydoxyl of silica and niobia can concur to the deuterium exchange.

Data presented in the same Table 2 show the results in the H/D exchange expressed as exchange rate. The experiments carried out with pure silica showed that the hydroxyl groups are not easily exchangeable, which is in perfect agreement with previous data [15]. Niobia showed a higher rate of H/D exchange than silica, and the preparation method had no significant effect. The deposition of cobalt improved this reaction. The comparative data on Co-SiO$_2$ and Co-Nb$_2$O$_5$ catalysts again suggest that the differences may be assigned to spillover species. Such a supposition is also sustained by the values measured for Co supported on mixed oxides. An increase of the reaction rate, nearly double, may be facilitated by very acidic OH groups of these materials

To make the contribution of spillover in this process more evident, we investigated the H/D exchange using physical mixtures of Co-Nb$_2$O$_5$ with silica, namely catalysts which showed a reduced exchange rate. Results are shown in Figure 1. The evolution of the curves representing the exchange rate in function of the composition of various physical mixtures indicates a maximum for Rm around 25, which corresponds to a composition that confers maximum acidity to this system. It is worth noting that these maximums in the exchange rates were very near to the values determined for Co supported on mixed oxides (see Table 2). Such a behavior may again recall the contribution of the acidic OH groups of niobia. They may allow an easy H/D exchange and the spillover of D species and thus the transfer to silica.

### 3. 4. Activity data

Figures 2-4 show the activity data on the investigated catalysts in structure sensitive butane hydrogenolysis at various temperatures. Cracking of butane on the same catalysts and in the same temperature conditions (reactions in nitrogen) is also presented in this figure. For both reactions, the rate exhibits a maximum in the temperature range 160 – 180 °C.
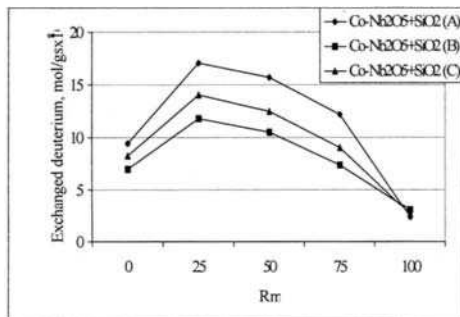
Fig. 1. Amount of deuterium exchanged as a function of composition of physical mixtures of $Co-Nb_2O_5$ and silica
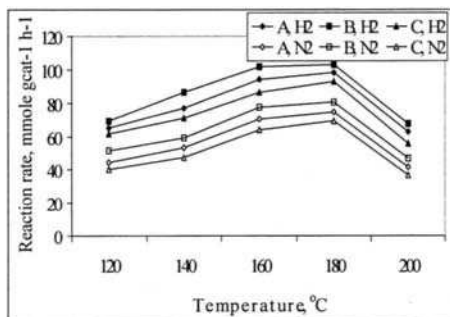
Fig. 2. Evolution of the reaction rate as a function of temperature on $Co-Nb_2O_5-SiO_2$ catalysts
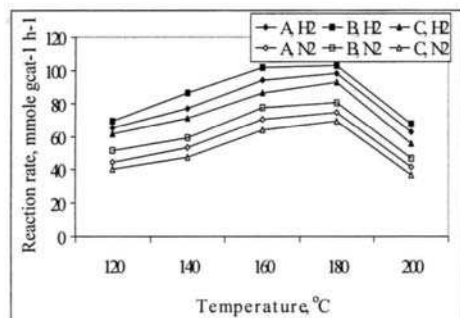


Fig. 3. Evolution of the reaction rate as a function of temperature on $Co-Nb_2O_5$ catalysts
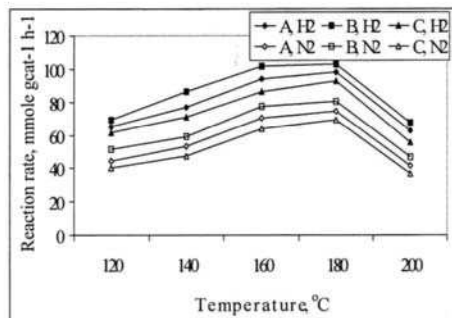
Fig. 4. Evolution of the reaction rate as a function of temperature on $Co-SiO_2$ catalysts

Figures 3-4 bring more evidence for the presence of hydrogen spillover species. The presence of hydrogen leads to an increase in the reaction rate irrespective of the catalyst used in the reaction. $Co-Nb_2O_5-SiO_2$ catalysts exhibited the highest reactivity and the activity decreased in the order $Co-Nb_2O_5-SiO_2 > Co-Nb_2O_5 > Co-SiO_2$. The preparation procedure also influenced the reaction rate. For $Co-Nb_2O_5-SiO_2$ the higher reaction rates were obtained on B, while for the other catalysts they were obtained on A.

Hydrogen spillover species also determined a scavenger effect. The decrease of the activity due to coke deposition appeared to be very inhibited. The analysis of this coke in the samples tested in hydrogen and in nitrogen for 30 min showed increased amounts for the latter.

258

## 4. DISCUSSIONS

The preparation of Co-niobia-silica catalysts following sol-gel procedures led to complex structures containing Co, $Co_3O_4$, $Nb_2O_5$, $CoNb_2O_6$, and $SiO_2$ in which both the degree of metal reduction and dispersion depended on the synthesis route. These systems may act as valuable bifunctional catalysts in hydroisomerization of high alkanes. Therefore their stability against hydrogenolysis and cracking are important characteristics.

Characterization data using $H_2$-TPR, $H_2$-chemisorption and H/D exchange led to the conclusion that hydrogen spillover exists and therefore may participate in these reactions. It can be associated to the presence of the acidic groups of the support. Mixed niobia-silica oxides led to very acidic systems which allow an increased mobility of hydrogen. Sol-gel synthesis led to a more intimate silica-niobia interaction which caused an increased density of the OH acidic groups. The direct consequence is that the results obtained on polymeric sol-gel mixed oxides indicated an increased contribution of these species. The situation is different for monocomponent oxides where the best results were obtained using samples A. On silica, the silanol groups are less acidic and therefore this effect is less evident. The contribution of the reduced niobia in these processes is still unclear. The investigation of physical mixtures of Co-$Nb_2O_5$ with $SiO_2$, or of Co-$SiO_2$ with $Nb_2O_5$, under the same experimental conditions, led to the same conclusions. Separate layers showed no indication about the existence of the hydrogen spillover species.

## 5. CONCLUSIONS

In conclusion, these studies have evidenced the presence of hydrogen spillover species using Co-$Nb_2O_5$-$SiO_2$ catalysts. H spillover species are generated on Co, where acidic OH groups exist or lead to acidic OH sites on the support.

## REFERENCES

1. K. Fujimoto and I. Nakamura, Stud. Surf. Sci. Catal., 112 (1997) 29.
2. A. M. Stumbo, P. Grange and B. Delmon, Stud. Surf. Sci. Catal., 112 (1997) 211.
3. G. M. Pajonk, Appl. Catal. B: General, 202 (2000) 157.
4. R. J. Willey, S. J. Teichner and G. M. Pajonk, J. Mol. Catal., 77 (1992) 201.
5. W. C. Corner, Jr. and J. L. Falconer, Chem. Rev., 95 (1995) 759.
6. I. Ibrahim and N. F. A. Bright, J. Am. Chem. Soc., 45 (1962) 221.
7. K. Tanabe, M. Misono, Y. Ono and H. Hattori, Stud. Surf. Sci. Catal., 51 (1989) 32.
8. V. Pârvulescu, M. Ruwet, P. Grange and V. I. Pârvulescu, J.Mol.Catal., 135 (1998) 75.
9. V. Pârvulescu, P. Grange and V. I.Pârvulescu, Catal.Today, 57 (2000) 193.
10. V. Ponec and G. C. Bond, Stud. Surf. Sci. Catal., 95 (1995) 284.
11. V. Pârvulescu, R. Crãciun, F. Tiu, S. Coman, P. Grange and V. I. Pârvulescu, Stud. Surf. Sci. Catal., 118 (1998) 691.
12. D.A. Monti, A. Baiker, J. Catal. 83 (1983) 323.
13. P. Malet, A. Caballero, J. Chem. Soc., Faraday Trans. 84 (1988) 2369.
14. W. M. H. Sachtler and A. Yu. Stakheev, Catal. Today, 12 (1992) 283.
15. D. Duprez, Stud. Surf. Sci. Catal. 112 (1997) 13.

# Effect of hydrogen spillover on toluene disproportionation and hydrogenation over HMOR-Pt/Al$_2$O$_3$

Zhu Zhirong, Chen Qinglin, Yang Deqin, Chen Wencai, Yu Gaoqin

Shanghai Research Institute of Petrochemical Technology, 1658 Pudong Beilu, Shanghai 201208, China

Besides the rapid regeneration of Bronsted acid sites through hydrogen spillover, the formation of new acidic OH groups in H$_2$ atmosphere greatly promotes the catalytic activity for toluene disproportionation over HMOR-Pt/Al$_2$O$_3$. Only under a higher reaction temperature, the acceptor sites of spilt-over hydrogen H$_s^+$, with Bronsted basicity, may convert into new acidic OH groups. On the other hand, the reaction of toluene hydrogenation, as a by-reaction, is activated by hydrogen spillover as well. Coke precursor strongly adsorbed on Bronsted/Lewis acid sites of catalysts is hydrogenated through hydrogen spillover, so that the formation of coke may be reduced.

## 1. INTRODUCTION

Mordenite (MOR) has been widely used as solid acid catalysts in practical processes of toluene disproportionation and other reactions [1~3]. Many methods have been used to improve its catalytic activity and lifetime in use, such as acid or steaming treatment, chemical vapor deposition and calcination etc. [4~7]. Additionally the introduction of transition metals is an efficient method for modifying mordenite catalysts. For example, Cu, Co or Ce – MOR was prepared by ion exchange respectively, which showed a good catalytic performance in hydroconversion process [8~11]. In the presence of hydrogen, some active metals may greatly promote the catalytic activity of mordenite as acid catalysts. Pd or Pt – HMOR was shown to have high catalystic activity and low rate of deactivation during hydrocracking and reforming of paraffins, but the mechanism of metal action was not explained during these reactions conclusively [12, 13].

The reaction of toluene disproportionation to yield benzene and xylene is catalyzed only by Bronsted acid sites of acid catalysts [14, 15]. The catalytic activity for toluene disproportionation over active metal - USY zeolite was much higher than that over USY alone in H$_2$ atmosphere, due to the effect of hydrogen spillover [16]. The similar phenomenon was also observed during 1,2,4-trimethybenzene disproportionation over Pd/Al$_2$O$_3$-HY [17]. In general, it is considered that hydrogen spillover promotes the acid catalyzed reaction, through regenerating Bronsted acid sites with the proton supply from the spilt-over hydrogen [16, 18]. On the other hand, it has also been suggested that new acidic OH groups are formed through hydrogen spillover, and greatly promote the catalytic activity for the acid catalyzed reaction, but the previous reports have not clearly explained the formation process of new acidic OH groups over Ir/NaY or CoMo/SiO$_2$-silica/aluminas [19, 20].

In this study, the effect of split-over hydrogen on toluene disproportionation and hydrogenation over HMOR-Pt/Al$_2$O$_3$ was investigated, and the formation process of new acidic OH groups through hydrogen spillover was discussed as well.

## 2. EXPERIMENTAL

0.5wt.% Pt/Al$_2$O$_3$ was prepared by impregnating$\gamma$-Al$_2$O$_3$ with an aqueous H$_2$PtCl$_6$ at the room temperature. HMOR-Al$_2$O$_3$ and HMOR-Pt/Al$_2$O$_3$ catalysts were obtained by mixing HMOR (Si/Al ratio = 20) with Pt/Al$_2$O$_3$ or Al$_2$O$_3$ physically in weight ratio of HMOR to Pt/Al$_2$O$_3$ or Al$_2$O$_3$ = 2/1. Then the above catalysts were reduced in the flow of H$_2$ at 773K for 2h. At the same time, TPR was conducted to find whether Pt over catalysts was completely reduced during the above process.

The reaction of toluene disproportionation was carried out in a fixed bed microreactor at 1.5MPa pressure and 633K, with molar ratio of H$_2$ or N$_2$ to toluene = 4/1 and WHSV 2.0h$^{-1}$. The reaction products were analyzed by on-line GC with FID and a fused silica capillary column. Benzene yield and methylcyclohexane yield were calculated respectively, with cracking products of methylcyclohexane being calculated into moles of methylcyclohexane according to carbon number. After catalysts were pretreated in situ under different conditions, IR-pyridine characterization was carried out to determine the acid property of catalysts, and IR spectrum of OH groups was conducted to investigate the change of acidic OH groups on catalysts as well. The coke formed over catalysts was characterized with both air-thermogravimetric method and C/H elemental analyzer. Besides, the amount of soluble coke in coke was determined with CH$_2$Cl$_2$ extraction method after catalysts were dissolved by HF acid according to the previous report [21].

## 3. RESULTS AND DICUSSION

### 3.1 The mode of hydrogen spillover over HMOR-Pt/Al$_2$O$_3$ and its effect on toluene disproportionation and hydrogenation

During the reaction of toluene disproportionation, the equal moles of benzene and xylene were produced, so the benzene yield may indicate the catalytic activity for toluene disproportionation. The experimental results in Figure 1 show that over HMOR-Al$_2$O$_3$, the benzene yield in H$_2$ atmosphere is nearly the same as that in N$_2$ atmosphere. With respect to HMOR-Pt/Al$_2$O$_3$, the benzene yield in H$_2$ atmosphere is much higher than that in N$_2$ atmosphere, and is also much higher than that over HMOR-Al$_2$O$_3$ in H$_2$ atmosphere. On the other hand, Pt/Al$_2$O$_3$ alone almost shows no catalytic activity for toluene disproportionation in H$_2$ or N$_2$ atomsphere.

Toluene hydrogenation, with forming methylcyclohexane and its cracking products, is a main by-reaction during toluene disproportionation. It is found in Figure 2 that in H$_2$ atmosphere, the catalytic activity for toluene hydrogenation over HMOR-Pt/Al$_2$O$_3$ is much higher than that over HMOR- Al$_2$O$_3$. Besides, Pt/Al$_2$O$_3$ alone in H$_2$ atmosphere also shows high catalytic activity for toluene hydrogenation, nearly equal to HMOR-Pt/Al$_2$O$_3$. However, in N$_2$ atmosphere, there is low catalytic activity for toluene hydrogenation over HMOR-Pt/Al$_2$O$_3$, or no catalytic activity for toluene hydrogenation over Pt/Al$_2$O$_3$ alone. Besides, HMOR-Al$_2$O$_3$ in H$_2$ atmosphere shows almost the same low catalytic activity for toluene hydrogenation as in N$_2$ atmosphere.
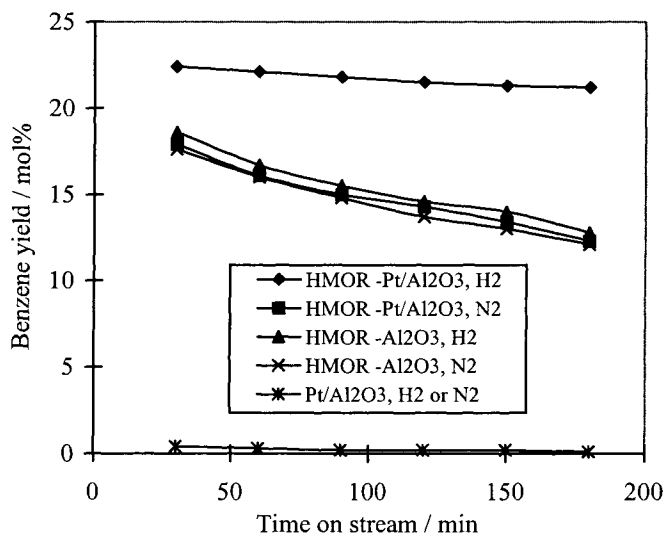
Figure 1. The catalytic activity of toluene disproportionation with time on stream over different catalysts in $H_2$ or $N_2$
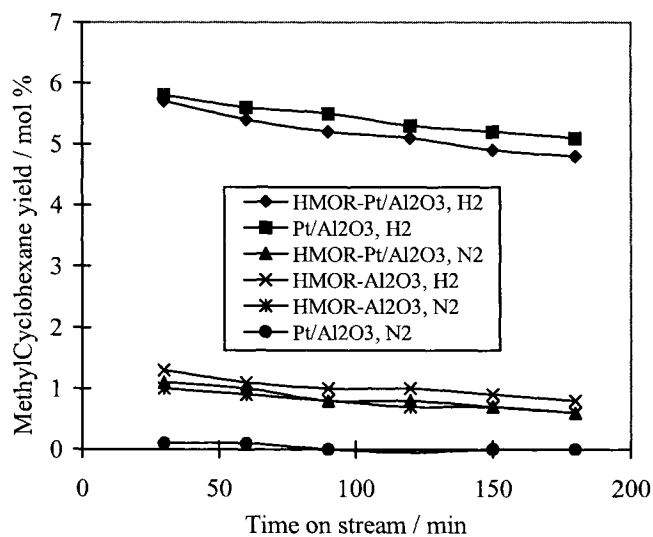


Figure 2. The catalytic activity of toluene hydrogention with time on stream over different catalysts in $H_2$ or $N_2$

The interaction between Bronsted acid sites and toluene is a necessary step during toluene disproportionation. Though the rapid regeneration of Bronsted acid sites through hydrogen spillover is a possible factor to promote the catalytic activity for toluene disproportionation, IR spectrum of OH groups in Figure 3 shows that in $H_2$ atomsphere at 633K, the number of 3590-3610 $cm^{-1}$ OH groups over HMOR-Pt/$Al_2O_3$, corresponding to Bronsted acid sites, is almost twice more than that over HMOR-$Al_2O_3$. Besides, compared to HMOR-$Al_2O_3$, the frequency of acidic OH groups over HMOR-Pt/$Al_2O_3$ decreases, which indicates that the strength of Bronsted acid sites increases. Consequently IR-pyridine characterization of catalysts in Table 1 also shows that the number of Brosted acid sites over HMOR-Pt/$Al_2O_3$ is nearly twice more than that over HMOR-$Al_2O_3$, and the strength of Bronsted acid sites increases as well. However, there is no similar phenomenon mentioned above over Pt/$Al_2O_3$ alone, with Lewis acid sites alone and no Bronsted acid sites in $H_2$ atomsphere.

Therefore, taking into account both authors' suggestion and catalysts used in the previous reports [19, 20, 22], it may be considered that new acidic OH groups are formed only over supports with Bronsted acid/base sites through hydrogen spillover. According to the theory on Bronsted acid-base pair [23], the $H_s^+$ acceptor sites with Bronsted basicity over HMOR-Pt/$Al_2O_3$, which may be produced by induction of their neigbour Bronsted acid sites, may convert into new acidic OH groups through combining with spilt-over hydrogen $H_s^+$.
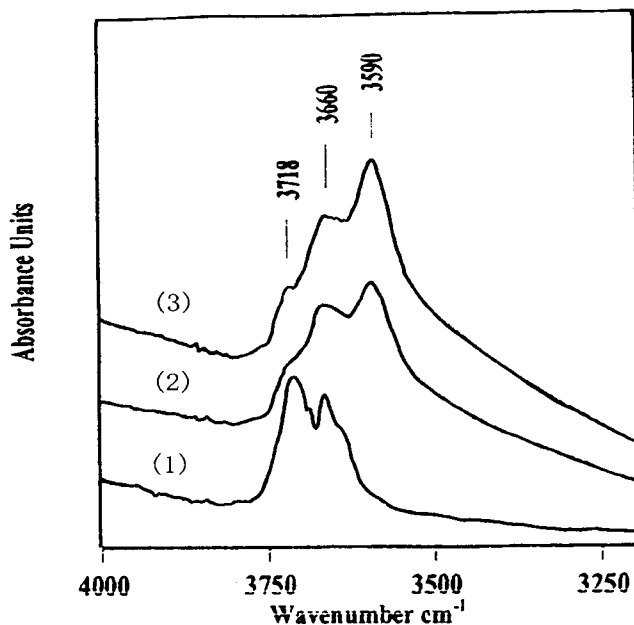


Figure 3. IR spectrum of OH Groups of different catalysts at 633K and in $H_2$
(1): Pt/$Al_2O_3$, (2): HMOR-$Al_2O_3$, (3): HMOR-Pt/$Al_2O_3$

Table 1
Bronsted acid sites and Lewis acid sites of different catalysts in $H_2$

| Catalyst | Bronsted acid sites | | Lewis acid sites | |
|---|---|---|---|---|
| | 473K | 673K | 473K | 673K |
| HMOR-Pt/Al$_2$O$_3$ | 11.8 | 6.9 | 5.4 | 2.8 |
| HMOR-Al$_2$O$_3$ | 6.4 | 2.7 | 6.0 | 3.1 |
| Pt/Al$_2$O$_3$ | 0.0 | 0.0 | 13.2 | 3.8 |

Note: Bronsted / Lewis acid was determined, after catalysts were pretreated in the flow of $H_2$ at 633K for 2 h. The number of Bronsted / Lewis acid sites was calculated in the relative unit.

Based on both the experimental results and the previous reports [16, 23], the mode of hydrogen spillover over HMOR-Pt/Al$_2$O$_3$ during toluene disproportionation and hydrogenation may be considered as following:
(1) Gas phase $H_2$ is dissociated into H atom ($H_s$ ) on Pt, and the charge transformation between Pt and $H_s$ takes place as well : $H_2 \rightarrow H_s + H_s$ , $H_s + Pt \rightarrow H_s^+ + Pt^-$.
(2) H atom or $H_s^+$ migrates onto Al$_2$O$_3$ or further onto HMOR. Then the following actions take place: $H_s^+ + HO-$ ( Bronsted acid sites ) $\rightarrow$ $H_sO- + H^+$ (the exchange of portons at Bronsted acid sites), $H_s^+ + O^-$ (acceptor sites with Bronsted basicity ) $\rightarrow$ $H_sO-$ (the formation of new acidic OH groups), $H_s + C_6H_6-CH_3 \rightarrow C_6H_{11}-CH_3$ (toluene hydrogenation on Bronsted/Lewis acid sites).

### 3. 2 The effect of reaction temperature on the formation of new acidic OH groups

The influence of temperature on the reactions of toluene disproportionation and hydrogenation in $H_2$ atmosphere, shown in Figure 4, indicates that with decreasing reaction temperature within 673K~523K, benzene yield over HMOR-Pt/Al$_2$O$_3$ decreases rapidly, but methylcyclohexane yield decreases very slowly. As a result, HMOR-Pt/Al$_2$O$_3$ still shows high catalytic activity for toluene hydrogenation, nearly without the catalytic activity for toluene disproportionation at reaction temperature of 523K. At the same time, it is seen that the difference of the catalytic activity for toluene disproportionation between HMOR-Pt/Al$_2$O$_3$ and HMOR-Al$_2$O$_3$, appears more and more obvious with increasing reaction temperature, when reaction temperature is higher than 583K. On the other hand, the catalytic activity for toluene hydrogenation over HMOR-Al$_2$O$_3$ increases gradually with increasing reaction temperature though it is much lower than that over HMOR-Pt/Al$_2$O$_3$. From above experimental phenomenon, it is found that the effect of hydrogen spillover on toluene disproportionation is certain to relate to reaction temperature, but the promote of hydrogen spillover on toluene hydrogenation is less influenced by reaction temperature in this temperature range.

Pyridine – IR characterization in Figure 5 shows that the number of Bronsted acid sites over HMOR-Pt/Al$_2$O$_3$ decreases with decreasing temperature in $H_2$ atmosphere, which is in agreement with the reported phenomenon [19]. Therefore, it may be considered that the formation of new acidic OH groups needs higher temperature than that of spilt-over hydrogen species. Only under a higher reaction temperature, the acceptor sites of $H_s^+$, with Bronsted basicity, may convert into new acidic OH groups.
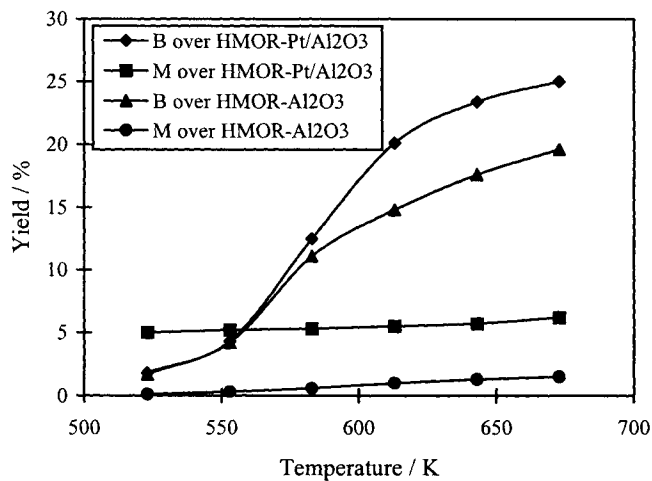
Figure 4. The catalystic activity of toluene disproportionation and hydrogenation over catalysts at different reaction temperatures in $H_2$
Note: B indicates benzene yield; M indicates methylcyclohexane yield.
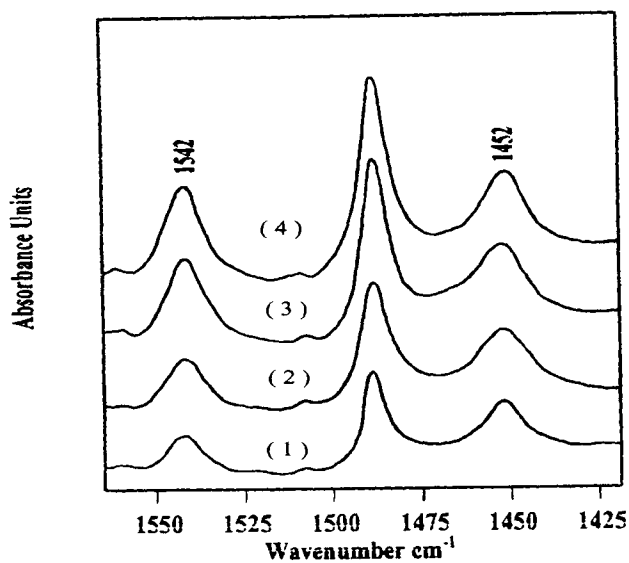


Figure 5. Pyridine-IR spectrum of HMOR-Pt/Al$_2$O$_3$ at different temperature in $H_2$
Note: After pretreated in $H_2$ for 2h at the temperature of (1): 523K, (2): 573K, (3): 623K, (4):673K respectively, Pyridine-IR spectrum of HMOR-Pt/Al$_2$O$_3$ was determined at 473K.

### 3.3 The effect of hydrogen spillover on coking rate and deactivating rate

The experimental results in Figure 6, show that coking rate over HMOR-Pt/Al$_2$O$_3$ is smaller than that over HMOR-Al$_2$O$_3$ during toluene disproportionation in H$_2$ atmosphere. As a result, the deactivating rate over HMOR-Pt/Al$_2$O$_3$ is also smaller than that over HMOR-Al$_2$O$_3$, as seen in Figure 1. Based on the analytic results of reaction products in Table 2, the amount of by–products with polyaromatics over HMOR-Pt/Al$_2$O$_3$, such as naphthalene and its derivates etc., is much less than that over HMOR-Al$_2$O$_3$, which is not easy to desorbed into gas phase and possibly changes into coke further.

It may be considered that coke precursor strongly absorbed on Bronsted/Lewis acid sites of catalysts, i.e., by-products with higher C/H ratio, is hydrogenated through hydrogen spillover, then desorbed into gas phase, so that the formation of coke may be resisted. The experimental results, shown in Figure 6, indicate that coke formed over HMOR-Pt/Al$_2$O$_3$ is of higher ratio of soluble coke in coke than that over HMOR-Al$_2$O$_3$. Besides, the elemental analysis shows that coke over HMOR-Pt/Al$_2$O$_3$ is of lower C/H ratio than that over HMOR-Al$_2$O$_3$. Soluble coke may convert into insoluble coke with higher C/H ratio through further dehydrogenation and condensation. It is because hydrogenation of coke is promoted by hydrogen spillover that the convert from soluble coke to insoluble coke may be reduced validly as well.

Table 2
Composition of reaction products over different catalysts in H$_2$ ( wt.% )

| Catalyst | alkane | Benzene | Toluene | Xylene | trimethyl–benzene | Tetramethyl-benzene | Alkyl-naphthalene |
|---|---|---|---|---|---|---|---|
| HMOR-Pt/Al$_2$O$_3$ | 5.8 | 23.6 | 46.0 | 21.4 | 2.4 | 0.8 | 0.05 |
| HMOR-Al$_2$O$_3$ | 1.3 | 16.9 | 63.9 | 15.3 | 1.8 | 0.6 | 0.24 |
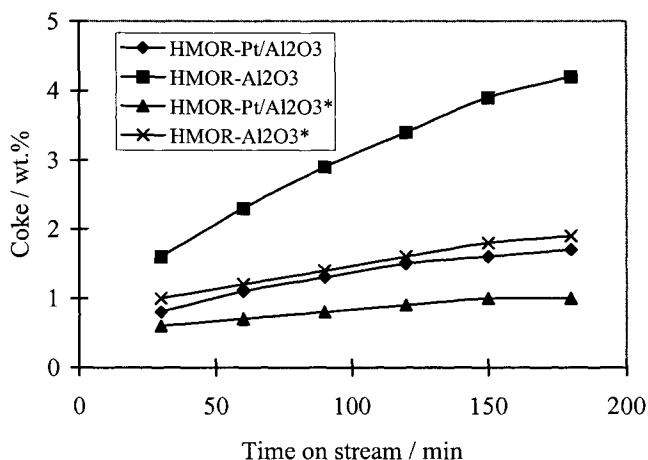


Figure 6. Coke and soluble coke with time on stream over different catalysts in H$_2$
Note: * indicates the amount of soluble coke in coke.

## ACKNOWLEDGMENTS

## REFERENCES

1. Y. Sugi and M. Toba, Catal.Today, 19(1994)187.
2. H. R. Ineland, C. Redini, A. S. Raff and L. Fava, Hydrocarbon Process, 58(1979)119.
3. H. G. Karge and J. Weitkamp, J. Chem. Ing. Tech. 58(1986)946.
4. R. W. Weber, K. P. Moller and C. T. O' Connor, Micropor. Mesopor. Mater., 35-36(2000)533.
5. F. Goovaerts, E. F. Vansant, J. Phillippaerts, P. Dehulsters and J. Gelan, J. Chem. Soc. Faraday Trans., 85 (1989) 3675.
6. L. Bertea, H. W. Kouwenhoven and R. Prins, Appl. Catal. A, 129 (1995) 229.
7. C. Mirodatos and D. Barthomeuf, J. Chem. Soc., Chem. Commun., 134 (1981) 39.
8. Y. Hong and J. J. Fripiat, Microporous Mater., 4 (1995) 323.
9. E. E. Miro, G. Imoberdorf, J. Vassallo and J. O. Petunchi, Appl. Catal. B, 22(1999)305.
10. D. Mravee, M. Michvocik and M. Hronee, Petro. Coal, 39(1997)27.
11. J. Patrick Carl and C. Sarak Larsen, J. Phs. Chem. B, 104(1999)6568.
12. C. Rhodes and G. J. Hutchings, J. Chem. Soc., Faraday Discuss., 93(1997)3593.
13. A. Martucci, G. Cruciani, A. Alberti, C. Ritter, P. Ciambelli and M. Rapacciuolo, Micropor. Mesopor. Mater., 35-36(2000)405.
14. W. W. Kaeding, C. Chu, L. B. Yong and S. A. Butter, J. Catal., 69(1981)392.
15. P. A. Jacobs, H. E. Leeman and J. B. Uytterhoeven, J. Catal., 33(1974)31.
16. M. G. Yang, I. Nakamura and K. Fujimoto, Appl. Catal. A, 127(1995)115.
17. T. Matsuda, T. Fuse and E. kikuchi, J. Catal., 106(1987)38.
18. J. Stephan, C. G. Khuan and Z. Ping, Stud. Surf. Sci. Catal., 121(1999)165.
19. F. S. Xiao and B. C. Gates, Stud. Surf. Sci. Catal., 112(1997)93.
20. A. M. Stumbo, P. Grange and B. Delmon, Catal. Letter, 31(1995)173.
21. S. M. Holmes, A. Garforth, B. Maunders and J. Dwyer, Appl. Catal. A, 151(1997)355.
22. T. Tanaka, K. Ebitani, H. Hattori and S. Yoshida, Stud. Surf. Sci. Catal., 77(1993)205.
23. A. Gutsze, U. Roland and F. roessner, Stud. Surf. Sci. Catal., 112(1997)417.

# Study on reactions between $H_2$ and $NO_x$ over noble metal-loaded $NO_x$-adsorbing metal oxides

M.Machida, D.Kurogi, and T.Kijima

Department of Applied Chemistry, Faculty of Engineering, Miyazaki University
1-1 Gakuenkibanadai Nishi, Miyazaki 889-2192, Japan

The reactivity of $NO_x$ adsorbed onto $MnO_x$-$CeO_2$ toward $H_2$ was studied in the presence of impregnated noble catalysts (1wt%Pd, Pt, and Ru) by the use of micropulse reactions and *in situ* DRIFT spectroscopy. The $NO_x$ adsorbability of the Pd-loaded catalyst after the saturation of NO uptake at 150 °C could be largely regenerated by micropulse $H_2$ injections, which ensure the reduction of $NO_x$ adsorbed on $MnO_x$-$CeO_2$ into $N_2$. Nitrite ($NO_2^-$) species were preferentially reacted with hydrogen at the boundary between Pd and the $NO_x$ adsorbing metal oxide.

## 1. INTRODUCTION

Sorptive removal has been applied to $NO_x$ control in the presence of excess $O_2$ [1,2]. Several researchers have already studied the $NO_x$ sorbing materials based on alkaline solids, metal oxides, and microporous materials. Regeneration of the $NO_x$-sorbents in such systems can be achieved simply by heating to liberated $NO_x$ and thus, sorption/desorption can be repeated by applying temperature-swing cycles[1-3]. In preceding papers[4,5], we reported sorption/ desorption properties of $NO_x$ over $MnO_x$-$CeO_2$ solid solutions with the fluorite-type structure. The oxides are useful as not only a $NO_x$ adsorbent, but also a support material that allows Pd to catalyze NO-$H_2$ reactions in the presence of excess $O_2$. Despite the nonselective character of Pd catalysts toward $NO_x$-$H_2$ reaction, Pd/$MnO_x$-$CeO_2$ attained 65% NO-conversion of a stream of 0.08%NO, 2%$H_2$, and 6%$O_2$ in He at a low temperature of 150 °C, compared to ca.30% for Pd/$\gamma$-$Al_2O_3$, the reaction on which was more suppressed by competitive $H_2$-$O_2$ reaction. The combination of $NO_x$ sorbability of $MnO_x$-$CeO_2$ and $H_2$ activation of Pd catalysts was found to give rise to a synergistic effect, thus paving the way to development of $NO_x$-sorbing catalysts for selective de$NO_x$ processes at low temperatures (<150 °C).

On the steady state NO-$H_2$-$O_2$ reaction over Pd/$MnO_x$-$CeO_2$, NO should be oxidatively adsorbed onto the binary oxide, whereas $H_2$ is activated on the surface of Pd and is partly consumed by $O_2$. The selective reduction is therefore dependent on the interaction between hydrogen and $NO_x$ adsorbed near the Pd/$MnO_x$-$CeO_2$ boundary. The aim of the present study is to obtain information of this type of $NO_x$-$H_2$ interaction by the use of micropulse injection method and *in situ* DRIFT spectroscopy.

## 2. EXPERIMENTAL

### 2.1. Preparation of catalysts

The equimolar binary oxide, $MnO_x$-$CeO_2$, was prepared by coprecipitation from aqueous solutions of nitrates. Calculated amounts of $Mn(NO_3)_2 \cdot 6H_2O$ and $Ce(NO_3)_3 \cdot 6H_2O$ (Wako Chemicals, Guaranteed reagent grade) were dissolved in distilled water. Addition of aqueous ammonia solution dropwise to the solution produced precipitates, which were evaporated to dryness and subsequently calcined at 450 °C for 5 h in air. An aqueous solution of $Pd(NO_3)_2$, $H_2PtCl_6$ and $RuCl_3$ was impregnated onto as prepared oxides and calcined at 450 °C for 5 h to metal-loaded samples (1.0 wt% loading). As prepared powder samples were pressed and crushed into 20 mesh granules before use.

### 2.2. $H_2$ micropulse injection during $NO_x$ adsorption

The reactivity of sorbed $NO_x$ to $H_2$ was also evaluated in pulse mode reactions. After reduction in $5\%H_2$/He at 400 °C, the sample (0.2 g) was placed in a stream of $NO_x$ (0.08% NO, 0-10%$O_2$ balanced with He, W/F=0.24 s·g/cm$^3$) at 150 °C. After the effluent $NO_x$ increased toward the saturation of adsorption, 1 cm$^3$ of $H_2$ was injected into the stream just before the catalyst bed every 10-20 min. $NO_x$ ($NO/NO_2$) and other gas species in the effluent were monitored by using a chemiluminescence $NO_x$ analyzer (Shimadzu NOA-305) and a mass spectrometer, respectively.

### 2.3. *in situ* DRIFTS

DRIFT spectra of $NO_x$ species adsorbed on the sample were measured by the use of temperature-controllable diffuse reflectance reaction cell connected to a gas flow system and a vacuum line. The sample was first outgassed in a stream of $5\%H_2$/He at 400 °C for 1 h and then exposed to the reaction gases containing $0.04\%NO$, $2\%O_2$, and He balance at 150 °C for 30 min. This was followed by treatment at 150 °C for 30 min in flowing 0.25-1.0%$H_2$, 2%$O_2$/ He and, subsequently, second $NO_x$ adsorption at 150 °C. After each treatment spectra were recorded in a flowing He at 150 °C.

## 3. RESULTS AND DISCUSSION

### 3.1. Structure and $NO_x$ uptake of $MnO_x$-$CeO_2$

The XRD pattern of as prepared equimolar binary oxide, $MnO_x$-$CeO_2$ (BET surface area: 64 m$^2$/g), shows the formation of the cubic fluorite-type solid solution with the surface atomic ratio of Mn/Ce=1.0. The calculated lattice parameter, 0,532 nm, was slightly less than that of $CeO_2$ (0.541 nm). The decrease of the lattice parameter is associated with the small ionic radius of $Mn^{3+}$ (0.66 nm) compared to $Ce^{4+}$ (0.94 nm) [6]. Generally, the formation of substitutional

Table 1 Properties of $MnO_x$-$CeO_2$

| BET surface area | 64 m$^2 \cdot$g$^{-1}$ |
|---|---|
| $NO_x$ uptake[a] | 0.10 mmol·g$^{-1}$ |
| $NO_x$ uptake[b] | 0.95 molecule·nm$^{-2}$ |
| $Ce_s$[c] | 3.25 nm$^{-2}$ |
| $(Mn/Ce)_s$[d] | 1.0 |
| $(NO_x/Ce)_s$[e] | 0.3 |

a) Determined from a breakthrough curve at 150 °C, 0.08%NO, 10%$O_2$/He.
b) ($NO_x$ uptake)/surface area.
c) Average on (100), (110), and (111) surfaces.
d) Determined by XPS analysis
e) ($NO_x$ uptake)/$Ce_s$.

solid solution is not favorable for the system having such a large difference of ionic radius. Nevertheless, the replacement of $Ce^{4+}$ by $Mn^{3+}$ in the fluorite structure seems to be possible when considering their structural similarity; the crystal structure of $Mn_2O_3$ is the C-rare earth type that is basically composed of anion-deficient units of fluorite structure [7]. As in the case of unloaded samples, $1wt\%Pd/MnO_x\text{-}CeO_2$ exhibited broad XRD peaks ascribable only to fluorite, but peaks corresponding to Pd phases were too weak to be observed because of the small amount and low crystallinity.

The NO adsorption property of the present system is briefly described for the latter discussion. As was reported previously[4,5], the formation of $MnO_x\text{-}CeO_2$ solid solution is significantly effective in oxidative adsorption of NO at <200 °C. Table 1 summarized the NO adsorbing properties. From the maximum $NO_x$ uptake at 150 °C, we could estimate that ca.30% of Ce ions exposed to the surface are occupied by $NO_x$. The coverage increases at decreasing temperatures, exceeding 50% at 30 °C. Such high surface coverage is due to not only the high oxidation activity of Mn and but also the moderate basicity of Ce. Impregnating Pd catalysts increased the NO uptake (ca.30%), because the NO oxidation is further accelerated in the presence of $O_2$. Because of the low loading (1wt%), however, NO adsorbed onto Pd should be far less than that onto $MnO_x\text{-}CeO_2$. Assuming monolayer chemisorption of NO on to Pd hemisphere with the radius of 2nm, the NO uptake should be less than 10%, compared to $MnO_x\text{-}CeO_2$.

## 3.2. Reactivity of adsorbed $NO_x$ to $H_2$

The reactivity of the $NO_x$ adsorbed on $MnO_x\text{-}CeO_2$ toward $H_2$ was evaluated by the method of micropulse injection of $H_2$. In this measurement, $1wt\%Pd/MnO_x\text{-}CeO_2$ was placed in a flowing gas mixture (0.08%NO, 0-10%$O_2$, and He balance) at 150 °C with monitoring $NO_x$ concentration in the reactor effluent as shown in Fig.1. On approaching the saturation of adsorption, the injection of 1 cm$^3$ of $H_2$ into the gas feed was repeated (shown as arrows in the figure). In
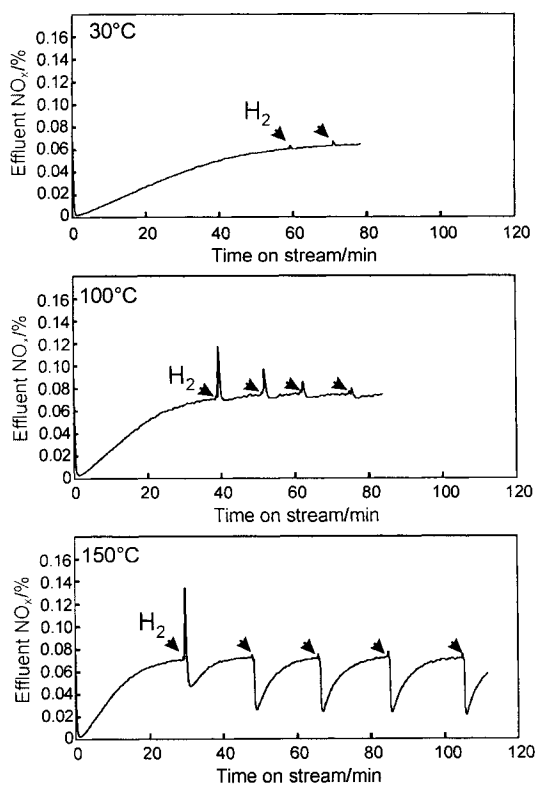


Fig. 1. Effect of $H_2$ pulses on the effluent $NO_x$ from $1wt\%Pd/MnO_x\text{-}CeO_2$ at 30 °C, 100 °C, and 150 °C. Each $H_2$ pulse was 1.0 cm$^3$, Gas feed: 0.08%NO, 2%$O_2$, He balance, W/F=0.24 g·s/cm$^3$.

all case in Fig.1, the incremental concentration from the beginning of the reaction corresponds to a breakthrough curve of $NO_x$ adsorption. The sorptive $NO_x$ removal at 30 °C lasted over 60 min without being affected by $H_2$ pulses. At 100 °C, the $H_2$ pulse immediately generated sharp but small evolutions of $NO_x$. The oxidation of $H_2$ over Pd would create a local exotherm and the resulting temperature rise would promote desorption of $NO_x$ species adsorbed thereon. However, the desorption peak decreased in intensity with repeating $H_2$ pulse injections. The most remarkable response was observed at 150 °C, i.e., the first injection of $1 cm^3$ $H_2$ immediately gave a sharp $NO_x$-desorption followed by a steep drop of the $NO_x$ concentration, accompanied by the evolution of $N_2$ as evident from parallel mass spectra measurement. The $NO_x$ concentration was then increased slowly again as was observed before the first $H_2$ pulse. Here, we define the adsorptive $NO_x$ uptake after each $H_2$ pulse as the regenerative capacity.

Figure 2 shows the regenerative capacity of $NO_x$ for each $H_2$ pulses at various $O_2$ concentrations (0, 2, and 10%) in the gas feed. Note that regenerative capacity becomes largest in the absence of $O_2$, which corresponds to ca.0.1



Fig. 2. Initial $NO_x$ uptake and regenerative capacity for 1wt%Pd/$MnO_x$-$CeO_2$ at 150 °C. $H_2$ pulse size: 1.0 $cm^3$ (0.22 mmol/g), Gas feed: 0.08%NO, 0-10%$O_2$/He, W/F=0.24 g·s/$cm^3$.

mmol/g. This is about 40 fold for the amount of monolayer chemisorption of NO onto Pd hemispheres with the radius of 2 nm. Assuming the stoichiometric reaction, $2NO_2+4H_2 = N_2+4H_2O$, the regenerative capacity corresponds to ca. 90% selectivity of $H_2$ in every injection to the reduction of $NO_x$ stored. Thus, a large part of $H_2$ injected was consumed to reduce $NO_x$ adsorbates on $MnO_x$-$CeO_2$. The regenerative capacity decreased with increasing $O_2$ concentration in the gas feed, suggesting that an incremental part of $H_2$ injected was reacted with $O_2$ to produce $H_2O$. However, it was still larger than 0.01mmol/g at 10%$O_2$, which is larger than the maximum NO uptake onto Pd. Thus, the hydrogen activated on the Pd catalyst could be utilized to reduce $NO_x$ adsorbates on $MnO_x$-$CeO_2$ even in the presence of excess $O_2$.

The $H_2$ pulse injection during $NO_x$ adsorption was also applied to unloaded $MnO_x$-$CeO_2$ as shown in Fig.3. The $NO_x$ breakthrough curve in this case was not influenced by the repeated injection of $H_2$ pulses, reaching toward saturation after ca.40 min reaction time without detectable drop of effluent $NO_x$ concentration. The reaction was also negligible in the absence of $O_2$ in the gas feed. This means that a catalyst to activate $H_2$ is indispensable for the reduction of $NO_x$ adsorbed on $MnO_x$-$CeO_2$.

We have also employed other noble metals, Pt and Ru, which are potential catalysts for the activation of $H_2$ at low temperatures (Fig. 4). Nevertheless, the adsorptive $NO_x$ removal in these cases were very small compared to the Pd-loaded sample. This is due to residual chloride

Fig. 3. Effect of $H_2$ pulses on the effluent $NO_x$ from unloaded $MnO_x$-$CeO_2$ at 150 °C. Each $H_2$ pulse was 1.0 cm³, Gas feed: 0.08%NO, 2%$O_2$, He balance, W/F=0.24 g·s/cm³.

ions originated from metal chloride precursors, which would be strongly bonded to the surface site for $NO_x$ adsorption. Therefore, the regenerative capacity of $NO_x$ adsorption for each $H_2$ pulse could not be clearly confirmed.

### 3.3. *in situ* DRIFTS study

*in situ* DRIFTS measurement was applied to clarify the structure of $NO_x$ adsorbates on the surface of $MnO_x$-$CeO_2$. Figure 5 shows one typical spectrum of $MnO_x$-$CeO_2$ taken after NO the uptake at 150 °C. The spectrum was characterized by strong bands at 1550, 1450, 1375, 1300, and 1035 cm$^{-1}$, which can be assigned to bidentate and unidentate nitrates ($NO_3^-$). It also includes a band of chelating nitrite ($NO_2^-$) at 1210 cm$^{-1}$. These assignments are almost consistent with those reported previously [8-12]. The intensity of these bands changed strongly depending upon the oxide composition (Mn/Ce), reaction temperature, and $O_2$ concentration in the gas feed[13]. The nitrite species were mainly produced at low $O_2$ concentration or at ambient temperature, whereas nitrate species became dominant with an increase of $O_2$ as well as temperature. Manganese in the lattice plays key role in oxidative adsorption of NO to $NO_2^-$ and then to $NO_3^-$.
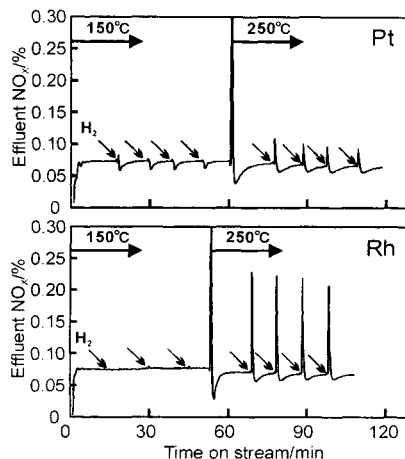


Fig. 4. Effect of $H_2$ pulses on the effluent $NO_x$ from 1wt%Pt- and Rh-loaded $MnO_x$-$CeO_2$. Each $H_2$ pulse was 1.0 cm³, Gas feed: 0.08%NO, 2%$O_2$, He balance, W/F=0.24 g·s/cm³.
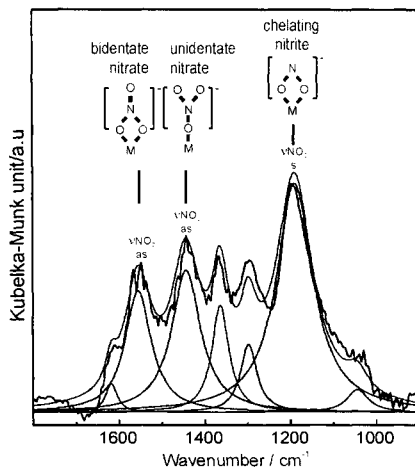


Fig.5. Assigned DRIFTS bands for NO adsorbed on $MnO_x$-$CeO_2$ at 150 °C. 0.04%NO/He for 30 min.

272
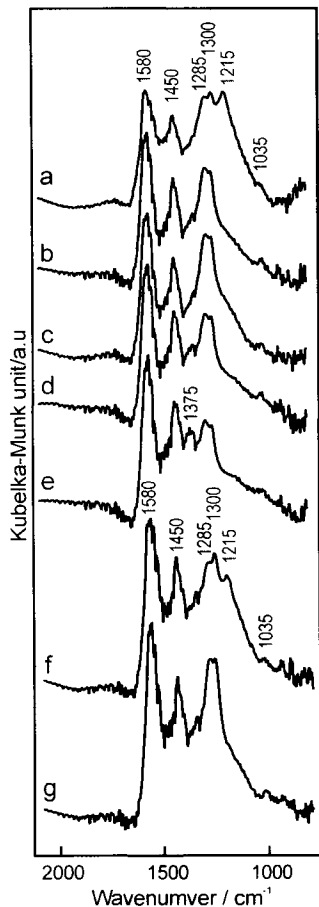


Fig. 6. *in situ* DRIFT spectra of 1wt%Pd/MnO$_x$-CeO$_2$ at 150 °C after exposing successively to a) 0.04%NO, 2%O$_2$/He, 30 min, b) 1%H$_2$/He, 5 min, c) 10 min, d) 20 min, e) 60 min, f) 0.04%NO, 2%O$_2$/He, 30 min, g) 0.25%H$_2$, 2%O$_2$/He, 10 min.
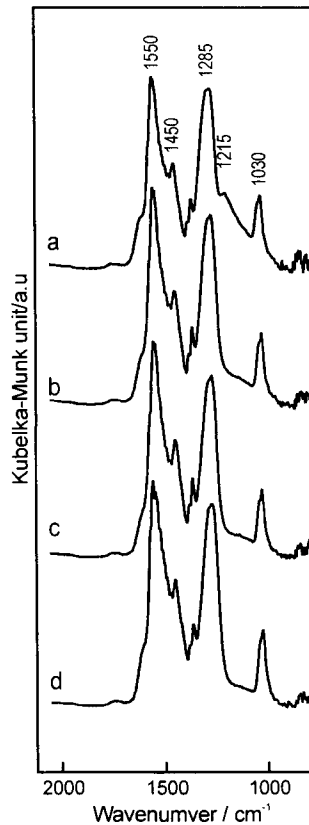
Fig. 7. *in situ* DRIFT spectra of MnO$_x$-CeO$_2$ at 150 °C after exposing successively to a) 0.04%NO, 2%O$_2$/He, 30 min, b) 1%H$_2$/He, 5 min, c) 10 min, d) 0.04%NO, 2%O$_2$/He, 30 min.

Figure 6 exhibits the spectral change of Pd/MnO$_x$-CeO$_2$ after NO uptake and subsequent exposure to a flowing mixture of 1%H$_2$/He at 150 °C. First, the nitrite band at 1210 cm$^{-1}$ disappeared after 5 min leaving strong bands of unidentate and bidentate nitrates (b). This was followed by very slow decrease of intensity of the band at 1285-1300 cm$^{-1}$ (c-e). The band of nitrite were reversibly restored after subsequent exposure to a stream of NO$_x$ mixtures (0.04% NO and 2%O$_2$/He) at 150 °C (f). Since this band could not be observed for other Pd-loaded

catalysts such as $Pd/Al_2O_3$, it should be attributed to nitrite species bound to the surface of $MnO_x$-$CeO_2$. These results suggest that the nitrite species on $MnO_x$-$CeO_2$ can be reduced by $H_2$ in the presence of Pd catalysts. Since the reduction also took place in the presence of excess $O_2$ (0.25%$H_2$, 2%$O_2$/He) (g), the reaction would proceed with a higher selectivity. During these reactions, the nitrate bands were negligibly affected by $H_2$, supporting the lower reactivity toward $H_2$. Indeed, more $H_2$ (ca.10% in He) was required to weaken the nitrate bands even in the absence of $O_2$ [5].



Fig. 8. A possible model for reaction between $H_2$ and $NO_x$ adsorbates at the $Pd/MnO_x$-$CeO_2$ boundary.

Figure 7 shows the spectra taken after $NO_x$ uptake onto unloaded $MnO_x$-$CeO_2$ and subsequent exposure to $H_2$. The spectrum of the NO-adsorbed sample was very similar to those for the Pd-loaded sample (Fig. 6) with an exception of very weak band at 1215 cm$^{-1}$. This is roughly consistent with that NO is mainly adsorbed onto the surface of $MnO_x$-$CeO_2$. Introducing 1%$H_2$/He removed the nitrite band without affecting other bands (b,c). Unlike the Pd-loaded catalyst (Fig. 6), however, the band was not restored by the subsequent exposure to 0.04%NO, 10%$O_2$/He (d).

Taking these results into consideration, a possible model for the $NO_x$-$H_2$ reaction can be illustrated as shown in Fig.8. The large regenerative capacity observed in the pulse reactions (Fig.2) cannot be explained by simple reactions over Pd catalyst. We have to consider the significant reactions between hydrogen and large amounts of $NO_x$ adsorbates stored on the surface of $MnO_x$-$CeO_2$, which require the assistance by the Pd catalyst. According to Table 1, the $(NO_x/Ce)_s$ ratio was more than 0.3, depending upon the $O_2$ concentration, i.e., the surface of $MnO_x$-$CeO_2$ was largely covered by $NO_2^-$ or $NO_3^-$. Since $H_2$ cannot be activated on $MnO_x$-$CeO_2$ at low temperatures, the reaction would take place in the vicinity of the boundary with Pd, where both hydrogen and $NO_x$ must be abundant. The $NO_x$-abundant surface near the Pd/$MnO_x$-$CeO_2$ boundary, so-called perimeter sites, may be effective in increasing the probability of reactions with hydrogen supplied from Pd catalysts. This supports data on the pulse reactions and DRIFTS results, indicating that the combination of two components, Pd and $MnO_x$-$CeO_2$, are essential to ensure the reaction between hydrogen and $NO_x$ adsorbates. Provided the $H_2$-$NO_x$ reaction takes place at the perimeter sites, the activity and selectivity will be affected by the $O_2$ partial pressure; more oxygen will cause competitive $H_2$-$O_2$ reactions on Pd as well as conversion of $NO_2^-$ to $NO_3^-$ with a less reactivity toward hydrogen.

## ACKNOWLEDGMENTS

274
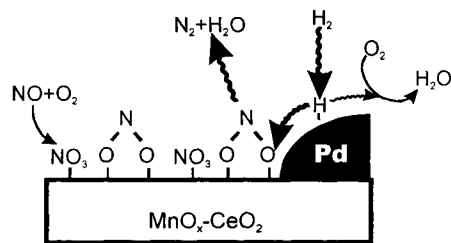
## REFERENCES

1.  M.Machida, in *Catalysis,* Vol.15, The Royal Society of Chemistry, Cambridge, 2000, p.73.
2.  H.Arai and M.Machida, *Catal. Today,* 22 (1994) 97.
3.  M.Machida, A.Yoshii and T.Kijima, *Int. J. Inorg. Mater.,* 2 (2000) 413.
4.  M.Machida, D.Kurogi and T.Kijima, *Chem. Mater.,* 12 (2000) 3158.
5.  M.Machida, D.Kurogi and T.Kijima, *Chem. Mater.,* 12 (2000) 3165.
6.  *CRC Handbook of Chemistry and Physics, 72nd ed.;* D.R.Lide, Ed. CRC Press, Boston, 1991.
7.  F.G.Galasso, *Structure and Properties of Inorganic Solids*, Pergamon, Oxford, 1970, p.115.
8.  K.Nakamoto, *Infrared and Raman Spectra of Inorganic and Coordination Compounds, 4th ed.;*Wiley, New York, 1986.
9.  B.Klingenberg and M.A.Vannice, *Appl. Catal., B: Environ.,* 21 (1999) 19.
10. S.J.Huang, A.B.Walters and M.A.Vannice, *Appl. Catal., B: Environ.,* 26 (2000) 101.
11. F.C.Meunier, V.Zuzaniuk, J.P.Breen, M.Olsson and J.R.H.Ross, *Catal. Today,* 59 (2000) 287.
12. A.Martinez-Arias, J,Soria, J.C.Consesa, X.L.Seoane, A.Arcoya and R.Cataluna, *J. Chem. Soc., Faraday Trans.,* 91 (1995) 1679.
13. M.Machida, D.Kurogi and T.Kijima, *J. Mater. Chem.,* 11 (2001) in print.

275

# Hydrogen spillover in Pt-Sn catalysts supported on activated carbon cloth.

A. Huidobro, A. Sepúlveda-Escribano and F. Rodríguez-Reinoso

Departamento de Química Inorgánica, Universidad de Alicante, Aptdo.99, E-03080, Alicante, Spain.

The effect of the tin content and the reduction temperature on the ability of bimetallic platinum-tin catalysts supported on activated carbon cloth (ACC) to retain hydrogen after the reduction treatments has been analysed by temperature-programmed desorption of hydrogen ($H_2$-TPD). A series of Sn/ACC samples with different tin contents has been prepared by impregnation of ACC with a solution of tin (II) oxalate in diluted $HNO_3$ and subsequent heat-treatment at 623 K under flowing helium. Platinum (1wt.%) was then introduced by impregnation of the Sn/ACC samples with aqueous solutions of $H_2PtCl_6$. Catalysts have been characterised by temperature-programmed reduction under diluted hydrogen and X-Ray Photoelectron Spectroscopy (XPS). The extent of hydrogen spillover from the metallic particles to the support has been determined by $H_2$-TPD, the products being analysed by on-line mass spectrometry. The presence of tin oxide provides anchoring sites for hydrogen atoms spilt-over from platinum, although the ability of the latter to dissociate $H_2$ molecules seems to be influenced by the presence of tin, both in an oxidised state after reduction at low temperature (523 K) and in the metallic state (possibility of alloy formation) after reduction at higher temperatures (623 and 723 K).

## 1. INTRODUCTION

The use of activated carbon as a catalyst support has been fuelled by its unique properties such as stability in both acid and basic media, easy recovery of precious metals, very high thermal resistance in an non-oxidising atmosphere and the possibility of changes in its textural and surface chemical properties. Activated carbons in the form of fibers and fabrics or cloths combine a series of properties that opens a new and very interesting research field as catalyst supports [1]. These have, among others, the advantage of superior contact efficiency and adsorption rate on dynamical experiments over granular activated carbons and the convenience of a resistant flexible cloth material. These materials are especially useful in processes carried out in triphasic reactions (gas-liquid-solid), such as the catalytic hydrogenation of organic molecules [2].

Bimetallic Pt-Sn systems supported on alumina, silica and carbonaceous materials have been extensively studied as catalysts for the selective hydrogenation of the carbonyl bond in $\alpha,\beta$-unsaturated aldehydes [3-5]. The importance of the surface composition of the catalyst to obtain the desired performance in terms of activity and selectivity towards the unsaturated alcohol has been reported. In this way, the presence of oxidised tin species close to Pt or PtSn alloy particles seems to be crucial [5].

An important aspect of hydrogenation reactions with supported metal-oxide catalysts is the possibility of hydrogen spillover from the metallic phase to the oxide promoter during either the reduction of the catalyst or the reaction itself. The mobility of adsorbed species from supported metals onto the nonmetallic support has been known since the 1950's and has been subjected to extensive research. These hydrogen species may play an important role such as partial reduction of the support, which may result in a large change in the metal-support interaction, leading to a modification of the adsorption mode of the substrate onto the active phase. It can affect, as well, the catalytic reaction and even participate in the it. It has been shown that spillover hydrogen can react with adsorbed organic species [6].

This work reports a study on hydrogen spillover in platinum-tin catalysts supported on an activated carbon cloth. Catalysts have been prepared with different tin loadings and subjected to several reduction temperatures.

## 2. EXPERIMENTAL PROCEDURE

### 2.1. Catalyst preparation

The support used has been an activated carbon cloth (ACC) (RS 1301, from Actitex$^{®}$) with a BET surface area of 1200 m$^2$g$^{-1}$, a mean pore diameter of 0.6-0.8 nm and an ash content of 0.48 wt.%. Tin oxide was deposited on the support at different loading (1, 6 and 12 wt.%) by impregnation with aqueous solutions prepared by dissolving the proper amounts of tin (II) oxalate in diluted HNO$_3$. The excess of solvent was removed with flowing nitrogen, and the resulting samples were dried at 393 K in air and subsequently heat-treated at 623 K under flowing helium. Platinum (1 wt.%) was introduced by impregnation of the Sn/ACC samples with aqueous solutions of H$_2$PtCl$_6$. After removing the excess of solvent, the solids were dried overnight at 393 K. A monometallic Pt/ACC catalyst was also prepared for the sake of comparison.

### 2.2. Catalyst characterisation

Temperature-programmed reduction measurements were carried out in a U-shaped quartz cell, using a 5%H$_2$/He gas flow of 50 cm$^3$·min$^{-1}$ and about 0.20 g of sample. X-Ray Photoelectron Spectroscopy XPS spectra were acquired with a VG Escalab 200R spectrometer equipped with a hemispherical electron analyser and $K\alpha$ (1253.6 eV) 300 W X-ray source. Reduction treatments were carried out in situ, previous to the spectra registration.

### 2.3. Temperature-programmed desorption of hydrogen

The extent of hydrogen spillover after different reduction treatments was studied by H$_2$-TPD, and the analysis of products was carried out by on-line mass spectrometry (MS). Two procedures were used. On one hand, samples were reduced in flowing hydrogen and then cooled down to room temperature in the same atmosphere. Then, H$_2$ was replaced by helium and, when the H$_2$ signal at the MS was equilibrated, a TPD (heating rate:10 K·min$^{-1}$) experiment was carried out. This method is labelled as *procedure A*. On the other hand, samples were reduced under a hydrogen flow and then swept with He at the same reduction temperature for 1.5 h; after that, they were allowed to cool under flowing helium. At a given temperature, helium was switched by hydrogen, which was allowed to flow over the sample for 30 min. After replacing hydrogen by helium flow, the TPD (10 K·min$^{-1}$) experiment was carried out when the H$_2$ signal at the MS was equilibrated. This method is labelled as *procedure B*.

# 3. RESULTS AND DISCUSSION

## 3.1. Reduction behaviour

Figure 1 shows the TPR profiles of catalysts Pt/ACC, 1Sn/ACC and Pt1Sn/ACC. The TPR profile of the monometallic Pt/ACC sample shows two small broad bands centred at about 655 and 965 K, respectively. As platinum should be reduced at lower temperatures, these peaks in hydrogen consumption rate can be assigned to the reduction of surface oxygen complexes on the support surface by hydrogen dissociated on the platinum atoms and spilt-over the carbon surface. In fact, XPS analysis reveals that Pt (IV) in $H_2PtCl_6$ is reduced to Pt (II) upon impregnation on the carbon support (binding energy: 72.8 eV) and it is already reduced to metallic platinum upon hydrogen treatment at 523 K (BE: 71.4 eV). The TPR profile of sample 1Sn/ACC shows a single reduction band centred at 915 K, which corresponds to the bulk reduction of tin oxide to metallic tin. However, the TPR profile of catalysts Pt1Sn/ACC shows two overlapping bands centred at 710 and 875 K, respectively. The band at a lower temperature is assigned to the reduction of tin oxide in close contact with platinum particles by means of hydrogen atoms generated on the platinum surface and spilt over tin oxide. The second peak of hydrogen consumption appears at a temperature close to that obtained for Sn/ACC, and corresponds to the reduction of tin oxide not interacting (or with a lesser interaction) with platinum.

XPS studies on the reduction behaviour of these catalysts [7] show that the reduction of oxidised platinum is hindered by the presence of tin. The Pt $4f_{7/2}$ band of the bimetallic catalysts reduced at 523 K appears at a binding energy of 72.0 eV, 0.6 eV higher than for the monometallic catalyst. At this reduction temperature tin is still in an oxidised state (B.E. at 487.3 eV) and may interact with platinum through the formation of Pt-O-Sn species. On the other hand, metallic tin is observed after reduction at 623 and 723 K. However even after reduction at these high temperatures, the Pt $4f_{7/2}$ band appears at B.E. values as high as 72.0 and 71.9 eV, respectively. Analogous positive shifts have been reported previously for Pt-Sn
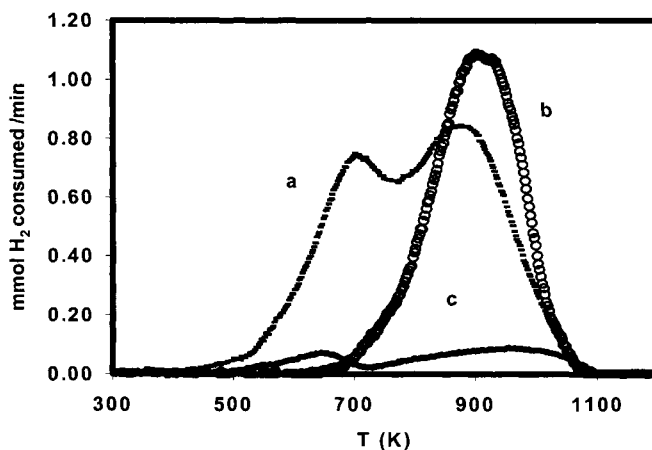


Fig. 1.Temperature programmed reduction profiles: (a) Pt1Sn/ACC, (b) 1Sn/ACC, (c) Pt/ACC.

bimetallic catalysts supported on alumina [10] and $ZrO_2$-$Al_2O_3$ [11], among others systems. In these cases, and assuming that platinum is reduced after the treatment at these relatively high temperatures, the high B.E. values were attributed to the formation of alloy phases between metallic platinum and metallic tin. In this way, TPR results correlate well with the XPS characterisation of these samples.

It can be concluded that samples reduced at 523 K contain metallic platinum in an electron deficient state (high binding energy) and oxidised tin species. Reduction at 623 and 723 K favours the partial reduction of tin oxide, with the subsequent formation of Pt-Sn alloy phases.

### 3.2. Monometallic Pt/ACC catalysts

Figure 2 shows several $H_2$-TPD profiles obtained with the monometallic catalyst Pt/ACC. When the experiment is carried out after reduction at 523 K and cooling down to room temperature in flowing $H_2$ (*procedure A*), two overlapping peaks for hydrogen desorption are observed (*profile a*). The most intense one (Peak I) is centred at about 623 K, whereas the other one (Peak II) appears as a shoulder at a somewhat higher temperature (710 K). In any case, both temperatures are much higher than those reported for the desorption of hydrogen chemisorbed on Pt [8, 9]. Accordingly, they are assigned to hydrogen species on the carbon support, distant from the Pt crystallites. These species are nearly removed if the catalyst is heat-treated in flowing He at 523 K after reduction (*profile b*). However, some of them are restored if, after reduction at 523 K and evacuation with flowing helium at the same temperature, hydrogen chemisorption is allowed for 30 min at 303 K (*profile c*). The hydrogen treatment at 303 K nearly restores the initial amount of hydrogen retained on the
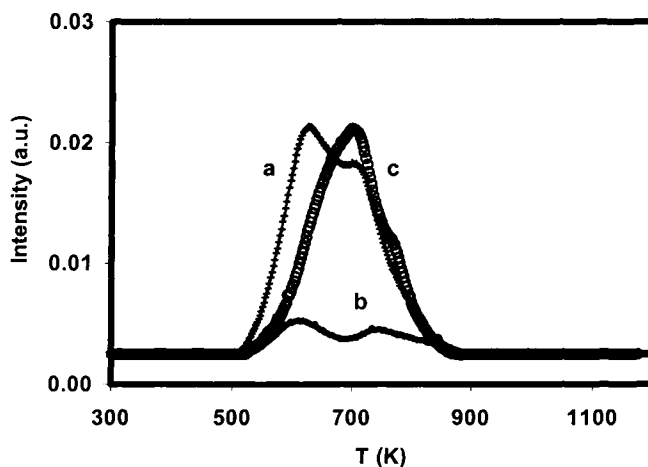


Fig. 2. $H_2$-TPD profiles of Pt/ACC reduced at 523 K: *(a) procedure A*; (b) heat treated in He at 523 K after reduction in $H_2$; (c) *procedure B* (303 K).

support, although a single band is now obtained, with the maximum centred at about 710 K. This is indicative of the existence of different anchoring sites for spilt-over hydrogen in this monometallic catalysts that are modified upon the thermal treatment in helium.

### 3.3. Bimetallic Pt-Sn catalysts. Effect of tin content

Catalysts with different tin loadings were submitted to *procedure A* after reduction at 523 K. The $H_2$-TPD profiles obtained are plotted in Figure 3, where the profile corresponding to the monometallic Pt/ACC catalysts has also been included for the sake of comparison. It can be observed that the profile corresponding to the bimetallic catalysts shows one single band, centred at about 610 K, whereas two bands are obtained with the monometallic catayst, the low temperature one appearing at nearly the same temperature as for the bimetallic catalysts. The amount of hydrogen desorbed from the bimetallic catalysts decreases as the tin content increases, although it is always higher than the corresponding to Peak I in the monometallic sample. XPS analysis of the catalysts reduced in situ at 523 K reveals that tin reduction has not yet started, as a relatively narrow band that appears in the Sn $3d_{5/2}$ region is centred at 487.0 eV in all cases. On the other hand, the Pt $4f_{7/2}$ peak appears close to 72.0 eV, a binding energy somewhat higher than the corresponding to the Pt/ACC catalyst (71.4 eV). Furthermore, the Pt $4f_{7/2}$ band of the catalyst Pt12Sn/ACC is broader that its counterparts, and can be deconvoluted into two peaks, centred at 71.7 and 72.5 eV, respectively. These results indicate the presence of reduced platinum in these samples after reduction at 523 K, although it seems to be affected by the presence of tin oxide, becoming electron deficient to different extents. It can be concluded that the presence of tin oxide in these catalysts provide new anchoring sites for spillover hydrogen, which are likely to block anchoring sites on the carbon support. However, the platinum-tin oxide interaction hinders the ability of platinum to chemisorb and dissociate hydrogen molecules.
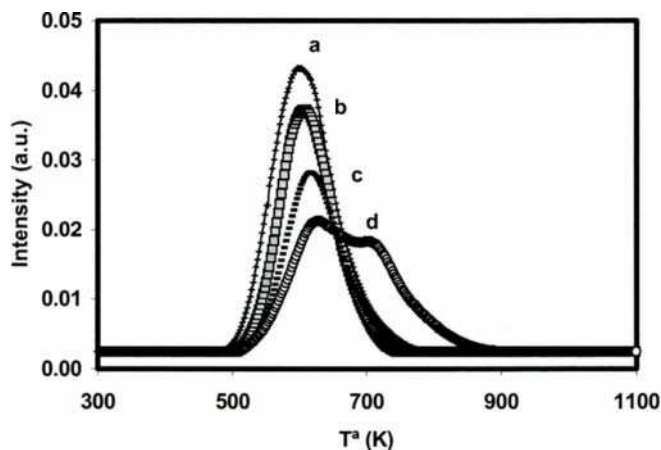


Fig. 3. $H_2$-TPD profiles of samples submitted to *procedure A*, after reduction at 523 K. (a) Pt1Sn/ACC, (b) Pt6Sn/ACC, (c) Pt12Sn/ACC, (d) Pt/ACC.

### 3.4. Effect of reduction temperature

Figure 4 shows the H$_2$-TPD profiles of catalyst Pt1Sn/ACC after reduction at different temperatures (523, 623, and 723 K), and then cooled down to room temperature under H$_2$ flow (*procedure A*). It can be seen that H$_2$ desorption peaks are strongly influenced by the reduction temperature: they become broader and the maxima are shifted to higher temperatures as the reduction temperature increases. This is an indicative of the creation of new anchoring sites for spillover hydrogen with increasing the reduction temperature, in which it is more strongly retained. It has been evidenced by XPS studies on this catalysts, after different reduction temperatures [7], that the surface concentration of platinum atoms is not modified by the increase in the reduction temperature and, furthermore, their electronic state also remains unchanged, the Pt $4f_{7/2}$ band appearing at a binding energy of 72.0 eV in all cases. However, the increasing reduction temperature does affect the chemical state of tin. Whereas, as discussed above, tin remains in an oxidised state after reduction at 523 K, it becomes reduced to an important extent (about 70%) after reduction at 623 and 723 K. This opens the possibility to the formation of Pt-Sn alloyed phases, with a distinctive behaviour as regard as their interaction with hydrogen.

In this way, bimetallic Pt-Sn particles are expected to show a lesser capability to dissociate and chemisorb hydrogen, due to the diluting effect of tin that breaks the platinum ensembles needed for the process. In spite of this, the amount of spillover hydrogen does not decrease with alloy formation, but even increases and H$_2$ desorbs at higher temperatures. It is also interesting to note that the highest amount of spillover hydrogen (sample reduced at 623 K), corresponds to the highest atomic Pt/Sn surface ratio in the catalyst after the reduction treatment, as measured by XPS. These modifications must be attributed to the presence of tin, as a very small desorption peak is observed with the monometallic sample reduced at 723 K, (profile d).
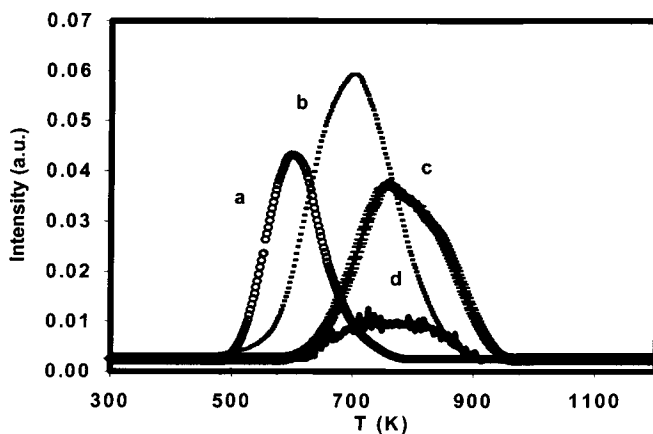


Fig. 4. H$_2$- TPD profiles of sample Pt1Sn/ACC submitted to *procedure A* after reduction at: (a) 523 K, (b) 623 K, (c) 723 K, and (d) Pt/ACC submitted to *procedure A* after reduction at 723 K.

## 4. CONCLUSIONS

Several conclusions can be drawn from this study on hydrogen spillover in Pt-Sn catalysts supported on an activated carbon cloth. Firstly, it has been shown that the presence of platinum favours the reduction of neighbouring tin species, and this has been explained on the basis of a spillover mechanism by which hydrogen atoms formed on the platinum surface migrate to the tin oxide particles close to the platinum atoms. On the other hand, a given amount of hydrogen is retained on these catalysts during the reduction treatment in hydrogen flow. These hydrogen species can be removed only by heat treatment in helium at a temperature higher than the reduction temperature, and produce different $H_2$ desoption peaks in the $H_2$-TPD profiles. The amount and thermal stability of these hydrogen species strongly depends on the tin loading in the catalyst and on the reduction temperature. When the reduction is carried out at low temperatures (523 K), in such a way that tin is completely in an oxidised state, the amount of $H_2$ evolved in $H_2$-TPD experiments decreases with tin loading in the bimetallic catalysts, although it is always higher than that obtained with the monometallic sample. It is postulated that tin oxide provides new anchoring centres for spillover hydrogen, although the ability of Pt to dissociate $H_2$ molecules is hindered by an electron effect of surrounding tin oxide. An important effect of reduction temperature has also been evidenced. Reduction at 623 and 723 K produce the reduction of a given amount of tin oxide, with the possibility of formation of Pt-Sn alloy phases. The maximum hydrogen evolution in $H_2$-TPD experiments is obtained after reduction at 623 K, which correlates with the highest Pt/Sn atomic ratio at the catalyst surface, as determined by XPS.

### Acknowledgements

## REFERENCES

[1] L.R. Radovic and F. Rodríguez-Reinoso, "Carbon Materials in Catalysis", ed. P.A. Thrower, Chemistry and Physics of Carbon, 25 (1997) 243.

[2] J.P. Reymond and P. Fouilloux, Stud. Surf. Sci . Catal., 130 (2000) 995.

[3] F. Coloma, A. Sepúlveda Escribano, J.L.G. Fierro, F. Rodríguez Reinoso, Appl. Catal. A: Gen., 136 (1996) 231.

[4] F. Coloma, A. Sepúlveda-Escribano, J.L.G. Fierro, F. Rodríguez-Reinoso, Appl. Catal. A: Gen., 150 (1997) 165.

[5] F. Coloma, J. Llorca, N. Homs, P. Ramírez de la Piscina, F. Rodríguez-Reinoso and A. Sepúlveda-Escribano, Phys. Chem. Chem. Phys., 2 (2000) 3063.

[6] D. Bianchi, M. Lacroix, G. M. Panjok and S. J. Teichner, J. Catal. 59, (1979) 467.

[7] A. Huidobro, F. Coloma, A. Sepúlveda-Escribano and F. Rodríguez-Reinoso, in preparation.

[8] J.T. Miller, B.L. Meyers, F.S. Modica, G.S. Lane, M. Vaarkamp and D.C. Koningsberger, J. Catal. 143, (1993) 395.

[9]  P. Ferreira-Aparicio, A Guerrero-Ruiz and I. Rodríguez-Ramos, J. Chem. Soc., Faraday Trans., 93(19) (1997) 3563.
[10] K. Balakrishnan, J. Schwank, J. Catal., 127 (1991) 287.
[11] C. Larese, J.M. Campos-Martín and J.L. G. Fierro, Langmuir, 16 (2000) 10294.

# Hydrogen Spillover Effect in the Reduction of Barium Nitrate of Ru-Ba(NO$_3$)$_2$/AC Catalysts for Ammonia Synthesis

Changhai Liang, Zhaobin Wei, Mengfei Luo, Pinliang Ying, Qin Xin and Can Li*

State Key Laboratory of Catalysis, Dalian Institute of Chemical Physics
Chinese Academy of Sciences, P.O. Box 110, Dalian 116023, China

Ru/AC catalysts promoted with nitrates of alkali metals, alkali earth metals and rare earth metals precursors were prepared by impregnation method and characterized by temperature-programmed reduction (TPR), differential thermal analysis (DTA) and chemisorption. The addition of promoters in the Ru/AC catalyst considerably improves the TOF of ammonia synthesis. The reduction of the promoted catalysts was investigated in detail. The promoter precursor can be reduced at much lower temperatures in the presence of Ru than that in the absence of Ru. It is suggested that H$_2$ spillover effect on the Ru/AC catalyst significantly promotes the reduction of the promoter precursors, and the hydrogen spills over from Ru to the remote nitrate through the carbon surface. The promoter precursors were converted to hydroxides or oxides under reaction condition.

## 1. INTRODUCTION

Ruthenium is an important catalyst for a number of reactions, especially for ammonia synthesis [1-7], Fischer-Tropsch synthesis [8], and methanol electro-oxidation [9]. The Ru/C catalysts promoted with nitrates of alkali metals, alkali earth metals and rare earth metals were found to be effective catalysts for ammonia synthesis [1-5]. However, the activation process of the Ru/C catalysts including the decomposition of promoter precursor (e.g. KNO$_3$ and Ba(NO$_3$)$_2$) has not been studied well. Here the promoted Ru/C catalysts were studied by H$_2$-TPR and H$_2$-DTA techniques in order to understand the activation process. H$_2$ spillover effect play an important role in the activation process of promoted Ru/C catalysts and the spiltover hydrogen can reduce the promoter precursor at much lower temperatures.

## 2. EXPERIMENTAL

### 2.1. Catalyst preparation

The catalyst preparation is previously reported in detail [10]. In brief, the activated carbon (AC) was impregnated with an aqueous solution of RuCl$_3$.3H$_2$O, and the ruthenium content is about 4.0 wt. %. After an evaporating and a drying, the as-prepared samples were reduced in a stream of hydrogen, and cooled in nitrogen to room temperature, and then passivated in a stream of 1% O$_2$/N$_2$ so as to avoid the violent oxidation. The promoter was

introduced by the incipient wet impregnation method with aqueous solution of $Ba(NO_3)_2$, $KNO_3$, $Ca(NO_3)_2$, $Ce(NO_3)_3$ and $La(NO_3)_3$, respectively.

## 2.2. Catalyst Characterization

Temperature-programmed reduction (TPR) of the sample was carried out in a stream of 95% argon and 5% hydrogen with a flowing rate of 30 $cm^3$/min. The catalyst bed was heated linearly at 20 °C/min from room temperature to 900 °C. TPR of CuO sample was used to calibrate the hydrogen consumption in a TPR.

DTA measurements were performed on a Perkin-Elmer DTA 1700 over the temperature range from room temperature to 600 °C at a heating rate of 15 °C/min, in a hydrogen flow of 40 $cm^3$/min.

Chemisorption measurements of CO were performed in the ASAP2800 chemisorption apparatus. The irreversible CO uptake was obtained by taking the difference between the total and the reversible amount of CO adsorbed. The dispersion of the ruthenium particles was estimated from the irreversible uptake by assuming that CO adsorbs with CO/Ru =1.

## 2.3. Measurement of ammonia synthesis activity

The ammonia synthesis activity of as-prepared catalysts was tested in a stainless steel reactor with a stoichiometric $H_2$ and $N_2$ mixture ($H_2/N_2$=3) flow at 3.0 MPa. About 0.5 g of the promoted Ru/C catalyst, with particles of 40-60 mesh was used. The gas effluent from the reactor was neutralized by sulfuric acidic solution containing an indicator (methyl red). As soon as the neutralizing reaction is over, the color of the solution changes from red to orange. The flow rate of residual hydrogen and nitrogen was determined by a wet flow meter.

## 3. RESULTS AND DISCUSSION

### 3.1. Reduction of Ru-Ba/AC catalyst

Figure 1 shows TPR profile of $Ba(NO_3)_2$/AC, $RuCl_3$/AC, RuOx/AC and Ru-Ba/AC with different Ba/Ru molar ratio. TPR of $RuCl_3 \cdot 3H_2O$ indicates that the $H_2O$ releases at 125 °C and $RuCl_3$ could be reduced at 175 °C [11]. TPR profile of $RuCl_3$/AC shows three peaks of $H_2$ consumption at 165 °C, 240 °C and 640 °C (Figure 1a). Because bulk $RuCl_3$ is reduced at higher temperatures than the dispersed $RuCl_3$ on support, the peak at 165 °C is due to $H_2$ consumption of $RuCl_3$, and hydrogen consumption is consistent with the reduction reaction:

$$RuCl_3 + 1.5H_2 = Ru + 3HCl \qquad (1)$$
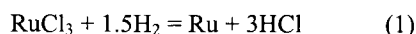
The peak at 240 °C is mainly due to the removal of the oxygen-containing functional groups on the carbon support. The peak at 640 °C is attributed to the methanation of surface carbon atoms producing $CH_4$. The latter two peaks have been proved by mass spectroscopy. From TPR experiment, a reduction temperature at 200 °C is high enough to reduce $RuCl_3$ into metal particle.

The RuOx/AC sample gives two TPR peaks of $H_2$ consumption at 140 °C and 700 °C (Figure 1b), which are due to removal of the oxygen on Ru and carbon support, and due to

methanation of surface carbon atoms. Actual $H_2$ consumption is less than the value for the reaction (2) with x=1.5.

$$RuO_x + xH_2 = Ru + xH_2O \qquad (2)$$
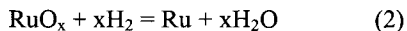
This means that Ru was not oxidized completely to $RuO_2$ during passivated and exposed to air. This indicates that Ru was in a partially oxidic form, RuOx, before the reduction.

For the $Ba(NO_3)_2/AC$ sample, no peak of $H_2$ consumption during TPR was observed below 400 °C (Figure 1g), while three peaks were detected at 450 °C, 600 °C and 700 °C, which correspond to the removal of surface functional groups on carbon support, decomposition and/or reduction of $Ba(NO_3)_2$ (reaction 3)

$$Ba(NO_3)_2 + 8H_2 = BaO + 2NH_3 + 5H_2O \qquad (3)$$
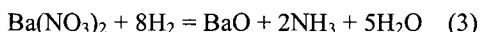
and methanation of surface carbon atoms, respectively. $Ba(NO_3)_2$ is not reduced with $H_2$ below 500 °C in the absence of Ru.
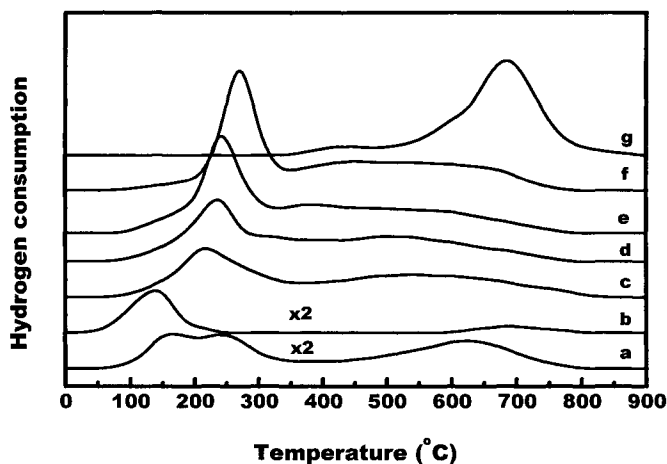


Figure 1. TPR profiles of Ru/AC samples. a: $RuCl_3/AC$; b: RuOx/AC; c: Ru-Ba/AC (Ba/Ru=0.5); d: Ru-Ba/AC (Ba/Ru=1.0); e: Ru-Ba/AC (Ba/Ru=2.0); f: Ru-Ba/AC ( Ba/Ru=6.2); g: $Ba(NO_3)_2/AC$.

For the $Ru-Ba(NO_3)_2/AC$ samples, it is noted that there exists a peak below 300 °C. The peak temperature of $H_2$ consumption is much lower than that of $Ba(NO_3)_2/AC$. The peak temperature at about 250 °C increases with the increase of Ba/Ru ratio, which may be due to more $Ba(NO_3)_2$ covering on Ru surface or poor dispersion of $Ba(NO_3)_2$. It can be seen that hydrogen consumption of the catalyst with promoters is higher than that without promoter. From Figure 1, it can be seen that the hydrogen consumption of the promoted catalysts is much more than that of catalyst without the promoter. Hydrogen is consumed mostly by the reduction of promoter precursor. Actual hydrogen consumption of catalysts with the Ba/Ru

ratio 0.5, 1, 2 and 6.2 amount to 94%, 84%, 60% and 40% of the value expected for reaction (2) and (3), respectively. The result is similar to that of Ru-Cs/Al$_2$O$_3$ catalyst measured by Aika et al. [11].

Figure 2 shows the DTA result of the samples. In the case of RuCl$_3$/AC, the exothermal peak at 140 °C is due to the reduction of RuCl$_3$ into Ru. No exothermal peak is observed below 400 °C for the Ba(NO$_3$)$_2$/AC and RuOx/AC samples. There is a strong exothermal peak at 220 °C that is due to reduction of promoter precursor. It is obvious that the result of DTA is consistent with that of TPR. This provides a proof for H$_2$ spillover phenomenon during the activation process of the Ru/C catalysts with Ba(NO$_3$)$_2$.

The surface of activated carbon, with the specific surface area of 1290 m$^2$.g$^{-1}$, could accommodate 38.0 mmolg$^{-1}$ Ba$^{2+}$ ions or 37.7 mmolg$^{-1}$ Ru when Ba$^{2+}$ ions or Ru are closely packed on the surface. The surface quantities of Ba$^{2+}$ and Ru with promoter/Ru = 6.2 and 4.0 wt.% Ru loading are about 2.5 mmolg$^{-1}$ and 0.4 mmolg$^{-1}$, respectively, and they cover only about 7 % and 1% of surface of AC, respectively. It is obvious that most Ru and Ba(NO$_3$)$_2$ are not closely contacted each other on the carbon surface. Therefore it is suggested that hydrogen on Ru must spills over Ba (NO$_3$)$_2$ through carbon surface. A schematic model of H$_2$-spillover on carbon support is given in Figure 3.
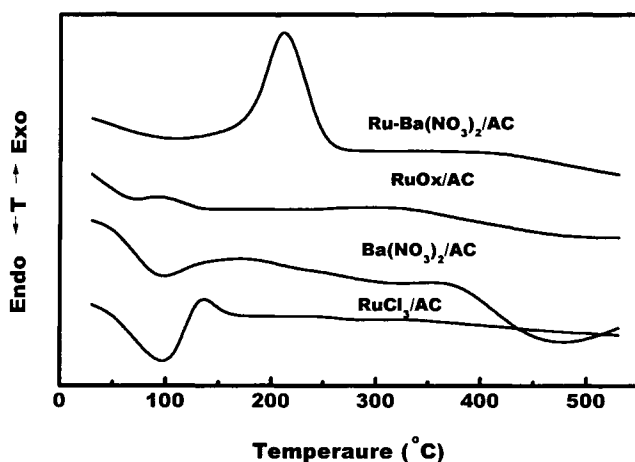


Figure 2. H$_2$-DTA of Ru/AC catalyst with and without promoter precursors
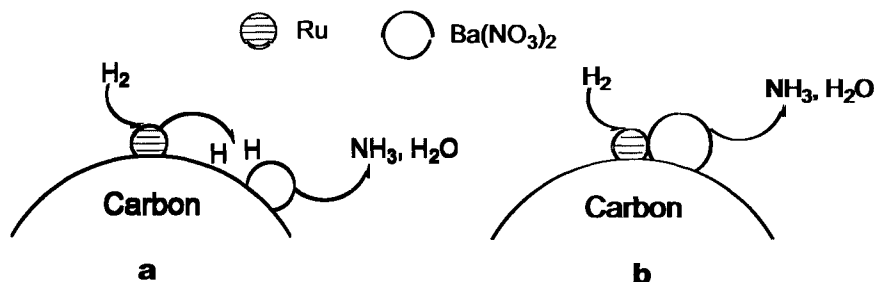
Figure 3. Schematic model of hydrogen spillover during activation process of the promoted Ru/AC catalyst. a Hydrogen spillover through carbon surface. b Hydrogen spillover through the interface between promoter and Ru.

## 3.2. Reduction of Ru-K(Ca, Ce, La)/AC catalysts

TPR and DTA profiles of the Ru/C catalysts promoted with $KNO_3$, $Ca(NO_3)_2$, $Ce(NO_3)_3$ and $La(NO_3)_3$ were measured and shown in Figure 4 and Figure 5. As shown in Figure 4, there is a strong peak of $H_2$ consumption between 200°C and 400°C for these samples, and peak temperatures is in the order: $KNO_3 <$ $Ce(NO_3)_3$ < $La(NO_3)_3$ < $Ca(NO_3)_2$. The high activation temperature for catalyst with $Ca(NO_3)_2$ can be attributed to formation of carbonate. However, Hydrogen consumption of these nitrate-promoted catalysts is much higher than that of catalyst without the promoter, and the peak temperatures of the promoted catalysts are much lower than those of corresponding nitrates, which are similar to the catalyst promoted with barium nitrate.
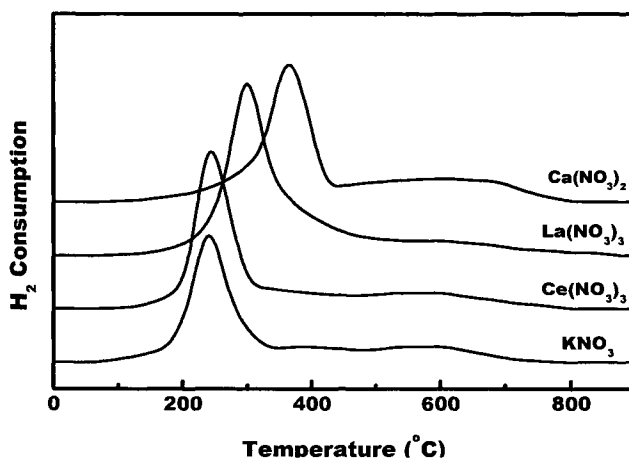


Figure 4. TPR profiles of Ru/AC catalysts promoted with $KNO_3$, $Ce(NO_3)_3$, $La(NO_3)_3$ and $Ca(NO_3)_2$, promoter/Ru=6.2.

As shown in Figure 5, there is an exothermic peak between 190 and 270 °C, which is assigned to decomposition of nitrates. The DTA profile also shows the same trend as the order of decomposition of promoter precursors shown by TPR. The reduction temperatures of these nitrates on Ru/AC catalyst are much lower than those of the nitrates without Ru/AC catalyst, indicating that $H_2$ spillover effect is common for the Ru/AC catalysts with other promoter precursors.
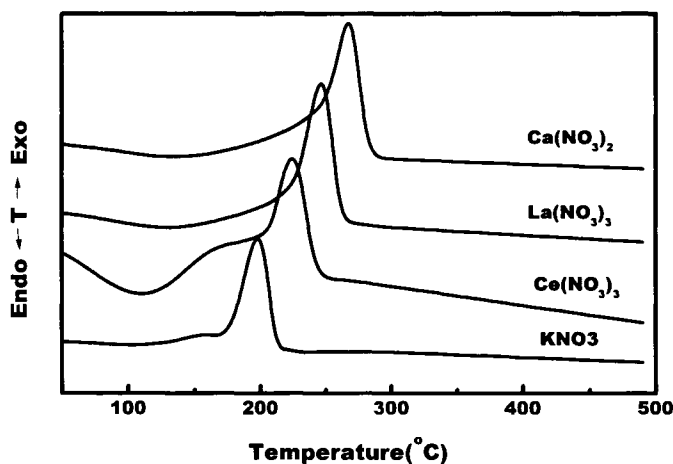


Figure 5. DTA of other Ru/AC catalysts promoted with $KNO_3$, $Ce(NO_3)_3$, $La(NO_3)_3$ and $Ca(NO_3)_2$, promoter/Ru=6.2.

### 3.3. Ammonia synthesis activity

CO chemisorption and ammonia synthesis activities for the Ru/AC catalyst and the Ru/AC catalysts promoted with different promoter are shown in Table 1. The activities are represented as TOF based on CO chemisorption because the measurement error is particularly severe for hydrogen chemisorption at room temperature [12]. The amount of CO chemisorption decreases with the increase of Ba/Ru molar ratio, suggesting that some Ru sites may be covered by the promoter. The TOFs of ammonia synthesis increase remarkably with the increase of Ba/Ru molar ratio, which can be explained in term of electron-donating effect of the promoters.

From Table 1, it can be seen that adding promoter in the catalyst decreases the amount of CO chemisorption and the Ru dispersion, suggesting that some promoters may located on the Ru metal surface. For the promoted Ru/AC catalysts, the order of ammonia synthesis activities is as following: no promoter < Ca < Ce < La < K < Ba.

Table 1
CO chemisorption and ammonia synthesis activity of Ru/AC catalysts

| Catalyst[a] | Promoter/Ru molar ratio | CO uptake ($\mu$mol/g) | Dispersion (%) | TOF $(s^{-1})^b$ |
|---|---|---|---|---|
| Ru/AC | 0 | 199.0 | 50 | Neg. |
| Ru-Ba/AC | 0.5 | 185.6 | 47 | 0.010 |
| Ru-Ba/AC | 1 | 145.9 | 37 | 0.027 |
| Ru-Ba/AC | 2 | 102.7 | 26 | 0.038 |
| Ru-Ba/AC | 6.2 | 74.9 | 19 | 0.048 |
| Ru-K/AC | 6.2 | 166.2 | 42 | 0.014 |
| Ru-La/AC | 6.2 | 69.9 | 18 | 0.016 |
| Ru-Ce/AC | 6.2 | 117.6 | 30 | 0.010 |
| Ru-Ca/AC | 6.2 | 92.6 | 23 | 0.006 |

[a] Ru loading is 4.0 wt.%.; [b] Ammonia synthesis rate at 400 °C and 3.0MPa expressed as $NH_3$ molecules/surface Ru atom/s.

Barium nitrate supported on the activated carbon does not decompose in the absence of Ru under reaction conditions as confirmed from TPR, and DTA results of $Ba(NO_3)_2/AC$. However, it is clear that the existence of Ru remarkably lowers the decomposition temperature of barium nitrate. DTA and TPR profiles suggest BaO and/or $Ba(OH)_2$ are the main product because BaO reacts easily with $H_2O$ from the reduction of surface oxygen-containing functional groups. But the formation of $BaCl_2$ can not be avoided due to reaction between residual chlorine ion from Ru precursor and barium salts, and $BaCl_2$ can not promote catalytic activity of ammonia synthesis. In the case of the $CsNO_3$-$RuCl_3$ system, Aika et al. had confirmed that the anion exchange occurred by XRD (peak of CsCl) of the $CsNO_3$-$RuCl_3$ sample before reduction [11].

A similar conclusion can be applied to other promoter systems, such as K and Ca. In particular, $KNO_3$ promoted catalyst and KOH promoted catalyst show the similar TOF [10], suggesting that the nitrate be converted to hydroxides under reaction conditions. But for the case of La and Ce system, the oxides are main products. Domka et al. have studied the $Ru/La_2O_3$ catalyst, and found that the crystalline LaOCl is formed during water-gas shift reaction although the main composition is $La_2O_3$ [13]. For the $Ru-La(NO_3)_3/AC$ catalyst, the formation of LaOCl is unavoidable due to the existence of residual chlorine and the basity of La oxides or hydroxides. The similar effect occurred for the other noble metal /rare-earth oxide catalysts [14].

## 4. CONCLUSION

$H_2$ spillover effect on the Ru/AC catalyst significantly promotes the reduction of promoter precursors, nitrates. It is suggested that the migration of hydrogen from Ru to the nitrate is possibly through the carbon surface which is the effective carrier for hydrogen spillover. The nitrates were converted to hydroxides or oxides under reaction condition. The promoters significantly improves the TOF of ammonia synthesis, and the activity is increased in the order: no promoter < Ca < Ce < La < K < Ba.

## ACKNOWLEDGEMENT

## REFERENCES

1.  K. Aika, H. Hori, A. Ozaki, J. Catal., 27 (1972) 242.
2.  K. Aika, K. Tamaru, in "Ammonia: Catalysis & Manufacture" (A. Nieson, Ed), p.104, Springer-Verlag, Berlin/Heideberg, 1995.
3.  L. Forni, D. Molinari, I. Rossetti, N. Pernocone, Appl. Catal. A, 185 (1999) 269.
4.  T. Becue, R. J. Davis, J. M. Garces, J. Catal., 179 (1998) 129.
5.  F. Rosowski, O. Hinrichsen, M. Muhler, G. Ertl, Catal. Lett., 36 (1996) 229.
6.  Fastrup, B., Catal. Lett. 48 (1997) 111.
7.  S. Dahl, A. Logadottir, R. C. Egeberg, J. H. Larsen, I. Chorkendorff, E. Tornqvist, J. K. Norskov, Phys. Rev. Lett., 83 (1999) 1814.
8.  H. Schulz, Appl. Catal., 186 (1999) 3.
9.  T. Mahmood, J. O. Williams, R. Miles, B.D. McNicol, J. Catal., 72 (1981) 218.
10. C. Liang, Z. Wei, Q. Xin, C. Li, Appl. Catal. A, 208 (2000) 193.
11. A.Aika, K. Shimazaki, Y. Hattori, A. Ohya, S. Ohshima, K. Shirota, A. Ozaki, J. Catal., 92 (1985) 294.
12. T. Narita, H. Miura, K. Sugiyama, T. Matsuda, R. D. Gonzalez, J. Catal. 103 (1987) 492.
13. A. Basinska, L. Kepinski, F. Domka, Appl. Catal. A, 183 (1999) 143.
14. F.L. Normand, J. Barrault, R. Breault, L. Hilaire, A. Kiennemann, J. Phys. Chem., 95 (1991) 257.

# Hydrogen Spillover Measured by Mass Spectroscopy during Reduction of Carbon Supported Palladium Catalysts: Effect of Carbon Properties

A. L. D. Ramos[a,*], D. A. G. Aranda[a,b] and M. Schmal[a,b,+]

[a]NUCAT/PEQ/COPPE, Universidade Federal do Rio de Janeiro, Caixa Postal 68502, CEP 219141, Rio de Janeiro, RJ, Brazil

[b]Escola de Química/UFRJ

Graphite and activated carbon samples of different nature or modified by chemical treatments with HCl and $HNO_3$ have been used as supports for palladium. Textural properties of supports were characterized by nitrogen adsorption at 77 K while the type and amount of surface oxygen groups were checked by temperature-programmed desorption in helium (TPDHe). The consumption of hydrogen as well the production of $CH_4$, CO and $CO_2$ were monitored by mass spectroscopy during the temperature-programmed reaction (TPR) of supports and catalysts. CO and $CO_2$ productions were generally lower during TPR of supports compared to TPDHe, which was attributed to the reduction of surface oxygen groups. This decrease was also observed comparing the reduction of supports and catalysts as well as an extra consumption of hydrogen and a higher production of $CH_4$. A phenomenon of spillover was proposed which intensity would be proportional to the amount of surface oxygen groups present on the support.

## 1. INTRODUCTION

Although carbon supported palladium catalysts have been used in a wide range of industrial reactions, especially hydrogenation reactions [1], their characterization still has a lot of points to be clarified, especially when hydrogen is involved. One important phenomenon that might occur with this system is the dissociation of adsorbed hydrogen on the metallic surface and migration of atomic hydrogen to the surface of the support, which is called spillover. There are some evidences of the occurrence of spillover on carbon supported noble metal catalysts by several methods, like hydrogen titration [2], hydrogen chemisorption [3], hydrogen temperature-programmed desorption [4], inelastic neutron scattering [5] and others. However, there are few works in the literature that monitor and quantify several gases simultaneously, like $H_2$, $CH_4$, CO and $CO_2$, during the reduction of the supports and catalysts. This is very important when carbon supported catalysts are used because of the possibility of occurring gasification reactions.

*Present Address: Campus II – Av. Murilo Dantas, 300 – Farolândia – Aracaju, SE, Brazil CEP: 49032-490

+Corresponding author. Fax: +55 21 590 7135; E-mail: schmal@peq.coppe.ufrj.br

Several factors are cited in the literature that affect the intensity of spillover. Boudart et al. [6] proposed that carbon atoms on the metallic surface would play a role in providing bridges for hydrogen atoms to be transported away from the metal to the carbon support itself. Suh et al. [2] concluded that the surface oxygen groups would promote the spillover phenomenon by reacting with atomic hydrogen produced from dissociative adsorption.

The objective of this work is to verify the occurrence of spillover during reduction of carbonaceous material supported palladium catalyst, monitoring several gases (like $H_2$, $CH_4$, CO, $CO_2$, $H_2O$ and HCl) by mass spectroscopy during the experiment. The influence of the carbon properties on the intensity of spillover will be also investigated.

## 2. EXPERIMENTAL

### 2.1. Support and Catalyst Preparation

High surface area graphite (GR) and two samples of activated carbon (VG and VP) produced by Carbomafra from wood precursors were the raw supports used in this study. The sample VP was submitted to two different chemical treatments. In the first one, the sample was immersed into an aqueous solution of HCl 0.5M and the slurry so formed was stirred for 6 h at reflux temperature (sample VPC). In the other one, the sample was oxidized in a solution of $HNO_3$ 0.5 M, at reflux temperature, for 6 h (sample VPN). In both cases the samples were washed after treatment with de-ionized water until a neutral pH and dried in air at 373 K.

Catalysts were prepared by wet impregnation using $PdCl_2$ as precursor aiming a loading of 1wt% of Pd. The precursor was dissolved in concentrated HCl and the final impregnation volume was 50 $cm^3$ of water per gram of support. The slurry was rotated for 18 h after which the fluid was evaporated at 353-373 K under vacuum for a period of 2-3 h. Subsequently the catalyst was dried overnight at 373 K and kept in a desiccator until use.

### 2.2. Support and Catalyst Characterization

The characterization of the porous texture of the supports was carried out by physical adsorption of nitrogen at 77 K in a conventional volumetric adsorption system. Total surface area was obtained via the BET equation [7], micropore properties with the Dubinin-Radushkevich method [8] and mesopore properties with the BJH method [9].

The amount and type of surface oxygen groups were determined by monitoring the production of CO and $CO_2$ during temperature-programmed desorption under helium (TPDHe). Samples (200 mg) were placed in a U-shaped quartz flow micro-reactor and dried in helium (60 $cm^3$ $min^{-1}$) at 423 K for 1 h. Then, after cooling the sample down to room temperature, the temperature was raised (10 K $min^{-1}$) to 1273 K in helium (60 $cm^3$ $min^{-1}$). The effluent gas was analyzed by a mass spectrometer, monitoring several masses simultaneously: m/e=2, 12, 15, 16, 17, 18, 28, 30, 32, 36 and 44. $H_2$, $CH_4$, CO and $CO_2$ were calibrated in order to have accurate measurements of the consumption or production of these gases.

Temperature Programmed Reduction (TPR) of the supports and catalysts was performed in the same apparatus as TPD experiments, monitoring the same signals of the mass spectrometer and calibrating the same gases. The difference is that after the drying step the sample was heated under flow of a mixture 1,65%$H_2$/Ar, at a heating rate of 5K $min^{-1}$ from room temperature to 1273 K.

## 3. RESULTS AND DISCUSSION

### 3.1. Textural Characterization

Table 1 reports the textural properties of supports. It can be concluded that graphite does not present the vast porous structure of the activated carbon samples, since the total surface area ($S_{BET}$), micropore surface area ($S_{D-R}$) and pore volume ($V_{D-R}$) are much smaller than the ones of activated carbon samples. Given that graphite is essentially microporous the BJH methodology that characterizes the mesoporosity cannot be applied to this sample. Among the activated carbon samples, support VG showed a higher proportion of micropores than the sample VP, which can be seen directly by the percentage of micropores obtained from the pore volumes (%micro) and by the higher micropore surface area ($S_{D-R}$) and smaller mesopore surface area ($S_{BJH}$). This higher proportion of micropores is responsible for a higher total surface area of this sample. The treatment with HCl did not affect considerably the textural properties while the oxidation treatment with $HNO_3$ has decreased slightly all the values of surface area and increased the proportion of micropores.

Table 1
Textural properties of supports

| Support | $S_{BET}$ $(m^2\,g^{-1})$ | $S_{D-R}$ $(m^2\,g^{-1})$ | $S_{BJH}$ $(m^2\,g^{-1})$ | $V_{D-R}$ $(cm^3\,g^{-1})$ | $V_{BJH}$ $(cm^3\,g^{-1})$ | %micro $\dfrac{V_{D-R}}{(V_{D-R}+V_{BJH})}$ |
|---|---|---|---|---|---|---|
| GR | 78 | 111 | - | 0.0362 | - | - |
| VG | 845 | 996 | 270 | 0.353 | 0.254 | 58.1 |
| VP | 664 | 755 | 355 | 0.268 | 0.426 | 38.6 |
| VPC | 646 | 760 | 336 | 0.257 | 0.403 | 38.9 |
| VPN | 599 | 703 | 320 | 0.245 | 0.366 | 40.1 |

### 3.2. Oxygen Surface Groups Characterization

Table 2 reports the production of $CH_4$, CO and $CO_2$ during the heating of supports in helium while Figure 1 shows TPD spectra of CO and $CO_2$.

Table 2
Quantification of gases produced during TPDHe

| | Amount Produced $(\mu mol\,g^{-1})$ Total | | | | Production T<873K Total production | | |
|---|---|---|---|---|---|---|---|
| Support | $CH_4$ | CO | $CO_2$ | $CO/CO_2$ | $CH_4$ | CO | $CO_2$ |
| GR | 96 | 519 | 329 | 1,6 | 0,84 | 0,50 | 0,85 |
| VG | 4 | 1958 | 310 | 6,3 | 0,48 | 0,10 | 0,57 |
| VP | 26 | 1322 | 309 | 4,3 | 0,13 | 0,17 | 0,68 |
| VPC | 43 | 1363 | 295 | 4,6 | 0,31 | 0,22 | 0,70 |
| VPN | 23 | 3342 | 1478 | 2,3 | 0,38 | 0,35 | 0,84 |

294
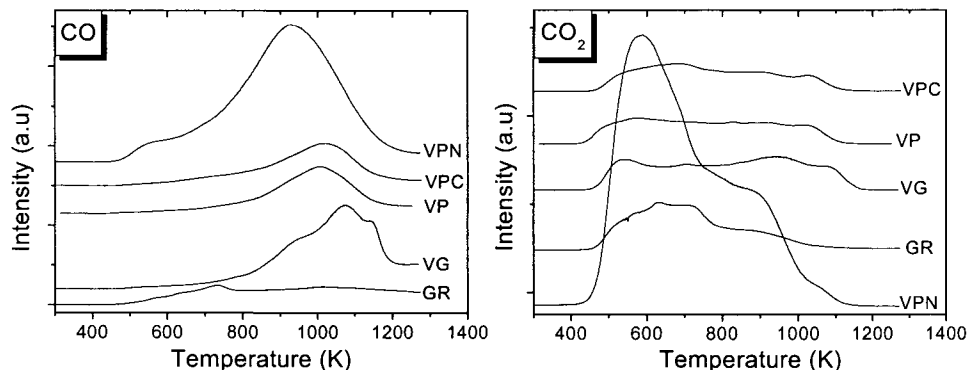


Fig. 1. Desorption of CO and CO$_2$ during TPDHe

It is well known in the literature that surface oxygen groups on carbon materials decompose upon heating by releasing CO and/or CO$_2$ at different temperatures. However it can be observed that graphite yielded much higher amount of methane than the activated carbon samples, especially in the low temperature (below 873 K) region which higher productions of CO and CO$_2$ can also be observed. These results indicate that some gasification reactions may be occurring during the experiment with graphite so that some amount of CO and CO$_2$ desorbed is not related to decomposition of surface oxygen groups. Even so amounts of CO and CO$_2$ produced were much lower than the ones produced by the activated carbon samples, indicating that graphite has much less surface oxygen groups than the others and these groups are less stable (decompose at lower temperatures).

Concerning the activated carbon samples the support VG showed higher production of CO and higher temperature of desorption. According to Figueiredo et al. [10], the oxygen groups that desorb as CO are less acid than the ones that desorb as CO$_2$, and temperatures of desorption of these groups follow this order: anhydride<phenol<ether<carbonyl~quinone. Therefore, the sample VG seems to have a higher proportion of quinone e lactone than the sample VP. However, temperature of peaks shows that for all the activated carbon samples quinone and lactone groups have a higher proportion than the other groups that desorb as CO. The treatment with HCl did not alter considerably the amount of surface oxygen groups and the proportion of them. Besides this treatment seems to have introduced chlorinated groups since it was observed a large m/e=36 peak at relatively high temperature (above 600 K). The treatment with HNO$_3$ produced much more modifications. First of all this treatment increases considerably the amount of surface oxygen groups, especially the ones that desorb as CO$_2$. Besides this treatment produces less stable groups, decreasing CO and CO$_2$ desorption temperature peak and increasing the proportion of desorption at temperatures lower than 873 K. According to Figueiredo et al. [10], the lower temperature of desorption of CO$_2$ indicates a higher proportion of carboxyl groups in relation to lactone and anhydride groups.

### 3.3. Temperature Programmed Reaction (TPR)

Figure 2 shows the evolution of hydrogen during TPR experiments of supports and catalysts. Supports showed a consumption peak (around 900 K) followed by a production peak (around 1100K). The production peak had been observed elsewhere during TPDHe experiment and is probably related to surface functionalities of the support like the aromatization of cyclic parts of the carbonaceous materials and elimination of hydrogen molecules attached to the surface oxygen groups or to the aromatic rings. Sample VG showed a higher temperature peak, indicating a great difficulty to eliminate hydrogen from this sample. Production of hydrogen from graphite was much lower than from activated carbon samples, which can be attributed to the low amount of surface oxygen groups and the presence of condensed aromatic rings, which in both cases is expected to have less hydrogen to be eliminated.

The consumption peak around 900 K is probably related to the reduction of surface oxygen groups [2] or to the adsorption on surface sites of the support formed upon the decomposition of oxygen complexes [11]. Actually peaks of water were observed in the same temperature range, corroborating the supposition that the following reactions may be taking place:

$$CO \text{ (sup)} + H_2 \rightarrow C \text{ (sup)} + H_2O \tag{1}$$
$$CO_2 \text{ (sup)} + 2 H_2 \rightarrow C \text{ (sup)} + 2 H_2O \tag{2}$$

Table 3 shows the production of $CH_4$, CO and $CO_2$ during TPR experiments of supports and catalysts. It can be observed that productions of $CO_2$ and especially CO of the supports are lower than the ones during TPDHe (Table 2), confirming that some of the oxygen surface groups, especially the ones that desorb as CO, have been consumed during TPR, according to reactions (1) and (2).
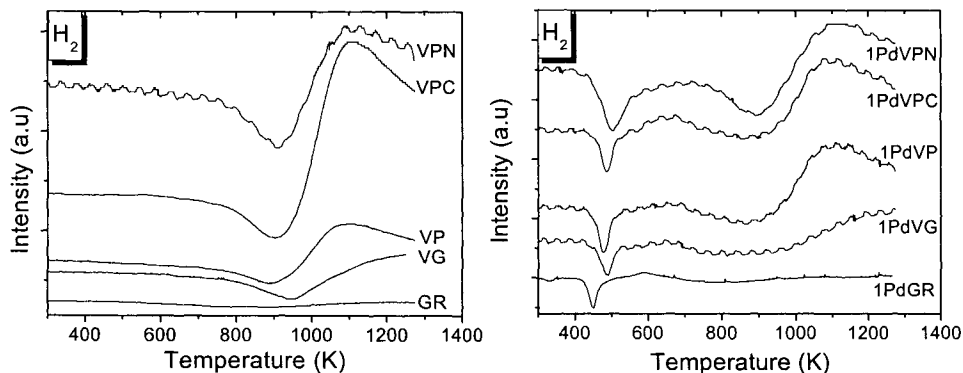


Figure 2- $H_2$ spectra during TPR of Supports and Catalysts

Table 3
Production of gases during TPR of supports and catalysts

| Sample | CH$_4$ | | CO | | CO$_2$ | |
|---|---|---|---|---|---|---|
| | Support | Catalyst | Support | Catalyst | Support | Catalyst |
| GR | 54 | 100 | 403 | 148 | 230 | 219 |
| VG | 24 | 76 | 991 | 115 | 254 | 191 |
| VP | 101 | 168 | 1015 | 764 | 286 | 252 |
| VPC | 108 | 167 | 837 | 1066 | 298 | 267 |
| VPN | 129 | 106 | 2466 | 1682 | 1783 | 1517 |

The "Amount Produced ($\mu$mol g$^{-1}$)" heading spans the CH$_4$, CO, and CO$_2$ columns.

Catalysts showed a new consumption peak around 500 K, which should be related to the reduction of the metallic precursor. This supposition was confirmed by the simultaneous production of H$_2$O and HCl, which would be expected if the precursor were an oxide or a chloride compound, respectively, according to the following reactions:

$$PdO_x + x\ H_2 \rightarrow Pd + x\ H_2O \qquad (3)$$
$$PdCl_x + x/2\ H_2 \rightarrow Pd + x\ HCl \qquad (4)$$

However, the consumption of hydrogen in this temperature range is much higher than the stoichiometric amount needed to the reduction of the metallic precursor, as can be observed by the quantification of this consumption showed in Table 4. It is important to say that any consumption of hydrogen was observed in this region (below 573 K) during the reduction of supports. Considering that the palladium oxidation state is +2, the relation H$_2$/Pd in both reactions should be one. However, this relation is much higher than one for all the catalysts. This way, it seems that the metallic phase is promoting the consumption of hydrogen through a spillover phenomenon. The intensity of spillover is higher for the sample with more surface oxygen groups (1PdVPN), indicating that these groups promote the phenomenon, as was proposed by Suh et al. [2]. Probably the metallic phase is responsible for the dissociation of the hydrogen molecule, creating hydrogen atoms that spilt over to the support:

$$H_2\ (g) \rightarrow 2H\ (Pd) \rightarrow 2H\ (C) \qquad (5)$$

Table 4
Consumption of H$_2$ below 573 K during TPR of supported palladium catalysts

| Catalyst | H$_2$ consumed below 573 K ($\mu$mol g$^{-1}$) | Moles H$_2$ / Pd atom |
|---|---|---|
| 1PdGR | 278 | 3,6 |
| 1PdVG | 568 | 7,4 |
| 1PdVP | 567 | 7,4 |
| 1PdVPC | 457 | 6,5 |
| 1PdVPN | 1528 | 20,1 |

There are some possibilities for the destiny of the hydrogen atoms spilt over to the support:

a) Reduction of surface oxygen groups – It was observed a new water production peak simultaneous to the hydrogen consumption peak. Besides, as can be observed in Table 3, productions of CO and $CO_2$ of the catalysts have decreased in relation to the support, indicating that the reduction of surface oxygen groups (reactions 1 and 2) may be promoted by the metallic phase.

b) Adsorption on the carbon surface, especially on surface sites of the support formed upon the decomposition or reduction of oxygen complexes:

$$C^* \text{ (sup)} + 2H \rightarrow {}^*CH_2 \tag{6}$$

c) Hydrogasification reaction- Table 3 showed that methane production was generally higher for the catalysts compared to the support. Besides a new methane peak was observed around 660 K, as can be seen in Figure 4. The peak temperature is higher than the hydrogen consumption peak (around 500 K), indicating that hydrogen species have a certain residence time on the support. One possibility is the formation of ${}^*CH_2$ species (reaction 6), which could then react with other hydrogen species, producing methane at temperatures near 660 K:

$$^*CH_2 + 2H \rightarrow CH_4 \tag{7}$$
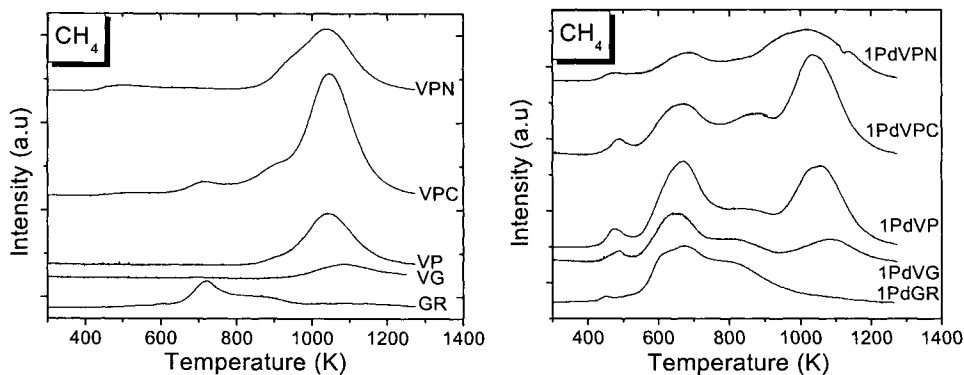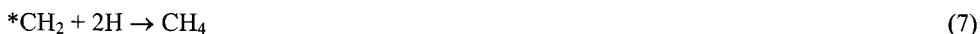


Fig. 4 – Production of $CH_4$ during TPR of supports and catalysts

Some authors postulated that hydrogen atoms spilt over from metallic particles could hydrogasify the most reactive surface carbon atoms that were left in a highly unsaturated state due to thermal removal of surface oxygen groups, yielding ${}^*CH_2$ in a first step and subsequently methane [4,12,13]. However, the fact that the sample 1PdVPN showed much more surface oxygen groups than the others and did not show a higher methane production

indicates that the possibility (a) and (b) should occur in a higher extent or else species $*CH_2$ formed by reaction (6) remain on the support without forming methane.

Comparing the nature of supports, the catalyst 1PdGR showed smaller $H_2/Pd$ ratio. This might be explained by the much lower amount of surface oxygen groups on this sample as observed by TPDHe, decreasing rates of reactions (1) and (2). This way, less active carbon atoms would be formed, decreasing rates of reactions (6) and (7). The catalyst 1PdVG showed a similar $H_2/Pd$ ratio than 1PdVP catalyst. This result may be explained by a compensation effect: although support VG has a higher amount of surface oxygen groups, especially the ones that decompose as CO, these groups are more stable than the ones in support VP which could decrease the rate of its reduction and the formation of active carbon atoms that would yield $*CH_2$ (reaction 6) or methane (reaction 7).

## 4. CONCLUSIONS

A phenomenon of spillover was observed during the reduction of graphite and activated carbon supported palladium catalysts based on an extra consumption of hydrogen measured by mass spectroscopy, as well as a decrease in the amount of CO and $CO_2$ desorbed and an increase in the amount of $CH_4$ produced compared to the supports. The hydrogen spilt over to the support could stay adsorbed on carbon surface, promote the hydrogasification reaction (producing methane) or be used to reduce oxygen groups presented on the carbon surface. It was showed a relation between the amount of surface oxygen groups and their stability with the intensity of spillover.

## REFERENCES

1. E. Auer, A. Freund, J. Pietsch et al., Appl. Catal. A: Gen. 173 (1998), 259.
2. D.J. Suh, T.J. Park and S.K. Ihm, Carbon, 31 (1993) 427.
3. S.T. Srinivas and P.K. Rao, J. Catal., 148 (1994), 470.
4. F. Coloma, A. Sepúlveda-Escribano, J.L.G Fierro and F. Rodríguez-Reinoso, Appl. Catal. A: Gen., 150 (1997) 165.
5. P. Albers, R. Burmeister, K. Seibold, G. Prescher, S.F. Parker and D.K. Ross, J. Catal., 181 (1999) 145.
6. M. Boudart, A.W.Aldag and M.A.Vannice, J. Catal.,18 (1970) 46.
7. S. Brunaer, P.H. Emmet and E. Teller, J. Am. Chem. Soc., 60 (1938) 309.
8. M.M. Dubinin, J. Colloid Interface Sci., 23 (1967) 487.
9. E.P. Barret, L.S. Jayner and P.P. Halenda, J. Am. Chem. Soc., 73 (1951) 373.
10. J.L. Figueiredo, M.F.R. Pereira, M.M.A. Freitas and J.J.M. Órfão, Carbon, 37 (1999) 1379.
11. A. Sepúlveda-Escribano, F. Coloma and and F. Rodríguez-Reinoso, Appl. Catal. A: Gen., 173 (1998) 247.
12. J.A. Menéndez, L.R. Radovic, B. Xia and J. Phillips, J. Phys. Chem., 100 (1996) 17243.
13. E. Baumgarten and L. Maschke, Appl. Catal. A:Gen., 202 (2000) 171.

# Direct FTIR Insight in the Spillover Hydrogen Reactivity: CO and NO Chemisorbed on Ru NaY Zeolite

Ruth Leibsohn Martins, Maria Auxiliadora S. Baldanza, Marcos Teixeira Lima, Martin Schmal

NUCAT/PEQ/COPPE, Universidade Federal do Rio de Janeiro, C.P. 68502, 21945-970, Rio de Janeiro, Brazil

The reactivity of Hydrogen species, provided by hydrogen backspillover, was detected, in absence of $H_2$ gas, by means of the different species of CO and NO chemisorbed on reduced RuNaY catalyst. Irreversible CO adsorption gives three bands observed at 2145, 2088 and 2031 $cm^{-1}$ which were assigned as CO bonded to oxidized Ru species (the first two bands) and to CO linearly bonded to $Ru^\circ$ (last band). After activation by heating Hydrogen reactive species were able to reduce the highly dispersed oxidized Ru particles (formed by oxidative disruption of $Ru^\circ$ clusters when the reduced surface was exposed to CO atmosphere), originating $Ru^\circ$ particles with lower dispersion than the catalyst that was only reduced. These new reduced particles readsorbed CO in the bridge form instead of the linear one, as expected on well dispersed $Ru^\circ$ particles. Also, NO adsorption gives bands at 1938 and 1881, assigned to NO adsorption on oxidized Ru and reduced particles, respectively. Hydrogen reactive species activated by heating can reduce the Ru oxidized particles (formed by dissociative adsorption of NO when this gas was exposed to the reduced catalyst) resulting in more NO adsorbed species on reduced $Ru^\circ$ particles.

## 1. INTRODUCTION

The phenomenon of spillover, first detected by Kuriacose in 1957 (1) with Pt promoted decomposition of $GeH_4$ on Ge film, was officially defined as involving the transportation of an active specie, which is adsorbed or formed on a phase, onto another phase that does not adsorb or form the species under the same conditions.

The most important species related with spillover are, unquestionably, dissociated hydrogen and oxygen but other species like nitrogen, oxygenated compounds (CO, NO, NCO, $CH_3O$, etc) are suitable to undergo this phenomenon.

With respect to the nature of hydrogen spillover species, the vast majority of the literature published concludes in favor of the migration of a monoatomic neutral particle, but charged and tri atomic neutral species were also advocated.

By interpreting a wide variety of experimental results Roland and Roessner (2), concluded that the nature of the hydrogen spillover species (H*) can be described by considering their electronic interaction with the solid. The H* species functions as an electron donors located on surface of the support. Its occupation with electrons corresponds to the ratio of weakly chemisorbed (neutral) and strong chemisorbed (ionized) hydrogen species.

Hydrogen atoms and $H^+$ ions coexist at the surface and the ratio of these species is determined by the electronic properties of the uniform system adsorbate/solid. In general, the experiments published in the hydrogen spillover field were done in the presence of $H_2$ in the gas phase.

In a previous work (3) the forms of irreversible chemisorbed CO on well dispersed Ru catalysts supported on Na, Ca and Ultrastable Y zeolite were investigated by Infrared Spectroscopy. This analytical tool showed to provide an excellent means to investigate support-metal interaction effects, oxidation state of surface metal atoms, nature of CO bonding species and metal particle size effects. In the present work "in situ" Infrared experiments were conducted in Ru/ NaY catalyst, by using the hydrogen spillover species stored in the support when the catalyst was reduced in hydrogen flow at 723K per one hour followed by evacuation $10^{-5}$ Torr at the same time and temperature. The reactivity of this stored hydrogen species was evaluated by monitoring the species formed at the catalyst surface when CO and NO were chemisorbed.

## 2. EXPERIMENTAL

NaY Zeolite supported Ru catalyst 1% (w/wt) was prepared by ion exchange with aqueous solution of Ru $(NH_3)_6 Cl_3$. The infrared measurements were obtained with a Fourier Transform spectrometer Perkin Elmer 2000 on self supported wafers (9.8 mg cm$^{-2}$) by using a Pyrex cell with $CaF_2$ windows. During sample pretreatment and gas adsorption, the cell was attached to a vacuum glass system. The spectral domain was between 4000 and 1000 cm$^{-1}$ with a 4 cm$^{-1}$ resolution.

The ion exchanged catalysts were decomposed "in situ" under vacuum at 723K, and then reduced with pure hydrogen at the same temperature, for one hour, followed by evacuation up to $10^{-5}$ Torr at same temperature and time. After cooled to room temperature, the infrared spectrum was recorded and used as background for the other experiments with irreversible adsorbed CO and NO. The spectrum in the hydroxyl region was obtained by rationing the spectra of reduced samples and the background of sample compartment.

Adsorption studies were conducted by exposing the reduced wafers to 30 Torr of CO or 7.6 Torr of NO at room temperature for 30 minutes followed by evacuation to $10^{-5}$ Torr.

## 3. RESULTS

Infrared spectrum of reduced RuNaY, in the hydroxyl region is shown in figure 1. After reduction, structural hydroxyl bands on zeolites appeared and were located at large mainly) and small cavities, allowing an indication of the cation positions susceptible to reduction.

### 3.2. CO adsorption

Irreversible adsorption of CO on the reduced samples as well as the thermal stability of adsorbed species produce the spectra shown in figures 2. Three bands are observed at 2145, 2088 and 2031 cm$^{-1}$. The intensities of those bands were diminished as the temperature of the wafer was increased and a new band appeared around 1843-1881 cm$^{-1}$ up to 573K when its intensity was greater. Also, this absorption band moves to higher wavelength as its intensity increased. After exposing that surface t o $O_2$ atmosphere (30 Torr) a slight decrease in 1881
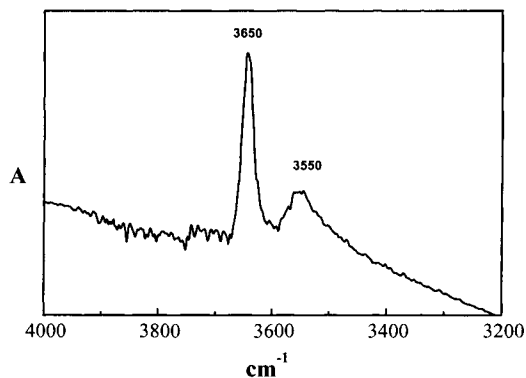
Figure.1-hydroxyl region of reduced RuNaY.
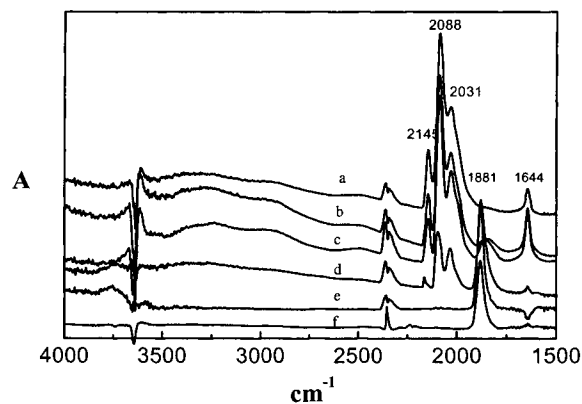


Figure 2 - a- Reduced Ru NaY zeolite: **a**-irreversible CO adsorption at 298 K. Desorption at **b**-323 K, **c**-373K, **d**-473K and **e**-573 K; **f**- after exposure to 30 Torr of $O_2$ at 298K, 30 minutes.

$cm^{-1}$ band was observed and, at the same time, the appearance of a band at 2350 $cm^{-1}$ suggest some $CO_2$ formation.

The next figure corresponds to an experiment where the reduced RuNaY was cooled to room temperature and, under vacuum, the temperature was risen up to 573 K when the wafer was then exposed to 30 Torr of CO. The spectrum **a** in Figure 3 shows the three bands of chemisorbed CO, as described before, and a very small band at 1852 $cm^{-1}$. When the wafer was cooled to room temperature and exposed again to 30 Torr of CO, (spectrum **b** in figure 3) the three bands increased their intensities to the level shown in figure 2 and decrease to the level of spectra **a** in figure 3 when heated again to 573K.
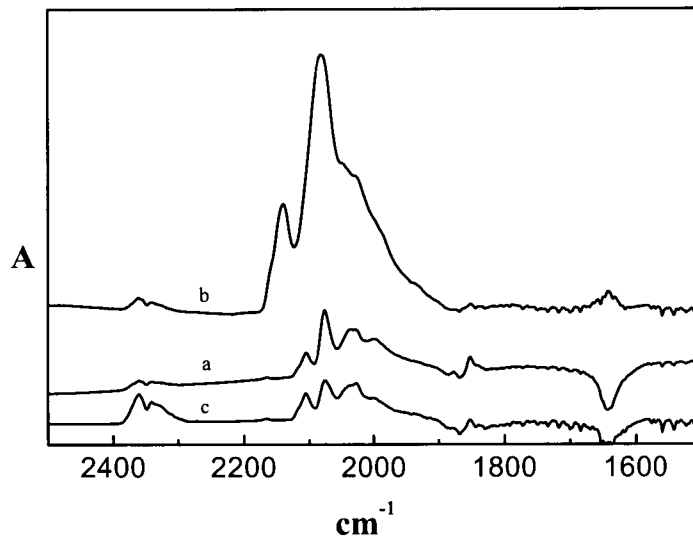
Figure 3 - Reduced RuNaY: a-CO chemisorbed at 573 K, b- CO chemisorbed at 298K, c- b heated to 573K.

## 3.2. NO adsorption

The exposure of RuNaY to NO resulted in the appearance of bands at 1938 and 1889 $cm^{-1}$, which were stable up to 473K. Above this temperature, only the 1889 $cm^{-1}$ band was preserved with its intensity increased. Bands at 1417 and 1270 $cm^{-1}$ also appeared, the latter one being more thermally stable and becoming more intense as temperature was raised.

It is interesting to note that after the exposure to NO, the reduced sample exhibit more structural hydroxyls than before. Bands absorbing at 3648 and 3540cm $^{-1}$ appeared at the same time as the other NO species chemisorbed on the surface.

## 4. DISCUSSION

The major findings regarding the FTIR study of CO and NO adsorption on RuNaY can be summarized as follows:

### 4.1. CO adsorption on Ru reduced catalyst

At least three major species, absorbing at 2145, 2068 and 2031 $cm^{-1}$ can be observed after irreversible adsorbed CO on reduced RuNaY catalyst. Goodwin (4) observed three main species after 155 Torr of CO was exposed to reduced RuNaY catalyst,: species A, absorbing at 2156, 2100, and perhaps a shoulder at 2075 $cm^{-1}$, which corresponds to CO multiply
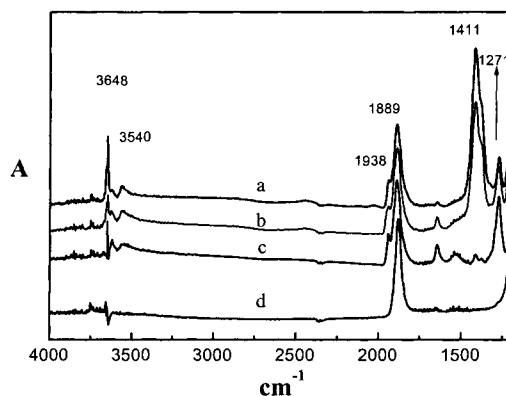
Figure 4 - **a**-NO adsorption on reduced RuNaY; desorption at **b**-373K, **c**-473K and **d**-573 K.

bound to an oxidized species of Ru in strong interaction with the support, species B having at least a band at 2075 cm$^{-1}$, which corresponds to a Ru carbonyl, perhaps Ru$_n$ (CO)$_{m-n}$, where n is greater than 3 and m is less than 4, that is, a carbonyl cluster compound with the Ru atoms highly coordinated with CO molecules, and species C having its main band at 2045 cm$^{-1}$ and possibly presenting bands at 2134 and 1934 cm$^{-1}$, attributed to the multiple adsorption of CO on the Ru surface atoms in a reduced metal surface. Goodwin related these three different species to different kinds of Ru atoms, the first being highly dispersed, probably atomically, the second existing in a cluster of Ru atoms which after adsorption of CO can form a carbonyl cluster, and the third existing on the surface of Ru metal particle with a diameter equal or greater than 1.0 nm. Prior to Goodwin, Dalla Betta (5) showed the effect of Ru particle size on the spectrum of CO adsorbed on alumina-supported Ru catalyst. For particles with a diameter of 90 Å only a single band at 2028 cm$^{-1}$ was observed while for particles of 60 Å and smaller, three bands in the vicinity of 2140, 2080 and 2040 cm$^{-1}$ were noted. The exact positions and relative intensities of the three bands changed with decreasing particle size. The low frequency band was assigned to CO adsorbed on low-index planes of Ru, while the two higher frequency bands were associated with CO adsorbed on low coordination edge and corner metal atoms. These band assignments however were questioned by Brown and Gonzalez (6). Based on their own experiments on silica-supported Ru, they observed that CO adsorption on reduced sample produced a strong band at 2030 cm$^{-1}$ and weak bands at 2150 and 2080 cm$^{-1}$, whereas CO adsorbed on an oxidized sample produced a strong band at 2080 cm$^{-1}$ and medium intensity bands at 2135 and 2030 cm$^{-1}$. The authors assigned the low frequency band to Ru-CO, while the high and medium frequency bands were assigned to CO adsorbed on a surface oxide and CO adsorbed on a Ru atom influenced by a nearby oxygen atom, respectively. However, Davydov and Bell (7) showed that CO adsorbed on fully reduced silica-supported sample produced a single band at 2040 cm$^{-1}$ which they assigned to linearly bonded CO. Oxidation of Ru and subsequent adsorption of CO produced bands at 2130 and 2070 cm$^{-1}$ which were assigned to the symmetric and asymmetric stretches of two CO molecules bonded to a single oxidized Ru site. While studying the interaction of CO with

alumina-supported Ru, Solymosi et al. (8) observed the oxidative disruption of Ru cluster as indicated by slow transformation of the band at 2020-2040 cm$^{-1}$ due to CO linearly bonded to Ru crystallites into bands at 2074 and 2140 cm$^{-1}$ due to $Ru^{n+}(CO)_2$ species, where n is equal to 1-3. The development of the medium and high frequency bands was favored by water and was almost not influenced by hydrogen and the authors suggested the involvement of OH groups from the support in the formation of those bands. In the present work, we also observe the consumption of zeolite OH structural band when CO was exposed to the reduced RuNaY catalyst and the possibility of the oxidative disruption mechanism with the contribution of OH group was considered. The intensities of the three main bands observed in the present work diminished as the temperature of the wafer was increased while a new band appeared around 1843-1881 up to 573K, when its intensity was greater. Furthermore this absorption band moved to higher wavelength as its intensity increased and the hypothesis of readsorption of desorbed CO species on a new reduced surface site, in a bridge form on two atoms of $Ru^o$, was proposed, the metal being in a different dispersion state as compared to the reduced catalyst. The new reduced particles were formed by reactive hydrogen species provided by back-spillover of hydrogen from the support, which was stored during the catalyst reduction. These new reduced sites could then readsorb the CO which desorbed from different oxidized Ru species and the observed shift toward higher wavelength is explained by the CO dipole-dipole coupling, as the CO coverage increased. After exposure of this surface to 30 Torr of $O_2$, a slight decrease in the band at 1881 cm$^{-1}$ band was observed with OH consumption and, at the same time, the appearance of a band at 2350 cm$^{-1}$ suggests $CO_2$ formation. Another consequence of hydrogen back-spillover was the water formation shown in figure 2 by the appearance of the 1644 cm$^{-1}$ band with a maximum intensity at 373K. The following experiment, which was shown in figure 3, supported the hypothesis of the necessity of hydrogen back-spillover species for the second reduced stage of $Ru^o$ and CO chemisorption on bridge form. After CO adsorption at 573K on a surface free from hydrogen back-spillover species (achieved by previous desorption at this temperature and vacuum of $10^{-5}$ Torr), no more new reduced sites were formed and the only species observed were the three ones observed in the reduced sample, but with lower intensities. If the high and medium frequency bands belong to different kinds of adsorption sites or correspond to the symmetric and asymmetric vibration of $Ru^{n+}(CO)_2$ species, it would become clear by the observation of the spectra taken at different temperature. The species desorbed at 473K and 573K showed that the possibility of the high and medium frequency bands belonging to the same adsorption site, symmetric and asymmetric stretching of $Ru^{n+}(CO)_2$, as proposed by Solymosi (9), can be ruled out, in the present case, as the ratio of the intensities of these two bands varies along the different desorption stages. As a matter of fact, the high frequency band contains in its envelope more than one band, absorbing at 2177 and 2144 cm$^{-1}$ as it became clear in the spectra of CO desorbed at 573 K. Based on CO desorption spectra, it can be suggested that the high and medium absorption bands belong to different sites of oxidized Ru, the first one being in close interaction with the support. These sites were formed probably by the oxidative disruption of Ru cluster The involvement of zeolite structural hydroxyls as observed by the presence of their negative bands on the spectra of Figure 2 will be discussed later.

### 4.2. NO adsorption Ru reduced catalyst

Bands at 1938 and 1889 cm$^{-1}$ as shown in figure 4, appeared after exposure of the reduced sample to NO and was attributed to NO chemisorbed on $Ru^{n+}$ and $Ru^o$ respectively.

The origin of oxidized Ru sites was explained by the partial dissociative adsorption of NO on the metal particles, resulting in some metal oxidation. Davydov and Bell (7), however, by studying NO adsorption on fully reduced Ru supported on silica, observed two bands at 1810 and 1860-1880 cm$^{-1}$ which were assigned as NO adsorbed on partially and more fully oxidized Ru sites. The differences in wavelength of the bands observed in the present case, when NO was adsorbed on RuNaY, was attributed to Ru-zeolite interaction involving negatively charged framework oxygens, resulting in NO absorptions in higher frequencies as the Ru-N bond strength decreased, and the N-O bond strength increased. Above 473K only NO chemisorbed on Ru$^{o}$ was observed. The increase in the intensity of this band was attributed to the reduction of oxidized Ru species by reactive hydrogen provided by back-spillover and, at the same time, readsorption of NO desorbed from those oxidized species. It is interesting to note that after exposed to NO, the reduced sample of RuNaY exhibited more structural hydroxyls than before exposure (reduced state), probably by the migration of active species of hydrogen provided by back-spillover. Bands at 3648 and 3540 cm$^{-1}$ appeared at the same time as the other NO species chemisorbed on the surface. It is probable that these hydroxyl bands also appeared in the case of the reduced sample exposed to CO, but were consumed when the oxidative disruption of Ru clusters happened. NO also adsorbs on zeolite matrix with bands at 1417 and 1270cm$^{-1}$. These bands correspond to nitrate and nitrite species, the latter one being more thermally stable and becoming more intense up to 573 K, and it was probably favored by the presence of a reductive atmosphere provided by reactive species of hydrogen from back-spillover which allowed that desorbed nitrate species were readsorbed as nitrite species.

## 5. CONCLUSIONS

Three major species, absorbing at 2145, 2068 and 2031 cm$^{-1}$ can be observed after CO being irreversibly adsorbed on reduced RuNaY catalyst. They were assigned, as proposed by Goodwin (4), as species A, which correspond to CO multiply bonded to oxidized Ru species with strong interaction with oxygen atoms of the support, species B, a carbonyl cluster compound with Ru atoms highly coordinated with CO molecules, and species C, which correspond to CO linearly bonded to Ru$^{o}$ particles, respectively. The possibility of the high and medium frequency bands belonging to the same site, being the symmetric and asymmetric vibration of Ru$^{n+}$(CO)$_2$ species as proposed by Davydov and Bell (7) and latter by Solymosi and Raskó (8), can be ruled out, in the present case, as the ratio of the intensities of these two bands varies along the different desorption stages. However, as proposed by the authors latter mentioned, those sites are believed to formed by the oxidative disruption of Ru clusters with the involvement of zeolite structural hydroxyls, formed when the catalyst was reduced. These three bands were not thermally stable and desorbed as the temperature of the wafer increased while a new band appeared around 1843-1881 up to 573K, when its intensity was greater. It was proposed that this new band corresponded to CO bonded in a bridge form on two atoms of Ru$^{o}$, the metal being in a different dispersion state as compared to the reduced catalyst. The new reduced particles were formed by reactive hydrogen species provided by back-spillover of hydrogen from the support, which was stored during the catalyst reduction.

The NO adsorption on RuNaY catalyst resulted in the appearance of bands at 1938 and 1889 cm$^{-1}$ which were attributed to NO chemisorbed on Ru$^{n+}$ and Ru$^{o}$ respectively. The origin of Ru oxidized sites was explained by the partial dissociative adsorption of NO on the metal particles, resulting in some metal oxidation. Above 473K only NO chemisorbed on Ru$^{o}$

306

was observed. At the same time as bands related to adsorbed NO were formed, new hydroxyl bands at 3648 and 3540 were observed and their appearance was related to the interaction of the hydrogen back spillover species with Ru particles, which remained in oxidized state even after the catalyst reduction.

Finally, the reactivity of Hydrogen species, provided by hydrogen backspillover, was then detected, in absence of $H_2$ gas, by means of the different species of CO and NO chemisorbed on reduced RuNaY catalyst. After activation by heating, Hydrogen reactive species were able to reduce the highly dispersed Ru oxidized particles (formed by oxidative disruption of $Ru^o$ clusters when the reduced surface was exposed to CO atmosphere), giving $Ru^o$ particles with lower dispersion than observed for the reduced catalyst. These new reduced particles readsorbed CO in the bridge form instead of the linear one, proper on well dispersed $Ru^o$ particles. Experiment, in which Hydrogen spillover species were evacuated prior the CO adsorption, supports the hypothesis that their presence is required for this second reduced stage of $Ru^o$ and CO chemisorption on bridge form. Also, Hydrogen reactive species activated by heating can reduce the Ru oxidized particles (provided by dissociative adsorption of NO when this gas was exposed to the reduced catalyst) resulting in more NO adsorbed species on reduced $Ru^o$ particles.

## REFERENCES

1. J. Kuriacose, Indian J. Chem., 5 (1957) 646.
2. U. Roland, F. Roessner, in "Spillover and Migration of Surface Species on Catalyst ( Can Li, Qin Xin edit.) Elsevier, Amsterdam 1997, p.191-200.
3. R. L. Martins, C. Barbosa, E. F. Souza-Aguiar, XV Simposio Iberamericano de Catalisis,.
4. J. G. Goodwin Jr., C. Naccache, J. Catal., 64 (1980) 482.
5. R.A. Dalla Betta, J. Phys. Chem., 79 (1975) 2519.
6. M.F. B rown and R.D. Gonzalez, J. Phys. Chem., 80 (1976) 1731.
7. A. A. Davydov, A.T. Bell, J. Catal., 49 (1977) 332.
8. F. Solymosi, J. Raskó, J.Catal., 15 (1989) 107.

# DUAL-FUNCTION CATALYSTS FOR RING OPENING OF CYCLIC COMPOUNDS

L.M. Kustov[a], A.Yu. Stakheev[a], T.V. Vasina[a], O.V. Masloboishchikova[a], E.G. Khelkovskaya-Sergeeva[a], and P. Zeuthen[b]

[a]N.D. Zelinsky Institute of Organic Chemistry, Russian Academy of Sciences, Moscow, 117334 Russia, e-mail: LMK@IOC.AC.RU

[b]Haldor Topsoe AS, Lyngby, DK-2800, Denmark

A series of Ni-containing catalysts were studied in the conversion of cyclohexane and decaline+n-octane mixture. Comparison of the performance of the catalyst bearing mainly metal active sites with acidic HY zeolite and the catalysts containing both functions revealed the importance of the acidic component for achieving high catalyst efficiency. Dual-function systems containing a metal function and strong acidity exhibited the best performance. It is shown that the strong acidity is particularly important for the ring opening of heavier naphthenes (decaline). Separation of these functions by using mixtures of an acid catalyst with a metal-containing system revealed the effect of spillover of reactive species in the course of the hydrocarbon conversion.

## 1. INTRODUCTION

The recent more stringent legislation impose severe requirements on motor fuels, including gasoline and diesel. These requirements limit the level of sulfur and aromatics, as well as other pollutants, carcinogenic agents, ozone destroying compounds, and soot. The improvement of the quality of the fuel is related to the enhancement of the octane number of gasoline (the content of branched paraffins) and cetane number of diesel (the content of normal paraffins). The challenge would be the improvement of the cetane number of diesel via ring opening of cycloparaffins formed upon hydrogenation of the aromatic compounds present in the fuel. However, the information on ring opening of naphthenes other than methylcyclopentane, such as cyclohexane and higher cyclic compounds on zeolite catalysts is scarce.

Earlier we studied ring opening of cyclohexane on metal-oxide catalysts [1]. The dramatic effect of the nature of both metal (Rh, Pt, Ru) and carrier ($Al_2O_3$, $Al_2O_3$-F, $La_2O_3$-$ZrO_2$, $SiO_2$ etc.) on the activity and selectivity in ring opening of cyclohexane was revealed.

Kubicka and Okal [2] showed that ring opening is a bifunctional reaction that requires both Broensted acid sites and metal (presumably electron-deficient) microparticles with well-defined properties. Ring opening activity was also reported for the conversion of toluene on NiHY zeolites [3]. It was shown that the activity enhances

with increasing Ni content. Ring opening of cyclic compounds was investigated in [4, 5]. The contribution of ring opening was found to increase with increasing reaction temperature, while that of skeletal isomerization diminished.

The most comprehensive analysis of the available data on various reactions involving hydrogen (ring opening, hydrogenation, hydrogenolysis) was done in the monograph by G.A.Somorjai [6]. However, this analysis covers basically ring opening of cyclopropane and cyclopentane derivatives and benzene. Only a short table illustrating the data on cyclohexane hydrogenolysis is presented.

The most interesting and commercially viable catalytic system based on 1%Pt/H-Beta zeolite was disclosed in the patent assigned to Mobil [7]. This catalyst exhibits rather high activity in ring opening of $C_6$ cyclic compounds and is used in a combination with the isomerization catalyst to upgrade the $C_6$ fraction. In this case, a 1:3 mixture of normal and isoparaffins was formed at the conversion of ~80% at 230-270°C under high-pressure conditions. Another catalyst proposed by the same authors for ring opening of $C_6$ cyclic compounds comprises an acidic $Pt/WO_3/ZrO_2$ system [8]. The performance of this catalyst is similar to that of Pt/H-Beta zeolite, but the reaction conditions are different. Two patents assigned to Exxon appeared [9,10], where new Ir-containing zeolite USY or alumina-based catalysts were shown to possess high activity and selectivity in ring opening of alkylcyclohexanes and alkylcyclopentanes with an aliphatic side chain containing at least 3 carbon atoms (propyl, butyl etc.), in particular, n-butylcyclohexane, as well as mixtures close in the composition to the real diesel fuel.

The main purpose of this paper was to study the role of metal and acid components of the catalyst in ring-opening transformation of lighter (cyclohexane) and heavier (decaline) naphthenes by comparison of the catalytic performance of the "hybrid" catalysts containing both functions and the individual components of the hybrid catalysts. HY zeolite was used as a catalyst bearing the acid function, and the Ni-W/$Al_2O_3$ catalyst, which showed promising results in preliminary tests was chosen as a catalyst with mainly metal function we used. "Hybrid" catalysts were prepared by mechanically mixing these components. For comparison, the catalyst prepared by introduction of Ni and W directly into HY zeolite was also studied.

## 2. EXPERIMENTAL

Various Ni-W-containing catalysts were prepared in two steps. The first step was the impregnation of the appropriate carrier ($Al_2O_3$ or HY) with an aqueous solution of nickel nitrate followed by drying and calcination in an air flow. After that the samples were impregnated with an aqueous solution of ammonium tungstate followed by calcination in air and reduction at 350-500°C in a hydrogen flow. The catalysts contained 3 wt. % of nickel and 6 wt. % of tungsten. The hybrid systems were prepared by mechanically mixing the metal-promoted oxide (Ni-W/$Al_2O_3$) and acidic components (HY zeolite). The mass ratio of the components in the mixture was 2.5 : 1. The resulting catalysts were mixed with an appropriate amount of $Al_2O_3$ for maintaning the constant catalyst volume.

Catalytic tests with cyclohexane and decaline + n-octane mixtures were carried out in a plug-flow unit at T = 280–440°C, P = 2.2–2.4 MPa, $H_2$ : hydrocarbon ratio of 10 : 1 (vol), LHSV = 1.7–2.1 $h^{-1}$. The catalyst loading was 2.1 g.

The catalysts were characterized by X-ray photoelectron spectroscopy using an XSAM-800 spectrometer (Kratos) with Al K $\alpha_{1,2}$ radiation for spectra excitation. A special home-made external reactor was used for studying the reduced catalysts. The catalysts were reduced in flowing hydrogen at 400-550°C and transferred into an analytical chamber without contact with air. The spectra of Ni $2p_{3/2}$ and W $4f$ lines were analyzed by a conventional peak synthesis procedure using Gaussian functions.

## 3. RESULTS AND DISCUSSION
### 3.1. XPS characterization

XPS data and the results of curve fitting analysis of the $Ni$-$W/Al_2O_3$ and Ni-W/HY samples after reduction are presented in Fig. 1. Reduction of the Ni-W/HY catalyst at 450°C results in almost complete reduction of Ni, while a significant fraction of Ni remains unreduced in the $Ni$-$W/Al_2O_3$ catalyst. The reduction degree of nickel in this catalyst does not exceed 30%. Analogous behavior was revealed for tungsten. In the Ni-W/HY catalyst, ~20% of tungsten is reduced at 450°C to metal and $W^{4+}$ state. In $Ni$-$W/Al_2O_3$, the reduction treatment does not change the initial $W^{6+}$ valence state.

The most plausible reason of such a low reducibility of Ni in the $Ni$-$W/Al_2O_3$ catalyst is the formation of a stable aluminate-like phase. The presence of Ni aluminate is clearly seen in XPS spectra due to the shift of the Ni $2p_{3/2}$ line toward higher binding energy by c.a. 2 eV with respect to the NiO signal. It is reasonable to assume that the
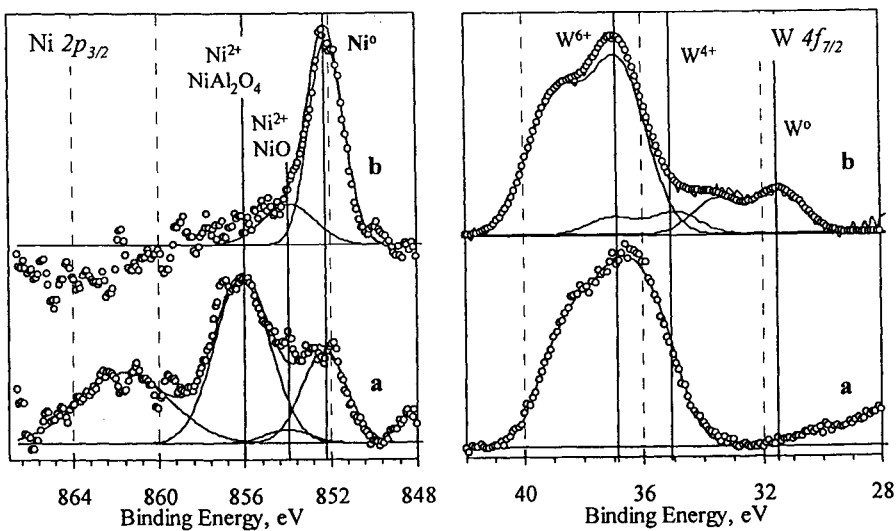


Fig. 1.   Ni $2p_{3/2}$ and W $4f7/2$ lines in $Ni$-$W/Al_2O_3$ (a) and Ni-W/HY (b) catalysts after reduction at 450°C in flowing hydrogen

formation of a similar stable surface compound is responsible for the low reducibility of tungsten in Ni-W/Al$_2$O$_3$. Broadening of the W 4$f$ line reveals the presence of such a surface compound. Unlike Ni-W/Al$_2$O$_3$, the reducibility of Ni and W in Ni-W/Al$_2$O$_3$ is markedly higher, which is indicative of weaker interaction between the support and metal precursors. Noteworthy that the positions of the Ni$^\circ$ 2$p_{3/2}$ lines in both samples are the same (~852.1 eV) and close to that found for the reference Ni foil sample. This indicates that the metal-support interaction in these samples is not pronounced. Presumably, nickel forms relatively large metal particles (>5 nm).

### 3.2. Cyclohexane conversion

Temperature dependencies of the overall cyclohexane conversion and the product distribution at 420°C over catalysts under study are shown in Fig. 2. Cyclohexane conversion over the Ni-W/Al$_2$O$_3$ catalyst starts at 350-360°C and approaches 90% at 430°C. The reaction products consist mainly of benzene (>60%), which points to the pronounced dehydrogenation activity of the catalyst, and methylcyclopentane (~30%). The C$_6$ fraction of the products of ring-opening is ~5%. Their formation over Ni-W/Al$_2$O$_3$ can proceed through MCP formation over acid sites on alumina followed by MCP ring-opening over metal sites. Note that the observed ratio of iso-C$_6$H$_{14}$/n-C$_6$H$_{14}$ is close to 1.5–2, which is typical for MCP ring-opening over metal sites.
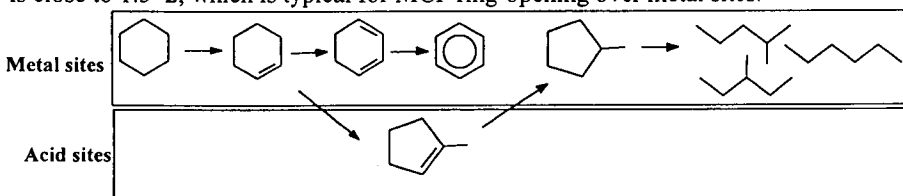


The overall C$_6$H$_{12}$ conversion on HY is lower and does not exceed 30%. The main reaction products (>75%) are methylcyclopentane (MCP) and the hydrocarbons with lower molecular weight. The product composition points to the pronounced cracking and isomerization activity of this catalyst. The main reaction route over this catalyst seems to be the isomerization of cyclohexane into MCP followed by its cracking. The observed ratio of iso-C$_6$H$_{14}$/n-C$_6$H$_{14}$ over this catalyst approaches 2.5–3, which is far from statistically expected ratio 1.5 and indicates the pronounced isomerization of C$_6$ hydrocarbons. The yield of the C$_6$ fraction of the products of ring-opening is also low for this catalyst and does not exceed ~5%.
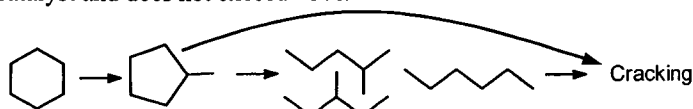


The mechanical mixture of these two catalysts demonstrates the behavior that cannot be explained by simple superposition of the reaction patterns. Thus, the activity of the mechanical mixture is markedly higher than the activity of the components. The conversion curve is shifted toward lower temperature by 50-60°C. Moreover, there is almost no benzene in the reaction products on the mixed catalyst. The yield of C$_1$-C$_5$ cracking products is higher over the mixed catalyst (~36%) compared to HY (~16%).
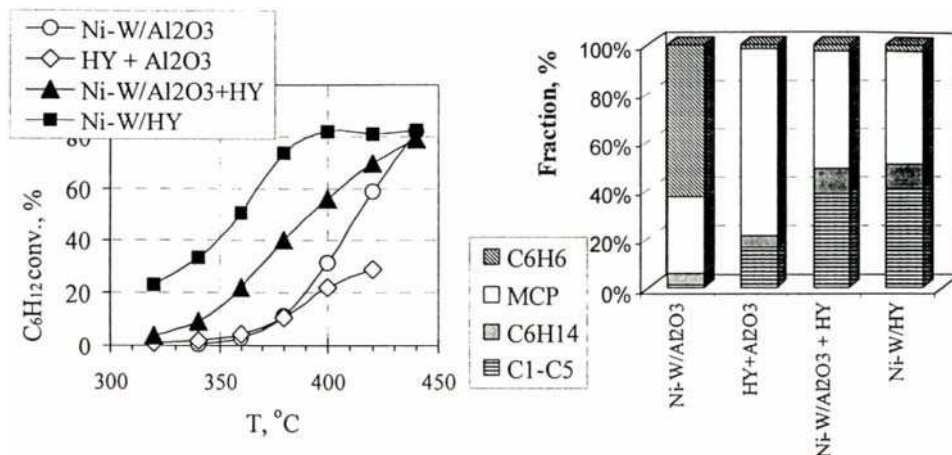
Fig. 2. Overall cyclohexane conversion (a) and product distribution at 420°C (b) for different catalysts

The most important fact is that the $C_6$ fraction of the ring-opening products markedly increased (from ~5% for individual components to >10% for the mixed catalyst).

Taking into account the pronounced synergy between metal and acid active sites in the mixed catalyst, it is of interest to compare the behavior of the mixed Ni-W/Al₂O₃ + HY catalyst and Ni-W/HY. In the first catalyst, the metal and active acid sites are spatially separated, while in the latter sample, they are located closer to each other. As can bee seen from Fig. 2, the overall conversion is markedly higher for Ni-W/HY: the conversion curve is shifted toward lower temperatures by ~60°C. This increase in the conversion may be attributed to a shorter distance between acid and metal sites in this catalyst, as well as to a higher degree of Ni reduction and possible formation of a Ni-W alloy (see section 3.1). Also, we should take into account that the mixed catalyst contains twice less of nickel and acid sites as compared to the Ni-W/HY catalyst. However, the composition of the reaction products is very similar for both catalysts; therefore, the reaction mechanism seems to be the same for both catalysts, and the spatial separation of the active sites is not a critical factor for the reaction mechanism.

Thus, the data obtained reveal the pronounced synergy between acid and metal active sites in the catalyst prepared by mechanically mixing the components or by direct impregnation of the zeolite with metal salts. The important observation is almost complete disappearance of benzene in the reaction products when the acid component is added to the metallic component in the hybrid catalyst. The most plausible explanation of this effect is based on the conversion of the intermediates of $C_6H_{12}$ dehydrogenation, which proceeds on the metal component, over acid sites of HY. For instance, it was shown that cyclohexene is the intermediate product of cyclohexane dehydrogenation [11]. We can suggest that over Ni-W/Al₂O₃+HY and Ni-W/HY, which contain significant amounts of strong acid sites, highly reactive intermediates undergo rapid conversion over these acid sites. On the one hand, this process explains the disappearance of benzene from the reaction products over the mixed catalyst. On

the other hand, due to high reactivity of the intermediates containing C=C bonds, they are rapidly converted over acid sites, thus increasing the fraction of the hydrogenolysis products: $C_1$-$C_5$ and $C_6H_{14}$.

The observed increase in the $C_6H_{12}$ conversion over hybrid catalysts can be attributed to two effects:

(1)The reaction rate over metal sites may be increased due to a decrease in the surface concentration of $C_6H_6$ and $C_6H_8$, which suppresses the dehydrogenation rate by strong adsorption [12].

(2) The reaction rate may be enhanced by supply of atomic hydrogen activated over metal sites toward acid sites by the spillover mechanism. The following reaction scheme summarizes the processes responsible for the observed reaction enhancement over the hybrid catalyst.
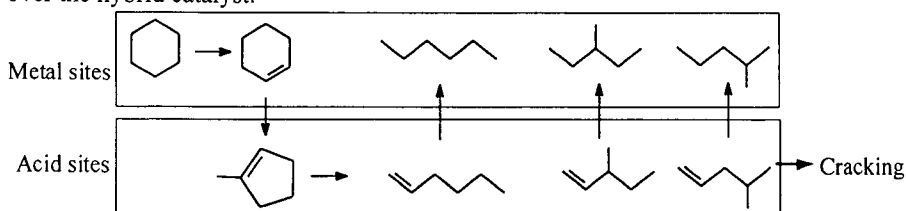


Additional evidence for the hydrogen spillover was obtained by comparing the variations of the catalyst activity with time on stream (Fig. 3). While the overall conversion on HY rapidly decreases, Ni-W/Al$_2$O$_3$ + HY and Ni-W/HY catalysts demonstrates fairly good stability.
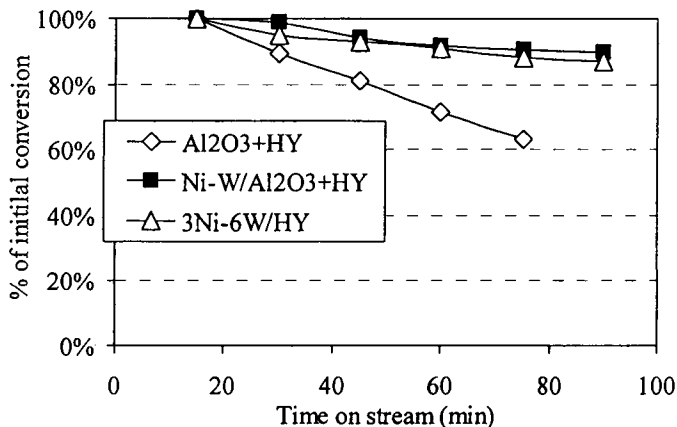


Fig. 3.  Variation of the overall $C_6H_{12}$ conversion with time on stream at 420°C
on different catalysts. The conversions are normalized as a percent of
the initial conversions.

Presumably, atomic hydrogen activated over the metal component, migrates toward the acid component and prevents formation of carbon deposits by

hydrogenation of coke precursors. Noteworthy that the deactivation rates are essentially the same for Ni-W/Al$_2$O$_3$+HY and Ni-W/HY catalysts despite the significant difference in spatial separation between acid and metal sites. This points to the high rate of hydrogen spillover under conditions of this study.

### 3.3. Conversion of the decaline+octane mixture

The catalytic performance of the hybrid catalysts and their individual components was compared in the conversion of the decaline+n-octane mixture modeling the composition of the real feedstock. The catalytic results are summarized in Table 1.

Table 1. Performance of Ni-containing catalysts in the conversion of the mixture of decaline (30.5%) and n-octane (69.5%) at H$_2$ : hydrocarbon ratio of 10 : 1 (vol.) and VHSV = 1.7 h$^{-1}$ (catalyst loading, 2.1 g)

| Catalyst mixture* | P, MPa | T, °C | Conversion, % | | | Yield, wt. % | | |
| --- | --- | --- | --- | --- | --- | --- | --- | --- |
| | | | Deca-line | n-Octane | C$_1$-C$_4$ | C$_5$-C$_8$ | C$_{10}$ | Aroma tics |
| 3%Ni-6%W/ | 2.2 | 280 | 0.7 | 0.6 | - | 0.4 | 0.2 | - |
| Al$_2$O$_3$ (1.5g) + | | 300 | 3.0 | 1.7 | 1.0 | 0.4 | 0.8 | - |
| Al$_2$O$_3$ (0.6g) | | 320 | 6.6 | 3.6 | 1.3 | 1.3 | 1.6 | 0.3 |
| 3%Ni-6%W/ | 2.2 | 280 | 31.2 | 2.3 | 1.4 | 1.2 | 8.4 | 0.1 |
| Al$_2$O$_3$ (1.5g) + | | 300 | 37.0 | 3.6 | 1.9 | 1.3 | 10.5 | 0.1 |
| H-Y (0.6g) | | 320 | 51.5 | 3.3 | 2.6 | 2.8 | 12.5 | 0.1 |
| Al$_2$O$_3$ (1.5g) + | 2.4 | 280 | 35.4 | 1.2 | 0.7 | 1.3 | 9.5 | 0.1 |
| H-Y (0.6g) | | 300 | 32.8 | 2.0 | 0.7 | 1.4 | 9.2 | 0.1 |
| | | 320 | 39.0 | 3.0 | 1.1 | 1.9 | 10.8 | 0.2 |
| 3%Ni-6%W/ | 2.4 | 280 | 64.3 | 3.5 | 2.7 | 4.2 | 15.1 | - |
| H-Y (1.5g) + | | 300 | 78.4 | 7.5 | 4.2 | 7.9 | 17.0 | - |
| Al$_2$O$_3$ (0.6g) | | 320 | 93.1 | 13.2 | 9.5 | 16.1 | 11.8 | 0.2 |

Unlike cyclohexane conversion, the decaline conversion over Ni-W/Al$_2$O$_3$ is significantly lower compared to HY. Taking into account that there is almost no aromatics in the reaction products over this catalyst, we can conclude that the main reason of the observed decrease in the activity is the suppression of dehydrogenation due to lower reaction temperature.

The decaline conversion on HY is markedly higher and approaches 35-36% at 280°C, which is indicative of the higher reactivity of decaline compared to cyclohexane in acid-catalyzed transformations. However, the catalyst is rapidly deactivated.

Comparison of the catalytic performance of the individual components and the hybrid catalyst reveals the pronounced synergy between metal and acid components. Decaline conversion is significantly enhanced over Ni-W/Al$_2$O$_3$+HY and Ni-W/HY. The latter catalyst exhibits the highest activity and the highest yield of the C$_{10}$ fraction was obtained over Ni-W/HY at 300°C. However, at increased temperature, the C$_{10}$ yield decreases due to cracking.

Taking into account that dehydrogenation over the metal component is low under these conditions, we can presume that the observed increase in the activity over the

hybrid catalyst is primarily attributed to the effect of hydrogen spillover from metal to the acid component. It is also noteworthy that the importance of the acid component for decaline ring-opening increased compared to cyclohexane ring-opening.

## 4. CONCLUSIONS

Comparison of the catalytic performance of hybrid catalysts and their individual components in ring opening of cyclohexane and decaline reveals the following major tendencies of the reaction mechanism.

- The acidic function is a necessary prerequisite of the high catalyst activity. The importance of the acid function is particularly pronounced in decaline conversion.
- The purely acidic catalyst exhibits quite high activity in decaline conversion, but it is rapidly reactivated. The presence of this function is not sufficient for achieving good performance and the presence of a metal is required;
- The observed synergy between metal and acid components can be attributed to two major factors: (1) formation of the dehydrogenated intermediates over the metal component followed by their transformations over the acid sites; (2) hydrogen spillover from the metal component toward acid sites. The first factor appears to play an important role in the case of ring opening of light naphthenes, while the second effect is particularly important for ring opening of heavier naphthenes (decaline).
- A tremendous effect of the hydrogen spillover is observed: even if the metallic and acidic functions are separated, the activity of such a hybrid catalyst is close to that of the Ni-W/HY catalyst where two functions are not spatially separated.

## 5. REFERENCES

1. L.M. Kustov, T.V. Vasina, O.V. Masloboishchikova, et al., Proc. 12th Intern. Congr. Catal., Granada, 2000; Stud. Surf. Sci. Catal., 130A (2000) 227.
2. H. Kubicka and J.Okal, Catal. Lett., 25 (1994) 157.
3. J. Fu, et al., Chem. J. Chin. Univ.-chin., 16 (1995) 461.
4. J.A. Martens, Thesis, Univ. Leuven, 1985.
5. D. Brower et al., Rec. Trav. Chim. Pays-Bas, 89 (1970) 211.
6. G.A. Somorjai, Introduction to Surface Chemistry and Catalysis, Wiley, 1994.
7. US Patent No. 5,382,730 (1995) (Mobil).
8. US Patent No. 5,382,731 (1995) (Mobil).
9. G.B. McVicker, M.S. Touvelle, C.W. Hudson, et al., WO 97/09288, 1997 (Exxon).
10. M.S. Touvelle, G.B. McVicker, M. Daage, et al., WO 97/09290, 1997 (Exxon).
11. R.K. Herz, W.D. Gillespie, E.E. Petersen, G.A. Somorjai, J. Catal., 67 (1981) 371.
12. W.M.H. Sachtler, G.A. Somorjai, J. Catal., 89 (1984) 35.

# Synergy effect between copper and manganese oxides in hopcalite catalysts

F.C. Buciuman[a], F. Patcas[a] and T. Hahn[b]

[a]Department of Chemical Technology, University Babes Bolyai, Cluj-Napoca, Romania

[b]Department of Technical Chemistry and Polymer Chemistry, University Martin Luther, Halle-Wittenberg, Germany

A hopcalite-type catalyst was prepared by coprecipitation of copper and manganese nitrates and calcination at 550°C. Its catalytic activity in the oxidation of hydrogen and carbon monoxide was compared with the activity of single phase CuO, $Mn_2O_3$ and $CuMn_2O_4$ and of the mechanical mixture $CuO \cdot Mn_2O_3$. It was found that the high catalytic activity of hopcalite does not arise from the interaction of copper and manganese cations within the spinel lattice of copper manganite, but from a synergistic cooperation of CuO and $Mn_2O_3$ phases in physical mixture. To account for this synergy, a model based on oxygen spillover was proposed.

## 1. INTRODUCTION

Hopcalite comprises a class of manganese-copper composite oxides that are employed in the combustion of exhaust gases loaded with carbon monoxide or volatile organic compounds. They are known as very active oxidation catalysts, even at low temperatures, but their thermal stability is poor: above 600-700°C they undergo an irreversible loss of activity [1, 2].

Regarding the origins of the outstanding activity of hopcalite, it is generally accepted that this arises from the inclusion of copper and manganese cations within the lattice of copper manganite spinel $CuMn_2O_4$ [1-3]. Each cation has its specific function (oxygen adsorption over $Cu^{1+}$ yielding $Cu^{2+}$, and reductant adsorption over $Mn^{4+}$ yielding $Mn^{3+}$) [3]. The regeneration of the active sites occurs in this model through a quick charge exchange between $Mn^{3+}$ and $Cu^{2+}$, mediated by the electronic orbitals of the oxygen anion that bounds them.

The present study was based on the observation that a hopcalite catalyst prepared by us after a common coprecipitation procedure and calcined at 550°C consisted mainly on copper and manganese oxides (CuO and $Mn_2O_3$) and showed a high oxidation activity, whereas the same mixture calcined at 1000°C and consisting almost exclusively on $CuMn_2O_4$ had a much lower activity [4]. It appeared that the origin of the oxidation activity was not to be searched in the

copper manganite spinel, but in the synergistic interaction of different copper and manganese oxide phases. Such effects were extensively studied in the case of other oxide couples and are involved in many catalytic materials used in partial oxidation reactions [5-7]. It is generally accepted that the synergy origins in an oxygen transfer (spillover) from a donor phase to an acceptor phase. The spillover oxygen (re)generates active sites, keeps the active acceptor phase in an optimal oxidation state [5] or participates as a reactant to the oxidation reaction [6, 7]. In the last few years synergy effects between mixed phases, related to oxygen transfer were also reported in relation to combustion catalysts. Thus, $Mn_2O_3$ acted as an oxygen donor for Ag [8] or Pd [9] in the oxidation of carbon monoxide. In another paper, $CeO_2$ was found to be an oxygen donor for CuO [10].

By taking into account this knowledge and our previous observations we attempted to propose an alternate model for the oxidation catalysis over hopcalite catalysts, based on the phase cooperation between copper oxide and manganese oxide. In order to rationalize the behavior of copper-manganese composite oxides we studied the catalytic properties of the following materials:

- hopcalite with a Cu:Mn atomic ratio of 1:2;
- copper manganite $CuMn_2O_4$ (spinel phase);
- simple oxides CuO and $Mn_2O_3$;
- a mechanical mixture of CuO and $Mn_2O_3$ in the molar ratio of 1:1.

## 2. EXPERIMENTAL

### 2. 1. Catalyst preparation

The catalysts were prepared by starting from the nitrates of copper and manganese, which were added to distilled water in the appropriate amount and ratio to yield firstly a 2M solution, and after decomposition the desired oxides or mixed oxides (Cu:Mn = 1:2, 1:0 and 0:1, respectively). After evaporation of water and decomposition of nitrates at 250°C, the material was calcined at different temperatures according to Tab. 1. The mechanical mixture $CuO \cdot Mn_2O_3$ was prepared by mixing the corresponding amounts of oxides in an agate mortar with no other ingredients and without any thermal treatment. The powders were pressed to obtain pellets, which were crushed and sieved to separate the fraction of 0.3-0.5 mm that was employed for the tests.

### 2. 2. Catalyst characterization

The phase analysis was performed by X-ray powder diffraction using a Seifert diffractometer with $CuK_\alpha$ ($\lambda = 0.15418$ nm) radiation.

BET surface areas of the materials were measured by krypton physisorption at 77K using a computer controlled volumetric device.

Temperature programmed reduction (TPR) with hydrogen was carried out in a conventional flow apparatus equipped with a thermal conductivity (TC) detector. A 30 cm$^3$/min (STP) flow of gas containing 10% (Vol.) $H_2$ in $N_2$ was passed over a 50 mg oxide sample in a quartz reactor and then through a cold

trap to the detector. The temperature was linearly increased at 10°/min from 20°C to 950°C, then kept constant at 950°C for 20 min. The peaks were calibrated by reducing a sample of commercial copper oxide CuO (99,7%, Alfa) in the same apparatus and the calibration was checked by injecting hydrogen pulses of known volumes in a nitrogen flow.

## 2. 3. Activity evaluation

The catalysts were tested for their activity in the oxidation of hydrogen (at 240-450°C) and carbon monoxide (at 110-270°C) by performing kinetic measurements. The tests were carried out in a differentially operated recirculation reactor using a membrane pump which yielded a recycle ratio of about 40:1. The perfect mixing behavior was verified by using the single step response method. A 20 mm inner diameter glass reactor, loaded with 0.05-1 g catalyst was placed in the recycle loop, and was heated with an electric furnace. The temperature was measured with a thermocouple placed inside the reactor through a narrow glass tube that ended at the middle of the catalyst bed. Cold traps were used to remove reaction products from the recycle loop and prior to the analysis. The feed contained various concentrations (0.2 to 2% (Vol.)) of $H_2$ or CO in synthetic air. The $H_2$ and CO outlet concentrations were monitored continuously with a TC detector and a infrared detector (Binos-Rosemount), respectively. Prior to the kinetic measurements the catalysts were kept overnight in the reactant flow at 450°C (for $H_2$ oxidation) and 270°C (for CO oxidation), respectively.

## 3. RESULTS AND DISCUSSION

### 3. 1. Catalyst characterization

The characteristics of the prepared catalysts are given in Tab. 1. The sample prepared at 550°C, a typical calcination temperature for hopcalites, consisted on a mixture of copper oxide, manganese sesquioxide and copper manganite (spinel phase). The same oxide mixture calcined at 1000°C was copper manganite with very low amounts of $Mn_3O_4$. The XRD analysis was performed also on the used catalysts (after reaction) and displayed no changes of the oxide phase composition.

The reduction of copper oxide occurred in a single step to metal copper, whereas manganese sesquioxide was reduced in two steps to MnO, at higher temperatures as copper oxide. The reduction of the copper manganese spinel took place at an intermediate temperature between those of copper and manganese oxides.

A different reduction behavior is displayed by the physical mixtures of copper and manganese oxide: the reduction temperatures are displaced towards lower values. The effect is stronger in the case of hopcalite, but can also be recognized in the mechanical mixture of CuO and $Mn_2O_3$. The ratio of lattice oxygen extracted in the first (CuO) and the second ($Mn_2O_3$) reduction stage, which

should be theoretically 1:1, was found to be 1.1:0.9 in our case. It appears that in the presence of manganese oxide, the copper oxide releases easier its lattice oxygen, and at the same time about 10% of the oxygen of the manganese oxide is removed at lower temperatures during the reduction of copper oxide.

Table 1
Catalyst characterization

| Catalyst | Calcination temperature, °C | Phase composition (wt.%) | $S_{BET}$, m²/g | Temperature programmed reduction | | |
|---|---|---|---|---|---|---|
| | | | | Peak 1, °C | Peak 2, °C | Peak 3, °C |
| CuO | 500 | CuO | 0.92 | 330 | | |
| $Mn_2O_3$ | 750 | $Mn_2O_3$ | 1.28 | 445 | 525 | |
| $CuMn_2O_4$-550 | 550 | $CuO(20)$, $Mn_2O_3(40)$, $CuMn_2O_4(40)$ | 2.55 | 260 | 320 | 380 |
| $CuMn_2O_4$-1000 | 1000 | $CuMn_2O_4(92)$, $Mn_3O_4(8)$ | 0.69 | 410 | | |
| $CuO \cdot Mn_2O_3$ | - | $CuO(34)$, $Mn_2O_3(66)$ | 1.23 | 300 | 445 | 505 |

## 3. 2. The oxidation of hydrogen and carbon monoxide

In order to eliminate the effect of the different surface areas of the catalysts used, the reaction rates reported here are all related to the unit area of the catalyst surface.

The concentration-rate data sets at different reaction temperatures obeyed the following kinetic equations [4]:

$$r_{H_2} = k_{H_2} \cdot C_{H_2} \tag{1}$$

$$r_{CO} = k_{CO} \cdot C_{CO}^{0.7} \tag{2}$$

The rate constants were calculated accordingly from the kinetic data and are displayed in Fig. 1 as a function of the reaction temperature. The activation energy of the catalysts are given in the Tab. 2. Only the rate constants that were

Table 2
The activation energy of hydrogen and carbon monoxide oxidation.

| Catalyst | CuO | $Mn_2O_3$ | $CuMn_2O_4$-550 | $CuMn_2O_4$-1000 | $CuO \cdot Mn_2O_3$ |
|---|---|---|---|---|---|
| Ea, kJ/mole (H₂) | 86 | 53 | 53 | 63 | 48 |
| Ea, kJ/mole (CO) | 96 | 61 | 46 | 45 | 67 |
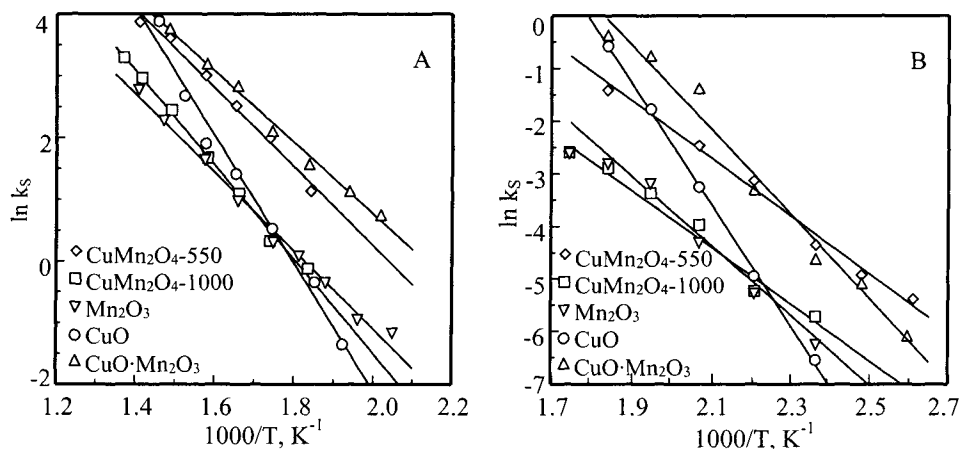
Fig. 1. The dependence of the rate constants on the reaction temperature: A) the oxidation of hydrogen; B) the oxidation of carbon monoxide

not influenced by internal or external mass transport processes were used in this calculation. The influence of the diffusion processes was evaluated on the basis of the Weisz-Prater and Hudgins criteria [11], and of the external mass transfer coefficient [12].

The data of Fig. 1 show that the catalytic activity of the catalysts consisting on physical mixtures of oxides is considerably higher than the activity of single phase oxides. Moreover, the latter catalysts group displays a compensation effect. The manganese sesquioxide is already active at lower temperatures, where copper oxide has a poor activity. In the oxidation of hydrogen, copper oxide becomes more active as manganese sesquioxide by starting with 330°C, the temperature corresponding to the maximum reduction rate with hydrogen as shown by the TPR experiments. The same occurs probably in the oxidation of carbon monoxide, by taking into account that TPR with carbon monoxide occurs at lower temperatures. The different catalytic behavior of manganese and copper oxides suggests different oxidation mechanisms. Manganese sesquioxide possesses $Mn^{3+}$ cations that can act as adsorption centers for oxygen, by donating the available electron. This feature makes it a good oxidation catalyst at lower temperatures, where the adsorption-desorption equilibrium of oxygen is favorable for achieving high surface concentrations of adsorbed oxygen. With increasing temperature this concentration is likely to decrease, and the increase of the reaction rate with temperature is low as shown by the value of activation energy. The lattice oxygen of manganese oxide becomes available for hydrogen oxidation only above 445°C, which was the limit of our experimental range. The copper cations in copper oxide can not adsorb oxygen, as they are already in the highest oxidation state; they have to be firstly reduced by the reducing gas, which is analogous to an oxidation mechanism after the Mars-van Krevelen (redox) model [13]. This reaction is very slow in the low temperature range and is strongly

accelerated above the reduction temperature of the oxide, as revealed by TPR. This accounts for the high values of the activation energy over copper oxide. The behavior of copper manganite lies between those of the single copper and manganese oxides. This proves that the inclusion of the copper and manganese cations with their complementary ways of action in the same oxide lattice brings no synergistic improvement of the catalytic properties; the activity of the spinel is merely an arithmetical mean of the activities of copper and manganese oxides.

The reaction rates found over physical mixtures of copper and manganese oxides are much higher, as shown by Fig. 1. The activity levels of the phase mixtures are similar, irrespective of their preparation method (that is, by coprecipitation or by mechanical mixing). This suggests that the source of the synergy must be found in some form of phase cooperation. By taking into account the properties of the copper and manganese single oxides, as previously discussed, the spillover of adsorbed oxygen from manganese oxide to copper oxide may be proposed as possible mechanism in order to explain the synergy. Thus, manganese oxide could act as an oxygen donor for the copper oxide especially in the low temperature range, which in turn might activate the reducing molecules and serve as oxidation site. The spillover oxidation mechanism is superimposed on the own oxidation mechanisms occurring on the single phase oxides and takes place probably mostly at the phase boundaries. The improvement of the catalytic activity of copper oxide by association with an oxygen donor as cerium oxide, and the use of manganese oxide as an oxygen donor for noble metal catalysts were previously described in the literature [8-10].

According to the model proposed, the extent of the synergistic effect should decrease in the higher temperature range where the oxygen adsorption-desorption equilibrium is defavored and the copper oxide mobilizes its own lattice oxygen anions for the catalytic reaction. In order to check if this really happen, the following definitions were used:

1. the absolute synergy $\Delta Y$, representing the difference between the activity of the mixture and the total activity of the single phase oxides:

$$\Delta Y_{CuMn_2O_4-550} = Y_{CuMn_2O_4-550} -$$

$$- (W_{CuO} \cdot Y_{CuO} + W_{Mn_2O_3} \cdot Y_{Mn_2O_3} + W_{CuMn_2O_4-1000} \cdot Y_{CuMn_2O_4-1000}) \qquad (3)$$

$$\Delta Y_{CuO. Mn_2O_3} = Y_{CuO. Mn_2O_3} - (W'_{CuO} \cdot Y_{CuO} + W'_{Mn_2O_3} \cdot Y_{Mn_2O_3}) \qquad (4),$$

2. the relative synergy $\left(\dfrac{\Delta Y}{Y}\right)$, representing the fraction of the total activity of the mixture brought by the synergy:

$$\left(\frac{\Delta Y}{Y}\right)_{CuMn_2O_4-550} = \frac{\Delta Y_{CuMn_2O_4-550}}{Y_{CuMn_2O_4-550}} \qquad (5)$$

$$\left(\frac{\Delta Y}{Y}\right)_{CuO\cdot Mn_2O_3} = \frac{\Delta Y_{CuO\cdot Mn_2O_3}}{Y_{CuO\cdot Mn_2O_3}} \tag{6},$$

where Y is the activity (taken as the reaction rate at a reductant concentration of $1.10^{-7}$ mole $cm^{-3}$), and W is the mass fraction of the oxide component in the mixture. The calculated values of the absolute synergy as a function of the reaction temperature are displayed in Tab. 3.

Table 3
The absolute synergy of the catalytic activity in the oxidation of $H_2$ and CO ($\Delta Y$, in $10^{-7}$ mole $m^{-2}$ $s^{-1}$)

| Temperature, °C | | 150 | 180 | 210 | 240 | 270 | 300 | 330 | 360 | 400 |
|---|---|---|---|---|---|---|---|---|---|---|
| $H_2$ | $\Delta Y_{CuMn_2O_4-550}$ | | | | | 2.28 | 5.89 | 9.28 | 14.63 | 23.34 |
| | $\Delta Y_{CuO\cdot Mn_2O_3}$ | | | | | 3.97 | 6.71 | 13.85 | 18.79 | 24.61 |
| CO | $\Delta Y_{CuMn_2O_4-550}$ | 1.33 | 4.79 | 8.12 | 13.29 | 10.57 | | | | |
| | $\Delta Y_{CuO\cdot Mn_2O_3}$ | 1.02 | 3.90 | 29.03 | 47.95 | 58.16 | | | | |

The absolute synergy increases monotonically with increasing temperature, which appears to contradict the expected behavior. But this finding can be accounted for by the Arrhenius dependence of the reaction rates with the temperature. By examining the temperature dependence of the relative synergy, (Fig. 2) a quite different conclusion arises. The synergy appears to pass a
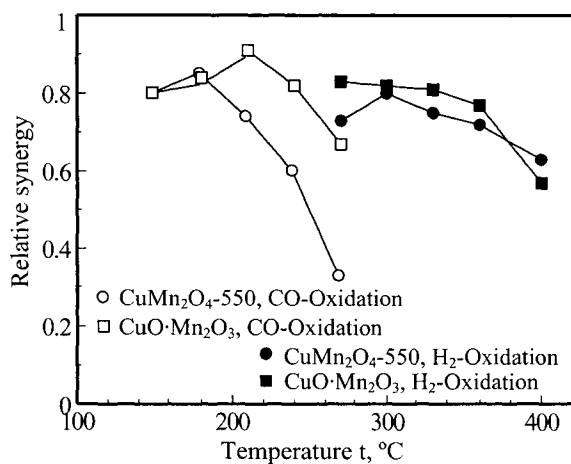


Fig. 2. The temperature dependence of the relative synergy

322

maximum with increasing temperatures, and the sudden decrease of the effect at higher temperatures is obvious. The suppression of the cooperation mechanism appears to be caused mainly by the onset of the redox mechanism over the copper oxide component. The slight increase in synergy in the low temperature range could be produced by the mobility improvement of the spilling oxygen.

The proposed model for the synergistic phase cooperation between copper and manganese oxides accounts also for the irreversible deactivation of hopcalite at temperatures above 600-700°C. In this temperature range the crystallization of the copper manganite spinel begins, and the single oxide phases $CuO$ and $Mn_2O_3$ are not longer available in the catalyst mixture.

## 4. CONCLUSION

The catalytic activity of hopcalite catalysts was shown to arise from the phase cooperation between manganese and copper catalysts. A model for the synergy found in the mixed oxide system is proposed, based on the oxygen spillover between manganese oxide as a donor and copper oxide as an acceptor.

## REFERENCES

[1]  G.J. Hutchings, A.A. Mirzaei, R.W. Joyner, M.R.H. Siddiqui and S.H. Taylor, Appl. Catal. A: Gen., 166 (1998) 143.
[2]  S. Veprek, D.L. Cocke, S. Kehl and H.R. Oswald, J. Catal. 100 (1986) 250.
[3]  G.M. Schwab and S.B. Kanungo, Z. Physik. Chem. N. Folge 107 (1977) 109.
[4]  F.C. Buciuman, F. Patcas and T. Hahn, Chem. Eng. Proc. 38 (1999) 563.
[5]  L.-T. Weng and B. Delmon, Appl. Catal. A: Gen. 81 (1992) 141.
[6]  Y. Moro-oka, Stud. Surf. Sci. Catal. 77 (1993) 95.
[7]  D. Duprez, Stud. Surf. Sci. Catal. 112 (1997) 13.
[8]  S. Imamura, H. Sawada, K. Uemura and S. Ishida, J. Catal. 109 (1988) 198
[9]  Y. Tsuji and S. Imamura, Stud. Surf. Sci. Catal. 77 (1993) 405.
[10] W. Liu and M. Flytzani-Stepanopoulos, J. Catal. 153 (1995) 317.
[11] J.B. Butt, V.W. Weekman, in: Standardization of catalyst test methods, S.W. Weller (Ed.), AIChE Symp. Ser. No. 143, Vol.70, 1974, p. 29.
[12] VDI-Wärmeatlas, 6th edn., VDI, Düsseldorf, 1991
[13] P. Mars, D. W. Van Krevelen, Chem. Eng. Sci. Suppl. 3 (1954) 41.

323

# Spillover of oxygen species in the catalysts for NO Decomposition

V. I. Pârvulescu[a]*, B. Delmon[b] and P. Grange[b]

[a]-University of Bucharest, Faculty of Chemistry, Department of Chemical Technology and Catalysis, B-dul Regina Elisabeta 4-12, Bucharest 70346, Romania, E-mail: V_PARVULESCU@chim.upb.ro.

[b]- Universite Catholique de Louvain, Unite de Catalyse et Chimie des Materiaux Divises, Place Croix du Sud 2/17, 1348 Louvain-la-Neuve, Belgium, E-mail: grange@cata.ucl.ac.be.

A series of Cu- and Cu-M-ZSM-5 (M= Ce, Sn, Tl) were prepared by ionic-exchange. The coresponding metal oxides were prepared by sol-gel method. Physical mixtures of Cu-ZSM-5 with M-ZSM-5, and with the metal oxides were prepared as well. These catalysts were characterized by adsorption isotherms of $N_2$ at 77K, NO-FTIR, $O_2$-TPD, and XPS. The correlation of these characteristics with catalytic data in NO decomposition provided a model, which supposes the role of oxygen spillover on zeolite surfaces, but only for short distances.

## 1. INTRODUCTION

NO decomposition is the most attractive solution for reduction of $NO_x$ air pollution because this process does not involve supplementary reductants and does not cause supplementary pollution. Data reported up to now focused on Cu-ZSM-5 because the performances obtained with this catalyst are the best reported for this process [1]. This is a quite unique system because ZSM-5 is the best support for this reaction and Cu is the most active species. The numerous investigation techniques used in characterization of this catalyst required that copper be located in certain positions. But even in these positions copper may easily deactivate in presence of water or in oxidative conditions. Bicomponent zeolites were also reported by several authors [2-9]. The addition of a second species like a rare-earth element was found to improve the performances of the parent Cu-ZSM-5. The causes of this enhancement in activity are still not clear, and none of these papers have proved a direct interaction between copper and the rare-earth element.

Physical mixtures have also been studied but in relation with reduction of NO with hydrocarbons. Misono [10] reported that some zeolites in an intimate mixture with oxides like $CeO_2$ or $Mn_2O_3$ may improve the catalytic performances in this reaction.

The aim of this study was to investigate if the positive effect of the second species may be associated with an oxygen spillover from copper to the rare earth species, thus leading to a decrease of the oxygen density around the active sites. Following this idea, physical mixtures of Cu-ZSM-5 with M-ZSM-5 (M=Ce, Sn, and Tl), or with the corresponding metal oxides were prepared and their behavior was investigated in NO decomposition. One of the main

reasons of this study was to identify the possible spillover species. Physical mixtures of M-ZSM-5 (M=Ce, Sn, and Tl) zeolites with the corresponding metal oxides were investigated as well.

## 2. EXPERIMENTAL

M-ZSM-5 (M= Cu, Ce, Sn, Tl) zeolites were prepared starting from a ZSM-5 (from Valfor PQ) with a Si/Al ratio of 25 using a one-step exchange procedure. Details about this preparation have been reported elsewhere [7]. Cu-M-ZSM-5 (M= Ce, Sn, Tl) were prepared as well using a co-exchange procedure [8]. The coresponding metal oxides were obtained by precipitation of the chloride salts of these elements with ammonia. All the samples were calcined at 500 °C for 6h, firstly in helium, and then for another 1h in air, using a heating rate of 0.3 °C min$^{-1}$. Samples were characterized by several techniques. Elemental analysis of Si, Al, Sm, and Cu was performed by atomic emission spectroscopy with inductively coupled plasma atomization (ICP-AES) after drying of the samples overnight at 373 K (Table 1). Adsorption and desorption curves of $N_2$ at 77 K were obtained with a Micromeritics ASAP 2000 apparatus after degassing the samples at 423 K for 12 h under vacuum. The TPD measurements with $O_2$ were carried out in the same fixed bed quartz microreactor as that used for the catalytic testing. 400 mg of sample were heated from room temperature to 773 K at a rate of 1 K min$^{-1}$ in a diluted flow of $O_2$ (40% $O_2$ in He at 27 ml min$^{-1}$) and kept at 773 K for 8 hours. After cooling to room temperature under an $O_2$ flow, the sample was purged with He (15 ml min$^{-1}$) for 3 hours. The temperature was then increased at a rate of 5 K min$^{-1}$ up to 773 K under the same He flow. The $O_2$ desorbed was analyzed by a Balzers Quadrupole QMG 311 mass spectrometer. Released O/M or O/(M+Cu) ratios were determined from the calibration of the M.S. signals and calculation of the peak areas using a subroutine program. The $O_2$-TPD measurements were carried out by taking various arrangements into consideration, namely, mixed bed or separate layers of components. FTIR spectra were recorded using a Brucker IFS88 instrument, equipped with KBr optics and a DTGS detector. Samples were placed into self-supported wafers (10-15 mg cm$^{-2}$) and placed in a special vacuum cell where they underwent evacuation and adsorptive treatments. The spectra corresponded to the accumulation of 50 scans at a 2 cm$^{-1}$ resolution. Before recording the first spectrum, the samples were heated at 400 °C for 6 h under vacuum to remove all adsorbed gases and then cooled to room temperature. Successive spectra were recorded after: i) introduction of 50 mbar NO at room temperature; ii) evacuation at 10$^{-5}$ Torr in order to remove weakly adsorbed NO; iii) one hour reaction at 400 $^0$C keeping a 50 mbar NO pressure in the cell; iv) evacuation at 10$^{-5}$ Torr at room temperature. The XPS spectra were recorded using a SSI X probe FISONS spectrometer (SSX -100/ 206) with monochromated AlKα radiation. The spectrometer energy scale was calibrated using the Au 4f$_{7/2}$ peak (binding energy 84.0 eV). The samples were moderately heated by a quartz lamp in the introduction chamber of the spectrometer to promote degassing, thus improving the vacuum in the analysis chamber. For the calculation of the binding energies, the C$_{1s}$ peak of the C-(C,H) component at 284.8 was used as an internal standard. The composite peaks were decomposed by a fitting routine included in the ESCA 8,3 D software. The superficial composition of the investigated samples was determined using the

same software, using the bands assigned to $Cu_{2p}$, $Ce_{3d}$, $Sn_{3d}$, $Tl_{4f}$, $Al_{2s}$, $O_{1s}$ and $Si_{2p}$ respectively.

All samples were tested for the decomposition of NO to $N_2$ and $O_2$ in a continuous flow system with a fixed bed quartz microreactor containing the catalyst. The reactant gas feed contained 4400 ppm of NO with He as carrier gas. The total flow was 30 ml min$^{-1}$. Each catalyst was tested between 623 and 873 K and the products of the reaction were analyzed with an on-line Balzers Quadrupole QMG 311 spectrometer scanning the masses from 28 to 46. The connection between the microreactor and the spectrometer was heated. The duration of one test was 4h. The activity of the catalysts was expressed in terms of NO total conversion and NO conversion to $N_2$.

## 3. RESULTS

### 3. 1. Textural characterization

Table 1 compiles the Langmuir surface areas of the investigated catalysts. Except for the bicomponent ones, the deposition of the various metals as Me-ZSM-5 did not caused an important decrease of the surface area compared to the parent zeolite, which may correspond to a good dispersion of these metals. In contrast with these values, their oxides exhibit much lower surface areas than zeolites, although these oxides were prepared following the sol-gel procedure.

Table 1.
Chemical composition and Langmuir surface area of the investigated zeolites

| Catalyst | Composition, wt. % | | | | Langmuir surface area, $m^2 g^{-1}$ |
|---|---|---|---|---|---|
| | Cu | Ce | Sn | Tl | |
| ZSM-5 | | | | | 490 |
| Cu | 3.06 | | | | 434 |
| Ce | | 3.15 | | | 396 |
| Cu-Ce | 2.13 | 3.04 | | | 367 |
| Sn | | | 3.39 | | 372 |
| Cu-Sn | 2.79 | | 3.11 | | 343 |
| Tl | | | | 3.05 | 415 |
| Cu-Tl | 2.68 | | | 2.87 | 382 |
| CeO$_2$ | | | | | 65 |
| SnO$_2$ | | | | | 76 |
| Tl$_2$O | | | | | 71 |

### 3. 2. O$_2$-TPD

Figure 1 shows O$_2$-TPD profiles corresponding to several monoexchanged zeolites compared with co-exchanged zeolites and physical mixtures of monoexchanged zeolites. This figure shows both common and specific trends of the investigated systems. Cu exhibits two peaks at 640 and 825 K. The peak located at 640 K corresponds to a collective property of copper and zeolite and results from the formation of species containing extra-lattice oxygen

(ELO). The additional release centered around 825 K corresponds to isolated Cu species [10]. The other monoexchanged zeolites exhibit peaks located at different temperatures than Cu: Sn and Tl have only one located to lower temperatures (415 and 540 K, respectively), while Ce presents two peaks, both at higher temperatures (725 and 855 K). The significance of the peaks is the same but the different temperatures show differences in the nature of the released oxygen. The released O-to-metal ratios as determined from these measurements varied in the following order: Cu (0.15) > Ce (0.08) > Tl (0.05) > Sn (0.02).
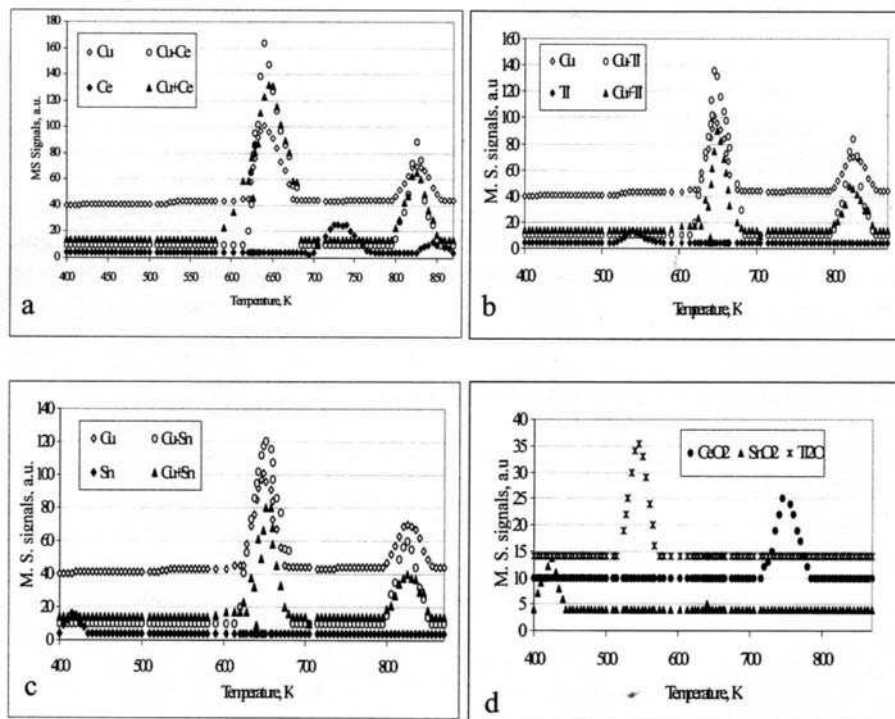


Figure 1. $O_2$-TPD profiles of the investigated zeolites and oxides. a: Cu, Ce, Cu-Ce, and physical mixture 1:1 Cu+Ce; b: Cu, Tl, Cu-Tl, and physical mixture 1:1 Cu+Tl; c: Cu, Tl, Cu-Tl, and physical mixture 1:1 Cu+Sn; d: pure oxides.

The co-exchange of zeolites determines a shift of the position of the first peak to slightly higher temperatures. $O_2$-TPD profiles of the physical mixtures of monoexchanged zeolites show maximums located at the same temperatures as the co-exchanged zeolites. However, the released O-to-metal ratio is in the order: Cu+Ce (0.21) > Cu+Tl (0.13) > Cu+Sn (0.10) corresponding to different values than those measured for monoexchanged zeolites. The

mixtures with Ce released more oxygen than pure Cu-ZSM-5, while those with Tl released an amount very close to pure Cu-ZSM-5. It is worth to note that even the mixtures with Sn released more oxygen than could be predicted from the contribution of the individual components. These data indicate a different behavior of co-exchanged zeolites comparatively with monoexchanged ones. The characterization of these zeolites with the different tools we have used showed no chemical modification of Cu or other elements as caused by co-exchange. This means that no other chemical compound was identified neither for the co-exchanged zeolites nor for the physical mixtures. Therefore, the only explanation of this behavior would be to consider the presence of oxygen spillover species. Separate layers showed no co-operative effects.

Physical mixtures of zeolites with metal oxides show curves which are a combination of those recorded for individual components, and the released oxygen was smaller than that determined for monoexchanged zeolites, suggesting an increased oxidation of copper by these oxides and a change in the metal arrangements.

### 3. 3. FTIR

NO-FTIR spectra recorded for the bicomponent zeolites showed bands located nearly in the same position as for Cu-ZSM-5, and a very different picture compared to M-ZSM-5. The main differences in these spectra occurred in the intensity of the bands associated to nitrate-nitrite species and to the position of the bands assigned to $(NO)^{\delta+}$ and $(N_2O_3)^{\delta-}$ species. The presence of the nitrate-nitrite species corresponds to a deactivation of the catalysts, and their population is reduced on bicomponent catalysts compared to Cu-ZSM-5. The band due to $(NO)^{\delta+}$ species is related to the possibility to keep copper in the initial active state, while that due to $(N_2O_3)^{\delta-}$ species is related to active intermediates in this reaction. Details about the particularities of the interaction of NO with the surface of these materials as resulted from FTIR investigation are given elsewhere [11].

Table 2.
Binding energies of Cu3p and Si2p components in the investigated zeolites

| Catalyst | XPS binding energies, eV | | | | | Cu(I)/ Cu(II) |
|---|---|---|---|---|---|---|
| | $Cu3p_{3/2}$ | $Cu3p_{3/2}$ | $Cu3p_{3/2}$ | $Cu3p_{3/2}$ | Si2p | |
| Cu | 932.9 | 934.8 | 941.2 | 944.4 | 102.5 | 0.48 |
| $Cu^r$ | 932.9 | 934.8 | 941.2 | 944.4 | 102.5 | 0.28 |
| Cu-Ce | 932.9 | 934.9 | 941.1 | 944.1 | 102.6 | 0.55 |
| $Cu-Ce^r$ | 932.9 | 934.9 | 941.1 | 944.1 | 102.6 | 0.36 |
| $Cu+Ce^r$ | 932.9 | 934.9 | 941.1 | 944.1 | 102.6 | 0.31 |
| Cu-Sn | 932.8 | 934.8 | 941.4 | 944.0 | 102.4 | 0.14 |
| $Cu-Sn^r$ | 932.8 | 934.8 | 941.4 | 944.0 | 102.4 | 0.11 |
| $Cu+Sn^r$ | 932.8 | 934.8 | 941.4 | 944.0 | 102.4 | 0.12 |
| Cu-Tl | 932.8 | 934.8 | 941.4 | 944.0 | 102.6 | 0.35 |
| $Cu-Tl^r$ | 932.8 | 934.8 | 941.4 | 944.0 | 102.6 | 0.23 |
| $Cu+Tl^r$ | 932.8 | 934.8 | 941.4 | 944.0 | 102.6 | 0.27 |

$^r$-after 4h reaction at 450 °C

328

## 3.4. XPS

Table 2 compiles the binding energies corresponding to levels $Cu_{3p3/2}$ and $Si_{2p}$, and the Cu(I)/Cu(II) ratios determined using a reported procedure [8]. These data show that after exposing the catalysts for 4h to the reaction mixture the XPS Cu(I)/Cu(II) ratios changed, copper being more oxidated. The behavior of the bicomponent catalysts is different according to the nature of the second species. Changes were also evidenced for physical mixtures. Except for Sn, XPS analysis indicated Cu(I)/Cu(II) ratios close to that of pure Cu-ZSM-5.
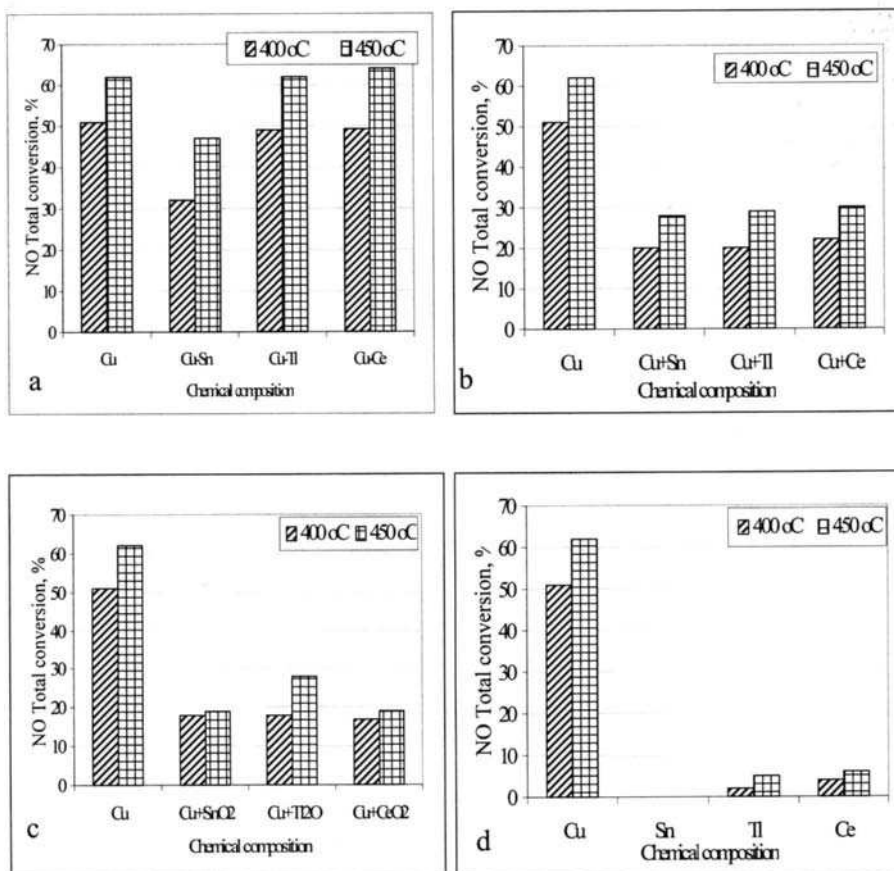


Figure 2. NO Total conversion on the investigated catalysts comparatively to Cu-ZSM-5
a: bicomponent zeolites; b: physical mixtures of metal-zolites; c: physical mixtures of Cu-ZSM-5 with metal oxides; d: metal-zeolites (total flow: 30 ml min$^{-1}$).

### 3.5. Catalytic activity

Figure 2 presents the NO total conversion data on the investigated catalysts. Considering the very poor performances of M-zeolites (see Fig. 2d), the experiments were made with the same amount of active Cu (i. e. 0.155g). All these catalysts exhibited a maximum of activity at around 450 °C. For the bicomponent catalysts (Fig. 2a), the conversion of those containing Ce or Tl is very close to that of the parent Cu-ZSM-5, while that of the catalyst with Sn is inferior to these systems. Physical mixtures of Cu-ZSM-5 with M-zeolites, or with metal oxides exhibit inferior activities than either Cu-ZSM-5 or bicomponent catalysts (Fig. 2b).

These data indicate an opposite behavior. In bicomponent catalysts the presence of Ce or Tl has a very small positive or near inert effect. But in the physical mixtures of Cu-ZSM-5 with M-ZSM-5, or with their oxides the influence is very negative, the conversion being much decreased.

## 4. DISCUSSIONS

The characterization measurements of the bicomponent catalysts did not support the hypothesis of a direct Cu-M interaction. Nevertheless, all of them suggested that the behavior of copper in the investigated catalysts was different. This may be associated with a different arrangement of the superficial atoms.

$O_2$-TPD curves indicated that in function of the chemical composition, the desorption temperatures were different, and also the released oxygen. An important result in this sense comes from the comparison of the shapes of the $O_2$-TPD curves and from the quantification of the amount of released oxygen. The co-deposition of the second metal with copper led to a small shift of the first TPD maximum to high temperatures (645 K for Cu-Ce, 645 K for Cu-Tl and 650 K for Cu-Sn). In the case of Cu-Tl and Cu-Ce, an increase in the amount of released oxygen (0.29 for Cu-Tl, 0.27 for Cu-Ce) was measured. This may be compared with 0.15 for Cu. Oxygen released from Cu-Sn (O/M = 0.17) was almost the same as that released by Cu-ZSM-5. Because no other modification in the nature of the catalysts was evidenced with the tools we have used, these changes may be associated with an oxygen spillover on the zeolite surface.

The modification of the reactivity of copper by the presence of cerium illustrated by the $O_2$-TPD profiles is in the same line as the data reported by Fernandez-Garcia et al. [12].

Changes in the $O_2$-TPD profiles compared to Cu-ZSM-5 or bicomponent catalysts were also evidenced for physical mixtures of zeolites. The quantification of the released oxygen showed different values than for copper or for the bicomponent catalysts. Except for Ce these were smaller than for copper. But physical mixtures of Cu-ZSM-5 with the oxides of cerium, tin, or thallium showed no effect comparatively to the parent zeolite. However, XPS measurements showed different Cu(I)/Cu(II) ratios than Cu-ZSM-5 even for these mixtures.

These data lead us to speculate that indeed the differences observed in the $O_2$-TPD profiles of bicomponent zeolites and physical mixtures of Cu-ZSM-5 with M-ZSM-5 are caused by the existence of oxygen spillover. Going further, we speculate that such spillover requires similar surfaces, and may exist only on short distances. In the case of the physical mixtures of Cu-

ZSM-5 with oxides there is no correspondence between their surfaces, and as a result the oxides act as simple oxidants of the Cu-ZSM-5 zeolite.

## 5. CONCLUSIONS

In conclusion, data obtained for catalysts for NO decomposition, namely Cu and Cu-M-ZSM-5 zeolites (M=Ce, Sn, Tl) suggest that the differences obtained in $O_2$-TPD experiments may be assigned to oxygen spillover. These species may exist only on similar surfaces, and only on short distances. The behavior of the mixtures of zeolites with oxides may be explained both by considering an advanced oxidation of the metal-zeolites by oxides and the incompatibility of their surfaces.

## ACKNOWLEDGMENT

## REFERENCES

1. G. Centi and S. Perathoner, Appl. Catal. A, 132 (1995) 179.
2. K. Eranen, N. Kumar and L. E. Lindfors, Appl. Catal. B: Environmental, 4 (1994) 213.
3. Y. Zhang and M. Flytzani-Stephanopoulos, *in* "Environmental Catalysis" (J. N. Armor, Ed.), p.7, American Chemical Society, Washington D.C., 1994.
4. Y. Zhang, T. Sun, A. F. Sarofim and M. Flytzani-Stephanopoulos, *in* "Reduction of Nitrogen Oxide Emissions" (U.S.Ozkan, Ed.), p.133, American Chemical Society, Washington D.C., 1995.
5. P. Budi, E. Curryhyde and R. F. Howe, Catal.Lett., 41 (1996) 47.
6. A. V. Kucherov, C. P. Hubbard, T. N. Kucherova and M. Shelef *in* "Progress in Zeolite and Microporous Materials" (H.Chon, S.K. Ihm and Y.S. Uh, Eds.), Stud. Surf. Sci. Catal., vol. 105, p.1469, Elsevier Science, Amsterdam, 1997.
7. V. I. Pârvulescu, P. Oelker, P. Grange and B. Delmon, Appl.Catal. B: Environmental, 16 (1998) 1.
8. Y. Zhang and M. Flytzani-Stephanopoulos, J.Catal., 164 (1996) 131.
8. V. I. Pârvulescu, M. A. Centeno, P. Grange and B. Delmon, J.Catal., 191 (2000) 445.
9. M. Misono, CATTECH, 3 (1998) 53.
10. E. V. Rebrov, A. V. Simakov, N. N. Sazonova, V. A. Rogov and G. B. Barannik, Catal. Letters, 51 (1998) 27.
11. V. I. Pârvulescu, P. Grange and B. Delmon, J. Phys. Chem., B, 101 (1997) 6933.
12. M. Fernandez-Garcia, E. Gomez Rebollo, A. Guerrero Ruiz, J. C. Conesa and J. Soria, J. Catal., 172 (1997) 146.

# Effects of oxygen spillover on the catalytic oxidation of BTEX in air with Pt/CeO$_2$ catalyst

Dong-Keun Lee, Dul-Sun Kim, Kee Chool Whang and Soo-Gon Kim

Department of Chemical Engineering/Environmental Protection, Research Institute of Environmental Protection, Gyeongsang National University, 900 Kajwa-dong, Chinju, Kyongnam 660-701, KOREA

Catalytic oxidation of BTEX was conducted over 1wt% Pt/CeO$_2$ and 1wt% Pt/Al$_2$O$_3$ catalysts. Much more efficient conversion of BTEX was obtained with the Pt/CeO$_2$ catalyst, and the higher activity was proved to be due to the continuous migration or spillover of the adsorbed dioxygen onto the Pt surface where dioxygen dissociates rapidly to produce essential monooxygen for the oxidation of BTEX. Pt/CeO$_2$ could also successfully be used for the oxidation of VOCs including BTEX in the vapor-laden air withdrawn from contaminated soils by gasoline.

## 1. INTRODUCTION

Soil may become contaminated with volatile organic chemicals such as industrial solvents and gasoline components in a number of ways. Soil vapor extraction is a cost-effective technique for the removal of volatile organic chemicals(VOCs) from contaminated soils. A soil vapor extraction system involves extraction of air containing volatile chemicals from unsaturated soil. Fresh air is injected or flows into the subsurface at locations around a spill site, and the vapor-laden air is withdrawn under vacuum from extraction vents.

BTEX(benzene, toluene, ethylbenzene and xylene mixtures) are main components of VOCs in the vapor-laden air withdrawn from the contaminated soils by gasoline. These components in the air should be removed before being transferred to the air where they may continue to pose environmental and health threats.

Catalytic oxidation of VOCs is currently receiving increased attention due to its low destruction temperature and its excellent selectivity towards formation of harmless reaction products [1-6]. CeO$_2$ has received much attention because it acts as an oxygen storage in three-way catalysts to maintain and enhance the activity of oxidation of hydrocarbons and carbon monoxide under working conditions [7-9]. There have been extensive studies showing that CeO$_2$ plays an important role on oxygen storage and therby increasing the activity of precious metals by supplying oxygen.

In this work Pt/CeO$_2$ catalyst was employed for the oxidation of BTEX in air, and the role of CeO$_2$ was investigated. To be this FTIR and ESR analyses were employed for the elucidation o the movement o adsorbed oxygen.

## 2. EXPERIMENTAL

CeO$_2$ was prepared by precipitating a solution of cerium(III) nitrate at pH 9 with ammonia. The resulting hydroxide precipitate was filtered, dried and calcined at 480°C for 5hr. Platinum(II) acetylacetonate was used as the precursor of Pt/CeO$_2$ catalyst. 1wt% Pt/CeO$_2$ catalyst was prepared by incipient wetness method. The prepared sample was dried and calcined at 400°C for 4hr in a programmable furnace. The calcined samples were finally reduced with a flowing 5% H$_2$/Ar gas mixture at 300°C for 4hr.

1wt% Pt/Al$_2$O$_3$ catalyst was also prepared by impregnating platinum (II) actylacetonate solution onto the surface of γ-Al$_2$O$_3$. In order to locate platinum particles mainly at the exterior surface of γ-Al$_2$O$_3$ powder (Strem Chemicals) the pores of γ- Al$_2$O$_3$ had been *a priori* saturated with n-hexane. A certain amount of platinum (II) acetylacetonate solution was added to γ- Al$_2$O$_3$ drop by drop. The prepared sample was then dried in vacuo at 323K. The above preparation steps were repeated ten times to have 1wt% Pt loading. The samples were dried and calcined at 400°C for 4hr, and were finally reduced with a flowing 5% H$_2$/Ar gas mixture at 300°C for 4hr.

The catalytic activities were measured in a fixed bed reactor with a reaction feed of air stream containing 500 ppm of benzene, toluene, ethylbenzene or o-xylene. The flow rate of gas feed was 120 cc/min over 0.2g catalysts. Analysis of the reactor outlet gas was performed by an on line gas chromatograph (HP 5890II) equipped with FID.

Dispersion of Pt particles in Pt/CeO$_2$ and Pt/Al$_2$O$_3$ was observed with a transmission electron microscopy (JEOL 2000X) using 160KeV electrons.

IR spectra were recorded on a JEOL JIR 100 FTIR spectrometer with 256 scans at 4cm$^{-1}$ resolution. About 50mg of the catalyst was pressed into a self-supporting wafer and the wafer was placed inside the IR cell designed by nearly the same method of Hicks et al.[10].

ESR spectra were recorded at X-band frequencies on a Varian E-4 spectrometer. DPPH and weak pitch were used as standards for the determination of g-values. The quartz sample tube was designed for *in situ* operation.

XPS analysis was performed with a VG ESCALAB 220iXL spectrometer with a MgKα-source operating at 20mA and 13KV.

BET surface areas were determined by adsorption of N$_2$ at 77K using a Micromeritics ASAP 2010.

## 3. RESULTS AND DISCUSSION

### 3.1. Oxidation of BTEX on Pt/CeO$_2$ and Pt/Al$_2$O$_3$

Figure 1 shows the light-off curves for BTEX oxidation as a function of reaction temperature on the reduced 1wt% Pt/CeO$_2$ and 1wt% Pt/Al$_2$O$_3$ at 300°C for 4hr. On Pt/CeO$_2$ catalyst conversion of ethylbenzene begins at 100°C and increases quickly so that complete oxidation is reached at 240°C. O-xylene begins to react at 120°C, but its oxidation rate is slow upto 160°C where 40% ethylbenzene was converted. At about 160°C reaction rate of o-xylene becomes faster and complete conversion of o-xylene is achieved at 300°C. Toluene shows practically the same behavior as o-xylene. Combustion of benzene takes place at higher temperatures than toluene, o-xylene and ethylbenzene in such a way that at 340°C its conversion was not higher than 97%.

Activity comparison between Pt/CeO$_2$ ad Pt/Al$_2$O$_3$ shows that Pt/CeO$_2$ is considerable more active than Pt/Al$_2$O$_3$ for the oxidation of BTEX. The activity difference might be due to the different size(or dispersion) of Pt particles in these catalysts. However, as shown in the TEM micrographs of these catalysts (Fig. 2) the size of the Pt particles in both the catalysts was nearly the same to have average diameter of 20Å. Therefore the effect of Pt particle size on the activity difference is , if any, believed to be not so significant.
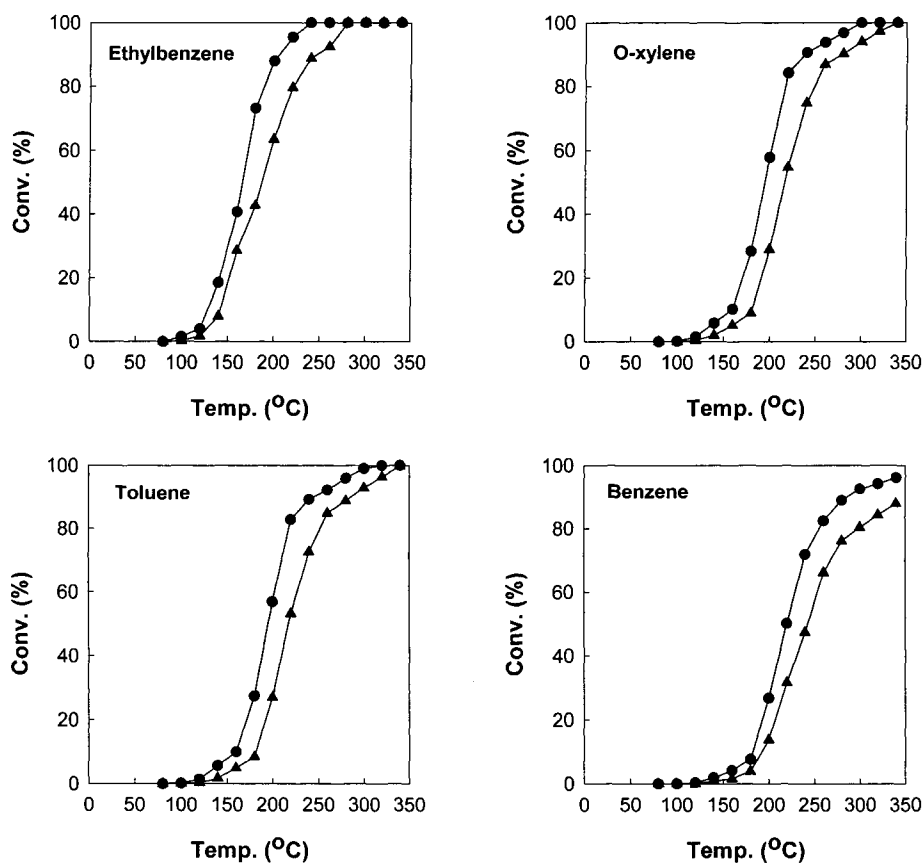


Figure 1. The temperature dependence of BTEX conversion on 1wt% Pt/CeO$_2$ catalyst(★) and 1wt% Pt/Al$_2$O$_3$ catalyst(π).

Another possibility for the activity difference might be the different electronic state of the active Pt surface which generally occurs through strong interaction between Pt and support. In order to verify this, XPS analysis of the catalysts was carried out. The Pt 4d$_{5/2}$ XPS spectrum of the fresh Pt/CeO$_2$ catalyst appeared at the binding energy of 314.2 eV, which was nearly the same as 314.1 eV of the fresh Pt/Al$_2$O$_3$ catalyst. In addition the binding energy of both the

used Pt/CeO$_2$ and Pt/Al$_2$O$_3$ after reaction with benzene at 350°C for 1hr was the same to each other and had 315.5 eV. Binding energy shifts from metallic Pt to PtO reported in the literature are 1.1[4], 1.4[5] and 2.2 eV[6]. The Pt 4d$_{5/2}$ XPS line shifting from 314.1 or 314.2 eV for the fresh catalysts to 315.5 eV for the used ones suggests the formation of surface PtO. The 0.1 eV difference in the binding energy of the fresh catalysts does not seem to be significant for the different electronic state of Pt to play a major role on the activity difference between the two catalysts. As mentioned CeO$_2$ acts as an oxygen storage. The stored oxygen might be able to migrate onto Pt, so that the Pt/CeO$_2$ catalyst can work well for the oxidation of BTEX. The migration of oxygen was investigated by using FTIR and ESR.
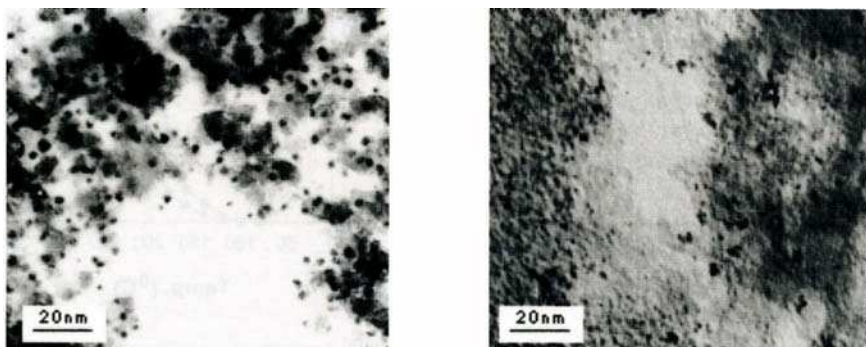


Figure 2. TEM micrographs of the fresh 1wt% Pt/Al$_2$O$_3$(left) and 1wt% Pt/CeO$_2$(right).

### 3.2. FTIR and ESR analyses

Figure 3 shows the IR spectra of adsorbed oxygen at room temperature on CeO$_2$ and Pt/CeO$_2$ which were reduced at 300°C for 4hr. A pair of bands at 2237 and 1126cm$^{-1}$ are clearly observed. These bands were assigned to adsorbed superoxide (O$_2^-$)[7-10]. The band at 1126cm$^{-1}$ was the characteristic frequency of O-O vibration, and the band at 2237cm$^{-1}$ was the first overtone of that at 1126cm$^{-1}$. The formation of the adsorbed superoxide species on the reduced CeO$_2$ might be due to surface defects or oxygen deficient sites where the superoxide species were formed.

The presence of Pt, however, decreased the intensity of these bands significantly, and the bands became undetectable at the adsorption temperature higher than 80°C. Since dioxygen species on Pt surface is known to dissociate rapidly into monooxygen species even at low temperature below room temperature [11], superoxide become unobservable on Pt surface. Hence the superoxide species observed on Pt/CeO$_2$ are adsorbed on CeO$_2$ surface instead of Pt surface. The respective surface area of CeO$_2$ and Pt/CeO$_2$ was 57m$^2$/g and 55m$^2$/g, indicating that surface area of CeO$_2$ in Pt/CeO$_2$ was just slightly decreased by the presence of Pt. If the adsorbed superoxide on CeO$_2$ does not migrate onto Pt, the intensities of superoxide

bands will reduce in proportion to the decrease in surface area. In this case intensities of superoxide bands on Pt/CeO$_2$ become almost the same as those on CeO$_2$ in spite of the presence of Pt. Although the superoxides species on the interface between CeO$_2$ and Pt or in the vicinity of Pt may dissociate, it is difficult to understand how the superoxide species located far from Pt particles can also dissociate into monooxygen rapidly.

A reasonable explanation for the significant decrease in band intensities by the presence of Pt is that the superoxide species formed on CeO$_2$ surface migrate or spillover continuously onto the Pt surface where they become monooxygen rapidly because Pt is an active catalyst for oxygen dissociation. Continuous migration or spillover of superoxide onto the Pt surface might be confirmed by measuring the changes in the adsorbed superoxide band intensities with time. Unfortunately the adsorbed superoxide on Pt/CeO$_2$ was so unstable that the changes in the intensity with time could not successfully be obtained.

Figure 4 shows the ESR spectra of adsorbed oxygen on the reduced CeO$_2$ and Pt/CeO$_2$. The spectra were recorded 1hr after oxygen introduction. For CeO$_2$, four typical signals at g values of 2.038, 2.029, 2.020 and 2.015 which were ascribed to adsorbed superoxide species [19,20]. For Pt/CeO$_2$, however, only the signals at g values of 2.038 and 2.015 are observed and the intensity of these signals was below one hundredth of that in CeO$_2$. This significant decrease in ESR signals by the presence of Pt coincides well with the result obtained from IR spectra.



Figure 3.FTIR spectra of adsorbed oxygen on CeO$_2$ and Pt/CeO$_2$.

### 3.3. Spillover of dioxygen from CeO$_2$ onto Pt

In order to confirm the aforementioned continuous migration or spillover of superoxide species onto the Pt surface, ESR signals on Pt/CeO$_2$ were measured with time after introduction of O$_2$ and the relative intensity of the signal at 2.015 was plotted versus time as shown in Figure 5. The relative intensity recorded on Y axis is the ratio of the intensity of the signal during the time and the intensity of the signal at 1min after introduction of O$_2$. The strong signal observed one minute after O$_2$ introduction attenuates rapidly with time, and only 5% of the intensity is left after 60min. The ESR signal on CeO$_2$ was, however, relatively stable with time, and about 35% of the intensity was lost in 60min. The superoxide species on CeO$_2$ must be more stable than those on Pt/CeO$_2$. The rapid disappearance of the superoxide species on Pt/CeO$_2$ can be explained by the continuous migration or spillover of the adsorbed superoxide on CeO$_2$ onto Pt surface where dioxygen dissociates rapidly into monooxygen. The monooxygen species on Pt, derived from spillover oxygen from CeO$_2$ surface, will
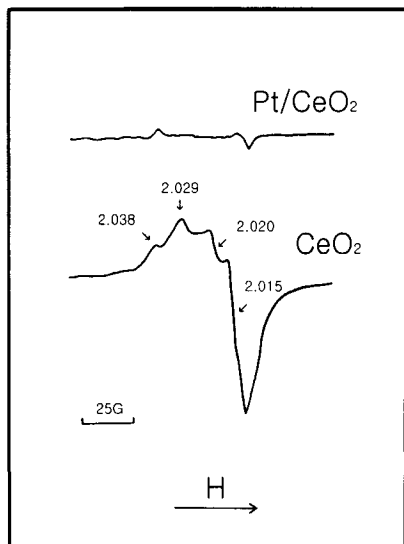
Figure 4. ESR spectra of adsorbed oxygen on $CeO_2$ and $Pt/CeO_2$.
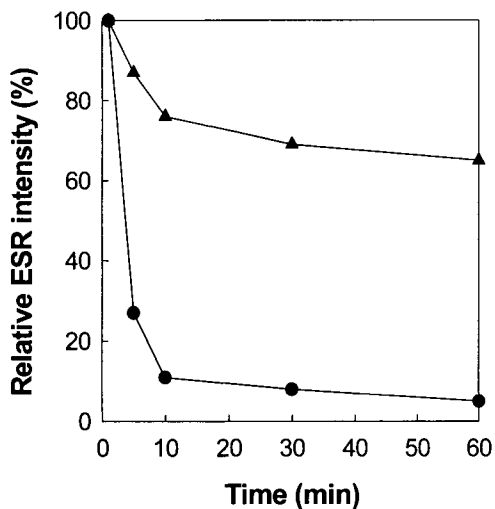
Figure 5. Changes in ESR signal (g value = 2.015) with time on $CeO_2$(▲)an d $Pt/CeO_2$(★).

accelerate the oxidation of BTEX. Accordingly the higher activity of $Pt/CeO_2$ for the oxidation of BTEX shown in Figure 1 is believed to be due to the spillover oxygen from $CeO_2$ onto Pt.

### 3.4. Catalytic oxidation of VOCs from contaminated soil by gasoline

Oxidation of VOCs in the vapor-laden air withdrawn from contaminated soils by gasoline was carried out at 250°C and 300°C with the $Pt/CeO_2$ catalyst. Fresh air was injected into the subsurface at locations around a gasoline spill site, and the vapor-laden air was withdrawn under vacuum from extraction vents. One hundred grams of $Pt/CeO_2$ catalyst was used, and the flow rate of the vapor-laden air was kept to be about 300cc/min. In the air stream were contained a lot of components together with BTEX. The initial concentration of BTEX in the air was 17000ppm, and huge amount of water vapor(15000ppm concentration) was also included.

GC chromatograms of the gasoline components before reaction and after reaction at 250°C and 300°C are shown in Figure 6. As seen, most of gasoline components could successfully be oxidized after reaction at 300°C with the $Pt/CeO_2$ catalyst. The $Pt/CeO_2$ catalyst was stable even in the presence of water vapor during the reaction, and could be a practical catalyst for the oxidation of BTEX from contaminated soils by gasoline.
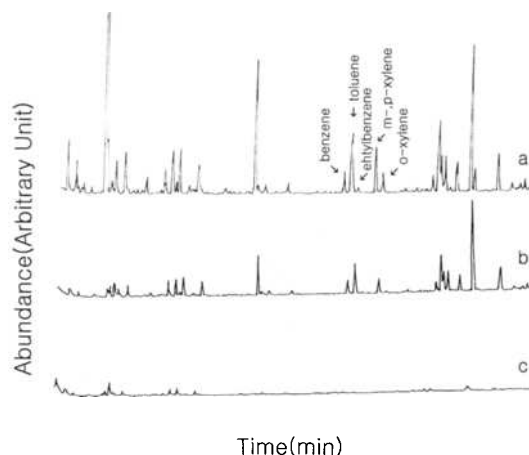
Figure 6. GC chromatograms of VOCs from contaminated soils before reaction(a) and after reaction at 250°C(b) and 300°C(c) with Pt/CeO$_2$ catalyst.

## 4. CONCLUSION

Catalyst oxidation of BTEX was investigated in the presence of Pt/CeO$_2$ and Pt/Al$_2$O$_3$ catalysts. The Pt/CeO$_2$ catalyst exhibited much higher activity in comparison to the Pt/Al$_2$O$_3$ catalyst. While ethylbenzene conversion over Pt/Al$_2$O$_3$ was 89% at 240°C, complete conversion of ethylbenzene was achieved in the presence of Pt/CeO$_2$.

The current work showed that the presence of Pt in the Pt/CeO$_2$ catalyst decreased the adsorption of superoxide($O_2^-$) species significantly. From the FTIR ad ESR analyses, the adsorbed superoxide species migrated or spiltover from CeO$_2$ onto the surface of Pt where the superoxide species dissociate very rapidly into monooxygen species. The spiltover oxygen from CeO$_2$ was suggested to promote the oxidationof BTEX on Pt/CeO$_2$ catalyst.

The Pt/CeO$_2$ catalyst could practically be applied to the oxidation of VOCs including BTEX in the vapor-laden air withdrawn from contaminated soils by gasoline.

## REFERENCES

1. R. Burch, P. K. Loader and F. J. Urbano, Catal. Today, 27(1996)243.
2. P.-O. Larsson, H. Berggren, A. Anderson and O. Augustsson, Catal. Today, 35(1997)137.
3. R. Burch, P. K. Loader, Appl. Catal., B, 5(1994)149.
4. J. J. Spivey and J. B. Butt, Catal. Today, 11(1992)465.
5. E. N. Ruddy and L. A. Carroll, Chem. Eng. Prog., 89(1993)28.
6. V. Labalme, N. Benhamou, N. Guilhaume, E. Garbowski and M. Primet, Appl. Catal., A, 133(1995)351.
7. D. Kalakkad and A. V. Dayte, Appl. Catal., B, 1(1992)191.
8. J. G. Hunam, H. R. Robota, M. J. Cohn and S. A. Bradley, J. Catal., 133(1992)309.
9. P. Marecot, L. Pirault, G. Mabilon, M. Prigent and J. Barbier, Appl. Catal., B, 5(1994)57.

10. R. F. Hicks, C. S. Kellner, B. J. Savatsky, W. C. Hecker and A. T. Bell, J. Catal., 71(1981)216.
11. J. Z. Shyu and K. Otto, Appl. Surf. Sci., 32(1988)546.
12. J. C. Vedrine, M. Dufaux, C. Naccache and B. Imelik, J. Chem. Soc. Faraday Trans. I, 74(1978)440.
13. J. A. Rossin, J. Mol. Catal., 58(1990)363.
14. C. Li, K. Domen, K. Maruya and T. Onish, J. Am. Chem. Soc., 111(1989)7683.
15. C. Li, K. Domen, K. Maruya and T. Onish, J. Chem. Soc., Chem. Commun., (1988)1541.
16. M. W. Urban, K. Nakamoto and F. Basolo, Inorg. Chem., 21(1982)3406.
17. D. McIntosh and G. A. Ozin, Inorg. Chem., 16(1977)59.
18. J. L. Gland, B. A. Sexton and G. B. Fisher, Surf. Sci., 95(1980)587.
19. M. Gideoni and M. Steinberg, J. Solid State Chem., 4(1972)370.
20. C. Li, Y. Song, Y. Chen, Q. Xin, X. Han and W. Li, Stud. Surf. Sci. Catal., 112(1997)439.

# The role of Cu in the reactivity of Cu/ZrO₂ catalysts for the SCR of NO with CH₄

A.Caballero[*,a], J.J.Morales[a], J.P.Holgado[a], J.P.Espinos[a], M.Ocaña[a], J.A.Anderson[b], A.R.González-Elipe[a]

[a]Instituto de Ciencia de Materiales de Sevilla (CSIC-USE) and Departamento de Química Inorgánica, Universidad de Sevilla. 41092-Sevilla, Spain.

[b]Dept. of Chemistry, University of Dundee, Dundee DD1 4HN, Scotland, UK

This paper provides some evidences about the role of the copper during the catalytic reduction of NO over Cu/ZrO₂ systems. The combination of catalytic test studies, DRIFTS and transmission FTIR spectroscopies and TPD measurements have shown how the general catalytic behaviour of this system is controlled by the zirconia support, the copper particles affecting principally the stability of the surface species adsorbed over the support in reaction conditions. In the copper containing system, less quantity of surface NOx species have been observed in reaction conditions, but also they are less stable, allowing its reduction with the methane molecules at lower temperature than in the ZrO₂ support.

## 1. INTRODUCTION

The removal of NOx from both stationary and automotive combustion processes is of great importance because of its effects on the health of living organisms and in the greenhouse effect. Selective catalytic reduction (SCR) of NO by hydrocarbons under oxidizing atmospheres offers a possible route to eliminate these toxic gases (1). The availability and use of methane as combustible has increased in recent years, and so, its use as reductant in the SCR process, despite its low reactivity, offers a possibility to simplify the practical application of the SCR process. Although this reaction has been extensively study, especially for Co-containing systems (2,3), also the Cu/ZrO₂ catalytic system has been recently reported as active in the SCR reaction with methane (4).

In this work, the catalytic behaviour of an ZrO₂ support, with and without copper, has been analysed for the NO-CH₄ reaction. The effect of the presence of copper in the reactivity of this oxide towards the reactive gas mixture has been studied by means of TPD and IR measurements.

## 2. EXPERIMENTAL

The ZrO₂ support was prepared by forced hydrolysis at 371 K of a 0.2M ZrOCl₂ solution for 72 h (5). The product obtained was dialysed for 3 days to eliminate the chloride ions, and calcined at 773 K for 3 h. After those treatments, the X-ray powder diffraction (XRD)
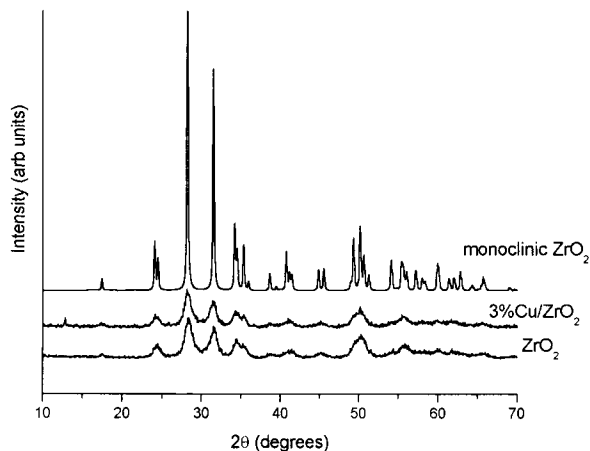
Fig.1. XRD patterns (Cu-Ka) of Cu/ZrO$_2$, the ZrO$_2$ support and a monoclinic phase.

patterns of the samples were carried out using Cu-Ka radiation in a Siemens D5000 diffractometer (Fig.1). They were consistent with the formation of a monoclinic phase of ZrO$_2$.

The TEM images (Fig.2) were recorded in a Philips CM200 microscope working at 200kV. They show particles of about 100nm, with a BET surface area of 45 m$^2$/g (Micromeritics ASAP 2010). The 3% Cu/ZrO$_2$ catalytic system was prepared by incipient wetness impregnation with a Cu(NO$_3$)$_2$ solution, drying at 393 K overnight and calcination in 3% O$_2$/He at 573 K for 3 h.
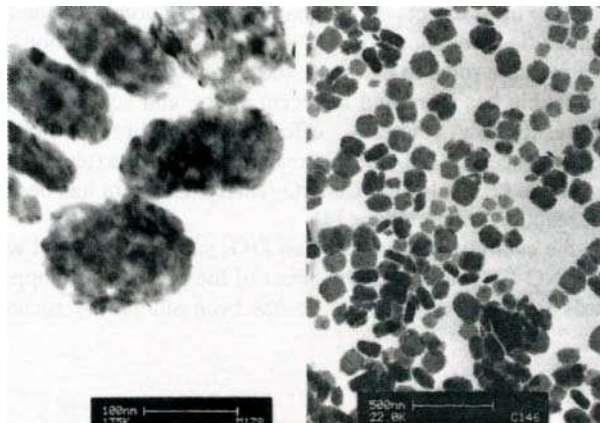


Fig.2. TEM images of ZrO$_2$ support after been calcined at 723K.

The catalytic reaction of NO with methane was carried out by measuring the light-out behaviour up to 823 K at 1K/min using a 1000 ppm NO + 2500 ppm $CH_4$ + 0 or 3% $O_2$ (He balance) mixture with a SV= 20000 $ml.h^{-1}.g^{-1}$. The product gases were analysed by means of a gas chromatograph (Varian 3800), equipped with a TCD detector and two columns packed with Porapak Q and molecular sieve 5A.

DRIFTS spectra were recorded with a Perkin-Elmer 1750 FTIR at 4 $cm^{-1}$ resolution (50 scans) equipped with a MCT detector and a Harrick environmental cell. Samples were calcined *in situ* in the DRIFTS cell at 773K in a flow of dry air, and treated with different $NO/CH_4/O_2$ mixtures at temperatures between 298 to 823K. Spectra were collected *in situ* during the thermal treatment at 298K, 473K, 623K and 773K. Transmission FTIR spectra were recorded with a Nicolet 510 spectrometer, using a Specac environmental cell that allows the recording in situ at temperatures up to 773K.

TPD experiments were performed in a flow system coupled with a TCD and a quadropole mass spectrometer. The samples were treated at room temperature with NO or with a mixture of $NO/O_2$ (1000ppm NO, 3%$O_2$, He balance), purged with helium and heated at 10 K/min from room temperature to 773 K.

## 3. RESULTS AND DISCUSSION

The catalytic performances of the $ZrO_2$ and $Cu/ZrO_2$ systems in the SCR reaction of NO with $CH_4$ in the absence and presence of oxygen are presented in Fig. 3. As shown, in the absence of oxygen the behaviour of the two system is quite distinct, with no conversion
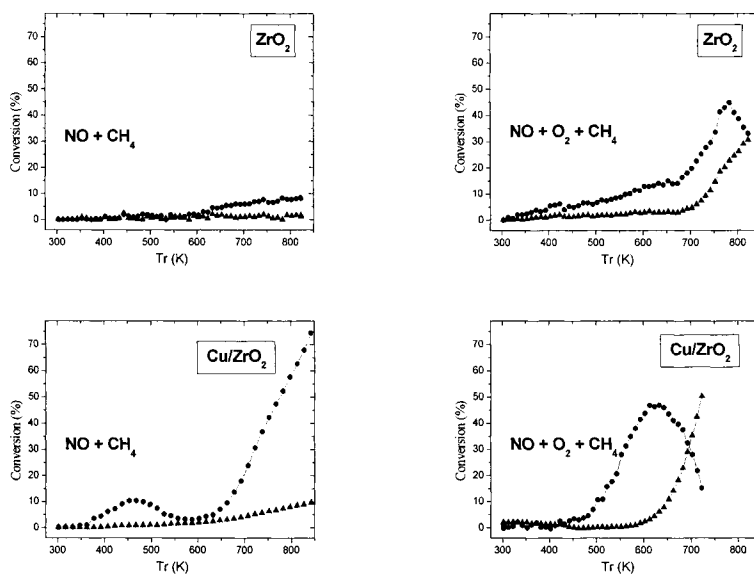


Fig.3. Conversion of NO (circle) and $CH_4$ (triangle) versus temperature for the SCR reaction over $ZrO_2$ and $Cu/ZrO_2$ systems.

in the ZrO$_2$ system over the whole temperature range, but up to 75% NO conversion at 823 K in the Cu/ZrO$_2$ system. In this last case, the methane and NO conversion are consistent with the stochiometric reaction of NO with methane:

$$4NO + CH_4 \rightarrow CO_2 + 2H_2O + 2N_2$$

The behaviour of the ZrO$_2$ and the Cu/ZrO$_2$ systems in the SCR reaction with the NO/CH$_4$/O$_2$ mixture is quite different. As can be seen in the figure, the NO conversion over these two catalytic systems are important, with maximum at about 50% NO conversion at 623 K for Cu/ZrO$_2$, and 150 K higher (773K) for the ZrO$_2$ support without copper. At temperatures above the maximum, the methane reaction with oxygen to form CO$_2$ dominates, with higher conversion of methane at 823 K for the Cu/ZrO$_2$ (100%) than the ZrO$_2$ alone (30%). So, this first results show that the ZrO$_2$ carrier is active for the SCR reaction with methane in these conditions, the copper affecting the reaction by decreasing significantly the temperature for the SCR reaction.

In order to elucidate the nature of the surface species formed on the catalyst in reaction conditions, both catalytic systems were investigated by DRIFTS, recording the spectra *in situ* at 623 K during the interaction of the systems with NO, O$_2$ and CH$_4$. At this temperature, no bands from mononitrosyl species over the Cu sites are detected, which appear at room temperature at about 1878 cm$^{-1}$. Figure 4 (full line) shows the DRIFTS spectra obtained after contact of ZrO$_2$ and Cu/ZrO$_2$ at 623K with NO and NO+O$_2$. As can be seen, these treatments produce the massive formation of bands located between 1700 and 1100 cm$^{-1}$, showing that various forms of NOx species adsorbed over the Cu and/or the ZrO$_2$ support are present in both systems.
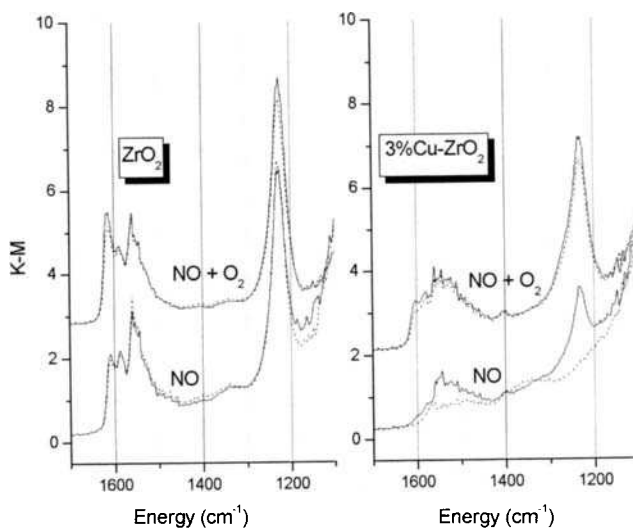


Fig.4. DRIFTS spectra of ZrO$_2$ and Cu/ZrO$_2$ systems after (full line) contact with NO (or NO+O$_2$) at 623K and subsequent addition of CH$_4$ (dotted line).

As known (6), is not possible to assign unambiguously the bands in this spectral region because of the existence of a wide variety of species with IR modes at similar frequencies, such as nitro, nitrates and nitrites bonded in different manners (mono and bidentate, bridged, etc.) to the surface sites. The comparison of the spectra obtained for the support and the Cu-containig catalysts show that the effect of copper on these species, is, initially, to decrease their stability, in agreement with the lower intensity of IR bands. Additionally, the spectra collected after the treatment of this systems with the $NO+O_2+CH_4$ mixture (figure 4, dotted line) show that the copper affects the lability of these adsorbed species, enabling, in some cases, their extensive reaction with $CH_4$. Both effects can be related with an higher mobility (spillover) of the surfaces species over the support induced by the copper active sites. These phenomena are especially relevant for the $NO-CH_4$ reaction, which almost eliminates adsorbed NOx species from the $Cu/ZrO_2$ system (figure 4).

In order to confirm this effect of copper on the adsorbed species, it have been conducted a study by temperature programmed desorption (TPD). These profiles, presented in Fig.5, have been obtained after the contact of the $ZrO_2$ and $Cu/ZrO_2$ systems with NO or $NO+O_2$ mixtures at room temperature.
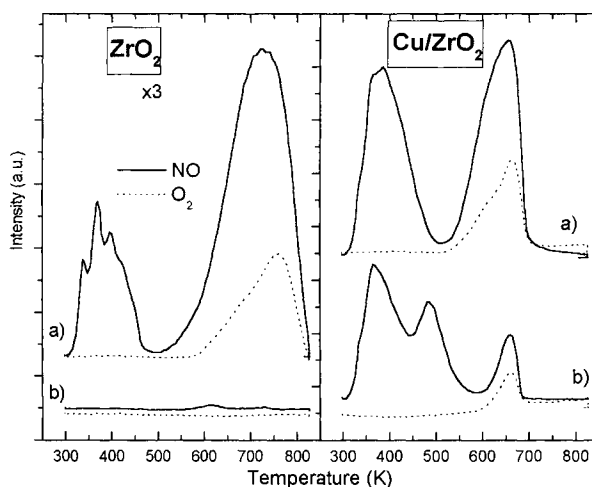


Fig.5. TPD profiles obtained after adsorption of a) $NO+O_2$ and b) NO at 298K .

The TPD profiles clearly show the important differences in the behaviour of both catalytic systems. First, the total adsorption of NOx species is much lower on the $ZrO_2$ system (note the x3 index in the $ZrO_2$ profiles), with almost no irreversible adsorption of NO in the absence of oxygen. The presence of copper and the coadsorption with oxygen drastically increase the adsorption capacity of the systems, with a great similarity between the profiles of $ZrO_2$ with and without copper after $NO+O_2$ coadsorption. It is important to note that these results are completely congruent with the previous DRIFTS spectra, because as can be seen in the TPD profiles, at 623K, more species are desorbed in the Cu-containing system than in the

ZrO$_2$ carrier. As a conclusion, these facts allow us to conclude that, contrary to what others authors suggest (7), the species desorbing from Cu/ZrO$_2$ during the TPD experiment can come also from the copper phase but, principally, from the ZrO$_2$ support, even although the TPD curves of NO adsorbed on unsupported CuO obtained previously by M.Shimokawabe et al. (8) present similar profiles to that obtained by us for the ZrO$_2$ systems.

Roughly, the NOx species desorbed in the TPD experiment can be classified in two different types. The low temperature desorption processes, between 298K and 550K, must correspond to mononitrosyl and dinitrosyl compound adsorbed on the support surface, coming from the nonreactive adsorption of NO. The high temperature region, up to 800K, show the simultaneous desorption of NO and O$_2$, which must come from the decomposition of the previous reactive adsorption of NO over the ZrO$_2$ surface, producing oxidized species as nitro, nitrites or nitrates. These species are less important but observed even when only NO is adsorbed on the Cu/ZrO$_2$ system (figure 4, right, b). In this case, the oxidation of NO to nitrites or nitrates species can proceed from the thermal decomposition of the CuO to Cu$^+$ species that, according to previous observations (9,10), occur during the TPD experiment.

Also very interesting is to observe in the thermal profiles of the Cu-containing system that the high temperature codesorption peak of NO and O$_2$ have the maximum around 673 K, 80 K lower than for the ZrO$_2$ alone. This effect also point out that the copper favours the spillover of NOx species over the ZrO$_2$ surface. This spillover phenomenum would operate increasing the ability of the support to adsorb NOx species, but also increasing the lability of the different adsorbed NOx species. It is worthy of note that the decrease in the catalytic activity at temperatures above that of maximum conversion observed for these systems in the SCR reaction with methane (figure 3) can be related with the thermal instability of the adsorbed species, thus eliminating from the surface the potential SCR intermediates and decreasing the conversion of NO, producing this volcano-shape curve.

This correlation between the temperatures of maximum activity in the SCR reaction (figure 3) with the high temperature peak in the TPD profile (figure 5) suggest also that the adsorbed species that, by decomposition, produce the codesorption of NO and O$_2$, could act as intermediates in the SCR reaction with methane, species that, once desorbed at higher temperatures, decrease the catalytic activity of the system. This fact suggest that, in agreement with the mechanism proposed by others authors for the SCR with methane, the oxidized NOx surface species operate activating the methane molecule (11,12), and allowing the reduction of these NOx species.

To clarify this point, a transmission FT-IR experiment has been carried out in similar conditions to that of the previous TPD experiment. So, IR spectra were recorded after coadsorption of NO and O$_2$ at room temperature (Fig.6), and after purge with argon at 473K and 623K. As can be seen, after the adsorption at room temperature, the spectrum present a great number of bands between 1700 and 1200 cm$^{-1}$, similar to that observed previously in the DRIFTS spectra (figure 4). The IR bands first disappearing after purge with argon at 473K are those around 1670cm$^{-1}$, which must be due to nitrosyls (NO) and dinitrosyls ((NO)$_2$) species (6). Most of the initial bands disappear after purge at 623K, remaining two bands at 1572 cm$^{-1}$ and 1370 cm$^{-1}$. After purge at 773K, all the bands disappear, resulting in a spectrum similar to that obtained after calcination at 573K. Assuming these bands correspond to the compound desorbing at 673K as NO and O$_2$ (figure 5), it could be assigned (6) to asymmetric and symmetric stretching modes of nitro NO$_2^-$ species adsorbed on the ZrO$_2$ support which, in agreement with previous discussion, might be considered as the intermediates capable to react with the hydrocarbon (methane) in the SCR reaction to rend CO$_2$ and N$_2$.
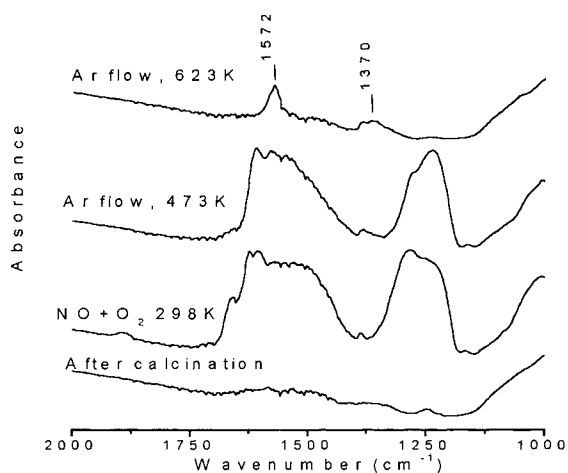
Fig.6. Transmission FTIR spectra of Cu/ZrO2 system after adsorption of NO+O$_2$ at 298K and purge with argon at increasing temperatures.

## 3. CONCLUSION

The Cu/ZrO$_2$ catalytic system have a good activity in the SCR reaction of NO by methane in oxidizing conditions, but, although less performance, the zirconia support is also active in this reaction. The adsorption-desorption processes over the support of zirconia determine the catalytic activity, and the copper play an essential role in these processes, providing by spillover a way for the NO to generate the appropriates intermediates at lower temperature than in the ZrO$_2$ support alone.

## REFERENCES

1. M. Iwamoto, H. Yahiro, N. Mizuno, W.-X. Zhang, Y. Mine, H. Furukawa, S. Kagawa, J. Phys. Chem., 96 (1992) 9360.
2. J.N. Armor, Catal. Today, 26 (1995) 147.
3. E.M. Sadovskaya, A.P. Suknev, L.G. Pinaeva, V.B. Goncharov, C. Mirodatos, B.S. Balzhinimaev, Stud. Surf. Sci. Catal., 130 (2000) 1505.

346

4.  H. Aritani, S. Kawaguchi, T. Yamamoto, T. Tanaka, Y. Okamoto, S. Imamura, Chem. Lett., 2000, 532.
5.  A. Bleier, R.M. Cannon, Mat. Res. Soc. Symp. Proc., Vol.73. 71-78 (1986).
6.  K.I. Hadjiivanov; Catal. Rev.-Sci. Eng., 71-144 (2000).
7.  G. Delahay, B. Coq, E. Ensuque, F. Figueras, Langmuir, 13 (1997) 5588.
8.  M. Shimokawabe, N. Hatakeyama, K. Shimada, K. Tadoroko, N. Takezawa, Appl. Catal. A: General, 87 (1992) 205.
9.  G.D. Lei, B.J. Adelman, J. Sarkany, W.M.H. Sachtler, Appl. Catal.B: Enviromental, 5 (1995) 245.
10. A. Dandekar, M.A. Vannice, Appl. Catal.B: Enviromental, 22 (1999) 179.
11. Y. Li, T.L. Slager, J.N. Armor, J. Catal., 150 (1994) 388.
12. E.A. Lombardo, G.A. Sill, L.J. dItri, W.K. Hall, J. Catal., 173 (1998) 440.

347

# Oxygen handling properties of Ce-Ca mixed oxides solutions

A. Iglesias-Juez[a], A.B. Hungría[a], O. Gálvez,[a] M. Fernández-García, [a,*] A. Martínez-Arias[a], A. Guerrero-Ruiz,[b] J.C. Conesa[a], J. Soria[a]

[a] Instituto de Catálisis y Petroleoquímica, CSIC, Campus Cantoblanco, 28049-Madrid, Spain
[b] Dept. Química Inorgánica y Técnica, UNED, Senda del Rey, 28040-Madrid, Spain

The doping of ceria with Ca ions is investigated. A microemulsion method of preparation allows to insert up to 33-40 at.% of Ca in the fluorite-type structure of the cerium oxide. Above such quantity, Ca is possibly spread on the mixed oxide surface, yielding stable bidentate Ca carbonate species. The incorporation of Ca into the $CeO_2$ lattice enhances significantly the number of surface oxygen vacancies created by outgassing. The interaction with $O_2$ is affected by the new nature of the surface, enhancing the activation/dissociation of the molecule, and by the change of the mobility through the bulk structure.

## 1. INTRODUCTION

Doping of ceria components with cations has technological implications for the present and future improvements of three-way catalysts [1] as well as of oxygen permeation membranes [2]. Cationic dopants with oxidation states lower than +IV are incorporated into the $CeO_2$ lattice leading to the formation of oxygen vacancies. Differences in oxygen handling properties of these oxides in respect to pure $CeO_2$ depend primarily on the size of the dopants (i.e. anion-cation bonding force) as well as on the energy of association between vacancy and electron and vacancy and dopant (influencing, respectively, the mobility of the electron and of vacancy). In particular, Ca is known to increase the oxygen storage capacity of ceria by 40% [3], giving a way to improve the properties of three-way catalysts.

In order to better understand the Ce-Ca binary oxide system, the synthesis of samples with Ca/Ce atomic ratios up to 1 has been attempted in this work. The surface and bulk properties of such complex materials have been analyzed by using a multitechnique approach.

## 2. EXPERIMENTAL

Three specimens were prepared by an inverse microemulsion method [4] with initial Ca/Ce atomic ratios of 0.1, 0.5 and 1 in the reacting mixtures, and calcined at 773 K for 2h, giving powders (hereafter referred as Ce9Ca1, Ce2Ca1 and Ce1Ca1) with, respectively, BET area of 111, 94 and 81 $m^2g^{-1}$. Reference materials of Ce ($S_{BET} = 92$ $m^2g^{-1}$) and Ca ($S_{BET} = 7$ $m^2g^{-1}$) were prepared using the same procedure.

Powder X-ray diffraction (XRD) patterns were recorded on a Siemens D-500

---
* Corresponding author ; e-mail: m.fernandez@icp.csic.es; fax: 34-91-5854760.

diffractometer using nickel-filtered Cu Kα radiation operating at 40 kV and 25 mA. Spectra were taken with a 0.025° step size and using a counting time of 1s.

Transmission Electron Microscopy (TEM) experiments were carried out using a JEOL 2000 FX (0.31nm point resolution) equipped with a LINK (AN 10000) probe for Energy dispersive x-ray spectroscopy (EDS) analysis. Portions of samples were crushed in an agate mortar and suspended in cyclohexene. After ultrasonic dispersion, a droplet was deposited on a copper grid supporting a perforated carbon film. Micrographs and electron diffractograms and, when necessary, dark-field images were recorded over selected areas with compositions previously characterized by EDS.

Raman spectra were obtained at room temperature (RT) with a Bruker RFS-100 FT-Raman spectrometer provided with a diode-pumped germanium solid-state detector, which operates at liquid nitrogen temperature. A NdYAG laser was used as excitation source with a power of ca. 10 mW. Powdered samples were pressed in a holder and analyzed (200 scans, 4 cm$^{-1}$ resolution) without further treatment.

EPR spectra in the X-band mode ($v \approx 9.5$ GHz) were recorded at 77 K with a Bruker ER 200D spectrometer calibrated with DPPH (g = 2.0036). Portions of ca. 40 mg of sample were placed inside a quartz probe cell where they can be subjected to outgassing treatments in high-vacuum conditions (ca. $10^{-4}$ Torr , dynamic vacuum). Oxygen adsorption experiments were carried out by admitting in the cell doses of 70 μmol of $O_2$ per gram of sample at 77 K, followed by thorough outgassing at 77 K and warming to room temperature. Prior to $O_2$ adsorption the samples were pretreated under 300 Torr of $O_2$ at 773 K for 2 h followed by outgassing at 773 K for 2 h.

Isotopic exchange experiments were carried out with ca. 15 mg of sample held inside a recirculating quartz reactor coupled to a grease-free standard vacuum system. Gas phase was analyzed with an on-line quadrupole spectrometer (Balzers QMG 421 C) connected to the reactor through a metering leak valve [5]. Calcined samples (100 Torr $^{16}O_2$ at 773 K, 1h) were subjected to evacuation at reaction temperature (573 K, 10 min) and to a subsequent circulation of ca. 87 Torr of $C^{18}O_2$ at 573 K through the catalytic bed, with continuous analysis of gaseous products ($C^{18}O_2$, m/Z = 48; $C^{18}O^{16}O$ m/Z = 46; $C^{16}O_2$ m/Z = 44; and secondary masses). Additional thermo-programmed surface reactions (TPSR) using ca. 49 Torr of $^{18}O_2$ were also performed at 10 K min$^{-1}$ from RT to 873 K on samples pre-calcined as above.

## 3. RESULTS

### 3.1 Morphological and structural characterization.

XRD patterns (Fig. 1) as well as Raman spectra (Fig. 2) give evidence that all solid synthesized contain crystalline phases with a fluorite-type structure. Cell parameters, calculated from the three strongest reflections, for the Ce-Ca materials are 5.40±0.01 Å, which can be compared with the reported, and here measured, value of 5.412 Å for pure cerium oxide. The practical invariance of the cell parameter is in broad agreement with the small elongation (less 2%) detected by neutron diffraction in samples with ca. 12 at. Ca % (see ref. 3 and references therein). The Ca reference does not correspond to a pure phase and the XRD pattern (data not shown) can be ascribed to a mixture of Ca oxide and carbonate (calcite). Interesting to note is that the full width at medium height (FWMH) grows markedly from Ce

and Ce9Ca1 to the remaining mixed oxide samples (Fig. 1b). Raman spectra confirm the fluorite-type structure of these materials, displaying a single band with a frequency red-shift and FWMH increasing with the Ca content of the specimens (Fig. 2).



Fig. 1. A; XRD patterns of Ce-Ca materials. B; Full width at maximum height of the most intense reflections.
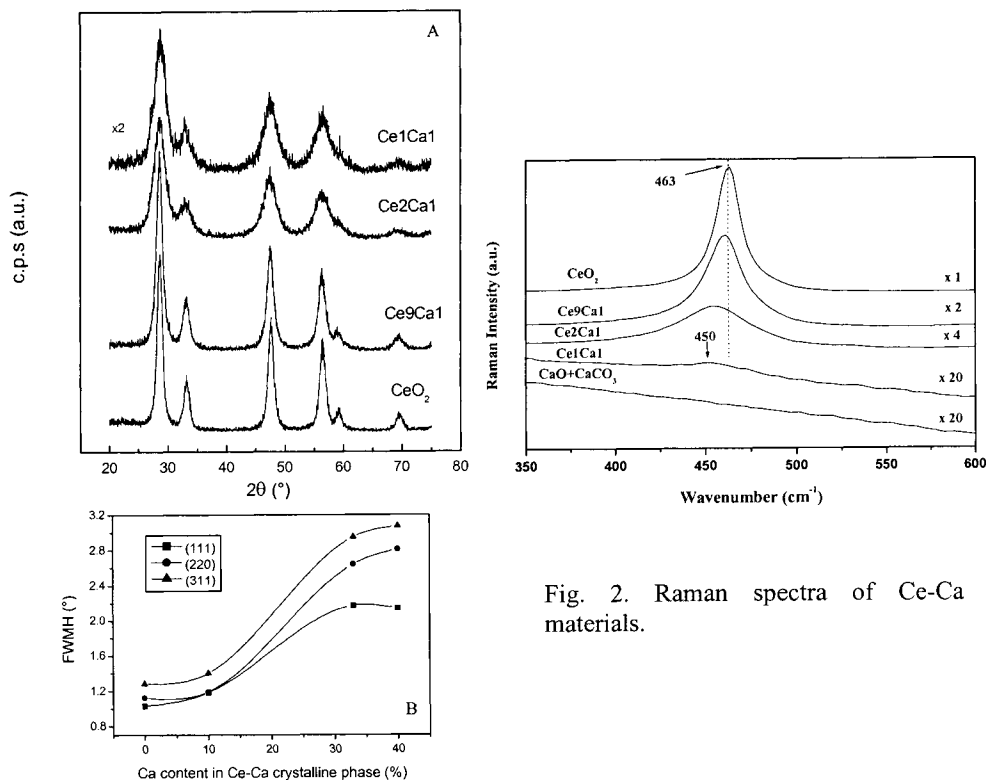
Fig. 2. Raman spectra of Ce-Ca materials.

EDS/TEM analysis of Ce1Ca1 gives evidence of its heterogeneous composition, with Ca-richer regions presenting a carbon component which implies carbonates (see below). In the carbonate-free zones, likely representative of the mixed oxide phase, the composition approaches a 60 at. % of Ce. No Ca-richer zones are systematically obtained in the remaining materials, so that the real compositions of the calcined mixed oxides corresponding to $Ce_{0.9}Ca_{0.1}O_{1.9}$, $Ce_{0.66}Ca_{0.33}O_{1.67}$ and $Ce_{0.6}Ca_{0.4}O_{1.6}$, with the last one showing differences in the

Ca/Ce ratio when comparing as-prepared and calcined samples. Electron diffraction yields rings exclusively ascribed to fluorite-type structures, independent of the zone analyzed. Dark-field TEM images, using the (111) and (220) reflections of fluorite-type structures, allows to estimate the average particle size of present crystalline phase, which is close to 2.5 nm for the two Ce-Ca samples with larger Ca content and ca. 6 nm for pure ceria. Assuming highly homogeneous materials, these figures can be compared with the ones extracted from XRD via Scherrer equation; values of 4 nm are obtained for Ce1Ca1 and Ce2Ca1, and of 7, 8 nm for Ce9Ca1 and $CeO_2$, respectively.

The analysis of IR bands (Fig. 3) reveals the presence of Ca carbonates on all samples. Ce9Ca1 contains unidentate (bands at ca. 1500, 1420 and 1060 $cm^{-1}$) and bidentate (bands at ca. 1550, 1315 and 1050 $cm^{-1}$) species [6,7]. The amount of the former grows at the expense of the latter with the Ca content of the materials. Notice that typical bands of bulk calcite, present in the Ca reference at about 2510 and 1795 $cm^{-1}$, are not observed on the Ce-Ca mixed oxides.
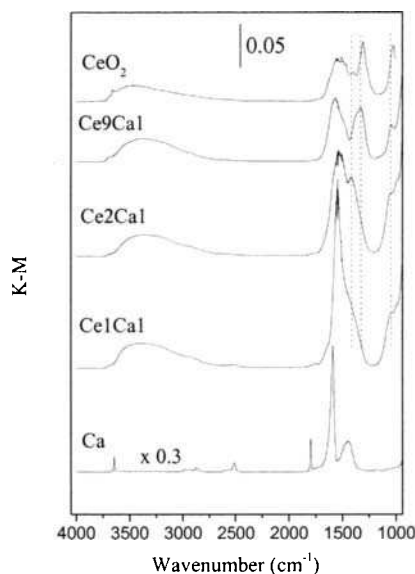


Fig. 3. DRIFTS spectra of Ce-Ca materials.

## 3.2 Surface properties.

Figure 4 shows the EPR spectra observed after oxygen adsorption on samples Ce, Ce9Ca1 and Ce1Ca1. The spectrum observed for sample Ce (Fig. 4a) is mainly formed by a signal OCe1 at $g_z = 2.047$, $g_y = 2.009$ and $g_x = 2.007$. A large intensity increase with respect to the Ca-free sample is observed for sample Ce9Ca1 (Fig. 4b). This spectrum shows the presence of signal OCe1 and a signal OCe2 at $g_{\parallel} = 2.036$ and $g_{\perp} = 2.011$ while a feature at $g = 2.002$ displays a significant intensity. This latter feature is related with formation of a new signal OCa, which largely predominates in the spectrum of sample Ce1Ca1 (Fig. 4c), at $g_y = 2.008$ and $g_x = 2.002$; $g_z$ is apparently dispersed in a relatively wide range for this signal, although sharp features at 2.095, 2.076 and 2.070 may be ascribed to this component.

Signals OCe1 and OCe2 are attributed to superoxide species adsorbed on cerium cations (formally $O_2^-$-$Ce^{4+}$) on the basis of previous works [8,9]. Differences between them are related to the degree of coordinative unsaturation of the adsorption centers where they are formed, which is higher for centers type OCe1 [8]. Note that the $CeO_2$ oxide prepared by microemulsion has a high degree of reduction (unsatured Ce valency) with respect to traditional ones [9]. Signal OCa can be attributed to superoxide species adsorbed on $Ca^{2+}$ cations [10].
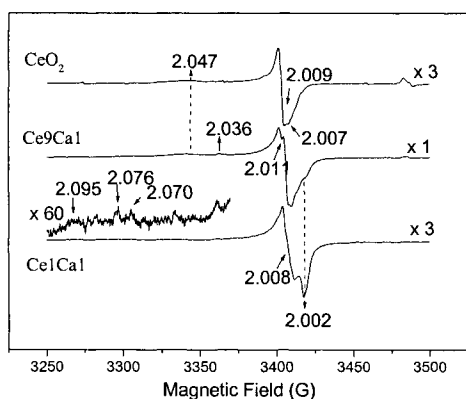


Fig. 4. EPR spectra following $O_2$ adsorption of Ce-Ca specimens evacuated at 773 K.
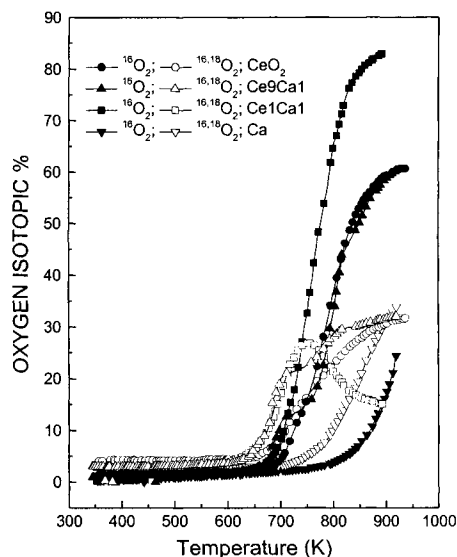
Fig. 5. Percentage of oxygen isotopomers obtained in TPSR experiments with $^{18}O_2$.

Differences in surface properties can be also revealed by isotopic exchange with $^{18}O_2$ (Fig. 5). Sample Ce2Ca1 is not plotted (for the sake of clarity) as it is very similar to Ce1Ca1. The presence of a 10 at.% Ca enhances the single ($R_1$, $\%^{16,18}O_2$) exchange mechanism, as it onsets at 30 K lower temperature than on $CeO_2$ , while higher quantities of Ca also contribute to enhance the multiple, $R_2$ ($\%^{16}O_2$) exchange mechanism. At higher temperatures, the $R_2$ mechanism becomes predominant for all Ce-containing materials. Close to 100% of exchange, Ce9Ca1 and the Ce reference reach similar levels of $R_1$,$R_2$ exchange while the remaining Ce-Ca samples display larger values (ca. 85%) of the $R_2$ mechanism. The Ca reference only contributes moderately to oxygen exchange above 750 K.

### 3.3 Bulk properties.

Fig. 6 displays the evolution with time of the isotopic labeling ($^{18}O$ fraction) of gaseous $C^{18}O_2$ obtained during recirculation experiments at constant reaction temperature, 573 K. Two regions, characterized by different slopes in Fig. 6, can be observed. The first one corresponds to exchange of surface oxygen, while the second one mainly measures oxygen diffusion from the bulk of the materials. Following the analysis of Martin and Duprez [10] the bulk diffusion coefficient has been measured and the results are presented in Table. 1.
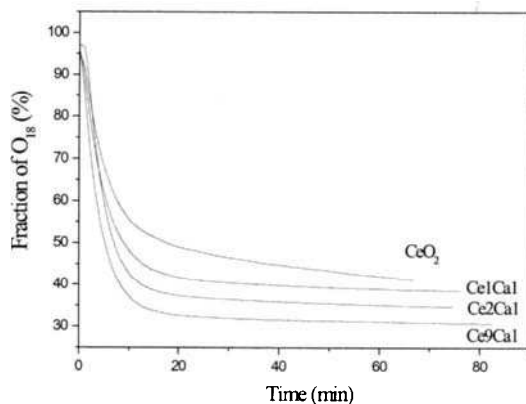


Fig. 6. Fraction of $^{18}O_2$ (percentage) present in the gas phase during a treatment with $C^{18}O_2$ at 573 K.

**Table 1.** Coefficients for oxygen bulk diffusion at 573 K.

| Sample | $D_b$ ($10^{21}$ cm$^2$s$^{-1}$) |
|--------|--------|
| CeO$_2$ | 44 |
| Ce9Ca1 | 2.2 |
| Ce2Ca1 | 8.5 |
| Ce1Ca1 | 10.4 |

## 4. DISCUSSION

The XRD and Raman characterization of the binary oxide samples indicate that they mainly contain crystalline phases of fluorite-type structure with a reasonably small average particle size of 8/7 nm for the Ce and Ce9Ca1 samples and of 4nm ( 2.5 nm if measured by TEM) for Ce2Ca1 and Ce1Ca1 samples. TEM analysis of materials indicates that Ca is inserted in the fluorite host up to about 33-40 at %. This may point out that the microemulsion method pushes the maximum Ca content inserted on a ceria host to a significantly higher value from those usually obtained with more classical methods of mixed oxide preparation [4]. In view of the similar XRD patterns obtained for Ce2Ca1 and Ce1Ca1 samples, which indicate the similar characteristics of the crystalline phase present on both materials, the excess Ca might be in an amorphous phase. The exclusive presence of unidentate carbonates, as no signal assigned to bidentate or hydroxyls species adsorbed on Ca is detected in the IR spectrum of the Ce1Ca1 specimen, could suggest that this Ca phase is located at the surface of the crystalline Ce-Ca mixed oxide phase and may be mainly constituted by dispersed Ca carbonate species. The strong contribution of EPR signals associated to Ca, which dominates the Ce1Ca1 spectrum, confirms the superficial location of the Ca-alone phase. EPR and IR also give evidence of Ca presence at the surface of Ce-Ca mixed oxide phases, although theoretical calculations predict that no significant Ca segregation is expected in these materials. [12]

The higher intensity of superoxide species in Ce9Ca1 with respect to Ce indicates that for this relatively low Ca loading, generation of oxygen vacancy (where superoxide species are stabilized [8,9]) is favored. The easier extraction of lattice oxygen in addition to the intrinsic vacancies present in Ce-Ca materials is likely in the origin of the easier activation/dissociation of the $O_2$ molecule detected with respect to ceria. On the other hand, appearance of signal OCe2 for Ce9Ca1 sample suggests that the huge increment in vacancy generation is mainly due to formation of isolated vacancies [8,9]. The favored presence of isolated vs. associated vacancies for Ce9Ca1 nicely correlates with the larger enhancement of the single, $R_1$, oxygen exchange mechanism with respect to the multiple, $R_2$ one, always taking ceria as reference. For higher Ca contents, the predominance of Ca-related vacancies on the EPR spectra does not allow to extend such correlation to the remaining Ce-Ca specimens. It can be noted, however, that bulk oxygen diffusion coefficients for all Ce-Ca samples are smaller that the one of ceria, suggesting that the improved oxygen handling properties observed with the Ce-Ca content below 750 K (Fig. 5), with respect to ceria, is dominated by surface (or near-surface) properties. This would mean that the increasing presence of Ca at the surface modifies the interaction with oxygen. Probably, this is related to the intrinsic arrangement of the dopant-vacancy pair, which, on the other hand, makes bulk diffusion more difficult with respect to pure ceria oxide.

## 5. CONCLUSIONS

The study shows that the microemulsion method allows to insert Ca up to about 33-40 at. % in a fluorite host. The surface of the mixed oxides formed are less reducible (larger isolated to associated vacancy ratio) than that of pure ceria, giving evidence of the strong effect of Ca in surface properties, even for the sample with a 10 at. %. Bulk properties are also

strongly affected; oxygen bulk diffusion coefficient are consistently lower for mixed oxides. In spite of all these facts, oxygen handling properties are clearly improved by the presence of Ca with respect to the single Ce oxide reference. Further studies would be required in order to understand the chemical basis of such behavior.

## Acknowledgments

## REFERENCES

1. J. Kaspar, P. Fornasiero, M. Graziani, Catal. Today, **50** (1999) 285.
2. Y. Nigera, K. Watanabe, J. Mizusaki, M. Ishigame, J. Electrochem. Soc., **144** (1997) 1050.
3. Y. Zhang, S. Anderson, M. Muhammed, Appl. Catal. B, **6** (1995) 325.
4. A. Martínez-Arias, M. Fernández-García, V. Ballesteros, L.N. Salamanca, J.C. Conesa, J. Soria, *Langmuir*, **15** (1999) 4796.
5. A. Guerrero-Ruiz, I. Rodríguez-Ramos, P. Ferreira-Aparicio, J.C. Volta, Catal. Lett., **45** (1997) 113.
6. Y. Fukuda, K. Tanabe, Bull. Chem. Soc. Japan, **46** (1973) 1616.
7. A. Mikkelsen, S.B. Engelsen, H.C.B. Hansen, O. Larsen, L.H. Skibsted, J. Crystal Growth, **177** (1997) 125.
8. J. Soria, A. Martínez-Arias and J.C. Conesa, *J. Chem. Soc. Faraday Trans.* **91** (1995)1669.
9. A. Martínez-Arias, M. Fernández-García, C. Belver, J.C. Conesa and J. Soria, *Catal. Lett.*, **65** (2000).197
10. M. Che and A.J. Tench, *Adv. Catal.*, **32** (1983).1
11. D. Martin, D. Duprez, J. Phys. Chem. B, **101** (1997) 4428.
12. S. De Carolis, J.L. Pascual, L.G.M. Petterson, M: Baudin, M. Wojcik, K. Hermansson, A.E.C. Palmqvist, M. Muhammed, J. Phys. Chem. B, **103** (1999) 7627.

355

# On the surface interaction between atomic oxygen and carbon: electronic and morphology changes in a model carbon material as studied by scanning probe microscopies

J.I. Paredes, A. Martínez-Alonso and J.M.D. Tascón

Instituto Nacional del Carbón, CSIC, Apartado 73, 33080 Oviedo, Spain

The surface modification of highly oriented pyrolytic graphite (HOPG) following exposure to atomic oxygen has been studied by means of atomic force and scanning tunneling microscopies (AFM/STM). At the nanometer scale, the atomically flat terraces typical of the pristine material disappear upon oxidation, giving rise to a smoothly roughened topography with nanometer-sized hillocks and pits. At the atomic scale, superstructures and protrusions are observed by STM. All these observations are accounted for in terms of the high reactivity of atomic oxygen, which combines with carbon atoms from both defect and perfect areas, but with somewhat different rates, leading to a relative chemical selectivity.

## 1. INTRODUCTION

The interaction of surfaces of different materials with plasmas presents interest both from the technological and the basic knowledge perspectives. In many cases, the changes brought about by the plasma can improve a number of surface characteristics of the materials, such as adhesion, wettability, lubricity, etc., which is beneficial for their application in a variety of fields: microelectronics, thin-film technology, biomedicine, etc. [1]. In the specific case of carbon materials, their surface modification is important in the realm of composite materials, where carbon fibers are being used as reinforcement of matrices for the aerospace industry or thermonuclear reactors [2,3]. To make these composites resistant and durable, the carbon fiber surface needs to be modified to improve its adhesion to the matrix [4]. This can be accomplished through oxygen plasma treatment of the fibers, by which they are exposed to the action of atomic oxygen (the main reactive species in an oxygen plasma). To be able to control this process, it then becomes obvious that a good knowledge of the interaction between atomic oxygen and carbon should be reached.

Due to its special characteristics (a well-known ordered structure with strong covalent carbon-carbon bonds within its basal planes and relatively weak interlayer forces), graphite has been used over the years as a model material for studying the interaction of carbon materials with oxidative environments, mainly molecular oxygen because of its importance in applications such as energy generation [5-7]. These studies have also led to a controlled modification of graphite by $O_2$ at the nanometer scale, called nanostructuring. This nanostructuring has proved extremely useful to isolate self-assembled molecular thin films (molecule corrals) for their study by scanning tunneling microscopy (STM) [8,9], to synthesize large numbers of polypyrrole nanostructures with potential applications in nanoscale electronic devices [10] or to adsorb proteins as a model for the interaction of biomolecules with more complex carbon based materials used as artificial heart valves [11].

In contrast to this, the interaction between graphite and atomic oxygen (or oxygen plasma) has received much less attention, though some examples can be found in the literature

[12], in spite of the fact that the study of the etching mechanisms of this material by atomic oxygen has a special relevance, not only owing to its status as model material, but also because of its specific applications. For instance, patterning of highly oriented pyrolytic graphite (HOPG) has been investigated recently [13], this being made with the ultimate aim of developing novel nanodevices by assembling carbon by design.

In the work presented here, HOPG has been employed as a model material for the study of the nanometer and atomic scale changes brought about by atomic oxygen attack of carbon. These changes are monitored by means of scanning tunneling and atomic force microscopies (STM/AFM). There has been extensive work by scanning probe microscopy on the oxidation of graphite by molecular oxygen [7,14-20]. However, that is not the case with atomic oxygen, so the imaging of its effects on graphite by this technique should help in understanding its interaction with carbon.

## 2. EXPERIMENTAL

The HOPG samples used in this study were obtained from Union Carbide and are of grade ZYH. To expose fresh surfaces to the oxidative environment, all the samples were cleaved with adhesive tape immediately before the treatment. Atomic oxygen exposure was carried out in a Technics Plasma 200-G treatment chamber where an oxygen plasma was generated using 2.45 GHz microwave (MW) radiation. The MW field was originated in a magnetron and a waveguide was employed to transfer MW power between this source and the point of use, which was a quartz reactor (batch type) where the plasma was created and the samples were placed. An oxygen pressure of 1.0 mbar was kept in the chamber during the treatment. To show evidence of the effect of some experimental parameters, several different samples were exposed at different MW powers and for different etching times.

After treatment, the samples were transferred to an STM/AFM microscope (Nanoscope Multimode IIIa, Digital Instruments) for their study in air at room temperature. STM was used for atomic-scale imaging, whereas the nanometer-scale topography was monitored by AFM. For the STM investigations, mechanically prepared Pt/Ir (80/20) tips were employed and the imaging was performed in constant current mode. Typical tunneling parameters were 250-300 mV for the bias voltage and 1 nA for the tunneling current. Lower bias voltages for the same tunneling current, such as those employed for pristine HOPG, were not possible, as the tip would crash the surface during engagement, implying a lower conductivity of plasma-treated HOPG. This was the first indication that atomic oxygen induces substantial changes on the graphite surface.

The AFM measurements were performed both in the contact and tapping modes of operation. The images were acquired at constant force (contact) or constant amplitude (tapping) to obtain topographical information of the surface. In the former mode, microfabricated $Si_3N_4$ cantilevers with a spring constant of 0.06 N/m and tip radius of curvature of 20-60 nm were used. The repulsive force was controlled and minimized. In the latter mode, the cantilevers are made of etched Si with a nominal tip radius of curvature of 5-10 nm and the tip-sample interaction was also minimized. It was observed that tapping mode yielded a better resolution than contact mode for images obtained at high magnifications, i.e., when a great detail at the nanometer scale was required. Two causes are responsible for this different behavior: i) In contact mode the capillary condensation between tip and sample leads to high shear lateral forces which disrupt the surface and therefore reduce the resolution of small features, whereas in tapping mode these forces are virtually suppressed [21], and ii) The smaller radius of curvature of the tips used in tapping mode. It is for this reason that high magnification images were obtained exclusively with tapping mode, while for low resolution imaging both modes could be used.

## 3. RESULTS AND DISCUSSION

Figure 1 shows low magnification AFM images evidencing the effects of oxygen plasma on the surface of HOPG. The pristine, untreated surfaces (Figure 1a) display large atomically flat areas (terraces) along with defects and discontinuities, such as steps. After exposure to atomic oxygen (Figure 1b), the large terraces have disappeared and have been replaced by a smoothly roughened topography with a considerable number of more or less circular pits spread all over the previously flat terraces and especially along cleavage steps. For comparison, the surface topography of HOPG following exposure to molecular oxygen at 650 °C is also presented in Figure 1c. It can be appreciated that the material essentially preserves the atomic flatness of the terraces of fresh HOPG and the reaction has progressed only along step edges, which have developed a jagged outline, and also at very limited locations of the
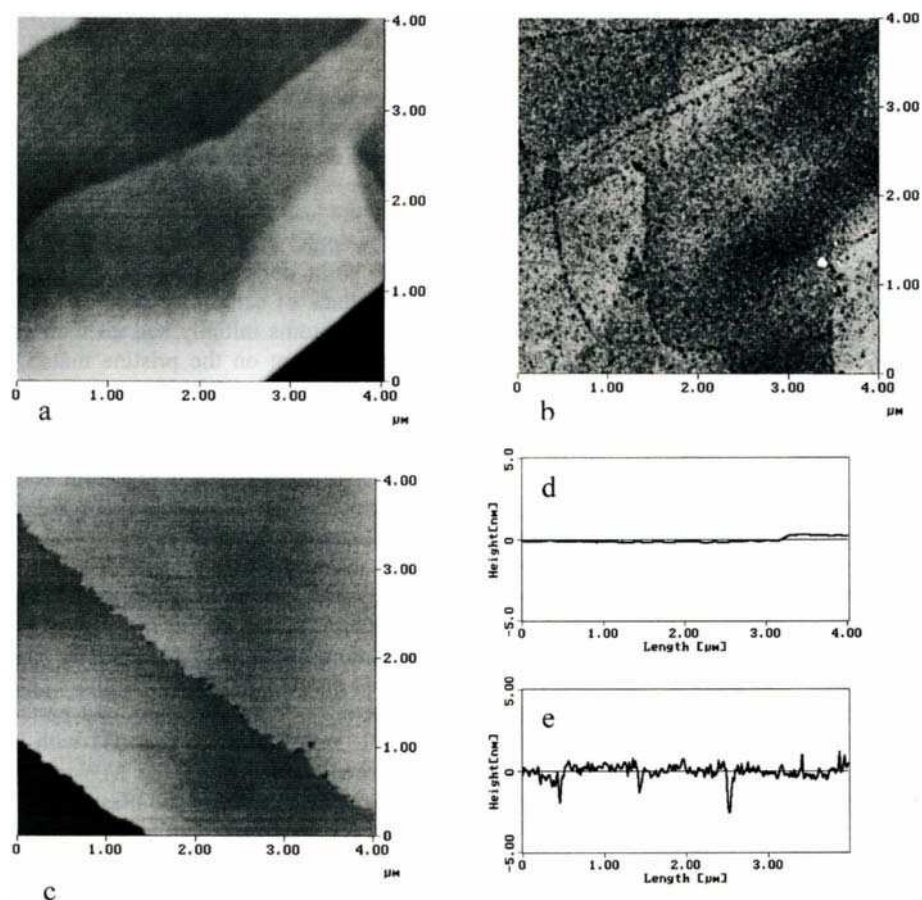


**Figure 1.** (a-c) Low magnification tapping mode AFM images of the HOPG surface: pristine (a) and after exposure to oxygen plasma for 10 min at a MW power of 100 W (b) or molecular oxygen at 650 °C for 10 min (c). The z-scale is 10 nm. (d-e) Typical line profiles for the pristine (d) and plasma-etched samples (e).

basal planes, where monolayer circular pits have appeared (e.g., near the upper step of Figure 1c). To emphasize the general roughness created by atomic oxygen on the graphite surface, typical line profiles of the pristine sample (Figure 1d) and plasma-etched surface (Figure 1e) are compared. It should be mentioned that the line profiles for molecular oxygen-etched surfaces are basically identical to those of the pristine material (Figure 1d).

The pits created by the action of atomic oxygen always displayed a variety of diameters and depths. For example, following a plasma treatment for 10 min at a MW power of 100 W (Figure 1b), diameters were found from 20 up to 80 nm and depths from 0.3 nm (1 graphite monolayer) to a few nm. The pit density for this sample was about 16 $\mu m^{-2}$. By increasing the exposure times it was observed that the pit density increased (e.g, densities of 28 $\mu m^{-2}$ were determined after a 20 min treatment). Also, the pit diameters tended to increase (diameters from 20 nm up to 240 nm were found in the 20 min sample). This is to be contrasted with the case of molecular oxygen, where the density of pits created on the HOPG surface was about two orders of magnitude smaller than in plasma-treated surfaces and all the monolayer pits had the same diameter for a given treatment time (~ 70 and 120 nm after 10 and 20 min exposure, respectively).

To understand these observations, it has to be first noted that in the case of molecular oxygen at temperatures below 700 °C (Figure 1c), the reaction with graphite takes place only at pre-existing defects on the surface, such as point defects (atomic vacancies) or line defects (dislocations, grain boundaries, step edges) [7], as a result of the existence of dangling $sp^2$ bonds. Point defects present on the surface of pristine graphite lead to the observed monolayer pits. In the case of atomic oxygen, the density of pits developed on the originally flat basal planes is much higher than the density of pre-existing point defects (i.e., the density of monolayer circular pits), so it can be concluded that the attack of carbon by atomic oxygen proceeds also at perfect sites of basal planes, where carbon atoms initially had all their $sp^2$ orbitals saturated, and not exclusively at defects initially existent on the pristine material. Thus, atomic oxygen, contrary to the case of molecular oxygen, can react with carbon atoms not only from defects but from basal planes as well [22], explaining the substitution of the atomically flat terraces typical of untreated HOPG by a general roughened topography after exposure to this reagent: the abstraction of carbon atoms (to form CO or $CO_2$) from basal planes at random locations would bring about, after a period of time, a rather disorganized topography and the addition of surface functional groups containing oxygen [23].

In any case, however, a certain degree of chemical selectivity between perfect sites of basal planes and defect areas is to be expected: due to the presence of highly reactive dangling bonds in carbon atoms of defect regions, these less ordered atoms should have a higher probability of reacting with atomic oxygen than carbon atoms with saturated orbitals from perfect areas of basal planes. This point has been observed previously by other authors [24]. Thus, the chemical selectivity would induce etching differences between defect and perfect areas, which should amplify with longer exposure time to atomic oxygen and also with its density in the plasma. The latter parameter can be varied by adjusting the MW power (increasing the MW power leads to higher densities of atomic oxygen in the plasma [25]). This mechanism would explain the formation of pits all over the HOPG surface: the defects created on the basal planes in the initial stages of the etching by the abstraction of carbon atoms by atomic oxygen would develop into pits after a period of time sufficiently long to make the chemical selectivity noticeable enough, which is the case of Figure 1b after an exposure to the plasma for 10 min. Considerably shorter exposure times (e.g., 5 min) gave rise to surfaces with not clearly developed pits, supporting the above interpretation. Likewise, as the abstraction of carbon atoms is an ongoing process and thus defects should be continuously created, pits with different diameters should consequently be present on the

graphite surface and their density should tend to increase with exposure time to the reagent. As a matter of fact, this is the behavior observed in the present work, as documented above.

Indication of the relative chemical selectivity of the attack by atomic oxygen was also found in other features observed on the etched HOPG surfaces. Figure 2 shows an AFM image displaying grooves that were occasionally encountered. The width and depth of the grooves increased with etching time and MW power applied and we attribute them to the etching of line defects such as grain boundaries. There is a strong correlation between the grooves found in the images (Figure 2 and many others not shown here) and the grain borders identified in HOPG by the electron channeling micrograph (ECM) technique [26]: both types of feature appear with the same frequency.
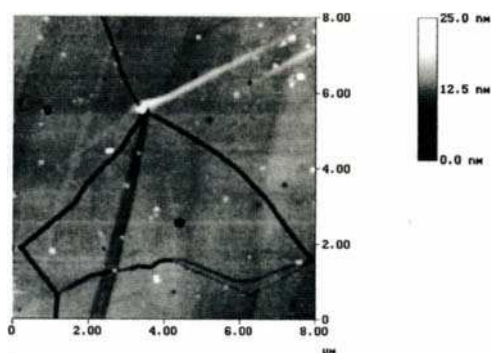


**Figure 2.** Low magnification contact mode AFM image showing the development of grooves in atomic oxygen-etched HOPG as a consequence of the relative chemical selectivity between defect and perfect areas.

The detailed nanometer scale topography of the HOPG surface after exposure to the oxygen plasma is shown in Figure 3 for an etching time of 5 min at a MW power of 50 (a) and 250 W (b). In the former case, the surface is made up of a large number of isolated hillocks (with lateral dimensions of 10-15 nm) surrounded by lower areas apparently in an arbitrary arrangement. When the MW power is increased to 250 W, the hillocks evolve into more rounded protuberances connected to each other and with no clear isolated peaks. This topographical change is explained in terms of the higher densities of oxygen atoms produced at increasing MW powers, as mentioned previously. Thus, at 250 W, the higher density of
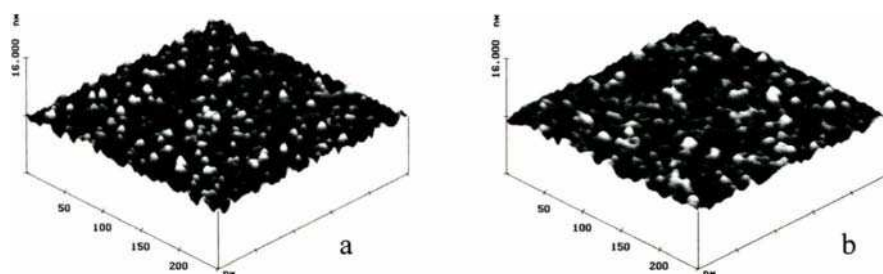


**Figure 3.** Three-dimensional tapping mode AFM images of HOPG surfaces following exposure to oxygen plasma for 5 min at MW powers of 50 (a) and 250 W (b).

reactive oxygen, as compared with that attained at 50 W, induces a greater chemical etching over the exposed tops of the hillocks, thereby limiting their development as isolated peaks and promoting the merging of the hillocks instead.
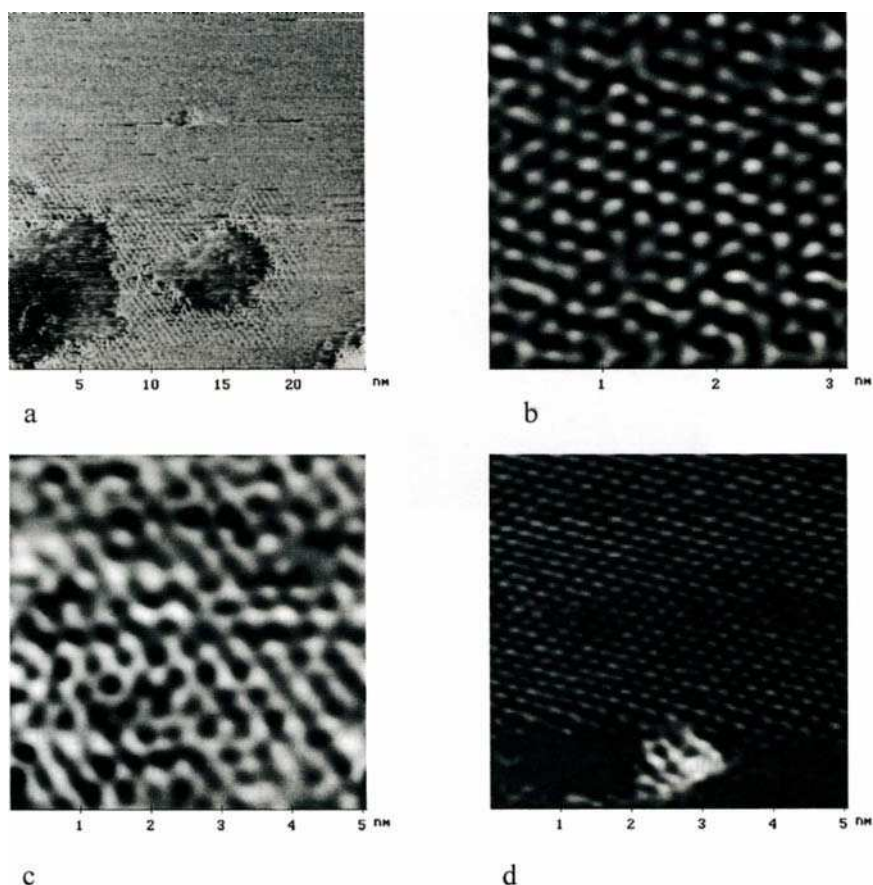


**Figure 4.** Atomic resolution STM images of the HOPG surface following exposure to an oxygen plasma for 10 min at a MW power of 100 W. (a) A superstructure can be seen around the pits in the bottom part of the image. (b) Detail of the upper part of (a), showing an unperturbed HOPG atomic conformation. (c) Detail of the superstructure around the pits. (d) Protrusion (1 nm wide) surrounded by an undisturbed atomic lattice.

Figure 4 shows some atomic resolution STM images of plasma-modified HOPG. This kind of images could only be obtained in the limited lower areas that lay between the aforementioned hillocks, where a relatively unperturbed arrangement remains. By contrast, the hillocks presented a highly disorganized structure which precluded the attaining of atomic resolution. In Figure 4a, a pit about 7 nm wide can be seen in the lower-center part of the image along with another one, somewhat bigger, on its left. As can be seen, the areas near the pits reveal a different structure to that of perfect, unperturbed basal HOPG. The usual perfect

atomic structure of HOPG, as observed by STM, consists of a triangular arrangement with a periodicity of 0.25 nm. This is what is observed in areas of Figure 4a far away from the pits: Figure 4b shows a magnification of one of these areas with unperturbed atomic-scale arrangement, which is located in the upper part of the image, displaying the typical periodicity of 0.25 nm. On the other hand, the region close to the pits also showed a triangular arrangement, but in this case with a periodicity of 0.44 nm, thus being what is termed a superstructure. Figure 4c is a magnification of the superstructure. Furthermore, the angle between the rows in the superstructure and the rows in the unperturbed HOPG lattice is around 30°, so it can be assigned to a $(\sqrt{3} \times \sqrt{3})R30^{o}$ superstructure. This type of superstructure has been previously observed in the vicinity of defects on the HOPG surface such as holes or adsorbed metal particles [27-29]. Figure 4d displays an area of the surface exhibiting a protrusion about 1 nm wide surrounded by a perfect HOPG structure. A few other similar protrusions were also observed in further locations.

These features of the effect of atomic oxygen on HOPG can be understood in terms of the local electronic density of states near the Fermi level of graphite, which is what the STM actually measures [30] and explains the observation of a triangular structure for perfect graphite with a repeat distance of 0.25 nm. Likewise, the $(\sqrt{3} \times \sqrt{3})R30^{o}$ superstructure is not attributed to atomic reconstructions around defects (a pit in this case), but to modulations in the electronic density at the Fermi energy induced by the defects instead. It has been suggested that these superstructures arise from the interference between normal electron wave functions and those scattered by the defect [28]. Starting from this idea, several authors were able to simulate theoretically the observed superstructures [31,32]. Concerning the protrusion of Figure 4d, its origin lies most probably in an atomic vacancy created by the abstraction of a carbon atom by atomic oxygen: recent semiempirical and ab initio theoretical calculations have shown that atomic vacancies in graphite induce an enhancement of the local electronic density near the Fermi level of the atoms immediately surrounding the vacancy [33,34]. Consequently, this electronic density enhancement is detected by STM as a protrusion in the images. Protrusions in the STM images are also observed on graphite after low energy ion impacts [35], which create atomic vacancies as well, although the actual topography of the defect is almost flat. In the present case, the atomic vacancies must have arisen from the chemical etching of basal plane carbon atoms by the highly reactive atomic oxygen, further supporting the mechanism of HOPG etching by atomic oxygen commented previously. It is believed that all these modulations in the graphite Fermi level electronic density may be very important for electronic devices based on carbon nanostructures and also for the use of carbon materials as catalysts or catalytic supports.

## 4. CONCLUSIONS

Scanning probe microscopy has proved to be a powerful tool for studying, both at the nanometer and atomic scales, the effects of exposure to atomic oxygen of highly oriented pyrolytic graphite used as a model carbon material. It has been shown that, contrary to the case of molecular oxygen, atomic oxygen attacks not only carbon atoms at pre-existing defects in the pristine material but also atoms from basal planes, continuously creating atomic vacancies which subsequently develop into nanometer-sized pits. However, a relative chemical selectivity was inferred from the images. The atomic scale superstructures and protrusions observed by scanning tunneling microscopy on the atomic oxygen-etched graphite surfaces were interpreted as local modulations in the electronic density at the Fermi energy in the vicinity of small pits and atomic vacancies, respectively.

362

**REFERENCES**

1. C.M Chan, T.M. Ko and H. Hiraoka, Surf. Sci. Rep., 24 (1996) 1.
2. H.O. Pierson, Handbook of Carbon, Graphite, Diamond and Fullerenes. Properties, Processing and Applications, Noyes Publications, Park Ridge, 1993, ch. 9.
3. V. Barabash, M. Akiba, J.P. Bonal, G. Federici, R. Matera, K. Nakamura, H.D. Pacher, M. Rödig, G. Vieider and C.H. Wu, J. Nucl. Mater., 263 (1998) 149.
4. J.B. Donnet and R.C. Bansal, Carbon Fibers, Marcel Dekker, New York, 1990, ch. 3.
5. J. Thomas, Chemistry and Physics of Carbon, P.L. Walker Jr. (ed.), vol. 1, Marcel Dekker, New York, 1965, p. 121.
6. P.L. Walker Jr., M. Shelef and R.A. Anderson, Chemistry and Physics of Carbon, P.L. Walker Jr. (ed.), vol. 4, Marcel Dekker, New York, 1968, p. 287.
7. H. Chang and A.J. Bard, J. Am. Chem. Soc., 113 (1991) 5588.
8. D.L. Patrick, V.J. Cee and T.P. Beebe Jr., Science, 265 (1994) 231.
9. D.L. Patrick, V.J. Cee, T.J. Purcell and T.P. Beebe Jr., Langmuir, 12 (1996) 1830.
10. J.D. Noll, M.A. Nicholson, P.G. van Patten, C.-W. Chung and M.L. Myrick, J. Electrochem. Soc., 145 (1998) 3320.
11. D.C. Cullen and C.R. Lowe, J. Colloid Interf. Sci., 166 (1994) 102.
12. C. Wong, R.T. Yang and B.L. Halpern, J. Chem. Phys., 78 (1983) 3325.
13. X. Lu, H. Huang, N. Nemchuk and R.S. Ruoff, Appl. Phys. Lett., 75 (1999) 193.
14. X. Chu and L.D. Schmidt, Carbon, 29 (1991) 1251.
15. A. Tracz, G. Wegner and J.P. Rabe, Langmuir, 9 (1993) 3033.
16. K.G. Vandervoort, K.N. McLain and D.J. Butcher, Appl. Spectrosc., 51 (1997) 1896.
17. D. Tandon, E.J. Hippo, H. Marsh and E. Sebok, Carbon, 35 (1997) 35.
18. Z. Klusek, Appl. Surf. Sci., 125 (1998) 339.
19. A. Mechler, P. Heszler, C.T. Reimann, K. Révész and Z. Bor, Vacuum, 50 (1998) 281.
20. F. Stevens, L.A. Kolodny and T.P. Beebe Jr., J. Phys. Chem. B, 102 (1998) 10799.
21. Q. Zhong, D. Inniss, K. Kjoller and V.B. Elings, Surf. Sci., 290 (1993) L688.
22. F.D. Egitto, F. Emmi, R.S. Horwath and V. Vukanovic, J. Vac. Sci. Technol. B, 3 (1985) 893.
23. M. Nakahara and Y. Sanada, J. Mater. Sci., 28 (1993) 1327.
24. W.P. Hoffman, Carbon, 30 (1992) 315.
25. S. Dzioba, G. Este and H.M. Naguib, J. Electrochem. Soc., 129 (1982) 2537.
26. A. Yoshida and Y. Hishiyama, J. Mater. Res., 7 (1992) 1400.
27. T.R. Albrecht, H.A. Mizes, J. Nogami, P. Sang-il and C.F. Quate, Appl. Phys. Lett., 52 (1988) 362.
28. H.A. Mizes and J.S. Foster, Science, 244 (1989) 559.
29. M. Kuwahara, S. Ogawa and S. Ichikawa, Surf. Sci., 344 (1995) L1259.
30. J. Tersoff and D.R. Hamann, Phys. Rev. B, 31 (1985) 805.
31. G.M. Shedd and P.E. Russell, Surf. Sci., 266 (1992) 259.
32. J. Valenzuela-Benavides and L. Morales de la Garza, Surf. Sci., 330 (1995) 227.
33. M. Hjort and S. Stafström, Phys. Rev. B, 61 (2000) 14089.
34. K.H. Lee, M. Causá, S.S. Park, C. Lee, Y. Suh, H.M. Eun and D. Kim, THEOCHEM-J. Mol. Struct., 506 (2000) 297.
35. J.R. Hahn, H. Kang, S. Song and I.C. Jeon, Phys. Rev. B, 53 (1996) R1725.

# Enhancement of the Catalytic Performance of NiMoO$_4$ and Modification of the Kinetic parameters of Oxidative Dehydrogenation of Propane over NiMoO$_4$/Sb$_2$O$_4$ Biphasic Catalyst by Oxygen spillover

H. M. AbdelDayem and P. Ruiz

Unité de catalyse et chimie des matériaux divisés, Université catholique de Louvain, Croix du Sud 2/17,1348 Louvain -la- Neuve, Belgium, Fax (3210) 473649.

Partial oxidation of propane to propene was investigated over monophasic NiMoO$_4$ and biphasic NiMoO$_4$/α-Sb$_2$O$_4$ in different proportions in heterogeneous reaction region. The existence of α-Sb$_2$O$_4$ in the mixture with NiMoO$_4$ produces a synergetic effect between the two phases. Selectivity towards propene was maximal with a mass ratio of NiMoO$_4$/(NiMoO$_4$+ α–Sb$_2$O$_4$) close to 0.25. The presence of α-Sb$_2$O$_4$ in the mixture with NiMoO$_4$ modifies the kinetic parameters of the reaction namely, decreases the partial pressure propane order and activation energy of propene formation. XRD and XPS characterization of pure NiMoO$_4$ and mechanical mixtures before and after reaction revealed neither formation of new oxide phases between NiMoO$_4$ and α-Sb$_2$O$_4$ nor contamination of one phase by an element of the other phase. Confocal LRS indicated that the addition of α-Sb$_2$O$_4$ to NiMoO$_4$ modifies the coordination state of Mo in the NiMoO$_4$. These results could be explained as an action of oxygen spillover.

## 1. INTRODUCTION

The selective oxidation of propane to propene is promising and important target in the field of partial oxidation of alkane. This reaction is the first step in the oxidation of propane to acrolein and in the ammoxidation of propane to acrylonitrile.

Recently, metal molybdate based catalysts have been reported by different authors as effective catalysts for the selective partial oxidation of propane [1]. One important characteristic of metal molybdate catalysts is the presence of a synergetic effect between different phases. NiMoO$_4$-MoO$_3$ catalyst oxidize butane to maleic anhydride with high performance than pure phases [2a]. NiMoO$_4$ with 15-40% "excess" MoO$_3$ exhibited higher selectivity and activity compared to single compound phase. Similar results have obtained with MnMoO$_4$-MoO$_3$ [2b]. A cooperation between oxide phases via oxygen spillover (O$_{so}$) has been postulated to explain such effects [2b]. In recent years evidences to explain synergetic effect between oxide phases by oxygen spillover has been accumulated. About 40 mixtures of pure single or mixed oxides, doped or not, investigated in different laboratories, exhibited similar synergy in different oxidation reactions and this cooperation was explained as results of oxygen spillover [3].

In this work the oxidative dehydrogenation of propane has been used as reaction test. The objective of this contribution is to show that the cooperation between phases via O$_{so}$ leads to a synergetic effect between the oxide phases and also to show that, for the first time, that

$O_{so}$ can modify the kinetic parameters of the reaction. This is demonstrated by using stoichiometeric $NiMoO_4$ as an $O_{so}$ acceptor phase and $\alpha$-$Sb_2O_4$ as a typical $O_{so}$ donor phase [3]. Aside from the oxygen spillover, a common explanation of synergy in such experiments is the formation of a surface contamination of elements of one phase on the surface of the other phase. Surface contamination was studied by photoelectron spectroscopy (XPS). Another explanation of the synergetic effects is the formation of a new phase associating two elements in a mixed compound in particular $NiSb_2O_6$. For this reason the catalytic activity of $NiSb_2O_6$ has been studied. X-ray diffraction measurements were performed to determine the crystalline phases and to detect phase modifications or formation of new compound. Mo coordination changes; were studied by using Raman spectroscopy analysis.

## 2. EXPERIMENTAL

Pure stoichiometeric $NiMoO_4$ was prepared (adapting the procedure described by Ozkan et al. [2a]) by coprecipitation from aqueous solutions of 750 ml of 0.057M ammonium heptamolybdate (Merck 99+%) and 750ml of 0.4M of nickel nitrate (Adrich 99+%), at pH=6 and at temperature of 60°C. The total addition period was 0.5 h. After filtration the precipitate was dried in air at 110°C for 12h; then calcined under a flow of oxygen at 500°C for 12h. The purity of the prepared $NiMoO_4$ from excess $MoO_3$ was checked by Raman Spectroscopy and thermal analysis (DTA/TGA).

$\alpha$-$Sb_2O_4$ was prepared by oxidation of $Sb_2O_3$ (Aldrich 99+%) by $HNO_3$ (65%) followed by calcination of the obtained solid at 500 °C in air after it has been cleaned from $HNO_3$ with water.

$NiSb_2O_6$ (Ni:Sb 1:2) was prepared by coprecipitation from nickel chloride (Aldrich 99.95%) and antimony pentachloride $SbCl_6$ (Aldrich 99%); they were dissolved in an aqueous HCl solution (Vel 37%). The catalyst precursor was dried overnight at 120°C and then calcined at 700°C for 16 h.

The biphasic catalysts were prepared mixing mechanically both oxides in n-pentane (Aldrich 98+%) in different mass ratio (Rm= 1.0, 0.5, 0.25 and 0.1, Rm= 1.0 is pure 100%$NiMoO_4$ and Rm= 0 for 100% $\alpha$-$Sb_2O_4$). Catalytic activity measurements were performed in a conventional fixed bed reactor system at atmospheric pressure by feeding $O_2$, $C_3H_8$ and He as diluent. Total feed rate was 30 ml/min. The partial pressures of oxygen and propane were varied between 5.08kPa and 30.4kPa. Conversion was kept below 10% to operate reactor in differential mode. The reaction was studied at three temperatures: 400, 450 and 490°C. No homogeneous gas phase for production of propene and no diffusion limitations were observed in this temperature range. The synergetic effect in selectivity are calculated according to a formula:

$$\text{Synergy effect} = \frac{S_{AB} - S_{(A+B)}}{S_{(A+B)}} \times 100$$

Where $S_{AB}$ is selectivity of the mixture and $S_{(A+B)}$ is the theoretical selectivity which would be observed in the absence of any synergetic effect, defined for mixture with a given Rm as:

$$S_{(A+B)} = \frac{Rm \times Y_A + (1 - Rm) \times Y_B}{Rm \times C_A + (1 - Rm) \times C_B}$$

In which $C_A$ and $C_B$ are the propane conversion and $Y_A$ and $Y_B$ are the yield in propene of the $NiMoO_4$ and $\alpha$-$Sb_2O_4$ respectively.

XRD was performed on a Kristalloflex Siemens D5000 diffractometer using the $K_{\alpha1,2}$ radiation of Cu ($\lambda = 1.5418\text{Å}$) for $2\theta$ angles varying from $10°$ to $80°$. The fluorescence contribution was eliminated from the diffracted beam using a curved graphite monochromator. The scan rate was 0.4 deg. $\text{min}^{-1}$ corresponding to a step size of 0.04 degree and a step time of 6s. The particle size ($t(\text{Å})$)of $NiMoO_4$ was calculated by using Scherrer formula: $t(\text{Å}) = 0.92\ \lambda\ /\ B\ \cos\theta$. where B is peak width at the half high of [330] peak of $NiMoO_4$ at $2\theta = 43.841$degree.

Specific surface areas (SBET) were measured on a Micromeritics ASAP 2000 instrument (adsorption of Krypton). Theoretical SBET were calculated both for the fresh and the used mechanical mixtures of $NiMoO_4$ and $\alpha\text{-}Sb_2O_4$ by using the formula:

Theoretical SBET = $(\text{SBET})_{NiMoO_4}$. $R_m$ + $(\text{SBET})_{\alpha\text{-}Sb2O4}$ $(1\text{-}R_m)$

In which $(\text{SBET})_{NiMoO_4}$ and $(\text{SBET})_{\alpha\text{-}Sb2O4}$ are the BET surface areas of nickel molybdate and antimony oxide respectively.

XPS analyses were performed with an SSX-100 model 206 X-ray photoelectron spectrometer. The binding energies were calibrated against the C([C-(C,H)] (carbon involved in a single bond with carbon or hydrogen) line fixed at 284.8 eV. The analysis first consisted in a scan of the binding energies between 0.0 and 1100 eV. This aimed at detecting all the different elements present at the surface of the samples. $C1s$, $Ni2p$, $Mo3d$, $Sb3d3/2$ and $O1s$ bands were thereafter recorded. The XPS peaks were decomposed by a least square routine provided by the manufacturer with an 85/15 Gaussian/ Lorentzian ratio and a non linear baseline.

Confocal laser Raman spectroscopy (LRS) was performed with a Dilor Labram Spectrometer equipped with a computerized X-Y transition stage. The Raman spectra were excited using a He-Ne laser (632.8nm, 10mW laser power at the sample surface). The spectrometer resolution was $7\text{cm}^{-1}$. The full spectra, hereafter shown for Raman shifts, between $200\ \text{cm}^{-1}$ and $1200\ \text{cm}^{-1}$, were built by merging three partial spectra successively, obtained by averaging 3 scans of 15 sec. It was checked that the spectra shown were not to be perturbed by any thermal degradation of the samples under the laser beam during the analysis. In addition, to have a representative picture and to check homogeneity of the surface, about 30 spectra were measured at different dispersed spots of a sample.

## 3. RESULTS

### 3.1. Catalytic activity and empirical kinetic parameters

Both $\alpha\text{-}Sb_2O_4$ and $NiSb_2O_6$ are fully inactive. For similar conversion the addition of $\alpha\text{-}Sb_2O_4$ in the biphasic catalyst increased the propene selectivity of pure $NiMoO_4$. Moreover the propene selectivity and synergetic effect in selectivity increased with increasing $\alpha\text{-}Sb_2O_4$ amount in the mixture and reached a maximum value for the $25\%NiMoO_4+75\%Sb_2O_4$ mixture (Rm= 0.25) followed by a decrease at higher $\alpha\text{-}Sb_2O_4$ content namely Rm= 0.1 as shown in Figures 1 and 2 respectively (Catalytic test conditions were partial pressures of $C_3H_8$, $O_2$ and He are 10.13, 5.07 and 86.1kPa respectively, temperature 450°C).

As shown in Table 1 the presence of $\alpha\text{-}Sb_2O_4$ in the mixture decreases the partial pressure propane order and the apparent activation energy of the reaction. The partial pressure oxygen order, for both 100% $NiMoO_4$ and mixtures, was near zero.
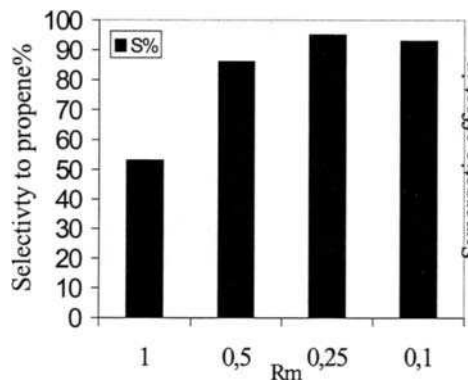
Figure 1. Variation of propene selectivity with the change of the composition of the mechanical mixture of $\alpha$-Sb$_2$O$_4$ and NiMoO$_4$ (R$_m$).
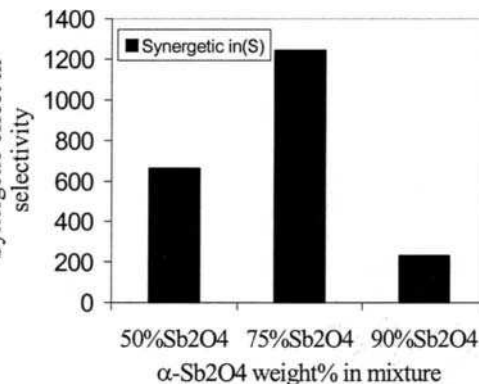
Figure 2. Variation of synergetic effect in propene selectivity with the change of the $\alpha$-Sb$_2$O$_4$ amount in the mechanical mixture of $\alpha$-Sb$_2$O$_4$ and NiMoO$_4$.

Table 1
Empirical oxygen (m) and propane (n) partial pressure orders at 450°C and activation energy (E) calculated from power law equation

| Catalyst | (n) | (m) | E (kJ mol$^{-1}$) |
|---|---|---|---|
| NiMoO$_4$(100%) | 1.0 | Near zero | 61.3 |
| NiMoO$_4$(50%)+Sb$_2$O$_4$(50%) | 0.6 | Near zero | 63.0 |
| NiMoO$_4$(25%)+Sb$_2$O$_4$(75%) | 0.5 | Near zero | 51.7 |

## 3.2 Characterization results

### 3.2.1. Specific surface area (SBET)

The SBET analysis of pure oxides and their mixture 25% NiMoO$_4$+75% $\alpha$-Sb$_2$O$_4$ before and after reaction are reported in Table 2. Values in parentheses are the theoretical values calculated on the basis of the composition of the mixture and the observed values of the corresponding constituting pure oxides.

Table 2
SBET values (m$^2$g$^{-1}$) of NiMoO$_4$, $\alpha$-Sb$_2$O$_4$ and mechanical mixture(Rm=0.25) before and after reaction (in parenthesis theoretical values after reaction).

| Catalyst | | SBET | $\Delta$ (SBET)% |
|---|---|---|---|
| 100%NiMoO$_4$ | before reaction | 41.0 | 0.0 |
| | after reaction | 35.6 | -13.2 |
| 100%Sb$_2$O$_4$ | | 1.1 | 0.0 |
| 25% NiMoO$_4$+75%Sb$_2$O$_4$ | before reaction | 11.3(11.1) | 0.0 |
| | after reaction | 10.4(9.7) | -8.0 |

Note: $\Delta$(SBET) is the variation in surface area (SBET) in %.

The SBET surface areas of 25% $NiMoO_4$+75% $\alpha$–$Sb_2O_4$ mixture are the same as those calculated theoretically and no difference are observed between the value of SBET of fresh and used mixture after reaction. Similar results have been obtained for the other mixtures of Rm= 0.5 and 0.1. Contrary the surface area of pure $NiMoO_4$ decreased by about 13% after reaction.

### 3.2.2. X-ray diffraction (XRD)

The XRD analysis (Table 3) of 100%$NiMoO_4$, 100%$\alpha$–$Sb_2O_4$ and their mixture 25% $NiMoO_4$ + 75% $\alpha$–$Sb_2O_4$ showed the presence of the monoclinic $\alpha$-$NiMoO_4$ phase of JCPDs file 31-902 and $\alpha$-$Sb_2O_4$ (Cervantite) of JCPDS standard 11-0964. No indication of the presence of $MoO_3$ and NiO was observed in the spectrum of $NiMoO_4$.

The XRD diffraction patterns of the mechanical mixtures of $NiMoO_4$ and $\alpha$–$Sb_2O_4$ in different proportions correspond to their pure oxide phases constituting the mixtures. After reaction, both the mixtures and pure $NiMoO_4$ showed no disappearance of any peak and no appearance of a new peak namely, no impurity was detected such as the formation of a new phase (e. g., $NiSb_2O_6$, $MoO_3$ and NiO). In Table 3 we also reported the calculated particle size of $NiMoO_4$ in 100%$NiMoO_4$ and in mixture of Rm= 0.25 before and after reaction (values in parentheses). In the case of the 100%$NiMoO_4$, the particle size is increased after reaction. however in the case of mixture no strong modification in the particle size was observed after reaction.

Table 3
Results of XRD analysis ((values in parenthesis after reaction).

| Catalyst | XRD phases | t(Å) | $\Delta$t(Å)% |
|---|---|---|---|
| 100%$NiMoO_4$ | $\alpha$-$NiMoO4$ | 681.0(792.0) | +16.3 |
| 100%$Sb_2O_4$ | $\alpha$–$Sb_2O_4$ | - | - |
| 25% $NiMoO_4$+75% $\alpha$–$Sb_2O_4$ | $\alpha$-$NiMoO_4$+$\alpha$–$Sb_2O_4$ | 677.0(730.0) | +7.8 |

*Note*: $\Delta$t is the variation in particle size in %.

### 3.2.3. X-ray photoelectron spectroscopy (XPS)

Tables 4 and 5 give the results of the XPS analysis obtained for $NiMoO_4$ and $NiMoO_4$+$\alpha$-$Sb_2O_4$ sample (Rm= 0.25). For both pure $NiMoO_4$ and mixture we can see that

Table 4
XPS results: atomic ratios for Mo/M, Sb/M, Ni/M and C/M for fresh and used $NiMoO_4$ and 25%$NiMoO_4$+75%$\alpha$-$Sb_2O_4$ mixture (Rm=0.25).

| Catalyst | | Mo/Mo+Ni | Mo/M | Ni/M | Sb/M | C/M |
|---|---|---|---|---|---|---|
| 100%$NiMoO_4$ | (before) | 0.43 | 0.43 | - | - | 1.23 |
| | (after) | 0.44 | 0.44 | - | - | 1.12 |
| 25%$NiMoO_4$+75% $\alpha$-$Sb_2O_4$ | | | | | | |
| | (before) | 0.44 | 0.31 | 0.38 | 0.32 | 1.30 |
| | (after) | 0.40 | 0.30 | 0.38 | 0.32 | 1.10 |

the surface composition is not changed after reaction namely Mo/M, Ni/M and Sb/M ratios (M=Mo+Ni +Sb) are not modified after reaction. In addition no carbon deposition is observed after reaction i.e., the carbon to metals ratio C/M is not modified after reaction.

On the other hand the binding energies (Table 5) of molybdenum ($Mo3d_{5/2}$ = 232.5eV, $Mo3d_{3/2}$ = 235.5eV), nickel ($Ni2p_{3/2}$ = 855.6eV and $Ni2p_{1/2}$ = 873.3eV), antimony ($Sb3d_{5/2}$ = 530.7eV and $Sb3d_{3/2}$ = 540.0eV) and oxygen ($O_{1S}$ = 530.4eV) were not modified after reaction. The significant differences between the binding energies of $Ni2P_{3/2}$ and $O_{1S}$ of $NiMoO_4$ and of NiO indicates that there is no NiO in the samples.

Table 5
XPS results: binding energies (BE±0.2 eV) for $Mo3d_{5/2}$, $Ni2p_{3/2}$, $Sb3d_{5/2}$ and O1s peaks for fresh and used $NiMoO_4$, 25%$NiMoO_4$+75%$Sb_2O_4$ mixture (Rm=0.25) and $\alpha$-$Sb_2O_4$.

| catalyst | | ($Mo3d_{5/2}$) | ($Ni2P_{3/2}$) | ($Sb3d_{5/2}$) | (O1s) |
|---|---|---|---|---|---|
| 100% $\alpha$-$Sb_2O_4$ | (before) | - | - | 530.7 | 530.4 |
| | (after) | - | - | 530.6 | 530.3 |
| 100%$NiMoO_4$ | (before) | 232.5 | 855.6 | - | 530.4 |
| | (after) | 232.4 | 855.5 | - | 530.4 |
| 25%$NiMoO_4$ | (before) | 232.3 | 855.6 | 530.7 | 530.5 |
| | (after) | 232.3 | 855.5 | 530.7 | 530.6 |
| NiO (reference) | | - | 853.9 | - | 529.3 |

### 3.2.4. Laser Raman spectroscopy (LRS)

Figure 3 shows the Raman spectra obtained for pure oxides $NiMoO_4$, $\alpha$-$Sb_2O_4$ and their mixture (25%$NiMoO_4$+75%$\alpha$-$Sb_2O_4$) before and after reaction. In the case of pure $NiMoO_4$ the Laser Raman bands at 707, 911 and 961 $cm^{-1}$ clearly indicated the presence of $\alpha$–$NiMoO_4$ [5] in which the $Ni^{+2}$ and $Mo^{+6}$ species are in octahedral oxygen environment. In addition to these bands we also observed a Raman bands at 817, 887 and 937 $cm^{-1}$ which have been assigned previously to deformed tetrahedral molybdenum species [5]. After reaction pure $NiMoO_4$ showed a similar spectrum as that observed before reaction. In the case of the fresh (25%$NiMoO_4$+75%$\alpha$-$Sb_2O_4$) mixture the spectrum obtained is described by a mixture of $\alpha$–$Sb_2O_4$ and $NiMoO_4$. A similar Raman bands of Mo octahedral and deformed tetrahedral of pure $NiMoO_4$ have been observed except a small shift have been observed in the Raman bands at 940, 890 and 821$cm^{-1}$ which were attributed to deformed tetrahedral Mo species. The important observation is that after reaction the Raman bands attributed to deformed tetrahedral Mo species have disappeared and only the bands characteristic for octahedral Mo of $NiMoO_4$ and the bands of $\alpha$-$Sb_2O_4$ have observed.

### 4. DISCUSSION

XRD and XPS characterization of pure $NiMoO_4$ and mechanical mixtures before and after reaction revealed that neither formation of a new phase between $NiMoO_4$ and $Sb_2O_4$ nor contamination of one phase by an element of other phase occurred during reaction. On the other hand we have observed that, an artificial contamination of $NiMoO_4$ by -$Sb_2O_4$ precursor (it consider that -$Sb_2O_4$ covered $NiMoO_4$ by monolayer) exhibited a strong tendency to disappear after long reaction time (48h)[4].
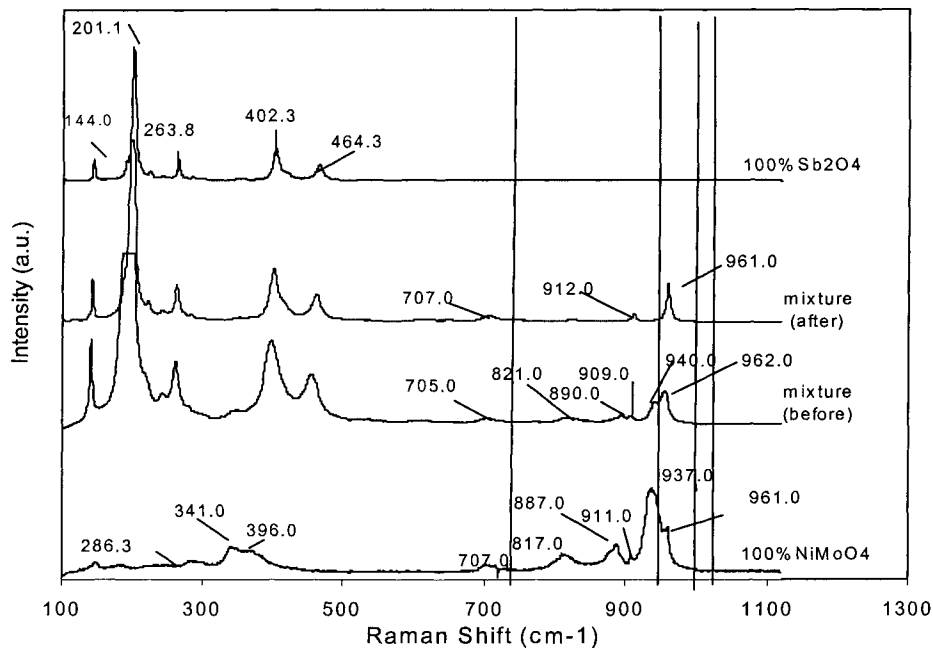
Figure 3. Confocal laser Raman spectra of 100%NiMoO$_4$ and 100%α-Sb$_2$O$_4$ and of their mixture (25%NiMoO$_4$+75%Sb$_2$O$_4$) before and after reaction.

This allowed to suggest that the role of α-Sb$_2$O$_4$ in the enhancement of propene selectivity and modification of kinetic parameters of the reaction is interpreted as a cooperation between two separate phases according to a remote control mechanism [3]. α-Sb$_2$O$_4$ is O$_{so}$ donor and NiMoO$_4$ is a oxygen spillover acceptor [3]. Even though, if NiSb$_2$O$_6$ is formed as a new phase between NiMoO$_4$ and α-Sb$_2$O$_4$ and it has not been detected by XRD. NiSb$_2$O$_6$ is considered as an effective oxygen spillover donor which increasing selectively the formation of acrylic acid from acrolein [6]. This suggestion is consistent with the the previous works done in our laboratory for the oxidative dehydrogenation of propane and ethane over MgVO/ α-Sb$_2$O$_4$ and MoVO or NiVO/ α-Sb$_2$O$_4$ respectively [7]. The principle consequence of this cooperation is the increase in the selectivity.

Previous studies for propane and ethane oxidation over NiCoMoO$_4$ and NiMoO$_4$ respectively [1b,8] demonstrated that the homolytic C-H bond break is the rate determining step (RDS), involving most probably an electron rich oxygen of molybdenum (octahedral) located adjacent to catalyst cation (Ni-O-Mo). It has also be concluded that the NiMoO$_4$ possessing octahedral co-ordination is not only more active but also more selective. In this study, the high dependence of the formation rate of propene on the partial pressure of propane confirm that the rate determining step is the activation of propane.

Our LRS results showed that in the case of pure NiMoO$_4$ the Mo species detected is not only MoO$_6$ octahedral but also MoO$_4$ tetrahedral. In the case of the mixture, only high electron rich octahedral MoO$_6$ sites have been detected. These results indicate that α–Sb$_2$O$_4$

370

inhibits the presence of tetrahedral molybdenum species on $\alpha$–NiMoO$_4$. This led us to suggest that the activation of propane (RDS) is easier over NiMoO$_4$ in mixture than in the case of pure NiMoO$_4$, which reflects the low dependence on propane pressure (low propane order), low activation energy and enhancement of propene selectivity when NiMoO$_4$ is mixed with $\alpha$-Sb$_2$O$_4$.

In addition, where tetrahedral Mo (MoO$_4$) species are believed to be more effective for chemisorption of propene than propane namely in the case of pure NiMoO$_4$, the adsorption of formed propene is very strong and easily decomposed to CO$_x$. However in the case of the mixture, propene is easily desorbed from the NiMoO$_4$ surface and the possibility to complete the oxidation to CO$_x$ is decreased. It can be suggested that $\alpha$-Sb$_2$O$_4$ facilitates the reoxidation (lower oxygen order) of the Mo sites to more active MoO$_6$ during reaction by O$_{so}$.

On the other hand SBET and XRD characterization indicated that the addition of $\alpha$-Sb$_2$O$_4$ to NiMoO$_4$ stabilized the surface of NiMoO$_4$ (no modification of SBET) after reaction. This might be due to $\alpha$-Sb$_2$O$_4$ inhibiting the sintering of NiMoO$_4$ particles (no change in particle size observed after reaction in the case of the mixture). $\alpha$-Sb$_2$O$_4$ inhibits the presence of Mo tetrahedral species on NiMoO$_4$ which might be it easily sintered.

## REFERENCES

1. (a) C. Mazzochia, C. Aboumrad, C. Diagne, E. Tempesti, J. M. Hermann and G.Thomas, Catal. Lett., 10 (1991) 181.
   (b) D. L. Stern and R. K. Grasselli, J. Catal. 167 (1997) 560.
2. (a) U. S. Ozkan. and G. L. Schrader, J. Catal., 95(1985)126.
   (b) U. S. Ozkan , R. C. Gill and M. R. Smith, Appl. Catal .62 (1990) 105.
3. L. T. Weng and B. Delmon, Appl. Catal. A, 81 (1992) 141.
4. (a) H. M. AbdelDayem, F. Christiaens, P. Ruiz and B. Delmon, submitted to 4th Int.Congr.on Oxidation Catalysis, September 16-21, 2001, Berlin Germany.
   (b) H. M. AbdelDayem and P. Ruiz, submitted to 4th Int. Symp. on Catalysts Deactivation, October 7-10, 2001, Lexington, Kentucky, USA.
5. J. Grimblot, E. Payen and J. P. Bonnelle, proc. 4[Th] Int. Conf. on the Chem.and Uses of Molybdenum (H. F. Barry, P. C.H. Mitchell, Eds.) Climax Molybdenum Cy, 1982, pp.261.
6. S. Briet, M. Estenfelder, H.-G. Lintz, A. Tenten and H. Hibst, Appl. Catal. A., 134 (1996) 81.
7. (a) S.R.G. Carrazàn, C. Peres, J. P. Bernard, M. Ruwet, P. Ruiz and B. Delmon, J. Catal. 158(1996)452.
   (b) T. Osawa, P. Ruiz and B. Delmon, Catal. Today 61 (2000) 317.
8. A. Kaddouri, R. Anouchinsky, C. Mazzocchia, L. Maderia and M. F. Portela, Catal. Today, 40 (1998) 20.

# Is spillover a key factor in SCR reaction over a physical mixture of $V_2O_5$ with $TiO_2$-$SO_4^{2-}$?

Seong Moon Jung* and Paul Grange

Unité de catalyse et chimie des matériaux divisés, Université catholique de Louvain,
Croix du Sud 2/17, B-1348 Louvain-la-Neuve, Belgium
Fax : +32-10-47.36.49.  e-mail : jung@cata.ucl.ac.be

The promotional effect of $V_2O_5$ on the SCR reaction of NO with $NH_3$ over a physical mixture of $V_2O_5$ and $TiO_2$-$SO_4^{2-}$ catalyst have been studied by DRIFTS (Diffuse Reflectance Infrared Fourier Transform Spectroscopy), $NH_3$-TPD and TPR (Temperature programmed reaction). In physical mixture, total conversion is observed at 300°C. $NH_3$-TPD performed on the separated catalyst layer confirm a synergetic effect between $V_2O_5$ and $TiO_2$-$SO_4^{2-}$. In addition, the spectra obtained by DRIFTS show that $NH_2$ species form at lower temperature than in pure $TiO_2$-$SO_4^{2-}$ catalyst and that the concentration of nitrate species on $TiO_2$-$SO_4^{2-}$ in physical mixture is improved. The improved activity in TPR is closely related with the enhanced formation of $NH_2$ species and nitrate. As a result, the high activity in the physical mixture can be explained by the promotional effect of $V_2O_5$ acting as an oxygen source.

## 1. INTRODUCTION

The elimination of nitrogen oxides emitted from the combustion process is particularly important in the reduction of the environmental problems caused by the formation of acid rain and ozone through secondary reactions in the atmosphere [1]. Several processes have been proposed for the elimination of NOx through the widespread application of available methods and/or via the development of new technologies [2]. Among the flue gas treatment methods, selective catalytic reduction (SCR) is well developed and used worldwide due to its efficiency, selectivity and economy. The SCR process is based on the reaction between NOx and NH₃, injected into the flue gas stream, to produce innocuous water and nitrogen.

Recently, several researchers have published reviews that cover the various range of SCR (catalyst preparation, chemical and mechanistic aspects, applications, analytical method)[1-3]. Based on the literature, it has been confirmed that both acid and redox properties are controlling factors of the reactivity of SCR catalysts [1-3]. The catalyst acid sites adsorb the ammonia, and the redox property of the catalyst dominates the activation rate of ammonia and/or the formation of intermediates like $NO_2$ [4-15]. The mechanism of SCR reaction leads to the fact that the activity and selectivity of SCR catalyst are very sensitive to temperature, since acidity is usually high at low temperature and redox property is highly improved at high temperature. Although there is no doubt that the catalytic redox and acid functions are the main controlling factors, the fundamental questions concerning the nature of the active ammonia species and of the active site are not clear and are still debated.

It is especially true in the case of $TiO_2$-$SO_4^{2-}$ catalyst [9,16], which shows higher reactivity than $V_2O_5$ based catalyst at high temperature. However, the possibility to substitute this

catalyst for a conventional SCR catalyst is limited because $TiO_2$-$SO_4^{2-}$ does not show any activity below 300°C.

We already suggested a new mechanism [15]: (i) $NH_3$ adsorbed on Lewis acid sites, (ii) NO oxidized to nitrate, (iii) nitrate intermediate reacted with adsorbed $NH_3$. This mechanism shows that $NO_2$ and/or nitrate formation rate plays an important role in the rate of reaction. Thus, if the rate of intermediates formation can be enhanced by another material, it could be imagined that the SCR reaction rate is also improved. $V_2O_5$ was firstly selected as a reducible material. In addition, a model catalyst was prepared through physical mixture of $V_2O_5$ and $TiO_2$-$SO_4^{2-}$.

This work is mainly focused on the identification of the improved reactivity on a physical mixture of $V_2O_5$ and $TiO_2$- $SO_4^{2-}$ catalyst during the SCR reaction. Then, we will propose a promotional effect on a reaction mechanism on the basis of the spectroscopic investigation of the intermediate species.

## 2. EXPERIMENTAL

Titanium hydroxide obtained through precipitation of $TiCl_4$ was dried at 100°C for 24h. The calculated $H_2SO_4$ solution (0.1N) was then added to the titanium hydroxide. Thereafter, the solids were dried for 24h at 100°C and calcined for 5h at 500°C. The BET surface is $104m^2/g$. Only anatase is detected. The loaded amount of sulfate on $TiO_2$ obtained from ICP analysis was 6.6wt%. The detailed characterization of sample is reported in previous papers (3). $V_2O_5$ used in this experiment is a commercial oxide (Aldrich). The specific surface area of the samples was $2.5m^2/g$.

In situ Diffuse Reflectance Infrared Fourier Transform Spectroscopy (DRIFTS) spectra were collected in a Brucker IFS88 infrared spectrometer with a DTGS detector. Pure samples were placed inside a commercial controlled environmental chamber (Spectra-Tech 0030-103) attached to a diffuse reflectance accessory (Spectra-Tech collector). Before adsorption, samples were pretreated under 30ml/min flow He at 400°C for 30min and then cooled to room temperature. The pretreated samples were exposed to ammonia followed by NO for 10 minutes for coadsorption of $NH_3$ and NO. To investigate the influence of the atmosphere on species adsorbed on the surface during temperature elevation, the spectra were also recorded under Nitric oxide 0.5vol% in helium at 100°C, 200°C, 300°C and 400°C (30ml/min).

An $NH_3$-TPD (temperature programmed desorption) spectrum was obtained by monitoring the desorbed ammonia, through increasing the temperature of the sample at a constant rate (10°C /min) under 50cc/min of diluted nitric oxide flow (0.5vol% in helium), after adsorbing ammonia on the catalyst at room temperature using ammonia (0.5vol% in helium). Outlet gas compositions were measured using a quadrupole mass spectrometer QMC 311 Balzers coupled to the reactor.

The TPR were carried out in a continuous flow fixed bed reactor operating at atmospheric pressure. 0.15g of catalyst were used. The total flow rate was 100ml/min and feed composition was: nitric oxide 0.1vol%; ammonia 0.105vol%; 2.5vol% oxygen, in helium. A mixture of reactants (NO, $NH_3$ and $O_2$) was diluted by helium and the flow rate was controlled by flow meter. The reactor was vertical and made of quartz. The rising rate of temperature was 10°C/min. The inlet and outlet gas compositions were measured using a quadrupole mass spectrometer QMC 311 Balzers coupled to the reactor.

## 3. RESULTS
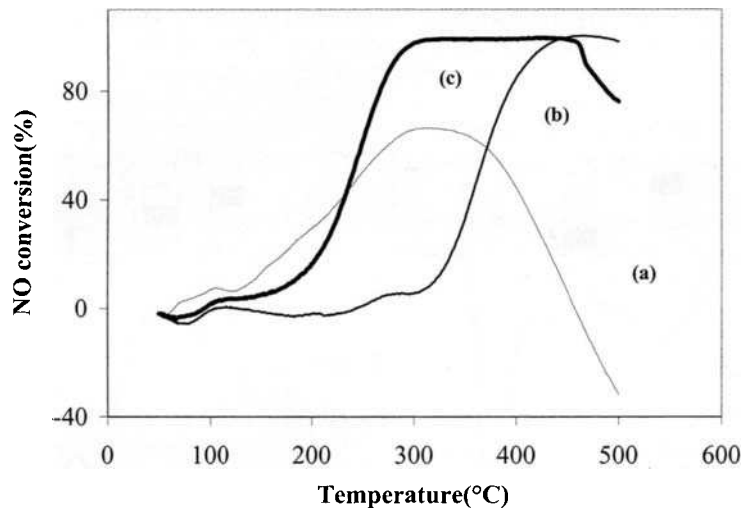


Fig 1. TPR (a) $V_2O_5$, (b) $TiO_2$-$SO_4^{2-}$, (c) $V_2O_5$ (50wt%)+ $TiO_2$-$SO_4^{2-}$(50wt%)

Fig 1 shows the TPR results over three catalysts. On $V_2O_5$ catalyst, the consumption of NO began at 100°C. The maximum of NO conversion was observed around 300-350°C. Above 350°C, the activity decreased and a concentration of NO higher than feed composition was detected after 450°C. It is suggested that the decrease in NO conversion is due to the increased rate of $NH_3$ oxidation to NO. The NO conversion of $TiO_2$-$SO_4^{2-}$ initiates at 300°C. The total conversion was observed at 450°C and preserved up to 500°C. As it has been mentioned in a previous paper [16], the high acid property on $TiO_2$-$SO_4^{2-}$ created by sulfation contributes to the improved activity at high temperature. Forzatti and Lietti proposed that the activity at low temperature depends on the reducibility of the catalyst, while the strong acid site is a key factor to control the activity at high temperature [2].

In the physical mixture, the threshold of NO consumption appeared at 200°C. Total conversion was detected at 300°C and preserved up to 450°C, although the decrease in NO conversion was observed after 470°C. This modified activity cannot be explained on the basis of individual property of each catalyst on SCR reaction.

Sobalik et al. [17] suggested that the mixing effect in physical mixture can lead to a modified activity due to the insertion of one material in another one during the mixing procedure. Accordingly, in order to see the real promotional effect without the potential effect of a mixing procedure, two experiments were performed without mixing, by only superposing the two solids separated or not by an inert material ($SiO_2$). Using these arrangements of catalyst, $NH_3$-TPD was carried out. The results are shown in Fig 2. All cases show almost same consumption of NO around 150°C, which is due to the reaction with ammonia adsorbed on $V_2O_5$ layer. But the feature of NO consumption at high temperature depends on the type of superposition.

When $V_2O_5$ placed in first layer (a) with $SiO_2$ as a middle layer, the feature of NO consumption at high temperature is almost the same as that observed on pure $TiO_2$-$SO_4^{2-}$ in $NH_3$-TPD, as reported previously [15]. This indicates that there is no promotional effect. On

the contrary, the use of TiO$_2$-SO$_4{}^{2-}$ as first layer (b) leads to the appearance of another peak concerning the NO consumption at 300°C, besides the peak at 400°C. In this case, it may be suggested that the stored NH$_3$ by TiO$_2$-SO$_4{}^{2-}$ is evolved during temperature increase and reacts with NO over V$_2$O$_5$ surface.
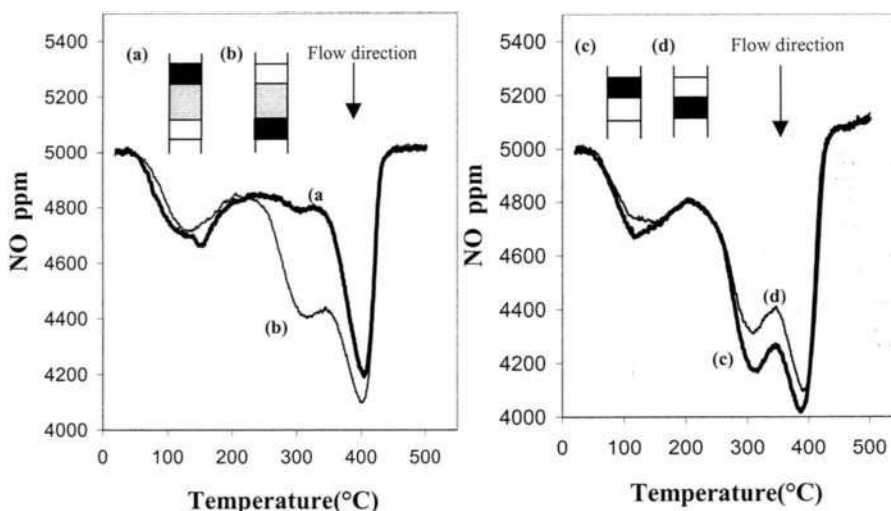


Fig 2. NH$_3$-TPD by NO(0.5vol% in He) after preadsorption of NH$_3$ over layered catalysts :
■ V$_2$O$_5$, ▭ TiO$_2$-SO$_4{}^{2-}$, ▭ SiO$_2$

Fig 2 (c) and (d) show the feature of NH$_3$-TPD without a middle layer of SiO$_2$. In both cases, peaks of NO consumption were observed at 300°C and 400°C. Especially, the first layered V$_2$O$_5$ shows the higher NO consumption, even compared with the reversed layer type. This result suggests that V$_2$O$_5$ promotes the reaction of NO with adsorbed NH$_3$ on TiO$_2$-SO$_4{}^{2-}$.

Comparing the results of (a) and (c), it can be imagined that the direct contact between two layers is an important factor to generate the synergetic effect and/or that the distance between two layers controls the activity.

In order to explain the improved activity of the physical mixture observed on TPR results, the surface species on the physical mixture of V$_2$O$_5$ and TiO$_2$-SO$_4{}^{2-}$ are detected by DRIFTS as a function of temperature. The mixture sample was prepared followed by the preadsorption of NH$_3$ on TiO$_2$-SO$_4{}^{2-}$, in order to avoid the influence of ammonia adsorbed on V$_2$O$_5$.

The spectra obtained under NO flow at 100°C-400°C on pure TiO$_2$-SO$_4{}^{2-}$ and on the physical mixture are presented and compared in Fig 3. In the case of pure TiO$_2$-SO$_4{}^{2-}$, the band at 1446 and 1623 cm$^{-1}$ attributed to bridging or chelating nitrate species dominated at 100°C. The band at 1446 cm$^{-1}$ further increases at 200°C. At 200°C, the decrease of the band at 1623 cm$^{-1}$ was detected, while the weakly broadened peak at 1506 cm$^{-1}$ increased. When the temperature reached 300°C, the band at 1623 and 1446 cm$^{-1}$ decreased, whereas the band at 1506 cm$^{-1}$ increased. At 400°C, the band at 1506 and 1446 cm$^{-1}$ disappeared. Meanwhile, the band related to S=O increased and shifted to higher wavenumber according to the temperature increase.

On the physical mixture, the intensity of the S=O band decreased due to the relative

decreasing amount of $TiO_2$-$SO_4^{2-}$. In spite of that, the band at 1506 cm$^{-1}$ can obviously be detected even at 100°C, while the band at 1446 cm$^{-1}$ assigned to nitrate shows an amount similar to that for pure $TiO_2$-$SO_4^{2-}$. Moreover, at 200°C, the band intensity at 1506 cm$^{-1}$ is higher than pure $TiO_2$-$SO_4^{2-}$. A decrease of the band was observed at 300°C. Considering that the increase of band at 1506 cm$^{-1}$ is shown even at 300°C and that this behavior is closely related with TPR results, it is suggested that the band at 1506 cm$^{-1}$ is a key clue to disclose the synergetic effect occurring between $V_2O_5$ and $TiO_2$-$SO_4^{2-}$. Ramis et al. suggested that the band at 1535 cm$^{-1}$ is assigned to an amide species NH$_2$ [7]. Tsyganenko et al. also proposed that NH$_2^-$ deformation mode is observed on 1505-1580 cm$^{-1}$ [18]. Accordingly the band at 1506 cm$^{-1}$ can be assigned to NH$_2$. Thus, it can also be suggested that $V_2O_5$ enhances the formation of amide species through the dissociation of hydrogen in ammonia.
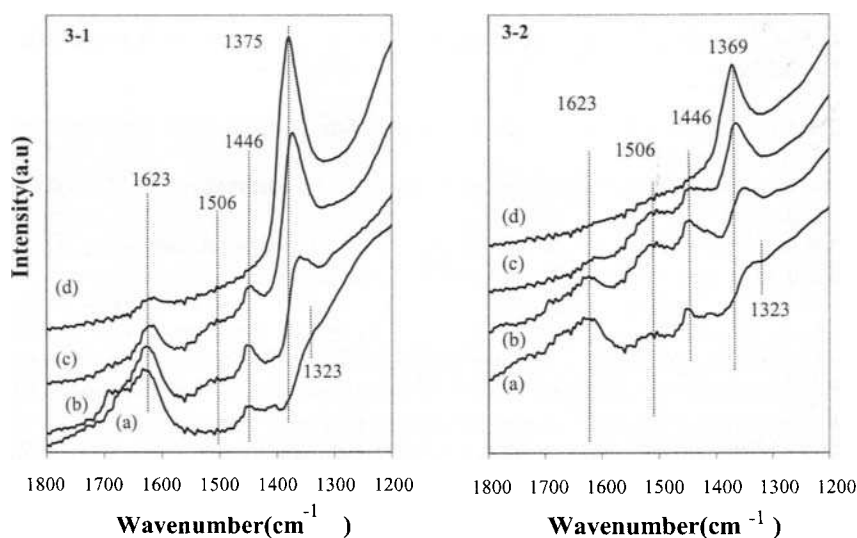


Fig 3. In situ DRIFTS spectra of adsorbed species on pure $TiO_2$ sulfate (3-1) and physical mixture (3-2) under NO flow with temperature, after adsorption of NH$_3$ at room temperature; (a) 100°C, (b) 200°C, (c) 300°C, (d) 400°C

## 4. DISCUSSIONS

Concerning SCR catalyst reaction, a large number of paper dealing with the mechanism have been published. More specifically, on $V_2O_5$/$TiO_2$ SCR catalyst, NH$_2$ species as main active intermediate have been emphasized by Ramis et al [7]. The mechanism of SCR could be described by the following steps, requiring a surface redox site adjacent to the surface acid site [3].

$$NH_3 + A \longrightarrow NH_3\text{-}A \ ( \ A : Acid \ site) \tag{1}$$
$$NH_3\text{-}A + O\text{-}(lattice) \longrightarrow NH_2\text{-}A + HO\text{-}(lattice) \tag{2}$$
$$NH_2\text{-}A + NO_x \longrightarrow N_2 + H_2O \tag{3}$$
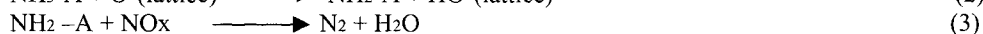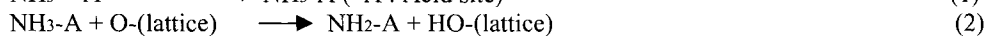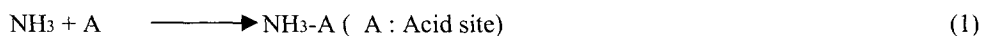
The first step in SCR reaction is adsorption of ammonia on a Lewis acid site. Then the

hydrogen on adsorbed ammonia would be dissociated by a neighbor oxidation site, in order to form the active intermediate through the reaction with NO. Thus, it has been proposed that the $NH_2NO$ formation rate controls the overall reaction rate of SCR. Lietti and Forzatti also explained that the liability of lattice oxygen atoms is the controlling factor to improve the SCR activity in the comparison of activity between isolated vanadyl and polymeric metavanadate species [19]. Based on those explanations, it can be suggested that SCR catalyst would be consisted of an $NH_3$ adsorption site and a labile oxygen source, which induce the dissociation of hydrogen attached ammonia.

In fact, pure $V_2O_5$ does not show considerable acidity after 300°C. But the rate of hydrogen transfer increases due to the increase of oxygen mobility. Thus, the excess dissociation of hydrogen to NH from $NH_2$ can happen at high temperature. Since NH species are known as the intermediate of ammonia oxidation, it is not surprising that in TPR over $V_2O_5$ catalyst, the NO concentration is higher than in the feed.

Meanwhile, in a previous paper, we proposed the SCR reaction mechanism on $TiO_2$ sulfate catalyst as follows:

i) Firstly, $NH_3$ adsorbs on the surface of $TiO_2$ sulfate and modifies the negative charge balance of the surface.
ii) Due to the generated negative charge on its surface, the adsorption of NO as $NO^-$ species is stimulated.
iii) $NO^-$ is oxidized to $NO_2$ and $NO_3^-$ by the oxygen from the structure and from NO.
iv) $NO_2$ and $NO_3^-$ may react with coordinated $NH_3$ adsorbed on Lewis acid sites.

Considering the above mechanism, the high activity at high temperature is explained by the increased oxidation rate of NO to nitrate. This mechanism is very similar to that suggested, based on zeolite catalyst [13,14], except for a kind of ammonia adsorption site. In DRIFTS, the band intensity at 1446 $cm^{-1}$ assigned to nitrate species is almost same in both the pure $TiO_2\text{-}SO_4^{2-}$ and the physical mixture. But, considering the difference in $TiO_2\text{-}SO_4^{2-}$ amount in both samples, the same trend of these species on both cases indicates that the nitrate concentration on physical mixture is double that in pure $TiO_2\text{-}SO_4^{2-}$. Thus, the change in band intensity concerning nitrate can explain the difference of activity observed by TPR and $NH_3$-TPD.

In our DRIFTS results, The band at 1506 $cm^{-1}$ also shows a clear difference between $TiO_2\text{-}SO_4^{2-}$ and the physical mixture. This band appeared even at 100°C in the physical mixture. Considering the assignment of this peak as a $NH_2$ species, it is shown that the formation rate of amide species is improved by addition of $V_2O_5$ to $TiO_2\text{-}SO_4^{2-}$ and effective oxygen able to dissociate the hydrogen on ammonia are already generated at 100°C.

$V_2O_5$ easily loses the surface oxygen as shown in Fig 4. When $V_2O_5$ is heated up to 300°C in helium flow, the surface modification verified by DRIFTS indicates the change of the band at 1996 and 2020 $cm^{-1}$. These bands can be assigned to V=O overtone band. The band intensity decreased with temperature increase. This result shows that V=O mobility on $V_2O_5$ is high and that oxygen can migrate to another phase.
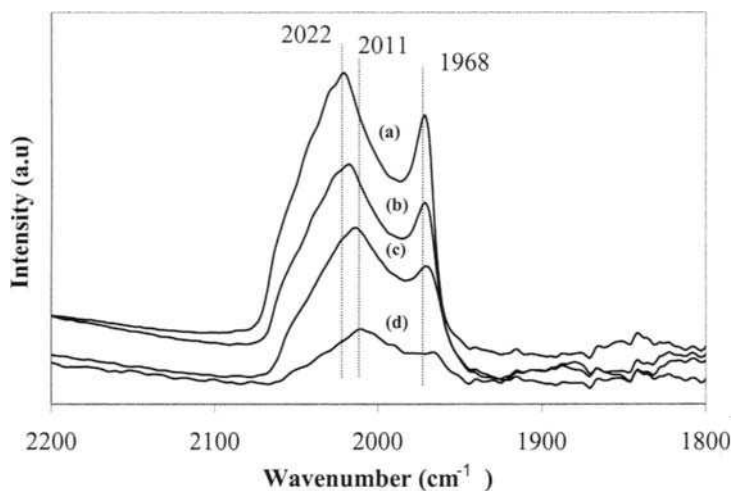
Fig 4. In situ DRIFTS spectra obtained over pure $V_2O_5$ under the condition of helium flow at (a) r.t, (b) 100°C, (c) 200°C, (d) 300°C

## 5. CONCLUSIONS

In the presence of $V_2O_5$, not only the formation rate of ammonia adsorbed on $TiO_2$-$SO_4^{2-}$ to amide but also of $NO_2$ to nitrate are improved. The positively modified reactivity in physical mixture can be explained by the different oxidation rates of $NO$ and $NH_3$. The oxygen of $V=O$ on $V_2O_5$ shows high labile properties. From these results, it is tentatively concluded that the oxygen from $V_2O_5$ can be attributed to the synergetic effect observed on physical mixture of $V_2O_5$ with $TiO_2$-$SO_4^{2-}$.

### Acknowledgments

### REFERENCES

1. V. I. Parvulescu, P. Grange, B. Delmon. Catal. Today 46 (1998) 233
2. P. Forzatti and L. Lietti, Heterogeneous Chem. Rev. 3 (1996) 33.
3. G. Busca, L. Lietti, G. Ramis, F. Berti Appl. Catal. B 18 (1998) 1.
4. M. Takagi, T. Kowai, M. Soma, T. Onishi and K. Tamaru, J.Catal. 50 (1977) 441.
5. M. Inomato, A. Miyamoto and Y. Murakami, J.Catal. 62 (1980) 140.
6. F. Janssen, F. Van den Kerkhof, H. Bosch and J.J. Ross, Phys.Chem. 91 (1987) 5931.
7. G. Ramis, G. Busca, F. Bregani and P. Forzatti, Appl. Catal. 64 (1990) 259.
8. T. Komatsu , M. Nunokawa, S. Moon, T. Takahara, S. Nanba and T. Yashima, J. Catal., 148 (1994) 427.
9. J.P. Chen and R.T. Yang, J. Catal. 139 (1993) 277.

10. H. Schneider, S. Tschudin, M. Schneider, A. Wokaun and A. Baiker, J. Catal., 147 (1993) 5.
11. N.Y. Topsøe, H. Topsøe and J.H. Dumesic, J. Catal. 151 (1995) 241.
12. Yu.M. Belokoptov, K.M. Kolyvenko and S.V. Gerei, J. Catal. 60 (1979) 1.
13. J. Eng and Calvin H. Bartholomew, J. Catal. 171 (1997) 27.
14. J. Eng and Calvin H. Bartholomew, J. Catal. 171 (1997) 14.
15. S. M. Jung and P. Grange, Appl. Catal. B 27 (2000) L11.
16. S. M. Jung and P. Grange, Catal. Today 59 (2000) 305.
17. Z. Sobalik, O. B. Lapina and V. M. Mastikhin, Proceeding of preparation of catalyst V, Elsevier, Amsterdam, p507 (1991)
18. A. A. Tsyganenko, D. V. Pozdnyakov and V. N. Filimonov, J. Mol. Structure, 299 (1975) 29.
19. L. Lietti and P. Forzatti, J. Catal., 147 (1994) 241.

# Comparative determination of surface and lattice oxygen mobility on vanadium phosphorus oxides by isotopic exchange with $C^{18}O_2$

B. Bachiller-Baeza[1], I. Rodríguez-Ramos[1], J.C. Volta[2], M. Cerro-Alarcón[3] and A. Guerrero-Ruiz[3]

[1] Instituto de Catálisis y Petroleoquímica, CSIC. Campus Cantoblanco 28049, Madrid Spain.

[2] Institut de Recherches sur la Catalyse, CNRS, 69626 Villeurbanne, France.

[3] Departamento de Química Inorgánica, Facultad de Ciencias, UNED, 28040 Madrid, Spain.

Graphite-supported vanadium-phosphorus-oxide catalysts, with different VPO contents, were prepared via impregnation with a homogeneous solution of V(V) ions in combination with phosphate ions. From the different characterisation techniques ($^{31}$P RMN, XRD, XPS and TEM) it was concluded that the VPO phase was amorphous and well dispersed over the surface of the support. These catalysts were tested for the n-butane mild oxidation to maleic anhydride reaction under "fuel-rich" conditions ($O_2/C_4$ = 0.6). A relationship between the VPO loading and the catalytic properties is stated. The maleic anhydride yield is increased for lower VPO contents. Comparison among these samples with respect to their surface characteristics as well as their oxygen exchange capacities determined using $C^{18}O_2$ was also performed. It is stated that these oxygen exchange capacities are responsible for the improved catalytic properties in the selective oxidation. The sample with lower VPO content, which is the most active in the oxygen exchange experiments and shows the highest oxygen diffusion rate, displays the best catalytic yield to maleic anhydride.

## 1. INTRODUCTION

Vanadium-phosphorus-oxide (VPO) is the heterogeneous catalyst industrially used for the production of maleic anhydride (MA) from n-butane. It is widely accepted that the active and selective phase is mainly the $(VO)_2P_2O_7$ formed in situ in the presence of the butane/air atmosphere [1,2] but it has also been claimed that V(V) phosphate phases operate in the reaction [3]. Several factors determine the final performance of the catalysts (preparation method, P/V ratio and activation process) and considerable effort has been done in order to gain an understanding on the nature of the active site for these catalysts [4]. Numerous techniques (XRD, Raman spectroscopy, XPS) have been used to study the surface and bulk properties of the V-P-O catalysts. Currently, two routes to improve the activity and selectivity have been proposed, the introduction of dopants and the use of supported VPO catalysts. The dispersion of the VPO phase over a carrier should offer some advantages such as an increase in surface area and exposition of active sites, but at the same time it could introduce support-oxide interactions that would affect the formation and final structure of the phases. Moreover,

supporting the VPO phase could avoid the bulk atoms contributions to the characterisation information obtained with most techniques and the local structure of the active site could be easily investigated. Few examples of VPO deposition on silica, titania or alumina have been described, and similarly to the unsupported catalysts, the catalytic activity has been related to the surface and bulk properties of the phases present in the catalysts [5,6,7]. Furthermore, redox processes ($V^{5+}/V^{4+}$) and the role of lattice oxygen may be crucial in the reaction mechanism but their involvement is still unclear. Different types of oxygen, terminal oxygen V=O, bridging oxygen V-O-V and V-O-P and activated molecular oxygen are present in the catalysts during the reaction and seem to be involved in the different steps of the mechanism. Particularly, the oxygen species of the V-P-O bond by its incorporation in the MA may be responsible for the selective oxidation [2]. Then, the oxygen availability and mobility are two facts that could determine the activity and selectivity in the selective oxidation by controlling the first step of $n$-$C_4$ activation as compared to the further O-incorporation in the carbon intermediates. So, the isotopic oxygen exchange, which has been applied to analyse lattice oxygen diffusion over different oxides, seems to be a very useful technique for the study of VPO catalysts [8,9].

In this communication graphite-supported VPO catalysts were prepared and tested in the oxygen isotopic exchange with $C^{18}O_2$ and compared with a bulk V-P-O catalyst. The final aim is to correlate the catalytic performance of the catalysts in the selective oxidation of $n$-butane to maleic anhydride with the oxygen surface exchange properties and with the lattice oxygen migration.

## 2. EXPERIMENTAL

### 2.1 Catalysts preparation

Five samples were studied in this work. Graphite-supported samples (VPOx/H) were prepared by impregnation with a water solution containing $NH_4VO_3$, $H_2C_2O_4·2H_2O$ and $(NH_4)_2HPO_4$ [10]. The samples were dried and calcined in static air at 653 K for 1h. The active phase nominal content was x = 5, 15, 20 and 30% (calculated on the basis of a $(VO)_2P_2O_7$ matrix). The graphite support used in this study is a high surface area graphite (HSAG) supplied by Lonza, with a 299 $m^2·g^{-1}$ surface area. Sample VPO was prepared by crystallisation of the impregnation solution. The resulting blue crystals were dried at 383 K and further calcined in static air at 653 K for 1h.

### 2.2 Catalyst Characterisation

The specific surface area of the samples was measured by the BET method with $N_2$ adsorption at 77K.

The $^{31}P$ NMR spectra were recorded with a Bruker DSX400 spectrometer at 161.9 MHz, equipped with a standard 4-mm probe head. The $^{31}P$ Spin Echo Mapping (SEM) spectra were obtained with a sweep width of 2 MHz, $t = 20$ μs and a 90° pulse length of 1.5 μs.

XPS analysis was performed in a VG Escalab 200R machine using Mg $K\alpha$ radiation. The electrical charge was corrected by setting the binding energy (BE) of adventitious carbon ($C_{1s}$) at 284.5 eV. For quantitative analysis, the integrated area under the $V_{2p3/2}$, $O_{1s}$, $P_{2p}$ and $C_{1s}$ peaks after smoothing and substraction of a non-linear Shirley background was used. The changes in the surface oxidation state of vanadium ($V^{5+}$, $V^{4+}$ and $V^{3+}$) were measured by the

analysis of the $V_{2p3/2}$ level from a peak decomposition and curve fitting technique already described [11].

The exchange experiments were carried out in a fixed bed quartz microreactor coupled to a vacuum volumetric apparatus [12]. Before experiments samples were treated under vacuum at 773 K for 1 h. Then, they were cooled to 673 K and a known amount of $C^{18}O_2$ was admitted in the reactor (the percentage of $^{18}O$ atoms in the system was kept at 10%). The gas phase was recirculated through the sample bed and analysed by an on-line mass quadrupole spectrometer (Balzers QMG 421C) connected to the reactor through a metering leak valve. The ion current of the products $C^{18}O_2$, $C^{18}O^{16}O$, $C^{16}O_2$ and secondary peaks were collected in a personal computer.

## 2.3 Catalysts testing

The catalytic experiments were carried out in a fixed bed reactor at atmospheric pressure. The reactor, a classical tubular Pyrex microreactor, was equipped with a thermocouple placed inside the catalytic bed for continuous temperature control. Sampling valves were inserted in a hot box heated at 150°C to avoid product condensation. Mass flow controllers regulated the gas flows of reactants. The feed consisted on a mixture of $n$-butane, oxygen and helium.

The tests were carried out at 380°C and "fuel-rich" conditions $O_2/C_4 = 0.6$ ($C_4/O_2/He = 10.0 / 6.0 / 84.0$) were chosen with a total flow rate of 16.7 $cm^3 \cdot min^{-1}$ at a constant GHSV of 2000 $h^{-1}$. These conditions were chosen in order to observe the effect of the oxygen availability in the samples when the oxygen supply in the feed is poor.

Reactants and reaction products were analysed by on-line gas chromatography using double FID detection and a combination of columns: a 10% AT 1200 with 1% $H_3PO_4$ on a chromosorb W-AW column (2 ft x 1/8 in., 80/100 mesh, 90°C) for separation of oxygenated products, and a Durapak column (4 ft x 1/8 in., 80/100 mesh, 60°C) to separate butane from butenes and butadiene. CO, $CO_2$, $O_2$ and He were analysed with a TCD detector and separated with a Carbosieve B column (4ft x 1/8 in., 80/100 mesh, 100°C).

## 3. RESULTS AND DISCUSSION

### 3.1 Catalysts characterisation

The catalysts tested in the selective oxidation of $n$-butane were previously characterised with different techniques. The BET surface areas, the V content and the P/V atomic ratio from the chemical composition are summarised in Table 1 for bulk VPO and graphite-supported VPO samples. It is displayed that the surface areas of the supported catalysts are lower than that of the support ($S_{BET} = 299$ $m^2 \cdot g^{-1}$). Moreover, the surface area markedly decreases with increasing vanadium content. This effect may be explained by the increasing coverage of the support's surface as the active phase content increases.

X-ray diffraction was applied for crystalline phase detection. However, due to the absence of any peak different to those obtained for graphite it can be concluded that the VPO phase is amorphous and is well dispersed over the surface of the support. This fact was corroborated for VPO15/H by Transmission Electron Microscopy (TEM), where no VPO particles could be detected.

Table 1 also shows the XPS results of the samples before and after the catalytic reaction. It can be observed that the P/V ratios obtained by XPS for the fresh samples are higher than those obtained from chemical analysis, indicating a phosphorus enrichment of the surface of the catalyst, as previously reported [6,7]. The same behaviour is observed for the samples after the catalytic test. Differences in the P/V surface ratio are observed for the samples before and after reaction depending on the VPO coverage on graphite.

Table 1
Catalysts characterisation before and after the selective oxidation of $n$-butane under "fuel-rich" conditions.

| Catalysts | | $S_{BET}$ $(m^2 \cdot g^{-1})$ | P/V | % V | XPS | | | | |
|---|---|---|---|---|---|---|---|---|---|
| | | | | | P/V | $V^{5+}/V^{4+}$ | $V^{5+}/V^{3+}$ | $V^{4+}/V^{3+}$ | $V_{ox}$[a] |
| VPO | fresh | 0.05 | | | 1.8 | | | 0.72 | 3.19 |
| VPO5/H | fresh | 179.1 | 1.1 | 1.5 | 2.2 | 0.45 | 1.20 | 2.67 | 4.04 |
| | used | | | | 1.3 | 0.38 | 0.95 | 2.50 | 3.99 |
| VPO15/H | fresh | 52.2 | 1.0 | 4.6 | 1.5 | 0.26 | 1.19 | 4.52 | 4.02 |
| | used | | | | 1.7 | 0.25 | 0.82 | 3.31 | 3.97 |
| VPO20/H | fresh | 33.8 | 1.1 | 6.2 | 1.9 | 0.18 | 1.16 | 6.47 | 4.02 |
| | used | | | | 1.7 | 0.18 | 0.90 | 5.09 | 3.99 |
| VPO30/H | fresh | 6.5 | 1.0 | 9.1 | 1.4 | 0.30 | 1.73 | 5.75 | 4.09 |
| | used | | | | 1.4 | 0.25 | 1.00 | 3.94 | 4.02 |

[a] Average oxidation state

The $V_{2p3/2}$ peak may be decomposed in three peaks of binding energies 518.0, 516.9 and 515.7 eV for $V^{5+}$, $V^{4+}$ and $V^{3+}$ respectively [3,13]. Considering the V ratios before and after reaction, both $V^{5+}/V^{3+}$ and $V^{4+}/V^{3+}$ decrease, while $V^{5+}/V^{4+}$ is maintained constant. This is due to the reduction in the reaction atmosphere of $V^{5+}$ and $V^{4+}$ to $V^{3+}$ species. Note that the decrease in the $V^{5+}/V^{3+}$ and $V^{4+}/V^{3+}$ ratios is much more pronounced for higher VPO loadings, which indicates that a higher concentration of $V^{3+}$ species is being generated. It is widely accepted that the $V^{4+}$- $V^{5+}$ redox cycle plays a role in the catalytic reaction. But, it has been also reported the importance of $V^{3+}$ species in the selective oxidation of butane. The presence of these species over vanadyl pyrophosphate catalysts has been evidenced by different methods [14,15] and it has been observed that an accumulation of such species takes place on the surface of the catalyst, particularly when mixtures containing low oxygen concentrations are used in the feed.

The average oxidation state of vanadium in the supported samples does not change considerably after the catalytic reaction or among samples, and it is maintained around 4. On the other hand, it can be noted the difference with the bulk VPO sample that displays an average oxidation state of 3.2, due to the absence of $V^{5+}$ species.

The $^{31}P$ NMR Spin Echo Mapping (SEM) spectra of samples VPOx/H before and after the catalytic reaction were recorded in order to observe the possible changes in structure due to the reaction atmosphere, and to observe the structure differences among samples. Sample

VPO and the four graphite-supported VPO fresh samples give spectra with a similar shape, showing a main peak around 0-ppm, characteristic of P atoms bonded to $V^{5+}$ centers in phosphate phases [3,11], and a small contribution in the 500-1500 ppm range which has been previously attributed to $V^{4+}$-$V^{5+}$ pairs [11,13]. This contribution in the 500-1500 ppm range is slightly higher for larger VPO loadings. When considering the spectra of the samples after the catalytic reaction, there is a considerable change in the relative intensities of the peaks compared to those for the fresh samples. While the intensity of the peak at 0-ppm decreases, the contribution of the 500-1500 ppm range increases. This fact indicates partial reduction of $V^{5+}$ to $V^{4+}$ species under the reducing atmosphere. Contrary to what is observed by XPS, no signals can be assigned to $V^{3+}$ centers, located around 4300-4700 ppm [3,11,13]. This fact seems to indicate that the total $V^{3+}$ concentration is very low and mainly located at the surface, and that these $V^{3+}$ sites are at a long distance from the P atoms.

In Figure 1A the gaseous carbon dioxide isotopic composition evolution with time during the oxygen exchange experiment is plotted for fresh samples VPO and VPO15/H. Figure 1B displays the $F(^{18}O)$ parameter evolution with time in reaction for these two samples. This parameter is defined as $F(^{18}O) = [I (46) + 2 I (48)] / \{2 [I (44) + I (46) + I (48)]\}$ (I = intensity in the mass quadrupole for a $m/z$ peak), and is indicative of the exchange kinetics [5]. For bulk oxides the first part of this curve is the surface oxygen contribution to the oxygen exchange. The last section of the curve is representative of the lattice oxygen exchange and its slope can be used to compare the catalysts. It has been found that the surface oxygen contribution to the oxygen exchange is very small for all the samples but increases slightly for the catalysts with lower active phase content.

The graphite support was also tested in the oxygen exchange experiment under the same conditions as the catalysts, and it was observed that it contributes to the exchange activity (Figure 1). There is a fast isotopic labelling decrease in the first minutes of the reaction characteristic of the surface oxygen exchange. After that, the oxygen exchange continues but at a lower rate. This activity shown by the support can be related to the oxygen functional groups of the material. The pre-treatment applied before the exchange modifies the amount of these groups by decomposition of the most acidic carboxylic surface groups [16]. Then, the most thermally stable carbonilic and phenolic groups are responsible for the oxygen exchange. The two oxygen exchange rates observed may be due to the presence of the two different types of oxygen groups and consequently to their different C-O bond strength and reactivity.

The slope of the $F(^{18}O)$ curves are presented in Table 2 for all the samples. It can be observed that the slope values follow the trend VPO5/H $\approx$ VPO15/H> VPO20/H> VPO30/H> VPO. Taking into account the behaviour of the support, it can be deduced that the oxygen exchange activity of the supported catalysts can be attributed to both the VPO phase and the graphite support. Therefore, the graphite contribution to the oxygen exchange will depend on the surface coverage, i.e. for higher coverage the amount of functional groups exposed should diminish. On the other hand, as it is shown in Table 2, the slope of the second section of the $F(^{18}O)$ curve is always higher for the supported catalysts than for the graphite ($13 \cdot 10^{-4}$), and increases for lower VPO contents. Moreover, increasing the oxide content increases the coverage of the support too, as it was deduced from the decrease in surface area (Table 1). This fact would explain the close behaviour obtained for catalysts VPO and VPO30/H. For catalysts with lower phase content, the graphite contribution may be mainly ascribed to the

surface exchange but the second contribution of the catalyst to the oxygen exchange would correspond to the active phase.
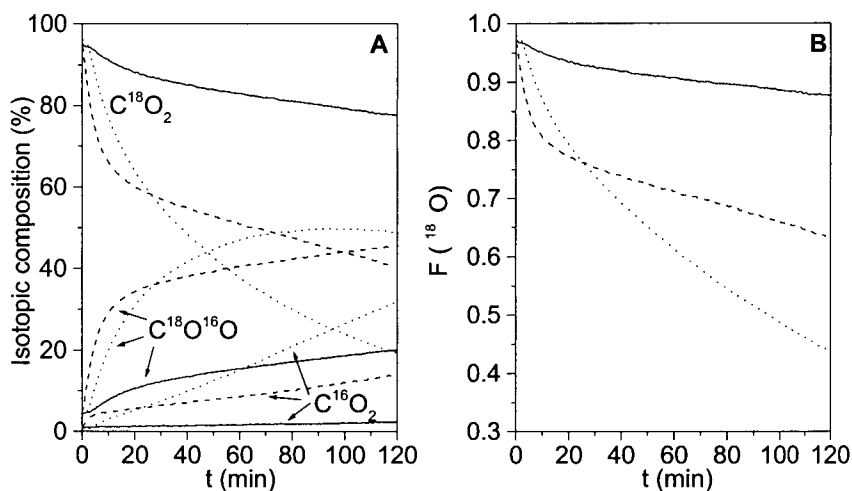


Figure 1. (A) Isotopic composition versus time in reaction and (B) gaseous $CO_2$ isotopic labelling for fresh samples VPO (solid), VPO15/H (dotted) and graphite H (dashed line).

Table 2
Slopes of the $CO_2$ isotopic labelling curves and catalytic results for the selective oxidation of $n$-butane to maleic anhydride under reducing atmosphere.

| Catalyst | Slope ($\times 10^{-4}$) | Activity $n$-$C_4$ ($\mu mol \cdot gV^{-1} \cdot s^{-1}$) | Selectivity MA (%) | MA Yield (%) |
|---|---|---|---|---|
| VPO | 11 | -[a] | -[a] | -[a] |
| VPO5/H | 24 | 10.6 | 77 | 2.5 |
| VPO15/H | 25 | 2.9 | 83 | 4.3 |
| VPO20/H | 20 | 1.6 | 81 | 3.5 |
| VPO30/H | 15 | 0.7 | 78 | 2.0 |

[a] Almost inactive

Previous isotopic exchange studies have suggested that a fast oxygen exchange on the surface of $(VO_2)P_2O_7$ takes place, but that the lattice oxygen diffusion is very slow [17]. In the case of $VOPO_4$, the overall oxygen exchange rate is lower than for the $(VO_2)P_2O_7$ phase, but it was observed that the lattice oxygen diffusion is very fast leading to a multiple exchange mechanism [9]. Comparing the unsupported and supported catalysts, the present

results suggest that the use of graphite to disperse the active microcristalline VPO phase favours the oxygen exchange properties of the catalysts, and particularly when the phase is well dispersed over the support. The modification in reactivity and in the oxygen diffusion of the VPO phase could determine the catalytic properties of the catalysts.

## 3.2 Catalytic results

Table 2 shows the catalytic performances for the $n$-butane oxidation to maleic anhydride reaction for the VPO and graphite-supported VPO samples, measured after 43.5h under stream ($n$-$C_4H_{10}$/$O_2$/He = 10.0/ 6.0/ 84.0, GHSV = 2000 $h^{-1}$). The VPOx/H catalysts reached the stationary state under these conditions only after 25h. It can be noted that the highest yield towards MA is obtained for sample VPO15/H. There is a general trend for the catalytic performances that follows the sequence VPO15/H > VPO5/H > VPO20/H > VPO30/H > VPO. This means that increasing the VPO loading leads to poorer catalytic results. This can be explained on the basis of the highest surface BET area exposed by samples with less VPO loading, fact that corroborates the high dispersion of the active phase on the support. When the VPO loading in the graphite-supported samples increases, the catalytic behaviour becomes close to that of bulk VPO. This fact is in agreement with the important role of the support in the catalytic performance, increasing the surface area and the exposition of the active and selective sites for MA production. As the sole exception, even though VPO5/H exhibits the highest surface area and activity towards $n$-butane conversion, it displays the lowest selectivity and yield towards MA, facts that will be explained later.

It is important to note that the general trend of the samples concerning the catalytic performances is the same as the trend that follows the oxygen exchange experiments. Catalyst VPO15/H, which is the most active for the selective oxidation of $n$-butane under fuel-rich conditions, gives the highest slope value corresponding to the last part of the F($^{18}$O) curve. This means that the catalytic properties can be correlated to the oxygen species availability. Centi et al. [15] proposed that the catalytic transformation of $n$-butane for MA production involves two types of redox pairs: $V^{4+}$/$V^{3+}$ pair for $n$-butane activation and oxidative dehydrogenation, and $V^{5+}$/$V^{4+}$ pair for selective oxygen insertion in MA production. Following this idea the activity and selectivity in the samples will depend on the availability of these species and on the maintenance of the optimal ratios among them. This latter will be determined by the possibility of re-oxidation of the sites that is given by the surface and lattice oxygen reactivity and, consequently, mobility. High oxygen mobility in the sample allows the re-oxidation of the catalytic sites and avoids an over-reduction of the catalysts.

For all the samples both $V^{5+}$/$V^{3+}$ and $V^{4+}$/$V^{3+}$ decrease after the catalytic reaction. Even though the $V^{5+}$/$V^{4+}$ ratio is maintained constant, what indicates that the quantity of $V^{5+}$ that is being reduced is the same as that of $V^{4+}$ for a given sample, the extent of the reduction among samples is not the same and is higher for higher active phase contents. For catalysts VPO20/H and VPO30/H the catalytic sites are over-reduced to $V^{3+}$ species as it was seen by XPS, and cannot be re-oxidised due to the poor mobility of the oxygen species. As the extent of over-reduction increases, selectivity towards MA decreases, as less oxidised $V^{5+}$ and $V^{4+}$ sites are available for selective O insertion. As it was remarked before, sample VPO5/H was the less selective and gave the lowest MA yield value. Catalyst VPO5/H displays the highest extension of reduced species ($V^{4+}$/$V^{3+}$ in Table1) and the highest specific activity related to

the V ions. Moreover, this sample with high efficiency for oxygen exchange (Table 2) is not able to improve the selectivity or the yield towards MA.

The best catalytic performances under fuel-rich catalytic conditions ($O_2/C_4 = 0.6$) are obtained for VPO15/H. Although the highest initial superficial $V^{3+}$ content is observed by XPS (Table 1) for this sample, the higher reactivity of the lattice oxygen atoms avoids an over-accumulation during the reaction. The initial concentration of $V^{3+}$ species is higher for the most active catalyst, as previously reported by Cavani et al. [18]. The absence of P-$V^{3+}$ bonds by $^{31}$P NMR SEM analysis is in agreement with the results obtained by Cavani et al. [18], indicating that the anionic vacancies created by the presence of $V^{3+}$ does not alter the basic structure of the VPO phase, and that these sites may be isolated.

It can be concluded that the higher dispersion of the active phase over the graphite support leads to an improvement in the oxygen exchange properties of the supported catalysts, which finally affects the catalytic performances in the selective oxidation of $n$-butane under fuel-rich conditions.

## REFERENCES

1. E. Bordes, Catal. Today, 16 (1993) 27.
2. G. Centi, Catal. Today 16 (1993) 5.
3. S. Mota, M. Abon, J.C. Volta, and J.A. Dalmon, J. Catal, 193 (2000) 308.
4. G.J. Hutchings, A. Desmartin-Chomel, R. Olier and J.C. Volta, Catal. Nature, 368 (1994) 41.
5. V.V. Guliants, Catal. Today, 51 (1999) 255.
6. R.A. Overbeek, P.A. Warringa, M.J.D. Crombag, L.M. Visser, A.J. van Dillen, J.W. Geus, Appl. Catal. A: Gen., 135 (1996) 209.
7. R.A. Overbeek, A.R.C.J. Pekelharing, A.J. van Dillen, J.W. Geus, Appl. Catal. A: Gen., 135(2) (1996) 231.
8. A. Guerrero-Ruiz, I. Rodríguez-Ramos, P. Ferreira-Aparicio and J.C. Volta. Catal. Lett., 45 (1997) 113.
9. C. Doorkamp, M. Clement, X. Gao, G. Deo, I.E. Wachs and V. Ponec, J. Catal., 185 (1999) 415.
10. K.E. Birkeland, S.M. Babitz, G.K. Bethke, and H.H. Kung, J. Phys. Chem. B, 101 (1997) 6895.
11. M. Abon, K.E. Béré, A. Tuel, and P. Delichère, J. Catal. 156 (1995) 28.
12. A. Guerrero-Ruiz, I. Rodriguez-Ramos, P. Ferreira-Aparicio, M. Abon and J.C. Volta, Catal. Today, 32 (1996) 233.
13. P. Delichère, K.E. Béré, M. Abon, Appl. Catal. A : Gen., 172 (1998) 295.
14. D. Wang, H.H. Kung, M.A. Barteau, Appl. Catal. A: Gen., 201 (2000) 203.
15. G. Centi, G. Fornasari, and F. Trifiro, J. Catal., 89 (1984) 44.
16. P. Badenes, L. Daza, I. Rodríguez-Ramos and A. Guerrero-Ruiz, Stud. Surf. Sci. Catal., 112 (1997) 241.
17. M. Pepera, J.L. Callahan, M.J. Desmond, E.C. Milberger, P.R. Blum, N.J. Bremer, J. Am. Chem. Soc., 107 (1985) 4883.
18. F. Cavani, S. Ligi, T. Monti, F. Pierelli, F. Trifirò, S. Albonetti, G. Mazzoni, Catal. Today, 61 (2000) 203.

# The structures, catalytic properties and spillover effects of the catalysts Co-Pt(Pd, Rh)/Ce-Al-O *

M. Meng, P.-Y. Lin, Y.-L. Fu and S.-M. Yu

Department of Chemical Physics, University of Science and Technology of China, Hefei, Anhui 230026, P. R. China

The catalytic synergy effects between cobalt phases and noble metals for CO oxidation are observed in Co-Pt(Pd, Rh)/Ce-Al-O catalysts. The results of XRD, XPS, EXAFS, $H_2$-TPR and TPO-MS suggest that hydrogen spillover may occur during the reduction pretreatment, and that oxygen spillover during the reaction is also potential. Additionally, the dispersion of cobalt phases is prominently enhanced by the small amount of noble metals. The essential for the synergy effect between cobalt phases and noble metals is elucidated from cobalt valence, cobalt phase dispersion and spillover effect of hydrogen and oxygen from noble metals to cobalt phases.

## 1. INTRODUCTION

Noble metals are the main active components in three-way catalysts (TWC), which are responsible for the complete oxidation of CO and hydrocarbons (HC) and the decomposition or reduction of nitrogen oxides (NOx). Although some transition metal oxides, such as cobalt, copper and manganese, also possess high catalytic activity for the oxidation of CO, alkenes and aromatics [1], these catalysts have less specific activity than noble metals for the oxidation of HC. Meanwhile, they normally show low thermal stability and poor activity for the reduction of NOx [2]. Many studies have indicated that if a small amount of noble metals is added to some transition metal oxides, their activity can be greatly enhanced, and their dispersion and thermal stability can be improved, too [3-6]. The complex oxides $La_{0.45}Sr_{0.15}Ce_{0.35}Zr_{0.05}M_{1.0}$ (M=Cu or Co) promoted by a small amount of Pt and Rh show a three-way activity quite similar to that of a commercial three-way catalyst containing four times as much Pt-Rh [3]. It is ever reported that the temperature for the conversion of CO and $C_3H_6$ is about 100°C lower over $Pd/Co/La/Al_2O_3$ than that over $Pd/La/Al_2O_3$ [4]. We have also found the similar phenomena in Co-Pt(Pd, Rh)/$\gamma$-$Al_2O_3$ catalysts used for CO and NO removal [5]. Up to now, the essential for the synergy effect between noble metals and transition metal oxides is still unclear, and few investigations are performed on the synergism from the view of spillover effect. In the present work, we aim to elucidate the synergism between cobalt phases and noble metals in Co-Pt(Pd, Rh)/Ce-Al-O catalysts for CO oxidation and the correlation between the structures and catalytic properties from spillover effect.

## 2. EXPERIMENTAL

### 2.1. Catalyst preparation

The support $\gamma$-$Al_2O_3$ was supplied by the Third Petroleum Manufacturer of Fushun of China from a dispersible boehmite calcined at 750℃ for 16h. The $\gamma$-$Al_2O_3$ powder was pelletized, ground and sieved to 40-60 mesh particle size (BET surface area: 152 $m^2$/g). The samples were prepared by the incipient wetness impregnation method, by impregnating $\gamma$-$Al_2O_3$ to a given aqueous solution of cerium nitrate. After drying at 120℃ and calcination at 500℃ for 4h, the Ce-Al-O support was impregnated in aqueous solution of cobalt nitrate, and was dried and calcined at the same condition to obtain Co/Ce-Al-O precursor. The precursor was then impregnated in the aqueous solution of $H_2PtCl_6$·$6H_2O$, $PdCl_2$ and $RhCl_3$·$3H_2O$, respectively. The wet Co-Pt(Pd, Rh)/Ce-Al-O precursors were dried at 120℃, and calcined in air at 500℃ for 2h. Before use, all samples were reduced with pure hydrogen (30ml/min) at 450℃ for 1h. The contents of the components in the catalysts are calculated according to the equations: Co/Al=5mol.%, M/Ce-Al-O=0.1wt.% (M=Pt, Pd or Rh), $CeO_2$/$Al_2O_3$=20wt.%.

### 2.2. Evaluation of catalytic activity

The CO oxidation activity of the samples was determined in a fixed bed reactor. A given amount of the sample (200 mg, 40-60 mesh) was used each time. The gas mixture was analyzed by means of a chromatograph (model GC 102, supplied by Shanghai Analyzing Instruments Factory, China) equipped with a thermal conductivity detector (TCD). The reaction gas contains 0.50 vol.% CO, 5.0 vol.% $O_2$, and is balanced with pure nitrogen to yield a space velocity (GHSV) of 4500h$^{-1}$.

### 2.3. X-ray diffraction (XRD)

X-ray diffraction measurement was carried out on a D/MAX-RA rotatory diffractometer, using Cu K$\alpha$ as radiation source ($\lambda$ = 0.15418 nm). The data were collected under the same conditions (40 kV and 100 mA).

### 2.4. X-ray photoelectron spectroscopy (XPS)

XPS spectra were recorded on ESCA-LAB MK-II type spectrometer using Mg K$\alpha$ as radiation source (1253.6 eV). The binding energies of the elements were corrected, using C1s (284.5 eV) peak as standard.

### 2.5. Extended X-ray absorption fine structure (EXAFS)

The EXAFS data of Co K-edge and Pt L-III-edge were collected on the XAFS station, 4W1B beamline of Beijing Synchrotron Radiation Facility of National Laboratory (BSRF NL), using transition mode for Co K-edge and fluorescence mode for Pt L-III-edge. The critical beam energy was 2.2 GeV with an average storage ring current of ~50 mA. Two Si(111) single crystals were used as monochromators. The structural parameters of the samples were obtained by curve-fitting method, using $CoAl_2O_4$ or Co metal as model compound for Co K-edge and $PtO_2$ or Pt metal for Pt L-III-edge. The details of EXAFS data treatment were described elsewhere [5].

## 2.6. Temperature-programmed reduction by $H_2$ ($H_2$-TPR)

TPR experiment was carried out in a micro-reactor with a quartz tube. A given amount of the sample (100mg, 40-60 mesh) was used each time. The reduced sample was initially pretreated at 500°C in air for 1h, then cooled to room temperature and finally reduced with hydrogen (5vol.% $H_2$ in $N_2$) at a flow rate of 30ml/min. The sample was heated up to 700°C at a rate of 10°C/min. The resulting gas mixture was analyzed by a gas chromatorgraph (model SP-2305, supplied by Beijing Analyzing Instruments Factory, China) equipped with a thermal conductivity detector (TCD) with the bridge current of 100 mA.

## 2.7. Temperature-programmed oxidation-mass spectroscopy (TPO-MS)

A given amount of the sample (500mg, 40-60 mesh) was fixed in a stainless tube of the micro-reactor, and pretreated in a flow helium (99.99%) at 500°C for 1h. After cooling to room temperature, the TPO experiment was performed, using the mixture of 1.0% $O_2/N_2$ as oxidation gas (30ml/min). The sample was heated up to 600°C at a rate of 10°C/min. The peak signal of m/z=32 ($O_2$ mass number) was detected by a quadruple mass spectrometer (model LZL-203, supplied by Beijing Analyzing Instruments Factory, China).

## 3. RESULTS AND DISCUSSION

### 3.1. The activity for CO oxidation

The results of activity evaluation are shown in Fig.1. From Fig.1, it can be seen that the Co/Ce-Al-O catalyst possesses good activity for CO oxidation. At ~180°C, the conversion of CO reaches 100%. When a small amount of Pt, Pd or Rh is added to Co/Ce-Al-O, the activity is greatly enhanced, the temperature for the 100% conversion of CO is decreased by about 70°C, 60°C and 40°C, respectively. The activities of Co-Pt(Pd, Rh)/Ce-Al-O are also higher than those of Pt(Pd, Rh)/Ce-Al-O. These results reveal that there exists a pronounced catalytic synergy effect between cobalt phases and noble metals, especially between cobalt and platinum or palladium.



Fig. 1. The relationships between CO conversions and reaction temperatures over the samples

(○) Co-Pt/Ce-Al-O    (■) Co-Pd/Ce-Al-O
(□) Co-Rh/Ce-Al-O    (▲) Pt/Ce-Al-O
(△) Pd/Ce-Al-O    (✕) Rh/Ce-Al-O
(●) Co/Ce-Al-O

### 3.2. XRD

The XRD patterns of Co-Pt(Pd, Rh)/Ce-Al-O are similar to each other, so, in Fig. 2, only that of Co-Pt/Ce-Al-O is presented. From Fig. 2(a), it is known that there are two groups of diffracted peaks, which correspond to $CeO_2$ and $\gamma$-$Al_2O_3$, respectively. No platinum phase is detected because of its very low content. For sample Co/Ce-Al-O, there is another peak appearing at $2\theta=36.9°$, which may come from $Co_3O_4$ or $CoAl_2O_4$ because the strongest

diffracted peaks of $Co_3O_4$ and $CoAl_2O_4$ are at the same positions. Considered that $Co_3O_4$ is relatively easy to reduce [7-9], while $CoAl_2O_4$ is very difficult to reduce [10,11], the peak at $2\theta=36.9°$ could be assigned to $CoAl_2O_4$ or $CoAl_2O_4$-like spinel. With the addition of a small amount of platinum to Co/Ce-Al-O, the peak at $2\theta=36.9°$ disappears, implying the complete reduction of the cobalt phase. Although no peaks of metallic cobalt are detected in Fig. 2(b) and (c), its existence is possible because the reduced cobalt phase may be highly dispersed in the catalysts or its amount is below the detecting limit of XRD.
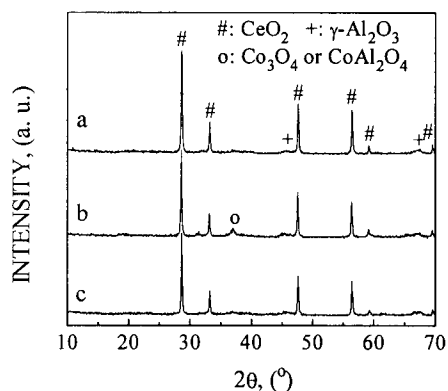
Fig. 2. The XRD patterns of the samples
(a) Pt/Ce-Al-O        (b) Co/Ce-Al-O
(c) Co-Pt/Ce-Al-O
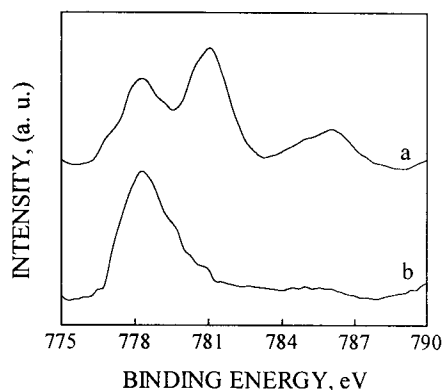
Fig. 3. XPS spectra of $Co2p_{3/2}$ of the samples
(a) Co/Ce-Al-O        (b) Co-Pt/Ce-Al-O

## 3.3. XPS

To confirm the state of the surface cobalt, the XPS spectra of $Co2p_{3/2}$ of the samples were recorded. The spectrum of $Co2p_{3/2}$ for Co/Ce-Al-O is shown in Fig. 3(a). There are two peaks at the position of low binding energy (778.3 and 781.2eV), and another weak peak at high binding energy position (786.0eV). According to references [12-14], the former could be assigned to $Co^0$ and $Co^{2+}$ in spinel, respectively, while the later weak peak is the typical satellite peak of $Co^{2+}$. Since the similarity of the $Co2p_{3/2}$ spectra of the samples containing noble metals, only the spectrum of Co-Pt/Ce-Al-O is presented in Fig. 3(b). It is obvious that there is only one peak in Fig. 3(b), which corresponds to metallic cobalt. These results means that the addition of a small amount of noble metals does enhance the reduction deepness of cobalt phase, which is in good agreement with that of XRD.

## 3.4. EXAFS

The radial structure functions (RSFs) of Co K-edge EXAFS of the samples and model compounds are presented in Fig. 4. For Co metal, there is a strong coordination peak appearing at ~0.21nm (uncorrected). Considering the phase scattering shift, this peak corresponds to the first Co-Co shell in Co metal, whose real coordination distance is 0.250nm. The RSFs of the samples promoted with a small amount of noble metals are very similar to that of Co metal, while the RSF of Co/Ce-Al-O is different from that of Co metal. There are

two peaks in the RSF of Co/Ce-Al-O, appearing at ~0.15 and ~0.27nm, respectively. The first peak can be fitted well by the first Co-O shell in $CoAl_2O_4$, while the second peak cannot be fitted by either the Co-Co shell in cobalt metal or the Co-Co shell in $CoAl_2O_4$. This peak may be contributed to both Co metal and $CoAl_2O_4$ or $CoAl_2O_4$-like spinel.

To obtain the structural parameters, curve-fitting was performed on the first shell, using Co metal and $CoAl_2O_4$ as the model compounds for Co-Pt(Pd, Rh)/Ce-Al-O and Co/Ce-Al-O, respectively. The best fitting values of the structural parameters are listed in Table 1.
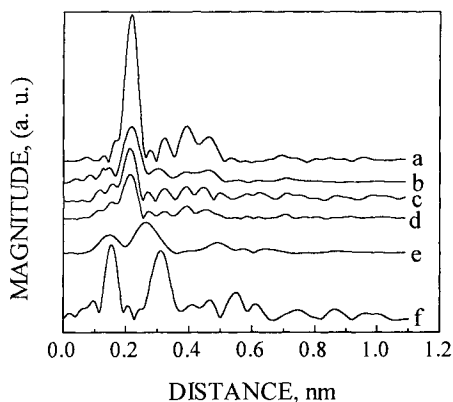


Fig. 4. The radial structure functions of Co K-edge of the samples and model compounds
(a) Co metal      (b) Co-Pt/Ce-Al-O
(c) Co-Pd/Ce-Al-O      (d) Co-Rh/Ce-Al-O
(e) Co/Ce-Al-O      (f) $CoAl_2O_4$
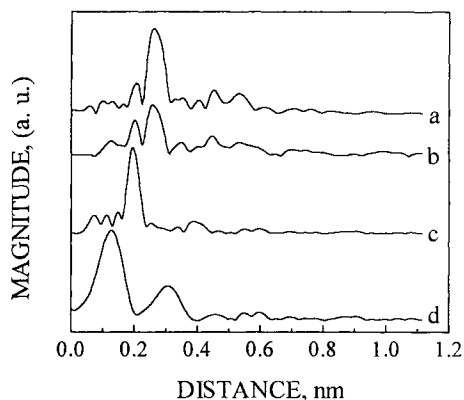
Fig. 5. The radial structure functions of Pt L-III-edge of the sample and model compounds
(a) Pt metal      (b) Co-Pt/Ce-Al-O
(c) $H_2PtCl_6 \cdot 6H_2O$      (d) $PtO_2$

Table 1
Best-fitting values of the structural parameters for the first coordination shells in the samples from Co K-edge EXAFS

| Sample | First coordination shell | | |
|---|---|---|---|
| | Shell | N | R/nm |
| Co-Pt/Ce-Al-O | Co-Co | 4.1 | 0.249 |
| Co-Pd/Ce-Al-O | Co-Co | 4.8 | 0.251 |
| Co-Rh/Ce-Al-O | Co-Co | 5.6 | 0.252 |
| Co/Ce-Al-O | Co-O | 2.6 | 0.194 |
| $CoAl_2O_4$ [*] | Co-O | 4.0 | 0.195 |
| Co metal [*] | Co-Co | 12.0 | 0.250 |

*The structural parameters of the model compounds come from Ref.[15].

From Table 1, it can be seen that the coordination distance(R) of the first shell for sample Co/Ce-Al-O is close to that of $CoAl_2O_4$, implying that there still exists some Co-O coordination. With the addition of the noble metals to Co/Ce-Al-O, the distances of the first

shells change to be almost the same as that of Co metal, indicating that the Co-O shells have completely disappeared. Combined with the results of XRD and XPS, it is deduced that the Co mainly exists as Co metal in the samples promoted with noble metals. While the Co in Co/Ce-Al-O exist as the mixture of Co metal and $CoAl_2O_4$ or $CoAl_2O_4$-like spinel. The presence of noble metals prominently enhanced the reduction of cobalt phases during the pretreatment. Additionally, the values of coordination number (N) indicate that the cobalt in the samples possesses high dispersion, the order for cobalt dispersion enhancement is Pt>Pd>Rh. This function of noble metals is a potential contribution for the catalytic synergy effect between cobalt phases and noble metals.

In order to confirm the state of the noble metals, we increased the platinum content to 1.0wt.% in Co-Pt/Ce-Al-O, and recorded the EXAFS data using fluorescence mode. The radial structure functions of Pt L-III-edge for Co-Pt/Ce-Al-O and the model compounds are shown in Fig. 5. From Fig. 5, it can be seen that the main coordination peaks of the model compounds $PtO_2$, $H_2PtCl_6 \cdot 6H_2O$ and Pt metal appear at ~0.16, ~0.21 and ~0.26nm, respectively. For Pt metal, there is another weak peak at ~0.22nm, which is resulted from the non-linearity of the phase shift function. Compared with those of model compounds, the RSF of Co-Pt/Ce-Al-O is analogous to Pt metal. However, the weak peak appearing at ~0.22nm is more obvious and the ratio of this peak to the main peak is much larger than that of Pt metal, which implies that there still exists some Pt-Cl coordination. These results indicate that most of platinum has been reduced to metal Pt, except for a small amount of platinum chloride. Similar phenomena have ever been found by Pirault et al. on Pt-Rh/$Al_2O_3$-$CeO_2$ system [16].

### 3.5. TPR results and hydrogen spillover

$H_2$-TPR characterization is a mirror to reflect $H_2$ spillover effect. In this work, the reduced samples were first reoxidized in air, then were used for TPR experiments. The TPR profiles of the reoxidized samples are shown in Fig. 6. For the support Ce-Al-O, there is a reduction peak at about 388℃. Since alumina cannot be reduced by $H_2$, this peak must correspond to the reduction of cerium species. Several studies [17-19] have ever indicated that there is a kind of oxygen species (capping oxygen) in the surface of $CeO_2$, which can be reduced below 500℃. Therefore, the peak in Fig. 6(a) is assigned to the reduction of the capping oxygen in $CeO_2$. When cobalt is supported on Ce-Al-O, there appear two reduction peaks at 351 and 467℃. According to the study by Bruce and co-workers [19], there exists strong interaction between cobalt and cerium oxides, which makes the reduction of the capping oxygen in $CeO_2$ easier. So, it is deduced that the peak at lower temperature corresponds to the reduction of the capping oxygen in $CeO_2$, while the other at higher temperature corresponds to the reduction of cobalt species. With the addition of noble metals to Co/Ce-Al-O, the two peaks shift obviously to lower temperature direction. Compared with Fig.6(b), it is found that the temperature for the first peak is decreased by 61, 76 and 94℃, and that for the second peak is also decreased by 81, 90 and 101℃ for Rh, Pd and Pt promoted sample, respectively. These results indicate that the presence of noble metals does make the reduction of cobalt and cerium species easier. Additionally, with increasing of noble metal contents, the reduction peaks shift monotonically toward the direction of lower temperature (not shown). Similar phenomena are also found by Lin et al. [3] and Van't Blik et al. [20] in other systems, where hydrogen spillover from platinum (or rhodium) to cobalt and from ruthenium to copper is proposed. It is well known that normally the hydrogen is chemically adsorbed on the noble

metal sites, and is readily dissociated into atomic species, which are very active spillover species [21]. Therefore, in our case, it is also assumed that the hydrogen first adsorbs on Pt (Pd or Rh, donor) and dissociates into atomic species. Then these active species spill over to the surrounding oxides (cobalt or cerium, acceptor) and react with them. The noble metals actually act as catalysts for the gas ($H_2$)-solid (cobalt or cerium oxides) reaction, which result in the decrease of the activation energy of this reaction. It is just reflected by the shift of the reduction peaks to lower temperatures in Fig. 6. The results of $H_2$-TPR reveal that during the sample pretreatment by $H_2$, the hydrogen spillover from noble metals to cobalt oxide may have taken place, which leads to the different reduction deepness between the samples with and without noble metals. Compared the peak area of the second peaks in Fig. 6, it is found that the amount of reducible cobalt species in Co/Ce-Al-O is less than that in the samples promoted by noble metals. Because there is some $CoAl_2O_4$ or $CoAl_2O_4$-like spinel, which cannot be reduced below 700°C. The $H_2$-TPR result is consistent with those of XPS and EXAFS. The enhancement effect of noble metals for the reduction of cobalt species may be an important source for the catalytic synergy effect between cobalt phases and noble metals.
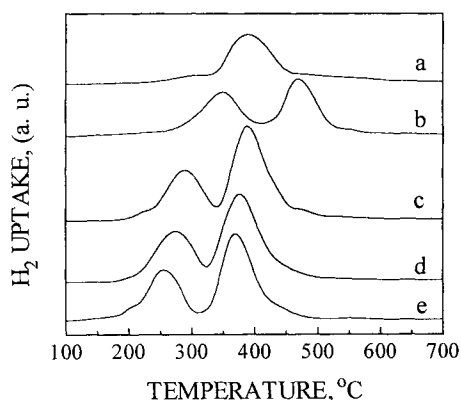


Fig. 6. The $H_2$-TPR profiles of the samples
(a) Ce-Al-O          (b) Co/Ce-Al-O
(c) Co-Rh/Ce-Al-O    (d) Co-Pd/Ce-Al-O
(e) Co-Pt/Ce-Al-O
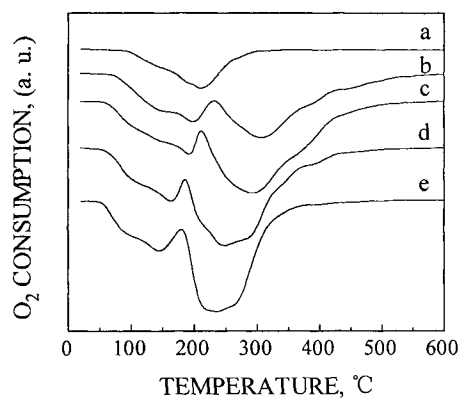
Fig. 7. The TPO-MS profiles of the samples
(a) Ce-Al-O          (b) Co/Ce-Al-O
(c) Co-Rh/Ce-Al-O    (d) Co-Pd/Ce-Al-O
(e) Co-Pt/Ce-Al-O

### 3.6. TPO-MS results and oxygen spillover

The TPO-MS profile for the support Ce-Al-O is presented in Fig. 7(a). There is a $H_2$-consumption peak at 212°C. It is well known that the cerium oxide is a non-stoichiometric compound ($CeO_x$, $1.5 < x < 2.0$). When reduced, some of the surface oxygen, such as capping oxygen, is removed, and the corresponding vacancies are generated. When exposed to the oxygen atmosphere at appropriate temperature, these vacancies can be eliminated through oxidation or storage. Therefore, the peak in Fig. 7(a) can be assigned to the oxidation of cerium species or the storage of oxygen. For Co/Ce-Al-O, there is another $H_2$-consumption peak appearing at 307°C, which may be resulted from the oxidation of cobalt species. With

394

the addition of noble metals to Co/Ce-Al-O, both the two peaks shift to lower temperature direction. The temperature for the first peak is decreased by 56, 37 and 12°C, and that for the second peak is also decreased by 65, 48 and 20°C for Pt, Pd and Rh promoted sample, respectively. With increasing of noble metal contents, the peaks shift further to lower temperatures. All these phenomena are similar to those found in $H_2$-TPR. Therefore, it is assumed that the oxygen spillover has taken place during the TPO process. The Pt, Pd or Rh acts as donor to provide active oxygen species, while the reduced phases act as acceptor to accept the spilled species and react with them. During the process of CO oxidation, it is believed that the noble metals play a key role for adsorbing, activating and providing oxygen species for cobalt phases through spillover. If the oxygen adsorption and dissociation is the rate-determining step, the oxygen spillover must lead to the decrease of the activation energy for CO oxidation and enhance the activity of Co/Ce-Al-O. The oxygen spillover during CO oxidation may be another important source for the catalytic synergy effect between cobalt phases and noble metals.

## REFERENCES

1. J.T. Kummer, Prog. Energy Combust. Sci., 6 (1980) 177.
2. P.-Y. Lin, W.-D. Chen and S.-M. Yu, Chinese J. Mole. Catal., 3 (1995) 179.
3. P.-Y. Lin, M. Skoglundh, L. Lowendahl, J.E. Otterstedt, L.Dahl, K. Jansson and M. Nygren, Appl. Catal. B, 6 (1995) 237.
4. M. Skoglundh, H. Johansson, L. Lowendahl, K. Jansson, L. Dahl and B. Hirshauer, Appl. Catal. B, 7 (1996) 299.
5. M. Meng, P.-Y. Lin, Y.-L. Fu, Catal. Lett., 48 (1997) 213.
6. Y. Chen, P.-Y. Lin and S.-M. Yu, Petrochem. Tech. (Chinese), 12 (1989) 834.
7. P. Arnoldy and J.A. Moulijn, J. Catal., 93 (1985) 38.
8. W.-J. Wang and Y.-W. Chen, Appl. Catal., 7 (1991) 223.
9. M. Meng, P.-Y. Lin and S.-M. Yu, Chinese J. Chem. Phys., 8 (1995) 66.
10. K.S. Chung and F.E. Massoth, J. Catal., 64 (1980) 320.
11. M. Meng, P.-Y. Lin and S.-M. Yu, Chinese J. Chem. Phys., 8 (1995) 176.
12. C.D. Wagner, W.M. Riggs, L.E. Davis, J.F. Moulder and G.E. Muilenberg (eds.), Handbook of X-ray photoelectron spectroscopy, Perkin-Elmer Corp., Physical Electronics Division, USA, 1979.
13. Y. Okamoto, T. Imanaka and S. Teranishi, J. Catal., 65 (1980) 448.
14. Y. Okamoto, T. Adachi, K. Nagata, M. Odawara and T. Imanaka, Appl. Catal., 73 (1991) 249.
15. G. Sankar, S. Vasudevan, C.N.R. Rao, J. Phys. Chem., 91 (1987) 2011.
16. L. Pirault, M. Guerin, F. Maire, P. Marecot and J. Barbier, Appl. Catal. A, 172(1998)249.
17. H.C. Yao and Y.F. Yu Yao, J. Catal., 86 (1984) 254.
18. A. Laachir, V. Perrichon, A. Badri, J. Lamotte, E. Catherine, J.C. Lavalley, J. El. Fallah, L. Hilaire, F.le Normand, E. Quemere, G.N. Sanvion and O. Touret, J. Chem. Soc. Faraday Trans., 87 (1991) 1601.
19. L.A. Bruce, M. Hoang, A.E. Hughes and T.W. Turney, Appl. Catal. A, 100 (1993) 51.
20. H.F.J. van't Blik, D.C. Koningsberger and R. Prins, J. Catal., 97 (1986) 210.
21. B. Delmon, Catal. Rev.-Sci. Eng., 1 (1996) 69.

# Effects of Ceria on Propane Reforming over Alumina Supported Palladium Catalysts

A.L. Guimarães , L.C. Dieguez and M. Schmal*

NUCAT-PEQ-COPPE, Universidade Federal do Rio de Janeiro, Ilha do Fundão, C.P. 68502, CEP 21941-970, Rio de Janeiro (Brazil) – *Schmal@peq.coppe.ufrj.br

Propane oxidation was investigated over $Pd/Al_2O_3$ and $Pd/CeO_2/Al_2O_3$ catalysts. In fuel rich conditions, the results pointed us two discrete domains of reaction: oxidation in low temperatures (< 20% of propane conversion) and steam reforming of propane after oxygen has totally disappeared. In regard to $Pd/CeO_2/Al_2O_3$, the selective steam reforming reaction has showed the strong attendance of ceria. Large quantities of hydrogen have been evidenced where specific reactions were unchained. Our results also exhibited the influence of initial state of palladium on these reactions. Oxidative atmospheres inhibited propane oxidation besides increasing steam reforming temperatures. Moreover, these results showed a great ratio $Pd^0/PdO$, which maximizes catalytic activity for hydrocarbon oxidation.

## 1. INTRODUCTION

Intensive research aiming to reduce air pollution caused by automotive exhaust gases has been performed in the last years. The catalytic oxidation of hydrocarbons has been investigated deeply in connection with a number of practical applications such as hydrocarbon detection in enclosed environments, odor control, volatile organic compounds, industrial boilers, gas turbines and fuel cells. It has shown early on that noble metals, platinum and palladium in particular, are the most active for promoting oxidation reactions. Therefore, a large effort has been focused on studying catalysts based on these elements [1]. Since exhaust gases contain normally 10 to 12% of steam, several authors have pointed kinetic inhibition by water. However, specific conditions of reaction may lead these systems to high catalytic activity [2].

Ceria is one of major components in current "three-way" catalysis. Its major roles are the stabilization of the active metal and the alumina support, the promotion of the water gas shift reaction and the enhancement of oxygen store capacity, thus enlarging the air fuel window [3]. The oxygen surface migration is quite important in oxidation reactions since the catalysts are submitted to reduction-oxidation cycles. Moreover, the metal-oxide combination may affect

strongly the oxygen mobility by chemical metal support interaction [4]. However, the role of rare earth oxides in steam reforming catalysis needs to be explored in greater depth.

The aim of this work is to study the effects of $CeO_2$ in catalytic steam reforming of propane as well as in its oxidation. In a specific way, the propane oxidation over $Pd/Al_2O_3$ and $Pd/CeO_2/Al_2O_3$ systems was studied varying the stoichiometric ratio of reaction from rich to lean mixtures. The effects of water attendance into inlet gas composition and the initial pretreatment atmosphere (oxidizing or reducing) were also performed.

## 2. EXPERIMENTAL

### 2.1. Catalyst preparation

The catalysts with 1 wt. % Pd were obtained by impregnation on $\gamma$ - $Al_2O_3$ (208 $m^2/g$) or $CeO_2/Al_2O_3$ (193 $m^2/g$) supports. $CeO_2/Al_2O_3$ system was prepared by the anchoring reaction between a cerium acetilacetonate precursor and alumina surface hydroxyl groups (18 to 20 wt. % $CeO_2$).

The precursor salts employed were $PdCl_2$ and $Pd(acac)_2$. $Pd/Al_2O_3$ and $Pd/CeO_2/Al_2O_3$ samples were prepared by incipient-wetness impregnation of $Al_2O_3$ and $CeO_2/Al_2O_3$, respectively. Hydrochloric acid solution was used to dissolve $PdCl_2$, meanwhile toluene to dissolve $Pd(acac)_2$. After impregnation, the samples were dried at 393 K, for 18 h, followed by calcination under air flow at 773 K for 4 h. Pd-X or PdCe-X (X = Cl or acac) was used to refer to $Pd/Al_2O_3$ or $Pd/CeO_2/Al_2O_3$ catalysts prepared by chlorine or acetylacetonate precursor.

### 2.2. Catalytic reaction – Oxidation and steam reforming of propane

$Pd/Al_2O_3$ and $Pd/CeO_2/Al_2O_3$ systems were pre-treated before reaction. $Pd/Al_2O_3$ samples were dried at 423 K for 30 min under He flow. $Pd/CeO_2/Al_2O_3$ catalysts were treated under flow of a mixture 5% $O_2/He$ at 673 K for 60 min, followed by flowing He at 773 K for 90 min. Then, the samples were reduced by $H_2$ or oxidized by a mixture 5% $O_2/He$ at 773 K for 1 h, followed by flowing He also at 773 K for 1 h and finally cooled down to reaction temperature.

The oxidation of propane was performed in a flow microreactor at atmospheric pressure. The catalyst bed was composed of 25 mg of fresh catalyst diluted in 250 mg of quartz. Catalysts were evaluated by studying their relative activity with a constant flow rate of the gas mixture, set at 150 $cm^3/min$, from 298 to 823 K at a heating rate of 20 K/min. Different reactions were investigated in this work - oxidation, steam reforming (SR) and steam reforming of propane in the presence of water into reaction mixture (SRO) – by varying the stoichiometric ratios of reaction (R and S) from rich to lean mixtures. R and S were defined as the ratio between the concentration of $O_2$ or water in the feed and the concentration of propane, respectively. The analyses of the reactor effluent were

performed by an online Quadrupole Mass Spectrometer (BALZERS QMS 420).
Table 1 shows the inlet gas concentrations of the reactants employed for the
different reactions.

Table 1
Reaction conditions and inlet gas concentrations.

| Reaction | Stoichiometric | | Feed composition ( vol - %) | | | |
|---|---|---|---|---|---|---|
| | R [1] | S [2] | $C_3H_8$ | $O_2$ | He | $H_2O$ |
| Oxidation | 10.0 | - | 0.30 | 3.00 | 96.70 | - |
| Oxidation | 5.0 | - | 0.50 | 2.50 | 97.00 | - |
| Oxidation | 2.5 | - | 0.70 | 1.70 | 97.60 | - |
| SR | - | 3.0 | 1.00 | - | 96.00 | 3.00 |
| SRO | 2.5 | 3.0 | 0.65 | 1.55 | 95.80 | 2.00 |

[1] $R=[O_2]/[C_3H_8]$    [2] $S=[H_2O]/[C_3H_8]$

## 3. RESULTS

### 3.1. Total propane combustion (reduced samples)
The propane oxidation reaction was performed under  some specific
conditions.
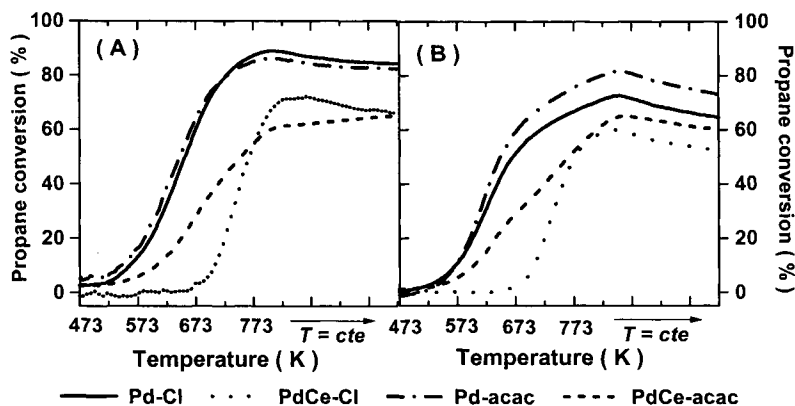


**Figure 1.** Effects of $O_2/C_3H_8$ ratio on total combustion of propane for reduced
samples. (A) R=10 and (B) R=5.0.

Figure 1 shows the "light-off" profiles for the total propane oxidation (R=5
and R=10) for different samples. These results are quite similar to general

behavior of the catalytic hydrocarbon combustion under lean conditions where the activity is very low for temperatures smaller than the activation temperature. When this temperature is reached the reaction rate raises exponentially. As shown in Figure 1, the Pd-Cl and Pd-acac samples exhibited similar performance, independently of the oxygen concentration in the reaction mixture. However, a strong inhibition was observed in the presence of cerium. The activity was always lower than the respective homologous without cerium.

## 3.2. Propane oxidation under reduction conditions without steam (reduced samples)

Figure 2 presents the results for the propane oxidation under reduction conditions (R=2.5). The catalysts Pd-Cl and Pd-acac show behaviors quite alike all along the temperature gap. In the beginning low conversions were observed up to 600 K (20% conversion of propane). From this point on, the conversion increased quickly up to 50 %, decreasing then at high temperatures.
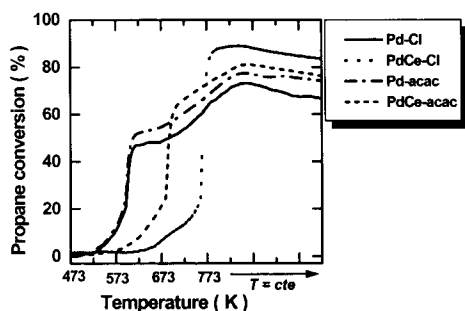
**Figure 2.** Propane oxidation profiles for R=2.5 without water into reaction mixture (reduced samples).
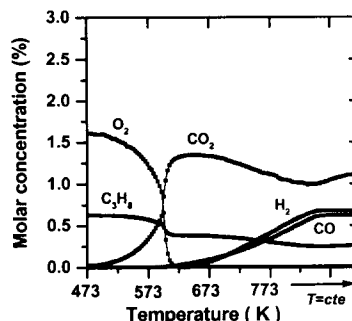
**Figure 3.** Reactant and product yields in propane oxidation for R=2.5 on Pd/Al$_2$O$_3$ catalyst.

With regard to PdCe-Cl and PdCe-acac catalysts, a strong inhibition was observed. Nevertheless, when the propane conversion was close to 20%, the activity increased continuously, overcoming significantly the activity of the catalysts without cerium.

The reactants and products yields involved in the oxidation of propane with excess of hydrocarbon are shown in Figure 3. These results agreed with Maillet et al [2] and Barbier et al [5], indicating that the light-off profiles brought out on two domains of reactions; the first one at low temperatures, corresponds to the oxidation reaction (1) and the second, when oxygen was totally consumed, corresponds to the steam reforming reactions (2 and 3) of water (produced by oxidation) with residual propane.

$$C_3H_8 \;+\; 5\,O_2 \;\rightarrow\; 3\,CO_2 \;+\; 4\,H_2O \qquad\qquad (1)$$

$$C_3H_8 \;+\; 3\,H_2O \;\rightarrow\; 3\,CO \;+\; 7\,H_2 \qquad\qquad (2)$$

$$C_3H_8 \;+\; 6\,H_2O \;\rightarrow\; 3\,CO_2 \;+\; 10\,H_2 \qquad\qquad (3)$$
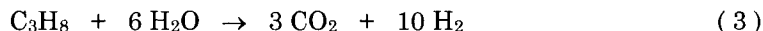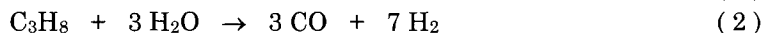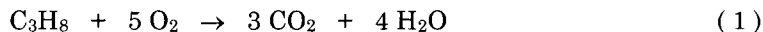
Indeed, these results demonstrate the occurrence of three simultaneous reactions in the catalyst bed – the total combustion of propane for low conversions (until 20%) and the steam reforming of propane at high temperature zone, when oxygen was totally consumed, that means they are closely depended on the oxygen concentration during reaction pathway.

### 3.3. Propane oxidation under reduction conditions with steam (SRO – reduced samples)

The influence of water was investigated on the propane oxidation under reduction conditions (R=2.5 and S=3.0). For this purpose, 2% steam was added into the inlet gas composition. Figure 4 shows a slight inhibition in the oxidation and an increase in the reforming temperature on the $Pd/Al_2O_3$ system (about 20 to 30 % of propane conversion – $T_{20-30\%}$). Pd-Cl and Pd-acac samples exhibited a shift toward higher temperatures, 60 and 35 K, respectively, when steam was introduced into reaction mixture.
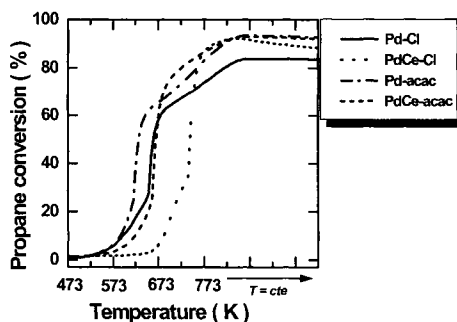


**Figure 4.** Propane oxidation profiles for R=2.5 in attendance of steam into reaction mixture (reduced samples).
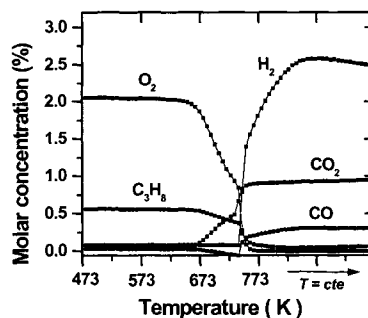
**Figure 5.** Reactant and product yields in propane oxidation for R=2.5 and S=3.0 on $Pd/CeO_2/Al_2O_3$ catalyst.

However, in the presence of cerium an opposite effect occurred. The reforming temperatures were shifted toward lower temperatures, around 20 K for PdCe-Cl and PdCe-acac catalysts. Noteworthy is also the great amount of hydrogen production, as shown in Figure 5.

Moreover, Table 2 presents the simultaneous influence of steam and cerium oxide addition for the SRO reaction and compared to the oxidation it reached higher conversion levels. These results suggest that from the point of

view of water it inhibits the propane combustion, but on the other side, it promotes the steam reforming reactions of the different systems.

Table 2
Influence of steam addition and ceria on propane reforming.

| Catalyst | Reforming Temperature ( K ) | | | Highest propane conversion (%) | | |
|---|---|---|---|---|---|---|
| | Oxidation[1] | SRO | SR | Oxidation[1] | SRO | SR |
| Pd-Cl | 593 | 653 | 603 | 70 | 84 | 32 |
| Pd-acac | 593 | 618 | 643 | 75 | 93 | 33 |
| PdCe-Cl | 758 | 738 | 593 | 89 | 92 | 50 |
| PdCe-acac | 683 | 660 | 588 | 80 | 93 | 57 |

[1] Propane oxidation under reduction conditions without steam  (R=2.5, S=0).

### 3.4. The selective propane steam reforming (SR - reduced samples)

The catalyst activity for the selective steam reforming of propane (R=0 and S=3.0) was also investigated and the results are presented in Figure 6.

These results showed low activity on $Pd/Al_2O_3$ system, as long as low conversion levels until 823 K. However, in the presence of cerium, the performance was much better, overcoming in almost 90 % that of $Pd/Al_2O_3$ system (Table 2).
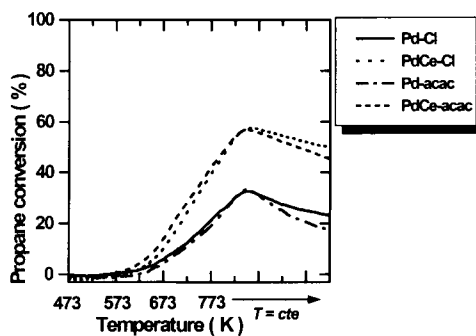


**Figure 6.** Steam reforming of propane (R=0 and S=3) for reduced samples.
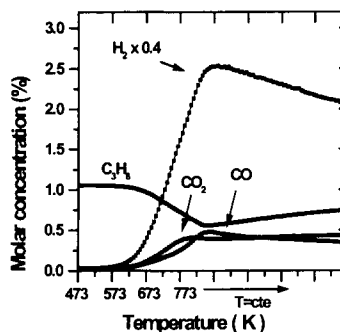
**Figure 7.** Reactant and product yields in steam reforming of propane on $Pd/CeO_2/Al_2O_3$ catalyst.

Figure 7 shows the reactant and product yields in steam reforming of propane on $Pd/CeO_2/Al_2O_3$ systems. The $Pd/Al_2O_3$ system showed just CO and $H_2$ production for specific experimental conditions (Table 1 and reaction 2). Meanwhile, $CO_2$ production was observed besides CO and a large amount of $H_2$ on

the Pd/CeO₂/Al₂O₃ system. High H₂/products ratio was obtained, probably due to the back spillover effect at the interface of the Ce/Pd sites.

### 3.5. The influence of pretreatment in propane oxidation under reduction conditions

Besides the influence of pretreatment conditions (oxidation or reduction) in the catalysts behaviors was investigated. The influence of the initial oxidation state of palladium sites on catalyst performance was evaluated. Figure 8 shows these results with and without water into inlet composition. The oxidative pretreatment pointed out a strong inhibition of the Pd/Al₂O₃ system for propane combustion at low temperatures. The steam reforming temperature was almost 100 K greater for Pd-Cl in the absence of water in the reaction mixture. However, a less sensitive effect was observed in the presence of ceria, independently of water addition in the reaction mixture.
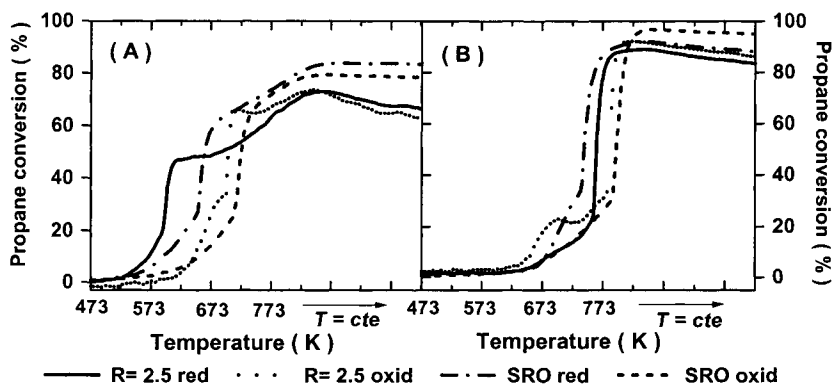


**Figure 8.** Influence of pretreatment atmosphere in propane oxidation under fuel rich conditions (R=2.5). (A) Pd-Cl, (B) PdCe-Cl. Red and oxide refer to reduced and oxidized samples, respectively.

## 4. DISCUSSION

### 4.1. The influence of steam on oxidation and selective reforming of propane

The propane oxidation profiles under fuel rich conditions (R=2.5) pointed out two discrete domains of reaction, according to reactions 1, 2 and 3. Maillet et al [2,6] investigated the performance of metal supported alumina catalysts for oxidation and steam reforming of light hydrocarbons. The authors also observed two regions of reaction: oxidation at low temperatures (T < 350 °C) and steam reforming above this temperature (T > 350°C). Besides, an apparent deactivation

was evidenced by the reduction of palladium oxide ($PdO_x$) to metallic palladium ($Pd^0$) during the reaction path. These results were confirmed later by XRD analysis [6]. However, steam in the reaction mixture avoided this phenomenon in spite of inhibiting oxidation.

Barbier and Duprez [5] corroborated these results, where $H_2$ and CO production were observed just on the steam reforming region, after wasting $O_2$ totally. Rhodium catalysts showed great performance for SR. Indeed, the bimetallic combination Pd-Rh presented results even so acceptable.

The influence of water on catalytic combustion of hydrocarbons has been reported by several authors [7] since automotive emissions brought out 10 to 12% of water. These investigations disclosed the stamped influence of water by inhibiting the kinetics of reaction in fuel lean conditions. Nevertheless, specific outcomes were observed in reduction conditions, guiding different catalytic systems to high activities.

The same results were observed by Bart et al [8], showing that water introduces two opposite effects: if for instance it inhibits hydrocarbon combustion, on the other side, raises its conversion by promotion of the steam reforming reactions.

Our results are in good agreement with these reports. TPSR results presented steam reforming reactions at high temperatures, from 20% of conversion of propane on. The oxidation inhibition by ceria and water were also evidenced. However, both effects increased the activities as much as the steam reforming favored temperature decrease.

## 4.2. The role of ceria on selective steam reforming of propane – the hydrogen production

The behavior of $Pd/CeO_2/Al_2O_3$ systems in relation to hydrocarbon oxidation has been very little reported in the last few years. H.S. So et al [9] investigated the promoting effects of ceria on "three-way" catalysis by DRX, TPR and oxygen store capacity measurements. Excellent performance and high thermal stability was observed for ceria mixture aged at 1000°C.

C.H. Lee et al [10] have shown great activities of $Pd/Al_2O_3$ catalysts promoted by $CeO_2$ and $K_2O$ for CO conversion in the presence of water. Basicity growth was evidenced when these promoters were added to the catalyst composition. On the other hand, no influence was observed on unpromoted samples exposed to low contents of water.

The oxygen storage properties of noble metals (Pd, Pt and Rh) supported on ceria have been investigated for water gas shift reaction [3]. These authors demonstrated a strong dependence of ceria structure in the CO conversion. Therefore, one may suggest that a $Ce_2O_3$ oxidation by water would conduct to a cyclic mechanism, especially under fuel rich conditions, where new reactions would be unchained. Water would be mainly adsorbed on reduced cerium species.

Therefore, this process would be responsible for cerium oxidation and can also promote hydrocarbon conversion into CO and $H_2$, besides the conventional steam reforming reactions. The symbol * represents an active site of palladium:

$$Ce_2O_3 \; + \; H_2O \; \rightarrow \; 2\, CeO_2 \; + \; H_2 \tag{4}$$

$$C_3H_8 \text{-} * \; + \; 6\, CeO_2 \; \rightarrow \; 3\, CO \; + \; 3\, Ce_2O_3 \; + \; * \; + \; 4\, H_2 \tag{5}$$

$$CO \text{-} * \; + \; 2\, CeO_2 \; \rightarrow \; CO_2 \; + \; Ce_2O_3 \; + \; * \tag{6}$$
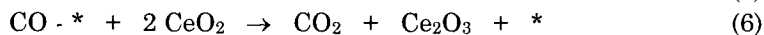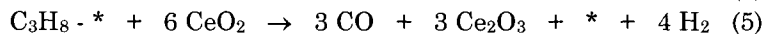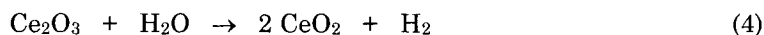
Our results showed that the molar ratios $H_2/CO$ and $H_2/CO_2$ presented very unlike relation to that required for steam reforming reactions. The first one was strongly higher and the second slightly lower. Therefore, it supports the proposed sequence of reactions in this work in this investigated system. According to some authors [5,8], still the "shift" reaction ($CO + H_2O \rightarrow CO_2 + H_2$) on $Pd/CeO_2/Al_2O_3$ would not be discarded in this system during the selective steam reforming of propane.

## 4.3. The influence of initial oxidation state of palladium

Figure 8 shows the influence of pretreatment atmosphere on propane oxidation under fuel rich conditions. These results evidenced that high oxygen contents into catalysts structure would be responsible for the significant increase in the steam reforming temperature ($T_{20\text{-}30\,\%}$) for the Pd-Cl and Pd-acac catalysts. Actually, these results pointed out a great $Pd^0/PdO$ ratio with a sensitive steam reforming inhibition in the pre-oxidized samples.

Yazawa et al [11] obtained quite similar results. The oxidation state of palladium on $SiO_2 - Al_2O_3$ during propane combustion was examined by XPS and XRD measurements. Beyond observing strong dependence of propane conversion with stoichiometric ratio $O_2/C_3H_8$, the oxidation state of palladium was strongly affected in their results. Partially oxidized palladium with an optimum ratio $Pd^0/PdO$, showed the best catalytic activity for combustion of light hydrocarbons. Groppi et al [12] used termogravimetric techniques in order to corroborate these results, ratifying the reversible transformation $Pd^0 - PdO$ during $CH_4$ combustion. Indeed, ceria shifted the temperatures of reduction of PdO and reoxidation of $Pd^0$ in almost 60 K above the corresponding temperatures observed on unpromoted samples.

Concerning the PdCe-Cl and PdCe-acac, the influence of pre-treatment atmosphere was less attempted, where low $T_{20\text{-}30\%}$ differences were observed.

Therefore, submitting $Pd/CeO_2/Al_2O_3$ system to oxidative pretreatment, besides oxidation inhibition, less sensitive steam reforming temperatures differences were noticed. In accordance with the literature [13-15], ceria would be capable of storing oxygen in its crystalline structure. As a matter of fact, ceria would contribute for diminishing active sites of palladium attendance, available for propane adsorption, as well as oxidizing propane under reducing conditions.

Considering that this is the rate determining step in the propane oxidation by $O_2$ [16], strong inhibition was evidenced as shown in Figure 8.

## 5. CONCLUSIONS

TPSR results showed markedly influences of the reaction conditions employed (R and S), water addition into reaction mixture, on the initial oxidation state of palladium and the promoting effects of cerium on propane steam reforming. The cerium attendance conducted the catalysts to a cyclic mechanism of reaction, evidenced by very unlike $H_2/CO$ and $H_2/CO_2$ ratios, in relation to that required for steam reforming reactions. That was probably attributed due to a back spillover effect on Ce/Pd sites. Therefore, these results demonstrated the essential effects of these parameters on post-combustion catalyst performance.

## REFERENCES

1.  M. Aryafar and F. Zaera, Catal. Lett., 48 (1997) 173.
2.  T. Maillet, J. Barbier and D. Duprez, Appl. Catal. B: Environ., 9 (1996) 251.
3.  T. Bunluesin, R.J. Gorte and G.W. Graham, Appl. Catal. B: Environ., 15 (1998) 107.
4.  G.P. Ansell, S.E. Golunski, H.A. Hatcher and R.R. Rajaram, Catal. Lett., 11 (1991) 183.
5.  J. Barbier and D. Duprez, Appl. Cat. A : Gen., 85(1992) 89.
6.  T. Maillet, C. Solleau, J. Barbier and D. Duprez, Appl. Cat. B: Environ., 14 (1997) 85.
7.  M.F. Luo, Z.Y. Hou, X.X. Yuan and X.M. Zheng, Catal. Lett., 50 (1998) 205.
8.  J.M. Bart, A. Pantenero and M. Prigent, Catalytic Control of Air Pollution, 495 (1992) 42.
9.  H.S. So, O.B. Yang, D.H. Kin and S.I. Woo, Stud. Surf. Sci. Catal., 130 (2000) 1379.
10. C.H. Lee and Y.W. Chen, Appl. Catal. B : Environ., 17 (1998) 279.
11. Y. Yazawa, H. Yoshida, N. Takagi, S. Komai, A. Satsuma and T. Hattori, Appl. Catal. B: Environ., 19 (1998) 261.
12. G. Groppi, C. Cristiani, L. Lietti, C. Ramella and Pio Forzatti, Catal. Today, 50 (1999) 399.
13. J. Kaspar, P. Fornasiero and M. Graziani, Catal. Today, 50 (1999) 285.
14. R.W. Mc Cabe, H.W. Jen, W. Chun, G.W. Grahan, L.P. Haack, A. Straccia and D. Benson, Appl. Catal. A : Gen., 184 (1999) 265.
15. M. Ozawa and C.K. Loong, Catal. Today, 50 (1999) 329.
16. R. Burch and T.C. Watling, J. Catal., 169 (1997) 45.

# Effect of ceria additive loading on Ni/SiO$_2$ catalysts for carbon dioxide reforming of methane

K.Kouachi[a] , S.Menad[b] , S.Tazkrit[b] and O.Cherifi[a]

[a]Laboratoire de Chimie du Gaz Naturel , Institut de Chimie,
USTHB BP32 , El Alia , Bab-Ezzouar , ALGER , ALGERIA

[b]Département de Chimie , Faculté des Sciences ,
Université Mouloud Mammeri , Tizi-Ouzou, ALGERIA

## ABSTRACT

The addition of CeO$_2$ to nickel catalyst dispersed on silica is found to improve the catalyst activity and carbon suppression in the carbon dioxide reforming of methane to syngas.
A weight loading of 5% Ce enhances greatly the catalytic activity suggesting that catalysis of Ni -CeO$_2$(5%)/SiO$_2$ is mainly connected with the surface of CeO$_2$ .
The study of Ni -CeO$_2$(5%)/SiO$_2$ catalyst aging reveals its ability of maintaining very low level of carbon depositing. The regeneration of the same catalyst suggests that its stability and its less coking are attributed to the oxygen storage capacity of CeO$_2$.

## 1. INTRODUCTION

There is a growing interest in the process of carbon dioxide reforming of methane to synthesis gas with a low ratio (1:1) that is desirable for F-T synthesis of olefins and oxo-synthesis of oxygenates [1,2]. Several studies have focused on developing Ni and Noble metals catalysts for methane reforming reaction. Although noble metals prove to be efficient catalysts for this reaction [3-6], nickel based catalyst seem more desirable due to their availability and their cost [7-10].
Many papers have been devoted to the study of Ni on several supports like SiO$_2$ [11-14] , Al$_2$O$_3$[13-15], MgO[11,12], TiO$_2$ [16-17], ZrO$_2$ [11,14,18] and activated carbon [12]. The main obstacles for practical nickel catalyst are the deactivation by carbon deposition, metal sintering or the phase transformation, such as the formation of NiAl$_2$O$_4$ in the case of Ni / $\gamma$-Al$_2$O$_3$ Catalyst [19].
The addition of metal additives could be a relatively simple and effective method to suppress carbon deposition and to improve the performance of catalysts .
As a matter of fact the addition of Mo or W to Ni (2 wt%) / Al$_2$O$_3$ catalysts revealed diminution of coking for Ni/Mo-Al$_2$O$_3$ and a total suppression of carbon deposition for Ni/W-Al$_2$O$_3$ catalysts [20]. In other respects Wang et al. [21] reported that a CeO$_2$ promoted Ni/Al$_2$O catalyst exhibited higher coking resistance than the unpromoted one and higher activity than

Ni/CeO$_2$ catalyst. Zamar et al. [22] have recently reported that mixed oxides of composition 80%CeO$_3$-20%MO$_2$ (with M=Zr or Hf) behave as efficient and stable catalysts for the total oxidation of CH$_4$.

In this paper, we report the results of investigation about the role of CeO$_2$ additive, the effect of its load and the aging/regeneration of Ni / CeO$_2$(5%)/ SiO$_2$ catalyst.

## 2. EXPERIMENTAL

### 2.1. Catalysts preparation and characterization

Silica supported nickel catalyst with Ni loading of 4.5 wt% was prepared by impregnating silica (Fluca, 208,36 m$^2$.g$^{-1}$) with Ni (NO$_3$)$_2$·6H$_2$O(Merk) using an incipient wetness technique . After impregnation this catalyst was dried overnight at 383K then calcined in air at 973K during 6h with heating rate 4 Kmn$^{-1}$. The Ni(4.5%)-Ce(x%)/SiO$_2$ catalysts were elaborated by wetness impregnation of Ni(4.5)/SiO$_2$ catalyst using Ce (NO$_3$)$_3$-6H$_2$O 5merk) salt solution and following the same procedure described above .

Structural characterization of catalysts was performed by powder X-ray diffraction (XRD) technique on a Philips Pw 1710 diffractometer using filtered CuKd radiation . Pattern were recorded from 0° to 80°(2θ) at 30mA and 40KV.

In order to determine the metal loading of our catalysts a spectrometer Perkin-Elmer 1100B was used.

The specific areas of prepared catalysts were obtained using a BET apparatus (Coultronics, Accusorb 2100E). Prior to adsorption the samples were outgassed for 12h under vaccum at 473K Scanning electron microscopy (SEM) performed with a Philips SEM 505 system was used to investigate the surface morphology of catalysts and to determine the catalyst grain size.

Hydrogen chemisorption was performed at 873K for all catalysts in order to estimate metal dispersion and particle size via application of the isotherm method.

### 2.2. Catalytic testing

Catalysts were tested in a fixed bed quartz tubular reactor at atmospheric pressure and 873K under hydrogen (1.2 $l$.h$^{-1}$), temperature rise rate 4K mn$^{-1}$ using a sample of 0.1g; particle size < 160 μm. The ratio CO$_2$/CH$_4$ = 4/1 of the feed was chosen with a total flow rate of 1.3 $l$.h$^{-1}$.

The reactants (air liquid) and products we analyzed on line using TCD gas chromatograph (Delsi; IGC 121 Ml) equipped with two 4 m carbosieve B columns.

The products formed are CO, H$_2$, H$_2$O and carbon balance has shown that coke was deposited.

Prior to analyze, the effluent was passed through water-trap at 273 K in order to condense H$_2$O. H$_2$ concentration was not analyzed.

The conversions of CH$_4$(%) and CO$_2$(%) are expressed as the ratio of mols converted divided by the number of mols in the feed .

## 2.3. Aging and regeneration of Ni–Ce(5%)/SiO₂ catalyst.

Aging regeneration experiments were realized in the same conditions as described above and the temperature heating was as following.
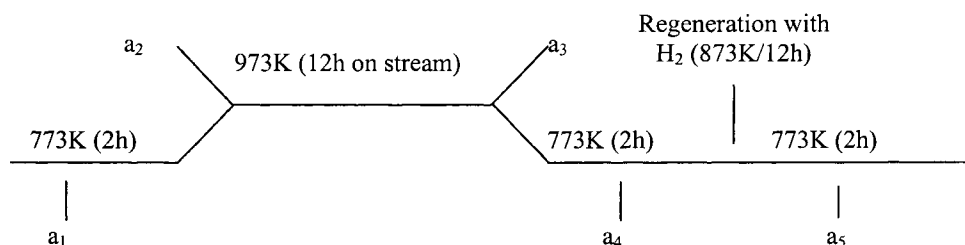


$a_1$, $a_2$, $a_3$, $a_4$ and $a_5$ represent the successive steady-state activities at 773K, 973K (after heating ), 973K (after 12h on stream), 773K after cooking and 773K after regeneration with $H_2$.

## 3. RESULTS AND DISCUSSION

### 3.1. Characterization

A summary of the weight loading of catalysts, BET areas and XRD spectra for each catalyst is provided in Table 1.

Table 1
Nickel and ceria loading , BET areas and XRD spectra for prepared nickel based catalysts

| Catalysts | Ni (wt%) | Ce (wt%) | BET area ($m^2g^{-1}$) | XRD phases |
|---|---|---|---|---|
| Ni/SiO₂ | 4.5 | 0 | 194 | Ni,SiO₂ |
| Ni-Ce(1%)/ SiO₂ | 4.5 | 0.8 | 189 | Ni,SiO₂ |
| Ni-Ce(2%)/ SiO₂ | 4.3 | 1.2 | 160 | Ni, CeO₂, SiO₂ |
| Ni-Ce(3%)/ SiO₂ | 4.0 | 2.4 | 155 | Ni, CeO₂, SiO₂ |
| Ni-Ce(4%)/ SiO₂ | 4.6 | 3.1 | 134 | Ni, CeO₂, SiO₂ |
| Ni-Ce(5%)/ SiO₂ | 4.6 | 5.5 | 166 | Ni,CeO₂, SiO₂ |

In general the agreement between nominal and analyzed metal loading is good. The surface area of Ni/SiO₂ catalyst decrease with the addition of CeO₂ however in comparison with other percentages higher CeO₂ loading (5wt%) increases sensibly the surface area .

A summary of the metal dispersion and particle size determined for each catalyst is provided in Table 2 . Dispersions calculated from hydrogen uptake indicate a low degree of nickel dispersion for all of the catalysts . The particles sizes determined by SEM are the size of ( metal + support ).

These values are remarkably higher than that obtained by $H_2$ chemisorption which estimates the nickel particles size. It seems that Ni-Ce(x%)/SiO₂ catalysts have a relatively bigger nickel particle sizes than that in Ni/SiO₂. Except for Ni-Ce(3wt%)/SiO₂, higher CeO₂ content result in big nickel particle size .

Table 2
Nickel dispersion and particle size for prepared Ni based catalysts.

| Catalysts | Dispersion(%) | d(nm) $H_2$ | d(μm) SEM |
|---|---|---|---|
| Ni/SiO₂ | 2.4 | 42.3 | 61.1 |
| Ni-Ce(1%)/ SiO₂ | 2.3 | 45.1 | - |
| Ni-Ce(2%)/ SiO₂ | 2.3 | 45.2 | - |
| Ni-Ce(3%)/ SiO₂ | 2.3 | 43.8 | 80.6 |
| Ni-Ce(4%)/ SiO₂ | 1.9 | 51.6 | 74.4 |
| Ni-Ce(5%)/ SiO₂ | 1.7 | 60.2 | 90.6 |

## 3.2. Catalytic performances

The carbon dioxide reforming of methane was carried out on a series of Ni(4.5 wt%)-Ce/SiO₂ catalysts with Ce loading of 0-5 wt% at 873K under atmospheric pressure. Figure1 presents the variation of $CO_2$ and $CH_4$ conversions with Ce content.

For the Ni(4.5 wt%)/SiO₂ catalyst, we observe a good activity ($CH_4$ conversion 46.7%) and (CO yield $16.20.10^{-2}$ mol·h⁻¹·g⁻¹) and a moderate deactivation by coking (carbon balance 78.3 ). This result agrees with those reported by Kroll et al. [23]. We can see also that cerium has a promoting effect on the nickel phase. The carbon monoxide yield increases from $16.20.10^{-2}$ mol·h⁻¹·g⁻¹ for the unpromoted catalyst to $17.9.10^{-2}$ mol·h⁻¹·g⁻¹ for the 1wt% Ce promoted catalyst.

The loading raising to 5wt% enhances greatly the catalytic activity. No carbon was formed over this latter (carbon balance 100%). This resistance to coking can be explained by the presence of sufficient amount of CeO₂ which suppress instantaneously the carbon formed from either carbon monoxide disproportionation (eq.1) or methane decomposition (eq.2).

$$2CO \;+\; * \;\rightleftarrows\; CO_2 \;+\; C* \qquad\qquad (eq.1)$$

$$CH_4 \;+\; * \;\rightleftarrows\; C* \;+\; 2\,H_2 \qquad\qquad (eq.2)$$
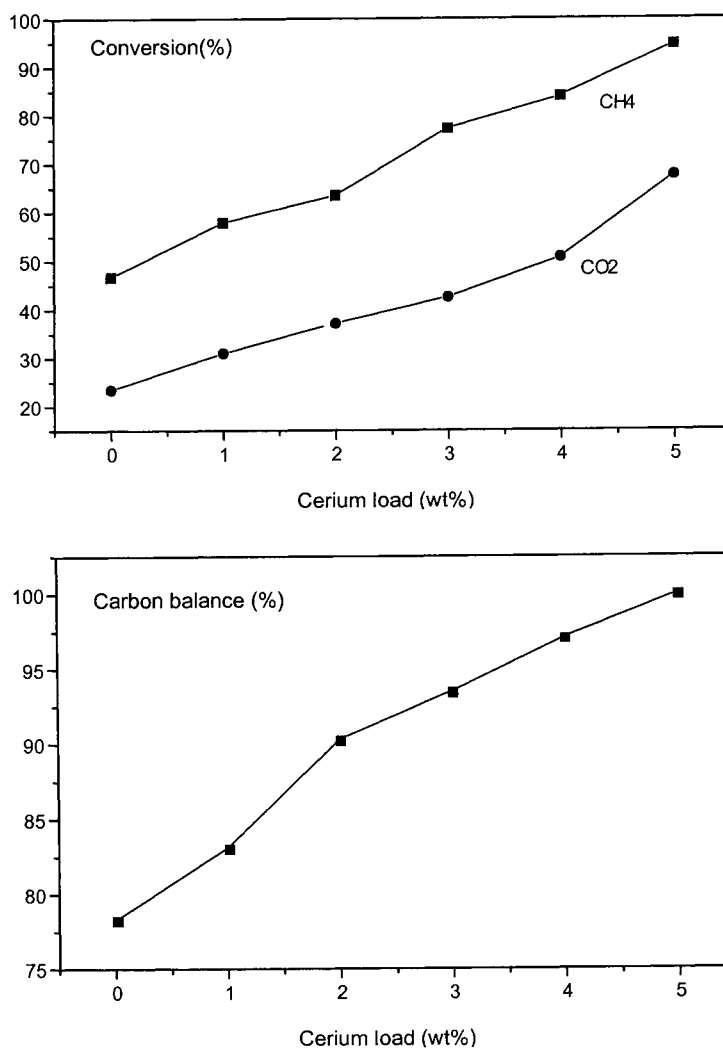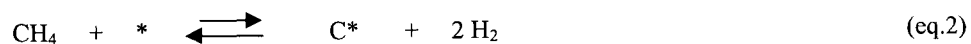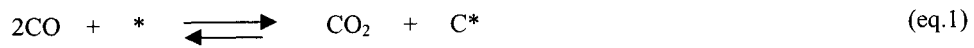


Fig. 1 activity results with cerium load

410

The high oxygen storage/transport capacity of $CeO_2$ permits a rapid cleaning mechanism. The carbon deposited on the nickel phase reacts with O coming from $CeO_2$. Jin et al. [24] reported that a significant conversion of CO to $CO_2$ in temperature-programmed desorption was observed. They explained this by the reversible reaction of CO observed on Pt with lattice oxygen.

In the case of our catalyst Ni-Ce(5%)/ $SiO_2$ , the total suppression of carbon deposited suggests that the mobility of lattice oxygen $CeO_2$ is accentuated by the presence of $SiO_2$ as a support.

### 3.3 Aging/regeneration

Table 3
Activity after aging and regeneration results in $CO_2$ reforming of $CH_4$ for Ce(5wt%)/$SiO_2$ catalyst.

| Operating Conditions | $CH_4$ conversion (%) | $10^2$ CO yield $(mol \cdot h^{-1} g^{-1})$ | Carbon balance (%) |
|---|---|---|---|
| $a_1$ | 26.9 | 12.3 | 98.2 |
| $a_2$ | 97.9 | 32.1 | 84.3 |
| $a_3$ | 96 | 27.6 | 86 |
| $a_4$ | 16.5 | 8.6 | 97.7 |
| $a_5$ | 19.4 | 10.5 | 99.4 |
| $a_4/a_1$ | 0.61 | 0.69 | - |
| $a_5/a_1$ | 0.72 | 0.85 | - |

Ni-Ce(5%)/ $SiO_2$ demonstrates a moderate activity at 773K (CO yield 12.3.$10^{-2}$ $mol \cdot h^{-1} \cdot g^{-1}$) with less coking (carbon balance 98.2%). Due to the endothermicity of the dry reforming of methane, the elevation of temperature to 973K increased greatly the activity of the catalyst (methane and carbon dioxide conversions and CO yield are multiplicated by 3). However carbon deposit increased as shown by carbon balance (98.2% against 84.3%).
After aging at 973K/12h, a slight decrease in the activity is observed (27.6 $10^{-2}$ against 32.1 $10^{-2}$ $mol \cdot h^{-1} \cdot g^{-1}$). However, this promoted catalyst exhibited a slight amelioration in coke resistance (carbon balance 86% against 84.2%). This suggests that the rate of elimination of carbon increased. The diminution in methane and dioxide of carbon conversions may be due to sintering of the active phase.
After aging and cooling to 773K a drop in activity is observed and a slight diminution in carbon deposit is signaled. After regeneration under $H_2$/873K/12h of Ni-Ce(5%)/ $SiO_2$ catalyst, the catalytic activity was not totally restored ($a_5/a_1$ = 0.72 for methane conversion) and ($a_5/a_1$ = 0.85 for CO yield) but an amelioration of coke resistance is realized (99.4% - 98.2% for carbon balance). This suggests that in reducing atmosphere there is a diminution

of carbon suppression or acceleration of carbon suppression. Stagg et al. [25] have shown by pulse experiments using $^{13}CH_4$, that in reducing atmosphere partial reduction of $ZrO_2$ support can occur. Due to the unusual redox properties of $CeO_2$, we can suggest the same behavior for this latter reduced in $H_2$ then re-oxidized by the O formed during the dissociation of $CO_2$ (eq.3). The decrease in the yield of CO is most probably attributed to a slight sintering of the active phase.

$$CO_2 \quad + \quad * \quad \rightleftharpoons \quad CO + \quad O* \qquad (eq.3)$$
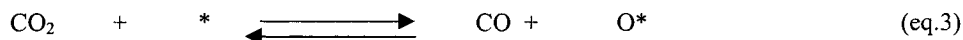
## 4. CONCLUSION

The $CO_2$ reforming of methane has been successfully performed over a series of Ni-Ce/ $SiO_2$ catalysts with varying Ce loadings from 0 to 5%. The promoted catalysts are more active than the unpromoted one. A loading of 5wt% of $CeO_2$ gives very high activity with carbon balance equal to 100%. The aging/regeneration of Ni-Ce(5%)/ $SiO_2$ catalyst revealed that the addition of Ce as a promoter suppresses totally the carbon deposition and maintains a high activity.

## REFERENCES

1. J.R. Rostrup-Nielsen and J.H.B. Hamsen, J.Catal., 144 (1193) 38.
2. J.A. Lercher, J.H. Bitter, W. Hally, W. Niessen and K. Seshen , Stud.Surf.Sci.Catal., 101 (1996) 463.
3. J.R. Rostrup-Nielsen, Stud.Surf.Sci.Catal., 36 (1988) 73.
4. P. Ferreira-Aparicio, A. Guerrero-Ruiz and I. Rodriguez-Ramos, Appl.Catal.A: General, 170 (1998) 177.
5. J.H. Bitter, K. Seshan and J.A. Lercher, J.Catal., 176 (1998) 93.
6. J.H. Bitter, K. Seshan and J.A. Lercher, Topics in Catalysis, 10 (2000) 295.
7. K. Tomishige, O. Yamazaki, Y. Chen, K. Yokoyama, X. Li and K. Fujimoto, Catal.Today, 45 (1998) 35.
8. Z. Zhang, X.E. Verykios, Appl.Catal.A: General, 138 (1995) 109.
9. Z. Cheng, Q. Wu, J. Li and Q. Zhu, Catal.Today, 30 (1996) 147.
10. S. Wang and G.Q. Lua, Energy and Fuels, 12 (1998) 248.
11. H.M. Swaan, V.C.H. Kroll, G.A. Martin, C. Mirodatos, Catal.Today, 21 (1994) 571.
12. M.C.J. Bradford and M.A. Vannice, Appl.Catal.A: General, 142 (1996) 73.
13. P. Ferreira-Aparicio, I. Rodriguez-Ramos, A. Guerrero-Ruiz, Appl.Catal.A: General, 148 (1997) 343.
14. R. Bouarab, S. Menad, D. Halliche, O. Cherifi and M.M. Bettahar, Stud.Surf.Sci.Catal., 119 (1998) 717.
15. D. Halliche, R. Bouarab, O. Cherifi and M.M. Bettahar, Catal.Today, 29 (1996) 373.
16. A. Erdohelyi, J. Cserenyi, F. Soymosi, J.Catal., 141 (1993) 287.
17. M.C.J. Bradford and M.A. Vannice, Catal.Today, 50 (1999) 87.
18. Xinsheng Li, Jong-San Chang and Sang-Eon Park, React.Kinet.Catal.Lett., 67 (1999) 375.

412

19. A.M. Gadalla and M.E. Sommer, Chem.Eng.Sci., 44 (1989) 2825.
20. A.P.E. York, T. Suhartanto and M.L.H. Green, Stud.Surf.Sci.Catal., 119 (1998) 777.
21. S. Wang and G.Q.(Max)Lua , Appl.Catal. , B: Environmental, 19 (1998) 267.
22. F. Zamar, A. Trovarelli, C. Leitenburg and G. Dolcetti, J. Chem. Soc. Chem Commun., (1995) 965.
23. V.C.H. Kroll, H.M. Swaan and C. Mirodatos, J. Catal., 161 (1996) 409.
24. T. Jin, Y. Zhou, G.J. Mains and J.M. White, J. Phys. Chem., 91 (1987) 5931.
25. S.M. Stagg and D.E. Resasco, Stud.Surf.Sci.Catal., 119 (1998) 813.

413

# Chlorine mobility in Pt/Al₂O₃ and Pt/Al₂O₃/Al complete oxidation catalysts.

M. Paulis[a], N. Burgos[a], C.López-Cartes[b], J.M. Gatica[b], J.J. Calvino[b] and M. Montes[a].

[a]Grupo de Ingeniería Química, Departamento de Química Aplicada, Facultad de Ciencias Químicas, UPV/EHU, Apdo. 1072, 20080 San Sebastián, España. ☎ 43-943-018183 ⌨ qppmoram@sc.ehu.es

[b] Departamento de Ciencia de los Materiales e Ingeniería Metalúrgica y Química Inorgánica. Facultad de Ciencias. Universidad de Cádiz, Apdo. 40, 11510 Puerto Real (Cádiz), España ☎ ⌨ jose.calvino@uca.es

The effect of chlorine presence on supported platinum oxidation catalysts has been studied. Apart from an initial inhibitory effect, unusual stability behaviour of chlorine containing Pt/Al₂O₃ catalysts was observed. Several experiments have been carried out in order to understand this behaviour. A chlorine mobility model has been suggested: the spillover of chlorine from Pt particle to the support, its backspillover to platinum and its final elimination. This chlorine mobility would be promoted by water produced during the hydrocarbon oxidation. The conclusions of the chlorine mobility model have been applied to fully activate a monolithic Pt/Al₂O₃/Al catalyst prepared from chlorinated precursors.

## 1. INTRODUCTION

Supported platinum catalysts are amongst the most active catalysts for complete oxidation of VOCs in environmental emission control [1]. The preparation of these catalysts have usually been carried out using platinum chlorinated precursors, which have been found to produce an activity inhibition during complete oxidation reactions [2, 3]. The inhibiting mechanism of chlorine on platinum containing oxidation catalysts is not fully understood, but the amount of information on chlorine spillover and mobility within the Pt/Al₂O₃ catalysts is huge. Cant et al. [4] deal with chlorine mobility between platinum particles and Al₂O₃ surface in different reducing and wet atmospheres, while the research by Stencel and coworkers [5] concentrated on the chlorine position within the platinum particle under reducing and oxidant atmospheres. It has also been reported an activation of the chlorinated catalysts due to the progressive elimination of chlorine with the H₂O produced in the oxidation reaction [2]. As a result, it seems that the surrounding atmosphere affects greatly the chlorine mobility on Pt/Al₂O₃ catalysts.

The main goal of this communication is to understand the chlorine mobility between the active-phase and the support during the catalytic oxidation of toluene over Pt/Al₂O₃ prepared from a chlorinated platinum precursor. The tools used for this purpose were toluene ignition curves, catalytic activity stability tests, platinum dispersion measurements, TPR and DRIFTS of adsorbed CO.

The results of this study are contrasted with the catalytic behaviour of platinum supported on a metallic monolith of anodised aluminium. This type of catalyst represents a more realistic type of catalyst, due to its monolithic form that allows a lower pressure drop, maintaining a high surface-to-volume ratio. Furthermore, the knowledge gained about chlorine spillover in these catalysts has been applied to devise a calcination pretreatment in wet air which eliminates the negative effects of chlorine on the catalytic activity of $Pt/Al_2O_3/Al$ metallic monolith.

## 2. EXPERIMENTAL

The $Pt/Al_2O_3$ powder catalyst was prepared by dry impregnation of $Al_2O_3$ (Spheralite SCS250, Rhône-Poulenc) with $(NH_4)_2PtCl_4$ (Johnson-Matthey, Alfa) (1% by weight of Pt). The sample was dried at 393K for 16 hours and calcined at 773K for 2 hours.

The preparation method of the metallic monoliths has been reported elsewhere [6]. An extensive study of the anodisation process of aluminium sheets led us to the utilisation of the anodisation conditions presented in Table 1.

Table 1.
Selected aluminium anodisation conditions for monolith preparation.

| Electrolyte | Current density | Anodisation time | Anodisation T | Agitation |
|---|---|---|---|---|
| $H_2SO_4$ 1.6M | 2 A/dm$^2$ | 50 minutes | 303K | By air bubbling |

Under these preparation conditions, a layer of 12-15 μm of $Al_2O_3$ was formed, with an average pore diameter between 17 and 19 nm and a specific surface area of around 28 m$^2$/g $Al_2O_3$. The construction of the monoliths from the anodised aluminium, combining flat and corrugated sheets, led to metallic monoliths with structural characteristics similar to the commercial ones [7], as it can be seen in Table 2. $Al_2O_3$ formed by the anodisation process was amorphous and remained in this form during calcination up to 973K, when the γ-$Al_2O_3$ phase started to be formed. The $Pt/Al_2O_3/Al$ metallic monolith was prepared by wet impregnation of the anodised monolith with $(NH_4)_2PtCl_6$ (Johnson Matthey, Alfa). The monolith contained 2.2 mg of Pt. It was dried at 393K for 30 minutes and calcined at 723K for 2 hours.

Table 2.
Structural properties of the prepared monoliths.

| Geometric volume | Number of cells | Free fraction | Wall thickness | $Al_2O_3$ surface area |
|---|---|---|---|---|
| 6 cm$^3$ | 350-360 cells/in$^2$ | 81% | 0.1mm | 40m$^2$/monolith |

The physico-chemical characterisation of the catalysts was carried out by $N_2$ adsorption (ASAP 2000, Micromeritics), X-ray diffraction (Philips PW 1729-1820), HREM (Jeol, JEM 2000EX), TPR (PulseChemisorb 2700, Micromeritics) and CO adsorption

followed by DRIFTS (Nicolet Protégé 460). The catalytic properties were studied by toluene ignition curves and isothermal stability tests. Toluene oxidation over $Pt/Al_2O_3$ was carried out at a $W/F_{Ao}$ ratio of 0.017 ($g_{Pt}$ min/cm$^3$$_{toluene\ NPT}$), with 200mg of catalyst (2 mg of Pt) and a total gas flow rate of 510 cm$^3$/min (GHSV 9700h$^{-1}$). The reaction conditions for monoliths were $W/F_{Ao}$ ratio of 0.019 ($g_{Pt}$ min/cm$^3$$_{toluene\ NPT}$) with a monolith (2.2 mg of Pt) and a total gas flow rate of 510 cm$^3$/min (GHSV 5100h$^{-1}$). The on-line analysis of the reaction products has been carried out by gas chromatography (Hewlett Packard 6890, TR-WAX 30m column), direct $CO_2$ detector (Digital Control Systems Model 300) and mass spectrometry (Omnistar, Balzers Instruments).

## 3. RESULTS AND DISCUSSION.

TPR analysis of the $Pt/Al_2O_3$ powder catalyst showed the presence of platinum oxychlorinated species, as denoted by the shift of 30K in the reduction maximum compared with a $Pt/Al_2O_3$ catalyst prepared from a non-chlorinated precursor.

The results obtained on the effect of the platinum precursor salt on the CO adsorption spectra can be summarised in the following way: The catalyst prepared with the chlorinated salt does not present bridged bonded CO species as catalysts prepared from non-chlorinated precursors do. The presence of bridge bonded CO has been attributed either to a less rough platinum surface or to a higher electronic density on the platinum due to a more alkaline character of the support [8]. The addition of chlorine to this catalyst, which has been used in catalysis to increase the electrophilic character of the $Al_2O_3$ [3], makes this support more acidic. In this way, the catalysts prepared with a chlorinated platinum salt will posses platinum with a lower electronic density.

The isothermal stability test of toluene complete oxidation over $Pt/Al_2O_3$ showed the trend shown in Figure 1.
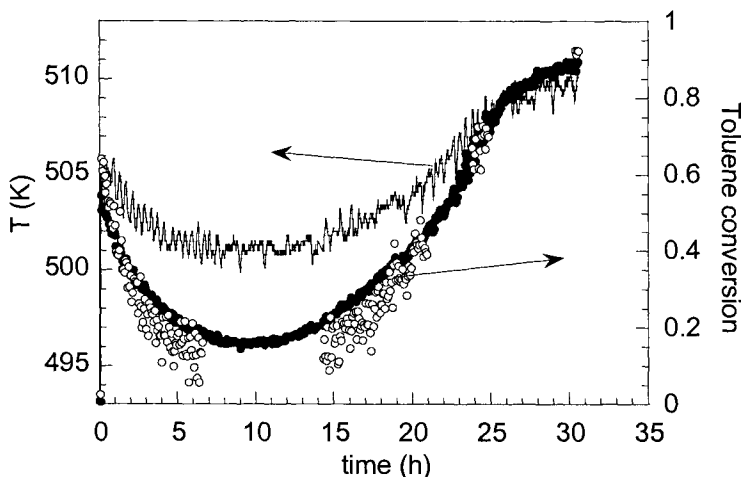


Fig. 1. Isothermal stability test of $Pt/Al_2O_3$ in toluene complete oxidation. Toluene conversion obtained from (O) toluene signal and (●) $CO_2$ signal.

Activity decayed initially from 50% of conversion to approximately 10% of toluene conversion. Consequently, even if the oven temperature remained constant, the bed temperature monitored inside the reactor decayed 4 degrees due to the exothermic character of the oxidation reactions. After 10 hours of reaction, the activity and the temperature decay was stabilised and they started to increase. After 30 hours of reaction, the activity and temperature values reached a plateau at 85% conversion and 510K, corresponding to an activity above the initial one.

In order to verify the different catalytic activity of the catalyst after different times of reaction, the toluene oxidation reaction was stopped after 10 and 30 hours of reaction, and the activity of such treated catalysts was compared with the fresh one. The toluene ignition curves of those catalysts are presented in Figure 2.
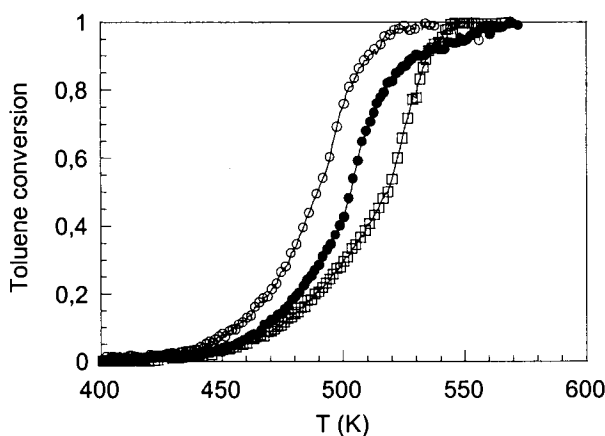


Figure 2. Toluene ignition curves for fresh Pt/Al$_2$O$_3$ (●), the catalyst after 10 h of reaction (□) and after 30 h of reaction (○).

As it can be seen, the Pt/Al$_2$O$_3$ catalyst showed initially a T$_{50}$ (temperature for 50% conversion) of 504K. After being treated under toluene oxidation conditions for ten hours, the T$_{50}$ increased to 518K, indicating catalyst deactivation. However, if the catalyst remained under reaction conditions for another 20 hours (30 hours of reaction) the T$_{50}$ shifted to 489K, showing that the catalyst had reached higher activity than the initial one.

In order to study this unusual behaviour, several experiments were carried out. First of all, Pt dispersion measurements of the catalyst at different points of the stability curve were carried out: before the reaction, after 10 hours under reaction conditions ("deactivated catalyst") and after 30 hours under reaction conditions ("reactivated catalyst"). The HREM technique gave us an initial metal dispersion of 36%, which decayed only slightly to 33% after 10 h, ending at 25% after 30 hours of reaction. As it can be seen, the small but constant decrease of the dispersion during the reaction cannot explain the important activity changes observed as sintering-redispersion phenomena.
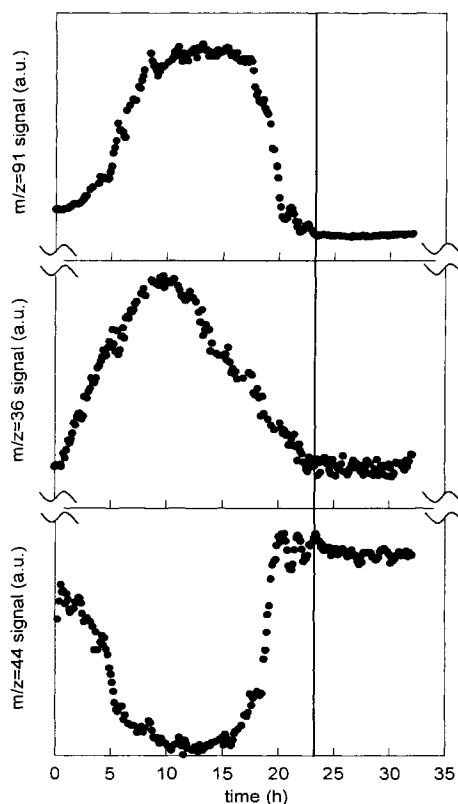
Fig. 3. Stability test of Pt/Al$_2$O$_3$ in the toluene complete oxidation reaction followed by on line mass spectrometry.

Furthermore, the stability test of the Pt/Al$_2$O$_3$ sample was repeated increasing the amount of sample, to allow on line MS analysis. The results of the evolution in time of toluene (m/z=91), CO$_2$ (m/z=44) and HCl (m/z=36) are shown in Figure 3. As it can be seen, the activity trend is the one described in Figure 1, with an initial decrease and a final increase. If we consider the m/z=36 signal, we can see that HCl evolves from the catalyst as the stability test runs, indicating that chlorine is being eliminated by reaction with water produced from toluene oxidation. The end of the HCl peak, when no more HCl flows out the reactor, comes together with a recuperation of the activity ending in a plateau.

This behaviour has been assigned to the mobility of chlorine between the Pt particles and the Al$_2$O$_3$ support, produced by the H$_2$O formed in the reaction [9]. The initial reduction would spillover the chlorine from the platinum particles to the support and to the inside of the platinum particles, as suggested by Cant et al. [4] and Stencel et al. [5]. The addition of toluene in the oxidising atmosphere would bring about the movement of chlorine to the surface of platinum particles and the back-spillover from the support to the platinum particles. This backspillover of the chlorine from the support to the Pt particle would be produced by the water generated in the oxidation of toluene which would spill over from the particle to the support. Both phenomena should decrease the catalytic activity. The subsequent chlorine elimination by the H$_2$O formed in the reaction will produce an increase of the activity reaching a higher activity than the initial one.

The same chlorine mobility can explain the activation of a Pt/Al$_2$O$_3$/Al monolith during the complete oxidation of toluene in air. In Figure 4 it can be seen how the activity increased greatly after maintaining the monolith under reaction conditions for 300 hours. The ignition temperature, T$_{50}$, passed form 460K to 440K after the reaction.

418
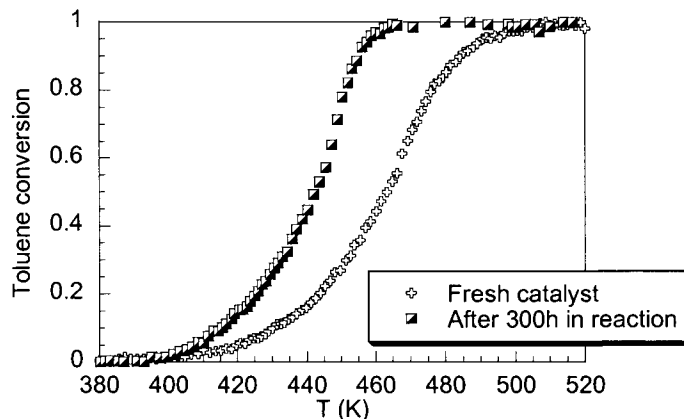


Fig. 4. Toluene ignition curves over fresh Pt/Al$_2$O$_3$/Al
and after 300h under reaction conditions.

Taking into account all these experiments and the chlorine mobility proposed to explain it, a wet calcination can be proposed to activate the Pt/Al$_2$O$_3$/Al monoliths. Indeed, heating up the system under wet air should facilitate the back-spillover of the chlorine present on the support to the platinum site and its final elimination as HCl. As a consequence, the maximum potential activity would be obtained from the beginning of the reaction. Figure 5 presents the activity tests obtained after different pretreatments. It can be seen that a 18 hours pretreatment in 3% H$_2$O in air at 773K is enough to obtain the maximum initial activity (T$_{50}$=443K), which coincides with the activity measured after 300 hours on reaction stream (Figure 4).
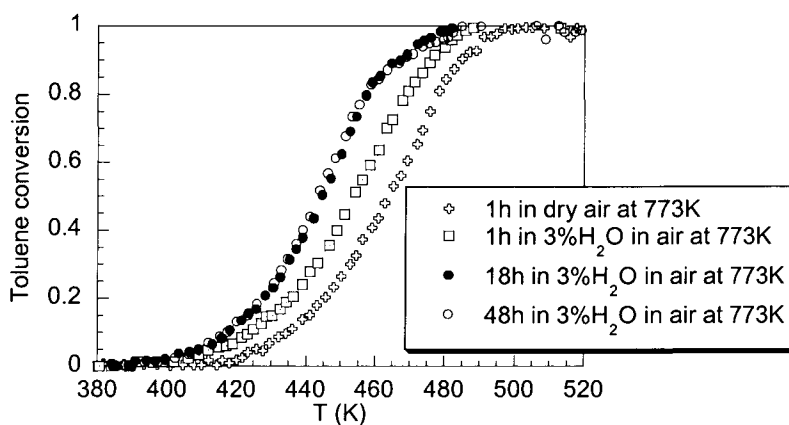


Fig. 5. Toluene ignition curves over fresh Pt/Al$_2$O$_3$/Al
and after different H$_2$O pretreatments at 773K.

## CONCLUSIONS

The effects of chlorine spillover on platinum supported on alumina have been detected through the change of activity during toluene oxidation. A model of chlorine mobility has been proposed, and its features can be summarised on Figure 6. The chlorine initially spread over the support and in the inner part of the platinum particle due to a reduction pretreatment [5], can be mobilised under reaction conditions (by the production of $H_2O$ during toluene complete oxidation) and under thermal wet conditions. Milder reaction conditions produce an initial increment of chlorine concentration in the particle, due to the water spillover from the platinum particle to the support and the HCl backspillover from the support to the particle, producing the initial activity decay observed in the $Pt/Al_2O_3$ stability test. The subsequent elimination of chlorine increases the platinum activity to reach conversions higher than the initial ones. A simple pretreatment at 773K in wet conditions for 18 hours produces the same complete elimination of chlorine, bringing about the complete activation of $Pt/Al_2O_3/Al$ monoliths for toluene oxidation.
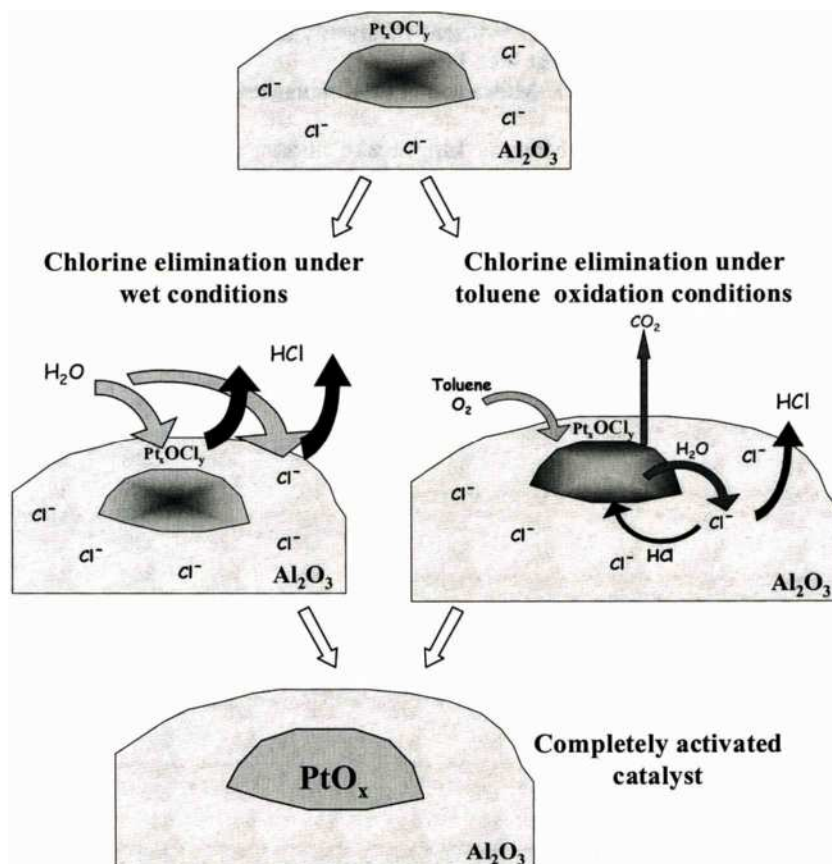


Figure 6. Chlorine mobility model proposed under reaction and wet conditions.

420

## REFERENCES

1. J.J. Spivey, , in "Catalysis, a Specialist Periodical Report" (J.R. Anderson and M. Boudart, Eds.) Vol. 8 p.157, The Royal Chemical Society, 1989.
2. P. Marècot, A. Fakche, B. Kellali, G. Mabilon, M. Prigent and J. Barbier, Appl. Cat. B: Env. 3 (1994) 283.
3. E. Marceau, M. Che, J. Saint-Just and J.M. Tatibouët, Catal. Today 29 (1996) 415.
4. N.W. Cant, D.E. Angove and M.J. Patterson, Catal. Today 44 (1998) 93.
5. J.M. Stencel, J. Goodman and B.H. Davis, Proc. 9th Int. Congr. Catal. 3 (1988) 1291.
6. N. Burgos, M. Paulis, J. Sambeth, J.A. Odriozola and M. Montes, Stud. Surf. Sci. Cat. 118 (1998) 157.
7. M.V. Twig and D.E. Webster, in "Structred Catalysts and Reactors" (A. Cybulski and J.A. Moulijn, Eds.) p. 59, Marcel Dekker Inc., 1998.
8. B.L. Mojet, M.J. Kappers, J.T. Miller and D.C. Koningsberger, Stud. Surf. Sci. Cat. 101 (1996) 1165.
9. M. Paulis, H. Peyrard and M. Montes, "Influence of chlorine on the activity and stability of Pt/Al$_2$O$_3$ catalysts in the complete oxidation of toluene" Journal of Catalysis (in press).

421

# Migration of carbonaceous materials formed during wet oxidation of phenol with supported Pt catalysts

Dong-Keun Lee, Sang-Jun Ahn and Dul-Sun Kim

Department of Chemical Engineering/Environmental Protection, Research Institute of Environmental Protection, Gyeongsang National University, 900 Kajwa-dong, Chinju, Kyongnam 660-701, KOREA

Removal of phenol by wet air oxidation was conducted with 1wt% $Pt/Al_2O_3$ and 1wt% $Pt/CeO_2$ catalysts. During the reaction carbonaceous materials were formed and deposited on the catalyst surface, and the materials deactivated the catalysts. The carbonaceous deposits were located on both the surface of Pt particles and the supports. The primarily formed carbonaceous deposit on Pt particles migrated continuously onto the supports.

## 1. INTRODUCTION

Many wastewater streams originating in chemical process industries contain high concentrations of organic materials which are difficult to be oxidized biologically. Phenol is one of the most common and important pollutants because it is extremely toxic to the environment even at very low concentrations.

Wet air oxidation (WAO) process is a very attractive and useful technique for treatment of effluents where the concentrations of organic pollutants are too low for incineration process and when biological treatments are ineffective, e.g., in the case of toxic effluents [1-3]. WAO was applied to removing total organic carbon(TOC) such as : insoluble polymers [4], wastewaters [5-8], and certain organic compounds [9,10]. The efficient removal of pollutants *via* WAO process requires very high temperature and pressure, typically in the range of 473~573K and 7~15MPa, respectively [11]. However, the severe reaction conditions can lead to high installation costs, and practical applications of this process are limited. Therefore, development of catalytic wet air oxidation (CWAO) using various catalysts has been attempted in order to reduce the severity of the oxidation conditions. The use of catalysts makes the process more attractive by achieving high conversion at considerably lower temperature and pressure [2,12,13].

Although many investigations dealing with heterogeneously catalyzed WAO have been reported, study of catalyst deactivation during WAO has been mostly unexplored. In the present work CWAO of phenol was carried at 423 K ad 1.4 MPa with $Pt/Al_2O_3$ and $Pt/CeO_2$ catalysts, and formation/migration of carbonaceous deposits on the catalyst surface were investigated.

## 2. EXPERIMENTAL

High purity phenol-$d_6$($C_6D_5OD$), supplied from Aldrich Co., was used without further purification. Platinum(II) acetylacetonate (Aldrich Co.) was used as the precursor of $Pt/Al_2O_3$ and $Pt/CeO_2$ catalysts. γ- $Al_2O_3$(Strem chemicals) and $CeO_2$(Aldrich Co.) were used as the support of $Pt/Al_2O_3$ and $Pt/CeO_2$ catalysts, respectively. All other chemicals used were of analytical reagent grade.

1wt% $Pt/Al_2O_3$ and 1wt% $Pt/CeO_2$ catalysts were prepared by incipient wetness method. In order to locate platinum particles mainly at the exterior surface of the supports, the pores of γ-$Al_2O_3$ and $CeO_2$ had been *a priori* saturated with n-hexane. A certain amount of platinum(II) acetylacetonate  solution was added to the supports drop by drop. The prepared samples were then dried *in vacuo* at 323K. The above preparation steps were repeated ten times to have 1wt% Pt loading. The samples were then calcined at 673K for 4hr in a programmable furnace. The liner rate of heating up to 673K was kept to be 0.5°C/min. The calcined samples were reduced with flowing $H_2$ at 573K for 4hr and were finally passivated at 298K with flowing 0.96% $O_2$/He gas mixture.

The oxidation of phenol solution was performed in a 1L SS316 autoclave (Parr Instrument Co.) equipped with a teflon liner and a gas entrainment impeller having a variable-speed arrangement.

Not only the dispersion of platinum particles but also the carbonaceous materials in the $Pt/Al_2O_3$ and $Pt/CeO_2$ catalysts were observed with a transmission electron microscopy (JEOL 200CX) using 160KeV electrons. XPS spectra of carbonaceous deposits were recorded by a VG ESCALAB 220 iXL spectrometer with a MgKα-source operating at 20mA and 13KV at room temperature.

The carbonaceous materials deposited on the catalyst during the wet oxidation reaction were analyzed by temperature-programmed oxidation(TPO) method using a mass spectrometer(HP 5970). In a typical TPO experiment, 0.2g of the used catalyst was loaded in a quartz microreactor which was then installed in a furnace coupled to a temperature programmer. The catalyst was first exposed to flowing helium(100mL/min) and the temperature was raised at a rate of 10K /min to 393K and kept at this temperature for 1hr before being cooled to room temperature. Subsequently the catalyst was heated under a flowing gas mixture of 0.96% oxygen in helium at a rate of 10K/min to 973K. Analysis of the microreactor outlet gas was performed by mass spectrometry.

Reaction intermediates and phenol residual were identified and quantified with HPLC(Waters Co.) equipped with a tunable absorbance detector and MS spectrometer (HP 5970). Separation of the components in HPLC was achieved by Nova-Pak C18 column. Elution was performed at 1mL/min flow rate of mobile phase(MeOH : $H_2O$ : $H_3PO_4$ = 40:60:0.5vol%).

Total organic carbon(TOC) was measured with a Shimazu 5000A TOC analyzer whose operation is based on the combustion/non-dispersive infrared(NDIR) gas analysis.

## 3. RESULTS AND DISCUSSION

### 3.1 Wet oxidation of phenol with $Pt/Al_2O_3$ and $Pt/CeO_2$

TEM micrographs of the 1wt% $Pt/Al_2O_3$ and 1wt% $Pt/CeO_2$ catalysts are shown in Figure 1. Platinum particles were finely dispersed on the surface of $Al_2O_3$ and $CeO_2$ support, and the average Pt particle size was estimated to be 20Å. To assess the extent of the uncatalyzed
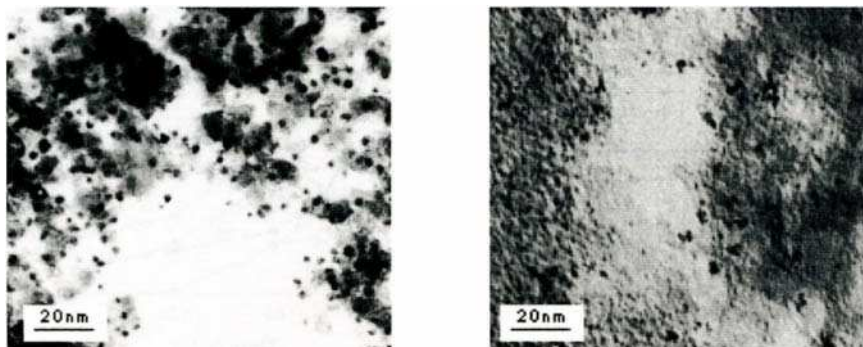
Figure 1. TEM micrographs of the fresh 1wt% Pt/Al$_2$O$_3$(left) and 1wt% Pt/CeO$_2$(right).

thermal oxidation of phenol and the effect of support, WAO tests were performed without catalyst and with metal-free support with phenol initial concentration 1000 mg/L. As can be seen in Figure 2, the uncatlayzed thermal oxidation did occur up to 5% in 3hr, and the use of metal-free Al$_2$O$_3$ support resulted in somewhat lower oxidation efficiency than uncatalyzed oxidation. The elevated temperature can lead to the formation of oxygen radical(O⊕), which in turn can read with water to form hydroxyl radical(HO⊕). This radical might have oxidized phenol. Metal-free Al$_2$O$_3$ support, however, scavenged some of the hydroxyl radical formed. The use of Pt/Al$_2$O$_3$ catalyst enhanced the oxidation appreciably. Almost complete conversion of phenol could be obtained in 60 min.

When analyzing the results of TOC that more than 95% of the initial TOC was removed in 60min reaction with Pt/Al$_2$O$_3$ catalyst(Fig. 3), most phenol in Figure 2 is believed to be completely mineralized into CO$_2$ and water.
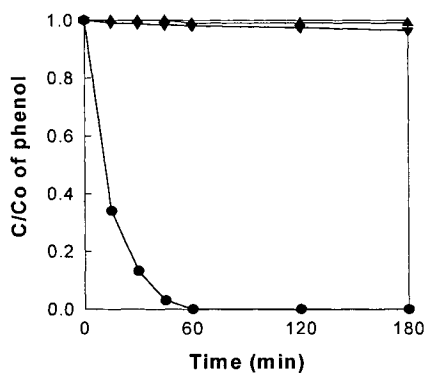


Figure 2. Catalytic wet oxidtion of phenol at 423K and 1.4MPa ($\pi$ : uncatalyzed reaction, $\theta$ : reaction with metal-free Al$_2$O$_3$, ✶ : reaction with 3g 1wt% Pt/ Al$_2$O$_3$ catalyst).
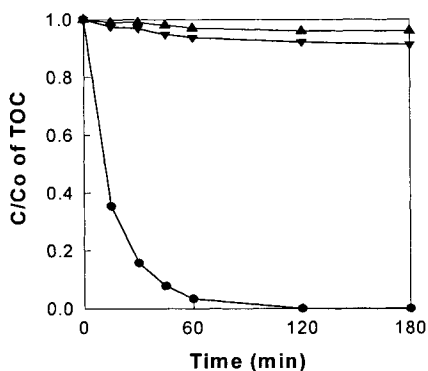
Figure 3. Change in TOC concentration during CWAO of phenol at 423K and 1.4MPa ($\pi$ : uncatalyzed reaction, $\theta$ : reaction with metal-free Al$_2$O$_3$, ✶ : reaction with 3g 1wt% Pt/Al$_2$O$_3$ catalyst).
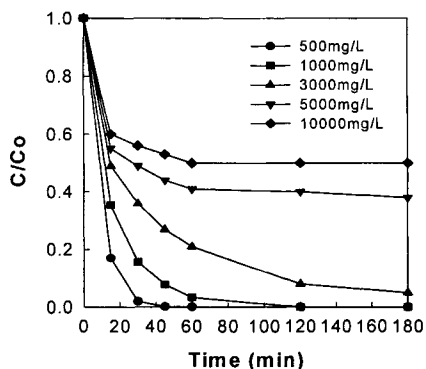
Figure 4. Effect of phenol initial concentration on wet oxidation of phenol at 423 K and 1.4 MPa with 3g Pt/Al₂O₃ catalyst.
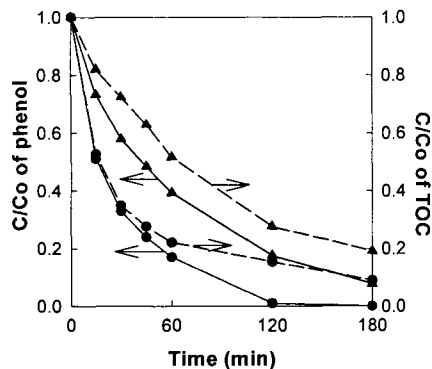


Figure 5. Time dependence of relative phenol and TOC concentrations during CWAO of phenol at 423K and 1.4MPa with 2g fresh Pt/ Al₂O₃ catalyst(★) and 2g used Pt/ Al₂O₃ catalyst(π).

The effect of initial phenol concentration was investigated in the range 500~10000 mg/L in the presence of 3.0g Pt/Al₂O₃. The results in Figure 4, showing the changes in phenol dimensionless concentration as a function of reaction time, indicate that the higher the phenol initial concentration, the lower the conversion. While complete phenol conversion was obtained within 60min operation with an initial phenol concentration of 1000 mg/L or less, only 50% conversion was achieved with the highest phenol initial concentration (10000 mg/L). In addition after 60min reaction the conversion of phenol did not proceed and remained almost constant. This implies that during the reaction there might have occurred catalyst deactivation whose extent is highly dependent on the phenol initial concentration.

When the CWAO of phenol was completed in 3hr, the used catalyst sample was filtered and washed with distilled deionized water. The sample was then dried at 353K for 24hr, and the CWAO of phenol was repeated with phenol initial concentration 1000 mg/L in the presence of the dried catalyst. As can be seen in Figure 5, the efficiency of phenol removal and TOC removal could not successfully be restored. This deactivation of the used catalyst might be due to either the leaching of the active component (Pt) of the catalyst during the reaction and/or accumulation of carbonaceous materials deposited on the catalyst.

To investigate the stability of the Pt/Al₂O₃ catalyst with respect to metal leaching, catalyst samples were taken after the reaction at various temperatures. The concentrations of dissolved Pt and Al metals were analyzed using ICP, but no detectable amount of dissolved Pt and Al metals could be measured. Accordingly at the reaction



Figure 6. Effect of phenol initial concentration on wet oxidation of phenol at 423 K and 1.4 MPa with 3g Pt/CeO₂ catalyst.
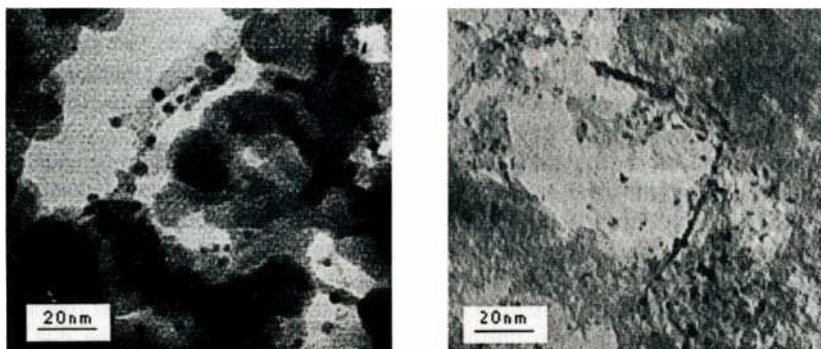
Figure 7. TEM micrographs of the Pt/Al₂O₃(left) and Pt/CeO₂(right) catalysts after 3hr reaction with phenol initial concentration 5000 mg/L.

conditions employed in this research no leaching can be said to occur.

In the case of reaction with Pt/CeO₂ catalyst (Figure 6), however, the dependence of conversion on phenol initial concentration appears somewhat different. When compared with the results from Pt/Al₂O₃, much higher conversions were obtained with Pt/CeO₂ at the corresponding phenol initial concentrations. While the oxidation reaction stopped after 1hr operation with initial phenol concentrations of 5000 mg/L and 10000 mg/L in the presence of Pt/Al₂O₃ catalyst (Fig. 4), the oxidation reaction continues to proceed upto 3hr operation on Pt/CeO₂ catalyst with initial phenol concentrations of 5000 mg/L and 10000 mg/L. Therefore catalyst deactivation of Pt/CeO₂, if any, seems to be not so strong as that of Pt/Al₂O₃ during the wet oxidation of phenol.

### 3. 2. Analysis of the deactivated catalysts

Figure 7 shows TEM images of the Pt/Al₂O₃ and Pt/CeO₂ catalysts which underwent wet oxidation of phenol for 3hr with phenol initial concentration 5000 mg/L. While the fresh Pt/Al₂O₃ and Pt/CeO₂ catalysts were kept clean and free of any deposited materials as previously shown in Figure 1, huge amount of a certain material was deposited on the surface of the used Pt/Al₂O₃ catalyst. In the case of the used Pt/CeO₂ catalyst, however, accumulation of the deposited material is not so outstanding and the deposited material acts as a bridge linking each Pt particles.

EDX analysis of the used catalysts had demonstrated that the dominant component of the deposited material was carbon. In addition XPS spectra of the catalysts after reaction with different phenol initial concentrations indicated the emergence of a strong C1s peak, confirming the presence of carbonaceous deposits on the catalyst surface. Figure 8 shows the representative XPS C1s spectrum of the Pt/Al₂O₃ catalyst after reaction for 3hr with phenol initial concentration 1000 mg/L.



Figure 8. XPS C1s spectrum of Pt/Al₂O₃ after reaction for 3hr.

The maximum intensity of C1s peak appears at binding energy of 286.3 eV. Although the peak intensity of C1s in $Pt/Al_2O_3$ and $Pt/CeO_2$ catalysts increased with increasing phenol initial concentration, both the shape and binding energy of the peak were almost unchanged. This indicates that the carbonaceous deposits on the catalysts have the same chemical composition and configuration.

Carbonaceous deposits on the catalysts were analyzed with TPO. Burn-off profiles of carbonaceous deposits on the catalysts after reaction for 3hr with initial phenol concentration 5000 mg/L are shown in Figure 9. As seen, in accordance with the consumption of oxygen formation of $CO_2$ occurs at a broad temperature range from 250°C to 700°C for $Pt/Al_2O_3$ and at a temperature range 250°C to 450°C for $Pt/CeO_2$. This result provides a further evidence that carbonaceous materials must have been deposited on the catalyst during wet oxidation of phenol, and the catalyst deactivation during wet oxidation of phenol must be due to the deposits of carbonaceous materials.

When considering the aforementioned XPS results that the carbonaceous deposits on $Pt/Al_2O_3$ and $Pt/CeO_2$ have the same chemical composition and configuration, carbonaceous deposits on both the catalysts are expected to be burned off at the same and narrow temperature range during TPO experiment. An interesting feature is, however, observed that the carbonaceous deposits on $Pt/Al_2O_3$ are less reactive toward oxygen (or more difficult to burn) than those on $Pt/CeO_2$. Carbon deposits on alumina support were reported to be oxidized at temperatures higher than 440°C[14]. On the other hand participation of Pt metal could catalyze oxidation of carbon deposits, and Pt-catalyzed oxidation of carbon is known to occur generally at temperatures around 280°C [15,16]. A separate TPO analysis was carried out with Pt powder alone after reaction for 3hr with initial phenol concentration 5000 mg/L, and the result is shown in Figure 10. The carbonaceous deposit on Pt powder was burned off at narrow temperature range around 250°C and was completely removed below 300°C.

The broad profiles of $CO_2$ formation in $Pt/Al_2O_3$ and $Pt/CeO_2$ imply that there are at least two types of carbon deposits burning at different temperatures. One type of deposits, locating on the surface of Pt particles, will burn at around 250°C, and the other type on $Al_2O_3$ or $CeO_2$ will burn at much higher temperatures. The presence of carbon deposits on $Al_2O$ and $CeO_2$ could be confirmed from the TEM micrographs in Figure 7.

$CeO_2$ has received much attention because it acts as an oxygen storage in three-way
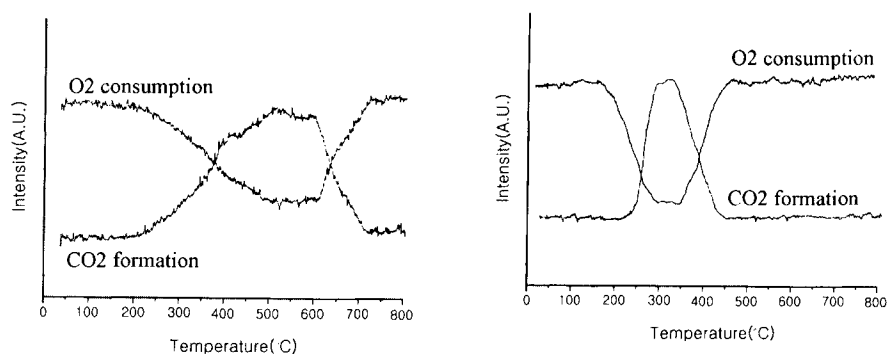


Figure 9. Profiles of $O_2$ consumption and $CO_2$ formation during TPO experiments with $Pt/Al_2O_3$(left) ad $Pt/CeO_2$(right) after reaction for 3hr with phenol initial concentration 5000 mg/L.
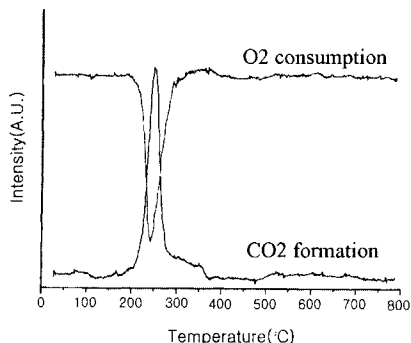
Figure 10. Profiles of $O_2$ consumption and $CO_2$ formation on Pt powder after reaction for 3hr with phenol initial concentration 5000 mg/L.

catalysts to maintain and enhance the activity of oxidation of hydrocarbons and carbon monoxide [17-19]. Although the reason why the carbonaceous deposit on $CeO_2$ rather than $Al_2O_3$ was burned off at lower and narrower temperatures can not clearly be answered at present, $CeO_2$ might have promoted the oxidation of the deposit on it.

### 3.3. Migration of carbonaceous deposits

Since the conversion of phenol on Pt-free $Al_2O_3$ support was almost negligible as shown in Figure 2, not only wet oxidation of phenol but also initial formation of carbonaceous deposits can be said to occur predominantly on the surface of Pt particles. The carbon deposits, primarily formed on the surface of Pt

particles, will then migrate onto the surface of $Al_2O_3$ and $CeO_2$ in the vicinity of Pt particles. In order to investigate the migration of carbonaceous deposits, TPO experiments were employed for $Pt/Al_2O_3$ and $Pt/CeO_2$ which underwent oxidation of phenol for 3hr with phenol initial concentrations 10, 50, 100, 500 and 1000 mg/L. The obtained profiles of $CO_2$ formation for $Pt/Al_2O_3$ and $Pt/CeO_2$ are shown in Figures 11 and 12, respectively. When phenol initial concentration was 50 mg/L or less, most $CO_2$ was produced at temperatures below 300°C. These $CO_2$ peaks are nearly the same as the $CO_2$ peak from Pt powder (Figure 10), indicating that carbonaceous deposits are primarily formed on the surface of Pt particles. At the phenol initial concentration 100 mg/L are found new higher temperature peaks which grow further with increasing phenol initial concentration. From the changes in the profiles of $CO_2$ formation with phenol initial concentration the primarily formed carbonaceous deposits on Pt particles are suggested to migrate onto the surface of $Al_2O_3$ and $CeO_2$. Furthermore, when looking carefully over the TEM micrographs of $Pt/Al_2O_3$ and $Pt/CeO_2$ (Fig. 7) carbonaceous materials on the supports were known to act as bridges connecting Pt particle



Figure 11. Effect of phenol initial concentration on $CO_2$ formation profiles of $Pt/Al_2O_3$.



Figure 12. Effect of phenol initial concentration on $CO_2$ formation profiles of $Pt/CeO_2$.

islands.

## 4. CONCLUSION

Catalytic wet oxidation of phenol was carried out with 1wt% $Pt/Al_2O_3$ and 1wt% $Pt/CeO_2$ in a batch reactor operated at 423 K and 1.4 MPa.

During the wet oxidation reaction catalyst deactivation was observed especially on $Pt/Al_2O_3$. From the TEM, EDX, XPS and TPO analyses the deactivation was proved to be due to the formation and deposition of carbonaceous materials on the catalyst surface. Although the carbonaceous deposits on $Pt/Al_2O_3$ and $Pt/CeO_2$ were known to have nearly the same chemical composition and configuration from XPS analysis, the profiles of $CO_2$ formation in TPO experiments were different to each other.

Carbonaceous deposits were located on the surface of Pt particles as well as supports. The deposit on Pt particles rather than the deposit on the support was much more reactive toward oxygen. The different reactivities of these deposits toward oxygen resulted in the appearance of broad $CO_2$ formation profiles at temperature range 250°C ~ 700°C for $Pt/Al_2O_3$ and 250°C ~ 450°C for $Pt/CeO_2$. The reason why the deposit on $CeO_2$ was burned off at lower and narrower temperatures was not clear, but $CeO_2$ was thought to have promoted the oxidation of the deposit on it.

From the sequential $CO_2$ formation profiles carbonaceous deposits were suggested to be primarily formed on the surface of Pt particles and then to migrate continuously onto the surface of $Al_2O_3$ and $CeO_2$ in the vicinity of the Pt particles.

## REFERENCES

1. J. Levec , Appl. Catal., 63 (1990) L1.
2. J. Levec and A. Pintar, Catal. Today, 24 (1995) 51.
3. T. L. Randall and P. V. J. Knopp, Water Pollut. Control Fed., 52 (1980) 2117.
4. D. Mantzavinos, R., Hellenbrand, A. G. Livingston and I. S. Metcalfe, Appl. Catal.: B, 11 (1996) 99.
5. C. J. Chang and J. C. Lin, J. Chem. Tech. Biotechnol., 57 (1993) 355.
6. A. Pintar and J. Levec, Chem. Eng. Sci., 47 (1992) 2395.
7. M. J. Dietrich, T. L. Randall and D. Channey, J. Environ. Progress, 4 (1985) 171.
8. S. H. Lin and S. Ho, Appl. Catal.: B:Environmental, 9 (1996) 133.
9. J. E. Atwater, J. R. Akse, J. A. Mckinnis and J. O. Thompson, Appl. Catal.: B: Environmental, 11 (1996) L11.
10. T. Hogan, R. Simpson, M. Kin and A. Sen, Catal. Lett., 40 (1996) 95.
11. E. Zimmerman, J. Chem. Eng., 56 (1958) 117.
12. F. Luck, Catal. Today, 27 (1996) 195.
13. D.-K. Lee and D.-S. Kim, Catal. Today, 63(2001)249.
14. S. M. Augustime, G. N. Alameddin and W. M. H. Sachtler, J. Catal., 115(1989)217.
15. S. Hamoudi, F. Larachi and A. Sayari, J. Catal., 177(1998)247.
16. C. L. Pieck, R. J. Verderone, E. L Jablonski and J. M. Parera, Appl. Catal., 55(1989)1.
17. D. Kalakkad and A. V. Dayte, Appl. Catal. B:Environmental, 1(1992)191.
18. J. G. Hunam, H. R. Robota, M. J. Cohn and S. A. Bradley, J. Catal., 133(1992)309.
19. P. Marecot, L. Pirault, G. Mabilon, M. Prigent and J. Barbier, Appl. Catal. B: Environmental, 5(1994)57.

429

# Possible role of spillover processes in the operation of NOx storage and reduction catalysts.

Allan J. Paterson, Daniel J. Rosenberg and James A. Anderson

Department of Chemistry, The University, Dundee, DD1 4HN, Scotland, UK

A series of catalysts containing $Pt-BaO-Al_2O_3$, have been prepared and characterised. Baria content was varied between 1 and 10 wt%. The processes which might involve spillover and thus contribute to the storage of NOx were studied using *in-situ* DRIFT and simultaneous temperature programmed reaction of the stored NOx. Experiments performed with $NO_2$ in place of NO and comparison of Pt containing with Pt-free samples were designed to show the role which is played by Pt in forming barium nitrate as the initial storage step. Even after $NO_2$ is formed, and is adsorbed as a nitro species at exposed baria surfaces, the subsequent transformation to nitrate species does not proceed readily in the absence of Pt suggesting that spillover of activated oxygen and/or an activated form of $NO_2$ may be required for the storage step and for the samples to behave as effective storage materials. Other differences between Pt and Pt-free sample observed during *in-situ* reaction, are the consequence of the Pt catalysed enhanced decomposition of barium carbonate, which otherwise acts as a poison for $NO_2$ adsorption and subsequent storage.

## 1. INTRODUCTION

Storage and reduction catalysts offer one possibility of controlling NOx emissions from automobile sources while allowing operation under predominantly lean-burn conditions [1]. Alkaline earth oxide components may be used to store NOx under lean conditions which is then released during intermittent rich/stoichiometric periods. The NOx released is then reduced by CO or HC over the noble metal component. Although certain mechanistic details of the processes involved are now emerging [2-4], much detail is still required. For example, it is uncertain to what extent the stored NOx is stable under warm-up conditions and to what extent spillover processes are involved in transferring NOx from the noble metal to the storage compound and vice versa. To address these aspects, combined FTIR-TPD studies were performed over Pt and Pt-free $BaO/Al_2O_3$ catalyst under different conditions using samples that have been previously exposed to $NO_2$.

## 2. EXPERIMENTAL

$BaO/Al_2O_3$ samples containing between 1 to 10 wt% BaO were prepared by precipitating the hydroxide from a barium nitrate solution using an ammonia solution onto γ-alumina (Degussa Aluminoxid C). The precipitate was filtered, washed and dried at 363 K for 16 h before being calcined in air (100 $cm^3$ $min^{-1}$) at 773 K (2 h). A fraction of each sample was

retained whilst the remainder was wet impregnated with 1 wt% Pt ($H_2PtCl_6$). Excess solvent was removed by heating under continuous stirring and the resulting powder dried overnight at 363 K prior to calcination in air (100 $cm^3$ $min^{-1}$) at 773 K (2 h). BET surface areas measurements were performed using Ar as adsorbate on samples outgassed at 573 K. Pt dispersion was measured using CO pulsed chemisorption on samples reduced in $H_2$ at 573 K. Barium dispersion was determined from $CO_2$ adsorption isotherms at 298 K on samples heated to 1013 K under $N_2$. DRIFT spectra were recorded at 4 $cm^{-1}$ resolution (100 scans) using an MCT detector and Harrick environmental cell. A computer-controlled gas blender fed the desired composition of reactant gases to the IR cell, with the exit gases passed to a chemiluminescence detector for $NO/NO_2$/total NOx analysis. A quadropole mass spectrometer and 2.5 m path length gas-phase IR cell were also available for on-line product analysis. 80 mg of powdered sample was calcined *in situ* at 673 K (1 h) in the DRIFT cell in a flow of dry air (50 $cm^3$ $min^{-1}$), and either exposed to $NO_2$ at 673 K, or cooled to 298 K and exposed to $NO_2$. Previous *in-situ* XRD studies [5] indicate that at 673 K in an air/$NO_2$ flow, barium carbonate species undergo decomposition. The IR cell was then flushed in air before a TPD of NOx from the samples was performed under air or air/propene/$N_2$ flows (50 $cm^3$ $min^{-1}$) between 298 to 873 K at 3 K $min^{-1}$. Spectra recorded in transmittance mode were obtained by heating samples in a quartz cell at the desired temperature followed by lowering the sample to the optical compartment, exposing the sample to the required adsorbate and measuring the spectra at beam temperature. $NO_2$ (99.5 %) was used as supplied.

## 3. RESULTS AND DISCUSSION

### 3.1 Sample characterisation

Table 1
Sample characteristics

| Sample | BET ($m^2g^{-1}$) | Pt Dispersion (%) | $CO_2$:BaO Ratio |
|---|---|---|---|
| $Al_2O_3$ | 93.5 | - | - |
| 1 % BaO/$Al_2O_3$ | 88.3 | - | 0.45 |
| 2.5 % BaO/$Al_2O_3$ | 91.1 | - | 0.36 |
| 5 % BaO/$Al_2O_3$ | 87.1 | - | 0.27 |
| 7.5 % BaO/$Al_2O_3$ | 92.7 | - | 0.16 |
| 10% BaO/$Al_2O_3$ | 101.7 | - | 0.09 |
| Pt, 1 % BaO/$Al_2O_3$ | 93.8 | 35.2 | 0.22 |
| Pt, 5 % BaO/$Al_2O_3$ | 92.6 | 46.3 | 0.23 |
| Pt, 10 % BaO/$Al_2O_3$ | 90.9 | 51.8 | 0.21 |

XRD patterns of as prepared samples, indicated (24 and 42° 2θ) that crystalline Ba(CO₃) was present at all baria loadings, with the 1wt% sample showing the weakest peaks. BET surface areas (Table 1) were reasonably constant with little change following the addition of baria, or subsequent addition of Pt and further calcination. BaO dispersion showed an almost linear decrease as a function of loading. Platinum dispersion (assuming Pt:CO =1) unexpectedly increased as the BaO loading was increased, even though the fraction of surface covered by baria was greater at higher loadings leaving less of the alumina surface free for interaction with the Pt salt. The subsequent addition of Pt appeared to influence the dispersion

of baria with a homogenisation of the baria apparent. Previous studies [6] suggest that this results from the use of the acidic $H_2PtCl_6$ solution which effectively redisperses the baria. To eliminate any possible differences in behaviour between Pt and Pt-free samples based on baria dispersion, results presented in this study were largely performed using $5\%Ba/Al_2O_3$ and $Pt5\%Ba/Al_2O_3$ which present very similar Ba dispersions.

## 3.2 Are spillover processes involved in the formation of stored NOx?
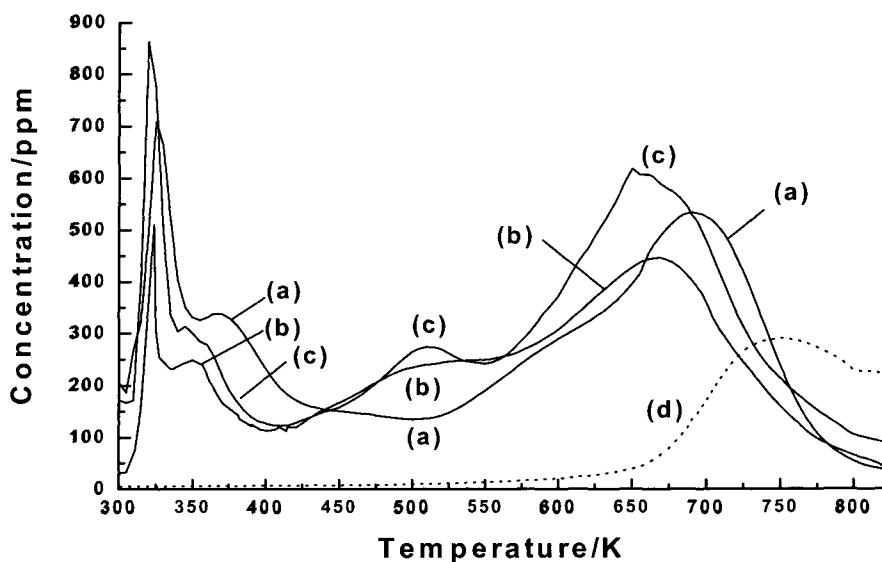


Fig. 1. TPD of $NO_2$ desorbed in air from (a) $Al_2O_3$, (b) 5% $BaO/Al_2O_3$ and (c) Pt-5% $BaO/Al_2O_3$ and (d) NO desorbed from Pt-5% $BaO/Al_2O_3$ after samples were previously exposed to $NO_2$ at 298 K

Fig.1 shows profiles of $NO_x$ desorbed from samples, which, according to XRD patterns may contain barium carbonates. FTIR spectra of the Pt-free samples show a band at *ca.* 1450 $cm^{-1}$ prior to exposure to $NO_2$ that may be attributed to such a species (Fig. 2a). However, exposure to $NO_2$ at 298 K led to the appearance of a triplet of bands around 1600 $cm^{-1}$ and another around 1300 $cm^{-1}$ which compare with those observed by Parkyns following exposure of alumina alone to $NO_2$ [7]. These bands are similarly attributed in the main to nitrate species on the alumina surface. The fact that the main contribution in IR spectra of $NO_2$ on $Ba/Al_2O_3$ is due to species on the alumina support explains why TPD profiles are similar for $Al_2O_3$, $Ba/Al_2O_3$ and $Pt/Ba/Al_2O_3$ (Fig. 1) with maxima around 350 and 650 K. The only desorption peak unique to the baria containing samples appeared at 500 K, suggesting that exposed baria sites, even though in the main covered with carbonate species, were available for adsorption of $NO_2$ after a 673 K calcination treatment.
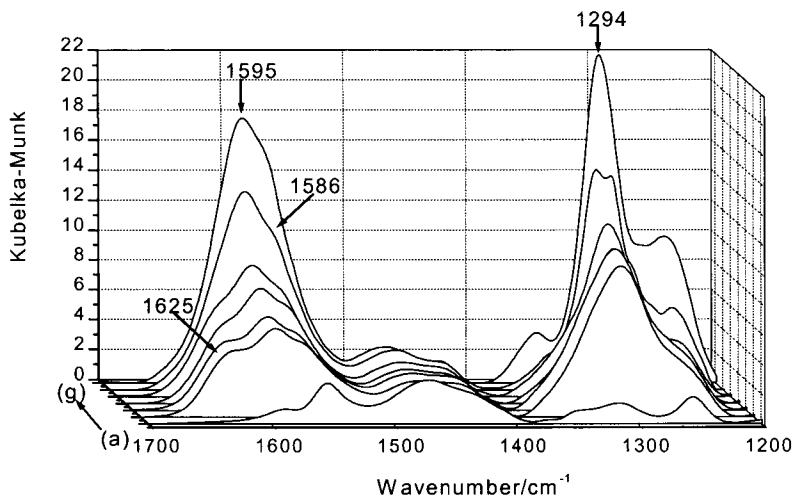
Fig. 2. FTIR of 5%BaO/Al$_2$O$_3$ (a) calcined in air at 673 K then (b) exposed to NO$_2$ at 298 K followed by heating in air (50 cm$^3$ min$^{-1}$) at (c) 345, (d) 440, (e) 530, (f) 605 and (g) 673 K.
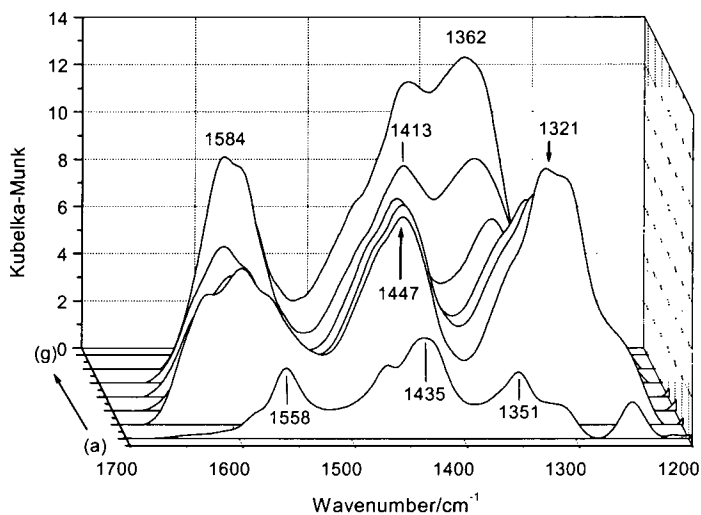


Fig. 3. FTIR spectra of Pt5%Ba/Al$_2$O$_3$ after (a) calcination in air at 673 K then (b) exposure to NO$_2$ at 298 K and then heating in air at (c) 363, (d) 400, (e) 523, (f) 623 and (g) 673 K.

Consistent with spectra of samples in the absence of Pt, a sample of Pt5%Ba/Al$_2$O$_3$ after calcination at 673 K showed bands in the 1600-1200 cm$^{-1}$ region (1558, 1469, 1351 and 1242 cm$^{-1}$) indicating that this treatment was not effective in completely removing all traces of carbonates from the sample. This is consistent with the work of others concerning the formation of stable carbonates on NOx storage catalysts [9]. Exposure to NO$_2$ generated similar species to those obtained in the absence of Pt with bands at *ca.* 1600 and 1300 cm$^{-1}$ (Fig. 3b) mainly due to adsorption on the alumina support. However an additional feature, at 1447 cm$^{-1}$ was present in the temperature range 298-523 K (Fig. 3 b-e) which was not detected for the 673 K calcined Ba/Al$_2$O$_3$ sample (Fig. 2) in the absence of Pt. To determine whether the presence of Pt was essential for the generation of this species, for example, by producing an activated form of NO$_2$ which is spiltover to exposed baria sites, samples of 5%Ba/Al$_2$O$_3$ were calcined over a range of temperatures and then exposed to NO$_2$. Fig 5 shows spectra of 5%Ba/Al$_2$O$_3$ outgassed at 1023 K and then exposed to NO$_2$ at 298 K.
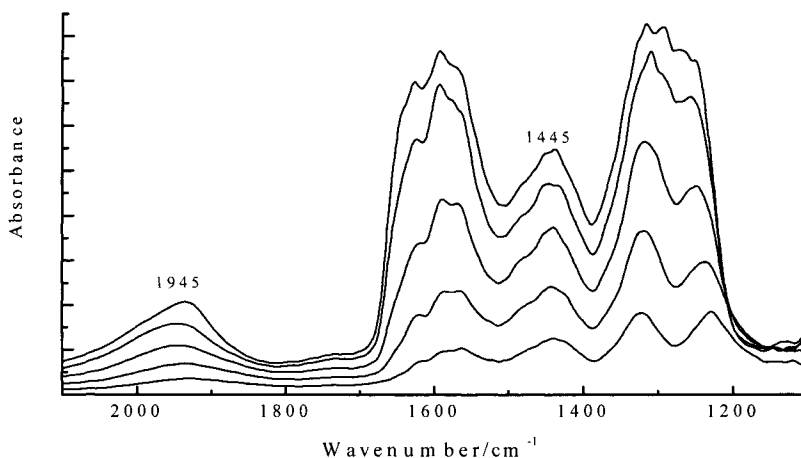


Fig. 4.   FTIR spectra of 5%Ba/Al$_2$O$_3$ outgassed at 1023 K then exposed to NO$_2$ at 298 K at pressures up to 1.0 Torr.

Spectra clearly show the growth as a function of NO$_2$ pressure of a feature at 1445 cm$^{-1}$ (Fig. 4). It would appear that the ability to observe the form of adsorbed NO$_2$ responsible for the band at *ca* 1447 cm$^{-1}$ is a function of the extent to which carbonate and other species are removed from the baria surface. The presence of platinum (compare Figs 2 and 3) apparently plays a role in assisting removal of these surface contaminants. The above experiment was conducted in vacuum thus indicating that the presence of oxygen is not required for formation of such an adsorbed nitro species. Fridell *et al.* [2] and Mestl *et al* [10-12] have proposed that oxygen is essential, however, for the nitrate formation process and that the presence of oxygen was required to convert ligated nitro species to nitrate.  Fridell *et al.* [2] suggest that Pt plays a role in this process by supplying dissociated oxygen atoms.

Initial evidence from Fig 3 might suggest that this baria adsorbed NO$_2$ species (1447 cm$^{-1}$ band) may have been a requirement for the changes observed at higher temperatures (Fig. 3 f,g) when bands at 1413 and 1362 cm$^{-1}$ became apparent. It is unclear as to whether the adsorbed NO$_2$ species (1447 cm$^{-1}$ band) was a precursor for this high temperature species.

434

However, a distinct shoulder (*ca.* 1450 cm$^{-1}$) of considerable intensity was still present in spectra recorded at 673 K (Fig. 3g), showing that such species were not significantly depleted. A similar feature (shoulder at 1460 cm$^{-1}$) was observed for our Ba/SiO$_2$ catalysts [3] and this was still present when intense bands at 1418 and 1360 cm$^{-1}$ were detected. The latter pair were assigned to the formation of barium nitrate [3] and so maxima for Pt/BaO/Al$_2$O$_3$ at 1413/1362 cm$^{-1}$ are similarly assigned. The maxima at 1413 and 1362 cm$^{-1}$ were depleted between 730 and 771 K [13], consistent with *in-situ* Raman studies [9] which indicate that crystalline Ba(NO$_3$)$_2$ was stable up to 770 K before being transformed into other species. Initial analysis of results would tend to suggest that the adsorbed nitro species giving the 1447 (1460 sh) cm$^{-1}$ band is not a precursor for barium nitrate formation and that the absence of such nitrate species for Pt-free samples (Fig. 1) results from other factors such as carbonate/other surface contamination whose removal is Pt assisted. *In-situ* XRD studies of these catalysts [5] indicate that under a NO$_2$/air flow, 673 K is the minimum temperature required to decompose bulk barium carbonate in the presence of Pt. FTIR spectra (Fig. 3f,g) indicate that under similar conditions, onset of nitrate formation occurs around 600 K, which might indicate bulk carbonate begins to decompose in the presence of NO$_2$ before reaching 673 K.
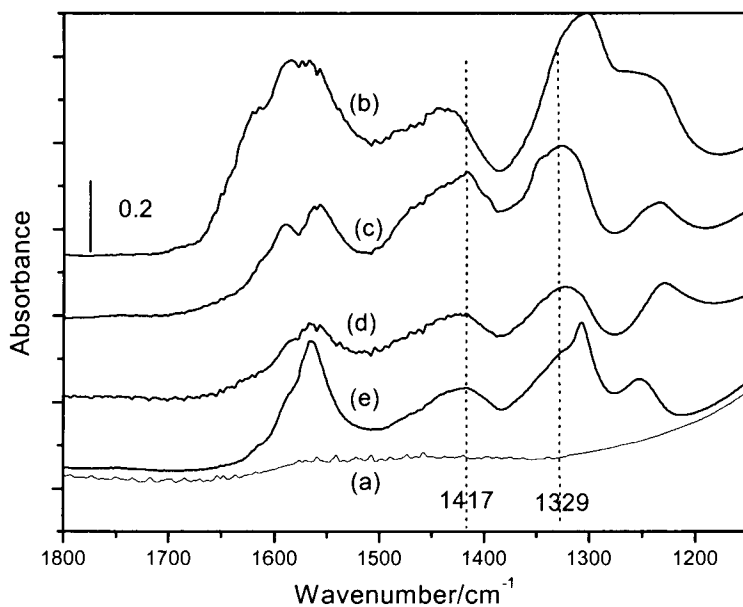


Fig.5 Transmittance IR spectra of 5%Ba/Al$_2$O$_3$ sample (a) outgassed at 1023 K and then (b) exposed to 1.0 Torr NO$_2$ at 298 K. Sample then heated to (c) 673 K in NO$_2$ before (d) addition of air (10 Torr) at 673 K and (e) evacuation at 673 K.

An alternative postulation, which would account for the co-existence of both the adsorbed nitro species and the nitrate species on the baria surface, involves a possible role of platinum in converting adsorbed nitro to nitrate. Only nitro species adsorbed on baria in intimate contact with Pt might be transformed to nitrate while nitro species adsorbed on isolated patches of baria, free from platinum are not transformed to nitrate. Note that Fridell et al. [2] report that no effective NOx storage occurs over pure BaO or $BaO/Al_2O_3$, even if $NO_2$ is used. To check this proposal, an experiment was conducted for a Pt-free sample of $5\%Ba/Al_2O_3$, which following high 1023 K outgassing (Fig. 5a), exhibited the 1445 $cm^{-1}$ band in the presence of $NO_2$ (Fig.5b) confirming the presence of adsorbed nitro species on the cleaned baria surface. The sample was then heated in the presence of $NO_2$ to determine whether conversion to nitrate in the absence of oxygen and Pt could proceed.

Spectra recorded after heating at 673 K (Fig. 5c) show two maxima at 1417 and 1329 $cm^{-1}$ which could be candidates for barium nitrate. However, in addition to differences in band positions, these band were much less dominant than those observed in spectra of $Pt5\%Ba/Al_2O_3$ recorded at 673 K (Fig. 3g) which had shown such a clear, well resolved doublet at 1413/1362 $cm^{-1}$ due to barium nitrate formation. One must conclude that spectra in figure 5 do not represent conversion of nitro to significant quantities of nitrate. Heating to 723 K did not lead to further significant changes in the spectrum. In an attempt to induce nitrate formation, dry air was introduced to the sample. Heating at 673 K in air/$NO_2$ (Fig. 5d) or by evacuation at 673 K (to eliminate re-adsorption of $NO_2$ on the alumina)(Fig. 5e) failed to increase the yield of these species or to shift the band positions towards those observed for the $Pt5\%Ba/Al_2O_3$ sample (Fig. 3g).

One plausible explanation for the above results is that bands at 1417/1329 $cm^{-1}$ for $Ba/Al_2O_3$ were due to a surface type nitrate and that only in the presence of platinum is bulk barium nitrate formation (1413/1362 $cm^{-1}$) possible. Note that Fridell et al. [2] suggest that Pt plays a role in nitrate formation by supplying dissociated oxygen atoms and that no effective NOx storage can occur over pure BaO or $BaO/Al_2O_3$, even if $NO_2$ is used. Our spectral interpretation would be consistent with these findings. As the dispersion of baria was similar for both Pt containing and Pt-free samples (Table 1), an interpretation of the different band frequencies in terms of different baria structures is dismissed.

If effective nitrate formation does require the presence of platinum, how is the surface nitrate species generated in Fig 5? It is worth considering other mechanisms of nitrate formation. Transmittance spectra in Fig. 4 clearly show an additional feature not readily observed in spectra obtained in the diffuse reflectance mode. The band at 1945 $cm^{-1}$ has been observed in previous studies of $NO_2$ adsorbed on alumina and alumina supported catalysts [7,8] and attributed to the nitrosonium ion ($NO^+$). The dimmer of $NO_2$ is known to undergo self-ionisation to produce nitrosonium and nitrate ions:

$$2NO_2 + \tfrac{3}{4} N_2O_4 \rightarrow \tfrac{3}{4} NO^+ + NO_3^-.$$
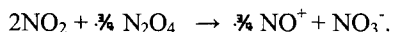
The adsorption of both types of ions would clearly shift the above equilibria towards the formation of such species. The direct formation of nitrate from $N_2O_4$ was used to explain barium nitrate formation over $Pt/BaCl_2/SiO_2$ catalysts [3]. While such a reaction would readily justify the formation of surface type nitrates formed on alumina, where the nitrate ion would coordinate to exposed aluminium cations at the surface [7], the above reaction is unlikely to account for the formation of barium nitrate species of longer range 3-D order, as this would leave the structure with a distinct oxygen ion excess. It is quite plausible that such a process is responsible for the formation of the surface nitrate species on baria (Fig. 5) formed by heating a cleaned baria surface in the presence of $NO_2$ but in the absence of

436

platinum. In the presence of platinum, a supply of, most likely some form of activated oxygen [2], allows the process to continue one step further, leading to the formation of bulk barium nitrate. Only on completion of this step does effective storage take place. Note that the same catalysts when examined by *in-situ* XRD [5] did not reveal the presence of 3-D nitrate species although similar treatments lead to the detection of IR bands at 1413 and 1362 cm$^{-1}$. This was interpreted in terms of $NO_2$ diffusion being limited to the first few surface layers.

## 4. CONCLUSIONS

$NO_2$ formed by NO oxidation over platinum is adsorbed by clean baria surfaces in the form of an adsorbed nitro species. The presence of carbonate blocks nitro formation on low temperature treated baria, although the presence of Pt in the process assists in the decomposition process. In the absence of Pt, conversion of nitro species to adsorbed nitrate is possible, however Pt is required for bulk nitrate formation, probably by providing some form of activated oxygen *via* spillover to the baria sites.

## REFERENCES

1. N. Takahashi, H.Shinjoh, T. Iijima, T. Suzuki, K. Yamazaki, K. Yokota, H. Suzuki, S. Matsumoto, T. Tanizawa, T. Tanaka, S. Tateishi and K. Kashara, Catal. Today, 27 (1996) 63.
2. E. Fridell, M. Skogludh, B. Westerberg, S. Johansson and G. Smedler, J. Catal., 183 (1999) 196.
3. J.M. Coronado and J.A. Anderson, J. Molec. Catal., 138 (1999) 83.
4. J.A. Anderson, A.J. Paterson and M. Fernández-García, Stud. Surf. Sci. and Catal., 130 (2000) 1331.
5. J.A. Anderson and M. Fernández-García, Trans IChemE., 78 (2000) 935
6. A. Sepulveda-Escribano, M. Primet and H. Praliaud, App. Catal. A., 108 (1994) 221.
7. N.D. Parkyns, Proc. 5$^{th}$ Inter Cong. Catal., p-255, J.W. Hightower (ed.) North Holland, Amsterdam, 1973.
8. J.A. Anderson, G.J. Millar and C.H. Rochester, J.C.S. Faraday Trans, 86 (1990) 86.
9. S. Hodjati, P. Bernhardt, C. Petit, V. Pichon and A. Kiennemann, Appl. Catal., 19 (1998) 209 and 221.
10. H.Knözinger and G.Mestl, Topics in Catal., 8 (1999) 45.
11. G.Mestl, M.P.Rosynek and J.H.Lunsford, J. Phys. Chem. B, 101 (1997) 9321
12. G.Mestl, M.P.Rosynek and J.H.Lunsford, J. Phys. Chem. B, 101 (1997) 9329.
13. A.J. Patterson, M. Fernández-García and J.A. Anderson, manuscript in preparation.

# Alumina supported molybdenum-nickel carbides as catalysts for the dry reforming of methane

P. Ferreira-Aparicio[a], S. Menad[b], A. Guerrero-Ruiz[c] and I. Rodríguez-Ramos[a].

[a] Instituto de Catálisis y Petroleoquímica. CSIC. Campus de Cantoblanco. 28049 Madrid. Spain.
[b] Departement de Chimie. Université de Tizi-Ouzou- M. Mammeri. Tizi Ouzou. Algeria.
[c] Dpto. de Química Inorgánica y Técnica. Facultad de Ciencias. UNED. C/ Senda del Rey, s/n. 28040 Madrid. Spain.

Bimetallic molybdenum-nickel catalysts supported on alumina have been studied in the carbon dioxide reforming of methane. Two different temperature-programmed reduction (TPR) pretreatments have been followed for their synthesis: using hydrogen to obtain metallic molybdenum and using a $CH_4/H_2$ reactant mixture to obtain molybdenum carbides, which have shown better performance in the reaction. Although in nickel catalysts the surface mobility of carbon species generated from methane decomposition leads to the accumulation of great amounts of carbon deposits in the support surface, the presence of molybdenum has been observed to avoid these migration processes. The synergic effect found between both metals in Ni-Mo bimetallic samples reduces the temperature of carburization of molybdenum, improves its catalytic activity and its selectivity to hydrogen in the $CH_4+CO_2$ reaction at the same time that avoids the formation of undesired carbon structures caused by methane decomposition.

## 1. INTRODUCTION

Since the last decade the conversion of methane by reforming with carbon dioxide has attracted a great deal of attention as an alternative way for syngas production [1]. In addition to the lower $H_2/CO$ ratio yielded by this reaction as compared with those from steam reforming and partial oxidation, this reaction is an interesting route for the recycling of carbon dioxide [2]. Its characteristic high endothermicity makes of this reaction one of the reversible chemical processes more suitable to be applied in chemical energy transmission systems.

Carbides of transition metals are of great interest because of their many and varied applications as result of their characteristics of hardness, their particular electronic and magnetic properties and their catalytic performance in a variety of chemical reactions [3]. These materials, and in particular molybdenum and tungsten carbides, have been proposed to be potential substitutes of VIII group metals as catalysts [4]. The main problem that the use of these carbides poses is the difficulty in obtaining materials with enough surface area to be used in

catalytic applications. Both molybdenum and tungsten carbides have been studied in a great variety of reactions but few publications have been devoted to processes involving the methane conversion reactions [4-5]. Nickel is one of the most active metals to catalyze this reaction, but its tendency to accumulate high amounts of carbon usually leads to deactivate catalysts.

In previous papers, different evidences concerning the importance of the surface mobility and reactivity of intermediate species on supported catalysts have been presented for this reaction [6]. In this paper we report a study of the catalytic properties for the dry reforming of methane of alumina supported molybdenum carbides, which have been prepared by temperature-programmed reduction of the supported oxide under a $H_2/CH_4$ mixture. Their activity and properties have been compared with those of the uncarburized samples prepared by temperature-programmed reduction in hydrogen. We have also studied the effects of adding a small amount of nickel to the catalysts and have compared their performances with an alumina-supported nickel catalyst with the same nickel loading following the same pretreatment.

## 2. EXPERIMENTAL

Three catalysts, $Mo/Al_2O_3$, $Mo-Ni/Al_2O_3$ and $Ni/Al_2O_3$, were prepared by impregnation of a $\gamma-Al_2O_3$ support (Puralox Condea) with aqueous solutions of the precursor salts: $(NH_4)_6Mo_7O_{24}\cdot4H_2O$ (Aldrich), $Ni(NO_3)_2\cdot6H_2O$ (Merck). The ammonium heptamolybdate concentration in the solution was calculated to obtain a nominal molybdenum loading in the catalysts of 10%-wt. The amount of nickel in the nickel-containing catalysts was the same, and was calculated to have a ratio Mo/Ni=10 in the bimetallic catalyst, approximately a loading of 0.5%-wt. The exact metal content was determined by chemical analysis. After impregnation the catalysts were dried at 393 K overnight and calcined in air at 873 K for 3 h.

Temperature programmed reduction and carburization reactions (TPR/TPRC) were performed in a flow micro reactor at atmospheric pressure. Mixtures of $H_2:N_2$ or $H_2:CH_4:N_2$ in proportions 10:90 and 10:10:80 respectively, were used for the experiments. Total flow rates of 3.0 $l\cdot h^{-1}$ were adjusted by means of mass flow controllers. For a typical TPR/TPRC experiment an amount of 0.5 g of catalyst was placed in the reactor between two quartz wool plugs and was heated under the required gas mixture at a rate of 4 K/min up to 1073 K. The gas phase composition at the reactor outlet was continuously analyzed by gas chromatography.

Reaction experiments with $CH_4$ and $CO_2$ were carried out with amounts of catalysts between 0.025 and 0.500 g in order to avoid reaching the thermodynamic equilibrium. A mixture of $CH_4:CO_2:N_2$ in proportions 10:10:80 at a total flow rate of 6.0 $l\cdot h^{-1}$ was used. A sample of unsupported molybdenum prepared from $MoO_3$ (Fluka) was also tested for comparison.

X-ray powder diffraction was carried out for structural characterization of the used samples. The nature of the different phases present on the catalysts

after each treatment was determined using the database of the Joint Committee on Powder Diffraction Standards (JCPDS).

## 3. RESULTS AND DISCUSSION

Table 1 summarizes the chemical composition of the different catalysts and their degree of reduction at 1073 K under hydrogen atmosphere calculated from the $H_2$ consumption during the TPR experiments.

**Table 1.** Chemical composition and degree of reduction of the catalysts after reduction in $H_2:N_2$ mixture. [a] Degree of reduction. [b] Unsupported sample of $MoO_3$ (Fluka). [c] Stoichiometric $H_2$ consumption for $Ni^{2+}:Ni^0$ ($mmol \cdot g^{-1}$).

| Catalyst | Metal loading (%) | | $H_2$ consumption from TPR (mmol/g) | | Stoichiometric $H_2$ consumption (mmol/g) | | $X^a$ |
|---|---|---|---|---|---|---|---|
| | Mo | Ni | Peak 700 K | Peak 1073 K | $Mo^{6+}:Mo^{4+}$ | $Mo^{4+}:Mo^0$ | |
| $Mo^b$ | 100 | -- | -- | 10.45 | 6.95 | 13.89 | 0.50 |
| $Mo/Al_2O_3$ | 9.2 | -- | 0.96 | 1.84 | 0.96 | 1.93 | 0.97 |
| $NiMo/Al_2O_3$ | 9.3 | 0.5 | 0.97 | 2.16 | 0.97 | $1.94(+0.17)^c$ | 1.00 |
| $Ni/Al_2O_3$ | -- | 0.5 | -- | -- | | 0.18 | -- |

The profiles obtained for bulk molybdenum and for the $Mo/Al_2O_3$ and Ni-$Mo/Al_2O_3$ samples are shown in Figure 1. The $Ni/Al_2O_3$ catalyst did not show any defined peak of reduction, so its profile has not been included in the figure.
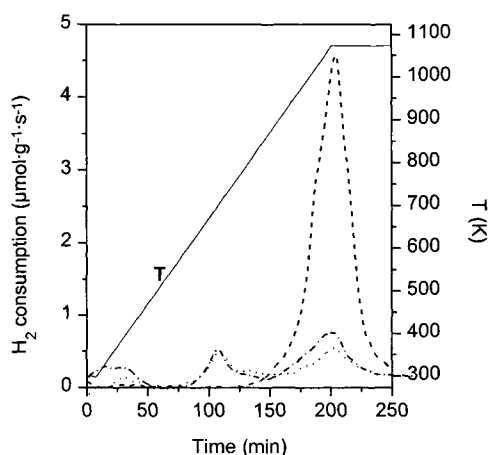


**Figure 1.** TPR profiles under $H_2:N_2$ mixture: (– – –) $MoO_3$, ($\cdots$) $Mo/Al_2O_3$, (– · – · –) Mo-$Ni/Al_2O_3$. (——)Temperature.

The reduction of $MoO_3$ in hydrogen to metallic molybdenum is known to occur in two stages: a first one from $MoO_3$ to $MoO_2$ and a second one from $MoO_2$ to Mo in metallic state [7]. In the case of unsupported molybdenum oxide only one reduction peak was observed up to 1073 K. The percentage of reduction in it, calculated from the $H_2$ consumed during the experiment (Table 1), indicates that it has been completely reduced to $MoO_2$ but the second reduction stage has not been completed. For the alumina-supported samples the molybdenum reduction process was observed to take place in two differentiated stages and at lower temperature: the first step at 705 K can be attributed to the reduction of $MoO_3$ to $MoO_2$, and the second one, at temperatures above 873 K, corresponds to the reduction of $MoO_2$ to metallic Mo. The hydrogen consumption in the case of the supported samples (Table 1) indicates that molybdenum is completely reduced to its metallic state at 1073 K. For the $Mo-Ni/Al_2O_3$ catalyst, an additional contribution in the second peak can be also appreciated at temperatures about 1000 K, which agrees well with the hydrogen consumption values estimated in Table 1 for the reduction of $Ni^{2+}$ present in the catalyst.

The reduction of the samples under the $CH_4:H_2:N_2$ mixture gave place to the TPRC profiles shown in Figure 2. As a general trend, the first reduction step from $MoO_3$ to $MoO_2$ gave place to $H_2$ consumption curves very similar to those obtained under diluted hydrogen. Once this stage was completed, methane consumption began and hydrogen was not consumed but produced by dehydrogenation of methane. $CH_4$ decomposition was accompanied in all cases with $H_2$ evolution, which was found to correspond to the complete dehydrogenation of methane. The carburization process of $MoO_2$ proceeded simultaneously with the reduction of $Mo^{4+}$ to its metallic state in agreement with previous studies [7]. The carbide formation in the bulk $MoO_3$ began after some time at the final temperature (1073 K). By considering that molybdenum was partially reduced under $H_2$ at that temperature, it is also probably that the carburization process of molybdenum was neither completed.

In the monometallic $Ni/Al_2O_3$ and $Mo/Al_2O_3$ catalysts methane decomposition was observed to take place above 975 K. The decrease observed in the temperature for the reduction-carburization process in the $Mo-Ni/Al_2O_3$ catalyst reveals a synergic effect between the two metals, Mo and Ni. Both metals are probably closely interacting in this catalyst forming an alloy with different properties. An estimation of the amount of $CH_4$ consumed during the TPRC in the supported samples indicates that the quantity of carbon retained in them exceeds in all cases by more than ten times the stoichiometry of the most stable nickel and molybdenum carbides ($Ni_3C$ and $Mo_2C$). It is well known that methane requires the presence of an active metallic surface for its decomposition (Ni or Mo). The presence of carbon in higher amounts than the stoichiometric ones suggests that processes of surface diffusion of carbon species from the metals to the support are probably taking place on these supported samples leading to the accumulation of some carbon deposits on the support surface.
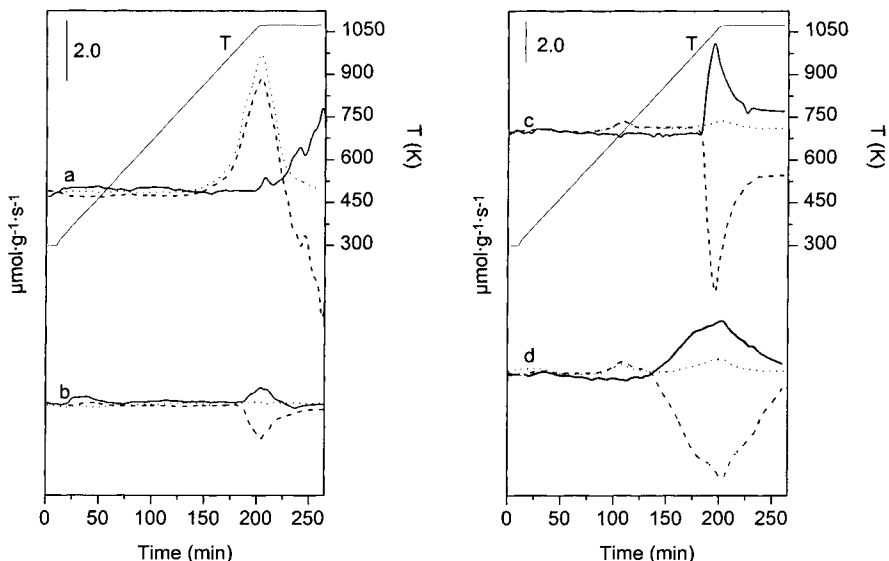
**Figure 2.** TPRC profiles under $H_2$:$CH_4$:$N_2$ mixture: (- - -) $H_2$ consumption, (——) $CH_4$ consumption. (a) $MoO_3$, (b) $Ni/Al_2O_3$, (c) $Mo/Al_2O_3$, and (d) $Mo-Ni/Al_2O_3$. (· · · ·) $H_2$ consumption under the $H_2$:$N_2$ mixture (TPR) is also plotted for comparison.

Catalytic activity data obtained in the $CH_4+CO_2$ reaction at 1073 K are compiled in Table 2 for both the reduced and carburized samples. In general, two main aspects should be stand out for the carburized molybdenum samples in comparison with those reduced under hydrogen. The carbide formation seems to induce in molybdenum a higher ability for $CH_4$ conversion giving place to more active catalysts. On the other hand, carburized samples also provide higher yields to $H_2$. The selectivity towards hydrogen is in this reaction an indicator of the reverse water gas shift (RWGS): $CO_2+H_2 \Leftrightarrow CO+H_2O$. The occurrence of this secondary reaction is also evidenced by the excess of carbon dioxide consumption with respect to methane, according to the stoichiometry of the dry methane reforming reaction ($CH_4+CO_2 \Leftrightarrow 2CO+2H_2$). The high ratios between the amounts of $CO_2$ and $CH_4$ converted for the uncarburized samples are probably consequence of an easier oxidation by $CO_2$ of metallic Mo to $MoO_2$ as compared to the molybdenum carbide. Data in Table 2 also reveals the enormous differences in catalytic performance between Mo and Ni. The modification of molybdenum samples with a small amount of nickel does not show an addition effect in their properties. For the reduced $Mo-Ni/Al_2O_3$ catalyst no significant changes in activity were observed as result of the nickel addition, in contrast with the carburized sample. In this latter case activity was increased by one order of magnitude, although its performance level is still far away from that of the

Ni/Al₂O₃ sample. This fact reveals, in agreement with the TPR/TPRC results, the strong interaction between both metallic components. This synergic effect between both metals acquires special relevance for the $CH_4+CO_2$ reaction after the carburization process.

**Table 2.** Catalytic activity data for the dry reforming reaction at 1073 K. Reactant gas mixture: $CH_4:CO_2:N_2$ (10:10:80). Flow rate: 6.0 l·h⁻¹.

| Catalyst | Treatment in $H_2/N_2$ | | | Treatment in $H_2/CH_4/N_2$ | | |
|---|---|---|---|---|---|---|
| | Activity | $CO_2/CH_4$ | $S_{H_2}$ | Activity | $CO_2/CH_4$ | $S_{H_2}$ |
| | ($\mu$mol $CH_4 \cdot g^{-1} \cdot s^{-1}$) | converted | (%) | ($\mu$mol $CH_4 \cdot g^{-1} \cdot s^{-1}$) | converted | (%) |
| Mo | 0.01 | 17.3 | 4.4 | 0.48 | 4.9 | 22.9 |
| Mo/Al₂O₃ | 1.20 | 2.5 | 26.2 | 1.41 | 1.4 | 63.7 |
| NiMo/Al₂O₃ | 1.28 | 2.4 | 30.0 | 11.55 | 1.3 | 66.3 |
| Ni/Al₂O₃ | 182.93 | 1.1 | 88.5 | 222.75 | 1.1 | 88.7 |

It must also be noticed that the carburization treatment did not lead to deactivate the Ni/Al₂O₃ sample, although great amounts of carbon were surely deposited in the catalyst during the treatment in $CH_4$. These carbonaceous species generated on the nickel surface by methane decomposition are probably accumulated in the support. The surface mobility and migration processes in this catalyst plays an important role by keeping the nickel surface free from carbon deposits.
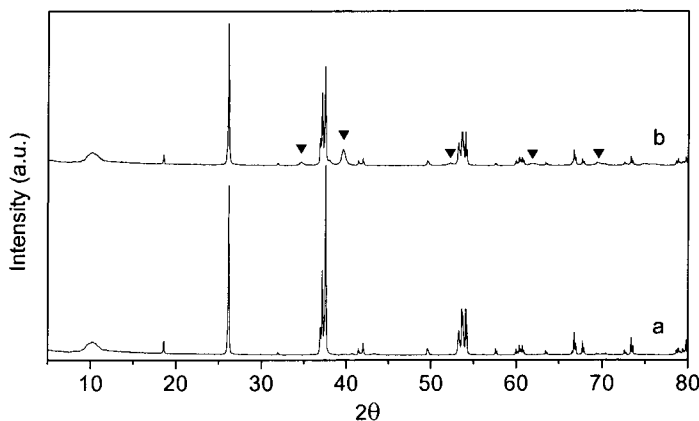


**Figure 3.** XRD profiles for the MoO₃ samples after 1 hour in reaction with $CH_4$ and $CO_2$ at 1073 K. (a) pretreated under the $H_2:N_2$ mixture at 1073 K, (b) pretreated under the $H_2:CH_4:N_2$ mixture at 1073 K. (▼): peaks corresponding to β-Mo₂C.

X-ray diffraction analysis of the MoO₃ samples after reaction with $CH_4$ and $CO_2$ (Figure 3) showed the presence of MoO₂ as the major phase in both reduced

and carburized samples, although $MoO_3$ pretreated under the $H_2:CH_4:N_2$ mixture at 1073 K also presented additional peaks corresponding to $\beta$-$Mo_2C$. The presence of $MoO_2$ agrees well with TPR and reaction results, which indicate that $MoO_3$ in bulk samples is mainly reduced to $MoO_2$ and metallic Mo is oxidized to $MoO_2$ with $CO_2$ under reaction conditions. In the case of the sample treated under the $H_2:CH_4:N_2$ mixture, the appearance of $MoO_2$ together with $Mo_2C$ correlates well with the TPRC results, which showed that 1073 K is a low temperature for the carbide formation in this kind of samples. Although methane decomposition was observed to begin at this temperature after $MoO_2$ formation, the carburization process was not completed and affected only to the most external layers of the sample.
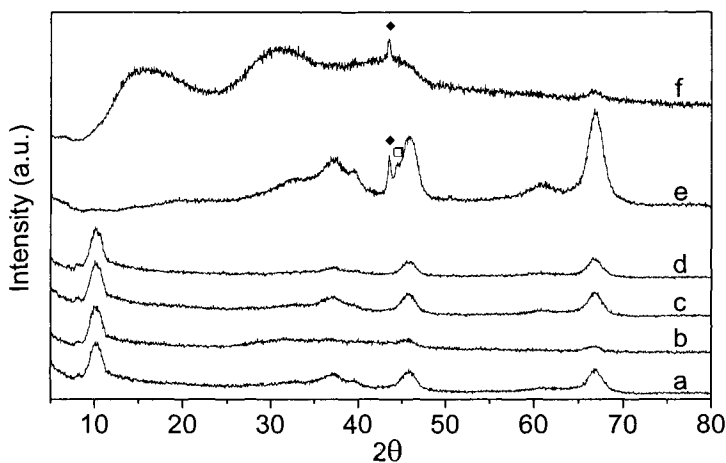


**Figure 4.** XRD profiles for the catalysts after 1 hour in reaction with $CH_4$ and $CO_2$ at 1073 K. (a) reduced $Mo/Al_2O_3$, (b) carburized $Mo/Al_2O_3$, (c) reduced Mo-$Ni/Al_2O_3$, (d) carburized Mo-$Ni/Al_2O_3$, (e) reduced $Ni/Al_2O_3$, (f) carburized $Ni/Al_2O_3$. (♦) NiO, (□) Ni.

For supported catalysts (Figure 4) the main peaks in the difractogram were observed to correspond to the alumina structure at 2θ values of 37.30°, 45.83° and 66.81°. Peaks corresponding to molybdenum phases were neither detected in reduced nor carburized samples. This fact gives indication of the good dispersion of the Mo active phase in these catalysts. Only a broadened peak at 2θ=12.28°, which also was observed in bulk molybdenum, was detected. For the $Ni/Al_2O_3$ sample treated under the $H_2:N_2$ mixture, in addition to the alumina features, peaks corresponding to metallic nickel at 2θ 44.52° and to nickel oxide (NiO) at 43.47° were also found. For the carburized $Ni/Al_2O_3$ the alumina peaks disappeared in the difractogram, fact that confirms the formation of large amounts of carbon on its surface. Only nickel oxide could be detected after the reaction on it. The broad bands observed at 2θ values of 15°, 31° and 44° concur with the diffraction features obtained for amorphous activated carbon. Nickel

444

catalysts are known to be prone to carbon deposition and it is generally claimed that carbon formation within the pores of the support leads to breakup the catalyst particles and to plug the reactor. In contrast with the results obtained for Ni/Al$_2$O$_3$, after the carburizing treatment molybdenum-containing samples did not revealed so high carbon accumulation and the structure of the alumina support remained practically unaffected even in the nickel modified catalysts. Furthermore, for the bimetallic Mo-Ni/Al$_2$O$_3$ sample no peaks due to any nickel phase were detected, indicating also a better dispersion of the nickel in the presence of molybdenum.

The obtained results indicate that the addition of small amounts of nickel to the alumina-supported molybdenum catalysts improves the behavior of molybdenum carbide as catalyst for the carbon dioxide reforming of methane. The synergic effect of both metals found in these samples not only reduces the temperature of carburization of molybdenum, but also improves its catalytic activity and its selectivity to hydrogen in the CH$_4$+CO$_2$ reaction at the same time that avoids the formation of undesired carbon structures caused by methane decomposition. The mobility of carbonaceous species, which are generated at higher rate in the nickel centers, is probably limited by molybdenum, which incorporates the carbon atoms to its structure to form the carbide. These preliminary results could establish the basis for further studies focused to optimize the Ni:Mo ratio in these bimetallic Ni-Mo catalysts. The reduction of the carbon deposition caused by molybdenum and the increase of the activity induced by nickel are promising properties of these samples, which would be interesting to apply to the design of new catalysts for the dry reforming of methane.

## REFERENCES

1   M. C. J Bradford and M. A. Vannice. Catal. Rev.-Sci. Eng. (1999) 1.
2   J. H. Edwards. Catal. Today 23 (1995) 59.
3   S. T. Oyama, *The Chemistry of transition metal carbides and nitrides*; S. T. Oyama, Ed., Blackie Academic & Professional: Glasgow. Scotland. (1996) 1.
4   J. B. Claridge, A. P. E. York, A. J. Brungs, C. Marquez-Alvarez, J. Sloan, S. C. Tsang and M. L. H. Green. J. Catal. 180 (1998) 85.
5   A. P. E. York, J. B. Claridge, A. J. Brungs, S. C. Tsang and M. L. H. Green. Chem. Commun. (1997) 39.
6   P. Ferreira-Aparicio, I. Rodríguez-Ramos, J. A. Anderson, A. Guerrero-Ruiz. J. Catal. 190 (2000) 296.
7   S. T. Oyama. Catal. Today 15 (1992) 179.

445

# Selective Hydrogenation of 1,3-Butadiene on Molybdenum Nitride Catalyst: Identification of the Adsorbed Hydrocarbonaceous Species

Zili Wu, Zhixian Hao, Zhaobin Wei, Can Li* and Qin Xin*

State Key Laboratory of Catalysis, Dalian Institute of Chemical Physics,
Chinese Academy of Sciences, P.O. Box 110, Dalian 116023, China
Fax +86 411 4694447, E-mail: canli@ms.dicp.ac.cn; xinqin@ms.dicp.ac.cn

The hydrogenation of 1,3-butadiene has been studied on $\gamma$-Mo$_2$N catalyst. The $\gamma$-Mo$_2$N catalyst was found to be selective to hydrogenate 1,3-butadiene to 1-butene (selectivity is 87% at the conversion of 35% at 333 K). But the activity decreased gradually with reaction time. The surface species from 1,3-butadiene adsorption and reaction on molybdenum nitride were studied by IR and temperature-programmed surface reaction (TPSR) techniques. The presence of surface hydrocarbonaceous species was identified by both IR and H$_2$-TPSR. They cause the deactivation of the nitride catalyst and increase the selectivity to 1-butene in the hydrogenation of 1,3-butadiene. Their participation in the hydrogenation reaction is interpreted by means of hydrogen transfer.

## 1. INTRODUCTION

The selective hydrogenation of dienes in C4 alkene cuts has received considerable attention because of its great importance in manufacturing high-purity alkene streams [1]. The active components of the catalysts for the reaction are usually noble metals such as palladium, platinum, etc. Unfortunately, a certain amount of carbon monoxide or some other poisons has to be added to the feed to inhibit the further hydrogenation of olefins [2], because olefins are very easily to be hydrogenated to alkanes on most noble metal catalysts. Therefore, it has been an attractive objective for a long time to develop catalysts, especially non-noble metal catalysts [3], for the selective hydrogenation of dienes to olefins, particularly for the selective hydrogenation of 1,3-butadiene to butene.

Recent studies on transition metal carbides and nitrides have shown that these catalysts resemble Group VIII metals in a number of hydrogen-involved reactions. For example, they are active in hydrogenation of ethene [4] and carbon monoxide [5]. Very recently, our studies have shown that molybdenum nitride catalyst has mild activity but high selectivity in hydrogenation of ethyne to ethene [6]. The results show a promising prospect for the application of transition metal nitride catalysts in the field of selective hydrogenation.

On noble metal catalysts, considerable attentions have been focused on the understanding of the role of hydrocarbonaceous species in the hydrogenation of diene because these species are assumed to be of importance for the activity and selectivity of the catalysts [7, 8]. Formation of various multiple bonded so-called spectator species and surface oligomers on

the metal sites leads to the decrease of hydrogenation activity and finally to the regeneration of the catalyst, meanwhile the presence of surface hydrocarbons alters the selectivity of alkene formation.

In this paper, the hydrogenation of 1,3-butadiene on $\gamma$-Mo$_2$N catalyst was tested. The activity decreased while the selectivity to 1-butene increased with reaction time. FT-IR spectroscopy and Temperature-Programmed Surface Reaction (TPSR) techniques were employed to investigate the surface hydrocarbonaceous species from 1,3-butadiene adsorption and reaction on molybdenum nitride catalyst. The possible roles of the surface hydrocarbons in the hydrogenation reaction were tentatively discussed.

## 2. EXPERIMENTAL

### 2.1. Catalyst Preparation

The starting material of the unsupported Mo nitride was a commercial MoO$_3$. MoO$_3$/$\gamma$-Al$_2$O$_3$ sample with Mo loading of 10 wt% was prepared by incipient wetness impregnation of $\gamma$-Al$_2$O$_3$ ($S_{BET}$ = 172 m$^2$/g) with an aqueous solution of (NH$_4$)$_6$Mo$_7$O$_{24}$, followed by drying at 393 K overnight and calcination at 773 K for 4 h.The unsupported molybdenum nitride and alumina-supported molybdenum nitride were prepared by the temperature-programmed reaction of their corresponding metal oxide precursors with ammonia as following procedures: the temperature was increased from room temperature (RT) to 623 K in 1 h and from 623 K to 973 K in 6 h, then the temperature was maintained at 973 K for another 2 h. Passivated Mo$_2$N/$\gamma$-Al$_2$O$_3$ sample were prepared from the nitrided sample which was passivated at RT in a stream of 1% O$_2$/N$_2$ so as to avoid the violent oxidation of the freshly prepared nitride.

### 2.2. Catalytic Tests and Temperature-Programmed Surface Reaction (TPSR) Studies

The hydrogenation of 1,3-butadiene was carried out in a fixed-bed continuous flow microreactor, which is made of quartz, at atmospheric pressure. The reactor is 300 mm long with a diameter of 7 mm. A thermocouple was placed in the middle of the catalyst bed to measure the reaction temperature. A temperature controller, connecting to an outside heater, was used to maintain the temperature of the reaction. The $\gamma$-Mo$_2$N catalyst was prepared in situ in the reactor and was treated with H$_2$ at 723 K for 1 h, then treated with Ar at the same temperature for 0.5 h and cooled down to reaction temperature at 333 K in Ar. The feedstock, which was a mixture of 2.0 vol% 1,3-butadiene and 3.0 vol% H$_2$ in pure Ar, was controlled by mass flowmeter. The products and the feedstock were analyzed on-line by a gas chromatograph using an activated silica gel column and an FID.

The $\gamma$-Mo$_2$N catalyst for TPSR studies was pretreated the same as before the hydrogenation reaction. Adsorption of 1,3-butadiene was carried out at 333 K for a certain time. Then the catalyst was purged with H$_2$ for 1 h at 333 K, and heated at 5 K/min in flowing H$_2$. The consumption of H$_2$ was analyzed by the gas chromatograph. An H$_2$-TPSR study of the post-reaction $\gamma$-Mo$_2$N catalyst was also conducted.

### 2.3. IR Studies

The procedure of IR studies is similar to those described in previous work [9-11]. Specifically, a passivated Mo$_2$N/$\gamma$-Al$_2$O$_3$ sample was pressed into a self-supporting wafer (ca. 15 mg/cm$^2$) and renitrided in flowing ammonia in a quartz IR cell with CaF$_2$ windows. The
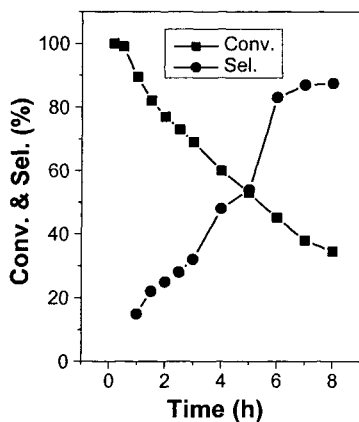
Fig. 1. Activity and selectivity of 1,3-butadiene hydrogenation on γ-Mo₂N as a function of reaction time at 333 K, SV= 7000 h⁻¹.
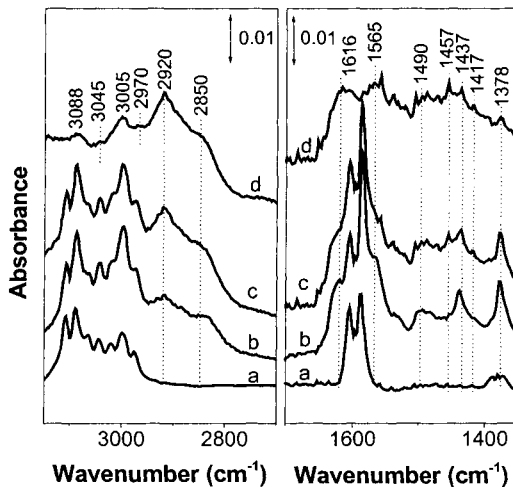
Fig. 2. IR spectra of 1,3-butadiene adsorbed on (a) nitrided Al₂O₃; (b) Mo₂Nγ-/Al₂O₃ catalyst for 1 min and (c) for 30 min; (d) outgassing of (c) at RT.

sample was heated from RT to 623 K in 30 min, then to 723 K in 100 min, further from 723 K to 873 K in 75 min, and finally held at this temperature for 60 min. The sample renitrided in the IR cell is called $Mo_2N/Al_2O_3$ or nitrided sample. Identical IR spectra of adsorbed CO were obtained for CO adsorption on the samples either from the nitridation of $MoO_3/\gamma-Al_2O_3$ or from the renitridation of passivated $Mo_2N/\gamma-Al_2O_3$. So passivated $Mo_2N/\gamma-Al_2O_3$ instead of $MoO_3/\gamma-Al_2O_3$ was used as the starting sample in the IR cell, otherwise it takes long time to nitride $MoO_3/\gamma-Al_2O_3$ sample.

The as-prepared sample was evacuated at 773 K for 60 min, and subsequently cooled down to RT. About 1 Torr (1 Torr = 133.33 Pa) 1,3-butadiene was introduced into the IR cell for adsorption experiment. IR spectra were collected at different adsorption time. After adsorption of butadiene for 2 h, the sample was outgassed at different temperatures and the corresponding spectra were acquired. All infrared spectra were collected at RT on a Fourier transform infrared spectrometer (Nicolet Impact 410) with a resolution of 4 cm⁻¹ and 64 scans in the region 4000-1000 cm⁻¹.

## 3. RESULTS

### 3.1. Selective Hydrogenation of 1,3-Butadiene on γ-Mo₂N

The main feature of 1,3-butadiene hydrogenation with reaction time on γ-Mo₂N is shown in Figure 1, where 1,3-butadiene conversion and 1-butene selectivity are presented as a function of reaction time at the reaction temperature of 333 K. The conversion of 1,3-butadiene drops

greatly from initial ca. 100% to about 35% after 8-h on steam. Meanwhile, the selectivity to 1-butene increases dramatically from about 15% to 87%.

Obviously, the γ-Mo₂N catalyst loses its activity slowly in the hydrogenation of 1,3-butadiene with the reaction time, indicating a deactivation/change of the surface active sites. It is possible to propose that some hydrocarbonaceous species form on the catalyst surface in the reaction condition, which leads to the deactivation of the nitride catalyst. But with the decrease of the activity, the selectivity to 1-butene increases, which may suggest that the new surface sites are favorable for the formation of 1-butene. To confirm the presence of these surface species, following IR and TPSR studies were carried out.

### 3.2. IR Results
### 3.2.1. Adsorption of 1,3-Butadiene on $Mo_2N/\gamma-Al_2O_3$

Figure 2 shows the IR spectra of 1,3-butadiene adsorbed on nitrided $\gamma-Al_2O_3$ and $Mo_2N/\gamma-Al_2O_3$ catalyst. In the 3150~1350 cm⁻¹ region, shown in Figure 2a, adsorbed butadiene on $\gamma-Al_2O_3$ gives similar IR bands to that of 1,3-butadiene in gas phase, indicating that the 1,3-butadiene is weakly or physically absorbed on the support. So it is reasonable to correlate the IR results of $Mo_2N/\gamma-Al_2O_3$ to pure $\gamma-Mo_2N$.

Figure 2b and 2c exhibit the IR spectra of adsorbed butadiene on $Mo_2N/\gamma-Al_2O_3$ catalyst for different adsorption time. When 1,3-butadiene was introduced onto the $Mo_2N/\gamma-Al_2O_3$ sample, IR bands at 2920, 2850, 1623, 1564, 1490, 1457, 1437, 1417 and 1378 cm⁻¹ appear together with the bands due to gas phase 1,3-butadiene. The differences between Figure 2a, 2b, and 2c manifest the chemical changes of the adsorbed butadiene on $Mo_2N$ surface. With the adsorption time, the following changes are observed in Figure 2: (a) In the ν(CH) region, the bands at 2920 and 2850 cm⁻¹, corresponding to ν (CH₂) as and ν (CH₂) as, respectively, become stronger in intensity. (b) In 1700~1300 cm⁻¹ region, the bands at 1490, 1437 and 1378 cm⁻¹ do not show evident change in intensity while the bands at 1457 and 1417 cm⁻¹ grow in intensity.

Figure 2d shows the IR spectrum recorded after an outgassing at RT of the gas phase 1,3-butadiene. The IR bands of gas phase 1,3-butadiene disappear after the outgassing. The ν(CH) region exhibits absorbances at 3088, 3005, 2920, and 2850 cm⁻¹, which do not decrease in intensity with further evacuation at RT. Additional bands with weaker intensity are observed at 3045 and 2970 cm⁻¹. Absorbance features are also observed at 1616, 1565, 1490, 1457, 1437, 1417, and 1378 cm⁻¹ in the ν(C=C) and δ(CH) regions.

The bands at 3088 and 3005 cm⁻¹ are due to the stretching modes of unsaturated C-H groups and could be ascribed to π-adsorbed species. The bands at 1616, 1565 and 1490 cm⁻¹ can be ascribed to C=C stretching modes. For C=C groups with only σ-type metal substitution, ν(C=C) is observed at lowered frequencies: 1650~1550 cm⁻¹; with π-bonding only, 1600~1460 cm⁻¹ [12]. So the band at 1616 cm⁻¹ could be attributed to σ-bonded species and the band at 1565 cm⁻¹ to single π-adsorbed butadiene (π_s). The 1490-cm⁻¹ band is probably due to di-π-adsorbed butadiene (π_d) according to the IR results of the Fe (CO)₃C₄H₆ complex: 1479 cm⁻¹ for ν(C=C) [13].

The strong absorbance at 2920 cm⁻¹ and the medium absorbance at 1437 and 1417 cm⁻¹ are also the evidence for the presence of σ-bonded species. The IR bands at 1437 and 1417 cm⁻¹ are suggested to be related to M-CH₂- or M-CH- group [14, 15]. These bands can be ascribed to the ν(CH₂) and δ(CH) modes of σ-bonded C₄H₆ species, respectively. These assignments
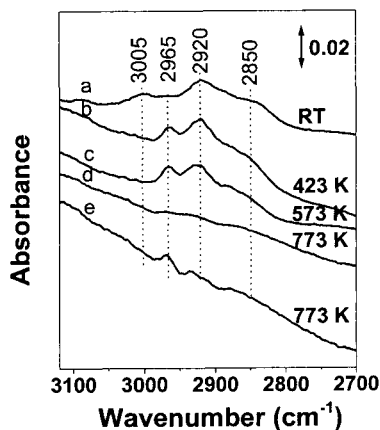
Fig. 3. IR spectra of 1,3-butadiene adsorbed on Mo₂N/γ-Al₂O₃ catalyst outgassed at different temperatures: (a) RT; (b) 423 K; (c) 573 K; (d) 773 K and (e) hydrogenation at 773 K.
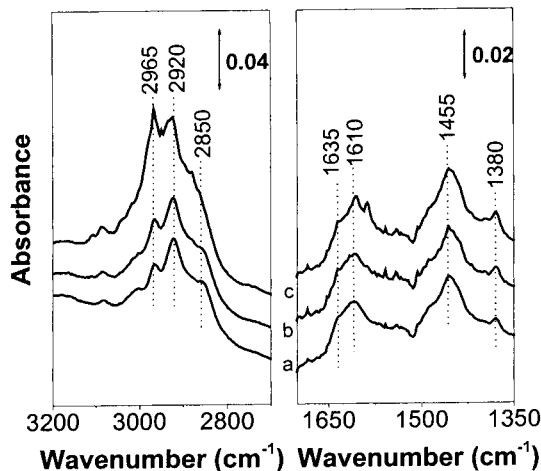
Fig. 4. IR spectra of 1,3-butadiene hydrogenation on Mo₂N/γ-Al₂O₃ catalyst outgassed at (a) 1 Torr; (b) 0.01 Torr and (c) 10⁻⁵ Torr.

are in agreement with those by Soma [16] for di-σ C₄H₆ on Ni/Al₂O₃ and by Sheppard [17] for the same structure on Pt (111).

### 3.2.2. Desorption and Hydrogenation of the Adsorbed Butadiene Species

Figure 3 shows the IR spectra of 1,3-butadiene adsorbed on Mo₂N/γ-Al₂O₃ catalyst after a subsequent heating in vacuum at different temperatures. The evacuation at higher temperature produces an obvious IR band at 2965 cm⁻¹, characteristic of ν (CH₃) as. The IR bands at 2965, 2920 and 2850 cm⁻¹ remain even after outgassing at 573 K, indicating the presence of very stable species derived from 1,3-butadiene adsorption. The increase of the intensities of these IR bands owns possibly to the hydrogenation of some dehydrogenated species at high temperatures. Although no strong IR bands are observed after outgassing at 773 K (Figure 3d), a subsequent hydrogenation at the same temperature produces again some distinct bands at 2967, 2935 and 2880 cm⁻¹ in the ν(CH) region, corresponding to ν(CH₃) (Figure 3e). This implies that there are some severely dehydrogenated species formed on the catalyst surface after a high temperature evacuation.

In summary, there are several kinds of hydrocarbon species derived from the adsorption of 1,3-butadiene on the Mo₂N/γ-Al₂O₃ catalyst: π (πs and πd) adsorbed butadiene, σ-bonded species and dehydrogenated species (11).

### 3.2.3. Surface Species from Hydrogenation of Butadiene

In situ hydrogenation of 1,3-butadiene on Mo₂N/γ-Al₂O₃ catalyst was also carried out in the
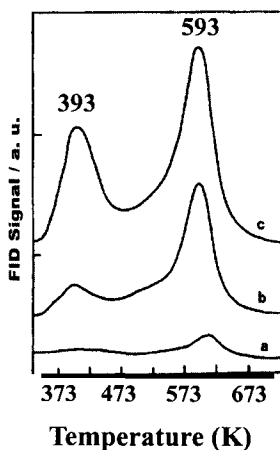
Fig. 5. TPSR profiles H$_2$ and adsorbate on γ-Mo$_2$N catalyst after 1,3-butadiene adsorption at 333 K with different time: (a) 1 h; (b) 3 h and (c) 6 h.
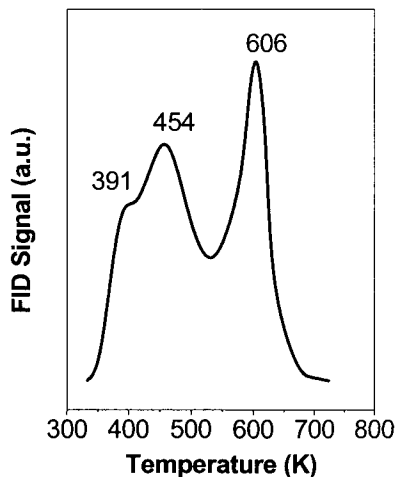
Fig. 6. TPSR profile of H$_2$ and adsorbate on γ-Mo$_2$N catalyst after 1,3-butadiene hydrogenation at 333 K.

IR cell with a mixture of 20 Torr 1,3-butadiene/H$_2$ (1:2 in volume) at RT. After a reaction time of 3 h, the IR cell was outgassed gradually and IR spectra were collected. Shown in Figure 4, IR bands at 2965, 2920, 2850 cm$^{-1}$ in the $v$(CH) region and bands at 1635, 1610, 1455, 1380 cm$^{-1}$ in the $v$(C=C) and $\delta$(CH) regions are clearly observed in the three spectra. Similarly to Figure 2, the three bands in the $v$(CH) region can also be assigned to σ-bonded surface species on the catalyst. The broad bands in the 1700~1300 cm$^{-1}$ region can be identified as C-C stretch and C-H bending vibrations of the carbonaceous deposits on the catalyst sample [18]. The 1635 and 1610-cm$^{-1}$ bands are located in the olefinic stretch region, indicating that the hydrocarbon species contain unsaturated components. The bands at 1455 and 1380 cm$^{-1}$ can be attributed to C-H bending modes of methylene groups in long aliphatic chains [19]. Therefore, it is evident that some carbonaceous species are formed on the nitride catalyst during the hydrogenation of 1,3-butadiene on Mo$_2$N/γ-Al$_2$O$_3$ catalyst.

### 3.3. H$_2$-TPSR Results

Figure 5 exhibits the H$_2$-TPSR profiles of 1,3-butadiene on γ-Mo$_2$N catalyst after adsorption for different times at 333 K. With adsorption time, from Figure 5a to 5c, two peaks at 393 and 593 K increase gradually and are assigned to weakly and strongly adsorbed species, respectively. In the initial stage, the peak at 593 K increase greatly; while for a longer adsorption time, this peak shows slow growth in intensity. These imply that the corresponding species has undergone an activation adsorption process. Considering its high desorption temperature, the strongly adsorbed species corresponds possibly to the dehydrogenated species in the IR study. And the weakly adsorbed species at 393 K can be due to the σ-bonded bonded species in the IR study. The π adsorbed butadiene species can be hydrogenated easily

at RT [11], so it is reasonable that no its corresponding peak in the TPSR profile is observed.

Figure 6 presents the $H_2$-TPSR profile of the adsorbate on $\gamma$-$Mo_2N$ catalyst after 1,3-butadiene hydrogenation at 333 K. Three peaks at 391, 454, and 606 K are observed. The peaks at 391 and 606 K can be assigned similarly as in Figure 5, namely, corresponding to $\sigma$-bonded and severely dehydrogenated species, respectively. The species for the peak at 454 K is possibly due to a kind of multiply $\sigma$-bonded species.

## 4. DISCUSSION

The presence of hydrocarbonaceous species ($\sigma$-bonded and dehydrogenated species) on Mo nitride catalyst is identified by both IR and $H_2$-TPSR studies (Figure 2-6). These strongly adsorbed species are formed slowly with adsorption/reaction time and are the precursors of coke, and can finally lead to the decrease of hydrogenation activity of 1,3-butadiene on $\gamma$-$Mo_2N$. This explains well the activity test that the conversion of 1,3-butadiene decreases with reaction time as shown in Figure 1.

Also as exhibited in Figure 1, the selectivity to 1-butene increases with reaction time. It is parallel to the formation of hydrocarbonaceous species on the $\gamma$-$Mo_2N$ catalyst. This suggests that the presence of these hydrocarbonaceous species is beneficial to the selectivity of 1-butene in the hydrogenation of 1,3-butadiene, partly due to their occupation of the more active sites on the catalyst surface. These species may also take part in the selective hydrogenation of 1,3-butadiene to butenes according to the suggestion that the hydrogenation process should be interpreted partly as *hydrogen transfer* between an adsorbed hydrocarbon species and the adsorbed olefin [20].

Previous work shows that 1,3-butadiene is adsorbed mainly on the Mo sites [11] while the hydrocarbonaceous species may be adsorbed on the [MoNxHy] sites [21] of molybdenum nitride. Thus the participation of the hydrocarbonaceous species in the selective hydrogenation of 1,3-butadiene can be tentatively proposed as following: in the presence of $H_2$, the adsorbed hydrogen is first added to the dehydrogenated surface species and then transfer to the adsorbed 1,3-butadiene on the Mo sites. As a result, the 1,3-butadiene is selectively hydrogenated to butenes on the Mo sites.

Our previous study [11] suggests that the high selectivity to 1-butene for the hydrogenation of 1,3-butadiene on $\gamma$-$Mo_2N$ catalyst can be explained in term of competitive adsorption, namely, the $\pi_d$-adsorbed butadiene strongly inhibits the adsorption of 1-butene and blocks its further hydrogenation and isomerization. Combination of this work, it is reasonable that both the $\pi_d$-adsorbed butadiene and the hydrocarbonaceous species contribute to the high selectivity to 1-butene in the hydrogenation of 1,3-butadiene on molybdenum nitride.

## 5. CONCLUSIONS

In the hydrogenation of 1,3-butadiene on $\gamma$-$Mo_2N$ catalyst, it is found that the activity decreases while the selectivity to 1-butene increases with reaction time. These are attributed to the presence of surface hydrocarbonaceous species on the catalyst as confirmed by IR and $H_2$-TPSR studies. The hydrocarbonaceous species not only influence the activity and selectivity of the nitride catalyst, but also take part in the hydrogenation process of 1,3-butadiene. Part of the 1,3-butadiene is proposed to be hydrogenated by the hydrogen transferred from the hydrocarbonaceous species to the adsorbed butadiene.

452

## ACKNOWLEDGMENTS

## REFERENCES

1. H.J. Müller, G. Kons, C. Herion, G. Meyer, M. Vicari, C. Freire-Erdbrügger, K. Flick, P. Polanek and H. Laib, Proceedings of the Ninth International Symposium on Large Chemical Plants, Antwerp, 4-6 October 1995.
2. Y.H. Park and G.L. Price, Ind. Eng. Chem. Res., 30 (1991) 1693.
3. J.J. Phillipson, P.B. Wells and C.R. Wilson, J. Chem. Soc., (1969) 1351.
4. B. Vidick, J. Lemaitre and L. Leclercq, J. Catal., 99 (1986) 439.
5. G.S. Ranhotra, A.T. Bell and J.A. Reimer, J. Catal., 108 (1987) 40.
6. Z. Hao, Z. Wei, L. Wang, X. Li, C. Li, E. Min and Q. Xin, Appl. Catal. A: General, 192 (1999) 81.
7. A. Sarkany, Appl. Catal. A: General, 165 (1997) 87.
8. A. Sarkany, Appl. Catal. A: General, 175 (1997) 245.
9. Z. Wu, Y. Chu, S. Yang, Z. Wei, C. Li and Q. Xin, J. Catal., 194 (2000) 23.
10. Z. Wu, Y. Chu, S. Yang, Z. Wei, C. Li and Q. Xin, Stud. Surf. Sci. Catal., 130 (2000) 2819.
11. Z. Wu, Z. Hao, P. Ying, C. Li and Q. Xin, J. Phys. Chem. B, 104 (2000) 12275.
12. N. Sheppard and C. De La Cruz, Adv. Catal., 41 (1996) 1.
13. G. Davidson, Inorg. Chim. Acta, 3 (1969) 596.
14. P. Basu and J.T. Yates, Jr., J. Phys. Chem., 93 (1989) 2028.
15. T.J. Campione and J.G. Ekerdt, J. Catal., 102 (1986) 64.
16. Y. Soma, Bull. Chem. Soc. Japan, 50 (1977) 2119.
17. N.R. Avery and N. Sheppard, Proc. R. Soc. London, A, 405 (1986) 27.
18. L.P.A.F. Elst, S. Eijsbouts, A.D. van Langeveld and J.A. Moulijn, J. Catal., 196 (2000) 95.
19. S.H. Wang and P.R. Griffiths, Fuel, 64 (1985) 229.
20. S.J. Thomson and G. Webb, J. Chem. Soc., Chem. Comm., (1976) 526.
21. Z. Hao, Z. Wu, Z. Wei, C. Li, Q. Xin and E. Min, Chinese J. Catal., 21 (2000) 367.

# Static purification-concentration process. Study of the system uranium, orthophosphoric acid –Di(ethyl-2-hexyl) phosphoric acid -Tri-n-octyl phosphine oxyde-Ammonium carbonate

F. Hassaine-Sadi[a] and A. Benhassaine[b]

[a] Chemistry Institute, University of sciences and Technology Houari Boumediene,
Bab-Ezzouar, Algiers, Algeria.
Tel/Fax : 213 (21) 24. 73. 11.

[b] Mining School of Alès, 6, Clavières Avenue, 30107 Alès, Cedex, French

A static purification-concentration process has been devised thanks to a liquid- liquid extraction-reextraction reactor where the extraction compartiment and the reextraction compartiment are put in contact with one another through the organic phase composed of an extractant and a diluent.

We have applied this process to the system : Uranium, orthophosphoric acid – Di(ethyl-2-hexyl) phosphoric acid -Tri-n-octyl phosphine oxyde-Ammonium carbonate. Interesting performances have been realized for diluted solutions (100ppm).
A chemical modelization has allowed to identify the extraction mecanisms. The classical behaviour obtained in agitated surroungings has been found again.
A physical modelization has allowed to demonstrate the existence of transfers which find their origins on the one hand , in a chemical potential gradient and on the other hand, in the transports related to concentration gradients. Three phases have been identified : a first phase where the transferred quantities are weak, a second phase where the transferred quantities are important and a third phase much slower.
The obtained results have put into evidence the process feasibility and the performances of the technique. This allows to foresee an industrial application of the static liquid- liquid extraction-reextraction combined, and to hope for wide applications as well in the marginal ores treatment as in the treatment of low-grade metal effluents.

## 1. INTRODUCTION

In the frame of a global process of marginal ores treatment and of the treatment of solid residues containing heavy metals, we can associate the techniques of static solid-liquid extraction to the techniques of static liquid-liquid extraction in a process flow-sheet represented on figure 1.
The static solid-liquid extraction or pile lixiviation is now well known in the processing of small-content ores [1] [2]. It could be easily used to abstract the lixiviable fraction of the residues and contribute to their inerting. It only remained the setting of systems of treatment of leaching solutions suitable with solid-liquid extraction from the kinetic, technological and economic point of vue. For this doing we have developed a static liquid-liquid extraction technique associating extraction to reextraction.
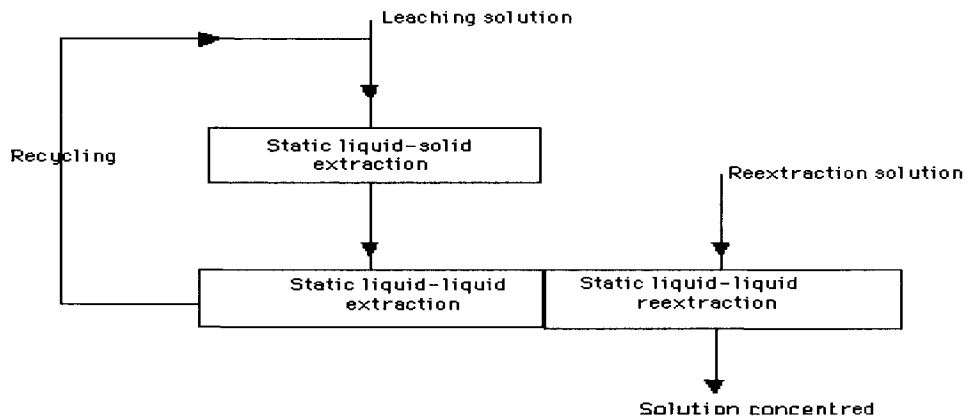
Figure1. Scheme global process of treatment of small-content ores .

# 1. THE STATIC LIQUID-LIQUID EXTRACTION-REEXTRACTION REACTOR

We have engineered and realized a combined comprising two static liquid-liquid extraction tubs.

### 1.1. The extraction-reextraction combined

The two extraction tubs are in pexiglass (material resisting to solvents, diluents and acids). The extraction compartment receives the feeding phase, that is the lixiviation solution. It is separated from the reextraction compartment which would contain the reextraction aquous phase in a waterproof manner. The two compartments and the two solutions are put into contact thanks to the organic phase composed of an extractant and a diluent. A scheme of the extraction-reextraction combined is drawn on figure 2 where the organic phase is the light phase. densities of both phases (light phase, heavy phase).
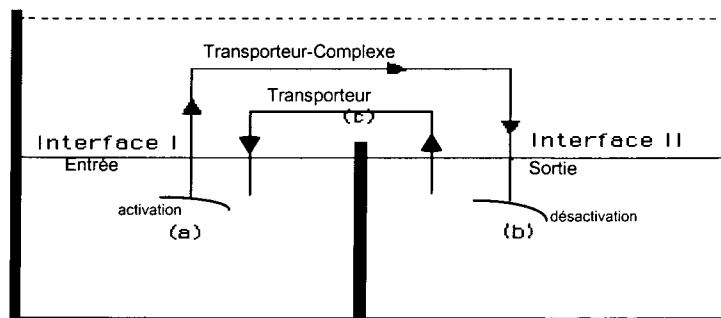


Figure 2. Scheme of extraction -reextraction combined. (a): Extraction compartment, (b): Reextraction compartment, (c): Junction organic : Membrane

The first great interest is related to the static nature of the extraction-reextraction operations. The elemination of agitation and dispersion and therefore of mixing and setting puts a considerable limite to the solubility of the organic phase in aquous phase.

The secund great interest of such disposition is also to allow processing of little clarified solutions and to get benefit from gravity phenomena which allow the interface to remain intact. The unclogging problems will thus be reduced considerably.

The third great interest is to avoid the regeneration of the solvent wich is intact at the end of operations.

## 1.2. The taking place of an experiment

Separate filling of the compartments is proceeded to, the aqueous phase loaded is first filled in the extraction compartment, the aqueous phase not loaded is then filled in the reextraction compartment , the aqueous solutions are put in contact with one another through the organic phase.

## 1.3. Used reactants

The aqueous phases are realized from orthosphoric acid at 30% and from solutions of uranyl nitrate ($UO_2(NO_3)_2$, $6H_2O$) (Merck) obtained by dissolving in distilled water. We have set the initial concentration of the feeding phase at 100 ppm in Uranium. The ammonium car bonate solutions have been utilized to make reextraction solutions.

The organic phase is made of an extractant the Di(ethyl-2-hexyl) phosphoric acid (B.D.H.), the phosphine tri-n-octyl oxyde (Merck) and of a kerosene diluent.

## 1.4. Measures

Regular samples have been made with the help of pipettes (2ml) from aqueous solutions, every week. The experiments period has been fixed to 60 days. The tests have been realized at room temperature. We have determined the uranium concentrations in the feeding phase and the reextraction aqueous phase. The dsings have been made by several analytical techniques[3] [4] : Volumetry, Colorimetry of the U(IV) complex- ArsenaZo III, Colorimetry of the U(VI) complex- Methane Dibenzoyl and Atomic emission spectroscopy [5] [6]  with plasma induced by high frequency or plasma flare.

## 2. STUDY OF THE STATIC PURIFICATION-CONCENTRATION PROCESS

In order to study the physico-chemical behaviour of the reactor, we have chosen system (choice of a system : extraction by synergism [7-10]) :

Extraction compartment / Organic phase / Reextraction compartment

$$UO_2^{2+}, H^+, PO_4^{3-} \ / \ \overline{HDEHP\text{-}TOPO} \ / \ (NH_4)_2CO_3$$

InterfaceI          InterfaceII

Every compartment and every interface have made the object of the examination.

## 2.1. Results and discussions

The extraction parameters and reextraction parameters examined have been the following :
- The concentration in TOPO, the rapport HDEHP/TOPO,
- the concentration in reextraction phase,
- the time of contact.

We have computed the extraction efficiencies (amount of uranium related to the initial amount remaining in the extraction compartment) and the rextraction efficiencies (amount of uranium in the reextraction compartiment related to initial uranium amount).

### 2.1.1. Influence of the concentration in TOPO

We have represented the variation of the extraction and reextraction efficiences in function of the time at the variables concentrations in TOPO and concentration in HDEHP constant. Figures 3 and 4 indicates the obtained results.
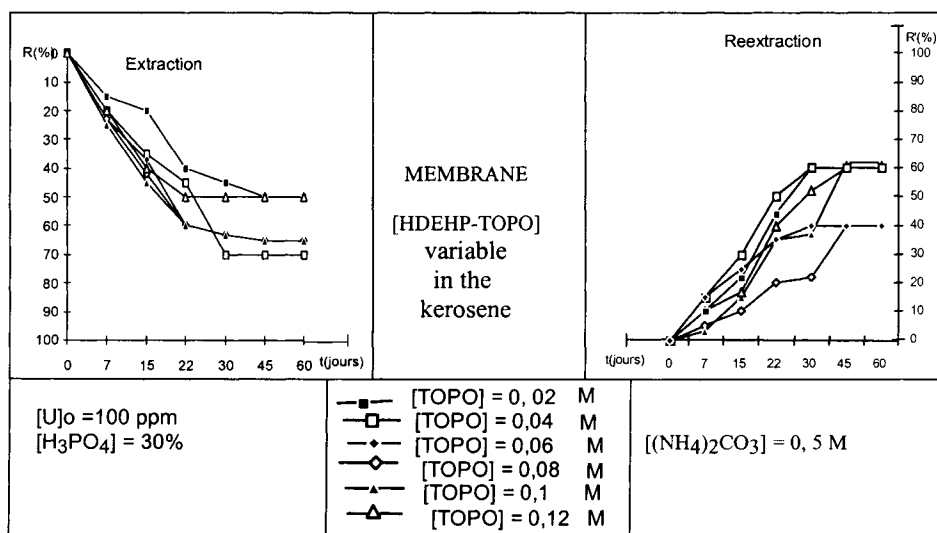


Figure 3. Influence of the phosphine tri-n-octyl oxyde concentration.
- Organic phase : [HDEHP] = 0, 4 M - [TOPO] variable.

We find back the influence of the concentration of solvatation agent. For the weak concentrations in phosphoric di(ethyl-2-hexyl) acid, we observe a slower exaltation of the efficients of the uranium extraction. The efficency of the uranium extraction is of the order of 70% for a time 60 days. We will notice that both compartments have a symetric behavior.

We have attempted to show the exaltation of the efficiencies of the uranium extraction in concentrated H3PO4 surroundings by the utilization of the HDEHP-TOPO mixture. We found an percentage of the uranium extraction maximum, it is of the order of 98% at the rapport H.D.E.H.P/TOPO to 5.
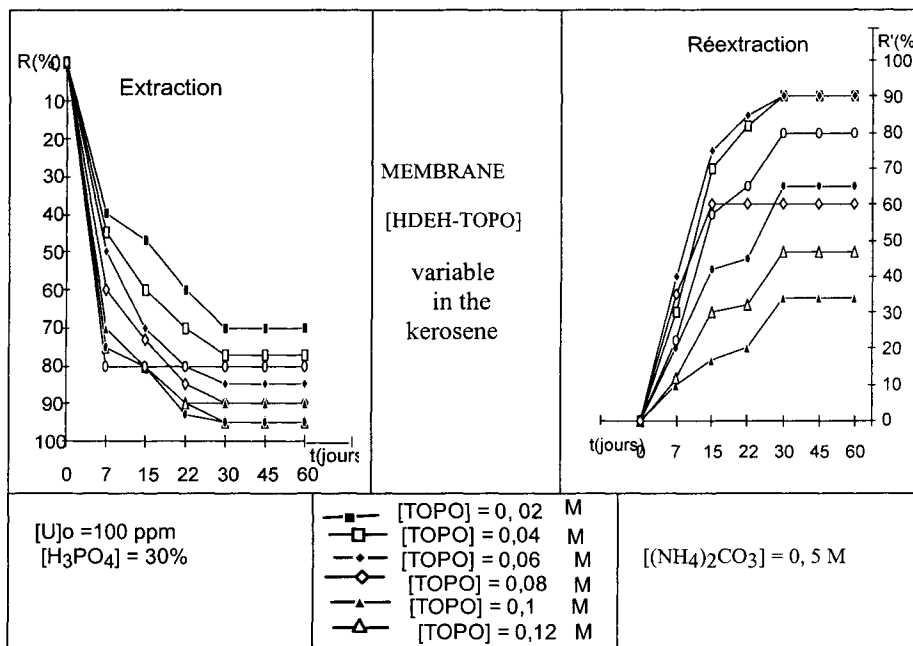
Figure 4. Influence of the phosphine tri-n-octyl oxyde concentration.
  - Organic phase : [HDEHP] = 0, 6 M - [TOPO] variable.

## 2.1.2. Influence in ammonium carbonate of the concentration of the reextraction phase

Uranium is reextracted by means of a mixture of ammonium carbonate and ammonia. In general we go up to the cristallization of the ammmonium tricarbonate uranyle. We have studied the influence of the concentration of $(NH_4)_2CO_3$ of the reextraction phase on the reextraction effeciencies. Figure 5 illustrate the increasing of the uranium reextracted amount when the ammonium carbonate concentration increases. The reextracted quantities are of the order of 60% for an ammonium carbonate concentration 0,5M and for a time 60 days.The mecanismes of active transport are represented on the sheme given in Figure 6.

The diffusion of the uranyl ions $UO_2^{2+}$ does by the activation of cosolute $HPO_4^{2-}$ at the interface I, we have the migration of complex formed across the membrane by active tansport and we have the desactivation of the molecular complex at the interface II. The diffusion at the interface II of cation $NH_4^+$ which is effectued in sens opposed that it is does by the contr-transport of the two ammonium ions at l'interface I.

## 3. KINETIC STUDY OF THE STATIC EXTRACTION-REEXTRACTION COMBINED

The efficiencies as a function of time present similar variations. We can sum-up the observations in the following way :
  - The behaviors of the two compartments are perfectly symetric. We have a total transfer through the organic phase .

458

- A 60 days period of time is sufficient to obtain high efficiencies in industrial terms.
- Chemical parameters carefully chosen allow to diminish the reaction times in a notable manner.



| [U]o =100 ppm | $-\blacksquare-$ [(NH4)2CO3]= | 0,01 M |
| [H3PO4] = 30% | $-\square-$ [(NH4)2CO3] = | 0,1 M |
| | $-\bullet-$ [(NH4)2CO3] = | 0,5 M |
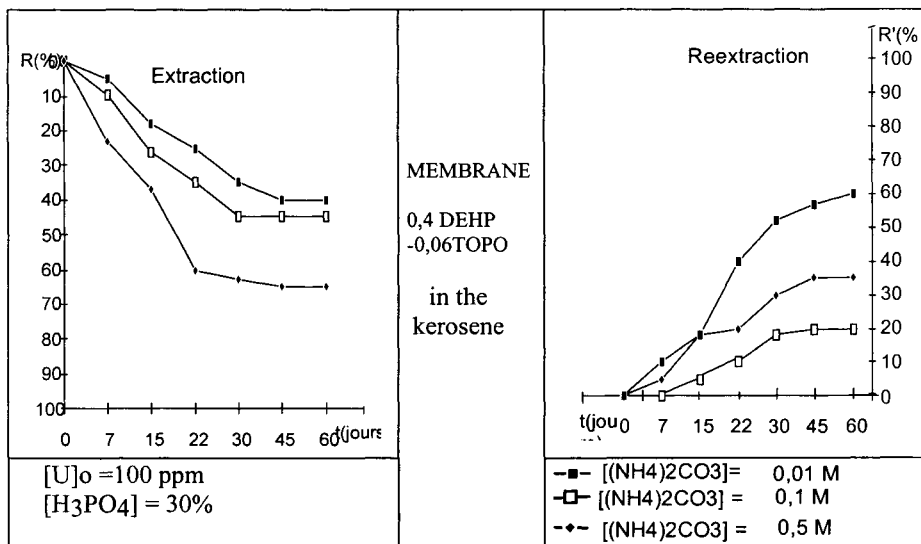
Figure 5. Influence of the ammonium carbonate concentration.
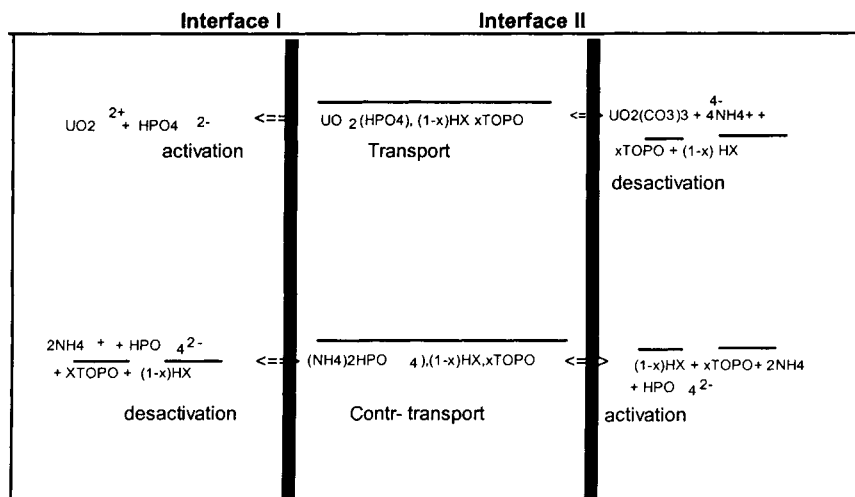


Figure 6. Schematic representation of the mecanismes of active transport.

A transfer model assuming a diffusion transport and an absence of interfacial resistance has been applied to two compartments. Approximations have allowed us to simplify the formulas and characterize our combined thanks to equations [11-14] :

$$Q_0 - Q_t = k\sqrt{Dt} \quad \text{Extraction compartment}$$

$$Q_t' = k\sqrt{Dt} \quad \text{Reextraction compartment}$$

Qo - Q(t) represents the quantity of uranium remaining in the extraction compartment and Q'(t) the quantity of uranium in the reextraction compartment. We have represented the variation of $Q_0 - Q_t = f\sqrt{t}$ and $Q_t' = f\sqrt{t}$ on figure 7.
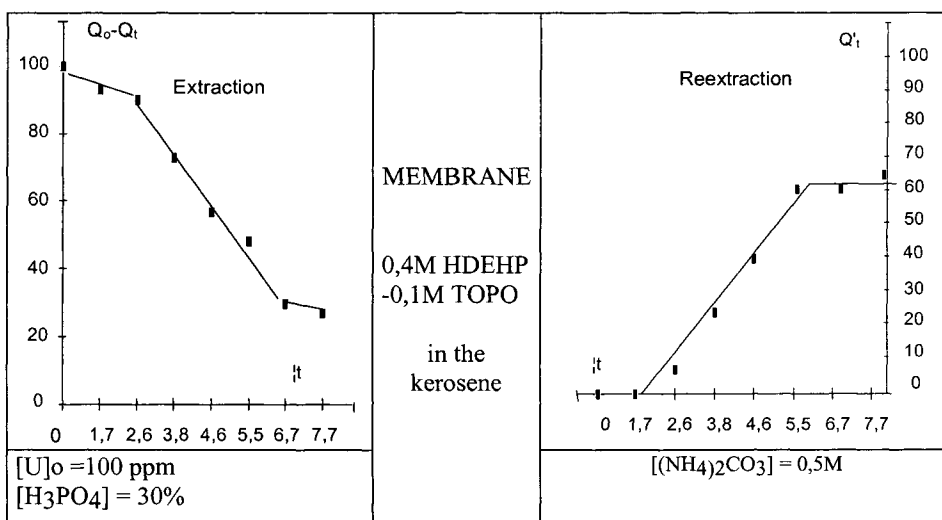


Figure 7. Variation de $(Q_0 - Q_t)$ et $Q_t'$ en fonction de √t.

In regard to cinetic curves, we can distinguish three phases for $Q_0 - Q_t = f\sqrt{t}$

1°) A first transfer phase where the transferred quantities are weak.

2°) A secund phase where the transferred quantities are important and follow a linear relation in function of the square root of t with avery high slope.

3°) A third phase of wearing out where the transferred quantities become weak again.

For the variation $Q_t' = f\sqrt{t}$ we can make the same observations :

        - A first phase where there is no transfer.

        - A secund phase where transfer is made according to a linear relation in function of √t.

        - A third phase much slower.

The obtained results in the kinetic curves show the existence of totally diffusive transfer processes.

## 4. CONCLUSION

A purification-concentration process for very dilute solutions has been set thanks to the conception and realization of a static liquid-liquid extraction combined characterized by the extraction-reextraction association.

We have applied this process for the system : uranium, orthophosphoric acid-Di(ethyl-2-hexyl) phosphoric acid, phosphine tri-n-octyl oxyde, kerosene-Ammonium carbonate.

The process has turned out to be very performing as well for extraction as for reextraction.

In spite of the existence of static systems, the chemical modelization has allowed to meet again the classical mecanisms obtained in agitated surroundings. It's about an extraction by synergy of uranium in orthophosphoric surroundings by the mixture HDEHP-TOPO.

A physical modelization has allowed to explain the existence of transfers which find their origin :

- in chemical potential gradients (interface reactions)
- and in transports related to concentration gradients.

Three transfer have been identified :

- a first slow transfer is governed by the diffusion process inside the organic phase.
- a secund fast transfer thanks to the high concentration gradient maintained between the two interfaces, justifiable of the classical laws of the diffusion.
- a third slow transfer that corresponds to the running out of the source.

These modelizations have allowed the phenomeno-logical characterisation of the combined that we have conceived and experimented. We have proposed the "Complex" combined allowing the transfer of several species.

The obtained results have put into evidence the process feasibility and the performances of the technique. This allows to foresee an industrial application of the static liquid-liquid extraction combined, and to hope for wide applications as well in the ores treatment field as in the solid residues fields.

## REFERENCES

[1] Processing of low-grade uranium ores, A. I. E. A., Vienne, 1967.

[2] Technique de l'ingénieur. Genie Chimique. J, 3.

[3] G. Charlot, The analytical chemistry method : Quanti. Analysis, Mass.ed., Paris, 1961.

[4] P. Fremaux and G. Cattin, Analytical Chemistry, 50, 1, 34-39, 1968.

[5] J ;M. Mermet C. R. Acad. Sc. PARIS, Serie B, 281, 273, 1975.

[6] Leroy M. J. F., Sutter E. M. M., An. Fals. Exp. chim., 718, n° 756, 400, 1977.

[7] M. Taube, S. Siekerski, Nucleonica, 6, 489, 1961.

[8] J. M. Josa and Coll., Junta Energia Nuclear, Madrid, 9, 33, 22-29, 1965.

[9] Process of extraction of uranium from wet process phosphoric acid. Brevet French 77, 20552, 5juill.1977.

[10] F.J. Hurst and D. J. Crouse. Oxidative stripping processs for the recovery of uranium from wet process phosphoric acid. US patent, 3-835214, 10 septemb. 1974.

[11] A. Fick. Pogg. Am. Physic., 94, 59, (1855).

[12] J. J. Moreau. Proceedings of symposium on a diffusion, Montpellier, (1955).

[13] J. Crank. Mathematics of diffusion, Clarendon Press, Oxford, (1956).

[14] C.Vidal, G. Dewel, P. Borckmanans. Au-delà de l'équilibre, Herman Ed., (1994).

# Improvement on the dry reforming of methane by hydrogen diffusion in a membrane reactor.

P. Ferreira-Aparicio[a], Y. H. Ma[b].

[a] Instituto de Catálisis y Petroleoquímica. CSIC. Campus de Cantoblanco. 28049 Madrid. Spain.

[b] Dept. of Chemical Engineering, Worcester Polytechnic Institute, 100 Institute Road, Worcester, MA 01609, U.S.A.

The applicability of commercial ultrafiltration ceramic membranes in the dry reforming of methane has been studied. The analysis of the permeability of pure gases through the membranes indicates that the transport process occurs mainly by Knudsen diffusion. Although preferential separation of the gases involved in the reaction is limited to a maximum value predicted by the diffusion mechanism, a significant conversion enhancement has been observed in the reaction when using the membranes. The preferential separation of $H_2$ as compared to the reactants leads to reduce the reverse water gas shift as secondary reaction and therefore to increase hydrogen selectivity. In membranes with similar separation coefficients, the permeance increase does not seem to have any significant effect in the catalytic performance.

## 1. INTRODUCTION

The dry reforming of methane has received a great deal of attention during the last decade as an interesting alternative to other methods for syngas production, particularly with concern over global warming and the utilization of natural gas [1]. Recent energy forecasts prepared by the International Energy Agency show that fossil fuels will predominate as an energy source during the 21st century, so that world emissions of $CO_2$ will increase by 50% in 2010 when compared to 1990 levels [2]. The limitation of world carbon dioxide emissions, that constitute the main contribution to the *greenhouse* effect, is currently one of the most ambitious challenges in the field of Catalysis. It is expected that over the medium to longer term future there will be a move towards the development of $CO_2$ recovery technologies [3]. The reaction between methane and carbon dioxide provides an attractive route for $CO_2$ recycling by converting these two abundant and inexpensive carbon-containing materials into industrially

important chemicals. The high reaction enthalpies associated to the methane reforming by carbon dioxide and its reverse reaction make this process one of the most suitable for application in the storage of renewable energy sources. The use of this kind of energy (solar or eolic), or other non fossil fuels sources (e.g., nuclear energy), in thermochemical heat pipe applications would allow large scale recycling of carbon dioxide that could substantially reduce its net emission to the atmosphere.

Up to now great effort has been devoted to the study and development of catalysts for this process. Most of Group VIII elements are active for this reaction. In particular, Rh and Ru dispersed on adequate supports ($Al_2O_3$, $ZrO_2$) have been shown to be very active and stable catalysts by enabling a bifunctional mechanism that requires the mobility and surface diffusion of species between the metal and the support [4,5]. However, the maximum conversion of methane in a conventional fixed bed reactor is limited by the reversibility of this process and quite high temperatures are needed to achieve a high conversion. The utilization of a membrane reactor that allows the preferential removal of one or more of the reaction products is a feasible way to overcome such thermodynamic equilibrium limitations [6].

Here we present a study concerning the applicability and the efficiency of different ultrafiltration ceramic membranes for the $CH_4+CO_2$ reaction. The effect of three different porous membranes on the conversion and hydrogen selectivity of the reaction will be analyzed. Permeance measurements of the different gases involved in the reaction will be correlated for each membrane with the catalytic performance of the reactor.

## 2. EXPERIMENTAL

Three commercial ceramic tubes of 10 mm OD with different composition and structural characteristics were used for this study: mullite (3 $Al_2O_3$-2 $SiO_2$) (Lomba), alumina ($\alpha$-$Al_2O_3$/$\gamma$-$Al_2O_3$) (SCT) and yttria-stabilized zirconia ($Y_2O_3$-$ZrO_2$) (SCT). The porous zone in the tubes was limited to a central section of the membrane by sealing the external surface of both sides of the tube with a glass enamel in order to ensure the absence of temperature gradients in it. The permeation zone had a length of 5 cm approximately.

The tubes were assembled in the membrane reactor by fitting their ends with graphite joints to an external stainless steel-tube. Gases were fed inside the tube and the permeated flow was collected in the shell side and measured with a soap-bubble flow meter. In order to determine the permeability of each membrane, gas flux measurements were carried out with pure gases ($H_2$, $CH_4$, $CO_2$ and Ar) at several temperatures as a function of the transmembrane pressure difference.

The methane dry reforming reaction was carried out at 823 K by feeding a undiluted equimolecular mixture of $CH_4$ and $CO_2$ at a total flow rate of 6 $l·h^{-1}$. Usually 0.800 g of a 1-%Rh/$Al_2O_3$ catalyst were loaded inside the membrane

between two quartz wool plugs. A thermocouple placed inside the ceramic tube allowed controlling the temperature in the catalytic bed. Gases flowing through the tube side and shell side were collected at the reactor outlet and analyzed together by gas chromatography. No sweep gas was fed in the shell side in order to avoid dilution effects that could mask the results. A blank reaction experiment was carried out in the membrane reactor without catalyst, in order to check the inertness of the reactor. Equilibrium conversion was also experimentally determined in the same reactor with identical conditions by using as membrane a non-porous quartz tube.

## 3. RESULTS AND DISCUSSION

Permeability measurements of $H_2$, $CH_4$, $CO_2$ and Ar across the membranes were carried out at different temperatures. Gas permeation values obtained were observed to vary linearly with the pressure difference between both sides of the membrane wall in all the experiments. Permeance of each gas, calculated as the ratio between the flux and the pressure difference between the tube side and the shell side, remained constant with pressure. The values obtained at 823 K for each membrane tube are shown in Figure 1.
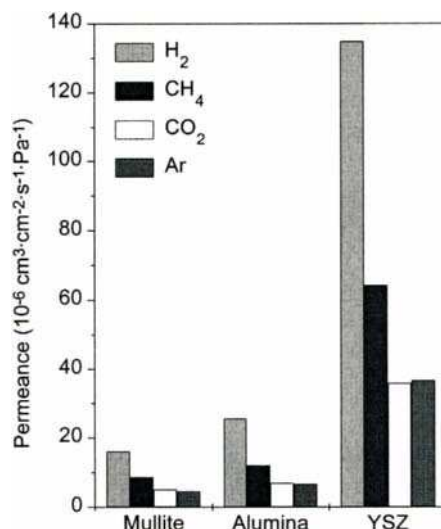


**Figure 1.** Permeance rate for $H_2$, $CH_4$, $CO_2$ and Ar at 823 K through the different commercial membranes: mullite, alumina and yttria-stabilized zirconia.

The permeability of the membranes increased in the following order: mullite<alumina<YSZ. The YSZ tube displayed the highest permeance, which

decreased by almost one order of magnitude in the alumina and mullite samples. There are at least two mechanisms that could be involved in the transport process across these membranes: Knudsen diffusion and viscous or Poiseuille flow. For non-adsorbable gases, the total permeance can be expressed as the sum of both Knudsen and viscous contributions [7]. For Knudsen diffusion, permeance does not depend on the pressure difference between both sides of the tube and is proportional to the reciprocal of the square root of the absolute temperature and the molecular weight of the gas. On the other hand, for viscous flow permeance should be proportional to the pressure and inversely proportional to the viscosity of the gas and to the absolute temperature. Results obtained seem to indicate that there is not any significant contribution of viscous flow in the gas transport process in the membranes used in this study. Gases are mainly permeated through the Knudsen diffusion mechanism. As an example, Figures 2a and 2b show that the permeance of the mullite membrane for the several gases is constant with pressure and that it varies linearly with the reciprocal of the square root of the absolute temperature according to the Knudsen diffusion mechanism.
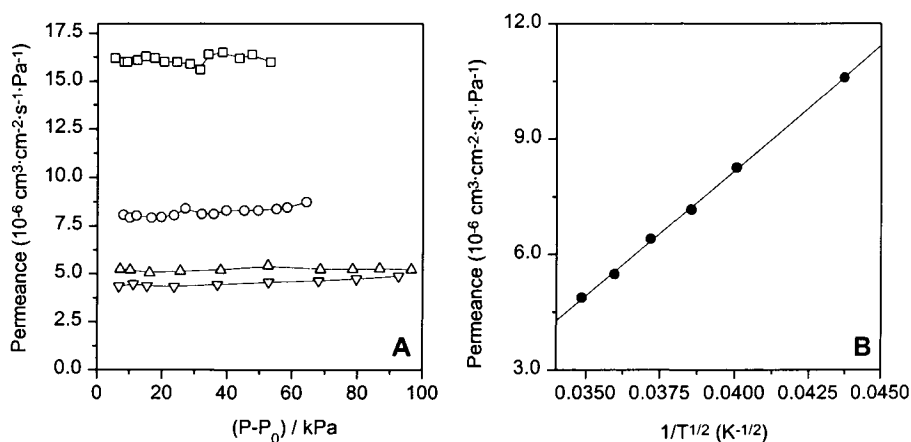


**Figure 2.** A: Permeance of $H_2$ (-□-), $CH_4$ (-○-), $CO_2$ (-△-) and Ar (-▽-) through the mullite membrane as a function of the gas pressure increase. B: Permeance of Ar through the mullite membrane as a function of the reciprocal of the square root of the absolute temperature.

The gas separation factors or selectivity coefficients, defined as the ratio between the permeances of two pure gases, have been estimated for the three membranes with respect to a non-adsorbable gas, such as Ar. These values are

compiled in Table 1 together with the pure Knudsen diffusion coefficients, which have been calculated according to the following equation:

$$\alpha(gas/Ar) = \frac{\sqrt{M_{Ar}}}{\sqrt{M_{gas}}} \qquad (1)$$

where $M_i$ is the molecular weight of the gas $i$.

In general, selectivity coefficients obtained for $CH_4$ and $CO_2$ respect to Ar are close to those predicted by Knudsen diffusion, although slightly higher values have been obtained for all the membranes. However, a considerable deviation can be found for $H_2/Ar$ coefficients. The decreased hydrogen separation factor experimentally obtained can be probably attributed to the surface interaction of hydrogen with the hydroxyl groups in the inner wall in the membranes at high temperatures. According to these results, the most selective membrane for hydrogen separation would be the alumina one, followed by the YSZ tube and finally the mullite membrane.

**Table 1.** Separation factors for the mullite, alumina and yttria stabilized zirconia (YSZ) membranes determined from individual gas permeabilities. Knudsen diffusion coeficients are also presented for comparison.

|                    | $H_2/Ar$ | $CH_4/Ar$ | $CO_2/Ar$ |
|--------------------|----------|-----------|-----------|
| Mullite            | 3.49     | 1.88      | 1.04      |
| Alumina            | 3.80     | 1.79      | 1.13      |
| YSZ                | 3.66     | 1.74      | 0.98      |
| Knudsen diffusion  | 4.47     | 1.58      | 0.95      |

As a matter of fact, the ideal membrane to be used in order to shift equilibrium conversion in a reaction, such as the dry methane reforming, would be one with high selectivity for hydrogen separation. However, for a preliminary study, the application of the ultrafiltration membranes we are studying in the $CH_4+CO_2$ reaction will allow us to evaluate how the preferential separation of hydrogen influences the equilibrium conversion and what effects predominate in the reactor performance: the higher permeance of a membrane respect to another or the higher selectivity to hydrogen as compared to the reactants.

The $CH_4+CO_2$ reaction was carried out in the membrane reactor assembled with a non-porous quartz tube. This experiment allowed determining the conversion for both reactants under real conditions in our experimental system in the same way it would be determined for the porous membranes afterwards. Figure 3 shows the equilibrium conversions obtained for the $CH_4+CO_2$ reaction in the 823-923 K temperature range and the Thermodynamics predicted values calculated for the stoichiometric reaction in the same conditions:

$CH_4+CO_2 \Leftrightarrow 2H_2+2CO$. The deviations observed between experimental and calculated values are due to the presence of secondary reactions such as the reverse water gas shift (RWGS). The occurrence of this reaction leads to enhance $CO_2$ consumption in comparison to that of $CH_4$ and to decrease the selectivity to hydrogen and the resulting $H_2/CO$ ratio. At 823 K the calculated value of 26% conversion for reactants resulted in a real methane and carbon dioxide conversion of 20% and 32% respectively. The high $CO_2/CH_4$ ratio obtained as result of the $H_2+CO_2$ reaction to produce $H_2O$ and CO is related to the low hydrogen selectivity reached (43%).
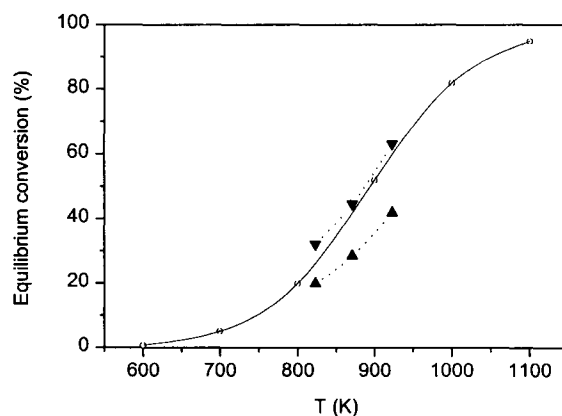


**Figure 3.** Equilibrium conversion experimentally obtained in the membrane reactor assembled with a non-porous quartz tube: (▲) $CH_4$ conversion and (▼) $CO_2$ conversion. Values calculated for the stoichiometric reaction with an equimolecular mixture $CH_4:CO_2$ (50:50) at a flow rate of 6 $l \cdot h^{-1}$ and 1 atm of pressure are also presented (solid line).

The experimental data obtained for the membranes at 823 K are summarized in Table 2. A blank experiment (without catalyst) was also carried out under the same conditions with the mullite membrane in order to ensure the inertness of the reactor. No conversion was detected in the absence of catalyst. On the contrary, both methane and carbon dioxide conversions were enhanced when using the different membranes as compared to the equilibrium values. Methane conversion increased from 20% for the non-porous system to 31, 34 and 38% for the mullite, YSZ and alumina membranes, respectively. An important effect of the membranes has also been found regarding the occurrence of the RWGS reaction, which can be directly correlated with the excess of carbon dioxide converted. The ratio between the converted amounts of $CO_2$ and $CH_4$ can be observed to be closer to unity when using the membranes. It decreased from a value of 1.7 for the non-porous quartz tube to 1.5, 1.3 and 1.1 for the mullite, YSZ

and alumina membranes respectively. On the basis of the results obtained, it seems that a correlation between the total conversion enhancement and the reduction in the excess of carbon dioxide consumption can be established. The preferential removal of hydrogen through the membranes, which would reduce its residence time in the catalytic bed, is probably the reason of the reduction in the carbon dioxide consumption and, therefore, of the improvement in hydrogen selectivity. The experimental results seem to indicate that the permeance is not a determining aspect in the equilibrium conversion enhancement. The high permeability in the YSZ membrane, which is almost one order of magnitude greater than those found in the mullite and the alumina tubes, does not seem to exert any significant influence in the system performance. On the contrary, the small differences in the hydrogen separation coefficient correlate well with the increase in conversion and selectivity to $H_2$ found under reaction conditions.

**Table 2.** Experimental data obtained for the dry reforming of methane at 823 K. Gas mixture: $CH_4:CO_2$ (50:50); Flow rate: 6 $l \cdot h^{-1}$. [a] Conversion values determined from the formation enthalpies of reactants and products for the stoichiometric reaction in the absence of the reverse water gas shift reaction.

| Experiment | Conversion (%) | | $CO_2/CH_4$ |
|---|---|---|---|
| | $CH_4$ | $CO_2$ | |
| Non-porous quartz / $Rh/Al_2O_3$ | 20 | 32 | 1.7 |
| Mullite / $Rh/Al_2O_3$ | 31 | 46 | 1.5 |
| Alumina / $Rh/Al_2O_3$ | 38 | 43 | 1.1 |
| YSZ / $Rh/Al_2O_3$ | 34 | 45 | 1.3 |
| Mullite / no catalyst | 0 | 0 | - |
| $CH_4+CO_2 \Leftrightarrow 2H_2+2CO$ [a] | 26 [a] | 26 [a] | 1.0 [a] |

The membranes used in this study, with relatively large pore diameters (between 5 and 20 nm), can be classified as ultrafiltration membranes. The hydrogen separation coefficients in them are limited to a maximum value predicted by Knudsen diffusion. Separation efficiencies in this kind of membranes are not the most adequate for equilibrium-restricted reactions because of removal of reactants along with products. However, their use in the methane dry reforming has provided moderate enhancements in conversion and improvements in hydrogen selectivity as compared to the operation in a conventional reactor. Further studies are required to investigate the effect of water produced along with the reaction in the membranes efficiency. In the light of the results obtained, the application of high temperature stable membranes with high selectivity for hydrogen separation is expected to yield promising results in the improvement of catalytic performance.

## CONCLUSIONS

The utilization of three different porous ceramic ultrafiltration tubes in a membrane reactor has allowed enhancing both methane conversion and hydrogen selectivity in the $CH_4+CO_2$ reaction in comparison with operation in a conventional reactor. Although $H_2$ is separated from the catalytic bed along with the reactants and other products, the preferential removal of hydrogen has been shown to shift the equilibrium and increase the $CH_4$ conversion. Furthermore, hydrogen separation also contributes to reduce the secondary reaction of reverse water gas shift and enhance hydrogen selectivity.

Gas permeation has been found to proceed mainly according to the Knudsen diffusion mechanism. However, the separation coefficient for $H_2$ seems to be affected by the interaction of hydrogen with surface hydroxyl groups of the ceramic materials at high temperatures. The selectivity coefficient for $H_2$ is under the conditions used in this study the key factor determining the methane conversion enhance. The permeance of the membrane does not seem to influence the reactor catalytic performance.

## ACKNOWLEDGMENTS

## REFERENCES

1    M. C. J. Bradford, M. A. Vannice. Catal. Rev.-Sci. Eng.; 1 (1999) 1.
2    P. R. Courty, A. Chauvel; Catal. Today 29 (1996) 3.
3    J. H. Edwards; Catal. Today 23 (1995) 59.
4    P. Ferreira-Aparicio, I. Rodríguez-Ramos, J. A. Anderson, A. Guerrero-Ruiz. J. Catal. 190 (2000) 296.
5    P. Ferreira-Aparicio, M. Fernández-García, A. Guerrero-Ruiz, I. Rodríguez-Ramos. J. Catal. 190 (2000) 296.
6    A. K. Prabhu, R. Radhakrishnan, S. T. Oyama. Appl. Catal. A: Gen. 183 (1999) 214.
7    R. J. R. Uhlhorn, K. Keizer, J. A. Burggraaf. J. Memb. Sci, 46 (1989) 225.

# Author Index

This Page Intentionally Left Blank

# Subject Index

This Page Intentionally Left Blank

# STUDIES IN SURFACE SCIENCE AND CATALYSIS

**Advisory Editors:**
B. Delmon, Université Catholique de Louvain, Louvain-la-Neuve, Belgium
J.T.Yates, University of Pittsburgh, Pittsburgh, PA, U.S.A.

This Page Intentionally Left Blank